WOODHEAD PUBLISHING SERIES IN ELECTRONIC AND OPTICAL MATERIALS

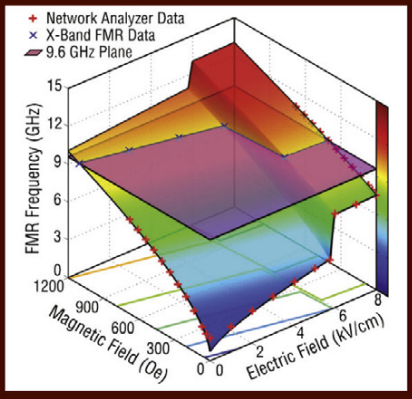

Composite Magnetoelectrics

Materials, Structures and Applications

Gopalan Srinivasan, Shashank Priya and Nian X. Sun

WP
WOODHEAD PUBLISHING

Composite Magnetoelectrics

Related titles

Metallic films for electronic, optical and magnetic applications: Structure, processing and properties
(ISBN 978-0-85709-057-7)

Advances in non-volatile memory and storage technology
(ISBN 978-0-85709-803-0)

Handbook of advanced dielectric, piezoelectric and ferroelectric materials: Synthesis, properties and applications
(ISBN 978-1-84569-186-8)

Woodhead Publishing Series in Electronic and Optical Materials: Number 62

Composite Magnetoelectrics

Materials, Structures, and Applications

Gopalan Srinivasan, Shashank Priya and Nian X. Sun

ELSEVIER

AMSTERDAM • BOSTON • CAMBRIDGE • HEIDELBERG
LONDON • NEW YORK • OXFORD • PARIS • SAN DIEGO
SAN FRANCISCO • SINGAPORE • SYDNEY • TOKYO
Woodhead Publishing is an imprint of Elsevier

WP
WOODHEAD
PUBLISHING

Woodhead Publishing is an imprint of Elsevier
80 High Street, Sawston, Cambridge, CB22 3HJ, UK
225 Wyman Street, Waltham, MA 02451, USA
Langford Lane, Kidlington, OX5 1GB, UK

Copyright © 2015 Elsevier Ltd. All rights reserved.

No part of this publication may be reproduced, stored in a retrieval system or transmitted in any form or by any means electronic, mechanical, photocopying, recording or otherwise without the prior written permission of the publisher.

Permissions may be sought directly from Elsevier's Science & Technology Rights Department in Oxford, UK: phone (+44) (0) 1865 843830; fax (+44) (0) 1865 853333; email: permissions@elsevier.com. Alternatively you can submit your request online by visiting the Elsevier website at http://elsevier.com/locate/permissions, and selecting Obtaining permission to use Elsevier material.

Notice
No responsibility is assumed by the publisher for any injury and/or damage to persons or property as a matter of products liability, negligence or otherwise, or from any use or operation of any methods, products, instructions or ideas contained in the material herein. Because of rapid advances in the medical sciences, in particular, independent verification of diagnoses and drug dosages should be made.

British Library Cataloguing-in-Publication Data
A catalogue record for this book is available from the British Library

Library of Congress Control Number: 2014957599

ISBN 978-1-78242-254-9 (print)
ISBN 978-1-78242-264-8 (online)

For information on all Woodhead Publishing publications visit our website at http://store.elsevier.com/

Contents

This page intentionally left blank

Woodhead Publishing Series in Electronic and Optical Materials

1 **Circuit analysis**
J. E. Whitehouse
2 **Signal processing in electronic communications: For engineers and mathematicians**
M. J. Chapman, D. P. Goodall and N. C. Steele
3 **Pattern recognition and image processing**
D. Luo
4 **Digital filters and signal processing in electronic engineering: Theory, applications, architecture, code**
S. M. Bozic and R. J. Chance
5 **Cable engineering for local area networks**
B. J. Elliott
6 **Designing a structured cabling system to ISO 11801: Cross-referenced to European CENELEC and American Standards**
Second edition
B. J. Elliott
7 **Microscopy techniques for materials science**
A. Clarke and C. Eberhardt
8 **Materials for energy conversion devices**
Edited by C. C. Sorrell, J. Nowotny and S. Sugihara
9 **Digital image processing: Mathematical and computational methods**
Second edition
J. M. Blackledge
10 **Nanolithography and patterning techniques in microelectronics**
Edited by D. Bucknall
11 **Digital signal processing: Mathematical and computational methods, software development and applications**
Second edition
J. M. Blackledge
12 **Handbook of advanced dielectric, piezoelectric and ferroelectric materials: Synthesis, properties and applications**
Edited by Z.-G. Ye
13 **Materials for fuel cells**
Edited by M. Gasik
14 **Solid-state hydrogen storage: Materials and chemistry**
Edited by G. Walker
15 **Laser cooling of solids**
S. V. Petrushkin and V. V. Samartsev

16 **Polymer electrolytes: Fundamentals and applications**
Edited by C. A. C. Sequeira and D. A. F. Santos
17 **Advanced piezoelectric materials: Science and technology**
Edited by K. Uchino
18 **Optical switches: Materials and design**
Edited by S. J. Chua and B. Li
19 **Advanced adhesives in electronics: Materials, properties and applications**
Edited by M. O. Alam and C. Bailey
20 **Thin film growth: Physics, materials science and applications**
Edited by Z. Cao
21 **Electromigration in thin films and electronic devices: Materials and reliability**
Edited by C.-U. Kim
22 **In situ characterization of thin film growth**
Edited by G. Koster and G. Rijnders
23 **Silicon-germanium (SiGe) nanostructures: Production, properties and applications in electronics**
Edited by Y. Shiraki and N. Usami
24 **High-temperature superconductors**
Edited by X. G. Qiu
25 **Introduction to the physics of nanoelectronics**
S. G. Tan and M. B. A. Jalil
26 **Printed films: Materials science and applications in sensors, electronics and photonics**
Edited by M. Prudenziati and J. Hormadaly
27 **Laser growth and processing of photonic devices**
Edited by N. A. Vainos
28 **Quantum optics with semiconductor nanostructures**
Edited by F. Jahnke
29 **Ultrasonic transducers: Materials and design for sensors, actuators and medical applications**
Edited by K. Nakamura
30 **Waste electrical and electronic equipment (WEEE) handbook**
Edited by V. Goodship and A. Stevels
31 **Applications of ATILA FEM software to smart materials: Case studies in designing devices**
Edited by K. Uchino and J.-C. Debus
32 **MEMS for automotive and aerospace applications**
Edited by M. Kraft and N. M. White
33 **Semiconductor lasers: Fundamentals and applications**
Edited by A. Baranov and E. Tournie
34 **Handbook of terahertz technology for imaging, sensing and communications**
Edited by D. Saeedkia
35 **Handbook of solid-state lasers: Materials, systems and applications**
Edited by B. Denker and E. Shklovsky
36 **Organic light-emitting diodes (OLEDs): Materials, devices and applications**
Edited by A. Buckley
37 **Lasers for medical applications: Diagnostics, therapy and surgery**
Edited by H. Jelínková

38 **Semiconductor gas sensors**
Edited by R. Jaaniso and O. K. Tan

39 **Handbook of organic materials for optical and (opto)electronic devices: Properties and applications**
Edited by O. Ostroverkhova

40 **Metallic films for electronic, optical and magnetic applications: Structure, processing and properties**
Edited by K. Barmak and K. Coffey

41 **Handbook of laser welding technologies**
Edited by S. Katayama

42 **Nanolithography: The art of fabricating nanoelectronic and nanophotonic devices and systems**
Edited by M. Feldman

43 **Laser spectroscopy for sensing: Fundamentals, techniques and applications**
Edited by M. Baudelet

44 **Chalcogenide glasses: Preparation, properties and applications**
Edited by J.-L. Adam and X. Zhang

45 **Handbook of MEMS for wireless and mobile applications**
Edited by D. Uttamchandani

46 **Subsea optics and imaging**
Edited by J. Watson and O. Zielinski

47 **Carbon nanotubes and graphene for photonic applications**
Edited by S. Yamashita, Y. Saito and J. H. Choi

48 **Optical biomimetics: Materials and applications**
Edited by M. Large

49 **Optical thin films and coatings**
Edited by A. Piegari and F. Flory

50 **Computer design of diffractive optics**
Edited by V. A. Soifer

51 **Smart sensors and MEMS: Intelligent devices and microsystems for industrial applications**
Edited by S. Nihtianov and A. Luque

52 **Fundamentals of femtosecond optics**
S. A. Kozlov and V. V. Samartsev

53 **Nanostructured semiconductor oxides for the next generation of electronics and functional devices: Properties and applications**
S. Zhuiykov

54 **Nitride semiconductor light-emitting diodes (LEDs): Materials, technologies and applications**
Edited by J. J. Huang, H. C. Kuo and S. C. Shen

55 **Sensor technologies for civil infrastructures**
Volume 1: Sensing hardware and data collection methods for performance assessment
Edited by M. Wang, J. Lynch and H. Sohn

56 **Sensor technologies for civil infrastructures**
Volume 2: Applications in structural health monitoring
Edited by M. Wang, J. Lynch and H. Sohn

57 **Graphene: Properties, preparation, characterisation and devices**
Edited by V. Skákalová and A. B. Kaiser
58 **Silicon-on-insulator (SOI) technology**
Edited by O. Kononchuk and B.-Y. Nguyen
59 **Biological identification: DNA amplification and sequencing, optical sensing, lab-on-chip and portable systems**
Edited by R. P. Schaudies
60 **High performance silicon imaging: Fundamentals and applications of CMOS and CCD sensors**
Edited by D. Durini
61 **Nanosensors for chemical and biological applications: Sensing with nanotubes, nanowires and nanoparticles**
Edited by K. C. Honeychurch
62 **Composite magnetoelectrics: Materials, structures and applications**
G. Srinivasan, S. Priya and N. X. Sun
63 **Quantum information processing with diamond: Principles and applications**
Edited by S. Prawer and I. Aharonovich
64 **Advances in non-volatile memory and storage technology**
Edited by Y. Nishi
65 **Laser surface engineering: Processes and applications**
Edited by J. Lawrence, C. Dowding, D. Waugh and J. Griffiths
66 **Power ultrasonics: Applications of high-intensity ultrasound**
Edited by J. A. Gallego-Juárez and K. F. Graff
67 **Advances in delay-tolerant networks (DTNs): Architectures, routing and challenges**
Edited by J. J. P. C. Rodrigues
68 **Handbook of flexible organic electronics: Materials, manufacturing and applications**
Edited by S. Logothetidis
69 **Machine-to-machine (M2M) communications: Architecture, performance and applications**
Edited by C. Anton-Haro and M. Dohler
70 **Ecological design of smart home networks: Technologies, social impact and sustainability**
Edited by N. Saito and D. Menga
71 **Industrial tomography: Systems and applications**
Edited by M. Wang
72 **Vehicular communications and networks: Architectures, protocols, operation and deployment**
Edited by W. Chen
73 **Modeling, characterization and production of nanomaterials: Electronics, photonics and energy applications**
Edited by V. Tewary and Y. Zhang
74 **Reliability characterisation of electrical and electronic systems**
Edited by J. Swingler
75 **Handbook of industrial wireless sensor networks: Monitoring, control and automation**
Edited by R. Budampati and S. Kolavennu
76 **Epitaxial growth of complex metal oxides: Techniques, properties and applications**
Edited by G. Koster, G. Rijnders and M. Huijben

77 **Semiconductor nanowires: Materials, synthesis, characterization and applications**
Edited by J. Arbiol and Q. Xiong
78 **Superconductors in the Power Grid**
Edited by C. Rey
79 **Optofluidics, sensors and actuators in microstructured optical fibres**
Edited by S. Pissadakis
80 **Magnetic Nano- and Microwires: Design, Synthesis, Properties and Applications**
Edited by M. Vázquez

This page intentionally left blank

Part One

Introduction to magnetoelectric materials and phenomena

This page intentionally left blank

Theory of magnetoelectric phenomena in composites

1

V.M. Petrov
Novgorod State University, Veliky Novgorod, Russia

1.1 Introduction

The magnetoelectric (ME) effect in a material is defined as the electric polarization induced by applied magnetic field or vice versa as the magnetization induced by applied electric field. The effect was first observed in antiferromagnetic Cr_2O_3 with a room temperature ME voltage coefficient of 20 mV/(cm Oe) (Astrov, 1961). An enhanced ME effect is obtained in magnetostrictive-piezoelectric composites (Ryu, Carazo, Uchino, & Kim, 2001; van Suchtelen, 1972). Since ME coupling in a composite is the product of the magnetostrictive deformation and the piezoelectric field generation, magnetostrictive-piezoelectric composites are expected to be ME (Laletin & Srinivasan, 2002; Nan, Bichurin, Dong, Viehland, & Srinivasan, 2008). The ME voltage coefficient is defined as $\alpha_E = \delta E/\delta H$ with δH and δE denoting the applied magnetic and induced electric ac fields, respectively. Lead zirconate titanate (PZT)−ferrite and PZT−Terfenol-D are the most studied composites to date (Srinivasan et al., 2001). One of the largest ME voltage coefficients of 500 V/(cm Oe) was reported recently for a high-permeability magnetostrictive piezofibre laminate (Dong, Zhai, Li, & Viehland, 2006). The huge increase of related publications on ME coupling in composites is stipulated by their important role in future ME devices.

It is clear that direct and converse ME susceptibilities are equivalent for strain-coupled two-phase systems (Lou, Pellegrini, Liu, Mathur, & Sun, 2012), that is, $\alpha = \frac{\partial P}{\partial H} = \mu_0 \frac{\partial M}{\partial E}$. ME coefficients for direct and converse ME effects can be expressed in terms of ME susceptibility. Thus, the ME voltage coefficient can be defined as $\alpha_E = \frac{\partial E}{\partial H}$ under an open electric circuit condition and can be expressed as $\alpha_E = \frac{\alpha}{\varepsilon}$, where ε is effective permittivity. Similarly, an electrically induced magnetic field can be determined as follows: $\alpha_H = \frac{\partial H}{\partial E} = \frac{\alpha}{\mu}$ under an open magnetic circuit condition, where μ is effective permeability.

The ME effect has been studied for low-frequency, electromechanical resonance (EMR) and ferromagnetic resonance (FMR) regions in our earlier work. In this chapter, we discuss detailed theoretical modeling approaches that are used to describe the dynamic behaviour of ME coupling in magnetostrictive-piezoelectric composites at low frequencies and in an EMR region. The ME voltage coefficients are estimated as functions of initial component parameters.

Composite Magnetoelectrics. http://dx.doi.org/10.1016/B978-1-78242-254-9.00001-9
Copyright © 2015 Elsevier Ltd. All rights reserved.

1.2 Low-frequency ME in composites

A series of difficulties that are characteristic of bulk composites can be overcome by using the layered structures. The giant ME effects in layered composites are enabled by (1) high piezoelectric and piezomagnetic coefficients in individual layers, (2) effective stress transfer between layers, (3) ease of poling and subsequent achievement of a full piezoelectric effect and (4) ability to hold charge due to suppression of leakage currents across composites with a 2−2 connectivity. In this work, we present a summary of a more recent theory of ME laminate composites (Bichurin, Petrov, & Srinivasan, 2002a, 2002b, 2003; Harshe, J. O. Dougherty, & Newnham, 1993).

We assume the symmetry of piezoelectric to be ∞ m and that of piezomagnetic to be cubic. The constitutive equation for the piezoelectric effect is as follows:

$$ {}^{p}S_i = {}^{p}s_{ij}\,{}^{p}T_j + {}^{p}d_{ki}\,{}^{p}E_k, \tag{1.1} $$

$$ {}^{p}D_k = {}^{p}d_{ki}\,{}^{p}T_i + {}^{p}\varepsilon_{kn}{}^{p}E_n, \tag{1.2} $$

where ${}^{p}S_i$ is a strain tensor component of the piezoelectric phase, ${}^{p}E_k$ is a vector component of the electric field, ${}^{p}D_k$ is a vector component of the electric displacement, ${}^{p}T_i$ is a stress tensor component of the piezoelectric phase, ${}^{p}s_{ij}$ is a compliance coefficient of the piezoelectric phase, ${}^{p}d_{ki}$ is a piezoelectric coefficient of the piezoelectric phase and ${}^{p}\varepsilon_{kn}$ is a permittivity matrix of the piezoelectric phase.

Although ferrites are not piezomagnetic, one can achieve a pseudo-piezomagnetic effect ($q = d\lambda/dH$, where λ is the magnetostriction) by subjecting the sample to a bias magnetic field H_0 and ac field H. The strain and magnetic induction tensors of the magnetostrictive phase can be presented similarly:

$$ {}^{m}S_i = {}^{m}s_{ij}\,{}^{m}T_j + {}^{m}q_{ki}\,{}^{m}H_k, \tag{1.3} $$

$$ {}^{m}B_k = {}^{m}q_{ki}\,{}^{m}T_i + {}^{m}\mu_{kn}{}^{m}H_n, \tag{1.4} $$

where ${}^{m}S_i$ is a strain tensor component of the magnetostrictive phase, ${}^{m}T_j$ is a stress tensor component of the magnetostrictive phase, ${}^{m}s_{ij}$ is a compliance coefficient of the magnetostrictive phase, ${}^{m}H_k$ is a vector component of magnetic field, ${}^{m}B_k$ is a vector component of magnetic induction, ${}^{m}q_{ki}$ is a piezomagnetic coefficient and ${}^{m}\mu_{kn}$ is a permeability matrix.

1.2.1 Asymmetric layered structure

In general, a layered structure exhibits the configurational asymmetry that results in bending the sample in an applied magnetic or electric field. One of the principal objectives of the present section is modeling of the ME interaction in a magnetostrictive-piezoelectric layered structure, taking into account the flexural deformations (Petrov, Bichurin, et al., 2009; Petrov, Srinivasan, et al., 2009). We calculated ME voltage coefficients α_E for transverse field orientations (in-plane dc and ac magnetic fields are

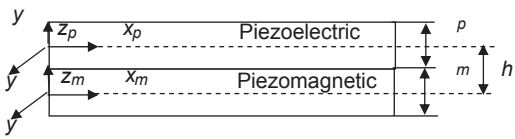

Figure 1.1 Schematic of a bilayer.

perpendicular to the electric field) to provide minimum demagnetizing fields and maximum α_E.

We demonstrate the computing sequence with a simple example of a magnetostrictive-piezoelectric bilayer as in Figure 1.1.

The thickness of the plate is assumed to be small compared to the remaining dimensions, and the width is assumed to be small compared to sample length. We assume the longitudinal axial strains of each layer to be linear functions of the vertical coordinate z_i to take into account bending the sample:

$$ {}^{m}S_1 = {}^{m}S_{10} + z_m/R_1, \tag{1.5} $$

$$ {}^{p}S_1 = {}^{p}S_{10} + z_p/R_1, \tag{1.6} $$

where ${}^{m}S_{10}$ and ${}^{p}S_{10}$ are the centroidal strains along the x-axis at $z_i = 0$ and R_1 is the radius of curvature.

To preserve force equilibrium, the axial forces in the three layers add up to zero:

$$ F_{p1} + F_{m1} = 0, \tag{1.7} $$

where $F_{i1} = \int_{-{}^{i}t/2}^{{}^{i}t/2} {}^{i}T_1 \mathrm{d}z_1$.

Equations (1.1), (1.3), (1.5) and (1.7) enable finding ${}^{m}S_{10}$:

$$ {}^{m}S_{10} = s_1 \left[(1 - V)\ {}^{m}Y {}^{m}q_{11} H_1 + V\, {}^{p}Y \left({}^{p}d_{31} E_3 + \frac{h}{R_1} \right) \right], \tag{1.8} $$

where h is the distance between the horizontal mid-planes of piezomagnetic and piezoelectric layers. The centroidal strain ${}^{p}S_{10}$ can be found from the relation ${}^{m}S_{10} - {}^{p}S_{10} = h/R_1$.

The moment equilibrium condition has the following form:

$$ F_{m1} h_m = M_{m1} + M_{p1}, \tag{1.9} $$

where $M_{i1} = \int_{-{}^{i}t/2}^{{}^{i}t/2} z_i {}^{i}T_1 \mathrm{d}z_1$.

Equations (1.6) and (1.7) enable calculating R_1, the axial stress components in the piezoelectric layer ${}^{p}T_1$ and ${}^{p}T_2$. Once the centroidal strains and radius of curvature are

determined, the axial stress ${}^{i}T_1$ can be found from Eqns (1.1) and (1.3). To obtain the expression for ME voltage coefficient, we use the open circuit condition on the boundary:

$$D_3 = 0. \tag{1.10}$$

Since electric induction is divergence free and has only one component, it is evident that D_3 is equal to zero for any z. In this case, Eqns (1.1) and (1.10) result in the expression for ME voltage coefficient:

$$\alpha_{E\ 31} = \frac{E_3}{H_1} = -\frac{\int_{-{}^{p}t/2}^{{}^{p}t/2} {}^{p}T_1\, {}^{p}d_{31}/{}^{p}\varepsilon_{33}\mathrm{d}z}{t\, H_1}, \tag{1.11}$$

where $t = {}^{m}t + {}^{p}t$ is the total thickness of the considered structure.

Under the assumption ${}^{p}K_{31}^2 = {}^{p}d_{31}^2/{}^{p}s_{11}{}^{p}\varepsilon_{33} \ll 1$, the ME voltage coefficient for a magnetostrictive-piezoelectric bilayer can be derived in the explicit form:

$$\alpha_{E\ 31} = \frac{\delta E_3}{\delta H_1} = \frac{\left[1{}^{p}s_{11} + {}^{m}s_{11}r^3\right]{}^{m}q_{11}\,{}^{p}d_{31}/{}^{p}\varepsilon_{33}}{{}^{p}s_{11}[2r{}^{m}s_{11}(2+3r+2r^2) + {}^{p}s_{11}] + {}^{m}s_{11}^2 r^4}, \tag{1.12}$$

where $r = {}^{p}t/{}^{m}t$ with ${}^{p}t$ and ${}^{m}t$ denoting the thickness of piezoelectric and piezomagnetic layers.

Expressions for ME voltage coefficients for longitudinal field orientation (dc and ac magnetic fields and ac electric fields are perpendicular to the sample plane and parallel to the poling direction) and for in-plane longitudinal field orientation (poling direction and dc and ac magnetic fields and ac electric fields are parallel to the sample plane) can be obtained by substituting the piezoelectric and piezomagnetic coefficients by appropriate components:

$$\alpha_{E\ 33} = \frac{\delta E_3}{\delta H_3} = \frac{\left[1{}^{p}s_{11} + {}^{m}s_{11}r^3\right]{}^{m}q_{31}\,{}^{p}d_{31}/{}^{p}\varepsilon_{33}}{{}^{p}s_{11}[2r{}^{m}s_{11}(2+3r+2r^2) + {}^{p}s_{11}] + {}^{m}s_{11}^2 r^4}, \tag{1.13}$$

$$\alpha_{E\ 11} = \frac{\delta E_1}{\delta H_1} = \frac{\left[1{}^{p}s_{11} + {}^{m}s_{11}r^3\right]{}^{m}q_{11}\,{}^{p}d_{11}/{}^{p}\varepsilon_{11}}{{}^{p}s_{11}[2r{}^{m}s_{11}(2+3r+2r^2) + {}^{p}s_{11}] + {}^{m}s_{11}^2 r^4}. \tag{1.14}$$

1.2.2 Symmetric layered structure

In the specific case of symmetric magnetostrictive-piezoelectric structure, one should neglect the flexural strains, and the radius of curvature in Eqn (1.5) must tend to infinity ($R_1 \to \infty$). It is clear that ${}^{m}S_1 = {}^{m}S_{10} + z_m/R_1$ and ${}^{p}S_1 = {}^{p}S_{10} + z_p/R_1$. It is easy to show that the expression for ME voltage coefficient reduces in this case to a well-known expression (Bichurin et al., 2003), which was obtained with the assumption of homogeneous longitudinal strains.

Under the assumption ${}^{p}K_{31}^{2} \ll 1$, the ME voltage coefficient for magnetostrictive-piezoelectric symmetric layered structure takes on the form

$$\alpha_{E\ 31} = \frac{{}^{m}q_{11}\,{}^{p}d_{31}/{}^{p}\varepsilon_{33}}{r\,{}^{m}s_{11} + {}^{p}s_{11}}. \tag{1.15}$$

For longitudinal and in-plane longitudinal field orientation, expressions for ME voltage coefficients take on the form

$$\alpha_{E\ 33} = \frac{{}^{m}q_{31}\,{}^{p}d_{31}/{}^{p}\varepsilon_{33}}{r\,{}^{m}s_{11} + {}^{p}s_{11}}, \tag{1.15a}$$

$$\alpha_{E\ 11} = \frac{{}^{m}q_{11}\,{}^{p}d_{11}/{}^{p}\varepsilon_{11}}{r\,{}^{m}s_{11} + {}^{p}s_{11}}. \tag{1.15b}$$

1.2.3 Examples of multilayer structures

The theoretical treatment referred to above resulted in expressions for the ME voltage coefficients for three different orientations of fields: longitudinal, transverse and in-plane longitudinal.

Next, we apply the theory for the calculation of ME coupling in layered composites of cobalt ferrite and lead zirconate titanate (CFO−PZT), which is a system that has been of significant prior interest. Since the value of α_E depends notably on the concentration of the two phases, the ME voltage coefficient has been determined as a function of the volume fraction v of the piezoelectric phase in composites. Material parameters used for estimates are given in Table 1.1. Results of calculations using the model are illustrated in Figure 1.2.

Results of $\alpha_{E\ 31}$ versus PZT volume fraction for a bilayer reveal a double maximum because the strain produced by the ferrite consists of two components: longitudinal and flexural. For a symmetric structure such as a trilayer, there are no flexural strains and the maximum ME coefficient occurs for $V = 0.6$ (Bichurin et al., 2003). Since the flexural strain is opposite in sign compared to the longitudinal one and reaches its maximum value for $V = 0.6$, the two types of strains combine to produce suppression of $\alpha_{E\ 31}$ at $V = 0.6$ and a double maximum in the ME coefficient as in Figure 1.2.

The ME voltage coefficient for symmetric structures of CFO and PZT is given for the in-plane longitudinal field orientation, taking into account that such structures result in higher values of ME coefficients.

The most significant prediction of the present model is that the strongest ME coupling should occur for in-plane longitudinal fields, as shown in Figure 1.3. The v-dependence of $\alpha_{E\ 11}$ reveals a rapid increase in the ME coefficient to a maximum value of $\alpha_{E\ 11} = 3600$ mV/(cm Oe) for $v = 0.11$, which is followed by a near-linear decrease with further increase of v. Such an enhancement in the in-plane longitudinal coefficient is understandable due to (1) the absence of demagnetizing fields in the in-plane configuration and (2) increased piezoelectric and piezomagnetic coupling

Table 1.1 **Material parameters (compliance coefficient s, piezomagnetic coupling q, piezoelectric coefficient d and permittivity ε) for lead zirconate titanate (PZT), cobalt ferrite (CFO) and lanthanum strontium manganite used for theoretical values**

Material	s_{11} (10^{-12} m^2/N)	s_{12} (10^{-12} m^2/N)	s_{13} (10^{-12} m^2/N)	s_{33} (10^{-12} m^2/N)	q_{33} (10^{-12} m/A)	q_{31} (10^{-12} m/A)	d_{31} (10^{-12} m/V)	d_{33} (10^{-12} m/V)	$\varepsilon_{33}/\varepsilon_0$
PZT	15.3	−5	−7.22	17.3	–	–	−175	400	1750
CFO	6.5	−2.4			−1880	556	–	–	10
LSMO	15	−5			250	−120	–	–	10

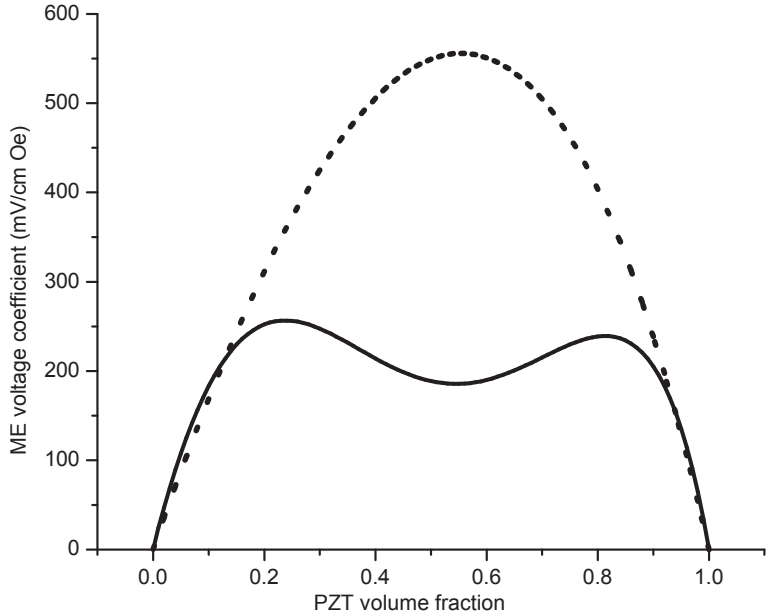

Figure 1.2 Transverse magnetoelectric voltage coefficient $\alpha_{E\,31} = \delta E_3/\delta H_1$ bilayer (solid line) and trilayer structure (dot line) of cobalt ferrite and lead zirconate titanate (PZT).

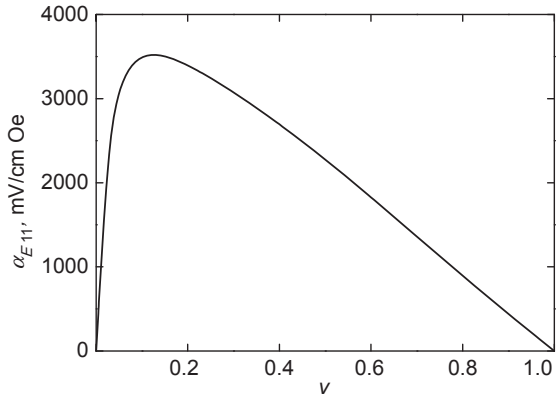

Figure 1.3 Magnetoelectric voltage coefficient for symmetric structure of cobalt ferrite and lead zirconate titanate for in-plane longitudinal field orientation. The poling field and dc and ac magnetic and electric fields are in the sample plane and parallel to each other.

coefficients compared to other orientations. The down-shift in the value of $v_{\max}$ (from 0.5 to 0.6 for longitudinal and transverse fields to a much smaller value of 0.1) is due to the concentration dependence of the effective permittivity.

Finally, we compare the theoretical predictions, illustrated above, with experimental data. Let us consider first a bilayer of CFO−PZT, taking into account the

flexural deformations. Figure 1.6 shows α_E as a function of v. These data were obtained at low frequencies (100−1000 Hz). The desired volume fraction v was achieved by careful control of the layer thickness. Data show an increase in α_E with v until a maximum is reached. However, these data clearly demonstrated that the actual experimental value is an order of magnitude smaller than that predicted in Figure 1.2. It is, therefore, reasonable to compare the data with calculated values of α_E as a function of v using reduced interface coupling parameters of $k = 0.1$ (Bichurin et al., 2003): in this case, agreement between theory and experiment can be seen, as shown in Figure 1.4. The key inference that can be made concerns the inherently poor interface coupling for CFO−PZT, irrespective of sample synthesis techniques.

Finally, we should comment on a possible cause of poor interfacial coupling for CFO−PZT and ideal coupling for nickel ferrite (NFO)−PZT. The parameter k can be expected to be sensitive to mechanical, structural, chemical and electromagnetic parameters at the interface. We attribute unfavourable interface conditions in CFO−PZT to inefficient magnetomechanical coupling. The magnetomechanical coupling k_m is given by $k_m = (4\pi\lambda'\mu_r/E)^{1/2}$, where λ' is the dynamic magnetostrictive constant, μ_r is the reversible permeability and E is Young's modulus. In ferrites, under the influence of a dc magnetic bias H and ac magnetic field δH, domain wall motion and domain rotation contribute to the Joule magnetostriction and, consequently, to the effective linear piezomagnetic coupling. A key requirement for strong coupling is unimpeded domain wall motion and domain rotation. A soft ferrite with a high initial permeability (i.e. low anisotropy), such as NFO, will have key material parameters favouring a high k_m, and, consequently, strong ME effects. Measurements have shown that NFO has an initial permeability of 20, whereas that of CFO is 2−3. Thus, one can infer that a plausible simple explanation of the near-interfacial parameter for NFO−PZT is (in part) favourable domain motion.

In deriving the above expression, we assumed the electric field to be zero in magnetic phase since magnetostrictive materials that are used in the case under study have a small resistance compared to piezoelectric phase. An estimate of ME voltage coefficient for CFO−PZT layered structure gives $\alpha_{E\ 33} = 325$ mV/(cm Oe), provided that the bending strains are ignored. However, considering CFO as a dielectric results in $\alpha_{E\ 33} = 140$ mV/(cm Oe) (Osaretin & Rojas, 2010), while the experimental value does not exceed 74 mV/(cm Oe) (Harshe, J. O. Dougherty, et al., 1993). We believe CFO should be considered as a conducting medium compared to dielectric PZT in the low-frequency region in accordance with our model. The discrepancy between theoretical estimates and data can be accounted for by features of piezomagnetic coupling in CFO and interface coupling of the bilayer (Bichurin et al., 2003).

1.2.4 Bulk composites

Making new ME composites assumes the use of reliable theoretical models, allowing prediction of properties for various material couples and over a range of laminate

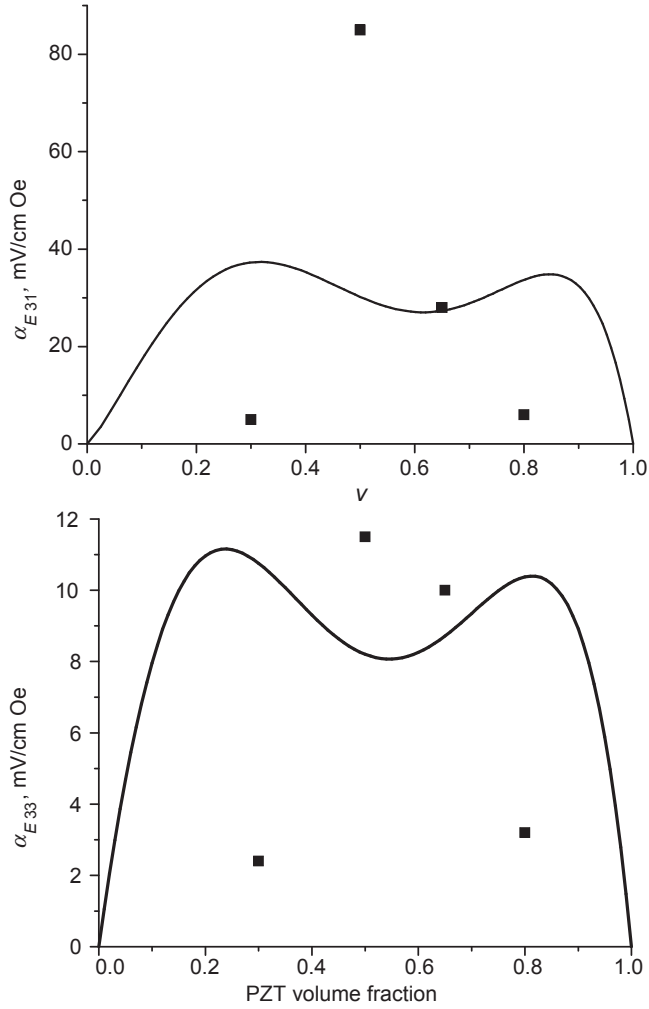

Figure 1.4 Lead zirconate titanate (PZT) volume fraction dependence of transverse (bottom figure) and longitudinal (top figure) magnetoelectric voltage coefficient of the cobalt ferrite (CFO) and lead zirconate titanate bilayer. Solid lines are theories for $k = 0.1$ and points are experiments.

parameters. Manufacturing methods of all-ceramic composites are based on an initial mixing of starting powders batched in proportion to the composite volume fraction, followed by pressing and densification/sintering to a net-shape. Clearly, if the concentration of one of the constituent phases is small, then that phase will consist of isolated particles in a matrix. Following accepted classification nomenclature (Newnham, Skinner, & Cross, 1978), this composite should be referred to as a 0−3 type, as one phase is isolated (i.e. connected in zero dimensions) and the second

is interconnected in three dimensions. If the volume fraction of the secondary phase in the matrix is increased, and a percolation limit is reached, then it is classified as a 1−3-type composite. If the secondary phase then crosses that initial percolation limit, and subsequently begins to be interconnected in two dimensions, the composite connectivity is known as the 2−3 type. We mention these things at this time to make the point that the same ceramic manufacturing technology allows the fabrication of a wide range of relative volume fractions of the different phases in an all-ceramic composite, and consequently, to various possible types of dimensional interconnectivities. Accordingly, it is very important to choose the correct method of calculation for effective constants of a composite at various relative volume fractions of components.

Exact solutions of three-dimensional problems related to the calculation of effective constants of inhomogeneous systems are unknown. Therefore, there is presently no precise structural classification of composites. Within the limited theory of heterogeneous systems of two-phase composites, there are two principal approaches to approximate solutions, matrix systems and two-component mixtures, for which behaviour of effective parameters continuously depends on concentration.

In the case of matrix systems, modification of the concentration from 0 to 1 does not change the qualitative structure of the composite: at any concentration, one of the components must form a coherent matrix that contains isolated particles of the second component. The system always remains essentially noncentral, and matching formulas for an evaluation of effective constants give their continuous dependence on concentration in the entire range from 0 to 1. We should note that the application of these formulas to the calculation of effective constants of composites is not always justified.

The case of two-component mixtures is characterized by a qualitative modification of the structure of the composite as the concentration is changed. It is well known that such systems are characterized by critical concentrations, at which point there are important property changes such as metal−insulator or rigid−plastic transformations. The metal−insulator transformation occurs in a composite consisting of insulating and conductive phases. Assume that the insulating phase is initially the matrix and that the conductive one consists of isolated particles. In this case, initially the composite is insulating; however, when the percolation limit is crossed, the conducting particles form an interconnected conduction pathway, dramatically lowering the resistivity near a critical volume fraction. In the second example (rigid−plastic transformation), it is supposed that the composite is a mixture in which the elastic compliance of one of the constituent phases tends to infinity (e.g., a porous composite). This composite type possesses a critical concentration of the second phase, above which the rigid framework of the composite loses its stability. It should be straightforward to see that any bulk composites will have numerous effective material properties, all of which change with relative phase volume fraction in a manner independent of other properties.

As an example, we consider a composite with a 3−0-type connectivity. Cubic models for ferrite−ferroelectric composites with a connectivity of 3−0 and 0−3 have been considered by Harshe (Harshe, J. P. Dougherty, Newnham, et al., 1993).

Numerically, the ME coefficient is equal to the ratio of the electric field induced on the composite by an applied magnetic field: the ME coefficient is equal to E_3/H_3. It is necessary to realize that the magnetic field was applied only to the ferrite phase: that is, $E_3/{}^{m}H_3$, where ${}^{m}H_3$ is the local magnetic field on the ferrite phases, which may exceed that applied to the entire composite. Harshe's study only considered the case of free cubic cells, and effective parameters of the composite in known model systems were not determined. However, in real composites, we must consider the case of non-free cells. It is also very important to use any such model to predict the effective composite parameters. In the following section, we present a generalized model for ferrite–piezoelectric composites that allows one to define and predict the effective parameters of the said composite using given conditions.

The properties of this ME composite will depend on the parameters of the corpuscles and also on the terminal conditions. Now, let us suppose that the geometrical model for ME composites in this figure is miniaturized to fine scales. If the given cubic model ME composite is considered as a material consisting of consecutive and parallel connections of cubic cells with legs of unit length, then it is obvious by the definition of properties of a composite that it is possible to consider only one cubic cell rather than the entire ensemble of cells. The magnetostriction phase is enclosed by piezoelectric ones along different directions.

To derive the effective material parameters of a composite, we use an averaging method similar to that at consideration of layered structures. To account for the external forces that act on the cells in the cubic model, it is necessary to consider the clamped condition. Thus, to the components of the stress tensor, one must add additional external stress components. In addition, it is necessary to use boundary conditions of the type

$$S_1 = -s_{c1}s_{11}T_1,$$

$$S_2 = -s_{c2}s_{22}T_2,$$

$$S_3 = -s_{c3}s_{33}T_3,$$

where $s_{ci} = {}^{c}s_{ii}/s_{ii}$ is the relative compliance of surroundings and ${}^{c}s_{ii}$ is effective compliance of the composite.

The dependence of the effective ME voltage coefficient on the piezoelectric phase volume fraction is shown in Figure 1.5.

Measurements of the ME voltage coefficient have been performed for bulk composites of NFO–PZT, using the experimental methodology mentioned above. Data are shown in Figure 1.6 for the ME voltage coefficient as a function of the piezoelectric phase volume fraction. These measured values are much lower in magnitude than the theoretical ones predicted for the free composite condition. However, considering a clamped condition defined by the matching $s_{c11} = s_{c22} = s_{c33} = 0.3s_{33}$, agreement between theory and experiment was found, as illustrated in Figure 1.6. These results indicate that in real 0–3 ferrite–piezoelectric ceramic composite mixtures, the

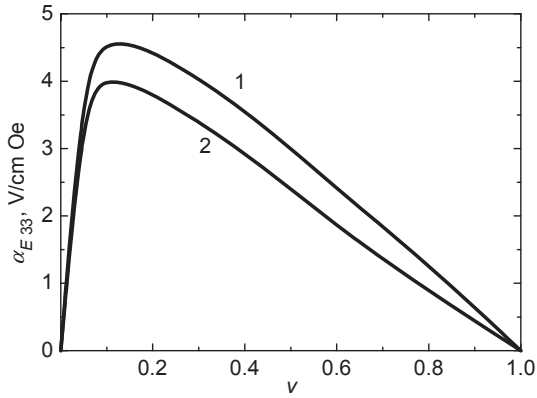

Figure 1.5 Lead zirconate titanate volume fraction dependence of magnetoelectric voltage coefficient for cobalt ferrite and lead zirconate titanate composite with connectivity 3−0 according to model (Petrov, Bichurin, Laletin, Paddubnaya, & Srinivasan, 2004) (1) and model (Harshe, J. P. Dougherty, et al., 1993) (2) for $\alpha_{E\,33} = E_3/^m H_3$.

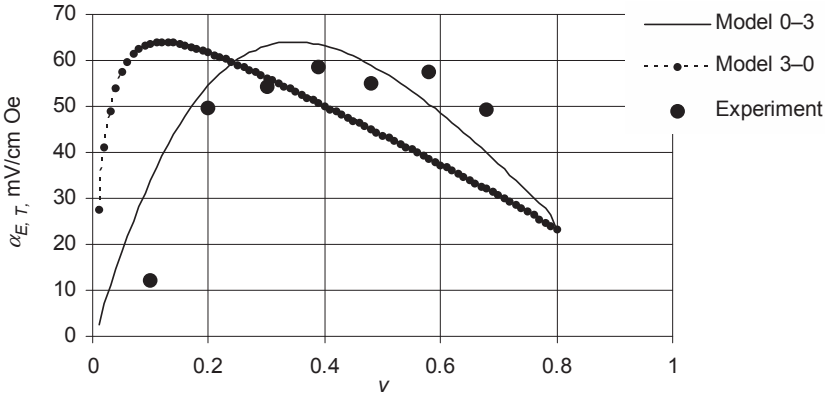

Figure 1.6 Magnetoelectric effect in bulk composites of nickel ferrite and lead zirconate titanate.

component phase grains are mechanically clamped by neighbouring grains and by environmental boundary conditions.

1.2.5 Layered composites of graded components

We consider ME effects in layered composites of functionally graded ferroelectric and ferromagnetic and limit ourselves to consideration of a bilayer (Petrov & Srinivasan, 2008). A linear grading of the piezoelectric coefficient and permittivity in the ferroelectric and a similar grading of piezomagnetic coefficient in the ferromagnet are assumed. The thickness dependence of piezomagnetic and piezoelectric coefficients leads to an additional flexural strain, and the theory predicts an enhancement in the

strength of ME coupling compared to homogeneous compositions. The enhancement in the case of a free-standing bilayer is on the order of 50% at low frequencies.

To take into account the z-dependent material parameters, one can use the theoretical model referred to above for ME coupling in asymmetric structures and consider material parameters as functions of z in Eqns (1.7) and (1.9). Then the ME voltage coefficient can be numerically estimated by using Eqn (1.11). As an example, we consider a bilayer of nickel zinc ferrite, $Ni_{1-x}Zn_xFe_2O_4$ (NZFO), and PZT. Studies show that when Zn is substituted in nickel ferrite, the room temperature piezomagnetic coefficient q varies linearly with increasing Zn concentration x for $x < 0.4$. Thus, it is possible to achieve a linear grading in q with a compositionally graded NZFO. Similar grading of the piezoelectric coefficient d (and the dielectric constant ε) is possible by compositional grading of PZT.

First we consider grading only in $Ni_{1-x}Zn_xFe_2O_4$ (NZFO) in which the piezomagnetic coefficient linearly varies with z:

$$ {}^{m}q_{11} = {}^{m}q_{110}\left(1 + 2kz_1/{}^{m}t\right), \quad -{}^{m}t/_2 \le z_1 \le {}^{m}t/_2, \tag{1.16} $$

where ${}^{m}q_0$ is the average value of this parameter and factor k specifies the grading strength and direction: $k > 0$ and $k < 0$ correspond to 'positive' and 'negative' magnetostriction grading, respectively. According to data on magnetostriction versus H of NZFO[21], ${}^{m}q_{11}$ varies from -680 pm/A for pure nickel ferrite to -1156 pm/A for NZFO with $x = 0.4$, with an average of -918 pm/A and a similar variation for ${}^{m}q_{12}$. In Eqn (1.16) we assume ${}^{m}q_{110} = -918$ pm/A and ${}^{m}q_{120} = 169$ pm/A and $|k| = 0.26$. In the calculations to follow, we use Eqn (1.16) for piezomagnetic coefficients of graded ferrites, and ${}^{m}q_{11}$ $(z_1 = 0) = {}^{m}q_{110} = -918$ pm/A for the homogeneous ferrite.

Similarly, the composition of PZT can be tailored to obtain linear grading of the piezoelectric coefficient and permittivity:

$$ {}^{p}d_{31} = {}^{p}d_{310}(1 + 2kz_2/{}^{p}t), \quad -{}^{p}t/_2 \le z_2 \le {}^{p}t/_2, \tag{1.17} $$

$$ {}^{p}\varepsilon_{33} = {}^{p}\varepsilon_{330}(1 + 2kz_2/{}^{p}t), \tag{1.18} $$

with ${}^{p}d_{310} = -175$ pm/A, ${}^{p}\varepsilon_{330}/\varepsilon_0 = 1750$ and $|k| = 0.35$.

Next we apply the theory to estimate the ME coefficients for (1) graded NZFO and homogeneous PZT, (2) homogeneous NZFO and graded PZT and (3) grading of both NZFO and PZT.

The ME coefficient versus PZT volume fraction V is shown in Figure 1.7 for the case of homogeneous PZT and homogeneous, positively or negatively graded NZFO. Results of $\alpha_{E\ 31}$ versus V reveal a double maximum for all cases because the strain produced by the ferrite consists of two components: longitudinal and flexural. In the absence of a flexural strain, the maximum ME coefficient occurs for $V = 0.6$ (Nan et al., 2008). Since the flexural strain is of opposite sign relative to longitudinal strain and reaches its maximum value for $V = 0.6$, the two types of strains

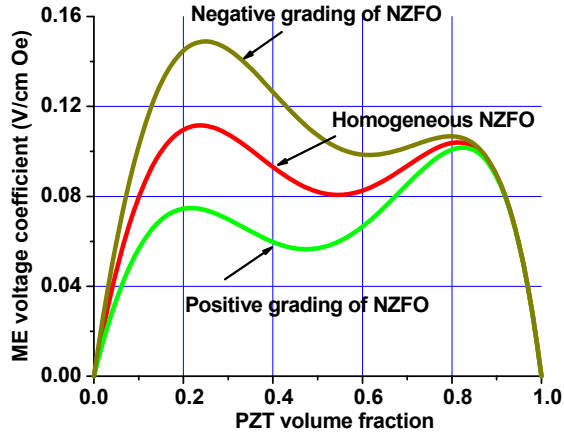

Figure 1.7 Low-frequency magnetoelectric voltage coefficient as a function of lead zirconate titanate (PZT) volume fraction for a free-standing PZT-$Ni_{1-x}Zn_xFe_2O_4$ (NZFO) bilayer. The results are for homogeneous PZT and homogeneous, positively or negatively graded NZFO.

combine to produce suppression of $\alpha_{E\,31}$ at $V = 0.6$ and a double maximum in the ME coefficient as in Figure 1.7. Negative grading of NZFO leads to a maximum in $\alpha_{E\,31}$ for low V, whereas positive grading gives rise to a maximum for high V. The ME coefficient shows a 50% increase in $\alpha_{E\,31}$ for negative grading of the piezomagnetic coefficient compared to the homogeneous case. Such dependence arises due to a decrease in the rotational moment of the ferrite layer for negative grading of q and an increase in the radius of curvature and longitudinal strain of PZT. It should be noted that the ME voltage according to Eqn (1.11) is determined by average longitudinal strains of the PZT layer.

The PZT volume fraction dependence of $\alpha_{E\,31}$ is shown in Figure 1.8 for the case of homogeneous NZFO and homogeneous or graded PZT. Simultaneous variations in ${}^{p}d_{31}$ and ${}^{p}\varepsilon_{33}$ lead to a constant value for the ratio ${}^{p}d_{31}/{}^{p}\varepsilon_{33}$, and the grading therefore cannot influence the ME voltage coefficient according to Eqn (1.11). But grading of

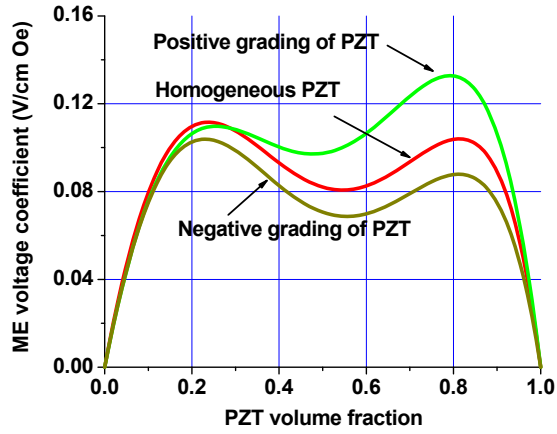

Figure 1.8 Similar results as in Figure 1.7, but for bilayers of homogeneous $Ni_{1-x}Zn_xFe_2O_4$ and homogeneous, positively or negatively graded lead zirconate titanate (PZT).

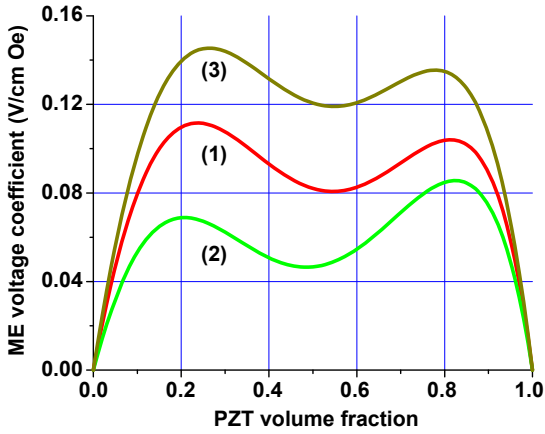

Figure 1.9 Lead zirconate titanate (PZT) volume fraction dependence of low-frequency magnetoelectric voltage coefficient for bilayers of homogeneous $Ni_{1-x}Zn_xFe_2O_4$ (NZFO)—PZT (1), positively graded NZFO and negatively graded PZT (2) and negative grading of NZFO and positive grading of PZT (3).

the piezoelectric coefficient results in an additional variation in the volume average of the stress ${}^{p}T_1$. Thus, z-dependence of ${}^{p}d_{31}$ induces an additional flexural moment, which gives rise to an increase in ME coefficient for positive grading and a decrease for negative grading, as seen in Figure 1.8.

Figure 1.9 shows the anticipated effects of grading of both PZT and ferrite. Simultaneous grading leads to the highest ME voltage coefficient when the ferrite is negatively graded and PZT is positively graded.

Next we consider ME effects in bilayers on a substrate. Estimates are shown in Figure 1.10 for homogeneous and graded bilayers with a thickness equal to the substrate thickness. It is seen that grading of NZFO and PZT leads to a general enhancement in the strength of ME coupling compared to the homogeneous composition. This could be attributed to the fact that the substrate yields a stress of the same sign as the

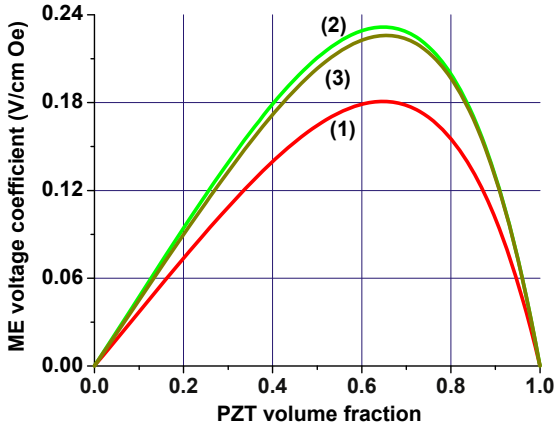

Figure 1.10 Lead zirconate titanate (PZT) volume fraction dependence of low-frequency magnetoelectric voltage coefficient for a bilayer of $Ni_{1-x}Zn_xFe_2O_4$ (NZFO) and PZT on a $SrTiO_3$ substrate of equal thickness. Results are for homogeneous NZFO—PZT (1), positively graded NZFO and negatively graded PZT (2) and negative grading of NZFO and positive grading of PZT (3).

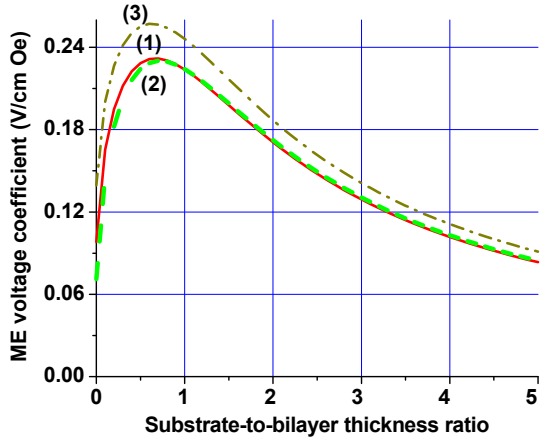

Figure 1.11 Substrate-to-bilayer thickness ratio dependence of magnetoelectric (ME) voltage coefficient for a bilayer on a substrate. The estimates are for a lead zirconate titanate (PZT) volume fraction of 0.7. Results are for homogeneous $Ni_{1-x}Zn_xFe_2O_4$ (NZFO)−PZT (1), positively graded NZFO and negative grading of PZT (2) and negative grading of NZFO and positively graded PZT (3).

axial stress of PZT. In a free-standing bilayer, however, half the PZT layer is under compression and the remaining under tension.

Figure 1.11 shows the variation in the ME coefficient as a function of the substrate thickness for a specific PZT volume fraction of 0.7.

Figure 1.11 shows that an increase in ${}^{s}t$ leads to a decrease in $\alpha_{E\,31}$ due to clamping effects. The ME voltage coefficient for negatively graded NZFO and positively graded PZT exceeds that of the homogeneous case by 20%. This is explained by an increase in the average stress of PZT due to additional rotating moments, which enters Eqn (1.11) for the ME voltage coefficient.

1.3 Resonance ME effect in composites

1.3.1 Longitudinal modes

A theory for the resonance enhancement of ME interactions in the EMR region is presented in this section. The frequency dependence of ME voltage coefficients is obtained using the simultaneous solution of electrostatic, magnetostatic and elastodynamic equations. The ME voltage coefficients are estimated from known material parameters (piezoelectric coupling, magnetostriction, elastic constants, etc.) of composite components. Estimates show that the resonance enhancement of ME coefficients exceeds the low-frequency values by more than an order of magnitude. The peak transverse ME coefficient at EMR is larger than the longitudinal one. The calculations exemplified by CFO−PZT composites are in agreement with the experimental data.

Because the ME effect in composites is due to mechanically coupled piezoelectric and magnetostrictive subsystems, it sharply increases in the vicinity of the EMR

frequency (Bichurin, Filippov, et al., 2003; Bichurin, Petrov, Averkin, & Filippov, 2010; Petrov, Bichurin, & Srinivasan, 2010; Srinivasan et al., 2005). If the length of the electromagnetic wave exceeds the spatial size of the composite by some orders of magnitude, then it is possible to neglect gradients of the electric and magnetic fields within the sample volume. We consider a composite sample that has the form of a narrow plate with length L. Based on elastodynamics and electrostatics, the equations of medium motion for longitudinal vibrations are governed by (Bichurin et al., 2010; Nan et al., 2008)

$$\overline{\rho}\frac{\partial^2 u_i}{\partial t^2} = V\frac{\partial {}^{p}T_{ij}}{\partial x_j} + (1-V)\frac{\partial {}^{m}T_{ij}}{\partial x_j}, \tag{1.19}$$

where u_i is the displacement vector component, $\overline{\rho} = V\,{}^{p}\rho + (1-V){}^{m}\rho$ is the average mass density, V is the ferroelectric volume fraction, and ${}^{p}\rho$ and ${}^{m}\rho$, ${}^{p}T_{ij}$ and ${}^{m}T_{ij}$ are the densities and stress tensor components of ferroelectric and ferrite, respectively.

Taking into account the elasticity Eqns (1.1) and (1.3), boundary conditions for free sample ends and the open circuit condition ($\int_A {}^{p}D_3\,\mathrm{d}A = 0$ with A denoting the cross-section), solution of Eqn (1.19) allows one to find the ME voltage coefficient. For transverse field orientation this expression takes the form (Bichurin et al., 2010)

$$\alpha_{E\ 31} = \frac{2\,{}^{p}d_{31}\,{}^{m}g_{11}\mu_{eff}\,{}^{p}s_{11}v(1-v)\tan(kL/2)}{s_2\left({}^{p}d_{31}^2 - {}^{p}s_{11}{}^{p}\varepsilon_{33}\right)kL - 2\,{}^{p}d_{31}^2 v\,{}^{m}s_{11}^{B}\tan(kL/2)}, \tag{1.20}$$

where $k = \omega\sqrt{\overline{\rho}\left[\frac{V}{{}^{p}s_{11}} + \frac{1-V}{{}^{m}s_{11}}\right]^{-1}}$, μ_{eff} is effective permeability of the piezomagnetic layer and $s_1 = V\,{}^{m}s_{11} + (1-V)\,{}^{p}s_{11}$.

The roots of the denominator in Eqn (1.20) define the maxima in the frequency dependence of the ME voltage coefficient. As one can see from Eqn (1.20) that the value of the ME coefficient is directly proportional to piezoelectric d_{31} and piezomagnetic g_{11} modules. To take into consideration the energy loss, we set ω equal to $\omega' - i\omega''$ with $\omega''/\omega' = 10^{-3}$. The resonance enhancement of the ME voltage coefficient is obtained at antiresonance frequency. ME voltage coefficient $\alpha_{E\ 13}$ for the bilayer of CFO and PZT increases with increasing PZT volume fraction, attains a peak value for $v = 0.5$ and then drops with increasing v as in Figure 1.12.

1.3.2 Bending modes

Application of the ME effect at longitudinal modes is suppressed due to the high resonance frequencies (approximately hundreds of kHz for nominal sample dimensions). The eddy current losses for the magnetostrictive phase can be high at such frequencies, in particular for transition metals and alloys and earth rare alloys, such as Terfenol-D, resulting in an inefficient ME energy conversion. To reduce the operating frequency,

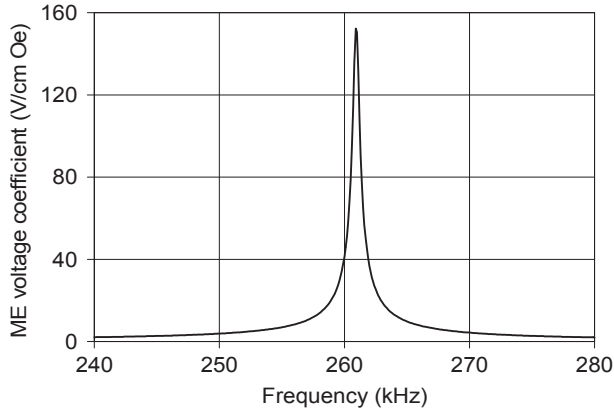

Figure 1.12 Frequency dependence of $\alpha_{E\ 13}$ for the bilayer of cobalt ferrite and lead zirconate titanate (CFO and PZT) with length of 7.3 mm and PZT volume fraction 0.5.

one must therefore increase the laminate size that is inconvenient for any applications. An alternative for getting a strong ME coupling is the resonance enhancement at bending modes of the composite. The frequency of applied ac field is expected to be much lower compared to longitudinal acoustic modes. Recent investigations have shown a giant ME effect at bending modes in several layered structures (Petrov, Bichurin, Srinivasan, Laletin, & Petrov, 2012; Petrov, Srinivasan, et al., 2009; Sreenivasulu, Petrov, Fetisov, Fetisov, & Srinivasan, 2012). In this section, we focus our attention on theoretical modeling of ME effects at bending modes (Petrov, Srinivasan, et al., 2009).

An in-plane bias field is assumed to be applied to a magnetostrictive component to avoid the demagnetizing field. The thickness of the plate is assumed to be small compared to the remaining dimensions. Moreover, the plate width is assumed to be small compared to its length. In that case, we can consider only one component of strain and stress tensors in the EMR region. The equation of bending motion of the bilayer has the form

$$\nabla^2\nabla^2 w + \frac{\rho\, b}{D}\frac{\partial^2 w}{\partial \tau^2} = 0, \tag{1.21}$$

where $\nabla^2\nabla^2$ is the biharmonic operator; w is the deflection (displacement in the z-direction); t and ρ are thickness and average density of the sample; $b = {}^{p}t + {}^{m}t$; $\rho = ({}^{p}\rho\, {}^{p}t + {}^{m}\rho {}^{m}t)/b$; ${}^{p}\rho$, ${}^{m}\rho$ and ${}^{p}t$, ${}^{m}t$ are densities and thicknesses of piezoelectric and piezomagnetic, respectively; and D is cylindrical stiffness.

Equation (1.21) relates to the middle plane, each point of which moves only in the z-direction. The boundary conditions for $x = 0$ and $x = L$ have to be used for finding the solution of the above equation. Here L is length of the bilayer. As an example, we consider the plate with free ends. At the free end, the turning moment M_1 and transverse force V_1 equal zero: $M_1 = 0$ and $V_1 = 0$ at $x = 0$ and $x = L$, where $M_1 = \int\limits_A zT_1\, \mathrm{d}z_1$, $V_1 = \frac{\partial M_1}{\partial x}$ and A is the cross-sectional area of the sample normal

to the x-axis. We are interested in the dynamic ME effect; for an ac magnetic field H applied to a biased sample, one measures the average induced electric field and calculates the ME voltage coefficient. Using the open circuit condition, the ME voltage coefficient can be found as

$$\alpha_{E\ 31} = \frac{E_3}{H_1} = -\frac{\int_{z_0-{}^{p}t}^{z_0} \frac{1}{{}^{p}\varepsilon_{33}} {}^{p}E_3 \mathrm{d}z}{t\, H_1}, \tag{1.22}$$

where E_3 and H_1 are the average electric field induced across the sample and applied magnetic field.

For the plate with free ends, Eqn (1.22) takes the form (Petrov et al., 2012)

$$\alpha_{E\ 31} = \frac{A \cdot {}^{p}d_{31} \cdot {}^{p}Y^{E} \cdot {}^{m}q_{11}}{\Delta \cdot {}^{p}\varepsilon_{33}} F(kL), \tag{1.23}$$

where $A = \frac{{}^{m}Y^{H} \cdot {}^{m}t \cdot (2 \cdot z_0 + {}^{m}t) \cdot (2 \cdot z_0 - {}^{p}t)}{4 \cdot D \cdot (1 - {}^{p}K_{31}^2)}$, D is cylindrical stiffness of the sample, $k^4 = \omega^2 \rho t / D$, L is the sample length, ${}^{p}K_{31}$ is piezoelectric coupling coefficient, $F(kL) = (4 \cdot r_2 \cdot r_3 - 2 \cdot r_2 \cdot r_3^2 + 2 \cdot r_2^2 \cdot r_4 - 2 \cdot r_2 \cdot r_4^2 + 4 \cdot r_1 \cdot r_4 - 2 \cdot r_4 \cdot r_1^2 - 2 \cdot r_4 - 2 \cdot r_2)$ and $\Delta = (r_3^2 - r_2^2 - 2 \cdot r_1 \cdot r_3 + r_1^2 + r_4^2)kL + (4 \cdot r_2 \cdot r_3 - 2 \cdot r_2 \cdot r_3^2 + 2 \cdot r_2^2 \cdot r_4 - 2 \cdot r_2 \cdot r_4^2 + 4 \cdot r_1 \cdot r_4 - 2 \cdot r_4 \cdot r_1^2 - 2 \cdot r_4 - 2 \cdot r_2) \cdot a_1$, with z_0 denoting the distance between the boundary and middle plane, $r_1 = \cosh(kL)$, $r_2 = \sinh(kL)$, $r_3 = \cos(kL)$, $r_4 = \sin(kL)$ and $a_1 = {}^{p}K_{31}^2 \cdot {}^{p}Y^{E} \cdot ((z_0 - {}^{p}t)^3 - z_0^3)/[3 \cdot D \cdot (1 - {}^{p}K_{31}^2)] + {}^{m}K_{31}^2 \cdot {}^{m}Y^{H} \cdot ((z_0 + {}^{m}t)^3 - z_0^3)/(3 \cdot D)$.

Assuming the electromechanical and magnetomechanical coupling coefficients to be small compared to unity, the resonance condition is $\cosh(kL) \cdot \cos(kL) = -1$, where k is wave number. Hence the fundamental resonance frequency can be expressed as the following:

$$f_r = \frac{1.758}{\pi L^2} \sqrt{\frac{D}{{}^{p}\rho\, {}^{p}t + {}^{m}\rho\, {}^{m}t}}, \tag{1.24}$$

Here D is the cylindrical stiffness, defined as $D = \frac{[z_0^3 - (z_0 - {}^{p}t)^3]}{3\, {}^{p}s_{11}} + \frac{[(z_0 + {}^{m}t)^3 - z_0^3]}{3\, {}^{m}s_{11}}$, and z_0 is the distance of a plane along the sample thickness where the axial force vanishes and can be estimated from the equation $z_0 = \frac{1}{2} \frac{{}^{p}Y\ {}^{p}t^2 - {}^{m}Y\ {}^{m}t^2}{{}^{p}Y\ {}^{p}t + {}^{m}Y\ {}^{m}t}$, where Y is the Young's modulus and ρ is the density. The peak ME voltage coefficient at bending mode frequency can be estimated as

$$\frac{\delta E_1}{\delta H_2} = \frac{0.0766\, Q_b}{D\, {}^{p}s_{11}\, {}^{m}s_{11}} {}^{m}t({}^{m}t + 2z_0)(2z_0 - {}^{p}t)\, {}^{m}q_{11}\, {}^{p}d_{11}/{}^{p}\varepsilon_{11}, \tag{1.25}$$

where Q_b is the quality factor for bending resonance.

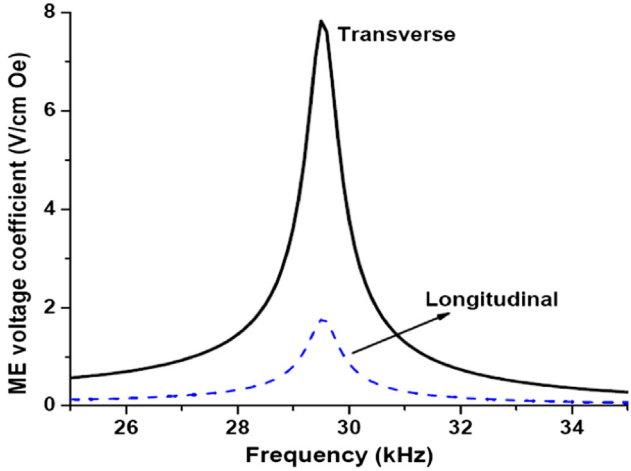

Figure 1.13 Frequency dependence of longitudinal and transverse magnetoelectric voltage coefficients for a bilayer of permendur and lead zirconate titanate (PZT), showing the resonance enhancement of ME interactions at the bending mode frequency. The bilayer is free to bend at both ends. The sample dimensions are $L = 9.2$ mm and total thickness $t = 0.7$ mm and the PZT volume fraction $v = 0.6$.

As an example, we apply Eqn (1.23) to the bilayer of permendur and PZT. Figure 1.13 shows the frequency dependence of the ME voltage coefficient at bending mode for a free-standing bilayer with length 9.2 mm and thickness 0.7 mm for PZT volume fraction 0.67. The graph of $\alpha_{E\ 31}$ reveals a giant value $\alpha_{E\ 31} = 6.6$ V/(cm Oe) and the resonance peak lies in the infra-low frequency range. Figure 1.14 reveals the theoretical and measured frequency dependencies of transverse ME voltage coefficients for a permendur−PZT bilayer that is free to bend at both ends.

According to our model, there is a strong dependence of resonance frequency on boundary conditions. The lowest resonance frequency is expected for the bilayer clamped at one end. One expects bending motion to occur at decreasing frequencies with increasing bilayer length or decreasing thickness.

1.3.3 Layered composites of graded components

In NZFO−PZT layered composites, a resonant enhancement of the ME coupling is expected when the ac magnetic field is applied at the same frequency as the longitudinal, thickness or bending modes of the structure. For nominal sample dimensions, longitudinal or thickness acoustic modes occur at several hundred kilohertz, whereas bending oscillations occur at a few kilohertz. Studies reveal a much higher enhancement in the strength of ME coupling for bending than for other modes. Here we focus only on modeling resonance ME effects due to bending oscillations in bilayers.

Consideration of ME effects in layered composites of functionally graded ferroelectric and ferromagnetic is limited to the bilayer. The thickness of the sample is assumed

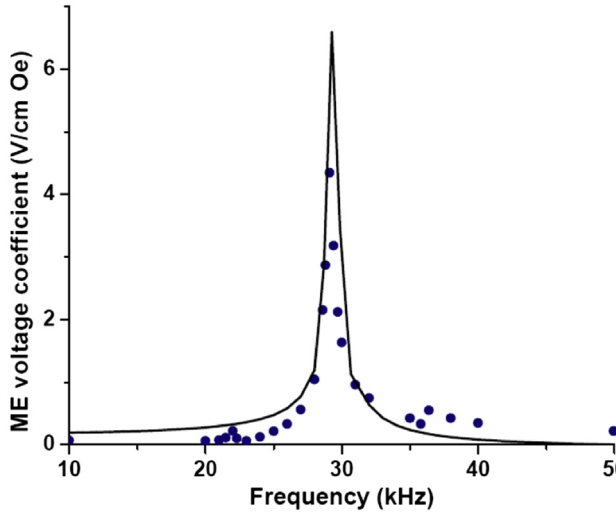

Figure 1.14 Theoretical (line) and measured (circles) frequency dependence of transverse magnetoelectric (ME) voltage coefficients for a permendur—lead zirconate titanate bilayer that is free to bend at both ends and with $v = 0.67$.

to be small compared to other dimensions. Moreover, the bilayer width is assumed to be small compared to its length. In that case, we can consider only one component of strain and stress tensors in the resonance region. A linear grading of the piezoelectric coefficient and permittivity in the ferroelectric and a similar grading of piezomagnetic coefficient in the ferromagnet are assumed. The thickness dependence of piezomagnetic and piezoelectric coefficients leads to an additional flexural strain, and the theory predicts an enhancement in the strength of ME coupling compared to homogeneous compositions. The enhancement in the case of a free-standing bilayer is on the order of 50% at low frequencies.

To take into account the z-dependent material parameters, one can use the theoretical model referred to above for ME coupling in asymmetric structures and consider material parameters as functions of z in Eqns (1.7) and (1.9). Then the ME voltage coefficient can be numerically estimated by using Eqn (1.22) (Petrov & Srinivasan, 2008).

As an example, ME coupling is estimated at bending modes in a graded NZFO—PZT bilayer on a substrate. Figure 1.15 shows the frequency dependence of the ME voltage coefficient for a free-standing bilayer of graded NZFO and homogeneous PZT with a length of 12 mm and a thickness of 2 mm (PZT volume fraction is $V = 0.3$). The resonance in bending oscillations occurs at 5 kHz. The profile of $\alpha_{E\,31}$ reveals a two order of magnitude increase in the maximum ME voltage coefficient compared to low-frequency coupling (Figure 1.2). A small shift in the resonance frequency due to grading is predicted. In comparison to the homogeneous composition, a 50% increase in $\alpha_{E\,31}$ for positive grading of the piezomagnetic coefficient and a 50% decrease for negative grading are expected.

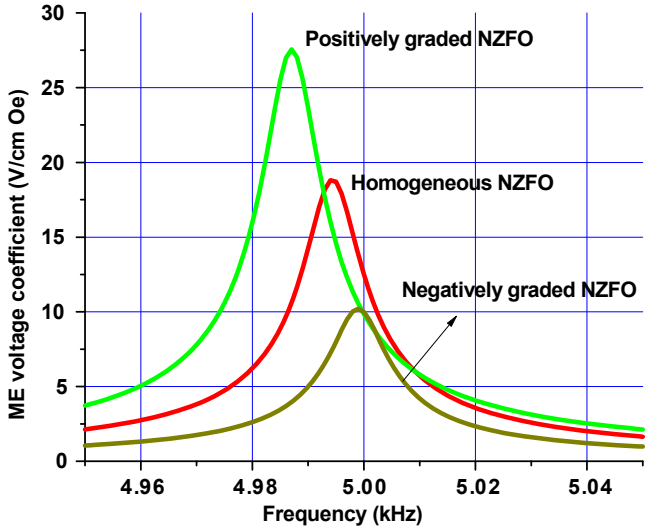

Figure 1.15 Frequency dependence of the magnetoelectric (ME) voltage coefficient for a free-standing lead zirconate titanate (PZT)-$Ni_{1-x}Zn_xFe_2O_4$ (NZFO) bilayer. The results are for homogeneous PZT and homogeneous, positively or negatively graded NZFO. The PZT volume fraction is 0.3. The peak in ME coefficient occurs at resonance frequency for bending oscillations in the bilayer.

Such dependence can be attributed to an increase in the rotating moment of the ferrite layer for positive grading and a corresponding increase in the longitudinal strain of PZT, resulting in an increase in the ME voltage.

A similar $\alpha_{E\ 31}$ versus f for bilayers of homogeneous NZFO and graded PZT is shown in Figure 1.16. It is seen that grading of PZT essentially leads to a shift of the resonance frequency, but no changes in the magnitude of $\alpha_{E\ 31}$. The constant magnitude for $\alpha_{E\ 31}$ is expected from Eqn (1.21). The ratio d_{31}/ϵ_{33} and ME voltage remain constant since both piezoelectric coupling and dielectric constant have the same grading-related variation. Based on the results in Figures 1.8 and 1.9, one expects maximum ME voltage coefficient for positive grading of both components.

Figure 1.17 shows the estimated resonance value of ME coefficient for homogeneous and graded bilayers. The results are shown as a function of PZT volume V. The maximum in the voltage occurs for a volume fraction of around 0.6, with the positive grading resulting in the highest voltage for all V values. The ME voltage coefficient vanishes at $V \approx 0.05$ for a bilayer of homogeneous components and is related to near-zero average axial stress in PZT due to lateral and flexural deformations.

Finally, we consider the resonance ME effects in a bilayer on a substrate. The estimated variation in the resonance frequency and ME voltage at resonance due to bending modes is shown in Figure 1.18. The results are for either positive or negative

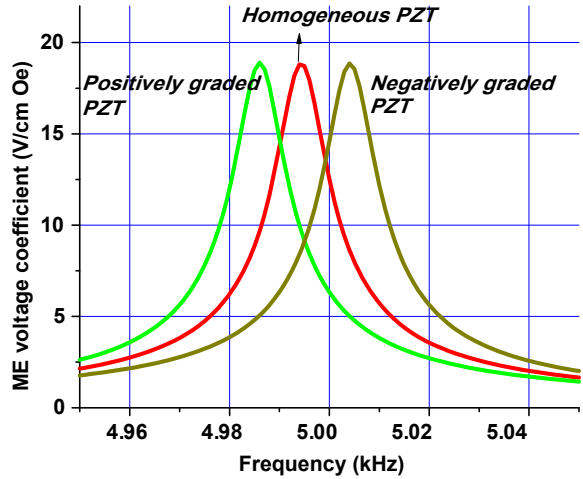

Figure 1.16 Frequency dependence as in Figure 1.7 for free-standing bilayers of homogeneous $Ni_{1-x}Zn_xFe_2O_4$ (NZFO) and homogeneous, positively or negatively graded lead zirconate titanate (PZT). The PZT volume fraction is 0.3.

grading of both PZT and NZFO. Estimates on the resonance frequency show a linear increase with increasing substrate thickness. The ME voltage initially shows a rapid decrease with increasing substrate thickness until it reaches a minimum at ${}^{s}t/({}^{p}t + {}^{m}t) \approx 0.3$. The minimum corresponds to sign reversal in the average axial stress of the PZT layer. The voltage coefficient then increases to show a broad

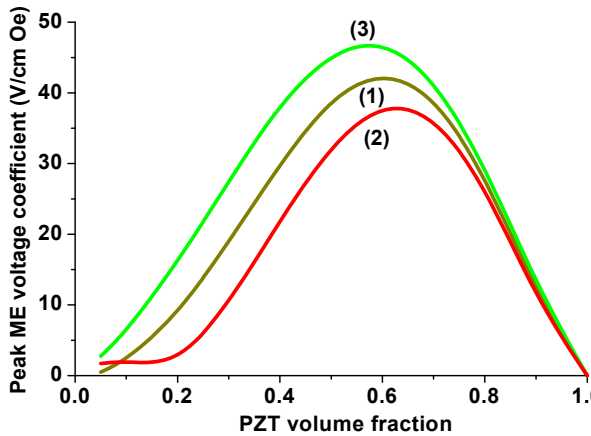

Figure 1.17 Lead zirconate titanate (PZT) volume fraction dependence of peak magnetoelectric (ME) voltage coefficient at resonance for bending modes. The results are for a free-standing bilayer of homogeneous components (1), negative grading of both PZT and $Ni_{1-x}Zn_xFe_2O_4$ (NZFO) (2) and positive grading of both PZT and NZFO (3).

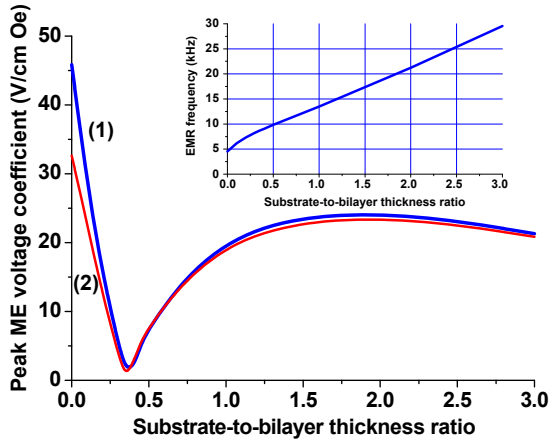

Figure 1.18 Substrate-to-bilayer thickness ratio dependence of peak magnetoelectric (ME) voltage coefficient at electromechanical resonance for a bilayer with positive grading of both lead zirconate titanate (PZT) and $Ni_{1-x}Zn_xFe_2O_4$ (NZFO) (1) and negative grading of both PZT and NZFO (2) for PZT volume fraction 0.5. The inset shows thickness ratio dependence of resonance frequency for bending modes for positive grading of both PZT and NZFO.

maximum centred at a thickness ratio of 1.8. The influence of grading slowly decreases with increasing substrate thickness.

1.4 ME effect at magnetic resonance

ME composites also offer important applications in the microwave range. In this frequency range, the ME effect reveals itself as a change in the magnetic permeability under an external electric field. Investigations of FMR line shift by an applied electric field are easily performed for layered ferrite—piezoelectric structures. In addition, layered composites are of interest for applications as electrically tunable microwave phase shifters, devices based on FMR, magnetic-controlled electro-optical and/or piezoelectric devices and electrically readable magnetic memories.

In this chapter, we discuss theoretical models of multilayer ME composites in the microwave range (Bichurin et al., 2001; Bichurin, Petrov, Kiliba, et al., 2002; Shastry, Srinivasan, Bichurin, Petrov, & Tatarenko, 2004). The model is a phenomenological theory, which is based on the magnetic susceptibility as a function of stress.

1.4.1 Electrically induced magnetic resonance line shift

Let us consider the simple model of a bilayer structure, consisting of a ferrite spinel with cubic (m3m) symmetry and poled PZT with a symmetry of ∞m.

The influence of an electric field on the piezoelectric PZT phase can be described as follows.

Based on elasticity equations and applying an electric field along the axis of polarization (i.e. $E_3 = E$, $E_1 = E_2 = 0$), we obtain the following expressions for stress components in the piezoelectric phase:

$$\begin{cases} {}^{P}T_{33} = -e_{33}E + {}^{P}c_{13}({}^{P}S_{11} + {}^{P}S_{22}) + {}^{P}c_{33}{}^{P}S_{33}, \\ {}^{P}T_{11} = -e_{31}E + {}^{P}c_{11}{}^{P}S_{11} + {}^{P}c_{12}{}^{P}S_{22} + {}^{P}c_{13}{}^{P}S_{33} = 0, \\ {}^{P}T_{22} = -e_{31}E + {}^{P}c_{12}{}^{P}S_{11} + {}^{P}c_{11}{}^{P}S_{22} + {}^{P}c_{13}{}^{P}S_{33} = 0. \end{cases} \tag{1.26}$$

Assuming the axis of polarization in the piezoelectric phase to coincide with the crystallographic [111] axis of the magnetostrictive phase, the stress components in the magnetostrictive phase are given by the following:

$$\begin{cases} {}^{m}T_1 = \left(\dfrac{{}^{m}c_{11} + {}^{m}c_{12}}{2} + {}^{m}c_{44}\right){}^{m}S_1 + \dfrac{{}^{m}c_{11} + 5{}^{m}c_{12} - 2{}^{m}c_{44}}{6}{}^{m}S_2 \\ \qquad + \dfrac{{}^{m}c_{11} + 2{}^{m}c_{12} - 2{}^{m}c_{44}}{3}{}^{m}S_3 + \dfrac{{}^{m}c_{11} - {}^{m}c_{12} - 2{}^{m}c_{44}}{3\sqrt{2}}{}^{m}S_4, \\ {}^{m}T_2 = \dfrac{{}^{m}c_{11} + 5{}^{m}c_{12} - 2{}^{m}c_{44}}{6}{}^{m}S_1 + \left(\dfrac{{}^{m}c_{11} + {}^{m}c_{12}}{2} + {}^{m}c_{44}\right){}^{m}S_2 + \dfrac{{}^{m}c_{11} + 2{}^{m}c_{12} + 4{}^{m}c_{44}}{3}{}^{m}S_3, \\ {}^{m}T_3 = \dfrac{{}^{m}c_{11} + 2{}^{m}c_{12} - 2{}^{m}c_{44}}{3}{}^{m}S_1 + \dfrac{{}^{m}c_{11} + 2{}^{m}c_{12} - 2{}^{m}c_{44}}{3}{}^{m}S_2 \\ \qquad + \dfrac{{}^{m}c_{11} + 2{}^{m}c_{12} - 2{}^{m}c_{44}}{3}{}^{m}S_3 - \dfrac{{}^{m}c_{11} - {}^{m}c_{12} - 2{}^{m}c_{44}}{3\sqrt{2}}{}^{m}S_4, \\ {}^{m}T_4 = \dfrac{{}^{m}c_{11} + 2{}^{m}c_{12} - 2{}^{m}c_{44}}{3}{}^{m}S_1 - \dfrac{{}^{m}c_{11} - {}^{m}c_{12} - 2{}^{m}c_{44}}{3\sqrt{2}}{}^{m}S_2 + \dfrac{{}^{m}c_{11} - {}^{m}c_{12} + {}^{m}c_{44}}{3}{}^{m}S_4. \end{cases} \tag{1.27}$$

To calculate the ME effect of bilayer structures in the FMR range, we should use the following procedure: (1) ${}^{m}S_3$ is defined as a function of the stress ${}^{m}T_3$; (2) ${}^{p}T_3$ is defined as a function of the strain ${}^{p}S_3$; and (3) use the known expressions for the dependence of the resonant magnetic field on stress to determine the FMR line shift. Thus, the task is reduced to the solutions of electrostatic equations under specific boundary conditions.

Let us then consider that the bilayer structure is mechanically clamped along the three-axis ferrite and piezoelectric subsystems. In this case, the boundary conditions, without taking into account forces of friction, have the form

$$\begin{aligned} {}^{p}T_3 &= {}^{m}T_3, \\ {}^{p}S_3 &= -\frac{{}^{m}v}{{}^{p}v}\cdot mS_3, \end{aligned} \tag{1.28}$$

where ${}^{m}v$ and ${}^{p}v$ are the volume fractions of the magnetostrictive and piezoelectric phases, respectively. Finally we find that the stress along the three axes is given by the following:

$$ {}^{m}T_3 = \frac{E_3\left(\frac{2{}^{p}c_{13}e_{31}}{{}^{p}c_{11}+{}^{p}c_{12}} - e_{33}\right)}{1+\frac{{}^{m}v}{{}^{p}v}\left(\frac{1}{3{}^{m}c_{44}}+\frac{1}{3+({}^{m}c_{11}+2{}^{m}c_{12})}\right)\left({}^{p}c_{33}-2\frac{{}^{p}c_{13}^2}{{}^{p}c_{11}+{}^{p}c_{12}}\right)}. \tag{1.29} $$

It is known that an applied electric voltage results in a change of the resonant magnetic field. We limit ourselves to the case when both the magnetic and electric fields are oriented along the polarization axis of the piezoelectric phases, which also corresponds to the [111] axis of the magnetostrictive one. In this case, the shift of the resonant magnetic field is given by

$$ \delta H_E = \frac{3\lambda_{111}{}^{m}T_3}{M_0} = AE_3, \tag{1.30} $$

where M_0 is the saturation magnetization of the magnetostrictive layer, and the ME constant is defined by

$$ A = \frac{3\lambda_{111}}{M_0} = \frac{\left(\frac{2{}^{p}c_{13}e_{31}}{{}^{p}c_{11}+{}^{p}c_{12}} - e_{33}\right)}{\left[1+\frac{{}^{m}v}{{}^{p}v}\left(\frac{1}{3{}^{m}c_{44}}+\frac{1}{3+({}^{m}c_{11}+2{}^{m}c_{12})}\right)\left({}^{p}c_{33}-2\frac{{}^{p}c_{13}^2}{{}^{p}c_{11}+{}^{p}c_{12}}\right)\right]}. \tag{1.31} $$

The theoretical values for the ME constant $A = \delta H_E/E_3$ were determined for composites of both NFO–PZT and yttrium iron garnet (YIG)–PZT. For these calculations, the following material parameters of two-component phases were used: YIG ${}^{p}c_{11} = 12.6 \times 10^{10}$ N/m^2, ${}^{p}c_{12} = 7.95 \times 10^{10}$ N/m^2, ${}^{p}c_{13} = 8.4 \times 10^{10}$ N/m^2, ${}^{p}c_{33} = 11.7 \times 10^{10}$ N/m^2, $e_{31} = -6.5$ Sim/m^2 and $e_{33} = 23.3$ Sim/m^2; $NiFe_2O_4$ ${}^{m}c_{11} = 22 \times 10^{10}$ N/m^2, ${}^{m}c_{12} = 10.9 \times 10^{10}$ N/m^2, ${}^{m}c_{44} = 8.12 \times 10^{10}$ N/m^2, $\lambda_{111} = -21.6 \times 10^{10}$ and $4\pi M_0 = 3200$ Gs.

In Figure 1.19, the dependence of the ME constant A on the relative volume fraction of the component phases in the bilayer structure is shown. In a composite of NFO and PZT, the ME effect has been reported to be stronger than that of YIG–PZT. This is because NFO has a much higher magnetostriction than YIG. Another notable feature in Figure 1.19 is the fact that theoretically the field shift should increase with increasing volume fraction of the piezoelectric phase. It should be noted that the magnetic resonance line will vanish if the volume fraction of the magnetostrictive phase is too low. This is uniquely different from results at lower frequencies, where the largest ME effect is found for an approximate volume fraction ratio of 50:50 (Nan et al., 2008). Assuming that ${}^{m}v/{}^{p}v = 1$, we can estimate that the resonance line shift under applied electric field is given by the relation

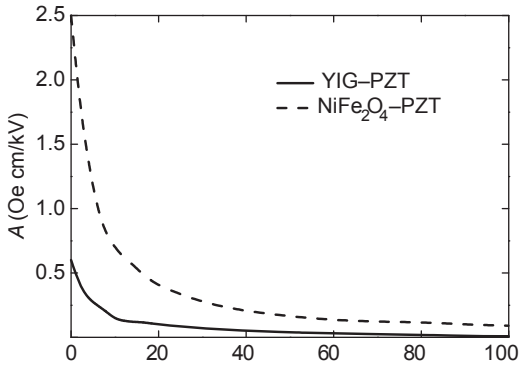

Figure 1.19 Dependence of magnetoelectric constant A on volume fraction of magnetostrictive and piezoelectric phases ${}^{m}v/{}^{p}v$. The results are for bilayer composites of nickel ferrite−lead zirconate titanate (PZT) and yttrium iron garnet (YIG)−PZT.

$\delta H = AE$, where $A \approx 2$ Oe cm/kV for $NiFe_2O_4$−PZT and $A \approx 0.45$ Oe cm/kV for YIG−PZT.

The values for the calculated resonance line shift are in good agreement with prior experimental data (Shastry et al., 2004): the theoretical line shift is 0.45 Oe cm/kV, which is comparable to the measured one of 0.2−0.56 Oe cm/kV depending on relative volume fraction of magnetostrictive and piezoelectric phases. Thus, we can see that it is necessary to use a piezoelectric component with large piezoelectric coefficients, and a magnetostrictive one with small saturation magnetization and high magnetostriction.

1.4.2 Magnetoelectric coupling at magnetoacoustic resonance

Now, let us investigate the resonant ME coupling at overlapping the electromechanical and ferromagnetic resonances. A theoretical model predicts a strong ME interaction at magnetoacoustic resonance (MAR) in the bilayer composite with ferrite and piezoelectric single crystal layers (Bichurin, Petrov, Ryabkov, Averkin, & Srinivasan, 2005; Petrov, Srinivasan, Ryabkov, Averkin, & Bichurin, 2007; Petrov, Zibtsev, et al., 2009; Ryabkov, Averkin, Bichurin, Petrov, & Srinivasan, 2007; Ryabkov, Petrov, Bichurin, & Srinivasan, 2006). The ferrite layer is supposed to be in a saturated single-domain state. A bias field is assumed to be applied perpendicular to the sample plane. This state has two important advantages. First, when domains are absent, acoustic losses are minimum. Second, the single-domain state under FMR provides the conditions necessary for achieving a large effective susceptibility.

The free energy density of a single crystal ferrite phase can be given as

$$ {}^{m}W = W_H + W_{an} + W_{ma} + W_{ac}, \tag{1.32} $$

where $W_H = -\mathbf{M}\cdot\mathbf{H}$ is Zeeman's energy, $W_{an} = K_1/M^4(M_1^2\,M_2^2 + M_2^2\,M_3^2 + M_3^2\,M_1^2)$ is cubic anisotropy energy, K_1 is a constant of the cubic anisotropy, $W_{ma} = B_1/M^2\cdot(M_1^2\,{}^{m}S_1 + M_2^2\,{}^{m}S_2 + M_3^2\,{}^{m}S_3) + B_2/M^2(M_1\,M_2\,{}^{m}S_6 + M_2\,M_3\,{}^{m}S_4 + M_1\,M_3\,{}^{m}S_5)$

is the magnetoelastic energy, B_1 and B_2 are magnetoelastic constants and $W_{ac} = {}^1\!/_2\,{}^m c_{11}({}^m S_1^2 + {}^m S_2^2 + {}^m S_3^2) + {}^1\!/_2 \quad {}^m c_{44} \quad ({}^m S_4^2 + {}^m S_5^2 + {}^m S_6^2) + {}^m c_{12} \quad ({}^m S_1 \quad {}^m S_2 + {}^m S_2 \; {}^m S_3 + {}^m S_1 \; {}^m S_3)$ is the elastic energy. In Eqn (1.32), it is supposed that the material is uniformly magnetized. On the basis of a generalized Hooke's law, we can write the stresses of the piezoelectric component phase as

$$\begin{aligned} {}^p T_4 &= {}^p c_{44}{}^p S_4 - e_{p15}{}^p E_2, \\ {}^p T_5 &= {}^p c_{44}{}^p S_5 - e_{p15}{}^p E_1, \end{aligned} \tag{1.33}$$

where e_{p15} is a shear piezoelectric coefficient. The equations of motion for the ferrite and piezoelectric phases are then

$$\begin{aligned} \partial^2({}^m u_1)/\partial t^2 &= \partial^2({}^m W)/(\partial\, x \partial {}^m S_1) + \partial^2({}^m W)/(\partial\, y \partial {}^m S_6) \\ &\quad + \partial^2({}^m W)/(\partial\, z \partial {}^m S_5), \\ \partial^2({}^P u_1)/\partial t^2 &= \partial({}^m T_1)/\partial x + \partial({}^m T_1)/\partial y + \partial({}^m T_1)/\partial z, \\ \partial^2({}^P u_2)/\partial t^2 &= \partial({}^m T_2)/\partial x + \partial({}^m T_2)/\partial y + \partial({}^m T_2)/\partial z. \end{aligned} \tag{1.34}$$

The equation of motion of the magnetization vector is given by

$$\partial \mathbf{M}/\partial t = -\gamma[\mathbf{M}, \mathbf{H_{eff}}], \tag{1.35}$$

where $\mathbf{H_{eff}} = -\partial({}^m \mathrm{W})/\partial \mathbf{M}$. To simplify calculations, we assume waves with the circular polarization:

$$\begin{aligned} m^+ &= m_1 + i\, m_2, \\ H^+ &= H_1 + i\, H_2, \\ E^+ &= E_1 + i\, E_2, \\ u^+ &= u_1 + i\, u_2, \end{aligned} \tag{1.36}$$

where m is a variable magnetization and u is the displacement. By taking into account Eqn (1.36), Eqns (1.34) and (1.35) take the form

$$\begin{aligned} \omega m^+ &= \gamma\left(H_0 m^+ - 4\pi M_0 m^+ - M_0 H^+\right), \\ -\omega^2 \; {}^m\rho \; {}^m u^+ &= {}^m c_{44} \partial^2\left({}^m u^+\right)/\partial \mathrm{z}^2, \\ -\omega^2 \; {}^p\rho \; {}^p u^+ &= {}^p c_{44} \partial^2\left({}^p u^+\right)/\partial \mathrm{z}^2. \end{aligned} \tag{1.37}$$

The boundary conditions at the interface between layers and at the top/bottom planes of the composite are given by

$$
\begin{aligned}
&{}^{m}u^{+} = {}^{p}u^{+} \text{ at } z = 0,\\
&{}^{m}c_{44}\partial\left({}^{m}u^{+}\right)/\partial z + \mathrm{B}_2 m^{+}/M_0 = 0 \text{ at } z = {}^{m}L,\\
&{}^{m}c_{44}\partial\left({}^{m}u^{+}\right)/\partial z + B_2 m^{+}/M_0 = {}^{p}c_{44}\partial\left({}^{p}u^{+}\right)/\partial z - {}^{p}e_{15}{}^{p}E^{+} \text{ at } z = 0,\\
&{}^{p}c_{44}\partial\left({}^{p}u^{+}\right)/\partial z - {}^{p}e_{15}{}^{p}E^{+} = 0 \text{ at } z = -{}^{p}L,
\end{aligned}
\tag{1.38}
$$

where ${}^{m}L$ and ${}^{p}L$ are the thicknesses of the ferrite and piezoelectric layers, respectively. Finally, the electric field E induced in the piezoelectric component can be defined by the open electric circuit condition $D^{+} = \frac{1}{{}^{p}L}\int_{-{}^{p}L}^{0} {}^{p}D^{+}\,\mathrm{d}z = 0$, where ${}^{p}D^{+} = {}^{p}e_{15}\,{}^{p}S^{+} + {}^{p}\varepsilon_{11}\,{}^{p}E^{+}$ is the dielectric displacement of the piezoelectric layer. Finally, we can derive an expression for the ME voltage coefficient (Bichurin et al., 2005):

$$
\begin{aligned}
\left|E^{+}/H^{+}\right| = {}&\gamma B_2\,{}^{p}c_{44}k_p{}^{p}e_{15}\left[1-\cos\left(k_p\,{}^{p}L\right)\right]^2\Big/\left\{(\omega-\gamma H_0+4\pi\gamma M_0)\right.\\
&\times\left[-\frac{1}{2}\,{}^{p}c_{44}{}^{p}\varepsilon_{33}k_p\,{}^{p}L\sin\left(2k_p\,{}^{p}L\right)\left({}^{p}c_{44}k_p+{}^{m}c_{44}k_m\right)+\left(\cos\left(k_p\,{}^{p}L\right)-1\right)\right.\\
&\left.\left.\times\,{}^{p}e_{15}^{2}\left[\left(\cos\left(k_p\,{}^{p}L\right)\left({}^{m}c_{44}k_m+2\,{}^{p}c_{44}k_p\right)+{}^{m}c_{44}k_m\right)\right]\right]\right\},
\end{aligned}
\tag{1.39}
$$

where

$$
k_m = \omega\sqrt{\frac{{}^{m}\rho}{{}^{m}c_{44}}} \text{ and } k_p = \omega\sqrt{\frac{{}^{p}\rho}{{}^{p}c_{44}}}.
$$

As follows from Eqn (1.39), there is a connection in the ferrite phase between the displacement and a homogeneous magnetization precession through boundary conditions on the plate surfaces. Expression (1.39) shows that if the frequency of an applied magnetic field equals that of the magnetization precession ($\omega_0 = \gamma H_0 - 4\pi\gamma M_0$), then the value of the ME voltage coefficient will be increased significantly. This enhancement is due to a coupling between the strain induced by an applied magnetic field in the range of the magnetic resonance and a corresponding one in the piezoelectric phase induced by an applied electric field.

Figures 1.20 and 1.21 show the dependences of the ME voltage coefficient for a bilayer composite of single crystal YIG and lead magnesium niobate−lead titanate (PMN−PT), both of which were calculated by Eqn (1.39). Calculations were performed by introducing a complex frequency to account for magnetoacoustic loss. The real component of the frequency was taken as $\omega_r = 10^7$ rad/s.

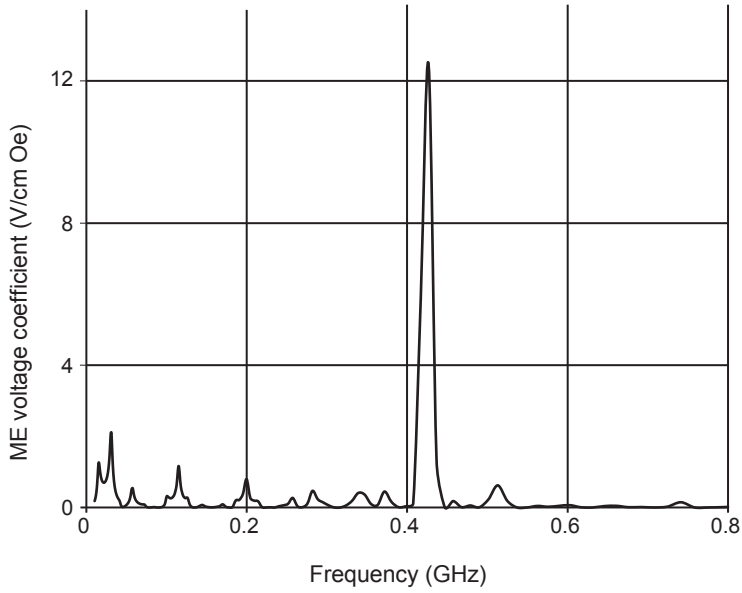

Figure 1.20 Frequency dependence of magnetoelectric voltage coefficient for $L1 = L2 = 0.05$ mm, $H_0 = 1.9$ kOe.

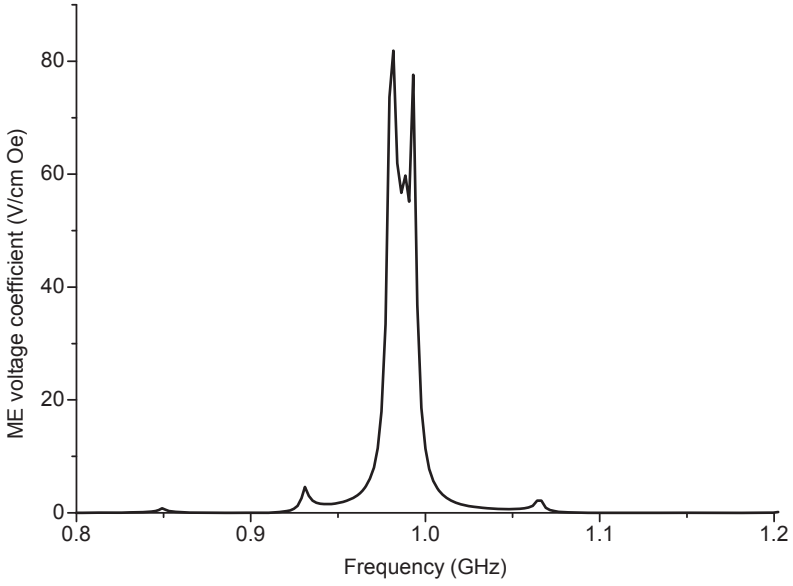

Figure 1.21 Frequency dependence of magnetoelectric voltage coefficient for $L1 = L2 = 0.01$ mm, $H_0 = 2.1$ kOe.

For frequencies less than that of the homogeneous magnetization precession, the microwave ME voltage coefficient has a maximum when driven by an electric field in the EMR frequency range. Essential to this increase in the microwave ME voltage coefficient is that the EMR frequency of the electric be equal to that for a uniform magnetization precession in the ferrite phase. Even after including magnetoacoustic loss factors (as mentioned above), the microwave ME coefficient can reach giant values of up to 64 V/(cm Oe).

Next we dwell on consideration of magnetic excitations in a ferrite−piezoelectric bilayer due to microwave electric field and ME interactions (Petrov et al., 2007). The magnetic response is described in terms of ME susceptibility, and a novel technique has been proposed for its determination for a YIG−PZT nanobilayer. It is assumed that the sample is positioned at the maximum of microwave electric field. An induced microwave magnetic field (parallel to the electric field) will result from ME interactions and, therefore, will lead to magnetic excitations in the bilayer. Such magnetic excitations originate from elastic modes in the piezoelectric component. These acoustic modes would in turn excite coupled magnetoelastic modes in the ferrite due to ME coupling. The excitations are standing waves along the thickness of the sample, and the wavelength is determined by the thickness of PZT and YIG and material parameters. These coupled magnon−phonon modes will be in the microwave region of the electromagnetic spectrum for YIG. Thus the focus here is high-frequency magnetic excitations, including FMR and ME susceptibility in a ferrite−ferroelectric bilayer. Traditional FMR at high powers in a ferrite will lead to nonlinear effects, such as saturation of main resonance and subsidiary absorption. The idea here is to eliminate those effects by locating a bilayer at the position of maximum RF electric field.

We consider a ferrite−PZT bilayer as in Figure 1.10 that is subjected to a bias field $\boldsymbol{H_0}$ perpendicular to its plane along the z-axis. The piezoelectric phase is electrically polarized with a field $\boldsymbol{E_0}$ parallel to $\boldsymbol{z}$. The expression for the space-variant microwave magnetization m_k can be obtained by solving combined equations of medium motion for ferrite and piezoelectric phases and the equation of motion of magnetization for the ferrite. Thus, $\partial m/\partial z$ will appear in the equation for mechanical displacement for ferrite, and the term $\partial u/\partial z$ will be present in the equation of motion of magnetization. The magnetization m_k in terms of circularly polarized mechanical displacement ${}^{m}u^{+}$ of the ferrite is obtained by solving the above equations and substituting in

$$m_k = \frac{B_2\gamma\frac{\partial({}^{m}u^{+})}{\partial z}}{\omega-\omega_k}. \tag{1.40}$$

The magnetic modes will have uniform magnetization in the plane of the film and a standing wave structure perpendicular to the film plane. Substituting the value for ${}^{m}u^{+}$ into Eqn (1.40) yields the following:

$$m_k = \frac{B_2\gamma e_{15}{}^{p}E{}^{m}k\,\sin[{}^{m}k({}^{m}L-z)]\,[1-\cos({}^{p}k\,{}^{p}L)]}{[{}^{p}c_{44}\,{}^{p}k\,\sin({}^{p}k\,{}^{p}L)\cos({}^{m}k{}^{m}L)+{}^{m}c_{44}{}^{m}k\,\sin({}^{m}k{}^{m}L)\cos({}^{p}k{}^{p}L)](\omega-\omega_k)}, \tag{1.41}$$

where ${}^{m}c_{44}^{+} = {}^{m}c_{44} + \gamma(B_2^2 + \omega^2 \quad {}^{m}\rho \quad M_0 \quad H_e)/[M_0 \quad (\omega - \gamma H_0 - 4\pi\gamma M_0)$, ${}^{m}k = \omega\sqrt{\frac{{}^{m}\rho}{{}^{m}c_{44}^{+}}}$, ${}^{p}k = \omega\sqrt{\frac{{}^{p}\rho}{{}^{p}c_{44}}}$.

Signal attenuation is taken into account by introducing a complex frequency and an imaginary component of $\omega'' = 10^{-3}\,\omega_k$. This imaginary component corresponds to a Q-value of 1000 for resonance absorption in the ferrite.

Next we apply the theory to the specific case of a YIG−PZT bilayer and calculate the ME susceptibility given by $\alpha = \mu_0\,\partial m_k/\partial^p E$. The choice of YIG for the ferrite is because of low losses at microwave frequency, a necessary condition for the observation of the enhancement in the ME coupling that is predicted by the theory. Figure 1.22(a) shows the susceptibility versus frequency f. We choose 100 nm YIG and 195 nm PZT so that the fundamental EMR will be around 6 GHz. A bias field of $H_0 = 2$ kOe is assumed, so it is smaller than the field H_r for the excitation of magnetic modes that include FMR. There are peaks in α at the fundamental EMR and higher order thickness modes. The susceptibility at the fundamental mode is an order of magnitude higher than the value at the higher harmonics.

Consider the results in Figure 1.22(b) for a bias field H_0 corresponding to magnetic resonance in YIG. When H_0 is set equal to $H_r = \omega/\gamma + 4\pi M_0$, α is expected to show a dramatic increase in magnitude, as in Figure 1.22(b) and (c), due to coincidence of resonance character for the mechanical displacement and magnetization. When the frequencies of magnon and phonon modes are matched, there is efficient transfer of energy between the electric and magnetic subsystems. In Figure 1.22(b) for $H_0 = 3.86$ kOe, the fundamental acoustic mode coincides with the uniform precession magnon mode that results in a 60-fold increase in α. When H_0 is increased to 6 kOe so that uniform precession frequency coincides with the higher order EMR mode, one expects a two orders of magnitude increase in α as in Figure 1.22(c).

Next we consider measurements of ME susceptibility for the case of a PZT−YIG bilayer. One could use a resonant cavity with the sample located at the ac electric field maximum. The dc magnetic bias field is selected so that homogeneous precession frequency coincides with the fundamental EMR mode. Thus the microwave electric field will result in FMR in YIG and absorption of microwave power. The electric-field-induced magnetization is equivalent to that induced by a microwave magnetic field:

$$H = m_k \frac{\gamma H_0 - 4\pi\gamma M_0 - \omega}{\gamma M_0}. \tag{1.42}$$

Equation (1.42) is obtained by solving the equation of motion of magnetization for a YIG plate placed in an antinode of ac magnetic field. The absorbed power P is given by $P = k_1 H^2$ with $k_1 = \frac{\pi M_0}{\Delta H}\omega V$, where V is volume of YIG and ΔH is half-width of resonance absorption. Thus, H can be determined from Eqn (1.42) and substituted in Eqn (1.41) to obtain m_k. The ME susceptibility can be determined from data on power absorbed.

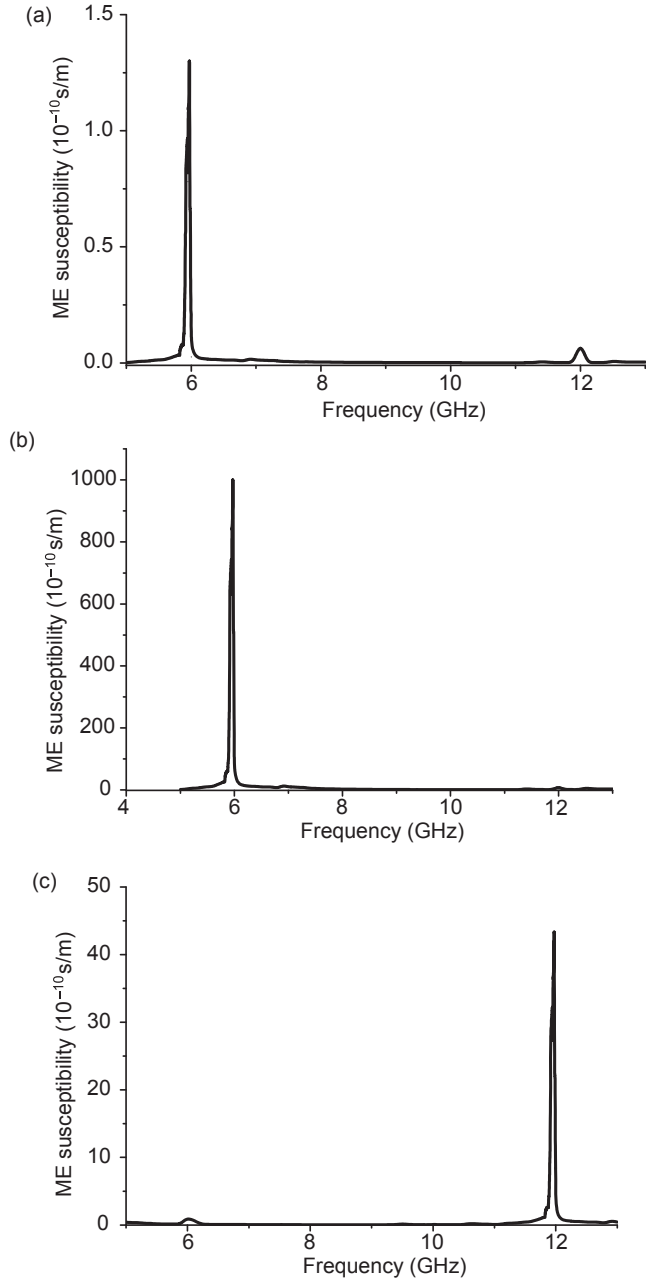

Figure 1.22 Theoretical frequency dependence of the ME susceptibility at the ferrite−piezoelectric interface ($z = 0$) for a bilayer of yttrium iron garnet (YIG) and PZT subjected to dc and ac fields. The bilayer is assumed at the microwave electric field maximum. (a) Results are for $H_0 = 2$ kOe that is well below the magnetic resonance field for YIG. The peaks correspond to elastic modes in PZT. (b) ME susceptibility for $H_0 = 3.86$ kOe, corresponding to coincidence of the fundamental elastic mode in PZT and magnetic resonance in YIG. (c) Similar data at $H_0 = 6$ kOe, at coincidence of higher order elastic mode and magnetic modes.

1.5 Conclusions

In this manuscript, a generalized theoretical model for low-frequency ME effects in layered composites was discussed. To describe the composite's physical properties, the exact solutions of elastostatic and electrostatic equations were obtained. Expressions for the ME coefficients were derived as functions of constituent phase material parameters, and relative volume fractions of phases. Longitudinal, transverse and in-plane cases were considered. For a bilayer that is an asymmetric structure, the influence of flexural deformations of the sample on ME output was estimated.

Predictions of the ME effect for various model composite systems were given, including CFO−PZT. It was shown that the ME effect in ferrite−PZT systems is maximum for in-plane magnetic and electric fields. The theoretical estimates of ME parameters were compared with experimental data.

The generalized theory allows for modeling of the low-frequency ME effect in bulk composites. To describe these low-frequency composite properties, an effective medium method was used. Calculations of the ME susceptibility and ME voltage coefficient were performed as functions of volume fractions and component parameters. Composites with connectivity types 3−0 and 0−3 were considered. Larger ME coefficients were found for 3−0 composites with magnetic and/or electric fields applied along the longitudinal direction. For composites of CFO−PZT, values as high as 4 V/(cm Oe) were predicted for the longitudinal ME voltage coefficient. For the transverse field orientation, the ME effect was found to be 2−3.5 times smaller than that for longitudinal orientation. Furthermore, clamping was shown to significantly reduce the ME effect.

We presented a theory for the resonance enhancement of ME interactions at frequencies corresponding to EMR. Frequency dependence for ME voltage coefficients is obtained using the simultaneous solution of electrostatic, magnetostatic and elastodynamic equations. The ME effect at bending mode in a bilayer is shown to be dependent on boundary conditions. It is shown that the ME coupling in the EMR region exceeds the low-frequency value by more than an order of magnitude.

The grading-related thickness dependence of piezomagnetic or/and piezoelectric coefficients leads to an additional flexural strain, and the theory predicts an enhancement in the strength of low-frequency ME coupling compared to homogeneous compositions. A similar increase in the ME coefficient has been predicted for mechanical resonance in bending modes in the sample. In graded bilayers, the ME voltage coefficient is expected to increase by 50% at low frequencies and at mechanical resonance. For a graded bilayer on a substrate, the low-frequency ME voltage coefficient is higher by 20% in comparison to the homogeneous bilayer. The maximum ME coupling occurs for equal thickness of bilayer and substrate. At EMR, the ME voltage shows a sharp drop with increasing substrate thickness and then increases to show a broad maximum.

A phenomenological theory is proposed to treat the ME coupling at frequencies corresponding to ferromagnetic resonance in a multilayer composite consisting of alternate layers of piezoelectric and magnetostrictive phases. Magnetic resonance line

shift is directly proportional to the product of the applied electric field and the ME coupling constant. The expression for ME coupling constant was obtained. For a nickel ferrite−PZT bilayer, the theory predicts a factor of 5 stronger effect than in YIG−PZT.

A theoretical model has been discussed for ME effects in a single-crystal ferrite−piezoelectric bilayer in the MAR region. The theory predicts a giant ME effect at MAR. The enhancement arises from interaction between elastic modes and the uniform precession spin-wave mode, resulting in magnetoelastic modes. The peak ME voltage coefficient appears at the coincidence of acoustic resonance and FMR frequencies. Estimates for nominal bilayer parameters for nickel ferrite−PZT and YIG−PZT predict MAR at 5−10 GHz and ME voltage coefficient on the order of 80−480 V/(cm Oe).

References

Astrov, D. N. (1961). Magnetoelectric effect in chromium oxide. *Soviet Physics JETP, 13*, 729.

Bichurin, M. I., Filippov, D. A., Petrov, V. M., Laletsin, V. M., Paddubnaya, N. N., & Srinivasan, G. (2003). Resonance magnetoelectric effects in layered magnetostrictive-piezoelectric composites. *Physical Review B, 68*, 132408.

Bichurin, M. I., Kornev, I. A., Petrov, V. M., Tatarenko, A. S., Kiliba, Yu. V., & Srinivasan, G. (2001). Theory of magnetoelectric effects at microwave frequencies in a piezoelectric/magnetostrictive multilayer composite. *Physical Review B, 64*, 094409.

Bichurin, M. I., Petrov, V. M., Averkin, S. V., & Filippov, A. V. (2010). Electromechanical resonance in magnetoelectric layered structures. *Physics of the Solid State, 52*(10), 2116−2122.

Bichurin, M. I., Petrov, V. M., Kiliba, Yu. V., & Srinivasan, G. (2002). Magnetic and magnetoelectric susceptibilities of a ferroelectric/ferromagnetic composite at microwave frequencies. *Physical Review B, 66*, 134404.

Bichurin, M. I., Petrov, V. M., Ryabkov, O. V., Averkin, S. V., & Srinivasan, G. (2005). Theory of magnetoelectric effects at magnetoacoustic resonance in single-crystal ferromagnetic-ferroelectric heterostructures. *Physical Review B, 72*, 060408.

Bichurin, M. I., Petrov, V. M., & Srinivasan, G. (2002a). Modelling of magnetoelectric effect in ferromagnetic/piezoelectric multilayer composites. *Ferroelectrics, 280*, 165.

Bichurin, M. I., Petrov, V. M., & Srinivasan, G. (2002b). Theory of magnetoelectric effects in ferromagnetic ferroelectric layer composites. *Journal of Applied Physics, 92*, 7681.

Bichurin, M. I., Petrov, V. M., & Srinivasan, G. (2003). Theory of low-frequency magnetoelectric coupling in magnetostrictive-piezoelectric bilayers. *Physical Review B, 68*, 054402.

Dong, S., Zhai, J., Li, J., & Viehland, D. (2006). Near-ideal magnetoelectricity in high-permeability magnetostrictive/piezofiber laminates with a (2-1) connectivity. *Applied Physics Letters, 89*, 252904.

Harshe, G., Dougherty, J. O., & Newnham, R. E. (1993). Theoretical modelling of multilayer magnetoelectric composites. *International Journal of Applied Electromagnetics in Materials, 4*, 145.

Harshe, G., Dougherty, J. P., & Newnham, R. E. (1993). Theoretical modelling of 3−0, 0−3 magnetoelectric composites. *International Journal of Applied Electromagnetics in Materials, 4*, 161.

Laletin, V. M., & Srinivasan, G. (2002). Magnetoelectric effects in composites of nickel ferrite and Barium Lead zirconate titanate. *Ferroelectrics, 280*, 177.

Lou, J., Pellegrini, G. N., Liu, M., Mathur, N. D., & Sun, N. X. (2012). Equivalence of direct and converse magnetoelectric coefficients in strain-coupled two-phase systems. *Applied Physics Letters, 100*, 102907.

Nan, C.-W., Bichurin, M. I., Dong, S., Viehland, D., & Srinivasan, G. (2008). Multiferroic magnetoelectric composites: historical perspectives, status, and future directions. *Journal of the Applied Physics, 103*, 031101.

Newnham, R. E., Skinner, D. P., & Cross, L. E. (1978). Connectivity and piezoelectric-pyroelectric composites. *Materials Research Bulletin, 13*, 525.

Osaretin, I. A., & Rojas, R. G. (2010). Theoretical model for the magnetoelectric effect in magnetostrictive/piezoelectric composites. *Physical Review B, 82*, 174415.

Petrov, V. M., Bichurin, M. I., Laletin, V. M., Paddubnaya, N., & Srinivasan, G. (2004). In M. Fiebig, V. V. Eremenko, & I. E. Chupis (Eds.), *Magnetoelectric interaction phenomena in crystals-NATO science series II* (Vol. 164, pp. 65−70). London: Kluwer Academic Publishers.

Petrov, V. M., Bichurin, M. I., & Srinivasan, G. (2010). Electromechanical resonance in ferrite-piezoelectric nanopillars, nanowires, nanobilayers, and magnetoelectric interactions. *Journal of the Applied Physics, 107*, 073908.

Petrov, V. M., Bichurin, M. I., Srinivasan, G., Laletin, V. M., & Petrov, R. V. (2012). Bending modes and magnetoelectric effects in asymmetric ferromagnetic-ferroelectric structure. *Solid State Phenomena, 198*, 281−284.

Petrov, V. M., Bichurin, M. I., Zibtsev, V. V., Mandal, S. K., & Srinivasan, G. (2009). Flexural deformation and bending mode of magnetoelectric nanobilayer. *Journal of the Applied Physics, 106*, 113901.

Petrov, V. M., & Srinivasan, G. (2008). Enhancement of magnetoelectric coupling in functionally graded ferroelectric and ferromagnetic bilayers. *Physical Review B, 78*, 184421.

Petrov, V. M., Srinivasan, G., Bichurin, M. I., & Galkina, T. A. (2009). Theory of magnetoelectric effect for bending modes in magnetostrictive-piezoelectric bilayers. *Journal of the Applied Physics, 105*, 063911.

Petrov, V., Srinivasan, G., Ryabkov, O. V., Averkin, S. V., & Bichurin, M. I. (2007). Microwave magnetoelectric interactions in ferrite−piezoelectric nanobilayers: theory of electric field induced magnetic excitations. *Solid State Communications, 144*, 50.

Petrov, V. M., Zibtsev, V. V., & Srinivasan, G. (2009). Magnetoacoustic resonance in ferrite-ferroelectric nanopillars. *European Physical Journal B, 71*, 367.

Ryabkov, O. V., Averkin, S. V., Bichurin, M. I., Petrov, V. M., & Srinivasan, G. (2007). Effects of exchange interactions on magnetoacoustic resonance in layered nanocomposites of yttrium iron garnet and lead zirconate titanate. *Journal of Material Research, 22*, 2174.

Ryabkov, O. V., Petrov, V. M., Bichurin, M. I., & Srinivasan, G. (2006). Magnetoacoustic resonance in tangentially magnetized ferrite-piezoelectric bilayers. *Technical Physics Letters, 32*, 1021.

Ryu, J., Carazo, A. V., Uchino, K., & Kim, H. (2001). Piezoelectric and magnetoelectric properties of Lead zirconate Titanate/Ni-ferrite Particulate composites. *Journal of Electroceramics, 7*, 17.

Shastry, S., Srinivasan, G., Bichurin, M. I., Petrov, V. M., & Tatarenko, A. S. (2004). Microwave magnetoelectric effects in single crystal bilayers of yttrium iron garnet and lead magnesium niobate-lead titanate. *Physical Review B, 70*, 064416.

Sreenivasulu, G., Petrov, V. M., Fetisov, L. Y., Fetisov, Y. K., & Srinivasan, G. (2012). Magnetoelectric interactions in layered composites of piezoelectric quartz and magnetostrictive alloys. *Physical Review B, 86*, 214405.

Srinivasan, G., De Vreugd, C. P., Laletin, V. M., Paddubnaya, N., Bichurin, M. I., Petrov, V. M., et al. (2005). Resonant magnetoelectric coupling in trilayers of ferromagnetic alloys and piezoelectric lead zirconate titanate: the influence of bias magnetic field. *Physical Review B, 71*, 184423.

Srinivasan, G., Rasmussen, E. T., Gallegos, J., Srinivasan, R., Bokhan, Yu. I., & Laletin, V. M. (2001). Magnetoelectric bilayer and multilayer structures of magnetostrictive and piezoelectric oxides. *Physical Review B, 64*, 214408.

van Suchtelen, J. (1972). Product properties: a new application of composite materials. *Philips Research Reports, 27*, 28.

This page intentionally left blank

Magnetoelectric characterization techniques

2

G. Srinivasan
Oakland University, Rochester, MI, USA

2.1 Introduction

Measurement techniques on magnetic field and electric field response of the multiferroic composites are considered here. A wide variety of techniques for frequencies ranging from DC to 110 GHz could be used (Nan, Bichurin, Dong, Viehland, & Srinivasan, 2008). There are two broad categories of magnetoelectric (ME) studies: (1) sample response to magnetic fields, termed direct-ME effect (DME) and (2) response to an electric field, called converse ME effect (CME). Several techniques have been reported so far for studies on direct and converse ME coupling. Studies on DME include low-frequency ME voltage coefficient, voltage response to magnetic fields applied at the bending and electromechanical resonance modes, nonlinear ME effects for large AC magnetic fields, static magnetic field induced polarization, and magneto-dielectric effects. For CME, one could measure low-frequency ME effects by applying an AC electric field and measuring the induced magnetic flux in a coil wound around the composite, static electric field E induced magnetization, E-tuning of inductance, or ferromagnetic resonance. Scanning probe microscopy is the preferred technique for ME measurements on nanoparticles, 1D structures (such as nanotubes and core−shell wires), and 2D structures (such as nanobilayers and nanopillars in a host matrix). These techniques are discussed in the sections to follow.

2.2 Direct-ME effects

2.2.1 Low-frequency ME effects

A parameter of importance for the DME is the magnetoelectric voltage coefficient (MEVC), that is, ratio of induced electric field to an applied magnetic field. The induced polarization P is related to the magnetic field H by the expression $P = \alpha H$, where α is the second rank ME-susceptibility tensor and is expressed in s/m in SI units (in Gaussian units $\alpha = 4\pi P/H$ is dimensionless). One generally determines $\alpha = \delta P/\delta H$ by subjecting the sample to a bias field H and an AC field δH and measuring δP or the electric field δE. The MEVC $\alpha_E = \delta E/\delta H$ (expressed in volts/ampere or volts/cm Oe) is related to α by $\alpha = \varepsilon_0 \varepsilon_r \alpha_E$, where ε_r is the relative permittivity of the material. For such measurements, it is necessary to first pole the ferroelectric phase in the composite in an electric field. In addition to the AC magnetic field δH,

Composite Magnetoelectrics. http://dx.doi.org/10.1016/B978-1-78242-254-9.00002-0
Copyright © 2015 Elsevier Ltd. All rights reserved.

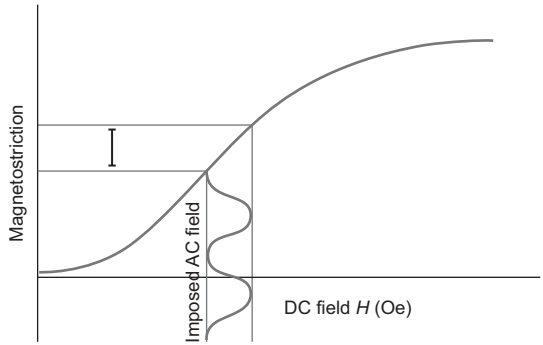

Figure 2.1 AC magnetostriction under DC bias H and an AC magnetic field.

a DC bias H is also applied so that the strength of ME coupling is enhanced. The need for DC bias is illustrated in Figure 2.1, in which schematic variation of magnetostriction λ of the ferromagnet is shown as a function of H. For $H = 0$, the mechanical deformation (or AC magnetostriction) is rather small and $\alpha_E \approx 0$. With a bias field, however, the AC magnetostriction can be substantially enhanced. It is also clear from Figure 2.1 that $\alpha_E \approx 0$ when the magnetostriction attains saturation.

Figure 2.2 shows a set up for the measurement of MEVC (http://www.ferrodevices.com/1/297/files/MER10-AMF2012Presentation.pdf). The sample is subjected to a bias field H (with the use of an electromagnet) and an AC field δH produced by a pair of Helmholtz coils. The coils must not be wound (or mounted) on the pole pieces of the magnet.

The sample must be shielded from picking up noise by placing it inside a metal box. It is necessary to use a three-terminal network for measurement of the differential

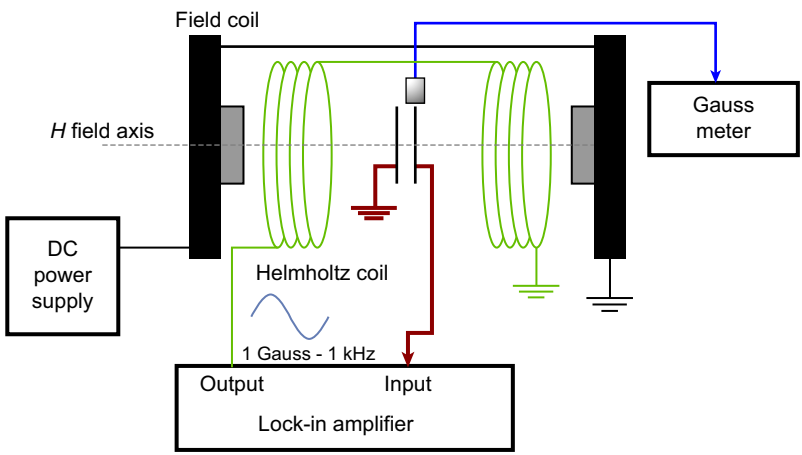

Figure 2.2 A set up for low-frequency magnetoelectric voltage coefficient (http://www.ferrodevices.com/1/297/files/MER10-AMF2012Presentation.pdf).

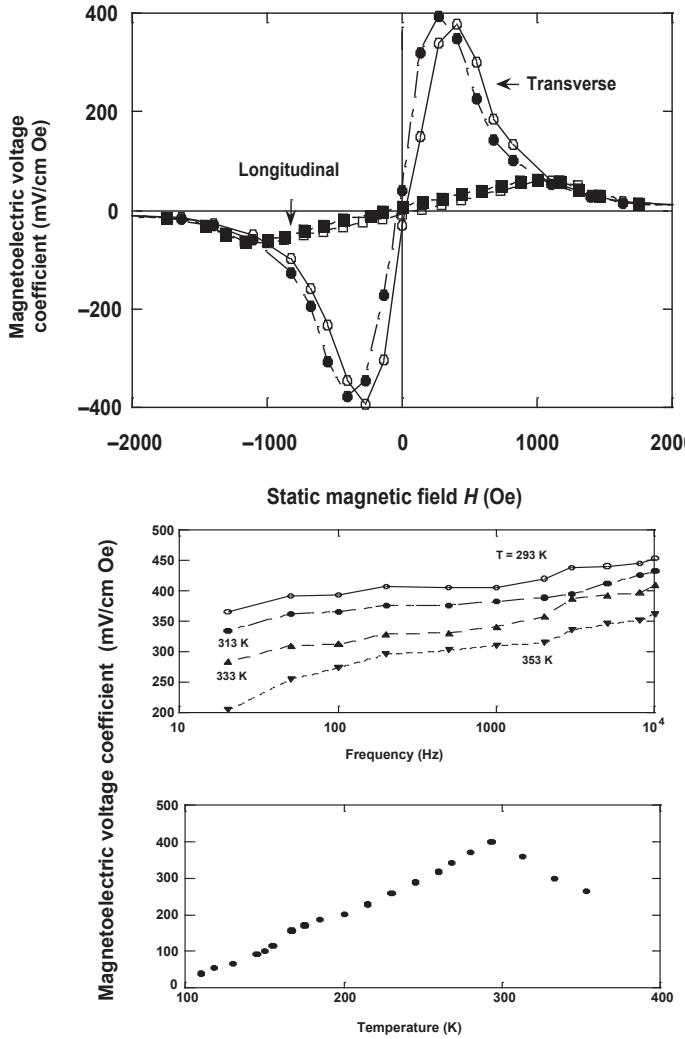

Figure 2.3 Representative data showing magnetoelectric voltage coefficient versus H and temperature dependence (Srinivasan et al., 2001).

voltage across the sample. Lock-in detection is preferable for accurate determination of MEVC. One measures MEVC as a function of the bias field H, frequency and amplitude of δH, applied field directions, and temperature. Typical MEVC dependence on H, f, and temperature is shown in Figure 2.3 (Srinivasan et al., 2001). The MEVC is relatively high when H and δH are parallel to each other and to the sample plane, compared to out-of-plane magnetic fields due to demagnetization associated with out-of-plane fields. Several composites show high MEVC at room temperature, as in Figure 2.3.

2.2.2 ME effects at electromechanical resonance (1 kHz–2 MHz)

A powerful tool for investigations on the nature of ME interactions is measurements at electromechanical resonance that could occur, depending on the sample dimensions, over a few hundred Hz to 2 MHz (Nan et al., 2008). The nature of coupling is the standard effect, that is, induced polarization due to AC magnetic field, but the frequency of the AC field is tuned to bending, longitudinal, or thickness electromechanical resonance mode. A pulsed-magnetic field technique for studies on frequency characteristics of ME coefficients was reported in Fetisov, Kamentsev, Ostashchenko, and Srinivasan (2004). As shown in Figure 2.4, the method is based on the excitation of a composite with magnetic field pulses, followed by the measurement of voltage across the sample and Fourier analysis of the signal.

2.2.3 Nonlinear ME effects

Most studies on ferromagnetic–ferroelectric composites have been devoted to investigation of ME interactions under AC magnetic field amplitudes, for which the voltage response is a linear function of the AC field. But the ferromagnetic materials are characterized by nonlinear magnetostriction λ versus field dependence (as in Figure 2.1), and ferroelectric materials are characterized by nonlinear dependence of the piezoelectric coefficient d on E. Thus, under certain conditions and rather high amplitude of the

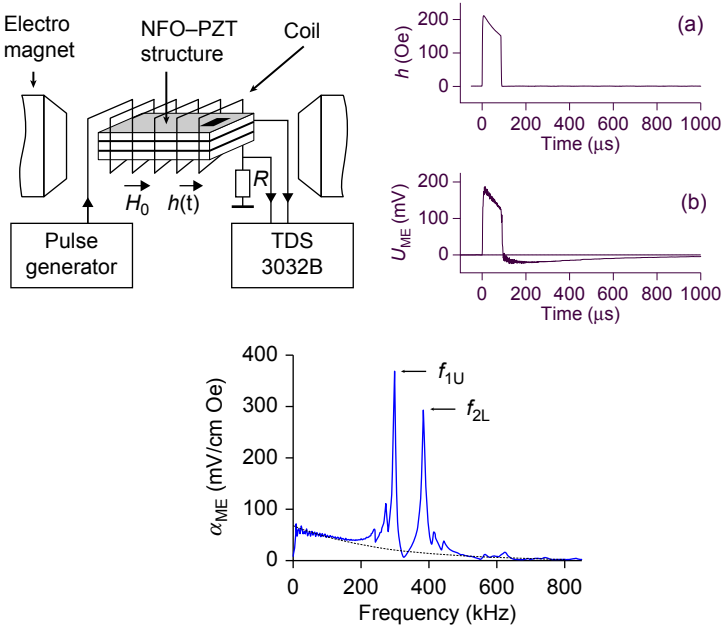

Figure 2.4 Schematics of pulsed-magnetic field ME measurement system, sample response to a pulsed magnetic field, and Fourier transform showing peaks in magnetoelectric voltage coefficient at acoustic resonance modes (Fetisov et al., 2004).

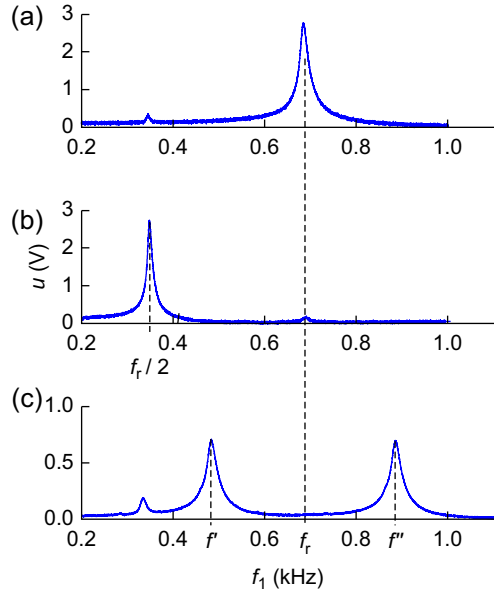

Figure 2.5 Measured dependences of the generated voltage u versus frequency: (a) for linear magnetoelectric (ME) effect showing a peak at the bending resonance, for bias field $H = 18$ Oe, and AC field $h = 2.8$ Oe; (b) nonlinear ME effect showing frequency doubling for $H = 0$, $h = 14$ Oe. The peak occurs when the excitation occurs at half the bending mode frequency; (c) for nonlinear field mixing showing peaks at sum and difference of two AC fields, $H = 0$, $f_1 = 700$ Hz, $h_1 = 10$ Oe, $f_2 = 0.2$ kHz, $h_2 = 10$ Oe (Burdin et al., 2013).

AC fields, a nonlinear ME response is expected in the composites. Several recent reports have dealt with nonlinear phenomena in ME composites. Frequency doubling and generation of harmonics were observed in composites such as layered ferrite−lead zirconate titanate (PZT) (Burdin et al., 2013). Figure 2.5 illustrates a specific example for linear and nonlinear ME effects. When a bias field H and an AC field of 10 Oe are applied to a composite, the mechanical deformation occurs at the excitation frequency (Burdin et al., 2013). One therefore measures a linear ME response characterized by a resonance ME coupling at $f = f_r = 700$ Hz as in Figure 2.5(a). But when $H = 0$ for the same AC field, the AC magnetostriction occurs at twice the excitation frequency. This frequency doubling leads to appearance of the peak in Figure 2.5(b) for an excitation frequency $f = f_r/2$. It was also reported that nonlinearity of the magnetostriction results in doubling of the frequency and generation of voltages with sum and difference frequencies when AC signals of two different frequencies are applied as in Figure 2.5(c) (Burdin et al., 2013).

2.2.4 Induced polarization

The strength of DME could also be measured in terms of the polarization induced by a static magnetic field H. A ferroelectric tester capable of measuring P versus E is used.

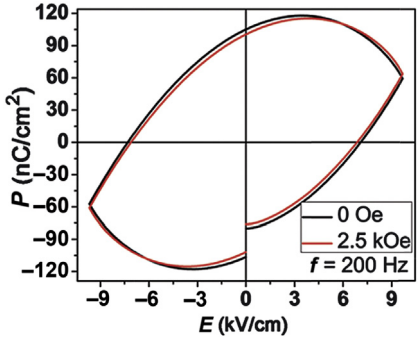

Figure 2.6 Polarization versus electric field E for static magnetic field $H = 0$ and 2.5 kOe for a disc of nanocomposites of barium titanate and nickel ferrite (Sreenivasulu et al., 2014).

Samples are placed in a measurement cell, and ferroelectric hysteresis are obtained for a series of in-plane or out-of-plane H as in Figure 2.6 (Sreenivasulu et al., 2014). Several composites are reported to show a change in the remnant polarization P_r and the coercive field E_c under H. The strength of ME coupling is then defined by the ratio $\Delta P_r/P_r(H = 0) = [P_r(H) - P(H = 0)]/P_r\,(H = 0)$, where ΔP_r is the change in P_r.

A related measurement procedure of importance is positive-up negative-down (PUND) measurements under H. In PUND measurements, a series of five voltage pulses are used for switchable polarization measurements in a composite as described in Evans.

2.2.5 Magneto-dielectric effects

The magneto-dielectric effect (MDE) involves studies on the influence of a static magnetic field on the dielectric constant of a material (Sreenivasulu et al., 2014). It is a powerful tool for investigations on the nature of direct-ME effects in composite multiferroics. A variety of measurements are possible: (1) magnetic field induced variation in the permittivity ε over a wide frequency range (from a few hundred Hz to 110 GHz), (2) ε versus H under dielectric resonance in the composite, and (3) dielectric resonance frequency f_r versus H. For MDE at low frequencies, one could perform magneto-capacitance measurements on the composite. MDE over 1−110 GHz usually requires the use of a vector network analyzer for measurements of reflected and transmitted power in a composite. Techniques including the transmission line method, which involves placing a sample of an appropriate shape inside a rectangular waveguide or coaxial airline, resonance cavity techniques, or horn antennas are used. Waveguide fixtures are band-limited but operate at higher frequencies than coaxial airlines. Composites must be rectangular in shape and completely fill the cross section of a waveguide without gaps at the fixture walls. Coaxial airlines require samples of specific shape and dimensions as well. During the measurements, a static magnetic field is applied either parallel or perpendicular to the sample plane. Figure 2.7(a) shows real part of the relative permittivity ε_r' versus f for a series of H for a composite of core−shell

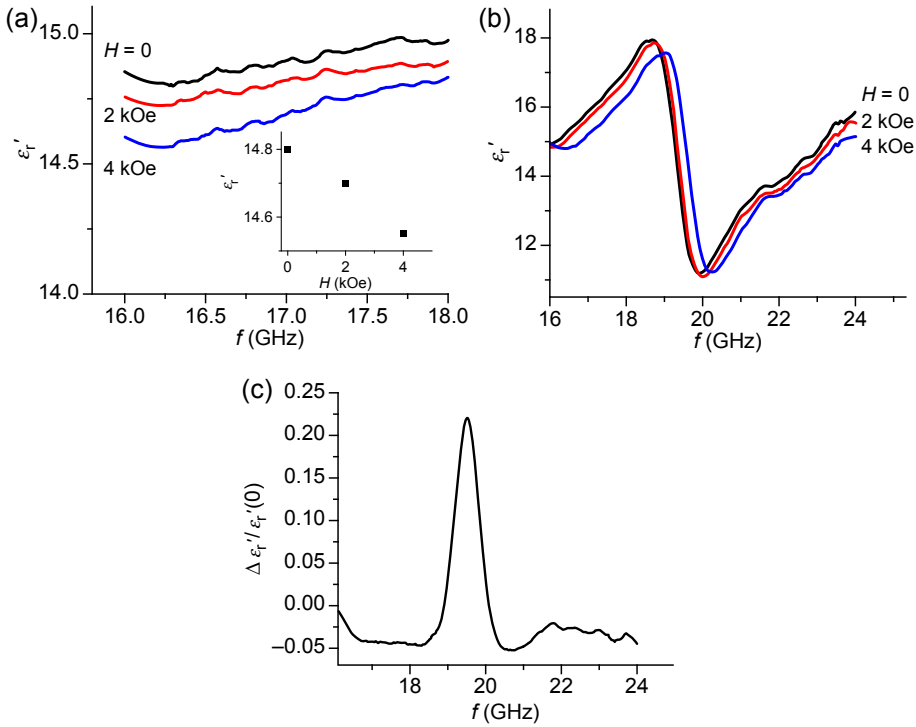

Figure: 2.7 Magneto-dielectric effects measured on a disc of core−shell nanoparticles of barium titanate and nickel ferrite (a) away from dielectric resonance, (b) at dielectric resonance, and (c) fractional change in ε_r' for the data in (b) for H = 4 kOe (Sreenivasulu et al., 2014).

nanoparticles of nickel ferrite and barium titanate (Sreenivasulu et al., 2014). These data were obtained for the sample placed in a waveguide. Figure 2.7(a) also shows the fractional change in the permittivity as a function of H.

Investigations on MDE at dielectric resonance in the composites are of interest since the resonance frequency is a function of the dielectric constant. Thus, any H-induced changes in ε_r' are directly reflected as a change in resonance frequency. One could measure (1) ε_r' versus f as a function of H in the region of dielectric resonance and (2) resonance frequency f_r versus H. It is essential that appropriate sample size for dielectric resonance over the specific frequency range is chosen. Typical data on ε_r' versus f for a series of H over the range 16−24 GHz are shown in Figure 2.7(b). A resonance is clearly seen in the data and is due to dielectric resonance in the sample of core−shell nanocomposite. With the application of H, a general decrease in ε_r' is observed except for a narrow frequency range extending from 19 to 20 GHz over which ε_r' is found to increase with increasing H. The fractional change in the dielectric constant defined as $\Delta\varepsilon_r'/\varepsilon_r'(0) = [\varepsilon_r'(H) - \varepsilon_r'(H = 0)]/\varepsilon_r'(H = 0)$for $H = 4$ kOe is shown in Figure 2.7. For frequencies away from the resonance region, one measures 1−5% decrease in ε_r', while at resonance the dielectric constant increases by 23%. Thus, a giant magneto-dielectric effect in the composite with a 28% net change in

permittivity is evident in the data. The change in the resonance frequency with H is also evident from the data in Figure 2.7. The shift in f_r with H could be attributed to the change in the permittivity that arises due to strain-mediated ME coupling in the composite (Sreenivasulu et al., 2014).

2.3 Converse ME effects

2.3.1 Low-frequency CME

In the case of converse ME effect, an external AC electric field E produces a deformation of piezoelectric layers, resulting in a change in the magnetic parameters of the composite (Fetisov, Petrov, & Srinivasan, 2007; Sun & Srinivasan, 2012). Thus with a pick up coil wound on a composite, one could apply an AC voltage across the piezoelectric and measure the resulting change in the magnetic induction B by measuring the induced voltage in the coil. The strength of the ME coupling is measured in terms of $\alpha_B = B/E$.

Figure 2.8 shows a schematic view of the setup. A trilayer composite of PZT−Ni−PZT is shown with a coil wound around the sample for measuring the induced B. A DC bias field H is applied to the sample. An AC voltage U_0 applied to PZT results in an induced U_{in} in the coil. The AC voltages generated in the coil could be measured as functions of frequency and magnitude of input AC fields and for different values and orientations of bias magnetic field H. Figure 2.8 shows typical U_{in} versus H for in-plane and out-of-plane bias magnetic fields (Fetisov et al., 2007).

2.3.2 Electric field induced magnetization

The nature of *static* E-tuning of magnetic parameters of composites is studied by electric field induced changes in the magnetic hysteresis loops with the use of a vibrating sample magnetometer. Figure 2.9 shows E-dependence of M versus H for a composite of nickel ferrite (NFO)/lead zinc niobate-lead titanate (PZN-PT). Data are for H along the [100] and [110] axes of PZN-PT (Li et al., 2011). Both

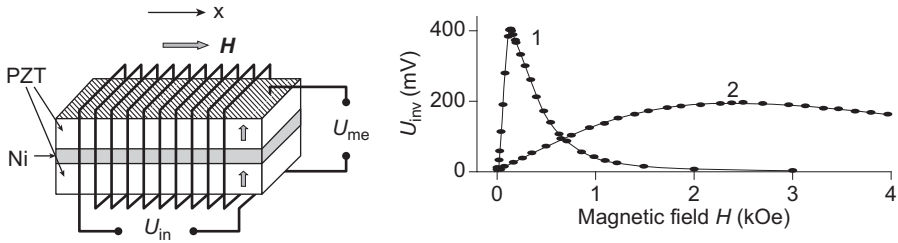

Figure 2.8 Low-frequency converse ME effects (CME) in a trilayer of Ni and PZT. An AC voltage is applied across the trilayers, and the resulting induced voltage due to CME is measured with the pick-up coil. The CME voltage is shown as a function of static field H for the field parallel (1) and perpendicular (2) to the sample plane (Fetisov et al., 2007).

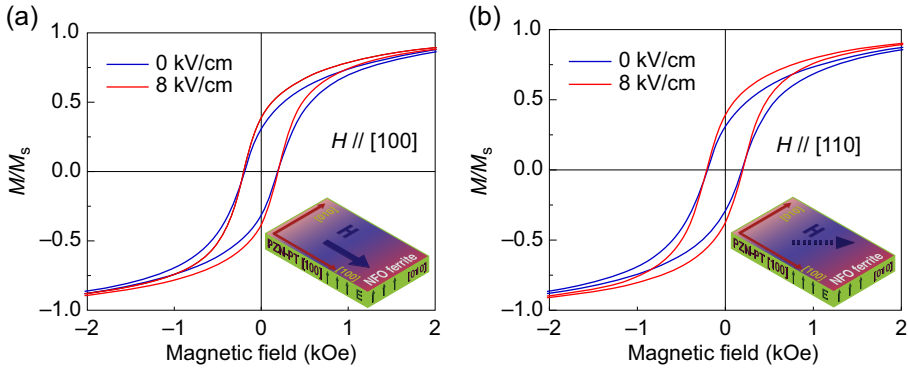

Figure 2.9 Magnetic hysteresis under static electric field for studies on CME. The figure shows influence *of E on M* versus *H* for a film of nickel ferrite deposited on PZN-PT substrates. *H* is applied parallel to either the [100] or the [110] axis of PZN-PT (Li et al., 2011).

orientations display an *E*-induced easy magnetization process. The fractional remanent magnetization change $\Delta M/M(E=0) = [M(E) - M(E=0)]/M(E=0)$ reaches 15% with $E = 8$ kV/cm applied across PZN-PT.

2.3.3 Static electric field tuning of inductance

A ferromagnetic−ferroelectric composite could potentially form the core of a high-frequency inductor. Such an inductor could be tuned with a DC electric field *E*. The strength of the ME effect could be expressed in terms of the change in the inductance (Lou, Reed, Liu, & Sun, 2009). Electrostatically tunable ME inductors with two layers of Metglas and one layer of PZT are shown in Figure 2.10. Measured inductance *L* versus *f* for a series of *E* is also shown in the figure. A decrease *in L* with *increasing E* is evident from the data (Lou et al., 2009).

2.3.4 Electrostatic tuning of ferromagnetic resonance

Ferromagnetic resonance (FMR) is ideal for studies on CME effects. There are two types of ME interactions at FMR: (1) coupling between microwave magnetic fields and DC electric fields and (2) coupling between microwave magnetic and electric fields (Nan et al., 2008). Only the first effect is considered here. The technique is based on the fact that magnetic resonance frequency is strain-dependent, and the magnitude of this strain-dependence is determined by the piezoelectric and magnetoelastic constants. The *E*-induced mechanical strain manifests as an internal magnetic field in the ferromagnetic layer, leading to a shift δH_E in the FMR field. The shift δH_E is strongly influenced by, among other factors, the sample magnetization, magnetostriction λ, and piezoelectric coupling *d*. Information on the nature of ME coupling could therefore be obtained from data on shift δH_E versus *E*. Such measurements of course could only be performed on composites in which the ferromagnetic resonance has a low FMR line-width.

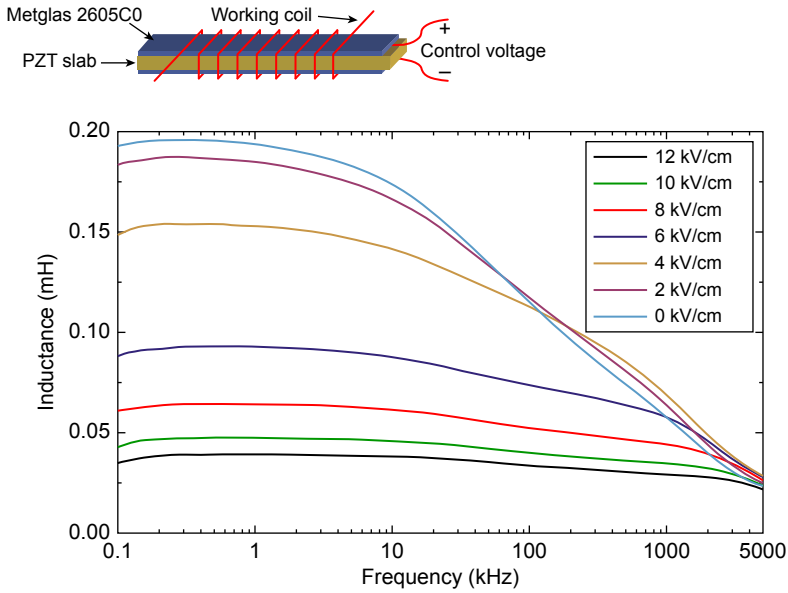

Figure 2.10 Inductance L measured for a coil wound around a Metglas−PZT composite. L is measured as a function of frequency for a series of static electric fields applied across PZT (Lou et al., 2009).

The measurements could be done with (1) cavity, (2) stripline, or (3) shorted waveguides. Measurements with cavities are done using a modified electron spin resonance spectrometer. A TE_{102} reflection-type cavity with holes (1 mm diameter) at the center of the cavity bottom or at one-quarter wavelength from the bottom on the narrow side was used in the work reported in Shastry, Srinivasan, Bichurin, Petrov, and Tatarenko (2004). The holes facilitated measurements by placing the sample *outside* the cavity so that the electric field can be applied to the piezoelectric layer. One then measures FMR profiles as a function of E, as illustrated in Figure 2.11. Data on field shift δH_{E} are obtained for a series of E, and the strength of ME coupling $A = \delta H_{\mathrm{E}}/E$ is estimated from the slope of δH_{E} versus E data (Shastry et al., 2004).

Resonant cavity techniques are appropriate for CME studies at a fixed frequency. Measurements over a wide frequency band are possible with a stripline transducer. The schematics of the setup with a microstripline structure are shown in Figure 2.12 (Fetisov & Srinivasan, 2006). A composite of yttrium iron garnet and PZT is shown on a microstrip transducer on an alumina substrate. The structure is placed between the poles of an electromagnet so that a bias magnetic field H could be applied parallel or perpendicular to the sample plane. A DC electrical field is generated across PZT by applying a voltage. Microwave measurements are carried out using a vector network analyzer. Low-input power on the order of 1 mW is chosen to prevent heating of the sample due to power absorption at FMR. Profiles of reflected power $P_{\mathrm{ref}}(f)$ versus f are recorded for a series of H and E. Figure 2.12 shows representative reflection spectra, $S_{11}(f) = 10 \log [(P_{\mathrm{ref}}(f)/P_{\mathrm{in}}(f)]$ versus f, for an in-plane $H = 1.12$ kOe.

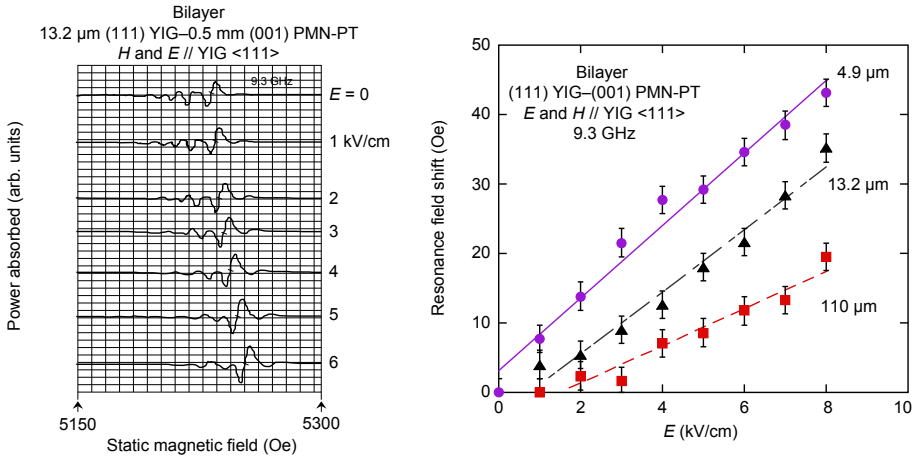

Figure 2.11 Profiles of power absorbed versus static field H showing ferromagnetic resonance in a YIG/lead magnesium niobate-lead titanate (PMN-PT) bilayer. Notice the shift in the profiles with the application of E to PMN-PT. Data on resonance field shift are shown as a function of E (Shastry et al., 2004).

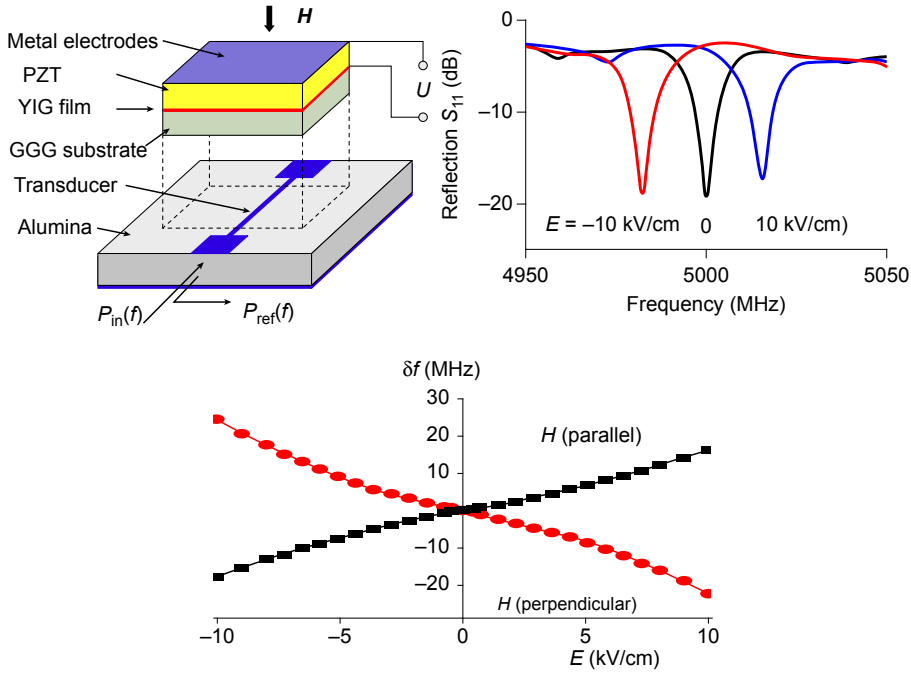

Figure 2.12 A microstripline transducer for wide-band converse ME effects studies by E-tuning of ferromagnetic resonance (FMR). Profiles of FMR are for $E = 0$ and ± 10 kV/cm. FMR frequency shift versus E data are for static field H parallel or perpendicular to the sample plane (Fetisov & Srinivasan, 2006).

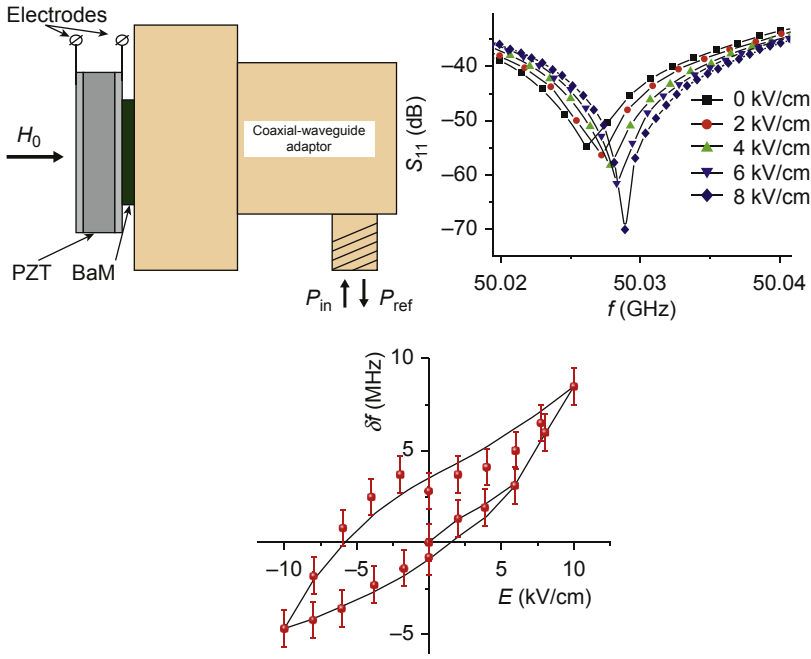

Figure 2.13 A shorted waveguide setup for converse ME effect studies by tuning of ferromagnetic resonance (FMR), FMR profiles for a series of E for bilayer of barium ferrite−PZT, and FMR frequency shift versus E for the bilayer. (Srinivasan et al., 2006).

For $E = 0$, the spectra contained a well-defined FMR absorption peak at ∼5 GHz with a 3-dB line-width $\Delta f = 3.4$ MHz. With the application of $E = 10$ kV/cm, the FMR peak shifted to a higher frequency by $\delta f_1 = 16$ MHz. When the polarity of E was reversed by reversing the voltage applied to PZT, the peak downshifted by $\delta f_1 = -18$ MHz. A similar electric field tuning of the absorption peak could be observed for H perpendicular to the bilayer plane, as shown in the figure. However, the shifts in FMR are usually higher in magnitude than for in-plane H (Fetisov & Srinivasan, 2006).

Since stripline measurements are limited to frequencies below 40 GHz, it is necessary to use resonance cavities or waveguide shorts for E-tuning of FMR for CME studies over 40−110 GHz. The measurement cell for such studies on a bilayer of barium ferrite and PZT is shown in Figure 2.13 and consists of a coaxial-to-(WR-17) waveguide adapter (Srinivasan, Zavislyak, & Tatarenko, 2006). A bilayer of M-type hexagonal barium ferrite (BaM) bonded to the silvered surface of PZT is shown. When the sample was placed at the open end of the waveguide, the silver electrode at the BaM−PZT interface acted as a classical short load of the waveguide. A vector network analyzer is then used for data on scattering matrix element S_{11} versus f for a series of H and for E. Typical profiles of FMR under E and shift in FMR frequency δf versus E are also shown in Figure 2.13 (Srinivasan et al., 2006).

2.4 Scanning probe microscopy techniques for ME effects in nanocomposites

Although there have been considerable efforts devoted to studies on ME interactions in bulk, layered, and thick film composites, a focused effort on nanostructured analogs of these structures is lacking at present. Once anticipates a strong ME coupling in nanocomposites due to a large surface-to-volume ratio. Some groups in recent years have reported on the synthesis of composites of core−shell nanoparticles, nanopillars in a host matrix, nanobilayers, coaxial tubes in a template, and core−shell wires. Some of these nanocomposites have been further self-assembled or magnetic and/or electric field-assisted assembly to obtain superstructures. Studies on the nature of ME coupling in these nanocomposites would require innovative techniques. The preferred tool so far has been scanning probe microscopy. Piezo force microscopy (PFM) under an applied magnetic field is used for studies on DME and magnetic force microscopy (MFM) in an applied voltage for CME. A few representative examples on the utility of these techniques for studies on bilayers, nanopillars, and nanotubes and wires are discussed here.

For DME in nanobilayers and core−shell fibers, several groups used PFM under H. PFM was used to monitor the ferroelectric domain characteristics and switching under the influence of a magnetic field (Xie, Ma, Liu, & Li, 2011). Data on PFM amplitude and phase images and piezoelectric displacement were used for quantitative estimates of ME coupling strength.

Similarly, MFM is used for information on the nature of CME. A strong CME was inferred in a nanocomposite from changes in the MFM image attributed to reversal in in-plane magnetization under an applied static electric field (Caruntu et al., 2012). CME studies by FMR were reported on an array of core−shell ferrite-ferroelectric nanotubes grown in an alumina template (Carignanet al, 2011). A microstripline deposited on the alumina template as in Figure 2.14 was used. One could also use a coplanar slotline shown in Figure.2.14 for FMR in nanocomposites (Beguhn et al., 2012).

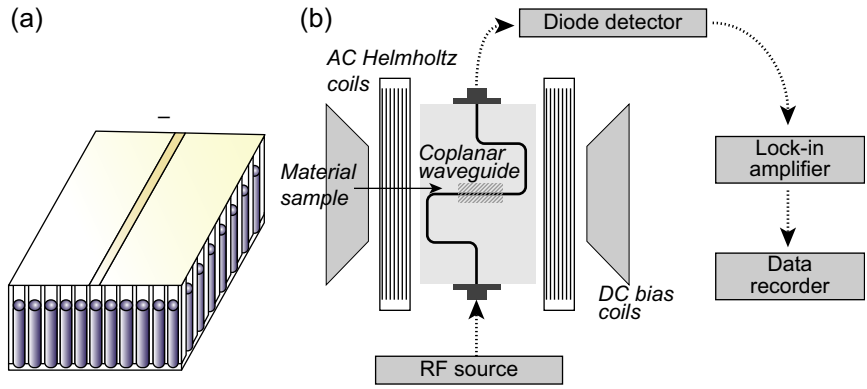

Figure 2.14 (a) Microstripline used for ferromagnetic resonance (FMR) in the ferrite−ferroelectric array of nanotubes in an alumina template (Carignanet al, 2011), (b) a high sensitivity FMR setup with coplanar waveguide for FMR in nanocomposites (Beguhn et al., 2012).

References

Beguhn, S., Zhou, Z., Rand, S., Yang, X., Lou, J., & Sun, N. X. (2012). *Journal of Applied Physics, 111*, 07A503.

Burdin, D. A., Chashin, D. V., Ekonomov, N. A., Fetisov, Y. K., Fetisov, L. Y., Sreenivasulu, G., et al. (2013). *Journal of Applied Physics, 113*, 033902.

Carignan, L., Yelon, A., Menard, D., & Caloz, C. (2011). Ferromagnetic nanowire metamaterials: Theory and applications. *IEEE Transactions on Microwave Theory and Techniques, 59*, 2568.

Caruntu, G., Ypurdkhani, A., Vopsaroiu, M., & Srinivasan, G. (2012). *Nanoscale, 4*, 3218.

Evans J.T. The relationship between hysteresis and PUND responses. http://www.ferrodevices.com/1/297/files/HysteresisEqualsPUND.pdf.

Fetisov, Y. K., Kamentsev, K. E., Ostashchenko, A. Y., & Srinivasan, G. (2004). *Solid State Communications, 132*, 13.

Fetisov, Y. K., Petrov, V. M., & Srinivasan, G. (2007). *Journal of Material Research, 22*, 2074.

Fetisov, Y. K., & Srinivasan, G. (2006). *Applied Physics Letters, 88*, 143503.

Li, N., Liu, M., Zhou, Z., Sun, N. X., Murthy, D. V. B., Srinivasan, G., et al. (2011). *Applied Physics Letters, 99*, 192502.

Lou, J., Reed, D., Liu, M., & Sun, N. X. (2009). *Applied Physics Letters, 94*, 112508.

Nan, Ce-W., Bichurin, M. I., Dong, S., Viehland, D., & Srinivasan, G. (2008). *Journal of Applied Physics, 103*, 031101.

Shastry, S., Srinivasan, G., Bichurin, M. I., Petrov, V. M., & Tatarenko, A. S. (2004). *Physics Review B, 70*, 064416.

Sreenivasulu, G., Popov, M., Chavez, Ferman A., Hamilton, Sean L., Lehto, Piper R., & Srinivasan, G. (2014). *Applied Physics Letters, 104*, 052901.

Srinivasan, G., Rasmussen, E. T., Gallegos, J., Srinivasan, R., Bokhan, Yu I., & Laletin, V. M. (2001). *Physics Review B, 64*, 214408.

Srinivasan, G., Zavislyak, I. V., & Tatarenko, A. S. (2006). *Applied Physics Letters, 89*, 152508.

Sun, N. X., & Srinivasan, G. (2012). *SPIN, 2*, 1240004.

Xie, S., Ma, F., Liu, Y., & Li, J. (2011). *Nanoscale, 3*, 3152.

Layered multiferroic composites

3

G. Srinivasan
Oakland University, Rochester, MI, USA

This chapter is on multiferroic composites with specific focus on thick film and thin film layered composites with ferroelectric oxides and ferromagnetic or ferrimagnetic metals/alloys or oxides. Ferromagnetic/ferrimagnetic oxides, including spinel ferrites, hexagonal ferrites, or lanthanum manganites for the magnetic phase and lead zirconate titanate (PZT), barium titanate (BTO), or lead magnesium niobate-lead titanate (PMN-PT) for the ferroelectric phase, are considered (Lawes & Srinivasan, 2011; Ma, Hu, Li, & Nan, 2011; Martin & Ramesh, 2012; Nan, Bichurin, Dong, Viehland, & Srinivasan, 2008; Srinivasan, 2010; Vaz, Hoffmann, Ahn, & Ramesh, 2010; Wang, Zhang, & et al., 2014). Composites with 3d transitions metals such as Ni, Co, Fe, and alloys such as Terfenol-D, Galfenol, permendur, or Metglas are discussed (Lawes & Srinivasan, 2011; Nan et al., 2008; Srinivasan, 2010). Recent efforts on composites with piezoelectric aluminum nitride (AlN), lanthanum-gallium-tantalate (langatate), and quartz are also addressed (Marauska et al., 2013; Sreenivasulu, Fetisov, Fetisov, & Srinivasan, 2012; Sreenivasulu, Petrov, Fetirov, Fetirov, & Srinivasan, 2012). Early works on magnetoelectric (ME) composites dealt with bulk composites prepared by mixing and sintering ferrite and barium titanate powders, whereas recent works have mainly focused on layered composites and nanostructures (Gao, Das, Xing, Li, & Viehland, 2010; Sun & Srinivasan, 2012; Viswan, Gray, Wang, & Li, 2011; Wang et al., 2011; Zheng et al., 2004). The strongest ME coupling is expected in a layered structure due to (1) low leakage currents and (2) ease of poling to align the electric dipoles and strengthen the piezoelectric effect (Nan et al., 2008; Srinivasan, 2010). Thick film layered samples are synthesized by laminating and sintering films of the two phases made by tape casting or by bonding single crystal or polycrystalline platelets (Nan et al., 2008). Efforts to date on nanocomposites include nanobilayers by deposition techniques, including molecular beam epitaxy (MBE), pulsed laser deposition (PLD), and chemical vapor deposition (CVD) (Vaz et al., 2010; Lawes & Srinivasan, 2011; Zheng et al., 2004).

Several techniques were employed for studies on direct ME effect (DME) and converse ME (CME) coupling in these composites (Nan et al., 2008). A giant low-frequency DME effect and resonance enhancement of the coupling at bending or electromechanical resonance were reported for a variety of systems (Nan et al., 2008; Srinivasan, 2010; Wang, Hu, Lin, & Nan, 2010). Studies on DME in nanocomposites utilized scanning probe microscopy techniques (Li et al., 2010; Zheng et al., 2004). Ferromagnetic resonance (FMR) is a powerful tool for studies on CME effects since E-field applied to the composite manifests as frequency or field shift in FMR profile, and the strength of CME coupling could be obtained from such data on shift δH_E versus E. Strong converse−ME effects in ferrite−ferroelectric composites were

Composite Magnetoelectrics. http://dx.doi.org/10.1016/B978-1-78242-254-9.00003-2
Copyright © 2015 Elsevier Ltd. All rights reserved.

reported with the use of FMR studies (Sun & Srinivasan, 2012). Models were developed for low-frequency and resonance DME effects and for CME at FMR (Srinivasan, 2010). Significant developments in the application aspects of metals/oxide-layered composites include magnetic sensors and E-tunable ferrite resonator, filter, phase shifter, and miniature antennas (Srinivasan, 2010; Sun & Srinivasan, 2012; Wang et al., 2011; Wang, Li, & Viehland, 2014). We conclude this chapter with comments on potential future efforts on the physics of ME coupling and applications.

3.1 Ferromagnetic–ferroelectric composites

The materials of choice for the oxide ME composites are ferrimagnetic spinel ferrites, M-, Y-, Z-type hexagonal ferrites, or yttrium iron garnet (YIG) and ferroelectric PZT or BTO due to their robust ferroic response at room temperature and high chemical, thermal, and mechanical stability (Bai, Zhang, Li, & Viehland, 2010; Bichurin, Viehland, & Srinivasan, 2007; Cho & Priya, 2011; Cross, 1993; Das, Kalinikos, Barman, & Patton, 2007; Deng, Zhang, Lin, & Nan, 2008; Gheevarughese, Laletsin, Petrov, Srinivasan, & Fedotov, 2007; Landolt & Bornstein, 1970; Li et al., 2011; Li, Wang, Lin, & Nan, 2009; Li, Zhou, et al., 2013; Liu, Obi, & Kai, 2010; Mandal, Sreenivasulu, Petrov, & Srinivasan, 2010; Mandal, Sreenivasulu, Petrov, & Srinivasan, 2011; Mathe, Srinivasan, & Balbashov, 2008; Park, Khachaturyan, & Priya, 2012; Petrov & Srinivasan, 2008; Ryu, Baek, &Han, 2012; Srinivasan, Rasmussen, Levin, & Hayes, 2002; Tatarenko & Srinivasan, 2011; Yan, Zhou, & Priya, 2013; Yang, Cho, Park, & Priya, 2011; Yang, Park, Cho, & Priya, 2010; Yang, Priya, Li, & Viehland, 2009; Zavislyak, Sohatsky, Popov, & Srinivasan, 2013; Zhang, Deng, Ma, Lin, & Nan, 2008; Zhang, Srinivasan, & Balbashov, 2009). The choice of ferrite is determined by (1) the magnetostriction λ, the piezomagnetic coefficient $q = d\lambda/dH$, and permeability μ that determine the strength of DME coupling and (2) desired magnetic anisotropy field for FMR over specific frequencies for studies on CME. Nickel ferrite and Ni–Zn ferrites have high values of λ, q, and μ for synthesizing composites with strong DME (Landolt & Bornstein, 1970). For strong CME and for E-tunable FMR devices such as resonators and filters, one prefers a ferrite with high λ, low high-frequency losses and with high magnetic anisotropy field so that FMR in the desired frequency range occurs for nominal bias magnetic fields (Sun & Srinivasan, 2012). Spinel ferrites and YIG with cubic anisotropy of 50–500 Oe are used in composites for strong CME and device applications over a range of 1–20 GHz (Landolt & Bornstein, 1970). Y-type hexagonal ferrites $Ba_2Zn_2Fe_{12}O_{22}$ (Zn_2Y) with easy plane anisotropy of 1–10 kOe are preferred for 20–40 GHz. M-type hexagonal ferrites with uniaxial anisotropy $BaFe_{12}O_{19}$ (BaM), SrM, and Al-substituted ferrites, including (Ba, Al) M and (Sr, Al) M, are ideal for the frequency range 40–110 GHz (Landolt & Bornstein, 1970).

Both PZT and PMN-PT are ferroelectrics of importance for use in the composite. For strong CME, one desires a high value of d, where d is the piezoelectric coupling coefficient (Cross, 1993). For strong DME, however, it is necessary to have a high value for d/ε (Marauska et al., 2013; Sreenivasulu, Fetisov, et al., 2012; Sreenivasulu, Petrov, et al., 2012; Viswan et al., 2011). The ferroelectric

nature of PZT, $Pb(Zr_{1-x}Ti_x)O_3$, is critically dependent on the Zr/Ti ratio, with $PbZrO_3$ being an antiferroelectric and $PbTiO_3$ ferroelectric at room temperature. Much interest is focused on compositions close to the morphotropic phase boundary (MPB) for Ti ratio of ~47% because of their large piezoelectric constants $d_{33} = 200-600$ pm/V (Cross, 1993). Similarly, PMN-PT, $(1-x)$ $Pb(Mg_{1/3}Nb_{2/3})O_3 - xPbTiO_3$, which is a relaxor ferroelectric, shows an MPB around 33%Ti and $d_{33} = 1000-2500$ pm/V (Cross, 1993). Nonferroelectrics such as ZnO, AlN, quartz, and langatate with very high values of d/ε have been used in recent years in composites showing strong DME for use as magnetic sensors (Marauska et al., 2013; Sreenivasulu, Fetisov, et al., 2012; Sreenivasulu, Petrov, et al., 2012; Viswan et al., 2011). Synthesis of layered thick film composites of ferrite–PZT, lanthanum calcium manganite (LCMO)–PZT, and lanthanum strontium manganite (LSMO)-PZT involved laminating and sintering thick films of the two phases by tape-casting or epoxy bonding of platelets of single crystal or polycrystalline oxides (Bai et al., 2010; Bichurin et al., 2007; Das et al., 2007; Gheevarughese et al., 2007; Li et al., 2010, 2011; Mathe et al., 2008; Srinivasan et al., 2002; Tatarenko & Srinivasan, 2011; Wang et al., 2010; Wang, Li, et al., 2014; Yang et al., 2009; Zavislyak et al., 2013; Zhang et al., 2009). Thin film composites are made by techniques including PLD, MBE, and CVD (Li et al., 2011; Wang et al., 2010).

Layered ferromagnetic metals/alloys–ferroelectric composites are of interest for studies on the nature of ME interactions and for useful technologies. The FM layer serves the dual role of ferromagnetic phase and electrodes for the structure. Studies on composites with 3d-transition metals (Ni, Fe, Co), permendur (an alloy of Fe–Co–V), Metglas, Galfenol (alloy of Fe and Ga), and Terfenol-D reveal strong ME coupling (Brintlinger et al., 2010; Chen, Li, Wen, & Zhu, 2014; Fetisov, Kamentsev, Chashin, Fetisov, & Srinivasan, 2009; Greve et al., 2010; Gribov et al., 2014; Guo, Zhou, & Liu, 2010; Hockel, Wu, & Carman, 2011; Kirchhof et al., 2013; Lage et al., 2012; Laletin, Paddubnaya, Srinivasan, DeVreugd, & Bichurin, 2005; Li et al., 2012; Li, Wen, et al., 2013; Liu, Lou, Li, & Sun, 2011; Liu et al., 2013; Nan, Hui, Rinaldi, & Sun, 2013; Nan et al., 2012; Onuta, Wang, Long, Lofland, & Takeuchi, 2012; Park, Cho, Arat, Evey, & Priya, 2010; Piorra et al., 2013; Shen, Gao, Wang, Li, & Viehland, 2014; Sreenivasulu, Laletin, Petrov, Petrov, & Srinivasan, 2012; Srinivasan, DeVreugd, Laletin, Paddubnaya, & Bichurin, 2005; Wang et al., 2012; Wu et al., 2013; Yao, Hou, Dong, & Li, 2011). Amongst the 3d-transition metals, Ni has the highest λ and q, whereas Fe has the lowest λ (Srinivasan et al., 2005). Both permendur and Galfenol have high ME coupling strength, whereas Metglas with very high q show the highest ME coupling (Brintlinger et al., 2010; Chen et al., 2014; Fetisov et al., 2009; Greve et al., 2010; Gribov et al., 2014; Guo et al., 2010; Hockel et al., 2011; Kirchhof et al., 2013; Lage et al., 2012; Li et al., 2012; Li, Wen, et al., 2013; Liu et al., 2013, 2011; Nan et al., 2013, 2012; Onuta et al., 2012; Park et al., 2010; Piorra et al., 2013; Shen et al., 2014; Sreenivasulu, Laletin, et al., 2012; Srinivasan et al., 2005; Wang et al., 2012; Wu et al., 2013; Yao et al., 2011). Terfenol-D has one of the highest λ, but the piezomagnetic coefficient is rather small compared to Metglas or Galfenol that results in weak DME in composites

with ferroelectrics (Chen et al., 2014; Guo et al., 2010; Hockel et al., 2011; Li, Wen, et al., 2013; Park et al., 2010; Yao et al., 2011). Some recent studies on composites involved the use of both ferromagnetic alloys and ferrimagnetic oxides (Yang et al., 2010).

3.2 Direct magnetoelectric effects

The electrical response of a composite to an applied magnetic field is termed direct ME (DME) effect. Measurement techniques for DME include (1) subjecting the sample to an AC magnetic field δH and a bias magnetic field H and measuring the ME voltage coefficient, (2) magneto-dielectric effect involving the measurement of ε as a function of bias field H, and (3) change in polarization P with H (Nan et al., 2008). This section focuses mainly on DME in layered composites.

3.2.1 Low-frequency ME effect

This measurement involves electric field response of samples that are first polarized in an electric field E and then subjected to an AC magnetic field δH and a bias field H. The resulting AC voltage δV is measured across the sample thickness. The ME voltage coefficient (MEVC) $= \delta E/\delta H = \delta V/(t\,\delta H)$, where t is the thickness of ferroelectric (or piezoelectric) layer, is measured as a function of bias field H and frequency f of δH and for a series of magnetic field orientation. Assuming the sample in the (1,2) plane, the MEVC is usually measured for two conditions: (1) for H and δH parallel to each other and to the sample plane (1,2) and δE measured along direction-3, and (2) all three fields parallel to each other and perpendicular to the sample plane. Figure 3.1 shows

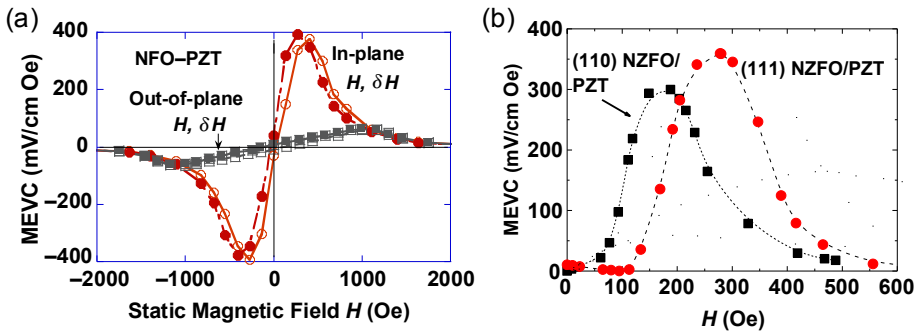

Figure 3.1 Low-frequency direct magnetoelectric (DME) effects in ferromagnetic oxide−PZT composites. The ME voltage coefficient (MEVC) is shown as a function of bias field H. (a) Multilayers of nickel ferrite (NFO)−PZT: data are for H and AC field δH (at 100 Hz) parallel to each other and for increasing (filled symbols) and decreasing (open symbols) bias field H. Results are for the fields applied either parallel or perpendicular to the sample plane. (b) MEVC versus H for (110) and (111) nickel zinc ferrite (NZFO)−PZT bilayers for in-plane magnetic fields.

representative data on H dependence of MEVC measured at 300 K for layered ferrite−PZT composites (Srinivasan, 2010). Figure 3.1(a) is for a multilayer of nickel ferrite (NFO)−PZT prepared by laminating and sintering 10−40 μm thick ferrite and PZT prepared by tape casting (Srinivasan, 2010). Data are for (1) δH_1 and H_1 parallel to each other and to the sample plane and (2) δH_3 and H_3 parallel to each other and perpendicular to the sample plane and $f = 100$ Hz. A general increase in MEVC is observed with H to a peak value, followed by a rapid drop. According to a recent model that assumes a one-dimensional composite with length much higher than the width and thickness, the MEVC for an in-plane field is given by (Sreenivasulu, Petrov, et al., 2012)

$$\text{MEVC} = \frac{\delta E_3}{\delta H_1} = \frac{{}^{m}q_{11}\ {}^{p}d_{11}/{}^{p}\varepsilon_{33}}{r\,{}^{m}s_{11} + {}^{p}s_{11}}, \tag{3.1}$$

where ${}^{p}s_{11}$, ${}^{m}s_{11}$, ${}^{p}d_{13}$, and ${}^{m}q_{11}$ are compliance and piezoelectric/piezomagnetic coupling coefficients for ferroelectric and piezomagnetic layers, respectively (${}^{p}\varepsilon_{33}$ is the permittivity of piezoelectric layer and $r = {}^{p}t/{}^{m}t$ with ${}^{p}t$ and ${}^{m}t$ denoting the thickness of piezoelectric and piezomagnetic layers). The coefficients are directly proportional to the piezomagnetic coupling $q = \mathrm{d}\lambda/\mathrm{d}H$ and the H dependence in Figure 3.1(a) tracks the slope of λ versus H. Saturation of λ at high field leads to an MEVC of zero. One measures an order of magnitude higher MEVC for in-plane magnetic fields compared to out-of-plane orientation for magnetic fields; this is due to large demagnetizing fields (and therefore small piezomagnetic coupling q) for out-of-plane magnetic fields. Similar studies were reported on bilayers of single crystal ferrites epoxy bonded to ferroelectrics. Representative MEVC data for such samples for in-plane magnetic fields are shown in Figure 3.1(b). The results are for PZT and (110) $Ni_{0.9}Zn_{0.1}Fe_2O_4$ (NZFO) or (111) NZFO (Gheevarughese et al., 2007). Although there is dependence of MEVC on the orientation of magnetic fields relative to crystallographic direction due to the directional dependence of λ, the overall MEVC is comparable to polycrystalline NFO−PZT data in Figure 3.1(a). Similar low-frequency ME coupling was investigated in bilayers of single crystal lead magnesium niobate-lead titanate (PMN-PT) and yttrium iron garnet (YIG) (Li et al., 2010).

It is clear from the data in Figure 3.1 that the ME response vanishes when magnetostriction saturates at high bias magnetic fields. But strong ME effects for H as high as 18 kOe were reported in bilayers of PZT and single-crystal hexagonal M, Y, or Z-type ferrites and is due to magnetic anisotropy fields of 10−40 kOe for the hexagonal ferrites (Mathe et al., 2008). Results in Figure 3.2 for Sr−Al−M or Zn_2Y and PZT show the weakest coupling in bilayers with M-ferrites and the strongest coupling for samples with Zn_2Y. In bilayers with Sr−Al−M, MEVC increases with increasing Al-substitution. Theoretical estimates of MEVC were in good agreement with the data in Figure 3.3 (Mathe et al., 2008).

Several groups reported on strong low-frequency ME effects in a variety of ferrite-based composites, including thin film piezoelectrics on nickel zinc ferrite (Park et al., 2012), dense films of nickel ferrite and a piezoelectric deposited by aerosol-deposition on Si (Ryu et al., 2012), and PLD grown NFO−BTO and cobalt ferrite

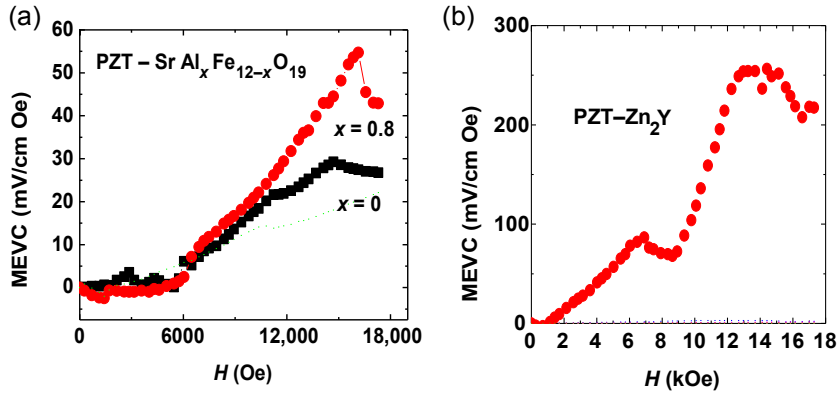

Figure 3.2 Bias field H dependence of MEVC for in-plane magnetic fields for bilayers of PZT and single crystal (a) M-type hexagonal Sr-Al-ferrite and (b) Y-type hexagonal ferrite.

(CFO)−BTO heterostructures on $SrTiO_3$ substrates (Deng et al., 2008; Zhang et al., 2008). Magnetic field dependence of Raman scattering studies were carried out on PZT−CFO to demonstrate strong strain mediated coupling in the system (Li et al., 2009).

The results in Figures 3.1 and 3.2 are for composites with ferrimagnetic oxides. Similar studies were reported for composites with ferromagnetic oxides. Lanthanum manganites with divalent substitutions such as Ba, Ca, or Sr show metallic conduction and ferromagnetism due to double exchange interactions. The oxides are of interest for studies on ME coupling in layered composites because of high λ and low resistivity. Bilayers and multilayers of polycrystalline and single crystal $La_{0.7}Sr_{0.3}MnO_3$ (LSMO)−PZT and $La_{0.7}Ca_{0.3}MnO_3$ (LCMO)−PZT were synthesized (Srinivasan et al., 2002; Zhang et al., 2009). The coupling was stronger in LSMO−PZT than in

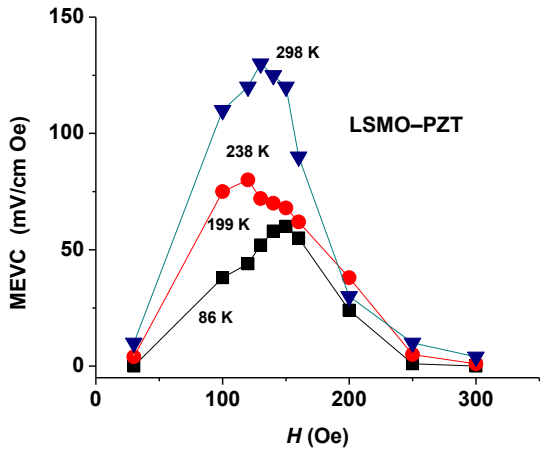

Figure 3.3 MEVC versus H data for in-plane magnetic fields and as a function of temperature for a bilayer of single crystal $La_{0.7}Sr_{0.3}MnO_3$ (LSMO) and PZT.

LCMO−PZT. Representative results on MEVC versus H for in-plane fields for bilayers with single crystal LSMO and PZT are shown in Figure 3.3. Strong ME interactions, comparable to ferrite−PZT (Figures 3.1 and 3.2), are evident. The data show a decrease in MEVC with decreasing temperature (Srinivasan et al., 2002; Zhang et al., 2009).

Although all-oxide composites show strong ME coupling, the highest MEVC were reported for composites with ferromagnetic metals or alloys. Most of the studies to date focused on layered samples of ferroelectrics with 3-d transition metal oxides (Nan et al., 2008; Srinivasan, 2010; Laletin et al., 2005), permendur (Laletin et al., 2005), Metglas (Greve et al., 2010; Kirchhof et al., 2013; Lage et al., 2012; Piorra et al., 2013; Shen et al., 2014; Wang et al., 2011, 2012), Galfenol (Brintlinger et al., 2010; Fetisov et al., 2009; Gribov et al., 2014; Onuta et al., 2012; Wu et al., 2013), FeGaB (Liu et al., 2013, 2011; Nan et al., 2013, 2012), Terfenol-D (Chen et al., 2014; Guo et al., 2010; Hockel et al., 2011; Li, Wen, et al., 2013; Park et al., 2010; Yao et al., 2011), or Heusler alloys (Li et al., 2012). Among the 3d-transition metals, Ni has the highest λ and q, whereas Fe has the lowest λ. At low frequencies, the highest MEVC was measured for Ni−PZT−Ni trilayers, and the weakest ME response was for samples with Co. Samples of Fe−PZT−Fe showed unique characteristics such as zero-crossing and sign reversal in MEVC versus H. One of the best values for low-frequency MEVC, $\sim$52 V/cm Oe, was measured in samples of Metglas and a piezofiber and was attributed to high q value for Metglas and excellent magnetic field confinement due to high permeability (Wang et al., 2011). The ME response of several ferromagnetic metal/alloy-based composites were found to be non linear under high ac field strengths or ac fields of different frequencies (Fetisov, Fetisov, Sreenivasulu, & Srinivasan, 2013). Such nonlinear ME effects and their dependence on thickness of a Metglas layer was studied in the composites with PMN-PT (Wang et al., 2012). Another alloy-based system of recent interest showing high MEVC has been high q, high permeability FeCoSiB alloy, and piezoelectric AlN (Greve et al., 2010; Kirchhof et al., 2013; Lage et al., 2012; Piorra et al., 2013). The system, in particular, shows excellent resonance ME coupling, as discussed later (Fetisov et al., 2009). Galfenol, an alloy of $Fe_{1-x}Ga_x$, has high magnetostriction. Compositions with $x = 0.15 - 0.3$ have saturation magnetostriction as high as $\lambda_S \sim 400 \times 10^{-6}$ in relatively low magnetic fields and, therefore, a high q. Composites of galfenol−PZT are found to show strong ME coupling (Brintlinger et al., 2010; Fetisov et al., 2009; Onuta et al., 2012; Wu et al., 2013). Another alloy-based system of importance is composites with Terfenol-D with MEVC comparable to all-oxide composites. Even though Terfenol-D has high magnetostriction, the q value is rather small. Ferromagnetic alloy-based composites show excellent ME response at mechanical resonance, as discussed in the following section.

3.2.2 ME coupling at bending and electromechanical resonances

It is of interest to investigate the dependence of the MEVC on the frequency f of the AC magnetic field. A bilayer of ferrite−PZT, for example, undergoes a bending deformation in a magnetic field due to its inherent asymmetry. One therefore anticipates a

resonance enhancement in the MEVC when f is tuned to the bending resonance frequency (Nan et al., 2008; Srinivasan, 2010). Such bending resonances, however, will be absent in a symmetric ferrite−PZT−ferrite trilayer. Similarly, a resonance enhancement is also expected at electromechanical resonance corresponding to radial, longitudinal, or thickness acoustic modes of the bilayer or symmetric trilayers. Several models have been proposed for ME coupling at bending modes, but most involve numerical solution of equations (Nan et al., 2008; Srinivasan, 2010). For longitudinal acoustic mode, under one-dimensional approximation, one obtains the following expressions for the resonance frequency f_L and MEVC. The fundamental EMR frequency is given by (Sreenivasulu, Petrov, et al., 2012)

$$f = \frac{1}{2L}\sqrt{\frac{{}^{p}s_{11} + r^{m}s_{11}}{{}^{p}s_{11}{}^{m}s_{11}(r^{p}\rho + {}^{m}\rho)}}, \tag{3.2}$$

where ρ is the density, and the peak MEVC at the axial mode frequency is

$$\frac{\delta E_3}{\delta H_1} = \frac{8Q}{\pi^2}\frac{{}^{m}q_{11}\,{}^{p}d_{13}\Big/{}^{p}\varepsilon_{33}}{r^{m}s_{11} + {}^{p}s_{11}}, \tag{3.3}$$

where Q is the quality factor for the EMR resonance.

Representative data for MEVC at bending and EMR are shown in Figure 3.4 for an epoxy bonded bilayer of (111) $Ni_{0.8}$ $Zn_{0.2}$ Fe_2 O_4 (NZFO) and PZT (Gheevarughese et al., 2007). The profile of MEVC versus f shows a peak MEVC of 48 V/cm Oe due to the bending resonance at ∼110 kHz and 45 V/cm Oe due to radial acoustic mode at ∼350 kHz. The secondary peak at 330 kHz is higher harmonics of the bending mode.

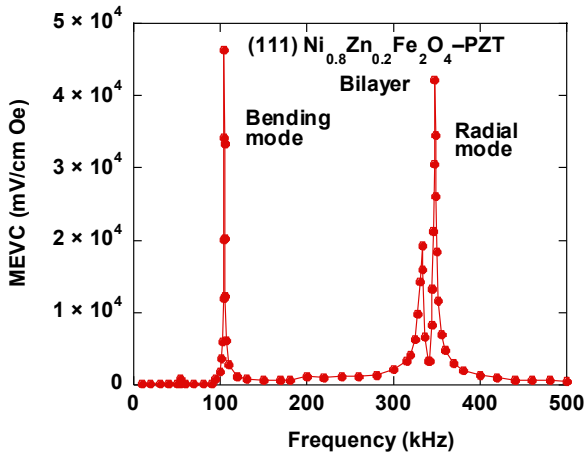

Figure 3.4 Frequency dependence of MEVC for a bilayer of NZFO and PZT. The peaks correspond to bending and radial acoustic resonances in the sample.

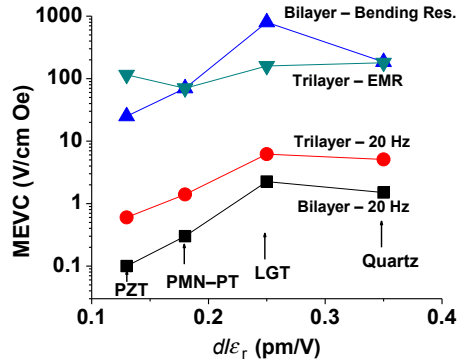

Figure 3.5 Low-frequency and resonance MEVC as a function of the ratio of the piezoelectric coupling coefficient d to the relative permittivity ε_r for bilayers and trilayers of permendur and ferroelectric PZT or PMN-PT and piezoelectric LGT or quartz.

Studies on trilayer composites of 3d-ferromagnetic metals and PZT revealed EMR at frequencies in the range of 100 kHz−3 MHz for radial and thickness modes. The corresponding MEVC was in the range 4−90 V/cm Oe (Laletin et al., 2005). A recent study compared the low-frequency and resonance ME effects in bilayers and trilayers of composites with permendur and ferroelectric PZT and PMN-PT and piezoelectric langatate and quartz (Sreenivasulu, Petrov, et al., 2012). Figure 3.5 shows the resonance value of MEVC as a function of the ratio of the piezoelectric coupling coefficient d to the relative permittivity ε_r. It is clear from the data in Figure 3.5 that the MEVC scales with the ration d/ε_r. But the highest resonance MEVC to date, 20 kV/cm Oe, was reported for AlN−FeCoSiB for measurements under vacuum that reduces damping of bending resonance in air (Kirchhof et al., 2013). A substantial enhancement in MEVC was reported under bending resonance in a cantilever of FeCo−SiB and PZT with interdigital electrodes (Piorra et al., 2013).

3.2.3 DME coupling in functionally graded composites

Magnetoelectric effects in composites with functionally graded ferroics are of fundamental and technological importance (Petrov & Srinivasan, 2008; Mandal et al., 2010, 2011; Yan et al., 2013; Yang et al., 2010). Since the MEVC is proportional to the product of the piezomagnetic coefficient q and piezoelectric coefficient d, models were developed recently for ME coupling in layered composites with graded q and d. The theory predicts stronger ME interactions in graded composites compared to homogeneous systems and strong ME coupling for zero external magnetic bias field (Petrov & Srinivasan, 2008).

The low-frequency ME interactions in functionally graded layered composites have been studied in several systems in recent years. Results for two such systems are provided in Figure 3.6. Figure 3.6(a) shows the low-frequency MEVC versus H data for bilayers of PZT and functionally graded ferromagnetic layer with two ferrites. The results are for graded ferrite layer with discs of NFO (Zn concentration $x = 0$) and

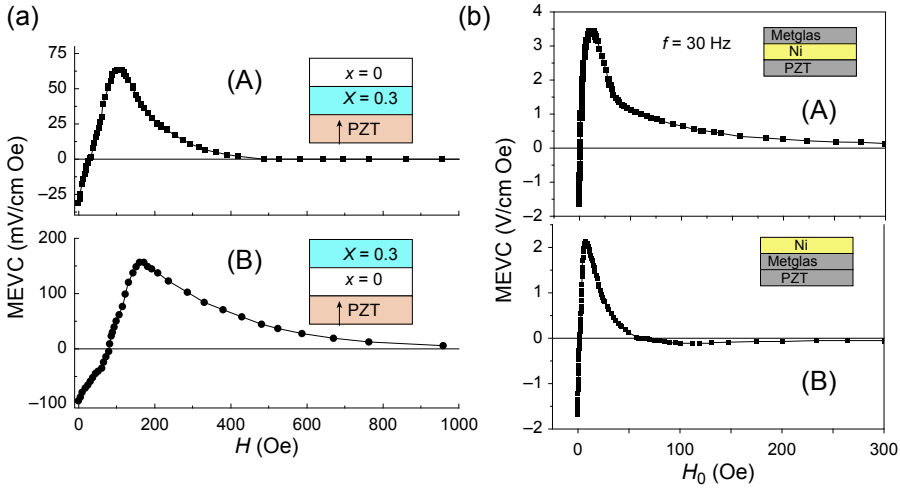

Figure 3.6 Low-frequency ME effects in functionally (magnetization) graded composites. (a) MEVC versus H data at room temperature for a sample of PZT−nickel ferrite−nickel zinc ferrite. Notice the large MEVC for zero-bias field and its dependence on the grading scheme. (b) Similar data for samples of PZT and graded ferromagnetic layer with Ni and Metglas.

$Ni_{0.7}Zn_{0.3}Fe_2O_4$ ($X = 0.3$) that were stacked to achieve grading of q (Mandal et al., 2010). A strong ME coupling arising out of grading and an ME response in the absence of an external bias magnetic field H are observed as shown in Figure 3.6(a) and the maximum MEVC is a factor two higher than for the homogeneous ferrite−PZT and is attributed to grading in q that counteracts the flexural deformation due to asymmetry associated with bilayers. An observation of significance in Figure 3.6(a) is the large MEVC for $H = 0$ for the graded systems and its dependence on the grading scheme. The zero-bias MEVC is due to a torque, which arises from interaction between in-plane ac induction δM produced by δH and a grading induced internal magnetic field H_{int} in the ferrite. Compositional grading of NZFO is shown to result in an internal field of magnitude $H_{\text{int}} \approx 30$ Oe in the grading direction (Mandal et al., 2010). Figure 3.6(b) shows results on the observation of a similar zero-bias ($H = 0$) ME effect in a bilayer of PZT and a ferromagnetic layer in which the magnetization is graded with the use of Ni and Metglas. One also observes a dependence of the zero-bias MEVC on the grading scheme (Mandal et al., 2011). Similar studies of significance are the use of nickel zinc ferrite and Ni for functional grading (Yan et al., 2013; Yang et al., 2010). A zero-bias MEVC was measured in the system and was attributed to an induced bias magnetic field due to the difference in the magnetic susceptibility and coercivity for Ni and the ferrite. Another study of importance is the exchange biasing of a composite to achieve zero-bias MEVC (Lage et al., 2012). In this study, the exchange bias field acting on the ferromagnetic layer was controlled by controlling the layer thickness so that the piezomagnetic coefficient was maximum for zero external bias magnetic field (Lage et al., 2012). A giant resonance ME effect at EMR frequency of 215 MHz was reported for a self-biased nano-cantilever of AlN/FeGa/Al_2O_3 (Nan et al., 2013).

One could also study the nature of direct ME effects in layered composites through other techniques involving measurements of H induced polarization, change in dielectric permittivity in H (i.e., magneto-dielectric effects), and by piezoforce microscopy under H (Lawes & Srinivasan, 2011; Nan et al., 2008; Sun & Srinivasan, 2012; Zheng et al., 2004).

3.3 Converse ME effects

The magnetic response of a composite to an applied electric field is termed converse ME effect, and the primary tools for studies on CME are measurements of magnetic hysteresis M versus H under E, tuning of FMR in E, and electric field control of magnetization or ferromagnetic domain switching by magnetic force microscopy. In this section, we discuss these tools for CME studies with two representative examples: M versus H for NFO/PZN-PT and FMR in a bilayer of single crystal Y-type hexagonal and PMN-PT (Li et al., 2011; Tatarenko & Srinivasan, 2011).

The converse ME effect was reported for direct liquid injection-chemical vapor deposition (DLI-CVD) grown NFO films on (001)-single crystal lead zinc niobate-lead titanate (PZN-PT) or PMN-PT substrates (Li et al., 2011). Models predicted a strong CME in such heterostructures because of high values of λ and d since such lattice-matched heterostructures are free of any foreign medium at the interface, as in epoxy bonded bilayers or even in polycrystalline films deposited directly on piezoelectric substrates. The nature of CME was studied by electric field-induced changes in the magnetic hysteresis loops, which were carried out using a vibrating sample magnetometer (VSM). Figure 2.9 shows E-dependence of M versus H for H applied along the [100] and [110] direction of NFO/PZN-PT, respectively. Both of them display an E-induced easy magnetization process. The fractional change in the remanent magnetization.

$\Delta M/M(E=0) = [M(E) - M(E=0)]/M(E=0)$ reaches 15% with $E = 8$ kV/cm applied across PZN-PT. Assuming $4\pi M_s = 3.2$ kG and for $M(E=0)/M_s = 0.3$ based on hysteresis data in Figure 2.9, an ME coupling coefficient of $A = \Delta M/E = 18$ G cm/kV is estimated and found to be in very good agreement with A obtained from static E-field tuning FMR (Sun & Srinivasan, 2012).

Another widely used technique for investigations on CME is static electric field tuning of FMR. An electric field E applied to the composite produces a mechanical deformation in PZT that results in an induced anisotropy in the ferrite, leading to a shift in the resonance field or frequency. The very first study was on bulk samples of 90% YIG−10% PZT, and the ME coupling was found to be quite weak because of low PZT concentration (Srinivasan, 2010). But in bulk samples with any higher PZT, FMR line broadening masked electric field effect on the resonance field. Such a line broadening, however, could be easily eliminated in layered samples. Models were developed for the phenomenon in bilayers (Srinivasan, 2010). The E-induced shift δH_E in the resonance field is determined by the magnetostriction λ and piezoelectric coupling d. When E and H are directed along a symmetry axis, <100> for example, perpendicular to the plane (1,2) of a bilayer, one obtains (Srinivasan, 2010)

$$\delta H_E = \frac{3\lambda_{100} d_{31} E_3}{M_0[({}^p s_{11} + {}^p s_{12})(1-v) + ({}^m s_{11} + {}^m s_{12})v]}, \tag{3.4}$$

where M_0 is the saturation magnetization and v is the volume fraction for the piezoelectric phase. Since the measurement accuracy depends very much on the FMR line width, the technique in general is appropriate for bilayers consisting of single crystal platelets or epitaxial films of low-loss ferrites such as YIG, lithium ferrite, nickel ferrite, and hexagonal ferrites (Sun & Srinivasan, 2012). In recent years, E-tuning of FMR has been utilized for CME in composites with FeGaB films (Liu et al., 2013, 2011; Nan et al., 2013, 2012).

Next, we discuss the E-tuning of FMR in a composite with hexagonal ferrite and a ferroelectric. Microwave ME effects over 8−25 GHz were studied in bilayers of single crystal Y-type hexagonal ferrite $Ba_2Zn_2Fe_{12}O_{22}$ (Zn_2Y) and polycrystalline PZT or single crystal PMN-PT (Tatarenko & Srinivasan, 2011). The bilayers were made by epoxy bonding or eutectic bonding the ferrite and piezoelectric. The strength of ME interactions $A = \delta H/E$ (or $\delta f/H$) were measured from data on resonance field shift δH or frequency shift δf in an electric field E. Studies on ME interactions were performed by placing the ferrite/PMN-PT bilayer on a microstripline transducer as shown in Figure 3.7. A static magnetic field H was applied parallel to the sample plane. Profiles of the scattering parameter S_{11} versus f in Figure 3.7 show absorption corresponding to FMR with a 3 dB frequency-width $\Delta f = 70$ MHz ($\Delta H = 25$ Oe). Data were obtained on frequency shift in FMR when a static field E was applied to PZT or PMN-PT for the estimation of ME coefficient A. For epoxy bonded Zn_2Y−PZT the measured $A = 1.2$ MHz cm/kV, and it is enhanced by almost an order of magnitude to $A \approx 10$ MHz cm/kV for eutectic bonded Zn_2Y/PMN-PT. The order of magnitude difference in A-value for samples with PZT and PMN-PT is primarily due to the difference in the strength of piezoelectric coupling constant $d \approx 400$ pC/N for PZT and $d \approx 2500$ pC/N for PMN-PT. The measured A for Zn_2Y−PZT is comparable to values reported for YIG−PZT, as expected since magnetic parameters for Zn_2Y ($\lambda = 1.8$ ppm, $4\pi M = 2.8$ kG) are close to that of YIG ($\lambda = 2$ ppm, $4\pi M = 1.78$ kG) (Sun & Srinivasan, 2012; Tatarenko & Srinivasan, 2011).

The A value for Zn_2Y/PMN-PT is comparable to measured values for single crystal nickel ferrite/PMN-PT (Li et al., 2011).

Similar studies on Fe_3O_4/PZN-PT demonstrated strong CME (Liu et al., 2010). The electric field was found to induce a magnetic anisotropy field as high as 400−600 Oe, depending on the field orientation, and an ME coefficient $A = 68$−100 Oe cm/kV (Liu et al., 2010). In another study on layered samples of Al-substituted nickel zinc ferrite and PZT, E-tuning of FMR was used to determine the strength of CME (Li, Zhou, et al., 2013). A related technique, that is AC electric field switching of magnetic induction in a ferrite−ferroelectric composite was employed for studies on self-biased CME (Yan et al., 2013; Yang et al., 2011).

Although one generally expects a large FMR line-width in composites of ferromagnetic alloys-ferroelectrics, studies on composites with thin films of FeGa revealed a line-width of less than 60 Oe (frequency half-width of 350 MHz) (Liu et al., 2013).

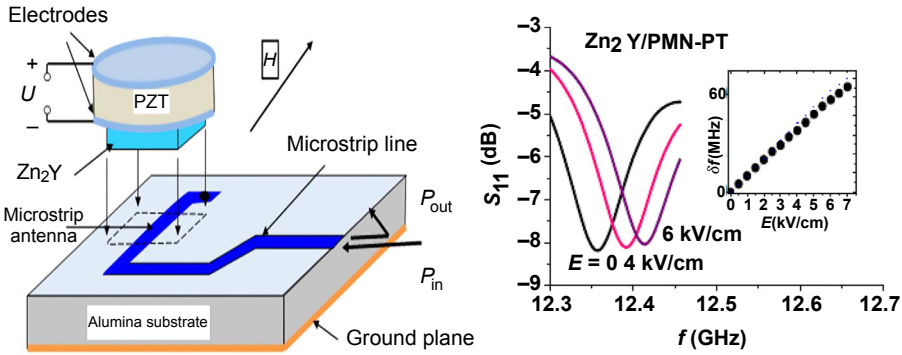

Figure 3.7 Data showing tuning of ferromagnetic resonance in a bilayer of single crystal Y-type hexagonal ferrite and PMN-PT. The insets show the stripline device used for the measurements and shift in FMR frequency versus *E*.

A giant E-tuning of FMR by 1200 Oe (equivalent to 5.3 GHz) and an ME coefficient $A = 880$ MHz cm/kV was achieved for the FeGa-based composite (Liu et al., 2013). Recent studies on low-frequency CME in ferromagnetic metals or alloys/ferroelectric composites involved resonant CME in FeGa−PZT−FeGa trilayers (Onuta et al., 2012; Wu et al., 2013), magnetic domain switching in FeGa−BTO and FeGa−PZT (Brintlinger et al., 2010; Nan et al., 2012), and electric field control of magnetization in Ni−ferroelectric composites (Buzzi et al., 2013; Cherepov et al., 2014; Finizio et al., 2014; Kim et al., 2013).

3.4 Conclusions

There have been considerable interests in recent years on mechanical strain mediated coupling in layered composites of ferromagnetic and ferroelectric phases. The nature of the ME coupling is studied by the sample response to a magnetic field or an electric field. Ferromagnetic metal or oxide and ferroelectric or piezoelectric-based composites show evidence for strong direct-ME coupling at low frequencies and further enhancement in the coupling strength under mechanical resonance conditions. A strong converse-ME effect was also evident from electric field switching of magnetization, magnetic domain switching, variation in inductance, or E-tuning of FMR. Several applications, including magnetic sensors, high-frequency inductors, memory devices, and high-frequency signal processing devices have been proposed and demonstrated. Most of the studies discussed in this chapter are on thick film layered composites or bonded bilayers. Ultra thin film multiferroic heterostructures have not been studied in detail so far. Difficulties in preparing high-quality heterostructures have impeded the studies on these composites. It is therefore necessary to overcome the challenges in depositing epitaxial films of the composite structures. It is also necessary to explore in detail the ME coupling in nanocomposites.

References

Bai, F., Zhang, H., Li, J., & Viehland, D. (2010). *Journal of Physics D: Applied Physics, 43*, 285002.

Bichurin, M. I., Viehland, D., & Srinivasan, G. (2007). *Journal of Electroceramics, 19*, 243−250.

Brintlinger, T., Lim, S., Baloch, K. H., et al. (2010). *Nano Letters, 10*, 1219.

Buzzi, M., Chopdekar, R. V., Hockel, J. L., et al. (2013). *Physical Review Letters, 111*, 027204.

Chen, L., Li, P., Wen, Y., & Zhu, Y. (2014). *Journal of Alloys and Compounds, 606*, 15.

Cherepov, S., Amin, P. K., Alzate, J. G., et al. (2014). *Applied Physics Letters*, 082403.

Cho, K., & Priya, S. (2011). *Applied Physics Letters, 98*, 232904.

Cross, L. E. (1993). Ferroelectric ceramics: tailoring properties for specific applications. In N. Setter (Ed.), *Ferroelectric ceramics*. Basel: Birkhäuser.

Das, J., Kalinikos, B. A., Barman, A. R., & Patton, C. E. (2007). *Applied Physics Letters, 91*, 172516.

Deng, C., Zhang, Y., Lin, Y., & Nan, Ce-W. (2008). *Acta Materialia, 56*, 405.

Fetisov, L. Y., Fetisov, Y. K., Sreenivasulu, G., & Srinivasan, G. (2013). *Journal of Applied Physics, 113*, 116101.

Fetisov, Y. K., Kamentsev, K. E., Chashin, D. V., Fetisov, L. Y., & Srinivasan, G. (2009). *Journal of Applied Physics, 105*, 123918.

Finizio, S., Foerster, M., Buzzi, M., Krüger, B., Jourdan, M., Vaz, C. A. F., et al. (2014). *Physical Review Applied, 1,* 021001.

Gao, J., Das, J., Xing, Z., Li, J., & Viehland, D. (2010). *Journal of Applied Physics, 108,* 084509.

Gheevarughese, V., Laletsin, U., Petrov, V., Srinivasan, G., & Fedotov, N. (2007). *Journal of Materials Research, 22*, 2130−2135.

Greve, H., Woltermann, E., Jahns, R., et al. (2010). *Applied Physics Letters, 97*, 152503.

Gribov, I. V., Osotov, V. I., Nosov, A. P., Petrov, V. M., Sreenivasulu, G., & Srinivasan, G. (2014). *Journal of Applied Physics, 115*, 193909.

Guo, Y., Zhou, J., & Liu, P. (2010). *Current Applied Physics, 10*, 1092.

Hockel, J. L., Wu, T., & Carman, G. P. (2011). *Journal of Applied Physics, 109,* 064106.

Kim, H. K. D., Schelhas, L. T., Keller, S., et al. (2013). *Nano Letters, 13*, 884.

Kirchhof, C., Krantz, M., Teliban, I., et al. (2013). *Applied Physics Letters, 102*, 232905.

Lage, E., Kirchhof, C., Hrkac, V., et al. (2012). *Nature Materials, 11*, 523.

Laletin, V. M., Paddubnaya, N., Srinivasan, G., DeVreugd, C. P., & Bichurin, M. I. (2005). *Applied Physics Letters, 87*, 222507.

Landolt, H., & Bornstein, R. (1970). Numerical data and functional relationships in science and technology, group III, crystal and solid state physics. In K.-H. Hellwege, & A. M. Springer (Eds.), *Magnetic and other properties of oxides* (Vol. 4(b)). New York: Springer-Verlag.

Lawes, G., & Srinivasan, G. (2011). *Journal of Physics D: Applied Physics, 44*, 243001.

Li, Z., Gao, Y., Yang, B., Lin, Y., Yu, R., & Nan, C. W. (2010). *Journal of the American Ceramic Society, 94*, 1060−1066.

Li, S., Liu, M., Lou, J., et al. (2012). *Journal of Applied Physics, 111*, 07C705.

Li, N., Liu, M., Zhou, Z., Sun, N. X., Murthy, D. V. B., Srinivasan, G., et al. (2011). *Applied Physics Letters, 99*, 192502.

Li, Z., Wang, Y., Lin, Y., & Nan, C. (2009). *Physical Review B, 79*, 180406(R).

Li, P., Wen, Y., Huang, X., et al. (2013). *Sensors and Actuators, 201*, 164.

Li, M., Zhou, Z., Liu, M., et al. (2013). *Journal of Physics D: Applied Physics, 46*, 275001.

Liu, M., Lou, J., Li, S., & Sun, N. X. (2011). *Advanced Functional Materials, 21*, 2593.
Liu, M., Obi, O., Cai, Z., et al. (2010). *Journal of Applied Physics, 107,* 073916.
Liu, M., Zhou, Z., Nan, T., et al. (2013). *Advanced Materials, 25*, 1435.
Ma, J., Hu, J., Li, Z., & Nan, C. W. (2011). *Advanced Materials, 23*, 1062−1087.
Mandal, S. K., Sreenivasulu, G., Petrov, V. M., & Srinivasan, G. (2010). *Applied Physics Letters, 96*, 192502.
Mandal, S. K., Sreenivasulu, G., Petrov, V. M., & Srinivasan, G. (2011). *Physical Review B, 84,* 014432.
Marauska, S., Jahns, R., Kirchhof, C., Claus, M., Quandt, E., Knochel, R., et al. (2013). *Sensors and Actuators A, 189*, 321−327.
Martin, L. W., & Ramesh, R. (2012). *Acta Materialia, 60*, 2449−2470.
Mathe, V. L., Srinivasan, G., & Balbashov, A. M. (2008). *Applied Physics Letters, 92*, 122505.
Nan, C. W., Bichurin, M. I., Dong, S., Viehland, D., & Srinivasan, G. (2008). *Journal of Applied Physics, 103*, 031101.
Nan, T., Hui, Y., Rinaldi, M., & Sun, N. X. (2013). *Scientific Reports*. http://dx.doi.org/10.1038/srep01985.
Nan, T. X., Zhou, Z. Y., Lou, J., et al. (2012). *Applied Physics Letters, 100*, 132409.
Onuta, T., Wang, Y., Long, C. J., Lofland, S. E., & Takeuchi, I. (2012). *Applied Physics Letters, 101*, 043506.
Park, C., Cho, H., Arat, M., Evey, J., & Priya, S. (2010). *Journal of Applied Physics, 107,* 094109.
Park, C., Khachaturyan, A., & Priya, S. (2012). *Applied Physics Letters, 100*, 192904.
Petrov, V. M., & Srinivasan, G. (2008). *Physical Review B, 78*, 184421.
Piorra, A., Jahns, R., Teliban, I., et al. (2013). *Applied Physics Letters, 103*, 032902.
Ryu, J., Baek, C., Han, G., et al. (2012). *Ceramics International, 38*, S431.
Shen, Y., Gao, J., Wang, Y., Li, J., & Viehland, D. (2014). *Journal of Applied Physics, 115*, 094102.
Sreenivasulu, G., Fetisov, L. Y., Fetisov, Y. K., & Srinivasan, G. (2012). *Applied Physics Letters, 100*, 052901.
Sreenivasulu, G., Laletin, U., Petrov, V. M., Petrov, V. V., & Srinivasan, G. (2012). *Applied Physics Letters, 100*, 173506.
Sreenivasulu, G., Petrov, V. M., Fetisov, L. Y., Fetisov, Y. K., & Srinivasan, G. (2012). *Physical Review B, 86*, 214405.
Srinivasan, G. (2010). *Annual Review of Materials Research, 40*, 153−178.
Srinivasan, G., DeVreugd, C. P., Laletin, V. M., Paddubnaya, N., & Bichurin, M. I. (2005). *Physical Review B, 71*, 184423.
Srinivasan, G., Rasmussen, E. T., Levin, B. J., & Hayes, R. (2002). *Physical Review B, 65*, 134402.
Sun, N. X., & Srinivasan, G. (2012). *Spin, 2*, 1240004.
Tatarenko, A. S., & Srinivasan, G. (2011). *Microwave and Optical Technology Letters, 53*, 261−264.
Vaz, C. A. F., Hoffman, J., Ahn, C. H., & Ramesh, R. (2010). *Advanced Materials, 22*, 2900−2918.
Viswan, R., Gray, D., Wang, Y., Li, Y., et al. (2011). *Physica Status Solidi (RRL) − Rapid Research Letters, 5*, 391.
Wang, Y., Gray, D., Barry, D., Gao, J., Li, M., Li, J., et al. (2011). *Advanced Materials, 23*, 4111.
Wang, Y., Hasanyan, D., Li, M., et al. (2012). *Physica Status Solidi, 6*, 265.
Wang, Y., Hu, J., Lin, Y., & Nan, C. W. (2010). *NPG Asia Materials, 2*, 61.
Wang, J., Li, J., & Viehland, D. (2014). *Materials Today, 17*, 269.

Wang, Z., Zhang, Y., Viswan, R., Li, Y., Luo, H., Li, J., & Viehland, D. (2014). *Physical Review B, 89*, 035118.

Wu, G., Nan, T., Zhang, R., Zhang, N., Li, S., & Sun, N. X. (2013). *Applied Physics Letters, 103*, 182905.

Yan, Y., Zhou, Y., & Priya, S. (2013). *Applied Physics Letters, 102*, 052907.

Yang, S., Cho, K., Park, C., & Priya, S. (2011). *Applied Physics Letters, 99*, 202904.

Yang, S., Park, C., Cho, K., & Priya, S. (2010). *Journal of Applied Physics, 108,* 093706.

Yang, Y., Priya, S., Li, J., & Viehland, D. (2009). *Journal of the American Ceramic Society, 92*, 1552−1555.

Yao, Y. P., Hou, Y., Dong, S. N., & Li, X. G. (2011). *Journal of Applied Physics, 110*, 014508.

Zavislyak, I. V., Sohatsky, V. P., Popov, M. A., & Srinivasan, G. (2013). *Physical Review B, 87*, 134417.

Zhang, Y., Deng, C., Ma, J., Lin, Y., & Nan, C. W. (2008). *Applied Physics Letters, 92*, 062911.

Zhang, N., Srinivasan, G., & Balbashov, A. M. (2009). *Journal of Materials Research, 44*, 5120−5126.

Zheng, H., Wang, J., Lofland, S. E., Ma, Z., Mohaddes-Ardabili, L., Zhao, T., et al. (2004). *Science, 303*, 661−663.

Multiferroic nanostructures

4

Z. Zhou[1], *N.X. Sun*[2]
[1]Argonne National Laboratory, Argonne, IL, USA; [2]Northeastern University, Boston, MA, USA

4.1 Introduction

Multiferroic materials with simultaneous ferroelectricity and magnetism provide a pathway to achieving strong magnetoelectric (ME) coupling with efficient voltage control of magnetism and compact and power-efficient electric-field-tunable magnetic devices (Eerenstein, Mathur, & Scott, 2006; Fetisov & Srinivasana, 2006; Martin et al., 2008; Nan, Bichurin, Dong, Viehland, & Srinivasan, 2008; Sun & Srinivasan, 2012; Vaz, Hoffman, Ahn, & Ramesh, 2010). From the viewpoint of their structures, nanoscale multiferroic ME composites can essentially be divided into several types: bulk magnetic on a ferro/piezoelectric slab; magnetic film on a ferro/piezoelectric slab; 2−2, 0−3, 1−3-type multiferroic nanostructures; and one-dimensional multiferroic composites. The bulk magnetic on ferro/piezoelectric slab multiferroic heterostructure will not be discussed in this chapter.

Compared with many bulk ME composites, multiferroic ME nanostructures have some unique advantages. For instance, the ferromagnetic and ferro/piezoelectric phase could be manipulated at the nanoscale. Furthermore, in bulk ME composites, the two constituent phases are usually combined/mixed by a cosintering or adhesive bonding method, which causes weakened ME coupling strength at the interface. Nevertheless, in ME composite nanostructures (e.g., thin films), the different phases are combined at the atomic level, reducing ME coupling loss at the interface significantly.

Recently, the advances in thin-film growth techniques (Zheng et al., 2004) and improved theoretical simulations (Duan, Jaswal, & Tsymbal, 2006; Hill, 2000; Lu, Wang, Zheng, & Ryba, 2007; Nan, Liu, Lin, & Chen, 2005; Zhang et al., 2007) accelerated the renaissance of multiferroic nanostructures. Novel nanostructures can be achieved by advanced growth techniques, and novel design of multiferroic nanostructures was also predicted by theory. Figure 4.1 shows three basic types of multiferroic nanostructures, 0−3, 2−2, and 1−3. The notation 0−3, 2−2, 1−3, etc. described the structure arrangement of two-phase composites (Newnham, Skinner, & Cross, 1978); each number implied the dimension of each phase. For example, a 0−3 composite represents the single-phase particles (represented by 0) embedded in a matrix of another phase (represented by 3), as shown in Figure 4.1(a). The 2−2 horizontal heterostructures represent a multilayer thin-film structure, where each single-phase layer can be denoted by 2 (see Figure 4.1(b)), and 1−3 vertical heterostructures show the one-dimensional single-phase nanopillars, denoted by 1, embedded in the

Composite Magnetoelectrics. http://dx.doi.org/10.1016/B978-1-78242-254-9.00004-4
Copyright © 2015 Elsevier Ltd. All rights reserved.

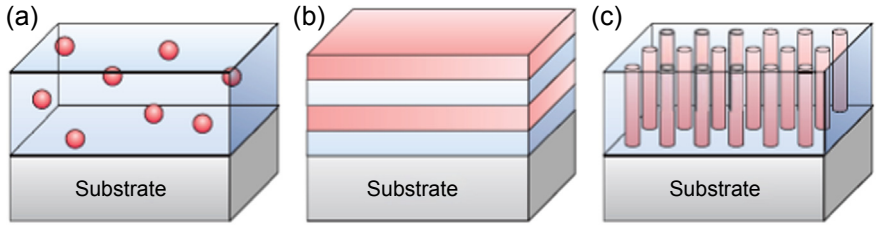

Figure 4.1 Schematic illustration of three kinds of ME composite nanostructures with common connectivity schemes: (a) 0−3 particulate nanocomposite films with magnetic particles (0) embedded in a ferroelectric film matrix (3); (b) 2−2 horizontal heterostructure with alternating ferroelectric (2) and magnetic (2) layers, or simply a ferroelectric (or magnetic) thin film grown on a magnetic (or ferroelectric) substrate; and (c) 1−3 vertical heterostructure with one-phase nanopillars (1) embedded in a matrix of another phase (3).

matrix of the second phase. These nanostructures, including magnetic thin film/ferroelectric slab structures, are discussed.

4.2 Magnetoelectric magnetic film/piezoelectric slab heterostructures

Multiferroic heterostructures with magnetic thin film deposited on a ferro/piezoelectric slab were widely studied (Liu et al., 2009, 2012; Liu, Obi, et al., 2009; Lou, Liu, Reed, Ren, & Sun, 2009; Nan et al., 2014; Zhou et al., 2012). Compared with bulk multiferroic composites, interface of ferromagnetic and ferroelectric with atomic level bonding introducing less ME coupling loss was obtained in magnetic thin film/ferroelectric slab heterostructures. Giant ME coupling coefficients were achieved in these magnetic thin film/ferroelectric slab heterostructures as there exists no substrate clamping effect that can diminish the strain/stress-mediated ME coupling effects. Several different deposition methods, such as spin-spray deposition (Liu et al., 2008, 2009; Liu, Obi, et al., 2009) and sputtering (Liu et al., 2012; Lou et al., 2009; Nan et al., 2014; Zhou et al., 2012), were studied to deposit magnetic thin film onto a piezo/ferroelectric slab.

4.2.1 Spin-spray-deposited ferrite film on piezo/ferroelectric substrate

The spin-spray deposition process, which was invented in 1983, is a novel technique to directly plate crystalline spinel ferrite film with different compositions from an aqueous solution at a temperature less than 90 °C. Conventional ferrite film preparation methods, such as sputtering, molecular beam epitaxy, pulsed laser deposition, etc., require high temperatures well above 600 °C; however, the spin-spray technique can produce high-quality polycrystalline ferrite films at a low temperature between 25 and 90 °C. Several chemical reactions are involved in the ferrite spin-spray process, which consist of (a) adsorption of Fe^{2+} and other ions Mn, Fe, Co, Ni, Zn, etc. on

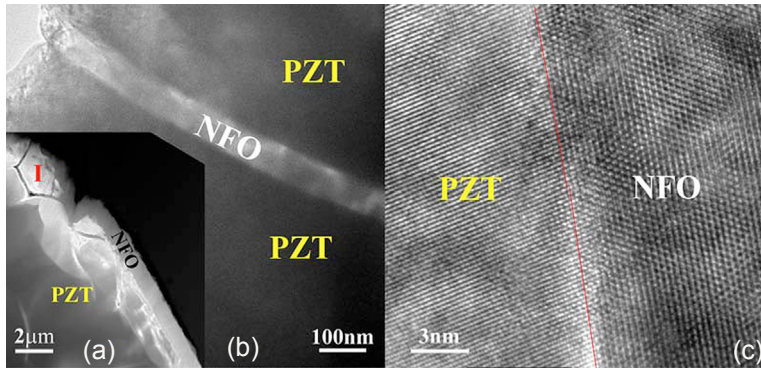

Figure 4.2 A cross-sectional HAADF image of NFO/PZT (a), HRTEM of Ni ferrite growing in the PZT crack (b), and HRTEM ferrite and PZT interface images (c).

the substrate surface mediated by OH groups, (b) oxidization expressed by $Fe^{2+} \rightarrow Fe^{3+} + e$, and (c) ferrite film formation accompanied by hydrolytic dissociation. Spin-spray-deposited ferrites provide great opportunities for low-temperature synthesized multiferroic composite materials on ferroelectric substrates.

$Ni_{0.23}Fe_{2.77}O_4$ (NFO)/$Pb(Zr,Ti)O_3$ (PZT) multiferroic composites were synthesized by spin-spray deposition of NFO film onto PZT ceramic substrate at 90 °C (Liu et al., 2008). The interface between NFO and PZT was investigated by a high-angle annular dark-field (HAADF) scanning transmission electron microscopy image (Z-contrast), as shown in Figure 4.2(a). A uniform ferrite film with a thickness of 1 μm can be identified on the PZT phase; no voids were observed at the NFO/PZT interface. It is interesting to note that the NFO ferrite phase was growing into the small surface crack of the PZT phase with a crack width of 100 nm area (I), as shown in Figure 4.2(b), which was proved by the energy-dispersive X-ray results. This indicates the excellent wetting between the NFO ferrite phase and the PZT phase during the spin-spray deposition process, which leads to a tight interface and a strong adhesion between the two phases. A high-resolution transmission electron microscope (HRTEM) image of the NFO/PZT interface is shown in Figure 4.2(c), which shows a clearly tight interface between the ferrite NFO and ferroelectric PZT phases without obvious lattice matching, even though the lattice parameter of the spinel NFO and the perovskite PZT phases match well, with the NFO lattice parameter being very close to two times that of PZT.

The in-plane M−H curves were measured by applying an external electric field of 0 and 1.3 MV/m across the thickness direction of PZT substrate, as shown in Figure 4.3. An obvious upward shift of the M−H curve was observed at a low external magnetic field, and the remnant magnetization was increased by 10% when applying an electric field of 1.3 MV/m. In addition, we found that both M−H curves reached the same saturation magnetization at a high external magnetic field, which indicated reduced ME coupling due to the saturated magnetostriction at a high-applied magnetic field.

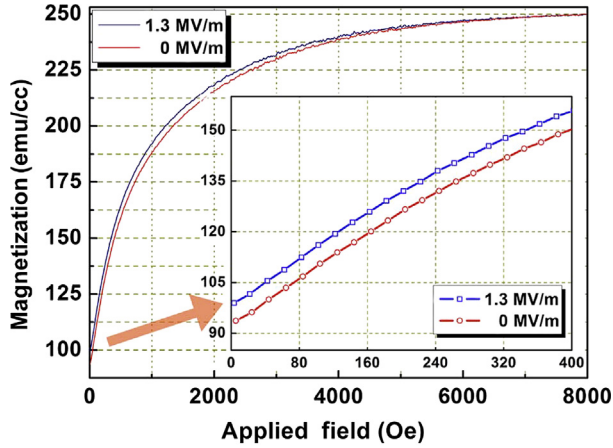

Figure 4.3 In-plane M−H curves of spin-sprayed Ni ferrite film on PZT when applying 0 and 1.3 MV/m electric fields through the PZT substrate.

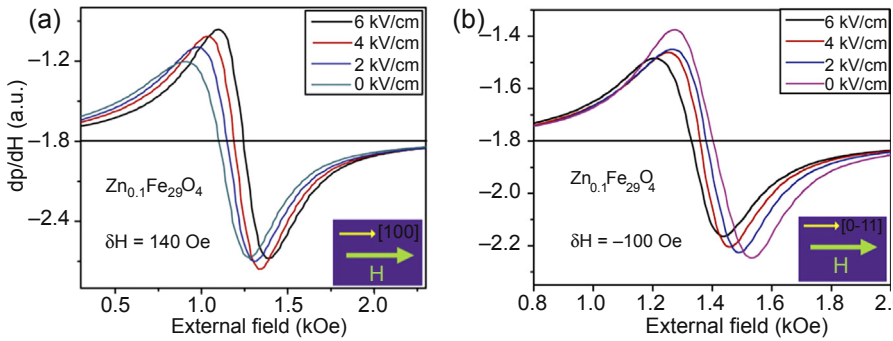

Figure 4.4 Ferromagnetic resonance absorption spectra of multiferroic composites ZFO/PMN-PT under different electric fields while applying an external magnetic field along the (a) [100] and (b) [01−1] directions.

Strong ME interaction was demonstrated at both dc and microwave frequencies in a novel $Zn_{0.1}Fe_{2.9}O_4$/PMN-PT (lead magnesium niobate-lead titanate) multiferroic heterostructure, which was prepared by spin-spray depositing a $Zn_{0.1}Fe_{2.9}O_4$ film onto a single-crystal PMN-PT substrate at a low temperature of 90 °C (Liu, Obi, et al., 2009). A large electric-field-induced ferromagnetic resonance (FMR) field shift up to 140 Oe was observed, corresponding to an ME coefficient of 23 Oe cm/kV (see Figure 4.4). In addition, a large squareness ratio change of 18% was observed in electrostatic field tuning of magnetic hysteresis loops. The spin-spray-deposited ferrite/piezoelectric multiferroic heterostructures exhibiting strong ME interactions at both dc and microwave frequencies provide great opportunities for novel electrostatically tunable microwave magnetic devices synthesized at a low temperature.

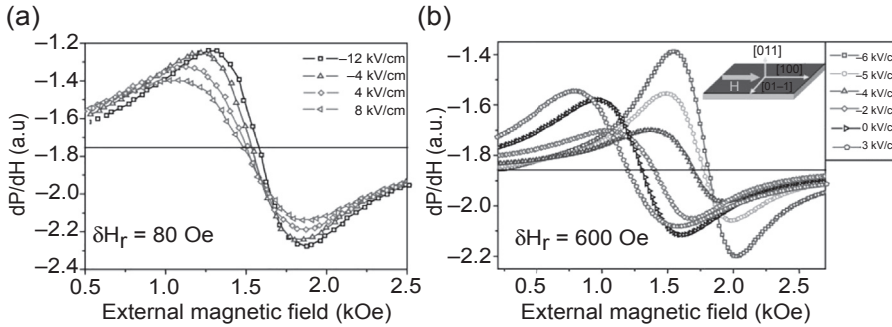

Figure 4.5 Ferromagnetic resonance absorption spectra of Fe_3O_4/PZT (a) and Fe_3O_4/PMN-PT (b) while applying different electric fields.

Multiferroic heterostructures of Fe_3O_4/PZT (lead zirconium titanate), Fe_3O_4/PMN-PT, and Fe_3O_4/PZN-PT (lead zinc niobate-lead titanate) are prepared by spin-spray depositing Fe_3O_4 ferrite film on ferroelectric PZT, PMN-PT, and PZN-PT substrates at a low temperature of 90 °C (Liu et al., 2009). Strong ME coupling and giant microwave tunability are demonstrated by an electrostatic-field-induced magnetic anisotropic field change in these heterostructures. Microwave ME interactions and magnetic tunability of Fe_3O_4/PMN-PT and Fe_3O_4/PZT composites were demonstrated by electrostatic-field-induced FMR field changes at room temperature, as shown in Figure 4.5. Here, a microwave cavity operating at TE_{102} mode at X-band (9.5 GHz) was used to perform FMR measurements of the ferrite/ferroelectric multiferroic composites. The external bias magnetic field was applied in the Fe_3O_4 film plane along the PMN-PT [100] or PMN-PT [01−1] directions, with the microwave RF field in-plane and perpendicular to the magnetic dc bias field. Clearly, giant microwave ME interaction was observed in Fe_3O_4/PMN-PT, which resulted in a high tunable FMR field range from 1185 Oe to 1786 Oe, or $dH_r = 600$ Oe, when the electric fields across the PMN-PT thickness were changed from 3 kV/cm to 6 kV/cm and when the external magnetic field was applied along the [100] direction of PMN-PT. This corresponded to a large microwave ME coupling coefficient of 67 Oe cm k/V. In comparison, the tunable FMR field range in Fe_3O_4/PZT was also measured as 80 Oe, which is much smaller than that of Fe_3O_4/PMN-PT due to the weak piezoelectric coefficient of PZT compared to PMN-PT.

In order to achieve a larger ratio of tunable FMR field over FMR linewidth, Fe_3O_4 ferrite films were also spin-spray deposited onto the (011)-cut PZN-PT single-crystal substrate, which has a higher piezoelectric coefficient and lower loss tangent compared to PMN-PT. The microwave and static ME coupling of the Fe_3O_4/PZN-PT heterostructures was investigated, and the results are shown in Figure 4.6. A record-high electric-field-induced FMR shift up to $dH_r = 860$ Oe was obtained when the external magnetic fields were applied along the in-plane [100] direction (d_{31}: 3000 pC/N), and the external electric fields were applied across the thickness of PZN-PT substrate starting from 0 kV/cm to 8 kV/cm, corresponding to an ME coefficient of 108 Oe cm/kV.

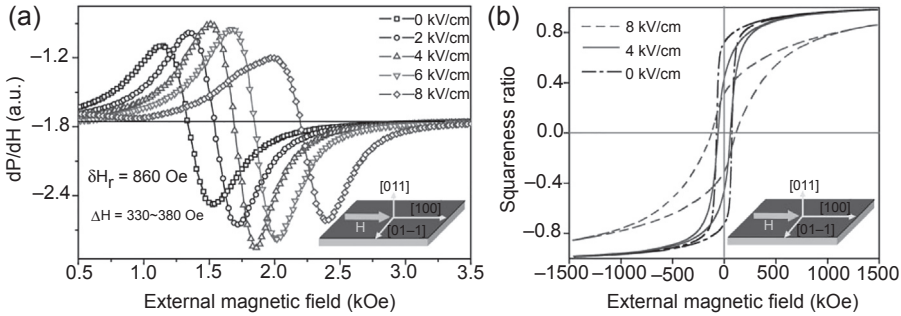

Figure 4.6 Ferromagnetic resonance absorption spectra of Fe_3O_4/PZN-PT (a) and magnetic hysteresis loops of Fe_3O_4/PZN-PT (b) while applying different electric fields.

Clearly, the FMR field tunable range and ME coefficient in Fe_3O_4/PZN-PT are larger than those in Fe_3O_4/PMN-PT, which are 600 Oe and 67 Oe cm/kV, respectively. In addition, the FMR linewidth obviously was reduced from $480 < \Delta H < 620$ Oe in Fe_3O_4/PMN-PT to $330 < \Delta H < 380$ Oe in Fe_3O_4/PZN-PT, leading to a significantly enhanced ratio of tunable FMR field over FMR linewidth of 2.5. The static ME coupling was shown in Figure 4.7(b), which displayed a significant squareness ratio change of 40% when an external magnetic field was along the [100] direction and 8 kV/cm external electric field was applied across the thickness of PZN-PT, which was also higher than that for the Fe_3O_4/PMN-PT.

The Fe_3O_4/PMN-PT can be shifted upward or downward, depending on whether the applied magnetic field is parallel or perpendicular to the effective magnetic field induced by the electric field across the (011)-cut PMN-PT, which is a natural result

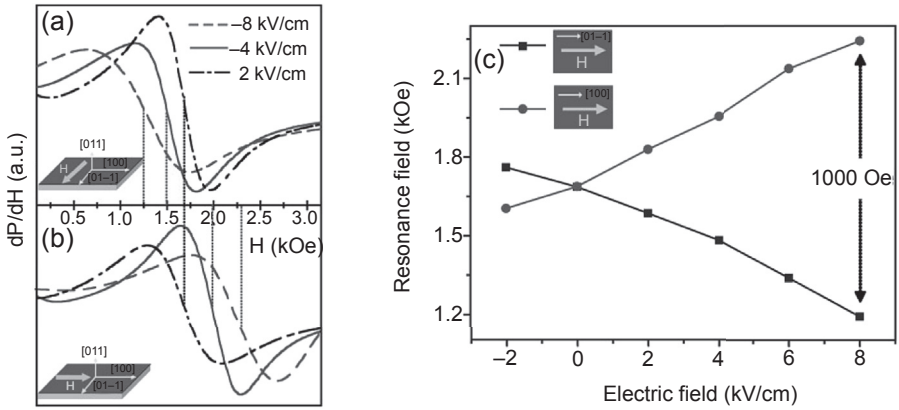

Figure 4.7 Ferromagnetic resonance absorption spectra shifts with the external magnetic field along tensional (a) and compressive (b) directions of PMN-PT. The cooperation of magnetic orientation and electric-field-generated resonance field change shift is up to 1000 Oe (c).

of the anisotropic piezoelectric coefficient of the (011)-cut PMN-PT. Considering the anisotropic in-plane piezoelectric coefficients of the (011)-cut PMN-PT, which can generate orthogonal tensile and compressive stresses under an electric field, a new concept is introduced that FMR frequency could be tuned up or down and achieve a larger tunable range by applying the external magnetic field parallel to the [100] (d_{31}) or [01−1] (d_{32}) direction of the (011)-cut PMN-PT. This idea was demonstrated in the Fe_3O_4/PMN-PT multiferroic composite. As shown in Figure 4.7, an external magnetic field applied along the [01−1] direction led to a reduced FMR field of 1200 Oe (Figure 4.7(a)). When the external field was parallel to the [100] direction, the FMR fields were shifted up to 2200 Oe (Figure 4.7(b)). Each of them had the same resonance field of 1680 Oe at zero electric field due to the in-plane isotropic magnetic property of the Fe_3O_4 film. The total resonance field shift was $dH_r = 1000$ Oe when the external magnetic field was applied parallel to [100] and [01−1] directions (Figure 4.7(c)). This constitutes a simple but effective approach for achieving twice the tunable FMR frequency range, leading to new opportunities of magnetostatically tunable magnetic device design with large effective magnetic field tunability.

4.2.2 Sputtering deposited magnetic alloy film on piezo/ferroelectric substrate

The spin-spray method can deposit magnetic thin film at a low temperature (<90°) with good adhesion onto piezo/ferroelectric substrate. Giant ME coupling effects were also observed in these multiferroic heterostructures. Nevertheless, the magnetic material type fabricated by spin spray is limited: only spinel ferrite can be done through this method. In order to discover the ME coupling in an alloy magnetic thin film/piezoelectric substrate, a sputtering technique is widely used to deposit alloy magnetic thin film onto ferroelectric substrates.

Multiferroic heterostructures of FeGaB/PZN-PT were made by direct deposition of 100 nm FeGaB films using a magnetron sputtering method onto PZN-PT single-crystal slabs (Lou et al., 2009). The field sweep FMR spectra of the FeGaB/PZN-PT multiferroic heterostructure under different electric fields are shown in Figure 4.8. The external magnetic field was applied parallel to the in-plane [011] direction of the PZN-PT single crystal and was swept between 0 and 1400 Oe. Clearly, the FMR spectra changed dramatically with the external electric field, indicating a giant ME coupling in the FeGaB/PZN-PT heterostructure. The theoretical calculation results were demonstrated in Figure 4.9. The FMR field shifted from 1172 to 898 Oe on changing the external electric field from 2 to 5.8 kV/cm. A sudden change of the FMR field from 898 to 425 Oe occurred at electric fields between 5.8 and 6 kV/cm. Such a dramatic change of the FMR field within a very narrow electric field range is closely related to the phase transition from the rhombohedral to the tetragonal phase in the PZN-PT single crystal, which has been reported previously (Liu et al., 2013). The FMR field barely changed at electric fields higher than 6 kV/cm, which was also consistent with the strain−electric field relation of the PZN-PT single crystal (Liu et al., 2013). It is important to emphasize that the overall electric-field-induced FMR field change (also the total electrostatically induced magnetic anisotropy) is c. 750 Oe, which is the largest value that has

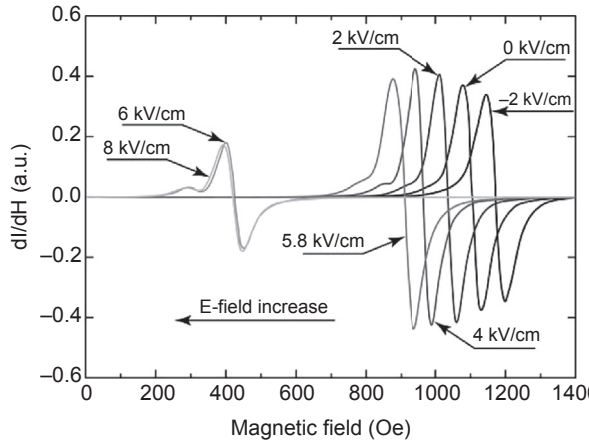

Figure 4.8 Electric field dependence of the in-plane field sweep FMR spectra of the FeGaB/PZN-PT multiferroic heterostructure measured at c. 9.6 GHz.

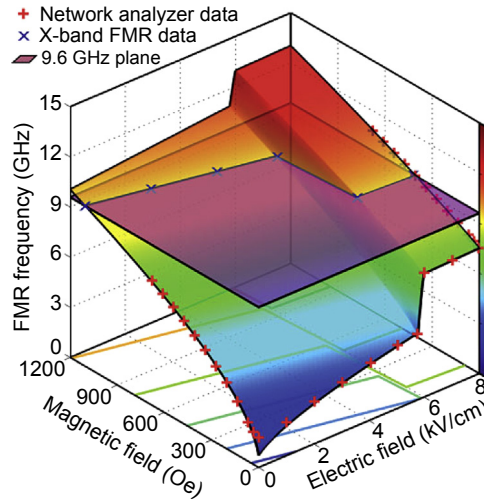

Figure 4.9 3D plot showing the FMR frequency of the FeGaB/PZN-PT multiferroic heterostructure as a function of external magnetic and electric bias fields.

ever been reported, corresponding to a mean ME coupling coefficient of 94 Oe cm/kV. Specifically, the ME coupling coefficient amounts to 2365 Oe cm/kV at the phase transition region of the PZN-PT single crystal. Meanwhile, the FMR linewidth of the FeGaB film, which is a critical parameter for microwave magnetic materials, stays at ∼50 Oe under different electric fields. The ratio between the total tunable magnetic field and the FMR linewidth is as high as c. 1500%, indicating an excellent figure of merit for tunable microwave devices.

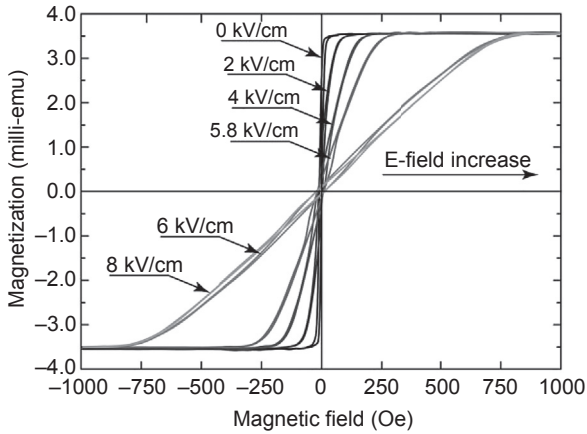

Figure 4.10 Magnetic hysteresis loops of the FeGaB/PZN-PT multiferroic heterostructure under different external electric fields measured by a vibrating-sample magnetometer.

The magnetic hysteresis loops of the FeGaB/PZN-PT multiferroic heterostructure were measured by a vibrating-sample magnetometer (VSM) along the [100] direction of the PZN-PT single crystal under different electric fields, which also confirmed the large electric-field-induced effective magnetic anisotropy changes, as shown in Figure 4.10. Clearly, the electric-field-induced magnetic anisotropy field is the largest at electric fields of 6 and 8 kV/cm, and lowest at 0 kV/cm. The in-plane magnetic anisotropy fields at different electric fields can be estimated from the hysteresis loops, with c. 20 Oe at 0 kV/cm and c. 700 Oe at 6 kV/cm electric field. This leads to an ME coefficient of c. 113 Oe cm/kV at dc, which is close to the value obtained from the FMR measurements at microwave frequencies.

To achieve a high-strain-mediated ME coupling effect in a magnetic thin film/ferroelectric slab, many efforts have been made in developing highly magnetostrictive RF magnetic materials. Recently, in magnetic/ferroelectric heterostructures, a low magnetization approach has been studied to generate large electric-field-induced effective magnetic fields. NiCr films with low magnetization and relatively large magnetostriction were discovered. NiCr alloy magnetic thin films were deposited by the dc magnetron cosputtering with Ni and Cr targets at room temperature on Si substrates with different Ni/Cr ratios (Zhou et al., 2012). All films were deposited for 600 s, leading to a film thickness of ∼50 nm. NiCr compositions were measured by an X-ray fluorescence system. The static NiCr hysteresis loops with different components were measured by a VSM. Microwave ME interaction was investigated by a broadband FMR spectrometer. A static electric field was applied across the NiCr/PZT and NiCr/PZN-PT samples thickness direction.

Strong converse ME coupling and large electric-field-tunable FMR bandwidths are achieved in layered NiCr/lead zirconate titanate (PZT) and NiCr/PZN-PT multiferroic heterostructures. A large electric-field-induced effective magnetic field of 260 Oe for NiCr/PZT and 756 Oe for NiCr/PZN-PT was observed, corresponding to a giant ME coupling coefficient of 13 Oe cm/kV in NiCr/PZT and 75.6 Oe cm/kV in NiCr/

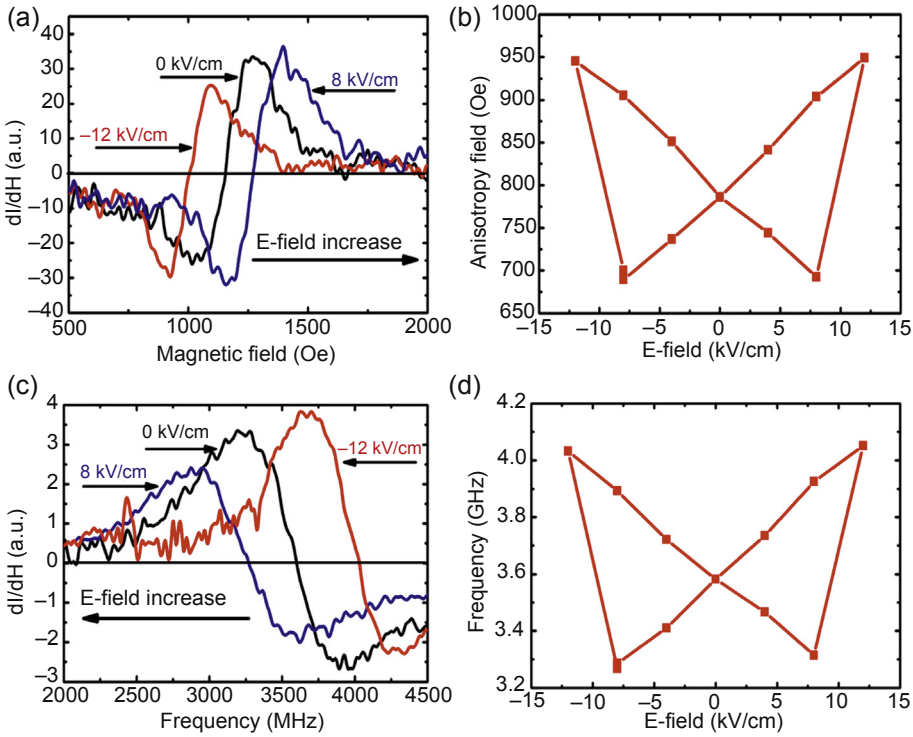

Figure 4.11 (a) Electric field dependence of the in-plane magnetic field sweep FMR spectra of NiCr/PZT multiferroic heterostructures measured at 6.85 GHz. (b) Butterfly plot of anisotropy magnetic field as a function of applied electric field from −8 to 12 kV/cm. (c) Electric field dependence of the in-plane frequency sweep FMR spectra of NiCr/PZT multiferroic heterostructure measured at 50 Oe. (d) Butterfly plot of resonance frequency as a function of applied electric field from −8 to 12 kV/cm.

PZN-PT multiferroic heterostructures (see Figures 4.11 and 4.12). A high-voltage tunable FMR frequency range was observed, with f_{max}/f_{min} being 124% and 325% for NiCr/PZT and NiCr/PZN-PT. The strong converse ME coupling of NiCr/PZT and NiCr/PZN-PT heterostructures provides great opportunities for electric-field-tunable RF magnetic devices.

Terfenol-D ($Tb_{0.7}Dy_{0.3}Fe_2$) exhibits the highest room temperature magnetostriction value and has been widely used as an actuator and sensor in either bulk or thin-film forms (Liu et al., 2012). Based on our previous model, the ME coefficient is proportional to the product of magnetostriction coefficient (k) and piezoelectric coefficient (d), which would enable a giant E-field-induced magnetic anisotropy once incorporating with ferroelectric materials. Terfenol-D will be a great candidate of magnetic thin film to realize a giant ME coupling coefficient. Amorphous and crystalline Terfenol-D films were grown on single-crystal (011) cut PZN-PT substrates that possess giant in-plane piezoelectric coefficients ($d_{31} = -3000$ pC/N [100];

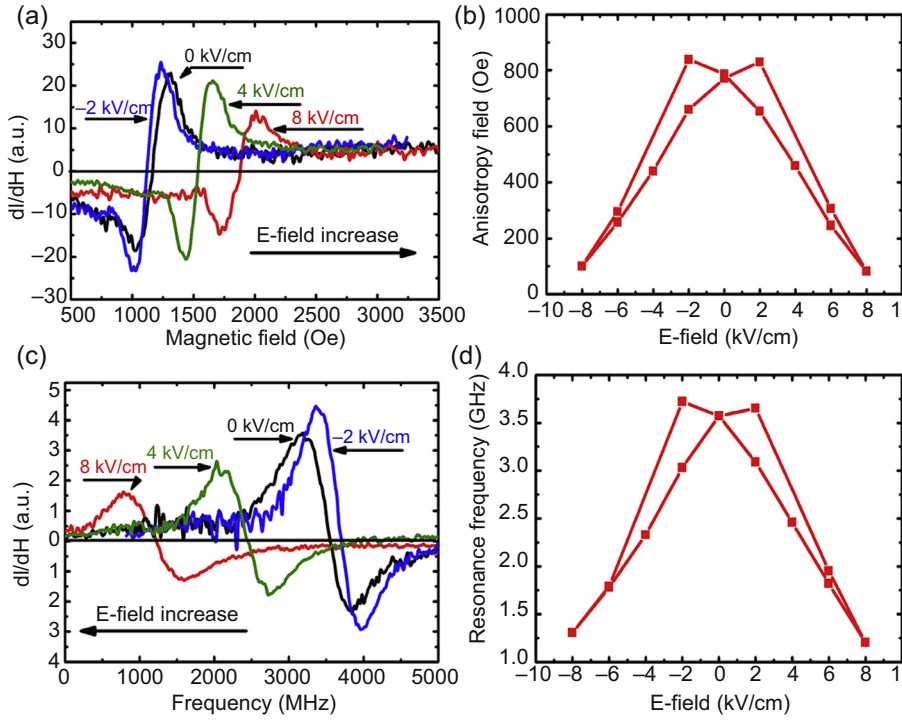

Figure 4.12 (a) Electric field dependence of the in-plane magnetic field sweep FMR spectra of NiCr/PZN-PT multiferroic heterostructures measured at 6.85 GHz. (b) Butterfly plot of anisotropy magnetic field as a function of applied electric field from −2 to 8 kV/cm. (c) Electric field dependence of the in-plane frequency sweep FMR spectra of NiCr/PZN-PT multiferroic heterostructure measured at 50 Oe. (d) Butterfly plot of resonance frequency as a function of applied electric field from −2 to 8 kV/cm.

$d_{32} = 1100$ pC/N [01−1]). Amorphous and crystalline Terfenol-D films were deposited onto Pt-coated Si substrates and PZN-PT slabs, magnetron sputtering under a variety of temperatures. The base pressure of the chamber was 10^{-8} Torr, while the deposition pressure was set at 3 mTorr. Accounting for the relative sputtering yields of two independent targets, $Tb_{0.3}Dy_{0.7}$ and Fe, we prepared Terfenol-D films by cosputtering with an estimated composition of $Tb_{0.3}Dy_{0.7}Fe_2$ and a thickness of approximately 100 nm.

Strain-engineered E-field tuning of magnetic properties of the Terfenol-D/PZN-PT film−substrate system was examined by E-field-induced changes in the magnetization process, as shown in Figure 4.13. For both amorphous (Figure 4.13(a)) and crystalline (Figure 4.13(c)) or intermediate (Figure 4.13(b)) Terfenol-D films, applying an E-field through the thickness direction of PZN-PT, the in-plane magnetization process along the [100] direction becomes increasingly more difficult, indicating a magnetic anisotropy was produced perpendicular to in-plane [100] orientation. This phenomenon can be interpreted as strong

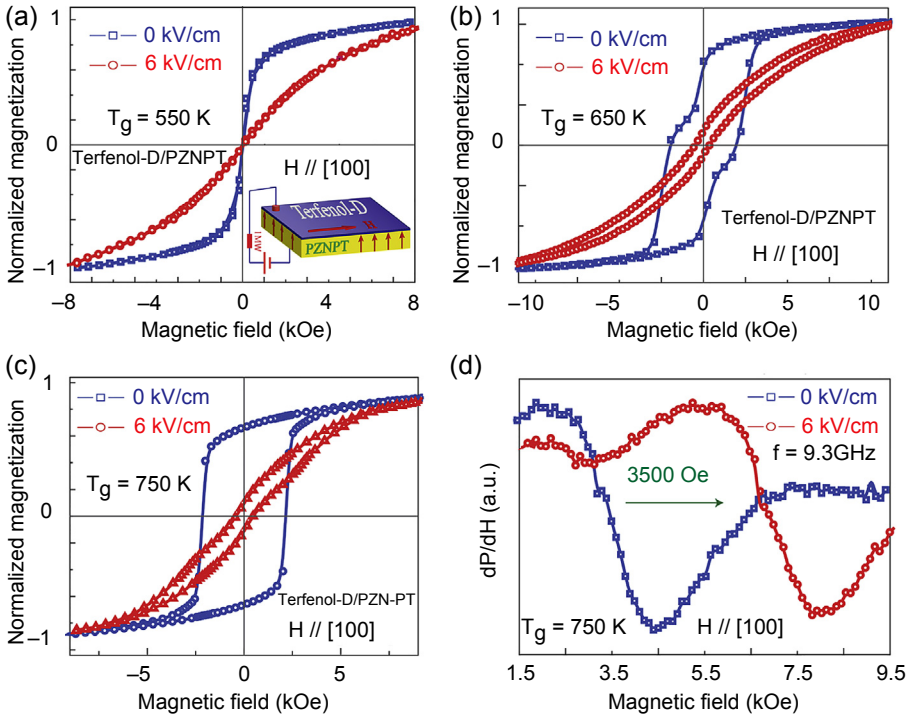

Figure 4.13 E-field dependence of in-plane magnetic hysteresis loops of Terfenol-D/PZN-PT deposited at 550 K (a), 650 K (b), and 750 K (c). The inset in (a) is the measurement configuration: E-field is applied through the thickness direction and magnetic field is applied along the in-plane [100] direction. (d) FMR spectra of polycrystalline Terfenol-D/PZN-PT at E = 0 kV/cm (blue) and E = 6 kV/cm (red).

magnetoelastic and piezoelectric effects. A dc field applied across the PZN-PT substrate results in a compressive stress along the in-plane [100] direction caused by the inverse piezoelectric effect. Once this mechanical strain coherently transfers to the Terfenol-D film, the magnetic moment undergoes a rotation away from the [100] direction due to the magnetoelastic effect. Given the complicated nature of the magnetization process involving domain wall motion, domain rotation, and nonlinear behaviors, E-field-induced magnetic hysteresis loop change is not sufficient to quantitatively determine this magnetic anisotropy, which is essential for fundamental and technologic study. According to the E-field dependence of the FMR spectrum plotted in Figure 4.13(d) for crystalline Terfenol-D/PZN-PT, the resonance field H_r is shifted upward by 3500 Oe as applying an electric field of 6 kV/m, indicating a record-high E-field-induced magnetic anisotropy of 3500 Oe is achieved, corresponding to an ME coefficient of 580 Oe cm/kV.

Besides strain/stress-mediated ME coupling, Tianxiang et al. revealed that the spin-polarized interfacial charge effect can also play an important role in magnetic thin film/

ferroelectric slab multiferroic heterostructure (Nan et al., 2014). The coexistence of strain and surface-charge-mediated ME coupling in an ultrathin (1 nm) $Ni_{79}Fe_{21}$ and (011) PMN-PT heterostructure was demonstrated. Voltage-controlled FMR of the $Ni_{79}Fe_{21}$/(011) PMN-PT heterostructures was utilized for quantitatively studying its ME behavior. A combination of strain-mediated butterfly curve and surface-charge-mediated hysteretic curve was observed with an effective magnetic field change of 375 Oe and a nonvolatile effective magnetic field change at zero voltage of 104 Oe. For a control sample, when a 5 nm Cu layer was inserted into NiFe and PMN-PT, a standard butterfly curve induced by pure strain-mediated ME coupling was observed. By subtracting the change of effective magnetic field induced by the strain effect, a pure charge-induced effective magnetic field of 201 Oe was achieved. The change of effective magnetic field shows a clear response to the polarization of ferroelectric PMN-PT.

As for NiFe/Cu/PMN-PT, the inserting Cu layer played a role as an isolation layer. In that case, no screening charge exists in the NiFe/PMN-PT interface. Thus pure strain-mediated ME coupling was controlled by strain and stress transferred through the Cu thin layer induced by the electric field on PMN-PT due to the piezoelectric effect. As expected, a standard "butterfly" curve of the FMR effective magnetic field as a function of electric field was observed shown in Figure 4.14(b), having a maximum H_{eff} tunability of 202 Oe. In FMR field sweeping mode, the magnetic field was applied along the in-plane [0−11] direction.

Interestingly, for comparison, NiFe/PMN-PT was measured in FMR field sweeping mode under similar experimental conditions, including the same circling electric field direction and applied magnetic field direction. By removing the isolating Cu layer, a completely different ME coupling phenomenon was observed, as shown in Figure 4.14(a). This possibly resulted from the surface charge induced by the polarization of PMN-PT. The maximum effective magnetic field shift was increased to ∼375 Oe. The FMR effective magnetic field was increased due to the different surface anisotropy of NiFe/Cu and NiFe/PMN-PT. More importantly, in NiFe/Cu/PMN-PT, the FMR magnetic effective field was unchanged (∼1940 Oe) when the electric field was 0 due to the linear piezoelectric effect; while in NiFe/PMN-PT, two different magnetic effective fields (∼3390 Oe and ∼3494 Oe, respectively) were induced depending on the polarization of PMN-PT, specifically the positive/negative remnant polarization induced by positive/negative electric field. Furthermore, the positive/negative remnant polarization could induce positive/negative charge between NiFe/PMN-PT interfaces, thus modifying the magnetic anisotropy via the screening charge effect. However, in NiFe/Cu/PMN-PT, because of the conductive Cu layer, the charge was unable to acuminate between the NiFe/Cu interfaces, resulting in nonexistence of the charge-mediated ME effect. The strain and charge-mediated ME coupling could possibly be involved in NiFe/PMN-PT at the same time. In NiFe/PMN-PT, like magnetic memory, two stable and reversible effective magnetic field states were established at zero electric field for achieving nonvolatile switching of the FMR field by reversing electric field.

In order to further investigate the distinct origin of the ME coupling effect between NiFe/Cu/PMN-PT and NiFe/PMN-PT, the angular dependence of FMR spectra was

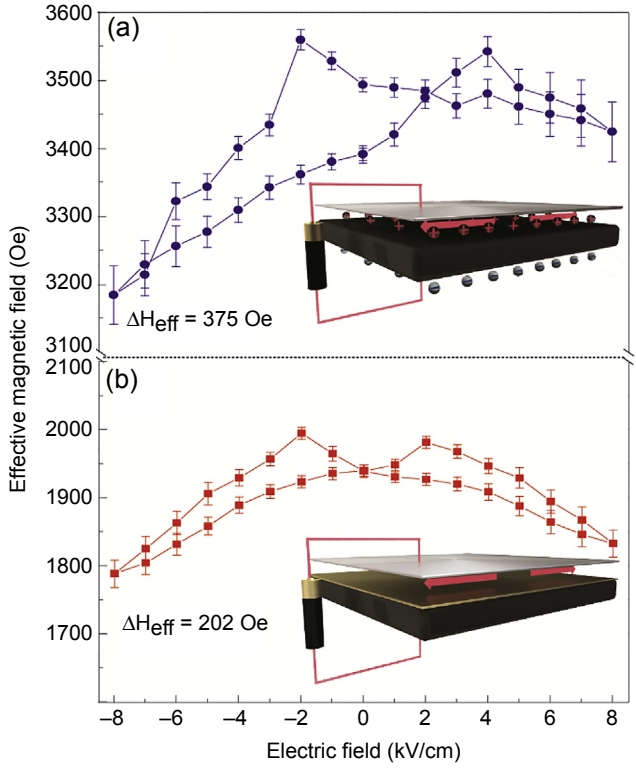

Figure 4.14 (a) FMR fields of NiFe/PMN-PT (011) and (b) NiFe/Cu/PMN-PT (011) by applying different electric fields with the bias magnetic field applied along the in-plane [0−11] direction. The blue and red arrow pointed the direction of the applied circling electric field.

acquired by an under-varied electric field. In FMR field sweeping mode, a magnetic field was first applied along the in-plane [0−11] direction defined as 0° (360°) and the step of the increment was 15°. Figure 4.15(a) and (b) show the angular dependence of the FMR effective magnetic field of NiFe/PMN-PT and NiFe/Cu/PMN-PT under a different electric field; Figure 4.15(c) and (d) show the polar graph transferred from (a) and (b), respectively. In NiFe/Cu/PMN-PT, with the applied electric field impulse of +8 kV/cm and −8 kV/cm electric field impulse, the FMR angular dependence depicts a uniaxial anisotropy with a magnetic easy axis along the [100] direction; however, due to the release of piezo-strain at zero electric field and symmetric behavior of the piezoelectric "butterfly" curve, there was no magnetic anisotropy change. While applying an electric field of 2 kV/cm, the effective magnetic field increased along the [0−11] direction and decreased along the [100] direction. The in-plane magnetic anisotropy change is due to the linear piezoelectric effect of (011)-oriented PMN-PT, in particular, anisotropic in-plane piezoelectric coefficients

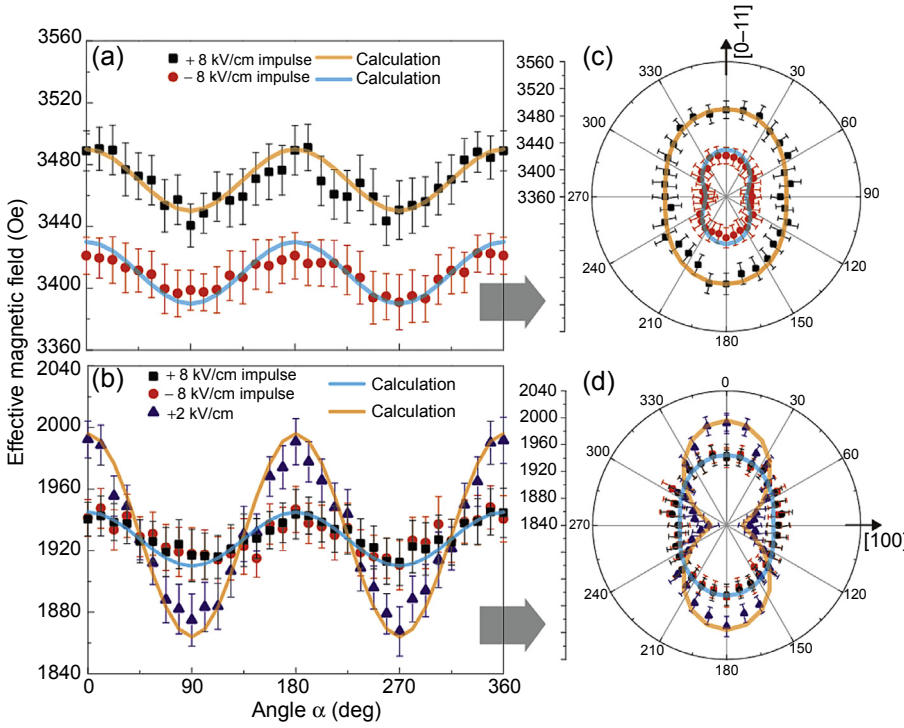

Figure 4.15 (a) Angular dependence of FMR effective magnetic fields of NiFe/Cu/PMN-PT and (b) NiFe/PMN-PT under different electric fields and the calculated curves. (a) is the angle between the applied magnetic field and the [0−11]direction. (c) and (d) show the polar graph transferred from (a) and (b), respectively.

of PMN-PT ($d_{31} = -1800$ pC/N, $d_{32} = 900$ pC/N). The change of effective magnetic field on both directions was ∼45 Oe, which is consistent with the FMR field response in Figure 4.14(b). A sharp contrast was observed in NiFe/PMN-PT shown in Figure 4.15(b) and (d) by measuring the angular-dependent FMR spectra after applying +8 kV/cm (black) and −8 kV/cm (red) electric field impulse (from 0 kV/cm through ±8 kV/cm to 0 kV/cm), respectively. The angular dependence FMR fields both exhibit uniaxial anisotropy behavior. However, the +8 kV/cm electric field impulse induced a high effective magnetic field, while −8 kV induced a low effective magnetic field. This is direct evidence of the existence of surface-charge-induced out-of-plane anisotropy change. The change of the effective magnetic field was around 80 Oe, which corresponds with Figure 4.14(a) where an FMR field of 100 Oe discrepancies in zero electric field exists. Figure 4.16 shows a voltage-impulse-induced FMR field tuning in NiFe/PMN-PT (011) with a magnetic field along the [0−11] direction, which demonstrated a robust and repeatable nonvolatile switching of an effective magnetic field.

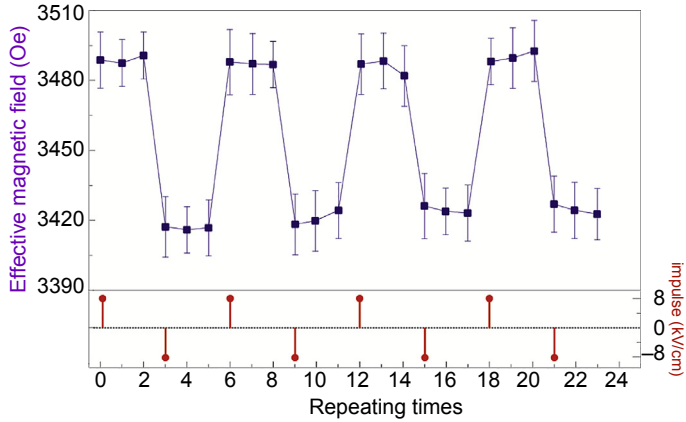

Figure 4.16 Electric-field-impulse-induced nonvolatile switching of the FMR field of NiFe/PMN-PT with a magnetic field applied along the [0−11] direction.

References

Duan, C.-G., Jaswal, S. S., & Tsymbal, E. Y. (2006). *Physical Review Letters, 97*, 047201.

Eerenstein, W., Mathur, N. D., & Scott, J. F. (2006). *Nature, 442*, 759.

Fetisov, Y. K., & Srinivasana, G. (2006). *Applied Physics Letters, 88*, 143503.

Hill, N. A. (2000). *Journal of Physical Chemistry B, 104*, 6694.

Liu, M., et al. (2008). *Applied Physics Letters, 92*, 152504.

Liu, M., et al. (2009). *Advanced Functional Materials, 19*, 1826−1831.

Liu, M., Li, S., Zhou, Z., Beguhn, S., Lou, J., et al. (2012). *Journal of Applied Physics, 112*, 063917.

Liu, M., et al. (2013). *Advanced Materials, 25*, 1435.

Liu, M., et al. (2009). *Journal of Physics D: Applied Physics, 42*, 045007.

Lou, J., Liu, M., Reed, D., Ren, Y. H., & Sun, N. X. (2009). *Advanced Materials, 21*, 4711−4715.

Lu, X. Y., Wang, B., Zheng, Y., & Ryba, E. (2007). *Applied Physics Letters, 90*, 133124.

Martin, L. W., et al. (2008). *Journal of Physics: Condensed Matter, 20*, 434220.

Nan, C. W., Bichurin, M. I., Dong, S. X., Viehland, D., & Srinivasan, G. (2008). *Journal of Applied Physics, 103*, 1101.

Nan, C.-W., Liu, G., Lin, Y., & Chen, H. (2005). *Physical Review Letters, 94*, 197203.

Nan, T., et al. (2014). *Scientific Reports, 4*, 3688.

Newnham, R. E., Skinner, D. P., & Cross, L. E. (1978). *Materials Research Bulletin, 13*, 525.

Sun, N. X., & Srinivasan, G. (2012). *Spin, 2*(3), 1240004.

Vaz, C. A. F., Hoffman, J., Ahn, C. H., & Ramesh, R. (2010). *Advanced Materials, 22*, 2900.

Zhang, J. X., et al. (2007). *Applied Physics Letters, 90*, 052909.

Zheng, H., et al. (2004). *Science, 303*, 661.

Zhou, Z., et al. (2012). *Journal of Applied Physics, 111*, 103915.

Epitaxial multiferroic heterostructures

5

Z. Hu, N.X. Sun
Northeastern University, Boston, MA, USA

5.1 Introduction

Recently, a new trend in the design of multiferroic systems is the control of properties at the nanoscale, along with a bottom-up approach where the properties are engineered at the atomic scale (Ma, Hu, Li, & Nan, 2011; Martin, Chu, & Ramesh, 2010; Vaz, Hoffman, Ahn, & Ramesh, 2010). The studies on epitaxial multiferroic heterostructures have been driven, in part, by the development of new thin-film growth techniques and the resulting access to high-quality epitaxial or self-assembled materials on various substrates (Martin et al., 2010). In strain-mediated multiferroic systems, strong magnetoelectric (ME) coupling is expected between the order parameters of the ferroelectric and ferromagnetic components, because the lattice-matched interface is free of any foreign medium, which can transfer the mechanical coupling more efficiently than that in epoxy bonded or polycrystalline bilayers (Li et al., 2011). Charge- or exchange-bias (EB) -mediated ME coupling that relies on uncompensated interfacial charges or spins can also be engineered at the nanoscale (Vaz, Hoffman, Ahn, et al., 2010). However, the controlled epitaxial growth of a magnetic layer on ferroelectrics or ferroelectrics on a magnetic layer is still challenging, because the two kinds of materials must be both chemically and structurally compatible: there should be no chemical reaction at high temperature, and they should have similar lattice parameters when being indexed by pseudocubic structures to help guide the heteroepitaxial growth. Therefore, in most of the studies on epitaxial multiferroic heterostructures, $BiFeO_3$ (BFO), Pb(Zr, Ti)O_3 (PZT), $Pb(Mg_{1/3}Nb_{2/3})O_3$-$PbTiO_3$ (PMN-PT), and $Pb(Zn_{1/3}Nb_{2/3})O_3$-$PbTiO_3$ (PZN-PT) have been used as the ferroelectric layer, while the magnetic materials of choice include La-manganite ((La,Sr)MnO_3) and Ni/Co-ferrite (i.e., $NiFe_2O_4$, $CoFe_2O_4$ (CFO)).

5.2 $BiFeO_3$ systems-related multiferroics

BFO is the most commonly studied single-phase multiferroic material because of its high ferroelectric and magnetic ordering temperatures, $T_C = 1123$ K, $T_N = 643$ K (Sosnowska, Neumaier, & Steichele, 1982). At room temperature, BFO has a large remanent polarization in excess of $\sim 100\ \mu C/cm^2$ along the $[111]_{pc}$ direction and a G-type antiferromagnetic local ordering (Wang et al., 2003). Weak ME coupling to the ferroelectric polarization leads to a slight canting of the magnetic moment that

Composite Magnetoelectrics. http://dx.doi.org/10.1016/B978-1-78242-254-9.00005-6
Copyright © 2015 Elsevier Ltd. All rights reserved.

averages to zero due to a long-range incommensurate spin cycloid, with a wavelength $\lambda \sim 62$ nm. The spin cycloid averages out any linear ME coupling between polarization (P) and magnetization (M); however, a high magnetic field (~ 20 T) can destroy the cycloid, thereby recovering the linear ME coupling (Zvezdin et al., 2006). The multiferroic properties of single-phase BFO are summarized in recent reviews (Catalan & Scott, 2009; Martin et al., 2010; Martin & Ramesh, 2012). In this section, we will focus specifically on the multiferroic composite heterostructures based on the epitaxial BFO system.

5.2.1 Epitaxial $BiFeO_3$–$CoFe_2O_4$ multiferroic columnar nanostructures

The early approach is to develop strain-mediated ME composites utilizing the piezoelectric response of BFO. Following the pioneering work of Zheng et al. on $BaTiO_3$–$CoFe_2O_4$ (Zheng et al., 2004), epitaxial $BiFeO_3$–$CoFe_2O_4$ multiferroic columnar nanostructures were demonstrated under appropriate growth conditions using pulsed laser deposition (PLD) (Dix et al., 2010; Yan, Yang, et al., 2009; Zavaliche et al., 2007; Zheng et al., 2006). In this structure, nanopillar arrays of the magnetic component form in a ferroelectric matrix; due to the close oxygen sublattice parameters, both phases grow epitaxially, both in-plane and perpendicular to the substrate. Only the piezoelectric properties of BFO are employed to modulate the magnetic state of $CoFe_2O_4$ via strain, and magnetization reversal induced by an electric field was observed at room temperature. Although the piezoelectric constant of BFO is relatively low (between 15 and 60 pm/V) compared with 100–1000 pm/V for other perovskite ferroelectrics (Catalan & Scott, 2009; Wang et al., 2003), the ME susceptibility of epitaxial $BiFeO_3$–$CoFe_2O_4$ columnar nanostructures is estimated to be $\alpha \sim 1.0 \times 10^{-2}$ Oe cm/V, which is comparable to the values obtained in laminate composites at resonant frequencies and to those obtained in particulate composites (Martin et al., 2010; Vaz, Hoffman, Ahn, et al., 2010). The ME coupling coefficient in similar structures has a peak value of $\alpha_E \sim 18$ mV/cm/Oe (Yan, Xing, et al., 2009). On the basis of these epitaxial $BiFeO_3$–$CoFe_2O_4$ columnar nanostructures, Zavaliche et al. proposed using an electric field to assist magnetic recording in multiferroic systems with high perpendicular magnetic anisotropy, as shown in Figure 5.1 (Zavaliche et al., 2007).

$BiFeO_3$–$CoFe_2O_4$ nanocomposites are an intriguing option for future memory and logic technologies due to the ME properties of the system. However, these nanocomposites form with CFO pillars randomly located within a BFO matrix, making implementation in devices difficult. To overcome this, Comes et al. developed a technique to produce patterned nanocomposites through self-assembly (Comes et al., 2012). CFO islands are patterned on Nb-doped $SrTiO_3$ to direct the self-assembly of epitaxial CFO–BFO nanocomposites, producing square arrays of CFO pillars, as shown in Figure 5.2.

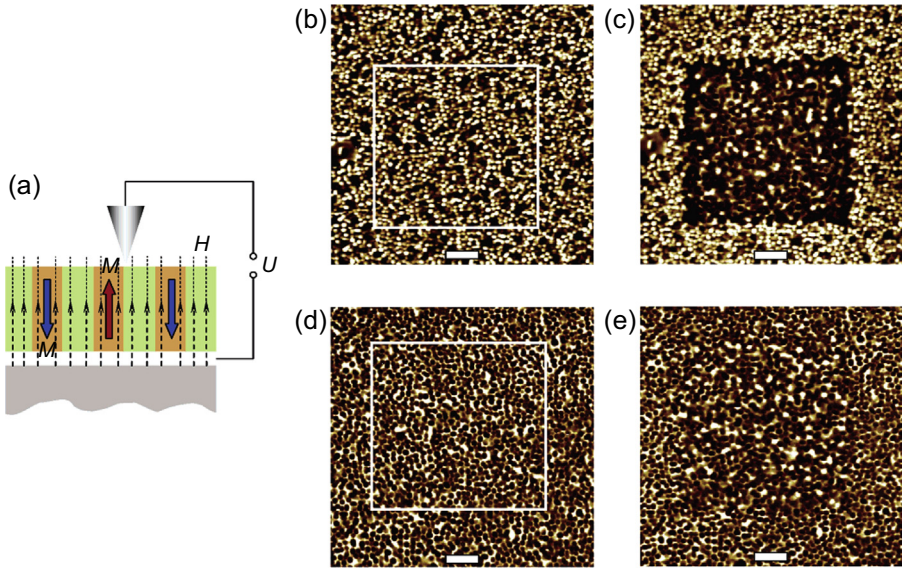

Figure 5.1 The principle of electrically assisted magnetic recording (EAMR) in $(BiFeO_3)_{0.65}$−$(CoFe_2O_4)_{0.35}$ multiferroic nanostructure. (a) Sketch of the experimental setup. (b) Magnetic force microscopy (MFM) after magnetization in a down 20 kOe field before and (c) after poling at −16 V in a 700 Oe up-magnetic field. (d) MFM after magnetization in an up 20 kOe field before and (e) after poling at −16 V in a 700 Oe up-magnetic field. The bars are 1 μm (Zavaliche et al., 2007).

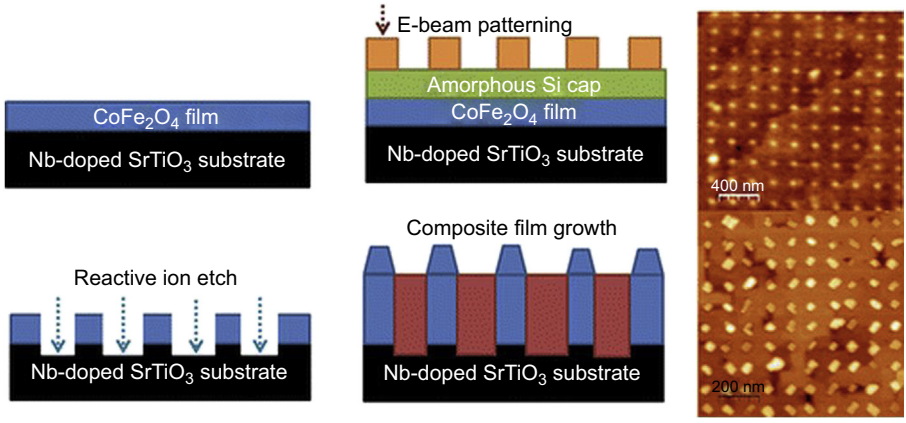

Figure 5.2 Sketch and scanning electron microscopy (SEM) images of directed self-assembly of epitaxial $BiFeO_3$−$CoFe_2O_4$ multiferroic nanocomposites (Comes et al., 2012).

5.2.2 Epitaxial BFO thin films for spintronic applications

More researchers are now focused on spintronic applications using epitaxial BFO thin films, for example, memories that can be written using a voltage and read using a magnetic field (Béa, Gajek, Bibes, & Barthélémky, 2008; Sando et al., 2013). In BFO, the magnetic state can be changed by a voltage through the rotation of ferroelectric polarization; however, the antiferromagnetic domains cannot be easily read. One solution to this problem consists in using the mechanism known as EB Crudely, EB is the magnetic interaction between the spins at the antiferromagnetic layer and a thin ferromagnetic layer attached to it. The voltage-induced changes to the underlying antiferromagnetic domains will result in changes to the ferromagnetic hysteresis of the upper layer, which can then be read by conventional mechanisms (Béa, Bibes, et al., 2008).

The implementations of this concept were first done using Cr_2O_3 and $YMnO_3$ and then in BFO, and several important milestones have been achieved so far. Dho et al. (Dho, Qi, Kim, MacManus-Driscoll, & Blamire, 2006) and Béa et al. (Bea et al., 2006; Béa, Bibes, et al., 2008) showed a sizable EB (50−60 Oe) in NiFe/BFO and CoFeB/BFO films at room temperature. Martin et al. indicated that there are two major interactions occurring in these heterostructures (Martin et al., 2007, 2008). One is a surface coupling between the spins in the antiferromagnet and the ferromagnet, which results in very little unidirectional pinning of the ferromagnetic layer and manifests itself as an enhancement of H_C (showing only exchange enhancement). The second interaction, EB, appears to be a coupling phenomenon at or near the few nanometers where the 109° domain walls in BFO intersect the film surface. It was found that the magnitude of this EB interaction can be tailored by engineering the underlying domain structure of the BFO film, thus presenting the ability to gain nanoscale control of EB interactions in an exciting multiferroic-based system. They observed a large EB field over 150 Oe in the CoFe/BFO bilayer with 109° domain walls in BFO films, as shown in Figure 5.3 (Martin et al., 2008).

Instead of using amorphous ferromagnetic alloys, epitaxially crystallized $La_{2/3}Sr_{1/3}$ MnO_3 was also utilized as a ferromagnetic layer. Thin BFO films can be used as a tunnel barrier between electrodes of $La_{2/3}Sr_{1/3}MnO_3$ (LSMO) and Co, which leads to a large positive tunnel magnetoresistance (TMR) up to 30% at low temperature (3 K) (Bea et al., 2006). In order to improve the magnetic and transport properties of LSMO, an $SrTiO_3$ (STO) protective layer was deposited before the BFO barrier to avoid the deoxygenation (Béa, Gajek, et al., 2008). A TMR up to 100% is obtained at 3 K and 10 mV with this double barrier junction, as shown in Figure 5.4. Moreover, the TMR remains up to 300 K, which is limited by T_C of LSMO films.

A novel ferromagnetic state is observed at the interface of multiferroic $BiFeO_3$ and ferromagnetic $La_{0.7}Sr_{0.3}MnO_3$ (LSMO) as a consequence of a complex interplay between the orbital degree of freedom and its coupling to the spin degree of freedom. This ferromagnetic state in the Fe sublattice gives rise to a significant EB interaction with the ferromagnetic LSMO (Yu et al., 2010). The electric field control of such an interfacial ferromagnetic state would be a significant step toward ME devices.

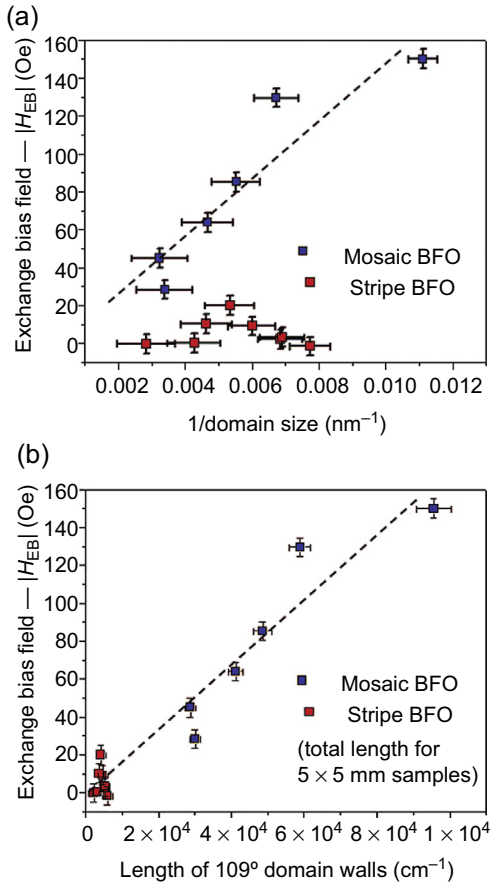

Figure 5.3 (a) Dependence of exchange bias field on domain size for CoFe/BFO heterostructures grown on mosaic-like (blue) and stripe-like (red) BFO films. (b) Exchange bias field of the same samples here graphed as a function of the total length of 109° domain walls/sample surface area in 5 × 5 mm samples (Martin et al., 2008).

Based on this concept, a multiferroic field-effect device was built by Wu et al., as shown in Figure 5.5 (Wu et al., 2010). Two distinct EB states can be reversibly switched by the ferroelectric polarization of $BiFeO_3$ at low temperature (5.5 K). The strain effect on EB can be ruled out in this BFO/LSMO heterostructure, since no EB existed in the BFO/STO/LSMO heterostructure. This type of low-current, low-power electrical switching has far-reaching implications for the field of spintronics.

The $BiFeO_3$-related epitaxial multiferroics are still an important focus and could have tremendous impact in many areas, including information storage, sensing and actuation, and spintronics. However, problems such as low ME coupling, low work temperature, and poor reproducibility should be addressed in the future for room temperature device applications.

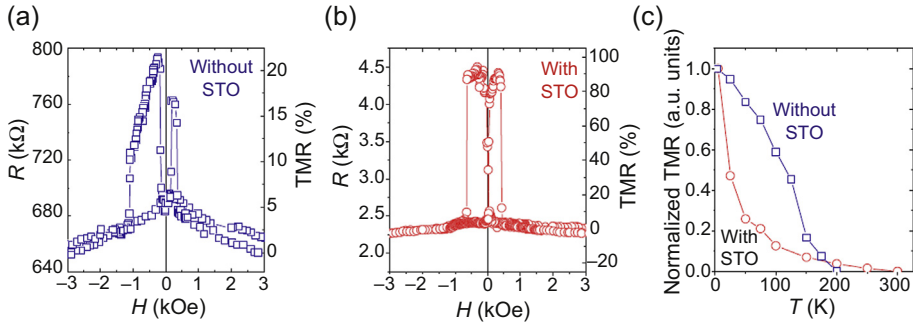

Figure 5.4 Resistance versus magnetic field for magnetic tunnel junctions with Co and LSMO ferromagnetic electrodes and multiferroic barriers measured at 3 K and 10 mV: (a) BFO (5 nm) single barrier, that is, without STO, and (b) BFO (2 nm)/STO (1.6 nm) double barrier, that is, with STO. (c) Evolution of the TMR with temperature for these two junctions (Béa, Gajek, et al., 2008).

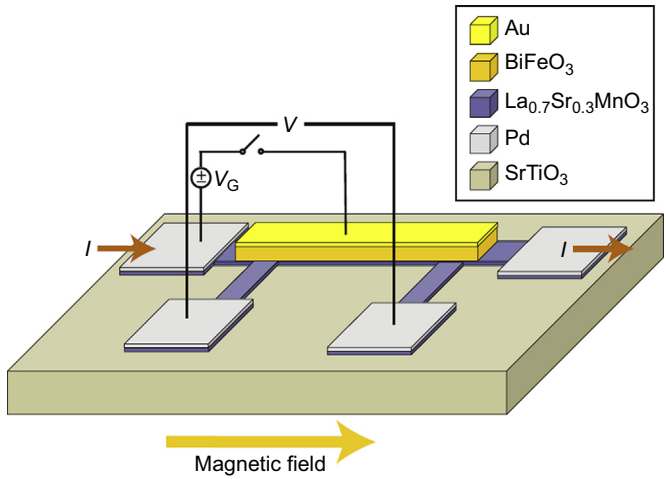

Figure 5.5 A schematic of the BFO/LSMO field-effect device (Wu et al., 2010). To change the BFO polarization, a voltage pulse V_G is applied between the gate and the LSMO channel. The magnetic field for magnetic remanence (MR) measurements is applied parallel to the direction of the current.

5.3 La-manganite-related multiferroics

La-manganite, such as $La_{1-x}Sr_xMnO_3$ (LSMO), is half metallic as well as magnetic, which can be used as electrode and ferromagnetic layer simultaneously. Besides, LSMO exhibits a similar perovskite structure (lattice parameters ~3.96 Å) with that of typical ferroelectric materials such as $BaTiO_3$ (BTO), PZT, and BFO. Therefore, epitaxial multiferroic structures are possible when combining LSMO and ferroelectric films together.

5.3.1 La-manganite/BTO heterostructures

Eerenstein et al. demonstrated electrically induced giant, sharp, and persistent magnetic changes (up to 2.3×10^{-7} s/m) at a single epitaxial interface in ferromagnetic 40 nm $La_{0.67}Sr_{0.33}MnO_3$ films on 0.5 mm ferroelectric BTO substrates (Eerenstein, Wiora, Prieto, Scott, & Mathur, 2007). The strain coupling via ferroelastic non-180° BTO domains was confirmed by X-ray diffraction. Those findings are valid over a wide range of temperatures, including room temperature, and the magnetic response to an electric field can be used in electric-write magnetic-read memory devices.

However, the bulky BTO substrates are not compatible with semiconductor industry processes. High-quality, thin ferroelectric films are desired to reduce the energy consumption and the device size. Garcia et al. reported the control of spin polarization by ultra-thin ferroelectric tunnel barriers based on BTO(1 nm)/LSMO(30 nm) bilayers grown epitaxially onto $NdGaO_3$ (001) single-crystal substrates (Garcia et al., 2010). To measure the TMR, a 5-nm-thick Fe layer was deposited on BTO/LSMO and capped by an Au(100 nm)/CoO(3.5 nm)/Co(11.5 nm) stack to increase coercivity. Using the half-metallic LSMO bottom electrode as a spin detector, TMR was found to be dramatically modified by the reversal of BTO polarization, as shown in Figure 5.6. The ferroelectric polarization can provide a local, reversible, nonvolatile, and potentially low-power means of electrically addressing spintronics devices (Garcia et al., 2010).

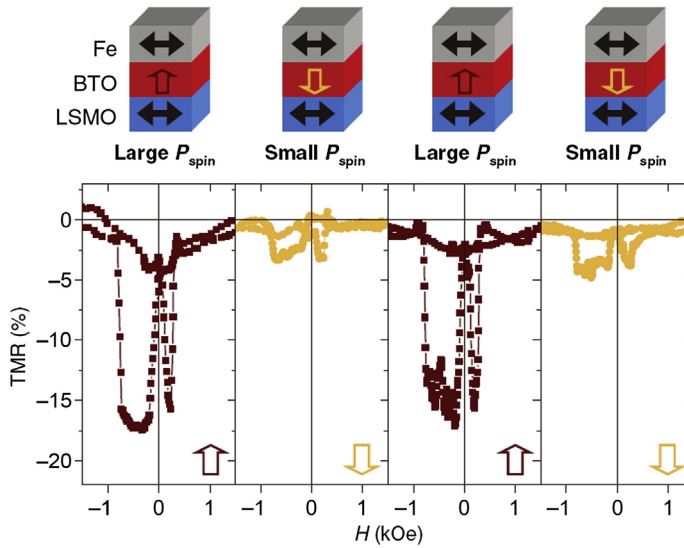

Figure 5.6 TMR (H) curves of Fe/BTO/LSMO tunnel junctions ($V_{DC} = -50$ mV, $T = 4.2$ K) after poling the ferroelectric polarization up (VP+), down (VP−), up (VP+), and down (VP−) (Garcia et al., 2010).

5.3.2 La-manganite/PZT

Perovskite $Pb(Zr,Ti)O_3$ (PZT) is one of the most widely studied ferroelectric and piezoelectric materials, especially in the vicinity of the morphotropic phase boundary between rhombohedral and tetragonal ferroelectric phases. Since PZT exhibits high ferroelectric polarization and high piezoelectric response, it is a promising candidate for strain-mediated multiferroic composites. Ziese et al. reported epitaxial $La_{0.7}Sr_{0.3}MnO_3$/PZT multilayers fabricated by PLD (Vrejoiu et al., 2008; Ziese et al., 2008). High ferroelectric polarization and stable piezoelectric switching were found for the lead zirconate titanate layers, whereas the manganite layers showed bulk-like resistivity and magnetoresistance, both attesting to the high quality of the layers. Multiple magnetization switching was observed in the multilayers, which was related to the complex strain state (Ziese et al., 2008).

Charge-mediated multiferroic properties were also demonstrated in a similar LSMO/PZT heterostructure, where an abrupt switching between a high and low magnetic state of the LSMO layer was found as a function of the PZT polarization state, as shown in Figure 5.7 (Molegraaf et al., 2009; Vaz, Hoffman, Ahn, et al., 2010). The origin of this ME effect is purely electronic, as recently demonstrated by probing directly the electronic structure of Mn in the LSMO via X-ray near-edge absorption spectroscopy (XANES), which demonstrates the direct modulation in the Mn valence state for the two directions of the PZT polarization (Vaz, Hoffman, Ahn, et al., 2010; Vaz, Hoffman, Segal, et al., 2010).

5.4 Ferrite-related multiferroics

Spinel ferrites, such as $CoFe_2O_4$ and $NiFe_2O_4$, are ferromagnetic oxides with relatively high resistivity. The perovskite ferroelectrics have a lattice parameter of ~4 Å,

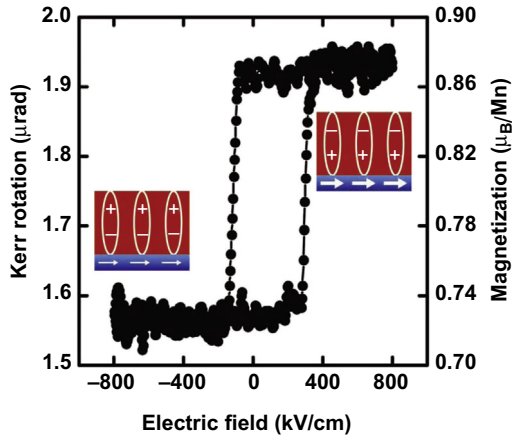

Figure 5.7 Magnetoelectric hysteresis curve showing the magnetic response of the PZT/LSMO system at 100 K as a function of the applied electric field. Insets represent the magnetic and electric states of the LSMO and PZT layers, respectively (Vaz, Hoffman, Ahn, et al., 2010).

which is generally within 5% of the basic building block of the spinels. The intrinsic similarities in crystal chemistry (i.e., oxygen coordination chemistry) between the spinel and perovskite families lead to compatible lattice dimensions and possibility of both in-plane and out-of-plane heteroepitaxy.

5.4.1 Ferrite/BTO heterostructures

By selecting materials that spontaneously separate due to immiscibility, such as spinel and perovskite phases, one can create nanostructured phases made of pillars of one material embedded in a matrix of another. These 1−3-type nanostructured composite films will produce much higher coupling interaction in comparison with 2−2-type films. Additionally, the large difference in lattice parameters between these phases leads to the formation of pillars with dimensions on the order of 10 nm, ensuring a high interface-to-volume ratio and strong coupling via strain (Martin & Ramesh, 2012). In 2004, Zheng et al. reported a pioneer work of multiferroic nanocomposite films consisting of magnetic $CoFe_2O_4$ nanopillars (diameters of 20−30 nm) embedded in a ferroelectric $BaTiO_3$ matrix (Zheng et al., 2004). Such structures were shown to exhibit strong ME coupling (Figure 5.8) via changes in magnetization occurring at the ferroelectric Curie temperature of the matrix material. These nanostructures, in which the interface is perpendicular to the substrate, remove the effect of substrate clamping and allow for better strain-induced coupling between the two phases (Martin & Ramesh, 2012; Zheng et al., 2004). However, the design, fabrication, and control of such heterostructures still remain a challenge.

It is more convenient to fabricate 2−2-type heterostructured multiferroic composite films. C.W. Nan's group reported the epitaxial growth of $NiFe_2O_4$−$BaTiO_3$ and $CoFe_2O_4$−$BaTiO_3$ heterostructures on $SrTiO_3$ (001) and (111) single-crystal substrates via PLD (Deng, Zhang, Ma, Lin, & Nan, 2007; Deng, Zhang, Ma, Lin, & Nan, 2008; Zhang, Deng, Ma, Lin, & Nan, 2008), in which the bottom $BaTiO_3$ layer epitaxially grown on the substrates acts as a buffer layer and effectively reduces the coherent constraint in the magnetic layer arising from the substrates. Microstructure studies from X-ray diffraction and electron microscopies showed good coherent epitaxy thin films of the spinels and perovskites on STO substrates, which exhibits simultaneously strong ferroelectric and ferromagnetic responses. A direct ME coupling effect was observed in the heterostructures. Jia's group reported a cost-effective, polymer-assisted deposition approach to prepare self-assembled epitaxial $NiFe_2O_4$−$BaTiO_3$ nanocomposite films on $LaAlO_3$ substrates, in which the ferroelectric $BaTiO_3$ is embedded in the ferrimagnetic spinel $NiFe_2O_4$ matrix. The composite shows both ferroelectric and ferrimagnetic properties (Luo et al., 2007). In theoretical analyses, the magnetically induced ferroelectric properties of the 1−3-type multiferroic $CoFe_2O_4$−$BaTiO_3$ nanocomposite films were calculated by the Landau−Devonshire thermodynamic theory (Zhong, Jiang, Fang, & Jiang, 2009). In addition, the magnetic-field-induced electric polarization in $CoFe_2O_4$−$BaTiO_3$ epitaxial thin films was studied by applying the transversal and longitudinal external magnetic fields to the magnetostrictive phase.

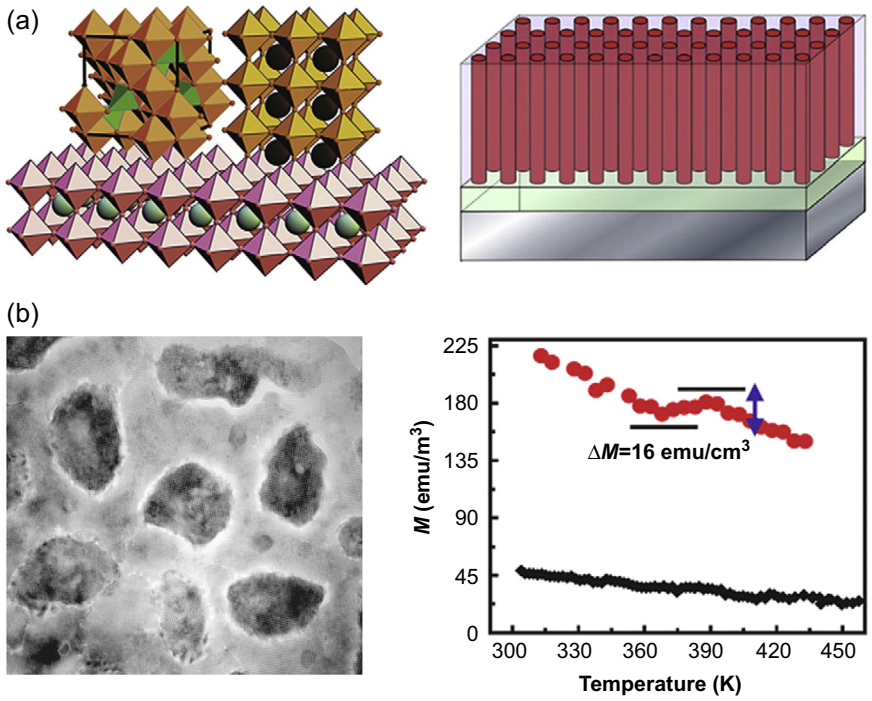

Figure 5.8 Multiferroic $CoFe_2O_4$−$BaTiO_3$ nanostructures. (a) Schematic illustrations of vertical nanostructure of spinel pillars embedded in a perovskite matrix grown on a perovskite substrate. (b) Magnetization versus temperature curve measured at 100 Oe, showing a distinct drop in magnetization at the ferroelectric Curie temperature, which is a proof of strong magnetoelectric coupling (Zheng et al., 2004).

5.4.2 Ferrite/PZT heterostructures

PZT has higher ferroelectric polarization and piezoelectric coefficient than that of BTO, thus leading to better ME coupling effects in multiferroic composites. Mukherjee et al. reported epitaxial growth of $CoFe_2O_4$−PZT bilayers on single-crystal $SrTiO_3$ (100) substrates by PLD (Mukherjee et al., 2010). The CFO−PZT bilayer films showed reduced values of magnetization as compared with those of the CFO single-layer films. A strain compression−relaxation mechanism was proposed in order to explain the structure−property relationships in the CFO−PZT bilayer thin films. To improve the ME coupling, Zhang et al. reported epitaxial CFO−PZT multilayer nanocomposite thin films with up to 11 alternative layers grown on Nb-doped $SrTiO_3$ (STO) substrates by PLD (Zhang, Dai, & Chan, 2010). An excellent epitaxial relationship between the PZT and CFO layers without interfacial reaction at their interfaces was confirmed by X-ray diffraction and high-resolution transmission electron microscopy. The magnetic, electric, and ME coupling effect could be tuned by the strain engineering in multiferroic

superlattices. Gao et al. reported a nanofabrication technique combining PLD and a nanoporous anodic aluminum oxide membrane mask to prepare various types of multiferroic nanocomposites (Gao et al., 2010): periodically ordered $CoFe_2O_4$ dots covered by a continuous PZT layer, PZT dots covered with $CoFe_2O_4$, and $CoFe_2O_4$−PZT bilayer heterostructure dots. By properly tuning the processing parameters, epitaxial nanodot-matrix composites can be obtained. An unexpected out-of-plane magnetic easy axis was induced by the top PZT layer. The nanocomposites display ME coupling revealed by magnetic-field-dependent capacitance measurement (Gao et al., 2010).

5.4.3 Ferrite/PMN-PT or PZN-PT heterostructures

The strain-mediated ME effect is expected to be enhanced in epitaxial ferrite/piezoelectric single-crystal heterostructures due to the combination of high values of the magnetostriction and piezoelectric coefficient. Park et al. reported an asymmetric bilayer structure in which the MR was controlled by the in-plane strain of the top $NiFe_2O_4$ layer epitaxially constrained by the bottom $Pb(Mg_{1/3}Nb_{2/3})O_3$-$PbTiO_3$ (PMN-PT) single-crystal substrates (Park, Jeong, Ryu, Son, & Jang, 2010). In this asymmetric structure, an electric-field-induced giant piezoelectric strain from the bottom PMN-PT layer is effectively transferred to the top $NiFe_2O_4$ layer. The room temperature MR of the 100-nm-thick $NiFe_2O_4$ layer was enhanced by 46% when an electric-field-induced in-plane compressive strain was about −0.1%. A synchrotron X-ray absorption near-edge structure study supported a scenario of the cation-charge redistribution between Ni^{2+} and Fe^{3+} ions under the condition of an electric-field-induced in-plane compressive strain.

Li et al. have demonstrated strong ME interactions at microwave frequencies in 1.5−2.0-μm-thick $NiFe_2O_4$ films grown heteroepitaxially on (001) PMN-PT and lead zinc niobate-lead titanate (PZN-PT) substrates, as shown in Figure 5.9 (Li et al., 2011). After poling, the $NiFe_2O_4$/PZN-PT heterostructure showed a high E-field-induced ferromagnetic resonance (FMR) field shift of ∼260 Oe. Under an electrostatic field of 8 kV/cm, FMR field shifts of 125−130 Oe were observed, corresponding to ME coefficient ∼16 Oe cm/kV. Static E-field control of magnetic hysteresis loop was also observed in the NFO/PZN-PT heteroepitaxial structures, which showed an E-field-induced remanance change of 15% (Li et al., 2011).

5.4.4 Other ferrite-based heterostructures

A change in bonding at the ferroelectric−ferromagnet interface could alter the interface magnetization when the electric polarization reverses. By first-principles density functional calculations of a model Fe/$BaTiO_3$ multiferroic heterostructure, Duan et al. have demonstrated an ME effect that arises from a purely electronic hybridization between Ti and Fe atoms not mediated by strain (Duan, Jaswal, & Tsymbal, 2006). Thus, this ME effect is driven by the coupling between ferroelectricity and magnetism through interface bonding. The displacement of atoms at the interface caused by ferroelectric instability alters the overlap between atomic orbitals

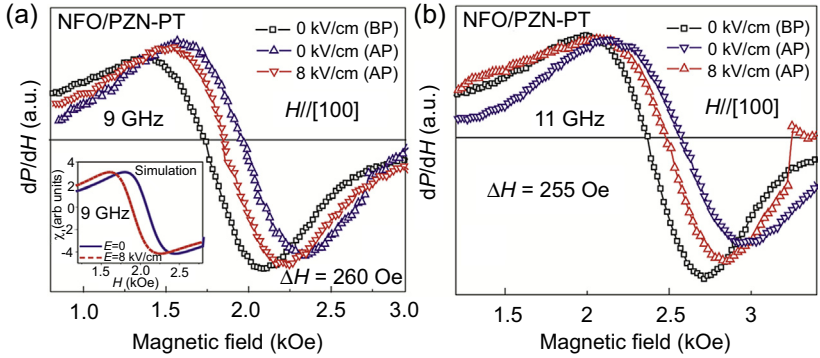

Figure 5.9 Ferromagnetic resonance absorption spectra as a function of external magnetic field measured with and without applied external electric field (Li et al., 2011). (a) $NiFe_2O_4$/PZN-PT heteroepitaxial structure measured at 9 GHz with magnetic field along [100] direction; (b) same heteroepitaxial structure as in (a) measured at 11 GHz with magnetic field along [110] direction. The terms "BP" and "AP" correspond to "before poling" and "after poling," respectively. The inset in (a) shows simulated FMR profiles at 9 GHz using an effective demagnetization factor method.

at the interface, which in turn affects the interface magnetization, resulting in an ME effect. In this case, the ME effect is confined to the interface and represents a change of the interface magnetic moment at the coercive field of the ferroelectric. Such an ME effect is possible in both vertical and horizontal heterostructures (Duan et al., 2006). Strong effects of ferroelectricity on electron and spin transport properties have also been predicted in $SrRuO_3/BaTiO_3/SrRuO_3$ multiferroic tunnel junctions by first-principles calculations, as shown in Figure 5.10 (Velev et al., 2009). Tunneling magnetoresistance and tunneling electroresistance effects will be coexistent in these junctions with asymmetric interfaces, indicating that magnetic tunnel junctions with ferroelectric barriers may serve as four-state resistance devices. However, all these theoretic results remain in need of experimental verification.

The room temperature interface-induced multiferroicity was experimentally demonstrated in 2011 in $Fe/BaTiO_3$ and $Co/BaTiO_3$ heterostructures by Valencia et al. (2011). They reported ferroelectricity-controlled TMR in artificial multiferroic tunnel junctions ($Fe/BaTiO_3$/LSMO and $Co/BaTiO_3$/LSMO), as well as the observation of a remanent magnetic moment in ferroelectric $BaTiO_3$ at the interface with Fe and Co at 300 K. Spin polarization of Fe/BTO and Co/BTO interfaces can be controlled by the direction of ferroelectric polarization in BTO and detected for both cases of a spontaneous and hysteresis magnetic moment in BTO. The most likely mechanism at play here involves formally Ti^{4+} ions and a spin-polarized iono-covalent bonding scheme with atoms in the adjacent ferromagnet. These results expand the possibilities for multiferroic interface engineering and indicate that magnetism extends over several unit cells in the ferroelectric layer, opening the way toward artificial multiferroic tunnel barriers that would be relevant for room temperature storage and logic devices (Valencia et al., 2011).

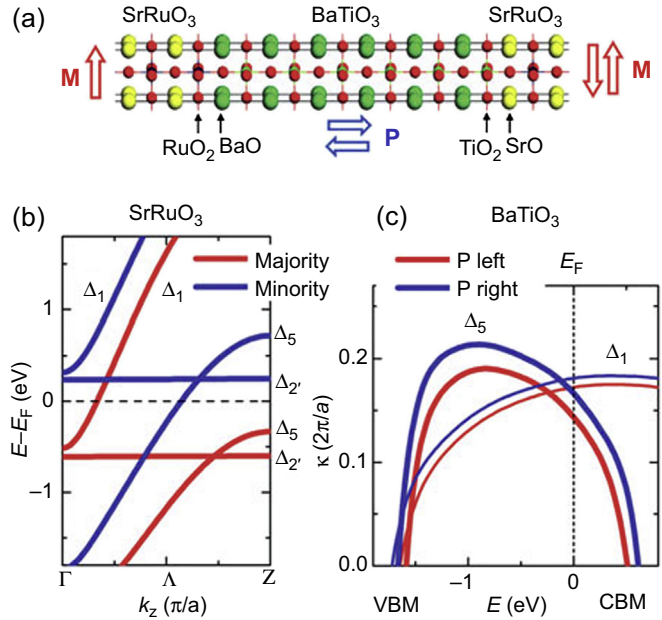

Figure 5.10 (a) Atomic structure of the $SrRuO_3/BaTiO_3/SrRuO_3$ multiferroic tunnel junctions (MFTJs) with different interface terminations. Switchable ferroelectric polarization of $BaTiO_3$ (indicated by blue arrows) is oriented normal to the planes. Magnetization of $SrRuO_3$ layers (indicated by red lines) is parallel or antiparallel. (b) Spin-polarized bands along the [001] direction in bulk $SrRuO_3$. Majority-spin (red) and minority-spin (blue) bands near the Fermi energy (EF) are labeled with their symmetry. (c) Decay constant for $BaTiO_3$ for the left (red) and right (blue) polarization states as a function of energy. VBM and CBM are valence band maximum and conduction band minimum, respectively (Velev et al., 2009).

5.5 Summary and prospects

Epitaxial multiferroic composites have become a popular topic for the last few years, and several prototypes of devices based on these heterostructures have been proposed. However, there are still many issues and opportunities remaining:

1. The controllable epitaxial growth of multiferroic composite thin films is still very difficult. A critical control of the desired ME composite thin films with precise composition, atomic arrangements, and especially the interface between different ferroic phases would have significant impact on the ME response (Ma et al., 2011).
2. Another big challenge facing the field of epitaxial multiferroics today is the need for large tunability at room temperature. For instant, large change in TMR, an FMR field, or EB under an electric field, is highly desired for device applications at room temperature.
3. It is essential to integrate multiferroic thin films onto semiconductor devices, especially on silicon substrates. The first choice for a buffer/temple layer between Si and the multiferroic composites is $SrTiO_3$ grown by MBE (Thomas, Scott, Bose, & Katiyar, 2010). A yttria-stabilized zirconia (YSZ)/CeO_2 bilayer has also been reported as a promising buffer

layer for epitaxial growth of multiferroic thin films (Hu et al., 2012), which was prepared by PLD. Additional attention should be given to realize a comparable process with that used in the semiconductor industry.

References

Béa, H., Bibes, M., Cherifi, S., Nolting, F., Warot-Fonrose, B., Fusil, S., et al. (2006). *Applied Physics Letters, 89*, 242114.

Béa, H., Bibes, M., Ott, F., Dupé, B., Zhu, X. H., Petit, S., et al. (2008). *Physical Review Letters, 100*.

Béa, H., Gajek, M., Bibes, M., & Barthélémy, A. (2008). *Journal of Physics: Condensed Matter, 20*, 434221.

Catalan, G., & Scott, J. F. (2009). *Advanced Materials, 21*, 2463−2485.

Comes, R., Liu, H., Khokhlov, M., Kasica, R., Lu, J., & Wolf, S. A. (2012). *Nano Letters, 12*, 2367−2373.

Deng, C., Zhang, Y., Ma, J., Lin, Y., & Nan, C.-W. (2007). *Journal of Applied Physics, 102*, 074114−074115, 074114.

Deng, C., Zhang, Y., Ma, J., Lin, Y., & Nan, C.-W. (2008). *Acta Materialia, 56*, 405−412.

Dho, J., Qi, X., Kim, H., MacManus-Driscoll, J. L., & Blamire, M. G. (2006). *Advanced Materials, 18*, 1445−1448.

Dix, N., Muralidharan, R., Rebled, J.-M., Estradé, S., Peiró, F., Varela, M., et al. (2010). *ACS Nano, 4*, 4955−4961.

Duan, C.-G., Jaswal, S. S., & Tsymbal, E. Y. (2006). *Physical Review Letters, 97*, 047201.

Eerenstein, W., Wiora, M., Prieto, J., Scott, J., & Mathur, N. (2007). *Nature Materials, 6*, 348−351.

Gao, X., Rodriguez, B. J., Liu, L., Birajdar, B., Pantel, D., Ziese, M., et al. (2010). *ACS Nano, 4*, 1099−1107.

Garcia, V., Bibes, M., Bocher, L., Valencia, S., Kronast, F., Crassous, A., et al. (2010). *Science, 327*, 1106−1110.

Hu, Z., Li, M., Zhu, Y., Pu, S., Liu, X., Sebo, B., et al. (2012). *Applied Physics Letters, 100*, 252908.

Li, N., Liu, M., Zhou, Z., Sun, N. X., Murthy, D., Srinivasan, G., et al. (2011). *Applied Physics Letters, 99*, 192502−192503, 192502.

Luo, H., Yang, H., Baily, S. A., Ugurlu, O., Jain, M., Hawley, M. E., et al. (2007). *Journal of American Chemical Society, 129*, 14132−14133.

Ma, J., Hu, J., Li, Z., & Nan, C.-W. (2011). *Advanced Materials, 23*, 1062−1087.

Martin, L. W., Chu, Y.-H., Holcomb, M. B., Huijben, M., Yu, P., Han, S.-J., et al. (2008). *Nano Letters, 8*, 6.

Martin, L. W., Chu, Y. H., & Ramesh, R. (2010). *Materials Science and Engineering: R: Reports, 68*, 89−133.

Martin, L. W., Chu, Y.-H., Zhan, Q., Ramesh, R., Han, S.-J., Wang, S. X., et al. (2007). *Applied Physics Letters, 91*, 172513.

Martin, L. W., & Ramesh, R. (2012). *Acta Materialia, 60*, 2449−2470.

Molegraaf, H. J., Hoffman, J., Vaz, C. A., Gariglio, S., Van Der Marel, D., Ahn, C. H., et al. (2009). *Advanced Materials, 21*, 3470−3474.

Mukherjee, D., Dhakal, T., Hyde, R., Mukherjee, P., Srikanth, H., & Witanachchi, S. (2010). *Journal of Physics D: Applied Physics, 43*, 485001.

Park, J. H., Jeong, Y. K., Ryu, S., Son, J. Y., & Jang, H. M. (2010). *Applied Physics Letters, 96*, 192503−192504, 192504.

Sando, D., Agbelele, A., Rahmedov, D., Liu, J., Rovillain, P., Toulouse, C., et al. (2013). *Nature Materials*.

Sosnowska, I., Neumaier, T. P., & Steichele, E. (1982). *Journal of Physics C: Solid State Physics, 15*, 4835.

Thomas, R., Scott, J. F., Bose, D. N., & Katiyar, R. S. (2010). *Journal of Physics: Condensed Matter, 22*, 423201.

Valencia, S., Crassous, A., Bocher, L., Garcia, V., Moya, X., Cherifi, R. O., et al. (2011). *Nature Materials, 10*, 753−758.

Vaz, C. A. F., Hoffman, J., Ahn, C. H., & Ramesh, R. (2010). *Advanced Materials, 22*, 2900−2918.

Vaz, C., Hoffman, J., Segal, Y., Reiner, J., Grober, R., Zhang, Z., et al. (2010). *Physical Review Letters, 104*, 127202.

Velev, J. P., Duan, C.-G., Burton, J. D., Smogunov, A., Niranjan, M. K., Tosatti, E., et al. (2009). *Nano Letters, 9*, 427−432.

Vrejoiu, I., Ziese, M., Setzer, A., Esquinazi, P. D., Birajdar, B. I., Lotnyk, A., et al. (2008). *Applied Physics Letters, 92*, 152506.

Wang, J., Neaton, J. B., Zheng, H., Nagarajan, V., Ogale, S. B., Liu, B., et al. (2003). *Science, 299*, 1719−1722.

Wu, S. M., Cybart, S. A., Yu, P., Rossell, M. D., Zhang, J. X., Ramesh, R., et al. (2010). *Nature Materials, 9*, 6.

Yan, L., Xing, Z., Wang, Z., Wang, T., Lei, G., Li, J., et al. (2009). *Applied Physics Letters, 94*, 192902−192903, 192902.

Yan, L., Yang, Y., Wang, Z., Xing, Z., Li, J., & Viehland, D. (2009). *Journal of Materials Science, 44*, 5080−5094.

Yu, P., Lee, J. S., Okamoto, S., Rossell, M., Huijben, M., Yang, C. H., et al. (2010). *Physical Review Letters, 105*.

Zavaliche, F., Zhao, T., Zheng, H., Straub, F., Cruz, M., Yang, P.-L., et al. (2007). *Nano Letters, 7*, 1586−1590.

Zhang, J., Dai, J., & Chan, H. (2010). *Journal of Applied Physics, 107*, 104105.

Zhang, Y., Deng, C., Ma, J., Lin, Y., & Nan, C.-W. (2008). *Applied Physics Letters, 92*, 062911−062913, 062911.

Zheng, H., Straub, F., Zhan, Q., Yang, P. L., Hsieh, W. K., Zavaliche, F., et al. (2006). *Advanced Materials, 18*, 2747−2752.

Zheng, H., Wang, J., Lofland, S. E., Ma, Z., Mohaddes-Ardabili, L., Zhao, T., et al. (2004). *Science, 303*, 661−663.

Zhong, C., Jiang, Q., Fang, J., & Jiang, X. (2009). *Journal of Applied Physics, 105*, 044901−044906, 044901.

Ziese, M., Setzer, A., Vrejoiu, I., Birajdar, B., Rodriguez, B., & Hesse, D. (2008). *Journal of Applied Physics, 104*, 063908.

Zvezdin, A., Kadomtseva, A., Krotov, S., Pyatakov, A., Popov, Y. F., & Vorob'ev, G. (2006). *Journal of Magnetism and Magnetic Materials, 300*, 224−228.

This page intentionally left blank

Recent advances in piezoelectric and magnetoelectric materials phenomena

6

S. Priya, S.C. Yang, D. Maurya, Y. Yan
Bio-inspired Materials and Devices Laboratory (BMDL), Center for Energy Harvesting Materials and Systems (CEHMS), Virginia Tech, USA

6.1 Introduction

The realization of a material with simultaneous presence of strong coupling between electric and magnetic order, termed as "multiferroic magnetoelectrics," would be a milestone for modern electronics and multifunctional materials. It will open the gateway for very high-density memory storage media using both magnetization and electric polarization, and the possibility of electrically reading or writing magnetic memory devices (and vice versa). These applications have already prompted a surge of activity in magnetoelectronics and spintronics, where phenomena such as carrier effects in magnetic semiconductors and high-correlation effects in colossal magnetoresistive compounds are being investigated. Investigations have revealed the presence of both ferroelectricity and magnetism in a number of materials, such as perovskite-type $BiFeO_3$, $BiMnO_3$, the boracite family, $BaMF_4$ compounds (M, divalent transition metal ions), hexagonal $RMnO_3$ (R, rare earths), and the rare earth molybdates, but none seem to provide large coupling between them (Boomgaard & Born, 1978; Boomgaard, Terrell, Born, & Giller, 1974; Dai et al., 2004; Fischer, Gorodetsky, & Hornreich, 1972; Hornreich, 1969; Kadomtseva, Zvezdin, Popov, Pyatakov, & Vorob'ev, 2004; Ruette et al., 2004; Srinivas, Kim, Hong, & Suryanarayana, 2004; Suchetelene, 1972; Suryanarayana, 1994; Wang et al., 2003). Recently, rare earth manganites such as $TbMnO_3$, $DyMnO_3$, and $TbMn_2O_5$ have been reported to exhibit reproducible electric polarization under magnetic fields; however, the magnitude of the magnetoelectric (ME) coefficient (units of V/cm Oe) is quite small (Ederer & Spaldin, 2004; Fiebig, 2005; Fiebig, Lottermoser, Frohlich, Goltsev, & Pisarev, 2002; Hur et al., 2004; Kimura et al., 2003; Lottermoser et al., 2004; Park, Ryu et al., 2009; Priya et al., 2009; Srinivas et al., 2004; Van Aken, Palstra, Filippetti, & Spaldin, 2004). Single-phase materials exhibiting ME effects require two coupled transitions, such as one from ferroelectric to paraelectric state and another from ferro/ferri/antiferromagnetic to paramagnetic state. The ME effect then arises due to coupling between the magnetic and polar sublattices. Unfortunately, all the known single-phase materials suffer from the drawback that the ME effect is considerably weak even at low temperatures.

Composite Magnetoelectrics. http://dx.doi.org/10.1016/B978-1-78242-254-9.00006-8
Copyright © 2015 Elsevier Ltd. All rights reserved.

In the single-phase ME materials, the upper limit for ME susceptibility can be given as

$$\alpha_{ij}^2 < \left(\kappa_{ii}^e \chi_{jj}^m\right) \tag{6.1}$$

where κ^e and χ^m are the electric and magnetic susceptibilities, respectively.

A similar relationship can be derived based on the thermodynamic considerations given as (O'Dell, 1963)

$$\alpha_{ij} < \left(\varepsilon_{ii}\mu_{jj}\right)^{1/2} \tag{6.2}$$

where ε and μ are the electric permittivity and magnetic permeability, respectively. The ME coupling coefficient has been defined as

$$k_{\mathrm{ME}} = \frac{U_{\mathrm{mutual}}}{\left(U_{\mathrm{electric}} \cdot U_{\mathrm{magnetic}}\right)^{1/2}} \tag{6.3}$$

where $U_{\mathrm{mutual}} \left(= \frac{1}{2}\alpha_{ij}E_iH_j, \text{ where } H_j \text{ is the magnetic field}\right)$ is the mutual energy, $U_{\mathrm{electric}} \left(= \frac{1}{2}\varepsilon_{ii}E_iE_i\right)$ is the electric energy, and $U_{\mathrm{magnetic}} \left(= \frac{1}{2}\mu_{jj}H_jH_j\right)$ is the magnetic energy. In order to evaluate the efficiency of energy conversion from magnetic to electric forms, or vice versa, a working definition of the coupling coefficient can be written as

$$k_{\mathrm{ME}}^2 = k_{ij,\mathrm{piezo}}^2 \, k_{ij,\mathrm{magnetic}}^2 \tag{6.4}$$

where $k_{ij,\mathrm{piezo}}$ is the coupling coefficient of the piezoelectric phase and $k_{ij,\mathrm{magnetic}}$ is the coupling coefficient of the magnetic phase.

Unfortunately, many of the single-phase materials possess low permittivity, low permeability, or both. As a consequence, the ME coupling of all the known single-phase materials is usually too small at room temperature to be practically applicable. Several researchers have explored this question and have presented alternative ways of overcoming the fundamental problem related to the filling of electronic states. Recent investigations on single-phase multiferroics have revealed that the origin of the ME effect is often associated with a particular exchange mechanism for various families of compounds, such as orbital ordering, Jahn−Teller distortion, super/double exchange, and/or geometric magnetic frustration: these have been cited as the origin source of ME effects. Two prominent families of Mn-based compounds—$TbMnO_3$, $DyMnO_3$, $TbMn_2O_5$—exhibit coupling due to frustrated spin, resulting in magnetoelastically induced lattice modulations, while buckling of the layered MnO_5 polyhedral accompanied by displacements of the Y ions results in finite ME coupling in $YMnO_3$. Detailed theoretical calculations have been conducted on these materials, but none seem to indicate the possibility of shifting the transition temperature to room temperature.

There are two approaches that are considered to be promising for room temperature multiferroic magnetoelectrics. One is based on solid solutions exhibiting morphotropic phase boundary (MPB) or polymorphic phase boundary (PPB), and the other is based on composite structure that utilizes product property. In this chapter, we first briefly report considerable progress on ME solid solutions. Then, a review on ME composites (piezoelectric−magnetostrictive) is provided, covering the significant progress made in the past decade (both experimentally and theoretically demonstrating that the strain-mediated ME coupling in magnetostrictive−piezoelectric layered composites or laminates is several orders of magnitude larger as compared to single-phase materials). After that, material issues related to ME composites are presented, with emphasis on (1) important achievements and new phenomena in piezoelectric materials, such as textured piezoelectric ceramics and functionally graded composites, and (2) new processes for fabricating ME composites, such as cofiring and 3D printing/patterning. Lastly, considering the importance of environmental concerns, recent developments of lead-free piezoelectric and ME composites are discussed.

6.2 Magnetoelectric solid solution

$BiFeO_3$−$BaTiO_3$ solid solution: $BiFeO_3$ (BFO) consists of a cycloidal spatially modulated spin structure in conjunction with antiferromagnetic order that deteriorates the macroscopic magnetization. We have conducted extensive investigations on the BFO−$BaTiO_3$ (BTO) solid solutions that show the presence of MPB as shown in Figure 6.1. The enhanced magnetic properties with decreasing BFO mole fraction from 0.775 to 0.750 were attributed to active spin modulation of ordered Fe−O−Fe. It was found that the substitution of large Ba^{2+} and Ti^{4+} ions on the A- and B-sites, respectively, enlarges the distortion of the bond angle of Fe−O−Fe to release the spiral magnetic modulation. The atomic pair distribution function (PDF) for pure BFO ($x = 1.0$) was found to fit with a rhombohedral structure model (S.G. R3c) with lattice parameters in a hexagonal setting ($a = 5.583$ Å, $c = 13.835$ Å, and gamma = 120°). The PDFs for BT−xBFO ($x = 0.725$) were found to fit at lower r values with a structure model featuring monoclinic structure (S.G. Cm) with parameters $a = 5.499$ Å, $b = 5.631$ Å, $c = 3.974$ Å, and beta = 91°. At higher r values, a rhombohedral model (S.G. R3c) ($a = 5.558$ Å, $c = 13.834$ Å, and gamma = 120°) provided better fit. Thus, this material was found to be rhombohedral on average with local monoclinic distortions/symmetry. These results are highly exciting toward the realization of a room temperature single-phase multiferroic ME material.

$Pb(W_{1/3}Fe_{2/3})O_3$(PFW)−$Pb(Zr,Ti)O_3$ (PZT) solid solutions: PFW is one of the classical systems exhibiting magnetic and electric ordering. The dielectric and magnetic properties of pure PFW can be changed by adding *$Pb(Zr,Ti)O_3$ (PZT)*. Kumar et al. reported that solid solutions of PFW and PZT exhibit both ferroelectric relaxor characteristics and magnetic relaxor phenomena and found that the composition of 0.2PFW−0.8PZT has a large ME effect at room temperature. Using a 0.2PFW−0.8PZT thin film sample prepared by the sol−gel method, three-state logic switching ($+P_r$, 0, $-P_r$) in 0.2PFW−0.8PZT at room temperature was observed, as

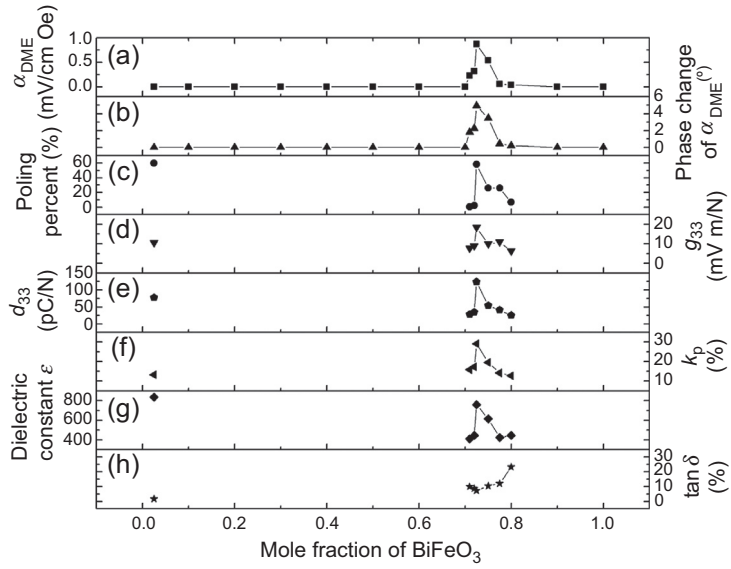

Figure 6.1 Variation of magnetoelectric, piezoelectric, and dielectric properties as a function of BFO mole fraction for BTO−xBFO ceramics with $x = 0.025-1.0$: (a) DME coefficient (α_{DME}), (b) phase change of α_{DME}, (c) poling percent, (d) piezoelectric voltage constant (g_{33}), (e) piezoelectric charge constant (d_{33}), (f) radial mode electromechanical coupling factor (k_p), (g) dielectric constant (ε), and (h) tangent loss factor (tan δ).
Journal of Applied Physics, *113*, 144101 (2013).

shown in Figure 6.2(a) (Kumar et al., 2009). The electric switching from $+P_r$ to $-P_r$ was observed at $E_c = 48$ kV/cm, and the magnetic switching from $+P_r$ to $-P_r$ was observed at 0.5 T (Kumar et al., 2009). Although a rather large switching magnetic field (0.5 T) is required, it would require only 100 G to switch if the device is under a field of 0.49 T (Kumar et al., 2009). This three-stage logic at a switching field of 100 G could be very useful for memory and sensory applications (Kumar et al., 2009). In order to further understand the reason of this behavior, frequency-dependent real and imaginary parts of the dielectric constant as a function of frequency under various applied magnetic fields were plotted in Figure 6.2(b) (Kumar et al., 2009). In this work, the authors clearly observed the effect of the magnetic field on the dielectric relaxation. The strong influence of the magnetic field on the dielectric susceptibility suggested strong coupling between spin fluctuations and polarization fluctuations. These results clearly demonstrated manipulation of polarization and dielectric behavior using the magnetic field, which could be used as extended logic states in memory devices and sensors.

6.3 Magnetoelectric composite

It has been shown both experimentally and theoretically that the strain-mediated ME coupling in a magnetostrictive−piezoelectric layered composite or laminate is several

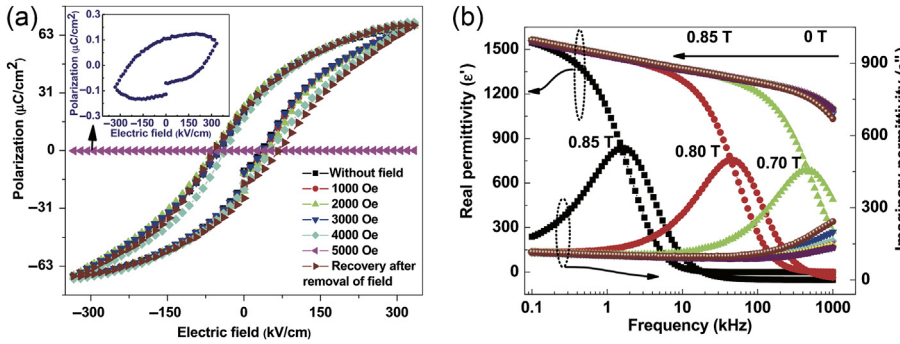

Figure 6.2 (a) Three-state switching ($+P_r$, 0, $-P_r$) in 0.2PFW/0.8PZT: P−E hysteresis under the application of an external magnetic field from 0 to 0.5 T changes the polarization from $|P_r|$ to zero; application of 1.4 V across 300 nm changes $+P_r$ to $-P_r$. The inset is the $P = 0$ relaxor state on expanded scale, showing a linear lossy dielectric. Note that the polarization values assume that the gold electrodes do not diffuse under the masks; due to such diffusion, the real values of P may be only about half the graphed values. (b) The real and imaginary part of dielectric permittivity (arrows show the direction of the real and imaginary part) as a function of frequencies under the application of an external magnetic field from 0 to 0.5 T. Journal of Physics: Condensed Matter, *21*, 7, 382204 (2009).

orders of magnitude larger as compared to single-phase materials. The direct ME (DME) and converse ME (CME) effect in the laminate composites consisting of a piezoelectric layer (P-layer) and a magnetostrictive layer (M-layer) can be represented by the following schematics:

$$\begin{aligned}
&\underbrace{\overset{(\mathrm{DME})}{H} \xrightarrow{\text{Magnetostrictive}} S}_{\text{Magnetic layer}} \underbrace{\xrightarrow{\text{Mechanical}} T \xrightarrow{\text{Direct piezoelectric}} D \xrightarrow{\text{Dielectric}} E}_{\text{Piezoelectric layer}} \\
&\underbrace{\overset{(\mathrm{CME})}{E} \xrightarrow{\text{Dielectric}} D \xrightarrow{\text{Converse piezoelectric}} T \xrightarrow{\text{Mechanical}} S}_{\text{Piezoelectric layer}} \underbrace{\xrightarrow{\text{Piezomagnetic}} M}_{\text{Magnetic layer}}
\end{aligned} \tag{6.5}$$

where H is magnetic field, S is mechanical strain, T is mechanical stress, D is electric displacement, E is electric field, and M is magnetization. In the off-resonance condition, the ME coefficient in the composites is given as (Cho, Park, & Priya, 2010)

$$\begin{aligned}
\alpha_{E,31} &= \frac{\mathrm{d}E_3}{\mathrm{d}H_1} = \frac{nq_{11}g_{31}^*}{nS_{11}^E\left(1-k_{31}^2\right)+(1-n)S_{11}^H} \\
g_{31}^* &= g_{31}\frac{1}{\exp\left(\tan\delta' + \tan\theta' + \frac{C-C_f}{C_f}\right)}
\end{aligned} \tag{6.6}$$

where H_1 is the longitudinally applied magnetic field along the 1 axis, E_3 is the generated electric field perpendicular to the H_1 direction (3 axis), n is the volume fraction of the magnetostrictive layer ($n = V_{\text{magnetic}}/(V_{\text{piezoelectric}} + V_{\text{magnetic}})$, V is the volume), q_{11} is the piezomagnetic coefficient, g_{31} is the piezoelectric voltage coefficient, k_{31} is the electromechanical coupling coefficient, piezoelectric loss is shown as $\tan\theta'$, dielectric loss is shown as $\tan\delta'$, C is the capacitance at a given frequency, C_f is the capacitance at 1 kHz, and S_{11}^E and S_{11}^H are the elastic compliances of the piezoelectric and magnetostrictive layers, respectively.

Composite geometry can be designed based on the connectivity. The connectivity in general can be given by the ratio $\frac{(n+3)!}{3!n!}$, where n is the number of phases. For a two-phase system, there are 10 types of connectivity. For three- and four-phase systems, there are 20 and 35 types of connectivity. Figure 6.3 shows three types of connectivity for multiphase ME composites. The 3−0-type particulate ME composites were constructed by embedding one-phase particles in a matrix of another phase and were found to exhibit coupling coefficients of several ten to hundred millivolts per centimeter Oersted at room temperature. The ME coefficient in 3−0-type particulate composites can reach up to several thousand millivolts per centimeter Oersted at resonance frequency, but this magnitude is still below the theoretical magnitude due to the problems related to the interdiffusion between piezoelectric and magnetostrictive phases during high-temperature sintering, thermal expansion mismatch between the two phases, and low resistivity. In order to improve the resistivity in ME composites, 2−2-type ME laminates have been synthesized by using piezoelectric and magnetostrictive layers and have been shown to exhibit ME coefficients of several thousand millivolts per centimeter Oersted at room temperature due to reduction of the leakage problem. The 1−3-type ME composites were investigated for high ME coefficient by exploiting contributions from both piezoelectric coefficient d_{33} and piezomagnetic coefficient q_{11}. The PZT/Terfenol-D composites were reported with an ME coefficient of 500 mV/cm Oe under off-resonance condition and 18,200 mV/cm Oe under resonance condition by Ma, Shi, and Nan (2007). Laminate composites are generally fabricated by bonding magnetostrictive and piezoelectric layers using silver epoxy followed by annealing at a lower temperature of $\sim$100 °C. The most common geometry for laminate composites is a "sandwich" structure, where the piezoelectric layer is arranged between two magnetostrictive ones. Under an applied magnetic field, the strain in the

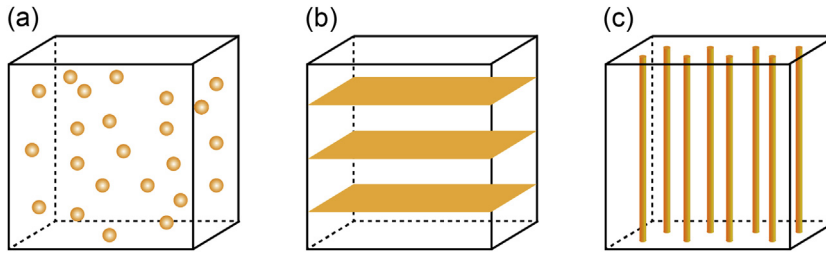

Figure 6.3 Schematic diagram for connectivity of multiphase magnetoelectric composites: (a) 3−0-type particulate structure, (b) 2−2-type laminate structure, and (c) 1−3-type cylinder-matrix structure.

magnetostrictive layer is transferred to the piezoelectric layer through the bonding layer, resulting in generation of electrical charge. In 2−2 ME laminate composites, there can be four possible modes, as shown in Figure 6.4. In $L-L$ mode, both the applied H field and the measured E field are parallel to the principal vibration mode; in $T-L$ mode, the applied H field is perpendicular to the induced E field, which is measured parallel to the principal mode; in $L-T$ mode, the applied H field is parallel and the induced E field is measured perpendicular to the principal mode; and in $T-T$ mode, the applied H field and induced E are perpendicular to the principal mode (Priya, Islam, Dong, & Viehland, 2007).

The ME coefficient for 2−2-type laminate composites has been modeled by Srinivasan et al. (2001). The transverse ME coefficient for the laminate composite was given as

$$\alpha_{E31} = \frac{\delta E_3}{\delta H_1} = \frac{-2d_{31}^{p} q_{11}^{m} v^{m}}{\left(s_{11}^{m} + s_{12}^{m}\right)\varepsilon_{33}^{T,P} v^{p} + \left(s_{11}^{p} + s_{12}^{p}\right)\varepsilon_{33}^{T,P} v^{m} - 2\left(d_{31}^{p}\right)^{2} v_{m}} \tag{6.7}$$

The longitudinal ME coefficient for the laminate composite was given as

$$\alpha_{E33} = \frac{\delta E_3}{\delta H_3} = \frac{-2d_{31}^{p} q_{13}^{m} v^{m}}{\left(s_{11}^{m} + s_{12}^{m}\right)\varepsilon_{33}^{T,P} v^{p} + \left(s_{11}^{p} + s_{12}^{p}\right)\varepsilon_{33}^{T,P} v^{m} - 2\left(d_{31}^{p}\right)^{2} v_{m}} \tag{6.8}$$

where d_{31}^{p} is piezoelectric coefficient, v^{m} and v^{p} are volumes of magnetostrictive and piezoelectric phases, s_{11}^{p}, s_{12}^{p} are elastic compliances for the piezoelectric phase, s_{11}^{m}, s_{12}^{m} are elastic compliances for the magnetostrictive phase, q_{11} is piezomagnetic coefficient of the magnetostrictive phase, and $\varepsilon_{33}^{T,P}$ is permittivity of the piezoelectric phase.

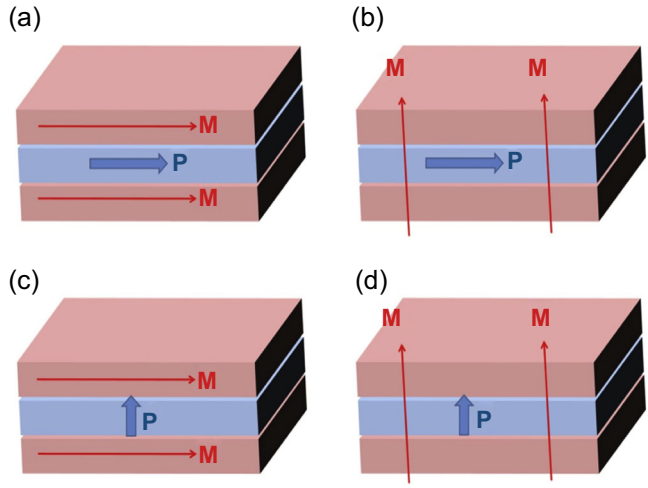

Figure 6.4 Laminate magnetoelectric composites operating in four types of vibration modes: (a) $L-L$ mode, (b) $T-L$ mode, (c) $L-T$ mode, and (d) $T-T$ mode.

In the case of laminate ME composites with 2−2 connectivity, detailed research has been conducted in the form of bilayers, trilayers, and multilayers of piezoelectric and magnetostrictive materials. Table 6.1 shows the ME properties of 2−2-type laminate ME composites. The push−pull mode ME laminates consisting of PZT, Terfenol-D, and Metglas were found to exhibit ME coefficients of ∼20,000 mV/cm Oe with high magnetic sensitivity in resonance condition (Dong, Zhai, Bai, Li, & Viehland, 2005). Partial texturing of the piezoelectric phase in 2−2 laminate composites was found to show 67% improvement of the ME coefficient compared to the randomly oriented laminate (Islam & Priya, 2009).

One of the problems related to the design of magnetic field sensors is the need for DC bias magnets. Additional magnets make the device bulky and require insulation. Thus, there is critical need for the design of self-biased ME laminates. In this section, a discussion is included on the magnitude of DC bias required for the 2−2-type laminates. 2−2-type laminate ME composites can be categorized by the type of magnetostrictive material used in the design: (1) ferrite, (2) Terfenol-D, and (3) Metglas. Each of these ME laminates has different ME behavior due to differences in coercive field (H_c), permeability (μ), and magnetization (M). In Table 6.2, varying ferrite oxides are available to cosinter with the piezoelectric matrix and were found to exhibit different magnetostriction due to their varying magnetic properties (Priya et al., 2007). Terfenol-D in Table 6.3 has the largest magnetostriction of 1400×10^{-6} with low permeability, while Metglas in Table 6.4 has an extremely high relative permeability of >40,000 and thus is a quite attractive magnetostrictive material in low-field ME sensors (Zhai, Xing, Dong, Li, & Viehland, 2008). Detailed research has been performed by our research group, exploring the 2−2 connectivity of the ME composites in the form of bilayers, trilayers, and multilayers of piezoelectric and magnetostrictive materials. Islam et al. have synthesized a PZT−NCZF bilayer and an NCZF−PZT−NCZF trilayer using the cofiring technique and have found a high ME coefficient on the order of ∼500 mV/cm Oe in trilayer structures (Islam & Priya, 2008). Lead-free 2−2 laminate ME composites of $BaTiO_3$ (BT)/$(Ni_{0.8}Zn_{0.2})Fe_2O_4$ (NZFO) were synthesized by cofiring, and the magnitude of the ME voltage coefficient reached saturation at a DC bias of 1000 Oe with a maximum magnitude of 152 mV/cm Oe (Islam & Priya, 2006). Dong et al. have studied several multilayered ME configurations by using materials PZT, Terfenol-D, and Metglas and have reported quite high ME coefficients on the order of 10 V/cm Oe in resonance condition (Dong, Cheng, Li, & Viehland, 2003; Dong, Li, & Viehland, 2003; Dong, Li, & Viehland, 2004a,b; Dong, Zhai, Bai, Li, Viehland, & Lograsso, 2005).

6.4 Recent advances in piezoelectric and magnetoelectric materials

According to Eqns (6.6)−(6.8), piezoelectric material with high d and g is required to achieve high ME charge and voltage coefficients. In this section, we will focus on the recent development of high-performance piezoelectric materials.

Table 6.1 List of magnetoelectric laminate composites

Year	Compositions	DC bias/frequency	d*E*/d*H* (mV/cm Oe)	References
2001	$Pb(Zr,Ti)O_3/TbDyFe_2$	4200 Oe/1 kHz	4680	Ryu, Carazo, Uchino, and Kim (2001)
2002	$Pb(Zr_{0.5}Ti_{0.5})O_3/Tb_{1-x}Dy_xFe_2$	4000 Oe/1 kHz	5900	Ryu, Priya, Uchino, and Kim (2002)
2004	$Pb(Mg_{1/3}Nb_{2/3})O_3-PbTiO_3/Tb_{1-x}Dy_xFe_2$	400 Oe/1 kHz	4300	Dong, Li, Viehland, Cheng, and Cross (2004)
2004	$BaTiO_3/Tb_{1-x}Dy_xFe_2$	350 Oe/1 kHz	2100	Liu, Nan, Cai, and Lin (2004)
2005	$Ni/Pb(Zr_{0.5}Ti_{0.5})O_3/Ni$	80 Oe/1 kHz	450	Laletin et al. (2005)
2006	$BaTiO_3/Ni_{0.8}Zn_{0.2}Fe_2O_4$	1000 Oe/1 kHz	152	Islam and Priya (2006)
2006	Terfenol-D/$Pb(Zr,TiO)_3$/μ-metal	240 Oe/1 kHz	>1400	Dong, Zhai, Li, and Viehland (2006)
2007	Fe-doped $BaTiO_3/Tb_{1-x}Dy_xFe_{2-y}$	350 Oe/100 Hz	2100	Zhang, Fan, Rong, Cao, and Wei (2007)
2008	$0.9Pb(Zr_{0.52}Ti_{0.48})O_3-0.1Pb(Zn_{1/3}Nb_{2/3})O_3/Ni_{0.6}Cu_{0.2}Zn_{0.2}Fe_2O_4$	400 Oe/1 kHz	468	Islam and Priya (2008)
2009	$BaTi_{0.99}Cr_{0.01}O_3/Tb_{1-x}Dy_xFe_{2-y}$	355 Oe/100 Hz	2753	Ke, Zhang, and Guo (2009)
2010	$Pb(Zr,Ti)O_3-Pb(Mg_{1/3}Nb_{2/3})O_3$ single crystal/Terfenol-D/Metglas	1011 Oe/1 kHz	5150	Yang, Park, Cho, and Priya (2010)
2010	Mn-doped $Na_{0.5}Bi_{0.5}TiO_3-BaTiO_3$ single crystal/Terfenol-D	400 Oe/1 kHz	1320	Zhang, Xia, Shrout, Zang, and Wang (2006)

Table 6.2 List of magnetoelectric laminates based on ferrite

Year	Compositions	DC bias (Oe)	References
2001	$Pb(Zr, Ti)O_3/NiFe_2O_4$—bilayer	100	Srinivasan et al. (2001)
2001	$Pb(Zr, Ti)O_3/NiFe_2O_4$—multilayer	400	Srinivasan et al. (2001)
2002	$Pb(Zr, Ti)O_3/Ni_{0.8}Zn_{0.2}Fe_2O_4$	100	Srinivasan et al. (2002)
2003	$Pb(Zr, Ti)O_3/Co_{0.6}Zn_{0.4}Fe_2O_4$	450	Srinivasan, Rasmussen, and Hayes (2003)
2003	$Pb(Zr, Ti)O_3/Ni_{0.8}Zn_{0.2}Fe_2O_4$	150	Srinivasan, Rasmussen et al. (2003)
2003	$Pb(Zr, Ti)O_3/Li_{0.35}Zn_{0.3}Fe_{2.35}O_4$	150	Srinivasan, Hayes, and Bichurin (2003)
2003	$Pb(Zr, Ti)O_3/Ni_{0.93}Co_{0.02}Mn_{0.05}Fe_{1.95}O_4$	700	Babu, Srinivas, Suryanarayana, & Bhimasankaram (2008)
2006	$BaTiO_3/Ni_{0.8}Zn_{0.2}Fe_2O_4$	1000	Islam and Priya (2006)
2006	$Pb(Zr, Ti)O_3/Ni_{0.8}Zn_{0.2}Fe_2O_4$	250	Zhang, Ke, Schneider, and Srinivasan (2006)
2008	$Ni_{0.6}Cu_{0.2}Zn_{0.2}Fe_2O_4$/0.9 $Pb(Zr_{0.52}Ti_{0.48})O_3$−0.1$Pb(Zn_{1/3}Nb_{2/3})O_3$/ $Ni_{0.6}Cu_{0.2}Zn_{0.2}Fe_2O_4$	400	Islam, Ni, Khachaturyan, and Priya (2008)

6.4.1 *Textured piezoelectric ceramics and magnetoelectric composites*

Since $Pb(Zr,Ti)O_3$ composition was discovered in the mid-1950s, many studies on developing high-performance piezoelectric materials have been conducted. As shown in Figure 6.5(a), commercialized piezoelectric ceramic compositions with high d_{33} values of 1000 pC/N or compositions with high g_{33} values of 40×10^{-3} V m/N can be found. However, compositions having high d_{33} usually show low g_{33} value, while high g_{33} compositions possess low d_{33}; thus, the achievement of high $d \cdot g$ coefficient from single piezoelectric composition is challenging.

Table 6.3 List of magnetoelectric laminates based on Terfenol-D

Year	Compositions	DC bias (Oe)	References
2001	$Pb(Zr,Ti)O_3$/Terfenol-D	4200	Ryu et al. (2001)
2002	$Pb(Zr_{0.5}Ti_{0.5})O_3$/Terfenol-D	4000	Ryu et al. (2002)
2003	$Pb(Zr,Ti)O_3$/Terfenol-D	200	Dong, Cheng et al. (2003)
2003	$Pb(Zr_{0.52}Ti_{0.48})O_3$/Terfenol-D	700	Wan et al. (2003)
2004	$Pb(Mg_{1/3}Nb_{2/3})O_3$−$PbTiO_3$/ Terfenol-D	400	Dong et al. (2004)
2004	$BaTiO_3$/Terfenol-D	350	Liu et al. (2004)
2005	$Pb(Zr_{0.52}Ti_{0.48})O_3$/Terfenol-D	700	Wan et al. (2005)
2005	$Pb(Mg_{1/3}Nb_{2/3})O_3$−$PbTiO_3$/ Terfenol-D	450	Dong, Zhai, Bai, Li, and Viehland (2005)
2007	Fe-doped $BaTiO_3$/Terfenol-D	350	Zhang et al. (2007)
2008	$Pb(Mg_{1/3}Nb_{2/3})O_3$−$PbTiO_3$/ Terfenol-D	400	Wang, Or, Chan, Zhao, and Luo, (2008)
2009	$Pb(Mg_{1/3}Nb_{2/3})O_3$−$PbTiO_3$/ $Tb_{0.3}Dy_{0.7}Fe_{1.92}$	400	Wang, Leung, Wang et al. (2009)
2009	$BaTi_{0.99}Cr_{0.01}O_3/Tb_{1-x}Dy_xFe_{2-y}$	355	Ke et al. (2009)
2009	$Pb(Mg_{1/3}Nb_{2/3})O_3$−$PbTiO_3$/ Terfenol-D	400	Wang, Leung, Or, Zhao, and Luo (2009)
2010	$Pb(Zr,Ti)O_3$/Terfenol-D	300	Guo, Zhou, and Liu (2010)
2010	Mn-doped $Na_{0.5}Bi_{0.5}TiO_3$−$BaTiO_3$ single crystal/Terfenol-D	400	Zhang, Xia et al. (2006)

As seen in Figure 6.5(a), the $d_{33}\cdot g_{33}$ values of commercialized piezoelectric ceramics are confined below $16{,}500 \times 10^{-15}$ m^2/N. This is a fundamental limitation imposed by the thermodynamics constraints. Using Landau−Devonshire theory, the energy due to the fluctuations in the polarization p and strain u can be written as $f = \frac{1}{2\chi^u}p^2 + apu + \frac{1}{2}c^p u^2$, where χ^u is the susceptibility under constant strain, a is the piezoelectric coefficient relating the polarization and strain, and c^p is the elastic stiffness under constant polarization. For simplicity, only one polarization and one strain component were taken into account. Thus, the derivative of polarization with respect to the applied stress X can be written as $dp/dX = -as\chi +$ higher order terms, where s is the elastic compliance. This implies that any increase in the piezoelectric constant is always accompanied by the increase in transversal dielectric susceptibility, and thus the product $(d\cdot g)$ is constant (Ishibashi & Iwata, 1999).

Table 6.4 List of magnetoelectric laminates based on Metglas

Year	Compositions	DC bias (Oe)	References
2006	PVDF/Metglas	8	Zhai, Dong, Xing, Li, and Viehland (2006)
2009	Pb(Zr,Ti)O_3 fiber/Metglas	<10	Wu, Chung, Chang, Keller, and Carman (2009)
2009	PVDF/Metglas	52	Dong, Wang, Wang, Wan, and Liu (2009)
2009	PVDF/Metglas	<10	Fang et al. (2009)
2009	$Pb(Zn_{1/3}Nb_{2/3})_x(Zr_{0.5}Ti_{0.5})_{1-x}O_3$/Metglas	100–325	Park, Ahn et al. (2009)

It is well known that ⟨001⟩-oriented relaxor-based piezoelectric single crystals such as $Pb(Mg_{1/3}Nb_{2/3})O_3$–$PbTiO_3$ (PMN-PT) and $Pb(Zn_{1/3}Nb_{2/3})O_3$–$PbTiO_3$ (PZN-PT) with rhombohedral structure near the MPB exhibit d_{33} values of >2000 pC/N and k_{33} values of >92% (Park & Shrout, 1997). The piezoelectric response strongly depends on composition and orientation, and is largest near the MPB, as illustrated in Figure 6.6. These giant piezoelectric properties of ⟨001⟩ rhombohedral crystals are related to their piezoelectric anisotropy and "engineered

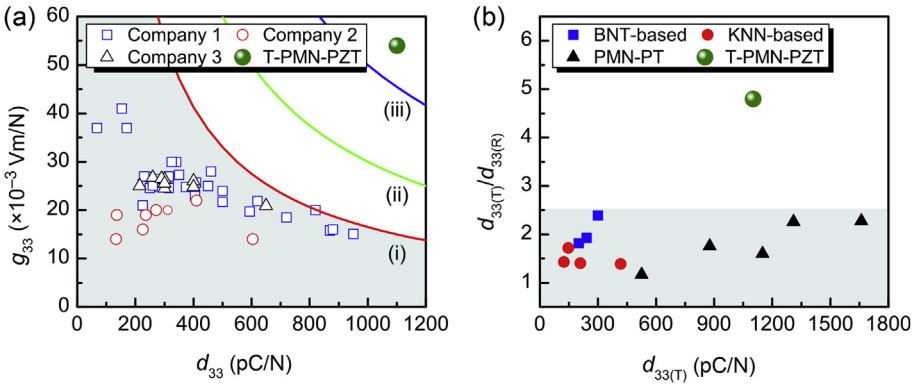

Figure 6.5 (a) Comparison of g_{33} and d_{33} values of various piezoelectric ceramics. Different colored lines (i), (ii), and (iii) indicate the plots of $g_{33} \cdot d_{33} = c$ function: (i) $c = 16{,}500 \times 10^{-15}$ m^2/N, (ii) $c = 30{,}000 \times 10^{-15}$ m^2/N, and (iii) $c = 50{,}000 \times 10^{-15}$ m^2/N. (b) Comparison of $d_{33(T)}/d_{33(R)}$ ratio versus $d_{33(T)}$ of various textured piezoelectric ceramics. $d_{33(T)}$ and $d_{33(R)}$ represent d_{33} of textured ceramic and that of the randomly oriented counterpart, respectively. BNT and KNN represent $(Bi_{1-x}Na_x)TiO_3$ and $(K_{1-x}Na_x)NbO_3$ compositions, respectively.
Applied Physics Letters, *102*, 042903 (2013).

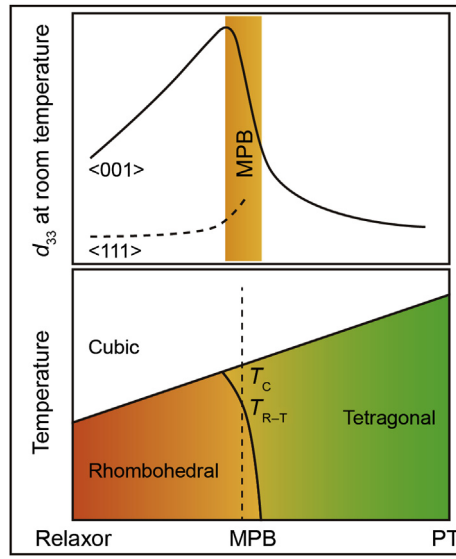

Figure 6.6 Schematic piezoelectric charge/strain coefficient, d_{33}, and phase diagram of relaxor-PT solid solution.

domain state" that facilitate the rotation of ⟨111⟩ polarization (⟨111⟩: pseudocubic ⟨111⟩ directions of spontaneous polarization in rhombohedral perovskite) toward the ⟨001⟩ direction (⟨001⟩: pseudocubic ⟨001⟩ directions in rhombohedral perovskite) (Zhang & Li, 2012).

PZT and relaxor-based ceramics with near-MPB composition exhibit high dielectric and piezoelectric properties but low energy density due to reduced piezoelectric voltage coefficient. Defects and substituents have been used to influence the electromechanical properties of the ceramics in poled conditions. Generally, acceptor doping (Fe, Mn, Ni, Co) in the PZT-based ceramics results in (1) decreased dielectric constant and loss, (2) lower elastic compliance, (3) lower electromechanical coupling factor, and (4) lower electromechanical losses. In contrast, donor doping (La, Sb, Bi, W) results in (1) increased dielectric constant and loss, (2) increased elastic compliance, (3) increased electromechanical coupling factor, and (4) increased electromechanical losses. However, the success through these doping methods has been limited. Domain engineered relaxor piezoelectric single crystals have been grown to achieve high performance. However, low ferroelectric rhombohedral to tetragonal phase transition temperature ($T_{R-T} \sim 60-90\ ^\circ C$) and low coercive fields ($E_C \sim 2-3$ kV/cm) limit the stability of electrical property in relaxor-based single crystals (Zhang & Li, 2012). Many attempts to grow PZT-based single crystals near MPB to achieve high and stable piezoelectric properties have been made, but there is a fundamental challenge in accomplishing this task. PZT-based compositions cannot be readily grown in single-crystal form because of incongruent melting behavior. For compositions near the MPB,

melting is incongruent and results in the precipitation of zirconia prior to PZT. Thus, any effort to grow MPB composition single crystal using liquid phase results in a mixture consisting of zirconia and Zr-deficient PZT grains. These considerations indicate the tremendous difficulty in synthesizing crystallographically oriented PZT materials.

A very different strategy for overcoming the fundamental limitations is via designing a textured microstructure, which can achieve a giant magnitude of the $d \cdot g$ coefficient with a value of 59,000 $\times$ 10^{-15} m^2/N (comparable to that of the single-crystal counterpart and 359% higher than that of the best commercial compositions) (Yan et al., 2013). The reason for realizing high $d \cdot g$ coefficients in textured ceramics is the following: (1) ⟨001⟩ texturing (grain orientation along the ⟨001⟩ crystallographic direction) of piezoelectric ceramics produces an engineered domain state similar to that of ⟨001⟩ single crystals, thus resulting in high d values, and (2) the existence of low ε templates produces a composite microstructure and suppresses the dielectric constant (ε) of piezoelectric ceramics.

In the TGG process, as illustrated in Figure 6.7, template crystals are aligned in ceramic matrix powder by a tape-casting process, then matrix crystals nucleate and grow on the aligned template crystals during the sintering. To yield textured ceramics, the template crystals should possess platelet morphology with the (001) plane to facilitate their homogeneous alignment in the matrix and oriented epitaxial growth along the ⟨001⟩ direction. Rhombohedral composition given as $0.4Pb(Mg_{1/3}Nb_{2/3})O_3{-}0.25PbZrO_3{-}0.35PbTiO_3$ (PMN-PZT) was used as the matrix because its ⟨001⟩ single-crystal counterpart shows excellent piezoelectric properties ($d_{33} = 1530$ pC/N, $k_{33} = 0.93$) and much better thermal and electrical stabilities ($T_C = 211$ °C and $E_C = 4.5$ kV/cm) than those of PMN-PT or PZN-PT crystals ($T_C = 130{-}170$ °C and $E_C = 2{-}3$ kV/cm) (Zhang, Lee, Kim, Lee, & Shrout, 2007, 2008). $BaTiO_3$ (BT) was selected as a template due to its chemical stability in PMN-containing ceramics and good lattice match with the PMN-PZT composition (lattice parameter: ~4.05 Å) (Messing et al., 2004; Yan, Cho, & Priya, 2011). Moreover, the low permittivity of ⟨001⟩ BT template crystal ($\varepsilon_{33}^T/\varepsilon_0 = 130$, ε_0: vacuum permittivity) (Zgonik et al., 1994) is very desirable to suppress the permittivity increase in ⟨001⟩-textured

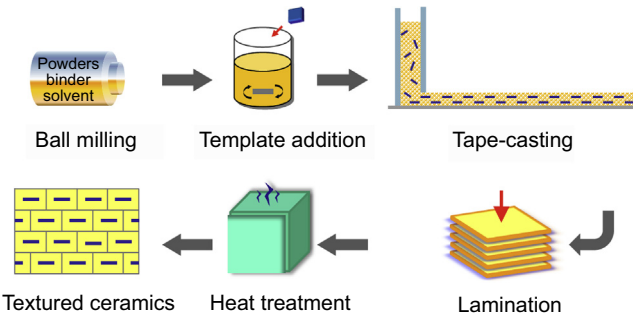

Figure 6.7 Schematic diagram of the texturing process of ceramics using the templated grain growth method.

PMN-PZT because the TGG processed textured ceramic is the "composite" material composed of matrix and monodispersed template crystals.

After embedding 5 vol% BT template crystals, the PMN-PZT ceramic was textured at different sintering temperatures. The microstructure evolution during the sintering is shown in Figure 6.8(a). At the sintering temperature of 600 °C, the matrix PMN-PZT particles were observed to surround the BT template without any growth in the matrix. The nucleation and growth on the surface of the BT template initiated around 800 °C, and interface migration was observed from the sample sintered at 900 °C. A high ⟨001⟩ Lotgering factor of 90% with highly textured microstructure was obtained from the specimen sintered at 1150 °C. Fine-grain size of the matrix preserved the driving force required for growth until the larger grains above 1150 °C started to impinge upon each other, resulting in low energy boundaries. The texture development is evidenced by X-ray diffraction (XRD) patterns in Figure 6.8(b). It can be seen that the intensity of (001) peaks is increased, while that of other peaks is decreased with increasing sintering temperature. Compared to randomly oriented ceramic in Figure 6.8(c), the highly textured sample in Figure 6.8(d) clearly shows a brick wall-like structure developed with larger grain size. Furthermore, electron backscatter diffraction (EBSD) mapping images in Figure 6.8(e) directly show that all grains in the textured sample were highly oriented along the ⟨001⟩ direction, unlike those in the randomly oriented sample.

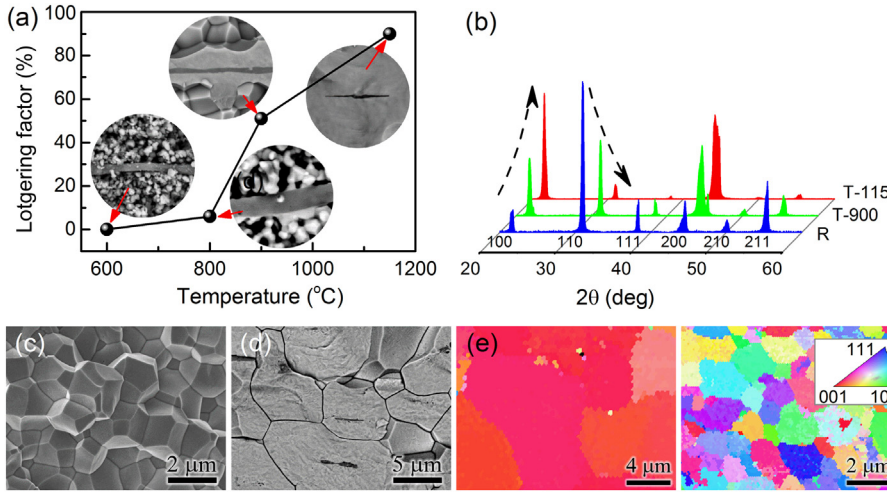

Figure 6.8 (a) ⟨001⟩ Lotgering factors of textured PMN-PZT samples sintered at various temperatures for 2 hours. Inset SEM images show the evolution of matrix PMN-PZT crystal growth on BT template crystal with variation of sintering temperature. (b) X-ray diffraction patterns of random and textured PMN-PZT samples. R and T-1150 denote the random and textured sample sintered at 1150 °C, respectively, and T-900 denotes the textured sample sintered at 900 °C. SEM images of (c) fractured random PMN-PZT and (d) fractured textured PMN-PZT. (e) EBSD inverse pole figure maps using stereographic projection of textured (left) and random (right) PMN-PZT ceramics.
Applied Physics Letters, *102*, 042903 (2013).

Table 6.5 Piezoelectric and dielectric properties of PMN-PZT: randomly oriented ceramic (R-ceramic), ⟨001⟩-textured ceramic (T-ceramic), and ⟨001⟩ single crystal (S-crystal)

Properties	R-ceramic	T-ceramic	S-crystal
d_{33} (pC/N)	230	1100	1530
k	0.4 (k_p)	0.84 (k_p)	0.93 (k_{33})
$\varepsilon_{33}/\varepsilon_0$	915	2310	4850
g_{33} ($\times 10^{-3}$ V m/N)	28.4	53.8	35.6
$d_{33} \cdot g_{33}$ ($\times 10^{-15}$ m^2/N)	6532	59,180	54,468
P_r (μC/cm^2)	30	36	29
E_C (kV/cm)	8.2	7.4	4.5
T_c (°C)	233	204	211

Applied Physics Letters, *102*, 042903 (2013).

Table 6.5 summarizes the piezoelectric and dielectric properties of randomly oriented ceramic (R-ceramic), ⟨001⟩-textured ceramic (T-ceramic), and ⟨001⟩ single crystal (S-crystal) of PMN-PZT composition. T-ceramic exhibited a giant d_{33} of 1100 pC/N, which is 4.8 times higher than that of R-ceramic (230 pC/N). This increasing ratio of d_{33} value between R- and T-ceramic (4.8) was much higher than that of the other textured piezoelectric ceramics (usually less than 2.5) as shown in Figure 6.5(b). Highly enhanced d_{33} of T-ceramic was also evidenced by strain versus electric field characteristics in Figure 6.9. Compared to R-ceramic, T-ceramic exhibited a much higher strain value (0.24% at 20 kV/cm), suggesting the high strain

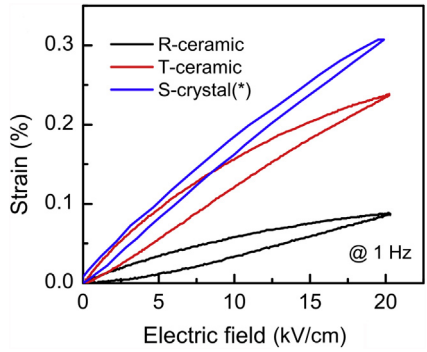

Figure 6.9 Strain versus electric field curves of randomly oriented ceramic (R-ceramic), ⟨001⟩-textured ceramic (T-ceramic), and ⟨001⟩ single crystal (S-crystal).
Applied Physics Letters, *102*, 042903 (2013).

coefficient and its superior feasibility for actuator applications. The planar mode coupling coefficient (k_p) of T-ceramic was found to be more than two times higher than that of R-ceramic. The most notable point is that via $\langle 001 \rangle$ texturing, the permittivity value was increased by only 2.5 times, while d_{33} was increased by 4.8 times. This suppressed the permittivity value of T-ceramic, resulting in a very high g_{33} of 53.8×10^{-3} V m/N (even much higher than the S-crystal value). High g_{33} of T-ceramic obtained by high d_{33} and suppressed permittivity yielded a giant transduction coefficient of $59{,}180 \times 10^{-15}$ m^2/N, which was nine times higher than that of R-ceramic and even higher than the S-crystal value.

The giant piezoelectric response of textured PMN-PZT ceramic was understood by noticing the role of special microstructure where BT templates were embedded in the matrix grains. The BT template inclusions were found to have comparatively higher polar anisotropy, suppressing rotation of its polarization under applied electric field. This was contrary to the properties of the matrix phase, PMN-PZT, which being near MPB had a drastically reduced polar anisotropy. In this scenario, the PMN-PZT matrix was regarded as a "soft ferroelectric" under the constant electric and stress fields imposed on this matrix by BT inclusions. These fields were generated by both fixed polarization of the BT template inclusions and crystal lattice misfit between the phases, which in turn were found to depend on the morphology, orientation relations with the matrix, polarization, and processing parameters. Given the low polar anisotropy of the PMN-PZT matrix, a direction of its energy-minimizing polarization was determined by a coupling with the BT-generated fixed electric and stress fields imposed on the matrix. Application of an external electric field produced a deviation of the polarization direction of the PMN-PZT matrix from its energy-minimizing direction. This deviation produced the dielectric and strain response that was significant due to the "soft" character of the matrix. A lifting of the applied electric field reversed the deviation and resulted in recovery of the initial energy-minimizing polarization direction. This reversal caused by a coupling with the BT-generated constant fields was practically hysteresis free. Therefore, the polar anisotropy of PMN-PZT in this two-phase composite was determined by the interaction of the polarization of PMN-PZT with the local static electric and stress fields generated by the BT rather than by the intrinsic properties of the PMN-PZT. This coupling, together with the low polar anisotropy of PMN-PZT, resulted in combination of the maximum piezoelectric strain inherent to the PMN-PZT with the enhancement of blocking force caused by the electrostatic and stress-induced interaction between the phases. The discovered processing regime provided a composite with very highly textured PMN-PZT grains with superior functionality.

To clearly show the advantage of high d, k, g in textured ceramic, ME laminate composite was fabricated in the form of a three-layer structure corresponding to Metglas (2605SA1, Metglas Inc., USA)/textured PMN-PZT/Metglas. Figure 6.10 shows the ME coefficients (α_{ME}) of random and textured PMN-PZT laminates, where the maximum was found to be 348 mV/cm Oe and 1490 mV/cm Oe, respectively. The 3.4 times improvement of α_{ME} was explained on the basis of the textured microstructure.

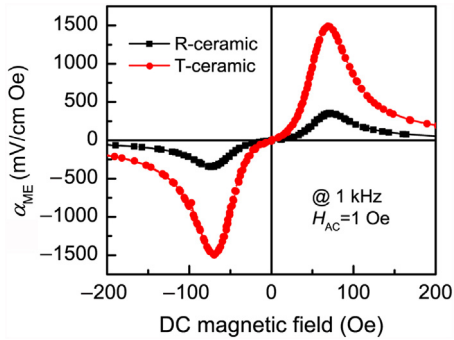

Figure 6.10 Magnetoelectric voltage coefficient of random and textured PMN-PZT ceramics. Applied Physics Letters, *102*, 042903 (2013).

6.4.2 Functionally graded composites

Functionally graded materials are the class of materials with variation in the properties across their dimensions. What makes functionally graded materials interesting are their overall unique properties, which are different from their individual components. There are a variety of functionally graded materials used in various fields, including defense and civilian applications (Miyamoto, Kaysser, Rabin, Kawasaki, & Ford, 1999). However, here we focus upon functionally graded ferroelectric materials and their potential applications, including ME devices.

The functional response of ferroelectric materials highly depends on the domain structure of a given material system. Domain structure depends on grain size to a certain extent. In our present work, we synthesized functionally graded laminate composites of ferroelectric materials with varying microstructure across the interface and consequently varying domain size across the interface. This kind of grading across the thickness provided an opportunity to have polarization-graded structure across the interface, and the coupling between the layers provided overall unique polarization characteristics, leading to interesting properties for the composite, which were not expected in the individual materials system.

The synthesis of bilayer and trilayer ferroelectric graded structures was performed with the following variations: (1) single-layer thick film of pure $BaTiO_3$ (BT) with a thickness of 1 mm, (2) bilayer structure with equal layer thickness of 0.5 mm for $BaTiO_3$ (BT) and $0.975BaTiO_3{-}0.025Ba(Cu_{1/3}Nb_{2/3})O_3$ (BTBCN), (3) bilayer structure with unequal thickness of 0.650 mm for BT and 0.350 mm for BTBCN, and (4) trilayer structure with a 0.40 mm layer of BT sandwiched between two layers of BTBCN with a thickness of 0.30 mm. Figure 6.11 shows the schematic of the various graded structures presented in the literature. The coupling between the layers due to the polarization mismatch was found to change the free energy function, dynamic hysteresis behavior, and power-law scaling relations.

In order to investigate the interface in graded structures, SEM images were recorded at various magnifications (Figure 6.12). The average grain size of ~32 μm on the BT

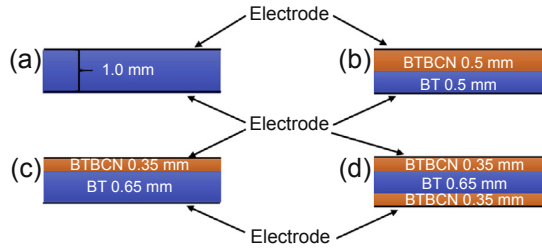

Figure 6.11 Schematic of various graded thick film structures: (a) BT, (b) bilayer with equal thickness of BT and BTBCN (0.5 mm each), (c) bilayer with higher thickness of BT (0.65 mm) and BTBCN (0.35 mm), and (d) trilayer with 0.3 mm thickness of each BTBCN layer and 0.4 mm BT layer sandwiched in between them.
Journal of Applied Physics, *108*, 124111 (2010).

side was found to be much larger than that on the BTBCN side (∼0.64 μm). The interface in this figure is marked with a red solid line. Figure 6.12(c) depicts the magnified view of the sharp interface, indicating the limited diffusion of Cu and Nb across the interface. From these micrographs, the effective thickness of the interfacial region was estimated to be ∼75 nm and therefore a trilayer specimen had thickness of interfacial regions on the order of ∼150 nm. In order to investigate the domain structure

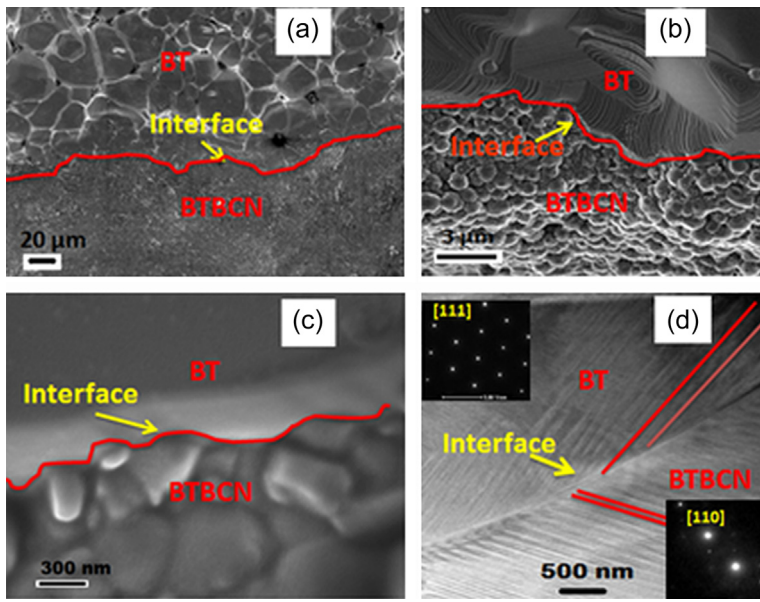

Figure 6.12 (a–c) SEM micrographs of the interface at various magnifications, and (d) TEM image of the domain structure across the interface (insets showing SAED patterns).
Journal of Applied Physics, *108*, 124111 (2010).

across the interface, transmission electron microscopy (TEM) was conducted (Figure 6.12(d)). The insets of Figure 6.12(d) show selected area electron diffraction (SAED) patterns on the corresponding side of the interface. These SAED patterns suggested that the zone axis of the BT side was [111] and the BTBCN side was [110]. Both the sides of the interface were found to show stripe-like domains; however, the size of domains was smaller on the BTBCN side than that of the BT side. This is a quite interesting phenomenon as it provides us the opportunity to modify the polarization response of a given system. The smaller size of grains was considered to have smaller domain size, which, in turn, affects the polarization response of the given system.

In polycrystalline ferroelectric ceramics, the domain size (D) could be related to grain size (G) as (Cao & Randall, 1996)

$$D \propto G^p \tag{6.9}$$

where

$$p < 1/2 \quad \text{for} \quad G > 10\ \mu\text{m}$$
$$p = 1/2 \quad \text{for} \quad 10\ \mu\text{m} > G > 1\ \mu\text{m}$$
$$p > 1/2 \quad \text{for} \quad G > 1\ \mu\text{m}$$

The domain sizes obtained from TEM images for BT and BTBCN sides were used to estimate the exponent $p \sim 0.52$ for the BTBCN side. The difference in domain exponents for BT and BTBCN sides gave rise to the polarization gradient across the interface. The difference in tetragonality of both the materials (BT and BTBCN) resulted in spontaneous strain gradient across the interface. Therefore, the polarization gradient along with the strain gradient across the interface leads to the formation of graded structure.

Figure 6.13(a) and (b) show the piezoresponse force microscopy (PFM) images of the BT and BTBCN sides, respectively. The variation in contrast in these images indicated regions with different piezoelectricity. From these images, it was observed that the domain size in BTBCN was much smaller than that of the BT side. Generally, materials with smaller domain size have been found to depict larger piezoelectric response. The longitudinal piezoelectric response (d_{33}) measured (using a Berlincourt d_{33} meter) on the individual BT and BTBCN layer was found to be 144 and 330 pC/N. Thus, PFM results were consistent with the measured bulk piezoelectric response.

The temperature dependence of relative permittivity (ε) and loss tangent ($\tan\delta$) plots at various frequencies for different samples are shown in Figure 6.14(a–e). The Curie temperatures of BT and BTBCN have been found to be 125 and 80 °C, respectively (Ahn, Maurya, Park, Nahm, & Priya, 2009). The peaks related to paraelectric (PE) to ferroelectric (FE) transition for both the samples (BT and BTBCN) could be observed in Figure 6.14(a) and (b). These peaks were marked in the $\varepsilon(T)$ plots. In graded bilayer and trilayer structures, the peaks related to the transition temperature were found to shift a little. The Curie temperatures of the BTBCN and BT sides

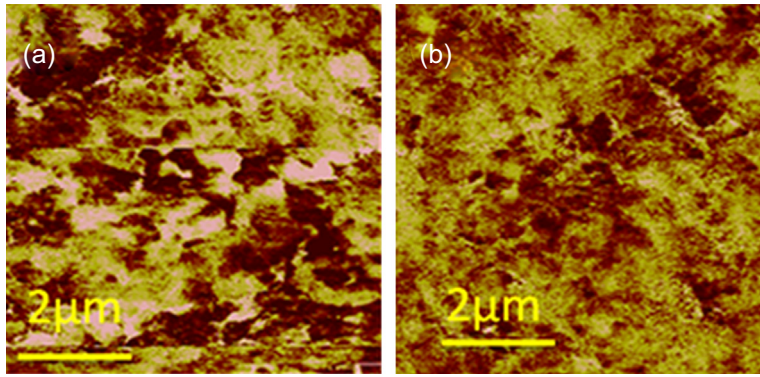

Figure 6.13 Piezoresponse force microscopy image of the (a) BT side and (b) BTBCN side. Journal of Applied Physics, *108*, 124111 (2010).

were found to shift toward higher (~90 °C) and lower temperature (~117 °C), respectively. This phenomenon was attributed to the strain gradient across the interface. Moreover, the maximum value of dielectric constant at transition temperature was also found to decrease for a composite specimen. The trilayer graded specimen was found to show higher intensity of the Curie peak related to BTBCN due to increased effective thickness of BTBCN layers.

From these results, the influence of interface on properties and functional response of a given composite was observed clearly, which was the combination of individual components of the composite. These results, along with the gradient in domain size across the interface, confirmed the formation of graded structure. By invoking phenomenology, further information about grading and interface coupling can be obtained. The free energy in terms of polarization can be expressed as follows for uncoupled and unconstrained tetragonal BT (Kao, 2004):

$$F_1(P,T) = F_{o1}(T) + \frac{1}{2}a_1P_1^2 + \frac{1}{4}a_2P_1^4 + \frac{1}{6}a_3P_1^6 \tag{6.10}$$

where $F_o(T)$ is the energy in the paraelectric state. For the isothermal case, the electric field acting on the ferroelectric material, expressed in terms of P_1, can be obtained as the following:

$$E_1 = \frac{dF_1}{dP_1} = a_1P_1 + a_2P_1^3 + a_3P_1^5 \tag{6.11}$$

Similarly, for BTBCN, the electric field can be written as

$$E_2 = \frac{dF_2}{dP_2} = b_1P_2 + b_2P_2^3 + b_3P_2^5 \tag{6.12}$$

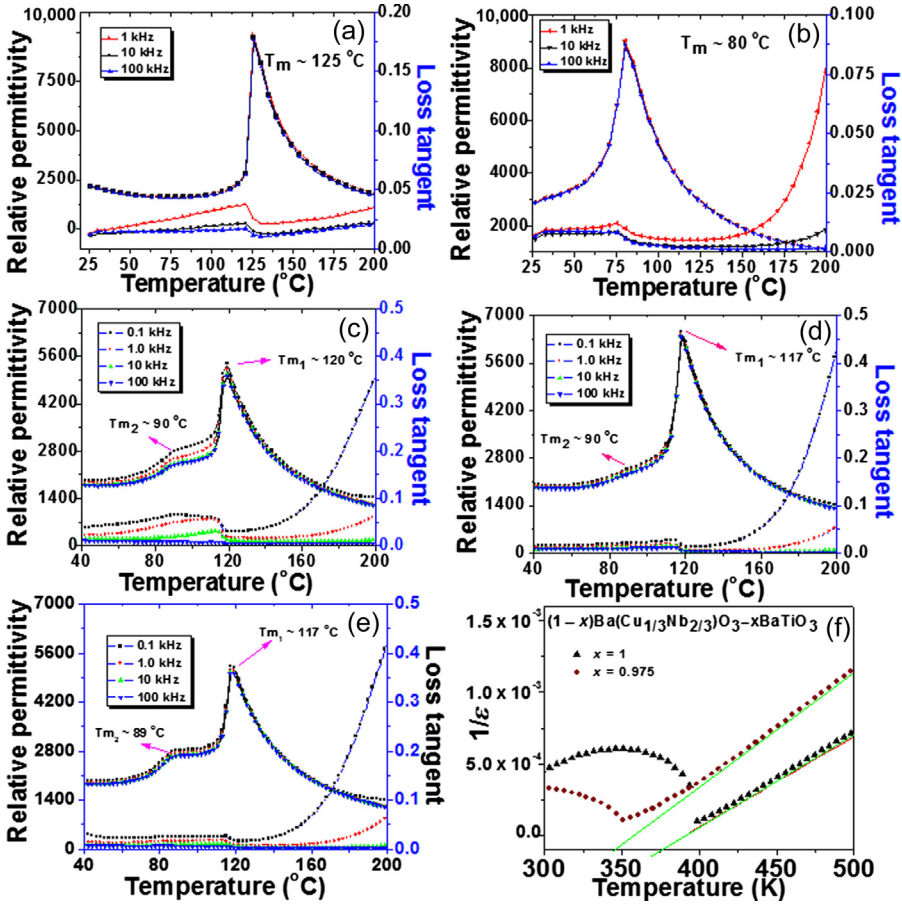

Figure 6.14 Temperature dependence of relative permittivity for (a) BT, (b) BTBCN, (c) bilayer with equal thickness, (d) bilayer with unequal thickness, (e) trilayer with BT layer sandwiched between two BTBCN layers, and (f) $1/\varepsilon$ versus temperature plot.
Journal of Applied Physics, *108*, 124111 (2010).

where F_1 and F_2 are free energy of layer 1 and 2 in its high-temperature PE state, P_1 and P_2 are the polarizations of layers 1 and 2, and a_1, a_2, a_3, b_1, b_2, b_3 are the Landau coefficients. The temperature dependence of coefficients a_1 and b_1 is given by the Curie−Weiss law as $a_1 = (T_o - Tc_1)/\varepsilon_0 C_1$ and $b_1 = (T_o - Tc_2)/\varepsilon_0 C_2$, where ε_0 is the permittivity of free space, and Tc_1, Tc_2 and C_1, C_2 are the Curie−Weiss temperature and constant of uncoupled layer 1 and 2. The other coefficients in free energy function are assumed to be temperature independent. By equating Eqns (6.4) and (6.5) to zero, spontaneous polarization (P) corresponding to two polarization states of each layer can be obtained. The magnitude of $(T_o - Tc_1) \sim -24.15$ K for the BT layer and $(T_o - Tc_2) \sim -5.88$ K for the BTBCN layer was computed using Figure 6.14(f).

Subsequently, these data were used to calculate the values of Curie constant (C) for BTBCN ($\sim 1.4 \times 10^5$ K) and BT ($\sim 1.6 \times 10^5$ K).

The coupling of layers in graded structures (bilayer and trilayer) was expected to result in different values of free energy (F) and electric field (dF/dP) as observed in the $\varepsilon(T)$ plots. Assuming E_{i1} and E_{i2} were the internal electric fields in BT and BTBCN layers (Kretschmer & Binder, 1979; Jena, Alpay, & Mantese, 2008),

$$E_{i1} = \frac{-1}{\varepsilon_0}(P_1 - \langle P \rangle) = \frac{\alpha}{\varepsilon_0(P_2 - P_1)} \tag{6.13}$$

and

$$E_{i2} = \frac{-1}{\varepsilon_0}(P_2 - \langle P \rangle) = \frac{(1-\alpha)}{\varepsilon_0(P_1 - P_2)} \tag{6.14}$$

where P_1 and P_2 are new polarization states in layer 1 and layer 2, respectively; after coupling, $\langle P \rangle = (1-\alpha)P_1 + \alpha P_2$ is the average polarization and α is the relative volume fraction. The total free energy function incorporating the potential energies of internal fields E_1 and E_2 was given by (Jena et al., 2008)

$$F_\Sigma = (1-\alpha)\left[F_1(P_1) - EP_1 - \frac{1}{2}\xi E_{i1}P_1\right] + \alpha\left[F_2(P_2) - EP_2 - \frac{1}{2}E_{i2}P_2\right] + F_S/h + F_{\text{el}} - JP_1P_2 \tag{6.15}$$

where F_{el} is the elastic energy of the polarization-free misfit. Because of the higher thickness of the bilayer (~ 1000 μm) and the very small correlation length of ferroelectric, the comparatively lower energy of interface F_S/h was neglected (Boris & Strukov, 1998; Jena et al., 2008). The last term in the above equation was described as interlayer (interfacial) coupling, while J is the coupling coefficient (interfacial exchange interaction coefficient) (Jena et al., 2008):

$$J = \alpha\,(1-\alpha)\xi/\varepsilon_0 \tag{6.16}$$

Equation (6.9) suggested that the coupling between layers could be controlled either by the volume fraction of each layer or by modifying free carrier content. The free charge density with respect to the bound charge at the interlayer interface was given by $\xi = 1 - \rho_f/\rho_b$, ρ_b, where ρ_f is the free charge density. The limiting values of ξ were given as 1 and 0, which were further related to the perfect insulating and semiconducting ferroelectric bilayers, respectively. The bound charge density, in the interfacial region with polarization ($\overrightarrow{P}$) varying point to point (assuming), was written as

$$\rho_b = -\vec{\nabla} \cdot \overrightarrow{P} \tag{6.17}$$

Using the differential form of Gauss's law, the divergence of electric field was given as

$$\vec{\nabla} \cdot \vec{E} = \frac{\rho}{\varepsilon_0} = \frac{\rho_b + \rho_f}{\varepsilon_0} \tag{6.18}$$

Combining Eqns (6.10) and (6.11), the relation for free charge density was derived as

$$\vec{\nabla} \cdot \varepsilon_0 \vec{E} = -\vec{\nabla} \cdot \vec{P} + \rho_f$$

or

$$\rho_f = \vec{\nabla} \cdot \varepsilon_0 \vec{E} + \vec{\nabla} \cdot \vec{P} = \vec{\nabla} \cdot \left(\varepsilon_0 \vec{E} + \vec{P}\right) = \vec{\nabla} \cdot \vec{D} \tag{6.19}$$

where $\vec{D} = (\varepsilon_0 \vec{E} + \vec{P})$ is the displacement vector. Below the subcoercive field and quasistatic frequency (<1 Hz), the free charge contribution to polarization was considered to be dominant. Alignment of domains contributed to resultant polarization in the saturated field and quasistatic frequency regime, which provided estimation of bound charge density. The values of polarization for the subcoercive field ($E_{c-} = 1$ kV/cm) and maximum polarization in the saturated field (E_{c+}) regime for layered systems at 0.1 Hz are depicted in Table 6.6. Taking the ratio of the polarization magnitudes in the E_{c-} and E_{c+} regime, an indication for the changes in free and bound charge density was obtained ($\sim \rho_f/\rho_b$). Table 6.6 shows the polarization ratio, which indicated a significant drop for the graded bilayer with unequal thickness and the

Table 6.6 Magnitude of polarization in the quasistatic frequency (0.1 Hz) regime

Systems	P_r (μC/cm^2) in subcoercive field (E_{c-}) regime (1 kV/cm)	P_{max} (μC/cm^2) in saturated field (E_{c+}) regime	Polarization ratio = $P_r(E_{c-})/P_{max}(E_{c+})$
BTBCN single layer	0.15	19.2	0.00781
BT single layer	0.11	16.8	0.00655
Bilayer with equal thickness	0.14	16.5	0.00848
Bilayer with unequal thickness	0.07	15.2	0.00461
Trilayer	0.07	12.1	0.00579

Journal of Applied Physics, *108*, 124111 (2010).

trilayer structure, which reflected the increase in coupling coefficient. The contribution from an unrealistic interface was neglected; however, it explained the changes observed in hysteresis behavior. Moreover, the observation on the influence of graded structure on ferroelectric properties was confirmed from this analysis.

The hysteretic PE loops at various frequencies (f) and electric fields (E_0) were recorded for BT single layer, BT−BTBCN graded bilayer with equal and unequal thicknesses, and BTBCN−BT−BTBCN graded trilayer ceramic systems. Figure 6.15(a) and (b) show examples of hysteresis profiles for a BT single-layer system. Other systems (graded bilayer with equal and unequal thicknesses and trilayers) exhibited very similar PE hysteresis behaviors. At fixed E_0, the hysteresis loop area $\langle A \rangle$, remnant polarization (P_r), and coercive field (E_C) were found to decrease with an increase of frequency (Figure 6.15(a)). This phenomenon was attributed to the delayed response of domain switching and polarization reversal, which also diminished the hysteresis loop size. On increasing E_0 at fixed f, remnant polarization (P_r) was found to increase (Figure 6.15(b)) as larger E_0 provides a higher level of driving force responsible for switching of ferroelectric domains. Higher driving force was

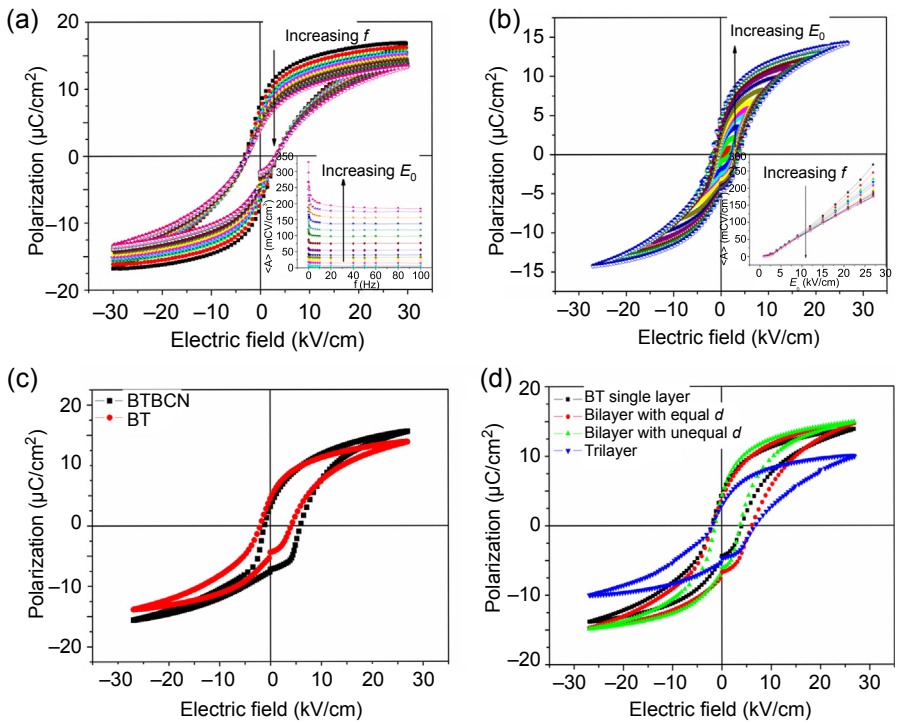

Figure 6.15 P−E hysteresis loops of a BT single-layer system: (a) various f with fixed $E_0 = 30$ kV/cm, and (b) various E_0 with fixed $f = 10$ Hz. (c) P−E hysteresis loops of BTBCN and BT layers at fixed $f = 50$ Hz and $E_0 = 27$ kV/cm, and (d) P−E hysteresis loops of multilayer systems with fixed $f = 50$ Hz and $E_0 = 27$ kV/cm.
Journal of Applied Physics, *108*, 124111 (2010).

found to enhance the domain volume and, consequently, total polarization, including other hysteresis parameters (Wongdamnern et al., 2010).

Figure 6.15(c) compares the P−E hysteresis loop of BTBCN with BT. Both these compositions were ferroelectric with tetragonal perovskite structure at room temperature and, as seen in this figure, the polarization of BTBCN was higher than that of BT. Furthermore, the P−E hysteresis loops for both the materials were found to be shifted toward the positive side on the electric field axis, implying the presence of an internal-bias field mainly arising from electronic defects. The polarization switching in BT single crystals was found to occur through nucleation of antiparallel domains and their growth by domain wall motion (Merz, 1954; Picinin, Lente, Eiras, & Rino, 2004). The polarization switching in polycrystalline ceramics was strongly influenced by grain boundaries, space charges, charged defects, and surfaces (Cohen, 2000; Lente & Eiras, 2001; Wongdamnern, Ngamjarurojana, Laosiritaworn, Ananta, & Yimnirun, 2009). As commonly observed in hard piezoelectric materials, the presence of charged defects resulted in the formation of an internal-bias field by pinning the domain boundaries. The coercive field broadness ($2E_C$) of BTBCN was found to be larger than that of BT. The P−E hysteresis loops of BT single layer and BT−BTBCN layers formed as graded bilayer and trilayer ceramic systems are compared in Figure 6.15(d). The graded trilayer system was found to show the lowest polarization value and largest coercive field (E_C) as compared with the rest of the structures. The higher value of coercive field on the positive side for all the structures further indicated the presence of a built-in internal-bias field.

The internal-bias field in each system was quantified using the following relations (Takahashi, 1981):

$$E_1 = E_C + E_i \tag{6.20}$$

$$E_2 = -E_C + E_i \tag{6.21}$$

$$E_i = (E_1 + E_2)/2 \tag{6.22}$$

where E_1 and E_2 are electric field intercepts on the positive and negative side, respectively, E_C is the magnitude of the coercive field with no internal bias, and E_i is the magnitude of the internal-bias field. The effect of internal-bias field on the coercive field was determined by expressing the rate of motion of domain boundaries as

$$v = \mu E \tag{6.23}$$

and

$$\mu = (3\delta)/2P_0\Gamma \tag{6.24}$$

where μ is the mobility of the domain wall, δ is its half-width, Γ is the viscosity of domain wall motion, and P_0 is the spontaneous polarization (Sidorkin, 2006).

The switching time was characterized by the time of intergrowth of the domain to the crystallite half-width $d/2$ as given by the relation

$$t = d/(2v(E_C)) = 1/f \tag{6.25}$$

combining Eqns (6.23)–(6.25)

$$E_C = (P_0 \Gamma df)/\delta \tag{6.26}$$

which is a linear dependence of internal-bias field modified coercive field on the frequency (Sidorkin, Nesterenko, Ryabtsev, & Sidorkin, 2009).

The BTBCN layer was found to show coercive field broadness ($2E_C$) ~7.2 kV/cm; however, the BT single layer was found to show $2E_C$ ~6.2 kV/cm. Generally, the coercive field broadness is expected to be between 6.2 and 7.2 kV/cm in uncoupled multilayer systems behaving like capacitors in series. However, graded bilayer and trilayer systems were found to show different behavior, as shown in Table 6.7. The lower coercive field broadness value found in a bilayer with an unequal thickness system and the higher coercive field broadness values found in a bilayer with equal thickness and trilayer systems implies that there was finite interaction across the layers. The internal-bias field was found to increase from the bilayer to trilayer system due to direct contribution of polarization mismatch, and, therefore, the system required additional energy for domain reversal to overcome the barrier due to internal-bias field. Therefore, the system with high internal-bias field was characterized by high coercive field. This clearly explained why the coercive field of the trilayer system was highest and was reduced sequentially for the bilayer with equal and unequal thickness systems, as shown in Table 6.7. However, the coercive field for the bilayer with an unequal thickness system was less than that for the BT single layer. This reflected the effect of interface coupling between layers in a bilayer with an unequal thickness system, which enhanced domain wall mobility.

Table 6.7 Magnitude of coercive field broadness ($2E_C$) and internal-bias field for various composite systems

System	Coercive field broadness, $2E_C$ (kV/cm)	Internal-bias field (kV/cm)
BTBCN single layer	7.2	2.9
BT single layer	6.2	1.0
Bilayer with equal thickness	8.2	2.1
Bilayer with unequal thickness	5.1	1.2
Trilayer	8.8	2.5

Journal of Applied Physics, *108*, 124111 (2010).

Interestingly, the graded trilayer ceramic system was found to exhibit double hysteresis loop-like behavior similar to that of antiferroelectric materials (Chew, Ong, Osman, & Tilley, 2000; Ong, Osman, & Tilley, 2002). Similar behavior in prior studies was attributed to the presence of multiple domain states when two factors were simultaneously occurring: (1) the coupling strength (J) was sufficient between layers and (2) both layers were expected to have almost equal polarization values in the antiparallel direction ($P_1 = -P_2$ or vice versa). The polarization of each layer was expected to depend on layer thickness, therefore, to provide equal polarization in the opposite direction. In the case of the same material, the layer thickness was required to be $L_1 \approx L_2$ (where L_1 and L_2 were thicknesses of layer 1 and layer 2, respectively). In the case of bilayers with equal thickness of the same material, when coupling strength was small, the overall polarization ($P = P_1 + P_2$) was nonzero, and the system was in weak ferroelectric phase. However, with the increase in the strength of coupling, P approached zero, and thereby the system exhibited double-loop behavior. In the case of graded bilayers consisting of two different materials, the polarizations P_1 and P_2 were variable with coupling strength (Ma, Shen, & Xu, 2000). The graded trilayer system had two interfaces between BTBCN−BT and BT−BTBCN. Since each couple of layers was composed of the same materials with the same layer thickness, it is possible that each couple induced equal polarization but in different directions, which explained the origin of double hysteresis loop-like behavior. Bilayers with equal and unequal thicknesses did not show double hysteresis loop-like behavior, which might be due to the smaller effective thickness of the interface.

Figure 6.15(c) shows that the polarization of BTBCN was higher than that of BT. Since polarization is directly proportional to layer thickness (Jena et al., 2008), an uncoupled state bilayer system with equal thickness should have higher polarization than that of a bilayer system with unequal thickness (lower volume fraction of BTBCN). However, the results exhibited that the polarization of a bilayer system with unequal thickness was almost similar to that of a bilayer with equal thickness at 50 Hz. At lower frequencies of 0.1 Hz, the polarization recorded for a bilayer with equal thickness was higher than that of a bilayer with unequal thickness (Table 6.6). This phenomenon indicated the presence of frequency-dependent finite coupling in the layered structure and was explained by considering the coupling of two layers, which established a new polarization state in each layer due to the internal-bias field arising from polarization mismatch (Jena et al., 2008). BTBCN was found to have higher polarization than BT, and therefore, even with smaller thickness of BTBCN, a bilayer system with unequal thickness depicted polarization comparable to that of BT. Thus, just by adjusting the thickness of BTBCN, a polarization mismatch in the graded bilayer was created. This polarization mismatch resulted in a weak internal-bias field, which was subsequently found to affect domain reversal. Thus, by tailoring the thickness of layers, a higher polarization in a graded bilayer system with unequal thickness was obtained (Figure 6.15(d)). For the composite having equal thickness of BT and BTBCN, the net polarization value in the BTBCN layer was expected to be higher as compared to that of BT, giving rise to polarization mismatch. As explained in earlier sections, the trilayer specimen had higher exchange coupling and increased internal bias due to finite interaction across the layers. Therefore, the

polarization value was expected to be lowest in the trilayer system as compared to the other systems. This phenomenon was confirmed experimentally in Figure 6.15(d).

In summary, a functionally graded ferroelectric bilayer and a trilayer bulk laminate composite of BT and BTBCN with different thicknesses of individual layers (while keeping the same overall effective thickness) have been investigated. A sharp interface with varying grain and domain sizes between two different layers of a composite was observed. The BT layer of the composite was found to have larger domain size than the BTBCN side. The functionally graded systems were found to exhibit shifting of the Curie peak with respect to each constituent material due to coupling between layers. Moreover, the polarization mismatch between the uncoupled BT and BTBCN resulted in an internal electric field in the composite specimen, which established new polarization states in each layer by perturbing the free energy of the composite specimen. The differences in grain size, tetragonality, and domain mobility of each layer also perturbed the ferroelectric response in coupled functionally graded composites. All graded structures exhibited similar trends where hysteresis area $\langle A \rangle$, remnant polarization (P_r), and coercive field (E_C) were found to decrease with increasing frequency due to delayed response. But the magnitude of these hysteresis parameters was found to increase with increase in applied electric field due to enlargement of electrical driving force. Interestingly, a functionally graded trilayer system was found to possess the strongest internal-bias field, while a graded bilayer with an unequal thickness system had the lowest magnitude. The trilayer functionally graded composite was found to exhibit a double hysteresis loop due to polarization mismatch between layers. Therefore, functionally graded ferroelectric composites were found to exhibit a unique overall functional response. These graded ferroelectric/piezoelectric composites, if used as piezoelectric elements in an ME composite, are expected to exhibit interesting novel phenomena like the appearance of a self-bias effect, etc.

6.4.3 Effect of functionally graded ferroelectric and ferromagnetic bilayers on magnetoelectric coupling

In order to understand the effect in grading on the properties of ferroelectric and piezoelectric layers, Petrov and co-workers performed theoretical calculations to predict ME properties of this system (Petrov & Srinivasan, 2008). They assumed a linear grading in the piezoelectric coefficient and permittivity of the ferroelectric. Similar grading was considered in the piezomagnetic coefficient of the ferromagnet component of the structure. For this analysis, bilayers of nickel zinc ferrite and lead zirconate titanate (PZT) with the grading axis perpendicular to the sample plane were considered (Petrov & Srinivasan, 2008). The schematic of the structure of the ME system is shown in Figure 6.16.

The theoretical calculations were further used to demonstrate the frequency dependence of ME voltage coefficient for a free-standing bilayer of graded NZFO and homogeneous PZT with a length of 12 mm and a thickness of 2 mm with PZT volume fraction $V = 0.3$ (Petrov & Srinivasan, 2008). The resonance in the bending oscillations was found to occur at 5 kHz. A two-fold-magnitude increase in the maximum ME voltage coefficient was obtained as compared to low-frequency coupling.

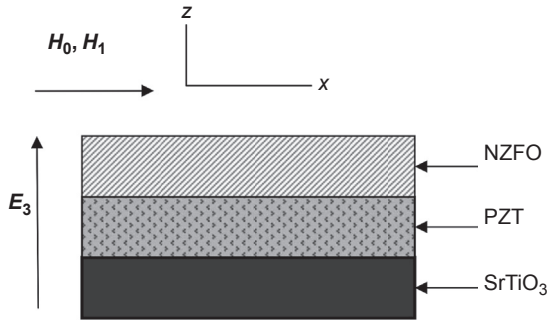

Figure 6.16 A graded nickel zinc ferrite−lead zirconate titanate bilayer on $SrTiO_3$ substrate. The ferrite is assumed to have a grading of composition, leading to a linear variation in the piezomagnetic coefficient along its thickness. Similarly, the PZT layer is assumed to have linear variation in the piezoelectric coefficient and dielectric constant along the z-axis. The bias magnetic field H_0 and the AC magnetic field H_1 are parallel to the x-axis. The piezoelectric layer is poled along z and the AC electric field E_3 is measured across the bilayer (Petrov & Srinivasan, 2008).
Physical Review B, *78*, 184421 (2008).

Furthermore, a 50% increase in the ME voltage coefficient was found for the composite with positive grading (Figure 6.17(a)) (Petrov & Srinivasan, 2008). On the other hand, a 50% decrease in the ME voltage coefficient was found for the composite with negative grading as compared to the homogeneous system (Petrov & Srinivasan, 2008). This behavior was attributed to an increase in the rotating moment of the ferrite layer for the positive grading and corresponding enhancement in the longitudinal strain of PZT, which consequently resulted in enhanced ME voltage. Similar experiments were performed for the bilayers of homogeneous NZFO and graded PZT (Figure 6.17(b); Petrov & Srinivasan, 2008). However, these results were found to exhibit a shift in the resonance frequency without any change in the magnitude of ME voltage coefficient. The ME voltage remained constant because of similar grading-related variations in the piezoelectric coupling and dielectric constant. Thus, the theoretical calculations demonstrated enhanced ME voltage coefficient in the system with positive grading in piezoelectric and ME components for a volume fraction of PZT $\sim$0.6 (Petrov & Srinivasan, 2008). It was further found that the ME voltage decreased rapidly with increasing substrate thickness until it reached a substrate to bilayer thickness ratio $\sim$0.3 (Petrov & Srinivasan, 2008).

In another interesting work on graded ferroics, Mandal et al. demonstrated the presence of a large zero-bias, low-frequency ME coefficient (0.3−1.6 V/cm Oe) for an ME system with grading in a magnetic component (Mandal, Sreenivasulu, Petrov, & Srinivasan, 2011). The grading in magnetization was created using Ni and Metglas (Mandal et al., 2011). The ME coupling was further found to be enhanced by a factor of 40 at bending modes on a clamping sample on one end (Mandal et al., 2011). The zero-bias ME coupling was attributed to strain-mediated coupling between transverse magnetization (originating due to magnetization grading at the interface of

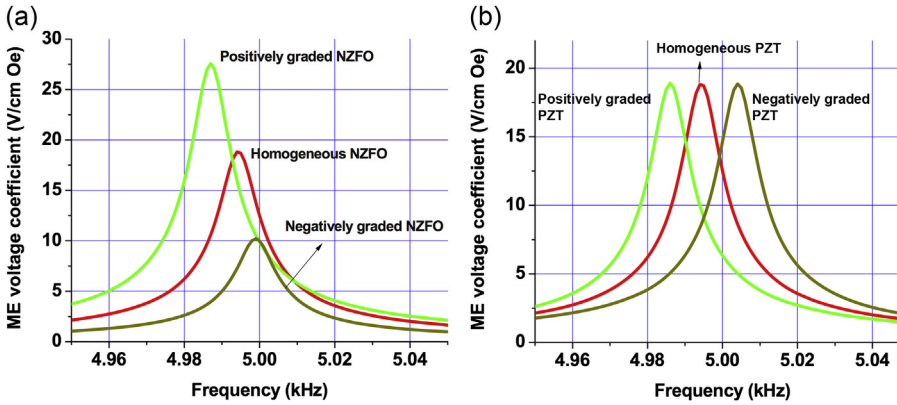

Figure 6.17 (a) Frequency dependence of the magnetoelectric (ME) voltage coefficient for a free-standing PZT−NZFO bilayer. The results are for homogeneous PZT and homogeneous, positively, or negatively graded NZFO. The PZT volume fraction is 0.3. The peak in ME coefficient occurs at resonance frequency for bending oscillations in the bilayer. (b) Frequency dependence as in (a) for free-standing bilayers of homogeneous NZFO and homogeneous, positively, or negatively graded PZT. The PZT volume fraction is 0.3 (Petrov & Srinivasan, 2008).
Physical Review B, *78*, 184421 (2008).

Ni-Metglas) and the in-plane AC magnetic field (Mandal et al., 2011). Recently, Laletin et al. reported a large remanent ME coefficient and coercivity in the static field dependence of the low-frequency ME effects for bilayers of PZT and a functionally graded ferromagnetic layer (Laletin et al., 2012). The grading in magnetization was achieved by using $Ni_{0.7}Zn_{0.3}Fe_2O_4$ (NZFO) and pure Ni layers (Laletin et al., 2012). They further demonstrated that the built-in magnetic field was created due to grading in the magnetization. This built-in field was found to depend on sequence and thickness of the NZFO and Ni layers (Laletin et al., 2012). This phenomenon resulted in strong hysteretic behavior of the total torque moment, flexural deformations in the composite, and the bias field dependence of ME voltage coefficient (Laletin et al., 2012). These results demonstrated that the grading in functional properties of the piezoelectric and magnetic layers of the ME composite system can be used to effectively manipulate the ME response to a great extent to achieve the self-bias effect. The detailed description of this self-bias effect is provided in a separate section of this chapter.

6.5 Recent advances in fabrication of magnetoelectric composites

The ME effect in ME composite is generated as a product property of the magnetostrictive effect (magnetic/mechanical effect) in the magnetic phase and the piezoelectric effect (mechanical/electric effect) in the piezoelectric phase. As a result, this

two-phase composite material can be represented as (Nan, Bichurin, Dong, Viehland, & Srinivasan, 2008)

$$\frac{\partial P}{\partial H} = \alpha_{\mathrm{ME}} = k_{\mathrm{c}} e^{m} e \tag{6.27}$$

where

$$e^{m} = \frac{\partial S}{\partial H} \quad \text{and} \quad e = \frac{\partial P}{\partial S} \tag{6.28}$$

k_{c} is the coupling factor ($0 \leq k_{\mathrm{c}} \leq 1$) between the two phases (Nan, 1993), α_{ME} is the ME coefficient of the composite, S is the strain, and e^{m} and e are piezomagnetic and piezoelectric coefficients, respectively. Therefore, besides a high piezoelectric coefficient (e) and a high piezomagnetic coefficient (e^{m}), a strong coupling factor (large k_{c}) will result in a large ME coefficient α_{ME}. In this section, we will focus on the recent development in the fabrication process to achieve high coupling in a ME composite.

6.5.1 Self-biased textured cofired laminate systems

The widely used method for synthesis of ME laminate composites is bonding of the magnetostrictive layer (such as Metglas, Terfenol-D) and the piezoelectric layer (such as PZT, PMN-PT) together using epoxy resin. This fabrication method is easy but the epoxy layer is much softer than both magnetostrictive alloy and ferroelectric ceramic and thus it dampens the generated strain, resulting in loss of efficiency. Cofiring of layered ME composite can avoid the interface weakening due to epoxy bonding and will also reduce the overall fabrication cost.

Magnetostrictive/piezoelectric/magnetostrictive (M/P/M) laminates with Ag inner electrodes have been cofired at 930 °C for 4 h as shown in Figure 6.18(a). $Pb(Mg_{1/3}Nb_{2/3})O_3{-}32.5PbTiO_3$ [PMN-PT] and $(Ni_{0.6}Cu_{0.2}Zn_{0.2})Fe_2O_3$ [NCZF] were used as piezoelectric and magnetostrictive materials, respectively. To improve the piezoelectric response, the PMN-PT piezoelectric materials were textured by using $\langle 001 \rangle$ $BaTiO_3$ (BT) microcrystals synthesized by the templated grain growth method. Figure 6.18(b) shows the cross-sectional scanning electron microscopy (SEM) images of cofired NCZF/textured-PMN-PT/NCZF (abbreviated as C-N/T/N) laminate composite. There was no trace of delamination or microcrack, and the thickness of the textured PMN-PT piezoelectric layer and NCZF ME layer was similar. Energy-dispersive spectroscopy (EDS) line scanning analysis results in Figure 6.18(b) show that the interfacial element diffusion and/or chemical reactions occurring during the sintering process at high temperature were negligible, indicating the high chemical stability of NCZF, Ag, and PMN-PT. In a prior study conducted on the NCZF/PZN-PZT system, the diffusion length for Cu was found to be in the range of 30 μm. EDS mapping images of C-N/T/N cross-sectional area (Figure 6.18(c)) show the dense microstructure and sharp interface across different layers. The thickness of the Ag electrode and the PMN-PT piezoelectric layer was 10 and 140 μm,

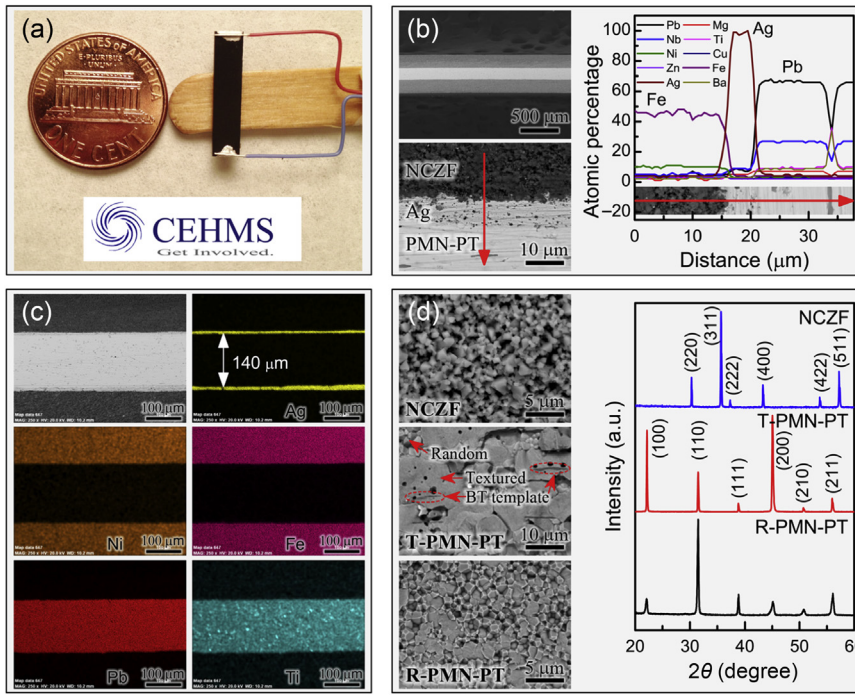

Figure 6.18 (a) Optical image of cofired NCZF/T-PMN-PT/NCZF laminate; (b) polished cross-sectional SEM images and EDS/SEM element line scanning analysis; (c) element mapping of cofired NCZF/T-PMN-PT/NCZF laminate; (d) fracture cross-sectional SEM images and planar X-ray diffraction patterns of different layers.
Applied Physics Letters, *102*, 052907 (2013).

respectively. The fracture surface SEM images and corresponding planar XRD patterns of different layers are shown in Figure 6.18(d). The textured PMN-PT layer displays brick wall-like microstructure with well-aligned BT templates (black lines) inside. Increase of (00l) XRD peak intensity and decrease of other peaks clearly indicates the formation of texture. The texture degree as calculated by the Lotgering factor was about 66%. In the TGG process, BT template crystals were aligned in PMN-PT matrix powder by a tape-casting process. PMN-PT matrix powders nucleate and grow on the aligned BT template crystals during the sintering, thereby yielding textured ceramics.

Figure 6.19(a) shows the ME voltage coefficient (α_E) as a function of DC magnetic field at off-resonance frequency of 1 kHz. The maximum α_E of cofired NCZF/random-PMN-PT/NCZF (abbreviated as C-N/R/N) was two times that of epoxy-bonded Metglas/random-PMN-PT/Metglas (abbreviated as B-M/R/M) laminate. It was seen that although the magnetostriction of Metglas ($\lambda = 40$ ppm) was twice that of NCZF ($\lambda \approx 20$ ppm), the strain transfer or coupling between magnetostrictive layer and piezoelectric layer by cofiring was much better than epoxy bonding. Via texturing,

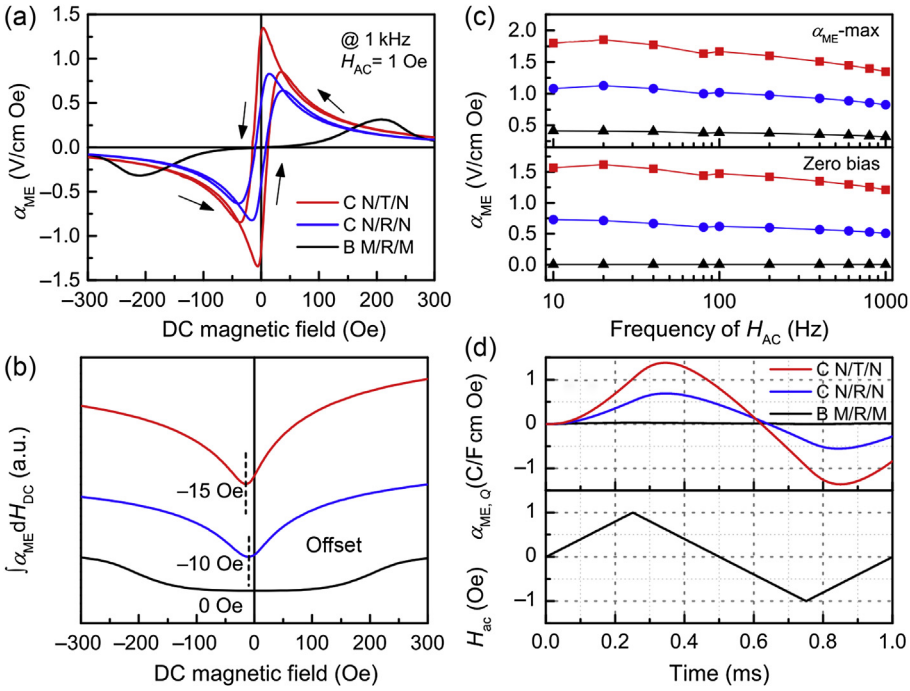

Figure 6.19 (a) ME voltage coefficients (α_{ME}) of cofired NCZF/T-PMN-PT/NCZF (C-N/T/N), NCZF/R-PMN-PT/NCZF (C-N/R/N), and epoxy-bonded Metglas/R-PMN-PT/Metglas (B-M/R/M) laminate; (b) integral values of α_{ME} with respect to the DC magnetic field; (c) ME voltage coefficients (α_{ME}) as a function of the frequency of applied AC magnetic field (H_{AC}); (d) dynamic ME charge coefficients (α_{ME}) and applied AC magnetic field spectra as a function of time for C-N/T/N, C-N/R/N composite, and epoxy-bonded Metglas/R-PMN-PT/Metglas (B-M/R/M) laminate under zero-DC magnetic field.
Applied Physics Letters, *102*, 052907 (2013).

further improvement was achieved in a cofired textured sample (C-N/T/N). The large enhancement in ⟨001⟩-textured ceramics was related to the formation of an "engineered domain state," which facilitates the rotation of ⟨111⟩ polarization toward the ⟨001⟩ direction. In Figure 6.19(a), it was also observed that there was a strong hysteretic ME response in the cofired composite. Considering the relation $\alpha \propto q = d\lambda/dH_{DC}$, we estimated the effective λ behavior by integrating α with respect to H_{DC}, as shown in Figure 6.19(b). The epoxy-bonded Metglas/PMN-PT/Metglas showed symmetrical λ behavior with respect to H_{DC}, while the tendency of λ for cofired composites was found to be asymmetric. The variation of α_E with frequency of applied H_{AC} is shown in Figure 6.19(c). It was seen that the maximum α_E displays excellent stability. A giant ME voltage coefficient (>1200 mV/cm Oe) at zero bias was obtained in both C-N/R/N and C-N/T/N samples. The dynamic change in charge (Q) or polarization (P) of ME composite (Radiant: Precision Premier II, USA) was measured under the condition

of $H_{AC} = 1$ Oe at $f = 1$ kHz and $H_{DC} = 0$ Oe. ME charge coefficient $\alpha_{ME,Q}$ can be written as

$$\alpha_{ME,Q} = \frac{dE}{dH} = \frac{dQ}{dH_{AC}} \times \frac{1}{Ct} = \frac{dP}{dH_{AC}} \times \frac{A}{Ct} \tag{6.29}$$

where C, A, and t are the capacitance, area, and thickness of the piezoelectric layer, respectively. As shown in Figure 6.19(d), large ME charge coefficients $\alpha_{ME,Q}$ under zero-DC bias are observed, which further confirms the presence of a strong ME effect under zero bias. The time delay of $\alpha_{ME,Q}$ related to H_{AC} was attributed to the interface between the magnetostrictive and piezoelectric layer. Compared to the ME coefficient of 30 mV/cm Oe obtained for NKNLS-NZF/Ni/NKNLS-NZF trilayer laminate (40×), ~100 mV/cm Oe was obtained for Ni-PZN-PZT bilayer laminate (12×), and ~400 mV/cm Oe was obtained for functionally graded Ni-NZFO-PZT laminate composites (3×) at zero bias. Recently, a slightly larger zero-bias ME coefficient of 1.65 V/cm Oe at 100 Hz in a quasi-one-dimensional ME sensor was reported compared to the cofired composite (1.47 V/cm Oe) (Chen et al., 2011). However, these cofired multilayer composites based on LTCC have the advantage of integration with other circuit components, such as multilayer capacitors, resistors, inductors, and conductors to fabricate fully packaged electronic devices.

The ME voltage coefficient can be written as the following:

$$\alpha_{ME} = \frac{\partial E}{\partial H} = \underbrace{\left|\frac{\partial E}{\partial D} \times \frac{\partial D}{\partial T} \times \frac{\partial T}{\partial H}\right|}_{\text{P-layer}} \times \underbrace{\left|\frac{\partial S}{\partial H}\right|}_{\text{M-layer}} = \left|\frac{d}{\varepsilon \times s}\right| \times q \tag{6.30}$$

where E is the output electric field, H is the applied magnetic field, S is the mechanical strain, T is the mechanical stress, D is the electric displacement, d is the piezoelectric constant, ε is the dielectric constant, s is the elastic compliance of the piezoelectric layer (P-layer), and q is the piezomagnetic coefficient of the magnetostriction layer (M-layer). Thus, the giant ME response of cofired composite and self-biased hysteretic behavior was explained by taking into account the piezoelectric and magnetostrictive characteristics separately. Since the parameters d, ε, and s of piezoelectric materials were independent of applied magnetic field (H), the self-bias should be related to the magnetostrictive materials. Figure 6.20(a) shows the magnetization (M) of NCZF as a function of the magnetic field in the longitudinal direction by using a vibrating sample magnetometer (VSM). The $M-H$ loop of NCZF shows hysteresis. The ME behavior can be correlated with magnetostriction (λ) and magnetization (M) as (Cahill, Watson, & Pohl, 1992)

$$\varphi \sim \frac{3\lambda\sigma}{(K + 2\pi M^2)} \quad \text{or} \quad \lambda \propto M^2 \tag{6.31}$$

where φ is the angle of magnetic moments and K and σ are the anisotropy constant and stress, respectively. M^2-H and $\partial M^2/\partial H-H$ curves were used to predict the nature of

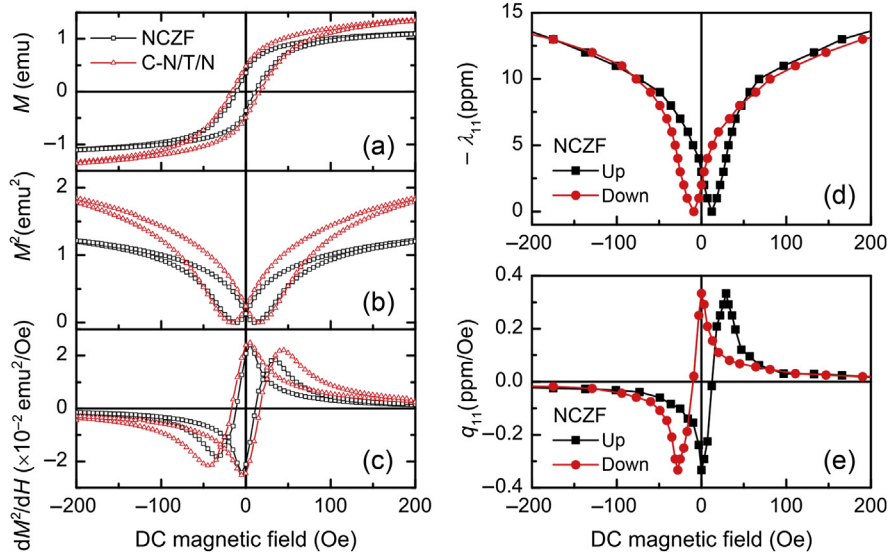

Figure 6.20 (a) Magnetization−magnetic field (M−H) loops, (b) square of magnetization as a function of magnetic field, and (c) differential of square magnetization−magnetic field [(dM^2/dH)−H] plot for pure NCZF (not cofired) and C-N/T/N structure. DC magnetic field (H_{DC}) dependence of (d) the magnetostriction (λ) and (e) piezomagnetic coefficients (q) of NCZF (not cofired).
Applied Physics Letters, *102*, 052907 (2013).

the magnetostriction coefficient (λ) and piezomagnetic coefficient ($q = d\lambda/dH$). To experimentally confirm the variation of q as a function of H_{DC}, the in-plane magnetostriction coefficient (λ_{11}) was measured in parallel to applied H_{DC} by the strain gauge method. The magnetostriction (λ) showed asymmetry and displayed "butterfly"-like characteristics (Figure 6.20(d)), and the in-plane piezomagnetic coefficient ($q_{ij} = d\lambda_{ij}/dH$) shows similar behavior as $\partial M^2/\partial H$ and $\alpha_{ME,Q}$−H. Therefore, the self-bias effect was mainly related to the hysteretic response of the ferrite layer.

Table 6.8 lists the dielectric and ME properties of cofired composites. The following conclusions can be drawn from these data: (1) the maximum α_E of NCZF/R-PMN-PT/NCZF was two to three times higher in magnitude (827 mV/cm Oe) compared to epoxy-bonded Metglas/PMN-PT/Metglas; (2) a 63% increase in the magnitude of α_E (1346 mV/cm Oe) was obtained via texturing; (3) textured composites exhibited low loss due to "engineered domain configuration"; (4) the dielectric constant of the textured sample was suppressed due to the introduction of low-permittivity BT template crystals; and (5) cofired textured composites exhibited large α_E under zero bias (1214 mV/cm Oe). Besides the increase in piezoelectric response, lower losses in the textured sample also play an important role in enhancing α_E. This was understood by taking into account the modified piezoelectric voltage coefficient (g_{31}) given as Eqn (6.6).

Table 6.8 Dielectric and magnetoelectric properties of cofired layered ME composites (1 kHz)

Sample	Electrode	ε_r	tan δ	dE/dH (max) (mV/cm Oe)	dE/dH (zero bias) (mV/cm Oe)
C-N/R/N	Cofired	1336	1.1%	827	510
C-N/T/N	Cofired	1135	0.7%	1346	1214

Applied Physics Letters, *102*, 052907 (2013).

In conclusion, NCZF/PMN-PT/NCZF layered composites with Ag inner electrodes were successfully cofired at low temperature (930 °C). The cofired NCZF/textured PMN-PT/NCZF layered composites exhibited a 5× increase in α_E compared to Metglas/PMN-PT/Metglas laminates. Further, these composites exhibited a giant self-bias phenomenon, which was associated with hysteresis of NCZF magnetostrictive materials. These cost-effective composites with excellent ME properties open the possibility of mass production of numerous ME applications.

6.5.2 3D printing and deposition

Figure 6.21(a) shows a schematic of the aerosol jet process. In this process, the ink was first aerosolized in the instrument's atomizer. After that, nitrogen gas carried the aerosols to the deposition nozzle, where the sheath gas (a secondary nitrogen stream) focuses the material into fine lines and draws the specific features. Structures for different capacitors and sensors were drawn using CAD software, which was then converted into a readable tool path. Prior to deposition, silicon substrates were ultrasonically cleaned in a beaker with acetone and ethanol for 5 min respectively. After cleaning the substrates, silver dispersion ink (Cabot) was printed to form square electrodes through a 150-μm-diameter opening tip at a deposition rate of 5 mm/s. The deposition rate below this speed resulted in overwetting of the substrate and did not provide a smooth layer. The substrate temperature was maintained at 60 °C during electrode deposition. The silver (Ag) electrode layer was found to have an average thickness of 1 μm. After the deposition, the Ag film was heated to a temperature of ∼200 °C to eliminate the solvents and organic additives from the ink. Figure 6.21(b) shows the schematic of the process for printing multilayer structures. There are two possibilities to design the MLCC structure: one utilizes vias to connect the electrode and ceramic layers, while the other is based on using the side wall. Both these possibilities are practical, as can be seen in the micrographs of Figure 6.21(c) that demonstrate that complex structures can be printed using an aerosol process. These Ag gear and hexagonal wall structures clearly show that the feature size for both vias and vertical wall can be in the range required to fabricate the MLCC structure shown in Figure 6.21(b). Figure 6.21(d) shows the printed structure before and after SLS. This figure also shows the effect of rapid sintering rate, which leads to delamination.

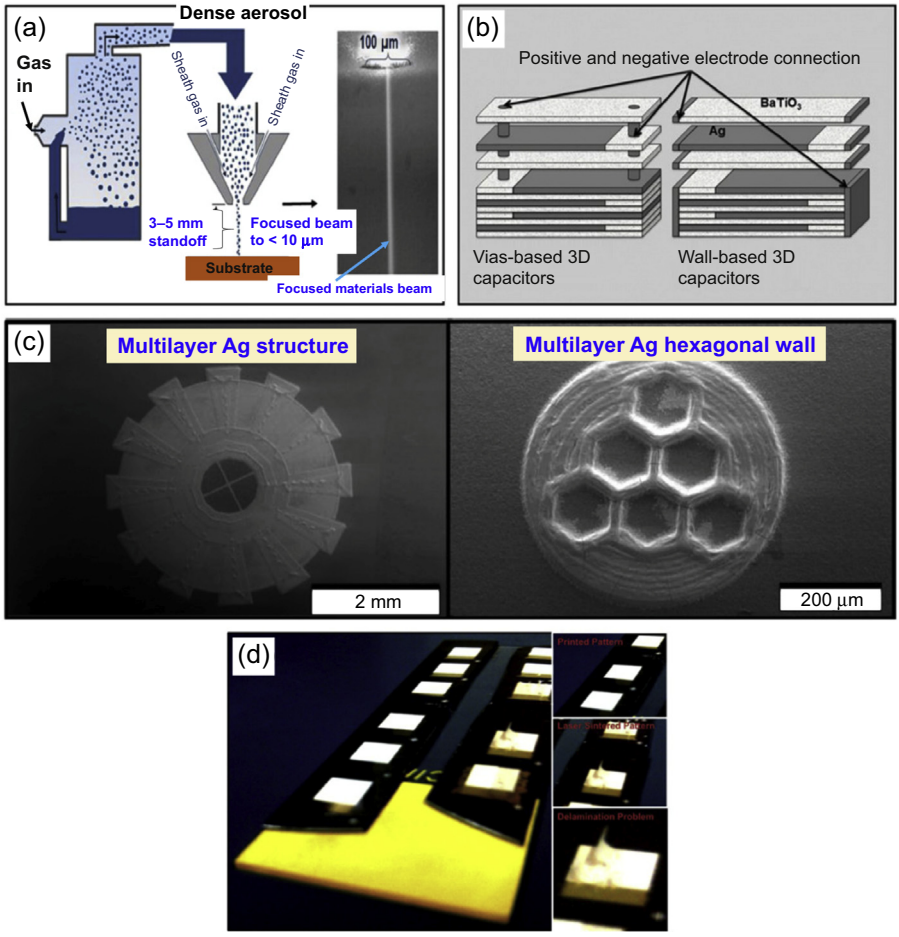

Figure 6.21 (a) Schematic of the aerosol jet process starting at the atomizer and finishing at the substrate. (b) Diagram of two types of multilayer structures under investigation: vias and wall-based 3D capacitors. (c) Multilayer 3D silver structures printed for wall-based capacitors technique. (d) Printed BTO layers before and after SLS: delaminating material can be observed during and after the sintering process.
Materials Letters, *65*, 1302−1307 (2011).

Strong ME coupling requires (1) large interphase elastic interactions, mediated via high interfacial areas, (2) a high effective permittivity, and (3) a high effective permeability. Recently, we have successfully implemented an aerosol deposition (AD) process to fabricate ME composite thick films, and we demonstrated one of the highest ME coefficients reported in the literature (Park, Ryu et al., 2009). Highly dense 3−2 nanocomposite thick films of $Pb(Zr,Ti)O_3$−$Pb(Zn,Nb)O_3$ (PZT-PZN) and $(Ni,Cu,Zn)Fe_2O_4$ (NCZF) with thickness >10 µm were synthesized on platinized

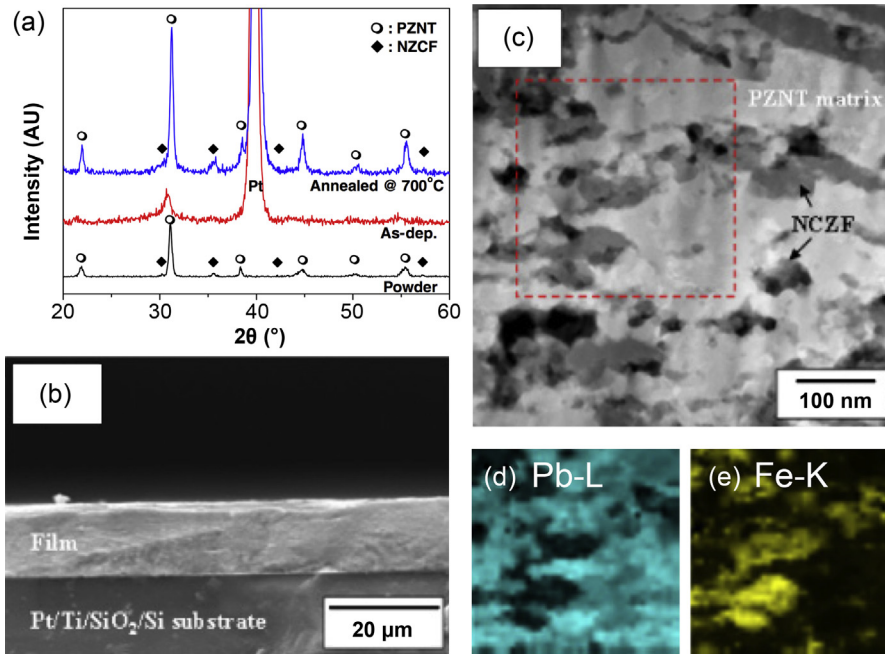

Figure 6.22 (a) X-ray diffraction patterns of powders and composite thick films, (b) cross-sectional SEM image, (c) STEM, and (d) EDX mapping of Pb, (e) EDX mapping of Fe. Japanese Journal of Applied Physics, *48*, 080204 (2009).

silicon substrate at room temperature. High ME response was associated with reduced clamping effect, effective poling of piezoelectric matrix, and enhanced elastic coupling due to laminate structure. The XRD and TEM microstructure is shown in Figure 6.22 along with elemental mapping, which illustrates well-defined 3−2 connectivity. In addition to improved ME characteristics, the deposition rate of ME films was exceptionally higher (over 1 μm/min) than any other conventional thin film process (Priya et al., 2009).

6.6 Recent advances in lead-free piezoelectric and magnetoelectric composites

Recently, investigations have focused on developing lead-free ME materials. $BaTiO_3$−$CoFeO_4$ lead-free composites were the first ones investigated by Boomgaard et al. in 1978 and were found to exhibit ME coefficients of 130 mV/cm Oe. Since that time, few studies have been conducted on lead-free ME composites, as shown in Table 6.9, mainly because of the poor piezoelectric performance of lead-free materials. This problem still remains, but the emphasis on developing lead-free ME composites has increased due to environmental concerns.

Table 6.9 List of lead-free magnetoelectric composites

Year	Compositions	Type	DC bias/frequency	d*E*/d*H* (mV/cm Oe)	References
2005	$BaTiO_3$−$CoFe_2O_4$	Particulate	270 Oe/160 kHz	2540	Ren et al. (2005)
2006	$0.7Sr_{0.5}Ba_{0.5}Nb_2O_6$−$0.3Ni_{0.8}Zn_{0.2}Fe_2O_4$	Particulate	1−3 kOe/100 kHz	26.6	Li, Chen, Lin, and Tang (2006)
2009	$BaTiO_3$−$CoFe_2O_4$	Particulate	2000 Oe/20 kHz	17.04	Nie, Xu, Yang, and Cheng (2009)
2009	$(K_{0.5}Na_{0.5})NbO_3$−$LiSbO_3$−$CoFe_2O_4$	Particulate	2200 Oe/1 kHz	15	Zhou et al. (2009)
2010	$0.75BaZr_{0.08}Ti_{0.92}O_3$−$0.25Co_{1.2-y}Mn_yFe_{1.8}O_4$ ($y = 0$−0.4)	Particulate	1500 Oe/1 kHz	2.5	Kambale, Shaikh, Bhosale, Rajpure, and Kolekar (2010)
2006	$BaTiO_3$/$(Ni_{0.8}Zn_{0.2})Fe_2O_4$	Laminate	1000 Oe/1 kHz	152	Islam and Priya (2006)
2010	$0.885Bi_{0.5}Na_{0.5}TiO_3$−0.05 $Bi_{0.5}K_{0.5}TiO_3$−0.015 $Bi_{0.5}Li_{0.5}TiO_3$−0.05$BaTiO_3$/Terfenol-D	Laminate	600 Oe/131 kHz	2500	Lo, Choy, Or, and Chan (2010)
2010	Mn-doped $Na_{0.5}Bi_{0.5}TiO_3$−$BaTiO_3$ single crystal/Terfenol-D	Laminate	400 Oe/1 kHz	1320	Zhang et al. (2006)

6.6.1 Sintered lead-free piezoelectric–ferrite composites

Lead-free piezoelectric materials considered for ME laminates can be classified into three material groups (ABO_3): (1) $K_{0.5}Na_{0.5}NbO_3$ (KNN), (2) $Na_{0.5}Bi_{0.5}TiO_3$ (NBT), and (3) $BaTiO_3$ (BT). Table 6.10 shows piezoelectric and electromechanical properties for compositions based on KNN, NBT, and BT. Among all the lead-free-based compositions, KNN-based ceramic has the highest piezoelectric response.

$0.948K_{0.5}Na_{0.5}NbO_3–0.052LiSbO_3$ (KNNLS) and $Ni_{0.8}Zn_{0.2}Fe_2O_4$ (NZF) ceramics were synthesized by the mixed oxide sintering method. The KNNLS powders were found to have a grain size <1 μm and exhibited perovskite structure as shown in Figure 6.23(a) and (b). The NZF powders had a grain size range of <300 nm with spinel structure, as shown in Figure 6.23(c) and (d). Figure 6.24(a–d) shows the XRD patterns for $(1-x)$KNNLS–xNZF ($x = 0.1$, 0.2, 0.3, and 0.4) composites sintered at varying temperatures (1040, 1050, 1060, and 1070 °C). The patterns clearly reflect that both phases of KNNLS and NZF stabilized, respectively, in perovskite and spinel structures without any trace of secondary phase in the composites. As the mole fraction of NZF was increased, the intensity of spinel peaks increased while the intensity of perovskite peaks decreased.

Variations of longitudinal piezoelectric strain constant (d_{33}) and radial mode electromechanical coupling factor (k_p) with composition for all composites are shown in Figure 6.25(a) and (b). The magnitude of both d_{33} and k_p decreased with increasing NZF concentration, and was found to maximize at sintering temperatures of both 1050 °C and 1060 °C regardless of x values. It can be noticed that there is a critical sintering temperature of 1070 °C, above which the electromechanical properties decreased. Clearly 0.9KNNLS–0.1NZF composites exhibit variation of piezoelectric properties with sintering temperature. The changes occurring in other KNNLS–NZF composites are relatively small, and this could be associated with varying factors, including poling percentage, grain size, resistivity, and space charge. Figure 6.25(c) and (d) show that the magnitude of dielectric constant ($\varepsilon_r/\varepsilon_o$) decreased with increasing NZF concentration and the magnitude of loss factor ($\tan\delta$) was found to minimize at the sintering temperatures of 1050 °C and 1060 °C. The low $\tan\delta$ at the optimum sintering points resulted from the composite structures possessing a high relative density of >95%. As the composites were sintered at 1040 °C and 1070 °C, the relative density was found to decrease below 95%, reflecting high porosity. Further, it is found in Figure 6.25 that the composites with high NZF concentration of $x = 0.4$ are still below the percolation threshold, as the dielectric and piezoelectric properties did not exhibit any significant drop.

Figure 6.26 (a–d) shows the magnetic hysteresis loops for the NZF particles and $(1-x)$KNNLS–xNZF ($x = 0.1$, 0.2, 0.3, and 0.4) composites measured by VSM at room temperature. The crushed NZF particles were found to exhibit a saturation magnetization (M_s) of 63.90 emu/g as shown in Figure 6.26(a) and (b), which decreased for the sintered KNNLS–NZF composites. The magnitude of M_s for the composites was found to increase from 6.58 to 23.48 emu/g with increasing NZF concentration, as shown in Figure 6.26(c) and (d). The remanent magnetization (M_r) for NZF particles was found to be 0.29 emu/g, and the magnitude of M_r for the composites

Table 6.10 List of lead-free piezoelectric materials

Year	Compositions	d_{33} (pC/N)	k_p	T_c (°C)	T_{O-T}/T_d (°C)	References
1959	$(K_{0.5}Na_{0.5})NbO_3$	80	0.35	420	195	Egerton and Dillon (1959)
2005	$(K_{0.465}Na_{0.465}Li_{0.07})NbO_3$	240	0.45	460	~20	Hollenstein, Davis, Damjanovic, and Setter (2005)
2006	$(K_{0.44}Na_{0.52}Li_{0.04})(Nb_{0.84}Ta_{0.1}Sb_{0.06})O_3$	410	0.61	253	25	Lang, Zhu, and Cross (2006)
2006	$0.95(K_{0.5}Na_{0.5})NbO_3-0.05SrTiO_3$	200	0.37	277	27	Wang et al. (2006)
2005	$0.95(K_{0.5}Na_{0.5})NbO_3-0.05LiTaO_3$	200	0.36	430	55	Guo, Kakimoto, and Ohsato (2005)
2004	$0.94(K_{0.5}Na_{0.5})NbO_3-0.06LiNbO_3$	235	0.42	460	70	Guo, Kakimoto, and Ohsato (2004)
2006	$0.95(K_{0.5}Na_{0.5})NbO_3-0.05LiSbO_3$	283	0.5	392	45	Zang et al. (2006)
2006	$0.7Bi_{0.5}Na_{0.5}TiO_3-0.2Bi_{0.5}K_{0.5}TiO_3-0.1Bi_{0.5}Li_{0.5}TiO_3$	216	0.401	350	160	Yuan, Zhang, Zhou, and Liu (2006)
2007	$x(Na_{0.5}Bi_{0.5})TiO_3-y(K_{0.5}Bi_{0.5})TiO_3-zBaTiO_3$ ($x+y+z=1$; $y{:}z=2{:}1$)	145	0.162	302	224	Zhang, Shrout, Nagata, Hiruma, and Takenaka (2007)
2006	$0.5Na_{0.5}Bi_{0.5}TiO_3-0.5K_{0.5}Bi_{0.5}TiO_3$	150	0.22	320	210	Zhao, Li, Ding, Wang, and Yin (2006)
1958	$BaTiO_3$	190	0.36	115	0	Jaffe (1958)
1957	$0.95BaTiO_3-0.05CaTiO_3$—Co	150	0.31	105	−45	Schofield and Brown (1957)

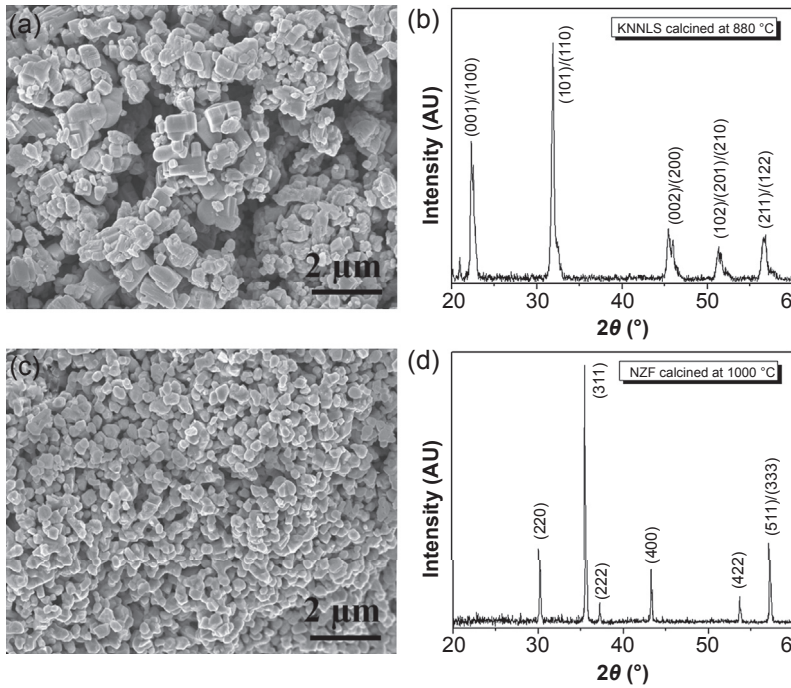

Figure 6.23 (a) SEM image and (b) X-ray diffraction (XRD) patterns of KNNLS calcined at 880 °C. (c) SEM image and (d) XRD patterns of NZF calcined at 1000 °C.
Journal of the American Ceramic Society, *94*(11), 3889−3899 (2011).

increased from 0.13 to 0.77 emu/g with increasing NZF concentration. The magnitude of coercive field (H_c) for KNNLS−NZF composites was found to be constant regardless of the change in composition.

In order to verify the coupling between magnetic polarization and mechanical strain for the $(1-x)$KNNLS−xNZF ($x = 0.1$, 0.2, 0.3, and 0.4) composites, magnetostriction (λ) and piezomagnetic coefficients (q) were determined in the range of 0−1000 Oe as shown in Figure 6.27(a−d). The parameters λ_{11} and λ_{12} correspond to in-plane parallel magnetostriction and in-plane perpendicular magnetostriction to applied magnetic field (H). With increasing NZF concentration, the magnitude of λ_{11} and λ_{12} was found to increase. The magnitude of λ_{11} and λ_{12} for composition $x = 0.4$ was found to be -8 ppm and 3 ppm. The in-plane piezomagnetic coefficients q_{11} and q_{12} were calculated by differentiating λ_{11} and λ_{12} with respect to magnetic field. As NZF concentration increases, the magnitude of q_{11} and q_{12} was found to increase and the peak shifted to low H. The position of the peak in the piezomagnetic constant is an important characteristic in the design of high-sensitivity magnetic field sensors as it corresponds with the peak observed in the ME coefficient.

Figure 6.28(a) and (b) show the variation of ME coefficient (α_E) and optimum DC bias (H_{bias}) for the $(1-x)$KNNLS−xNZF ($x = 0.1$, 0.2, 0.3, and 0.4) composites

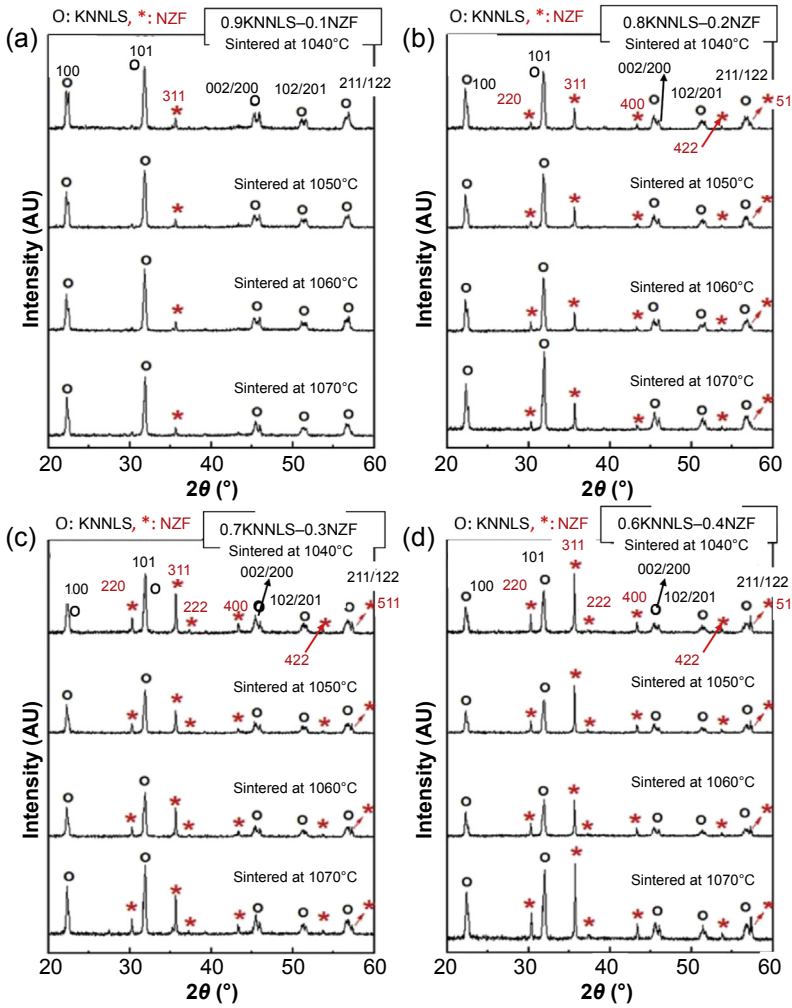

Figure 6.24 X-ray diffraction patterns for $(1 - x)$KNNLS$-x$NZF composites. (a) $x = 0.1$, (b) $x = 0.2$, (c) $x = 0.3$, and (d) $x = 0.4$.
Journal of the American Ceramic Society, *94*(11), 3889–3899 (2011).

with sintering temperatures, measured at 1 kHz under $H_{AC} = 1$ Oe. With increasing NZF concentration, the magnitude of α_E was found to increase to 20.14 mV/cm Oe under $H_{bias} = 380$ Oe at $x = 0.3$ and then slightly drop to 18.17 mV/cm Oe under $H_{bias} = 330$ Oe at $x = 0.4$. For all the compositions, the composites sintered at 1050 and 1060 °C were found to exhibit maximum α_E due to their optimized piezoelectric and dielectric values, as shown in Figure 6.25. The magnitude of optimum H_{bias} decreased from 545 to 326 Oe with increasing NZF concentration. The reason for shift in H_{bias} is related to the difference in magnetic susceptibilities of the composites and variation in peak piezomagnetic coefficient, as shown in Figure 6.27.

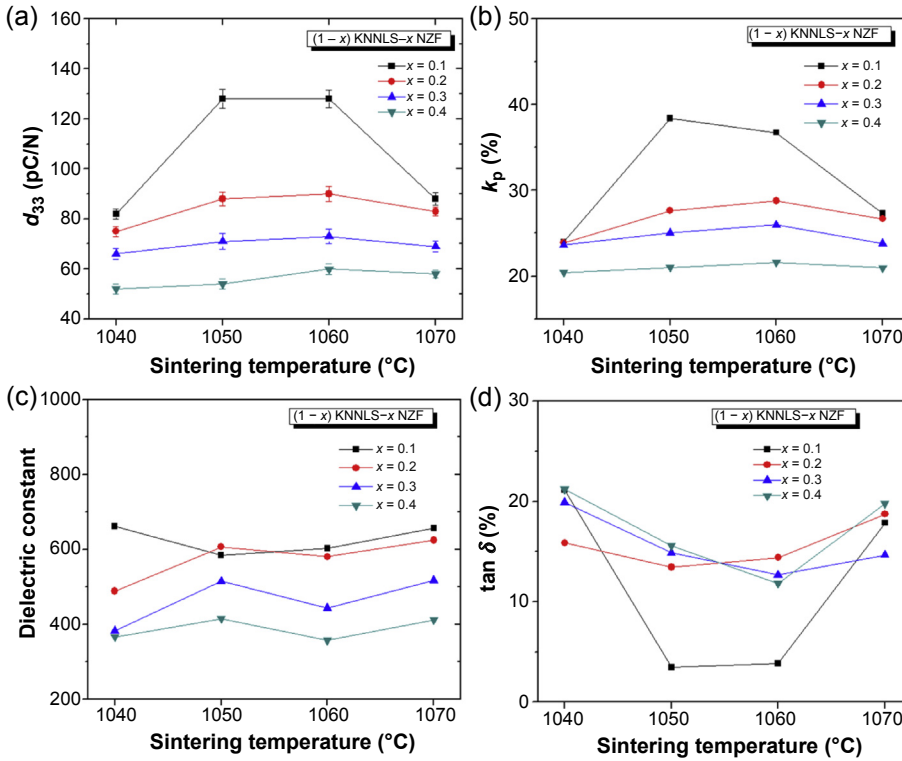

Figure 6.25 Piezoelectric and dielectric properties for $(1 - x)$KNNLS−xNZF composites. (a) Longitudinal piezoelectric constant, (b) radial mode coupling factor, (c) dielectric constant, and (d) tangent loss factor.
Journal of the American Ceramic Society, *94*(11), 3889−3899 (2011).

In order to form the island−matrix composite, the following considerations were taken into account: (1) the matrix had smaller particle size than that of the island to achieve control of the surface area, and (2) sintering temperature of the matrix and the island was quite different to eliminate the elemental diffusion. Bordia et al. have described the sintering phenomenon with rigid inclusions in terms of transient stresses and strain rates (Bordia & Scherer, 1988). The analysis shows that the volume fraction of the inclusion is an important parameter in determining the sintering of the composite. The KNNLS matrix normally has residual porosity due to the cubical shape of grains, but the KNNLS−NZF composites were found to exhibit a high relative density of >95%. This high density can be associated with NZF, which provides an interface for nucleation and growth. The densification rate of the composite is expressed as

$$\frac{1}{\rho_m}\frac{d\rho_m}{dt} = \frac{1}{\rho_c}\frac{d\rho_c}{dt}\left(\frac{\rho_{co}}{\rho_{co} - v_{io}\rho_c}\right) \tag{6.32}$$

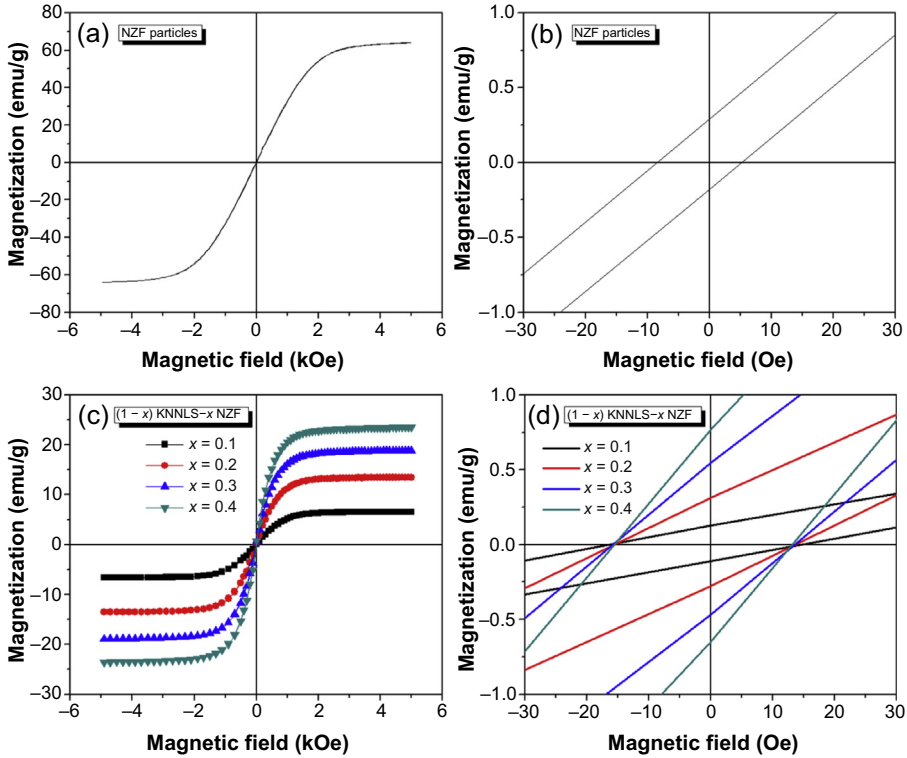

Figure 6.26 $M-H$ curves for NZF particles and $(1-x)$KNNLS$-x$NZF composites: (a) magnetization as a function of magnetic field for NZF particles, (b) amplified curve in the low magnetic field region shown in (a), (c) magnetization as a function of magnetic field for $(1-x)$KNNLS$-x$NZF composites, and (d) amplified curve in the low magnetic field region shown in (c).
Journal of the American Ceramic Society, *94*(11), 3889−3899 (2011).

where ρ_c and ρ_m are the relative densities of the composite and the matrix, and ρ_{co} and v_{io} are initial values for density and volume fraction of inclusion. Three stages of sintering were identified in these systems. The first stage corresponds to rearrangement of a random-shape particle to form a stack of plate-type particles. The second stage is characterized by rapid grain growth promoted by liquid phase. The liquid phase formation was found to be related to Na_2O volatilization. In the final stage of sintering, densification slows and microstructural coarsening becomes the dominant process. The fraction control of the liquid phase was an important factor to obtain a dense and uniform microstructure. Muffling was used to reduce the loss of the alkali ions during high-temperature sintering, and sintering temperature and time was used to control the volume fraction of the liquid phase.

Figure 6.29(a−d) shows the SEM micrographs for 3-KNNLS−NZF composites with island−matrix microstructure sintered at 1060 °C. All the compositions exhibited dense

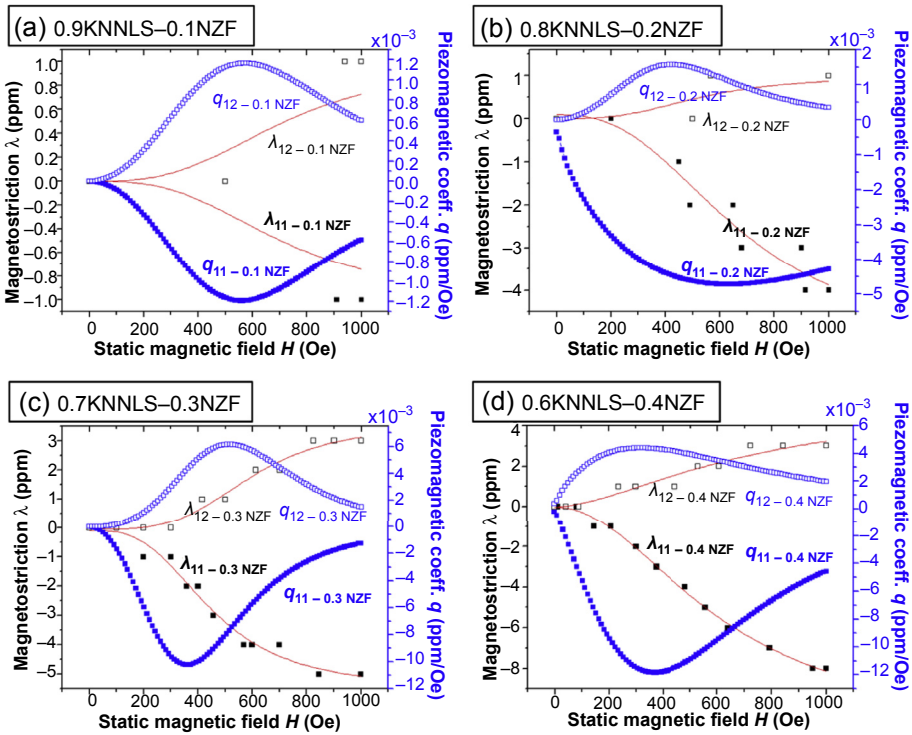

Figure 6.27 Magnetostrictions and piezomagnetic coefficients for $(1 - x)$KNNLS−xNZF composites. (a) $x = 0.1$, (b) $x = 0.2$, (c) $x = 0.3$, and (d) $x = 0.4$.
Journal of the American Ceramic Society, *94*(11), 3889−3899 (2011).

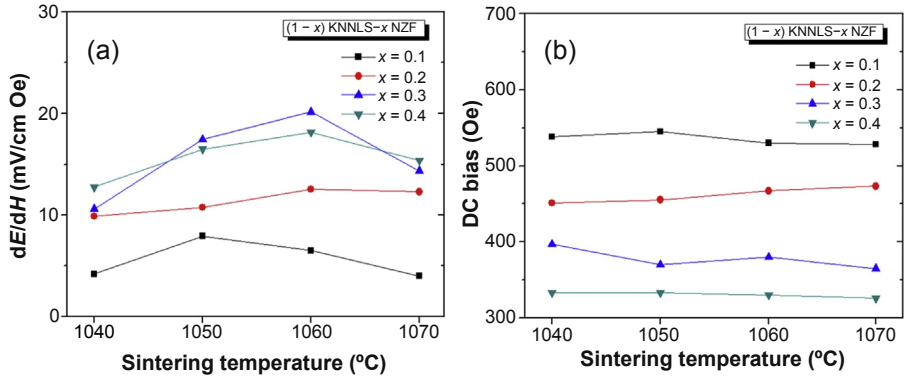

Figure 6.28 Variation of (a) ME coefficient and (b) H_{bias} for $(1 - x)$KNNLS−xNZF composites with $x = 0.1$, 0.2, 0.3, and 0.4 as a function of sintering temperature.
Journal of the American Ceramic Society, *94*(11), 3889−3899 (2011).

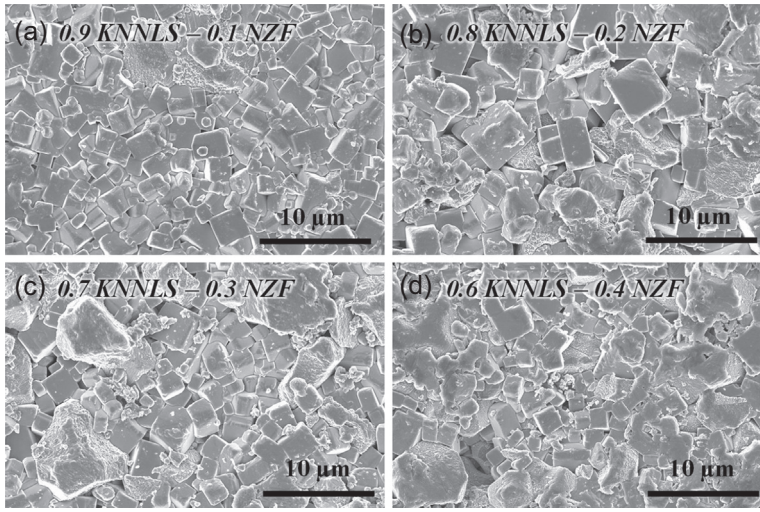

Figure 6.29 SEM micrographs for $(1 - x)$KNNLS−xNZF composites sintered at 1060 °C. (a) $x = 0.1$, (b) $x = 0.2$, (c) $x = 0.3$, and (d) $x = 0.4$.
Journal of the American Ceramic Society, *94*(11), 3889−3899 (2011).

microstructure with high density, which illustrates that growth occurred at the NZF interface leading to bridging of the residual porosity. The NZF islands were randomly dispersed in the KNNLS matrix, which is highly beneficial for the poling of the piezoelectric matrix. Two different grain structures can be noticed in the microstructure, cubical large grains corresponding to matrix and random-shaped small grains corresponding to island. There was no significant change observed in the size of the islands during sintering. From this microstructure, the connectivity of composites can be considered to be 3−0.

The EDS elemental mapping images shown in Figure 6.30(a−h) further confirm this conclusion. In this figure, the element Nb (white color in Figure 6.30(a−d)) represents the KNNLS matrix and Fe (white color in Figure 6.30(e−h)) represents the NZF islands. It can be seen that the NZF islands were isolated from each other for the composition $x = 0.1$−0.3 but the connectivity pattern changes at a high mole fraction of $x = 0.4$.

6.6.2 Enhanced magnetoelectric response in ME composites with textured lead-free piezoelectric $Na_{0.5}Bi_{0.5}TiO_3$−$BaTiO_3$ ceramics

The ME response of (001)-textured and randomly oriented NBTBT in Metglas/NBTBT/Metglas configuration was quantified. At 1 kHz, an ME coefficient of 222 mV/cm Oe was obtained, which was enhanced by ∼3× compared with laminates with random NBTBT, as shown in Figure 6.31.

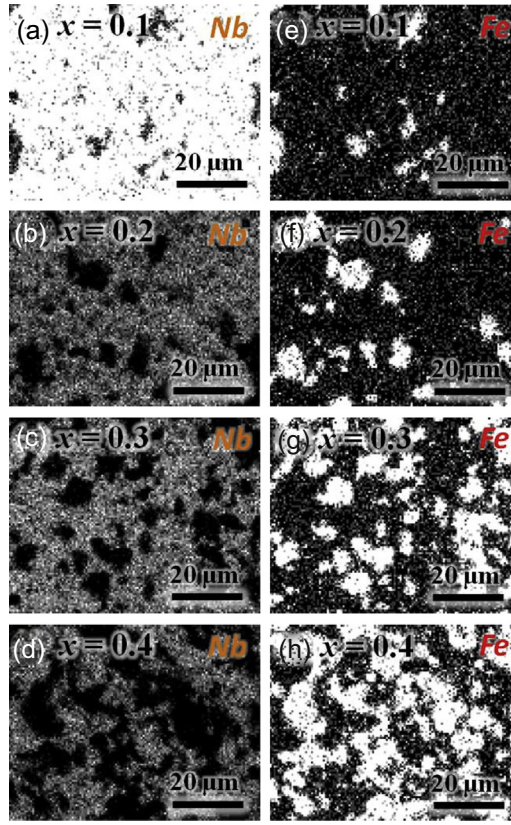

Figure 6.30 EDS elemental mapping images for $(1 - x)$KNNLS−xNZF composites sintered at 1060 °C. (a−d) SEM images for $x = 0.1$−0.4, (e−h) Nb mapping for $x = 0.1$−0.4, and (i−l) Fe mapping for $x = 0.1$−0.4.
Journal of the American Ceramic Society, *94*(11), 3889−3899 (2011).

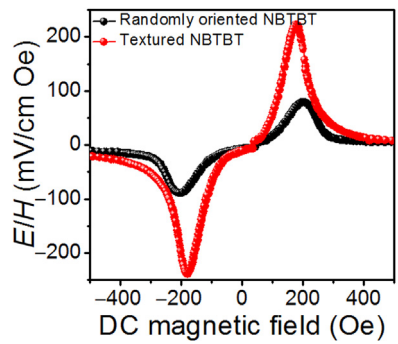

Figure 6.31 ME voltage coefficients for trilayer laminates of Metglas/NBTBT/Metglas for randomly oriented and textured NBTBT systems.
Journal of Materials Chemistry C, *1*, 2102−2111 (2013).

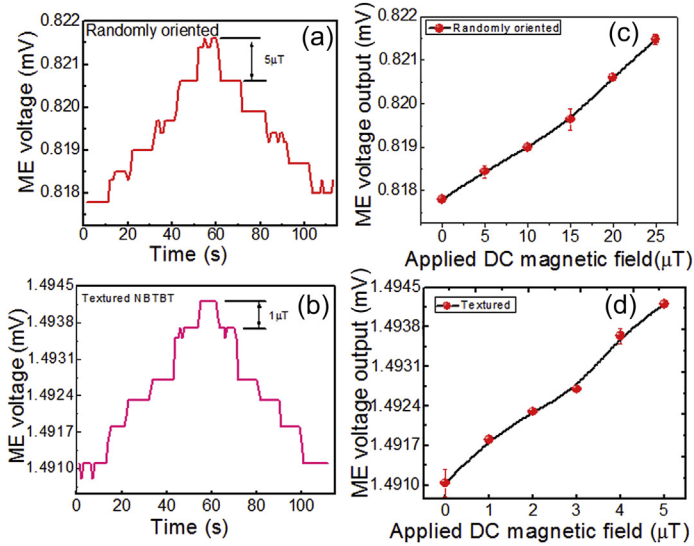

Figure 6.32 (a) Sensitivity limit for DC magnetic field for randomly oriented NBTBT, (b) sensitivity limit for DC magnetic field for textured NBTBT, (c) ME voltage output versus applied DC magnetic field for randomly oriented NBTBT, and (d) ME voltage output versus applied DC magnetic field for textured NBTBT.

Further, we measured the magnetic field sensitivity limit of the $L-T$ mode ME laminate to small DC magnetic field variation under $H_{AC} = 1$ Oe at 1 kHz. The voltage induced by step-like changes under small DC bias was measured by using the time domain capture mode (Figure 6.32(a) and (b)). These results indicated rapid and stable response in the induced voltage across the piezoelectric layers in response to ΔH_{DC}. It was observed that ME laminates with textured NBTBT were able to correspond to an applied small DC magnetic field of 1 μT, compared with 5 μT for random-based ME laminate, which could be considered extremely good performance for a trilayer structure in such small size. Previous studies on Metglas/Terfenol-D/PMN-PZT single crystal/Terfenol-D/Metglas laminate structure showed that at 1 kHz frequency, the sensor was able to deterministically measure step changes of 0.5 μT. Thus, compared with lead-based ME composite, our textured lead-free ME composite shows similar sensitivity.

6.7 Conclusion

Multiferroic magnetoelectrics have recently attracted ever-increasing interest due to potential applications in novel multifunctional devices, such as sensors, transducers, memories, and spintronics. Unfortunately, all the known single-phase materials suffer from the drawback that the ME effect is considerably weak even at low temperatures. There are two approaches that are considered to be promising for room temperature

multiferroic magnetoelectrics. One is based on solid solutions exhibiting MPB or PPB, and the other is based on composite structure that utilizes product property.

In this chapter, we first briefly reported the progress on ME solid solutions. $BiFeO_3$−$BaTiO_3$ (BTO) solid solutions show the presence of MPB ($BiFeO_3$ mole fraction from 0.750 to 0.775). The enhanced magnetic properties were attributed to active spin modulation of ordered Fe−O−Fe. These results are highly exciting toward the realization of a room temperature single-phase multiferroic ME material.

We further presented recent progress on ME composite. To achieve high ME charge and voltage coefficients, a piezoelectric material with high d and g is required. The high-performance, cost-effective textured piezoelectric materials were developed with a piezoelectric response similar to their single-crystal counterparts. Due to high d, k, and g in textured ceramic, the 3.4 times improvement of ME voltage coefficient was achieved. Besides high piezoelectric properties of textured ceramics, functionally graded piezoelectric composites were presented, which exhibit unique overall functional response. These graded ferroelectric/piezoelectric composites, if used as piezoelectric elements in an ME composite, are expected to exhibit interesting phenomena.

Further, the strong coupling factor is an important factor to achieve large ME response. Here we presented two new processes (cofiring and 3D printing/deposition) for fabricating ME composites, which offer large interphase elastic interactions. Lastly, due to environmental concerns, recent developments in the area of lead-free piezoelectric and ME composites were discussed.

Acknowledgments

Y.Y. acknowledges the financial support from the Office of Basic Energy Science, Department of Energy. S.P. would like to acknowledge the support from the Office of Naval Research through the Center for Energy Harvesting Materials and Systems (CEHMS).

References

Ahn, C.-W., Maurya, D., Park, C.-S., Nahm, S., & Priya, S. (2009). *Journal of Applied Physics, 105*, 114108.

Babu, S. N., Srinivas, K., Suryanarayana, S. V., & Bhimasankaram, T. (2008). *Journal of Physics D: Applied Physics, 41*(1), 165407.

Boomgaard, J. V. D., & Born, R. A. J. (1978). *Journal of Materials Science, 13*, 1538.

Boomgaard, J. V. D., Terrell, D. R., Born, R. A. J., & Giller, H. F. J. I. (1974). *Journal of Materials Science, 9*, 1705.

Bordia, R. K., & Scherer, G. W. (1988). *Acta Metallurgica, 36*, 2411.

Boris, A. P. L., & Strukov, A. (1998). *Ferroelectric phenomena in crystals*. Springer.

Cahill, D. G., Watson, S. K., & Pohl, R. O. (1992). *Physical Review B, 46*, 6131.

Cao, W., & Randall, C. A. (1996). *Journal of Physics and Chemistry of Solids, 57*, 1499.

Chen, Y. J., Gillette, S. M., Fitchorov, T., Jiang, L. P., Hao, H. B., Li, J. H., et al. (2011). *Applied Physics Letters, 99*, 042505.

Chew, K.-H., Ong, L.-H., Osman, J., & Tilley, D. R. (2000). *Applied Physics Letters, 77*, 2755.

Cho, K. H., Park, C. S., & Priya, S. (2010). *Applied Physics Letters, 97*, 182902.
Cohen, R. E. (2000). *Journal of Physics and Chemistry of Solids, 61*, 139.
Dai, Y. R., Bao, P., Zhu, J. S., Wan, J. G., Shen, H. M., & Liu, J. M. (2004). *Journal of Applied Physics, 96*, 5687.
Dong, S. X., Cheng, J. R., Li, J. F., & Viehland, D. (2003). *Applied Physics Letters, 83*, 4812.
Dong, S. X., Li, J. F., & Viehland, D. (2003). *IEEE Transactions on Ultrasonics, Ferroelectrics, and Frequency Control, 50*, 1253.
Dong, S. X., Li, J. F., & Viehland, D. (2004a). *IEEE Transactions on Ultrasonics, Ferroelectrics, and Frequency Control, 51*, 794.
Dong, S. X., Li, J. F., & Viehland, D. (2004b). *Journal of Applied Physics, 96*, 3382.
Dong, S. X., Li, J. F., Viehland, D., Cheng, J., & Cross, L. E. (2004). *Applied Physics Letters, 85*, 3534.
Dong, X. W., Wang, B., Wang, K. F., Wan, J. G., & Liu, J. M. (2009). *Sensors and Actuators A: Physical, 153*, 64.
Dong, S., Zhai, J., Bai, F., Li, J. F., & Viehland, D. (2005). *Applied Physics Letters, 87*(6), 062502.
Dong, S. X., Zhai, J. Y., Bai, F. M., Li, J. F., Viehland, D., & Lograsso, T. A. (2005). *Journal of Applied Physics, 97*(10), 103902.
Dong, S. X., Zhai, J. Y., Li, J. F., & Viehland, D. (2006). *Applied Physics Letters, 89*(25), 252904.
Ederer, C., & Spaldin, N. A. (2004). *Nature Materials, 3*, 849.
Egerton, L., & Dillon, D. M. (1959). *Journal of the American Ceramic Society, 42*, 438.
Fang, Z., Lu, S. G., Li, F., Datta, S., Zhang, Q. M., & El Tahchi, M. (2009). *Applied Physics Letters, 95*(11), 112903.
Fiebig, M. (2005). *Journal of Physics D: Applied Physics, 38*, R123.
Fiebig, M., Lottermoser, T., Frohlich, D., Goltsev, A. V., & Pisarev, R. V. (2002). *Nature, 419*, 818.
Fischer, E., Gorodetsky, G., & Hornreich, R. M. (1972). *Solid State Communications, 10*, 1127.
Guo, Y. P., Kakimoto, K., & Ohsato, H. (2004). *Applied Physics Letters, 85*, 4121.
Guo, Y., Kakimoto, K-i., & Ohsato, H. (2005). *Materials Letters, 59*, 241.
Guo, Y. Y., Zhou, J. P., & Liu, P. (2010). *Current Applied Physics, 10*, 1092.
Hollenstein, E., Davis, M., Damjanovic, D., & Setter, N. (2005). *Applied Physics Letters, 87*(18), 182905.
Hornreich, R. M. (1969). *Solid State Communications, 7*, 1081.
Hur, N., Park, S., Sharma, P. A., Ahn, J. S., Guha, S., & Cheong, S. W. (2004). *Nature, 429*, 392.
Ishibashi, Y., & Iwata, M. (1999). *Japanese Journal of Applied Physics Part 1-Regular Papers Short Notes & Review Papers, 38*, 800.
Islam, R. A., Ni, Y., Khachaturyan, A. G., & Priya, S. (2008). *Journal of Applied Physics, 104*(4), 044103.
Islam, R. A., & Priya, S. (2006). *Applied Physics Letters, 89*(15), 152911.
Islam, R. A., & Priya, S. (2008). *Journal of Materials Science, 43*, 2072.
Islam, R. A., & Priya, S. (2009). *Journal of Materials Science, 44*, 5935.
Jaffe, H. (1958). *Journal of the American Ceramic Society, 41*, 494.
Jena, D., Alpay, S. P., & Mantese, J. V. (2008). In C. J. Wood, & Debdeep (Eds.), *Polarization effects in semiconductors* (p. 307). Springer Science+Business Media, LLC.
Kadomtseva, A. M., Zvezdin, A. K., Popov, Y. F., Pyatakov, A. P., & Vorob'ev, G. P. (2004). *Jetp Letters, 79*, 571.

Kambale, R. C., Shaikh, P. A., Bhosale, C. H., Rajpure, K. Y., & Kolekar, Y. D. (2010). *Journal of Alloys and Compounds, 489*, 310.
Kao, K. C. (2004). *Dielectric phenomena in solids*. San Diego: Elsevier Academic Press.
Ke, W. L., Zhang, N., & Guo, Y. S. (2009). *Materials Research Innovations, 13*, 15.
Kimura, T., Goto, T., Shintani, H., Ishizaka, K., Arima, T., & Tokura, Y. (2003). *Nature, 426*, 55.
Kretschmer, R., & Binder, K. (1979). *Physical Review B, 20*, 1065.
Kumar, A., Sharma, G. L., Katiyar, R. S., Pirc, R., Blinc, R., & Scott, J. F. (2009). *Journal of Physics: Condensed Matter, 21*, 382204.
Laletin, V. M., Paddubnaya, N., Srinivasan, G., De Vreugd, C. P., Bichurin, M. I., Petrov, V. M., et al. (2005). *Applied Physics Letters, 87*(22), 222507.
Laletin, U., Sreenivasulu, G., Petrov, V. M., Garg, T., Kulkarni, A. R., Venkataramani, N., et al. (2012). *Physical Review B, 85*, 104404.
Lang, S. B., Zhu, W. Y., & Cross, L. E. (2006). *Ferroelectrics, 336*, 15.
Lente, M. H., & Eiras, J. A. (2001). *Journal of Applied Physics, 89*, 5093.
Li, Y. J., Chen, X. M., Lin, Y. Q., & Tang, Y. H. (2006). *Journal of the European Ceramic Society, 26*, 2839.
Liu, G., Nan, C. W., Cai, N., & Lin, Y. H. (2004). *Journal of Applied Physics, 95*, 2660.
Lo, Y., Choy, S. H., Or, S. W., & Chan, H. L. W. (2010). *Journal of Applied Physics, 107*(9), 093907.
Lottermoser, T., Lonkai, T., Amann, U., Hohlwein, D., Ihringer, J., & Fiebig, M. (2004). *Nature, 430*, 541.
Ma, Y-q., Shen, J., & Xu, X-h. (2000). *Solid State Communications, 114*, 461.
Ma, J., Shi, Z., & Nan, C.-W. (2007). *Advanced Materials, 19*, 2571.
Mandal, S. K., Sreenivasulu, G., Petrov, V. M., & Srinivasan, G. (2011). *Physical Review B, 84*, 014432.
Merz, W. J. (1954). *Physical Review, 95*, 690.
Messing, G. L., Trolier-McKinstry, S., Sabolsky, E. M., Duran, C., Kwon, S., Brahmaroutu, B., et al. (2004). *Critical Reviews in Solid State and Materials Sciences, 29*, 45.
Miyamoto, Y., Kaysser, W. A., Rabin, B. H., Kawasaki, A., & Ford, R. G. (Eds.). (October 31, 1999). *Functionally graded materials: Design processing and applications* (Vol. 5). Norwell, MA 02061, USA: Springer.
Nan, C. W. (1993). *Progress in Materials Science, 37*, 1.
Nan, C. W., Bichurin, M. I., Dong, S. X., Viehland, D., & Srinivasan, G. (2008). *Journal of Applied Physics, 103*, 031101.
Nie, J. W., Xu, G. Y., Yang, Y., & Cheng, C. W. (2009). *Materials Chemistry and Physics, 115*, 400.
O'Dell, T. H. (1963). *Philadelphia Magazine, 8*, 411.
Ong, L.-H., Osman, J., & Tilley, D. R. (2002). *Physical Review B, 65*, 134108.
Park, C. S., Ahn, C. W., Ryu, J., Yoon, W. H., Park, D. S., Kim, H. E., et al. (2009). *Journal of Applied Physics, 105*(9), 094111.
Park, C.-S., Ryu, J., Choi, J.-J., Park, D.-S., Ahn, C.-W., & Priya, S. (2009). *Japanese Journal of Applied Physics, 48*, 080204.
Park, S. E., & Shrout, T. R. (1997). *Journal of Applied Physics, 82*, 1804.
Petrov, V. M., & Srinivasan, G. (2008). *Physical Review B, 78*, 184421.
Picinin, A., Lente, M. H., Eiras, J. A., & Rino, J. P. (2004). *Physical Review B, 69*, 064117.
Priya, S., Islam, R., Dong, S., & Viehland, D. (2007). *Journal of Electroceramics, 19*, 149.
Priya, S., Ryu, J., Park, C.-S., Oliver, J., Choi, J.-J., & Park, D.-S. (2009). *Sensors, 9*, 6362.

Ren, S. Q., Weng, L. Q., Song, S. H., Li, F., Wan, J. G., & Zeng, M. (2005). *Journal of Materials Science, 40*, 4375.

Ruette, B., Zvyagin, S., Pyatakov, A. P., Bush, A., Li, J. F., Belotelov, V. I., et al. (2004). *Physical Review B, 69*, 064114.

Ryu, J., Carazo, A. V., Uchino, K., & Kim, H. E. (2001). *Japanese Journal of Applied Physics, 40*, 4948.

Ryu, J., Priya, S., Uchino, K., & Kim, H. E. (2002). *Journal of Electroceramics, 8*, 107.

Schofield, D., & Brown, R. F. (1957). *Canadian Journal of Physics, 35*, 594.

Sidorkin, A. S. (2006). *Domain structure in ferroelectrics and related materials*. Cambridge International Science Publishi.

Sidorkin, A. S., Nesterenko, L. P., Ryabtsev, S. V., & Sidorkin, A. A. (2009). *Physics of the Solid State, 51*, 1348.

Srinivas, A., Kim, D. W., Hong, K. S., & Suryanarayana, S. V. (2004). *Materials Research Bulletin, 39*, 55.

Srinivasan, G., Hayes, R., & Bichurin, M. I. (2003). *Solid State Communications, 128*, 261.

Srinivasan, G., Laletsin, V. M., Hayes, R., Puddubnaya, N., Rasmussen, E. T., & Fekel, D. J. (2002). *Solid State Communications, 124*, 373.

Srinivasan, G., Rasmussen, E. T., Gallegos, J., Srinivasan, R., Bokhan, Y. I., & Laletin, V. M. (2001). *Physical Review B, 64*(1), 214408.

Srinivasan, G., Rasmussen, E. T., & Hayes, R. (2003). *Physical Review B, 67*(1), 014418.

Suchetelene, J. V. (1972). *Philips Research Report, 27*, 28.

Suryanarayana, S. V. (1994). *Bulletin of Materials Science, 17*, 1259.

Takahashi, S. (1981). *Japanese Journal of Applied Physics, 20*, 95.

Van Aken, B. B., Palstra, T. T. M., Filippetti, A., & Spaldin, N. A. (2004). *Nature Materials, 3*, 164.

Wan, J. G., Liu, J. M., Chand, H. L. W., Choy, C. L., Wang, G. H., & Nan, C. W. (2003). *Journal of Applied Physics, 93*, 9916.

Wan, J. G., Li, Z. Y., Wang, Y., Zeng, M., Wang, G. H., & Liu, J. M. (2005). *Applied Physics Letters, 86*(20), 202504.

Wang, Y. J., Leung, C. M., Or, S. W., Zhao, X. Y., & Luo, H. S. (2009). *Journal of Alloys and Compounds, 487*, 450.

Wang, Y. J., Leung, C. M., Wang, F. F., Or, S. W., Zhao, X. Y., & Luo, H. S. (2009). *Journal of Physics D: Applied Physics, 42*(13), 135414.

Wang, J., Neaton, J. B., Zheng, H., Nagarajan, V., Ogale, S. B., Liu, B., et al. (2003). *Science, 299*, 1719.

Wang, Y. J., Or, S. W., Chan, H. L. W., Zhao, X. Y., & Luo, H. S. (2008). *Journal of Applied Physics, 103*(12), 124511.

Wang, R. P., Xie, R. J., Hanada, K., Matsusaki, K., Bando, H., Sekiya, T., et al. (2006). *Ferroelectrics, 336*, 39.

Wongdamnern, N., Ngamjarurojana, A., Laosiritaworn, Y., Ananta, S., & Yimnirun, R. (2009). *Journal of Applied Physics, 105*, 044109.

Wongdamnern, N., Triamnak, N., Unruan, M., Kanchiang, K., Ngamjarurojana, A., Ananta, S., et al. (2010). *Physics Letters A, 374*, 391.

Wu, T., Chung, T. K., Chang, C. M., Keller, S., & Carman, G. (2009). *Journal of Applied Physics, 106*(5), 054114.

Yan, Y. K., Cho, K. H., Maurya, D., Kumar, A., Kalinin, S., Khachaturyan, A., et al. (2013). *Applied Physics Letters, 102*, 042903.

Yan, Y. K., Cho, K. H., & Priya, S. (2011). *Journal of the American Ceramic Society, 94*, 1784.

Yang, S.-C., Park, C.-S., Cho, K.-H., & Priya, S. (2010). *Journal of Applied Physics, 108*, 093706.

Yuan, Y., Zhang, S. R., Zhou, X. H., & Liu, J. S. (2006). *Japanese Journal of Applied Physics, 45*, 831.

Zang, G. Z., Wang, J. F., Chen, H. C., Su, W. B., Wang, C. M., Qi, P., et al. (2006). *Applied Physics Letters, 88*(21), 212908.

Zgonik, M., Bernasconi, P., Duelli, M., Schlesser, R., Gunter, P., Garrett, M. H., et al. (1994). *Physical Review B, 50*, 5941.

Zhai, J. Y., Dong, S. X., Xing, Z. P., Li, J. F., & Viehland, D. (2006). *Applied Physics Letters, 89*(8), 083507.

Zhai, J., Xing, Z., Dong, S., Li, J., & Viehland, D. (2008). *Journal of the American Ceramic Society, 91*, 351.

Zhang, N., Fan, J. F., Rong, X. F., Cao, H. X., & Wei, J. J. (2007). *Journal of Applied Physics, 101*(6), 063907.

Zhang, N., Ke, W., Schneider, T., & Srinivasan, G. (2006). *Journal of Physics: Condensed Matter, 18*(48), 11013.

Zhang, S. J., Lee, S. M., Kim, D. H., Lee, H. Y., & Shrout, T. R. (2007). *Journal of Applied Physics, 102*, 114103.

Zhang, S. J., Lee, S. M., Kim, D. H., Lee, H. Y., & Shrout, T. R. (2008). *Applied Physics Letters, 93*, 122908.

Zhang, S. J., & Li, F. (2012). *Journal of Applied Physics, 111*, 031301.

Zhang, S. J., Shrout, T. R., Nagata, H., Hiruma, Y., & Takenaka, T. (2007). *IEEE Transactions on Ultrasonics, Ferroelectrics, and Frequency Control, 54*, 910.

Zhang, S. J., Xia, R., Shrout, T. R., Zang, G. Z., & Wang, J. F. (2006). *Journal of Applied Physics, 100*(10), 104108.

Zhao, S., Li, G., Ding, A., Wang, T., & Yin, Q. (2006). *Journal of Physics D: Applied Physics, 39*, 2277.

Zhou, Y., Zhang, J. C., Li, L., Su, Y. L., Cheng, J. R., & Cao, S. X. (2009). *Journal of Alloys and Compounds, 484*, 535.

This page intentionally left blank

Part Two

Applications of composite magnetoelectrics in devices

This page intentionally left blank

Magnetoelectric energy harvester

7

Y. Zhou[1], *D.J. Apo*[1], *M. Sanghadasa*[2], *M. Bichurin*[3], *V.M. Petrov*[3], *S. Priya*[1]
[1]Center for Energy Harvesting Materials and Systems (CEHMS), Virginia Tech, Blacksburg, VA, USA; [2]Aviation & Missile Research, Development, and Engineering Center, U.S. Army RDECOM, Redstone Arsenal, Huntsville, AL, USA; [3]Novgorod State University, Veliky Novgorod, Russia

7.1 Introduction

The performance, capabilities, and deployment of wireless sensor networks (WSNs) and remote monitoring devices have been rising. This rapid proliferation of WSNs is related to the significant progress being made in complementary metal-oxide-semiconductor (CMOS) electronics that has brought down the power requirements considerably. Energy harvesters (EH) are being developed to meet the power requirements of the WSNs and remote monitoring devices in order to enhance the lifetime and limitations of conventional batteries (Apo, Sanghadasa, & Priya, 2014; Nibir, Dhar, & Dutta, 2011). There are many different sources available for energy harvesting, including solar radiations, thermal gradients, vibrations, magnetic fields, ocean waves, and wind. Vibration energy harvesting (VEH) has been pursued both as an alternative and as a supplement to the batteries, and between 2000 and 2010, there has been a surge in the number of publications in this area. In order for VEH to become practical, the size and weight of the harvester should be compatible with the mm-scale electronics and sensors, and the resonance characteristics of the harvester must be tailored to match the low natural frequencies and accelerations inherent in most vibration sources. Further, the performance of VEH devices could be improved by simultaneously harvesting the surrounding magnetic fields available that can be converted into electricity through magnetoelectric (ME) material/devices. The focus of this chapter is on describing ME harvesters that can be operated in dual mode, converting vibrations and magnetic field into electricity.

7.1.1 Classification of energy harvesting systems

Energy harvesting systems can be broadly classified based on the voltage generation mechanism, such as piezoelectric, electromagnetic, ME, dielectric elastomers, and electrets. The output power ($P = U^2/R$, where U is the output voltage and R is the load resistance) is dependent on the voltage generated and the impedances present within the energy harvesting device. For piezoelectric harvesters, the voltage generated ($U = \sigma_j\, g_{ij}\, t$) is dependent on the stress applied on to the piezoelectric material (σ_j), the piezoelectric voltage constant (g_{ij}), and the thickness of the piezoelectric material (t). For electromagnetic harvesters, $U = NA\frac{\partial B}{\partial t}$, where N is the number of turns in coil, $\partial B/\partial t$ is the change in magnetic flux cutting the coil, and A is the cross-sectional

Composite Magnetoelectrics. http://dx.doi.org/10.1016/B978-1-78242-254-9.00007-X
Copyright © 2015 Elsevier Ltd. All rights reserved.

area of the wire. For ME harvesters, $\frac{\partial U}{\partial H} = \frac{\partial \sigma_m}{\partial H} g_{ij} t_p$, where σ_m is the stress generated by magnetostrictive material, H is the applied magnetic field, and t_p is the thickness of piezoelectric material. For dielectric elastomers, $U^2 \propto \frac{\varepsilon_r \varepsilon_0}{C_p} * V * E_{\max}^2 * \left[1 - \frac{A_{\min}^2}{A_{\max}^2}\right]$, where C_p is the capacity of the generator, A is the surface area, V is material volume, $E_{\max}$ is the maximum electric field strength, ε_r is relative permittivity, and ε_0 is the permittivity of vacuum. For electret power generators, $P = \left(\left[\frac{4\varepsilon_0 \varepsilon_E}{t_E}\left(\frac{\varepsilon_E g}{\varepsilon_A t_E} + 1\right)\right]^{-1} * \sigma^2 * \frac{\mathrm{d}A(t)}{\mathrm{d}t}\right) \propto t_E^2$, where σ is the surface charge density, $A(t)$ is the variable overlap area between top and bottom electrodes, ε_E is the dielectric constant of the electret, ε_0 is the permittivity of vacuum, ε_A is the dielectric constant of air, g is the distance between top electrode and electret surface, and t_E is the electret thickness.

Current state-of-the-art EH are mostly focused on the piezoelectric and electromagnetic mechanisms. Piezoelectric EH mostly operate in the vicinity of the electromechanical resonance frequency to generate electrical power. Most of the piezoelectric harvesters utilize unimorph or bimorph bending mode structures to couple with the external vibrations. Unimorph harvesters are composed of one layer of piezoelectric material laminated on a substrate with different elastic stiffness. Bimorph harvesters are composed of two layers of piezoelectric material laminated on either side of a substrate. Electromagnetic-induction-based harvesters consist mainly of magnets and coils. The modus operation involves the induction of magnetic flux field through a coil of wire, thus inducing current in the coil. Table 7.1 shows that the electromagnetic (EM) EH generally exhibit higher power outputs and power densities than the piezoelectric (PE) harvesters. However, piezoelectric harvesters exhibit higher power densities at the microscale.

7.1.2 Modeling and characterization of energy harvesters

The experimental characterization of a piezoelectric or electromagnetic harvester is usually carried out in a simple vibration testing setup. Usually, the harvester is attached to a vibrating base, which actuates the harvester at arbitrary frequencies and accelerations. As shown in Figure 7.1, the harvester can be clamped to a shaker and a laser vibrometer can be used to detect the motion of any parts which move relative to the shaker. The relative motion can be subtracted from the induced acceleration results recorded from an accelerometer attached to the shaker or clamp. A central digital signal processor can be used to supply an output voltage signal to the shaker and receive input voltage signals during testing as controlled by a computer.

Most piezoelectric harvesters are designed in the form of a simple cantilever (with more than one material layer) with a tip mass as depicted in Figure 7.2. The most commonly used piezoelectric material is lead zirconate titanate (PZT) because of its significantly high piezoelectric properties (e.g., piezoelectric strain constant) when compared to other piezoelectrics. Piezoelectric harvesting systems tend to exhibit linear behavior in their dynamic and voltage responses and are heavily reliant on

Table 7.1 Piezoelectric and electromagnetic energy harvesters reported in the literature

Source	EH	Power (mW)	Frequency (Hz)	Acc. (g)	Normalized power density ($mW/cm^3\ g^2$)	Ref.
MIDE	PE	7.1	50	1.27	0.11	Figueras, Sabadell, Teres, & Serra-Graells (2011)
KCF	PE	4.1	360	0.24	0.34	Figueiredo et al. (2011)
Cedrat	PE	95	110	2.194	0.56	Wang, Yang, et al. (2011)
Beeby et al.	PE	0.0021	80.1	0.235	0.304	Beeby, Tudor, and White (2006)
Roundy et al.	PE	0.21	120	0.255	3.23	Roundy, Wright, and Rabaey (2003)
Roundy et al.	PE	0.375	120	0.255	5.767	Roundy et al. (2003)
Kim et al.	PE	0.0011	870	8	0.0047	Kim et al. (2008)
Williams et al.	EM	0.0003	4400	39	3.586E-5	Williams et al. (2001)
Glynne-Jones et al.	EM	0.037	322	5.43	0.0015	Glynne-Jones, Tudor, Beeby, and White (2004)
Cepnik et al.	EM	20.6	50	0.102	1.01	Cepnik, Radler, Rosenbaum, Ströhla, and Wallrabe (2011)
Byung-Chul et al.	EM	1.52	16	0.2	1.07	Byung-Chul, Md Ataur, Seung-Ho, and Gwiy-Sang (2012)
Hatipoglu et al.	EM	0.4	24.4	15	0.017	Hatipoglu and Urey (2009)

Continued

Table 7.1 Continued

Source	EH	Power (mW)	Frequency (Hz)	Acc. (g)	Normalized power density ($mW/cm^3\ g^2$)	Ref.
Ching et al.	EM	0.83	110	9.74	0.0087	Ching, Wong, Li, Leong, and Wen (2002)
Shuo et al.	EM	0.55	9.2	0.8	0.023	Shuo and David (2010)
Saha et al.	EM	2.46	2.75	1	0.194	Saha, O'Donnell, Wang, and McCloskey (2008)
Beeby et al.	EM	0.005	52	0.06	4.5E-8	Beeby et al. (2007)
Marin et al.	EM	25.5	50	0.2	0.541	Marin, Turner, Ha, and Priya (2013)
Marin et al.	EM	19	168	0.7	0.347	Marin, Heitzmann, Twiefel, and Priya (2012)
von Büren et al.	EM	0.025	20	–	0.0096	von Büren and Tröster (2007)
Wang et al.	EM	0.00212	280	0.82	0.101	Wang, Liu, et al. (2012)
Pan et al.	EM	0.1	60	–	0.86	Pan, Hwang, Hu, and Liu (2006)
Apo et al.	EM	5.9	13	0.25	15.33	Apo and Priya (2014a)
Apo et al.	EM	12.9	16	1	2.09	Apo and Priya (2014a)

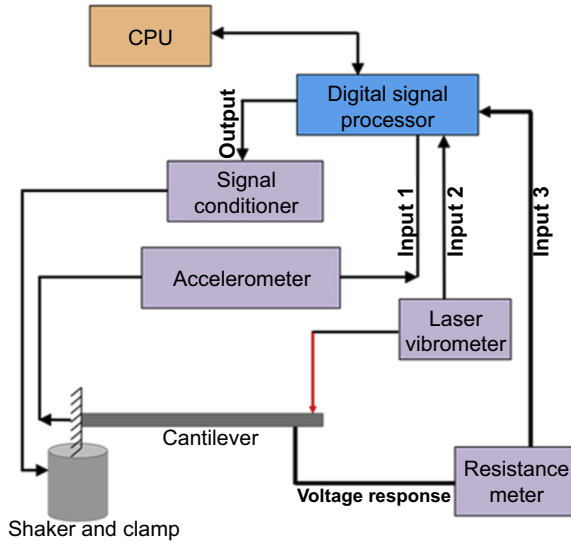

Figure 7.1 Typical vibration test schematic for piezoelectric and electromagnetic energy harvesters.

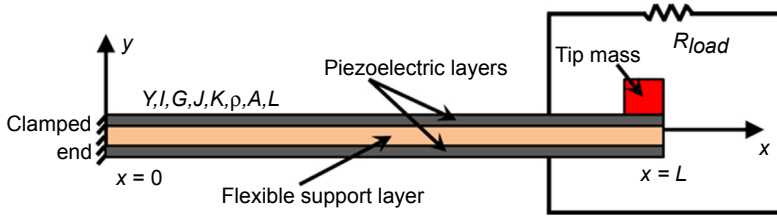

Figure 7.2 Schematic of bimorph piezoelectric energy harvester.

cantilever resonance frequencies for appreciable energy harvesting output. In some cases, electromagnetic harvesters consist of a magnetic mass (placed at the end of a cantilever beam) vibrating through a stationary coil. The positions of the magnetic mass and coil may also be switched (Zorlu & Külah, 2013). These electromagnetic systems can be modeled for their vibration characteristics similar to piezoelectric cantilevers.

A simplified derivation of the fundamental frequency (first mode) of a simple cantilever is based on the lumped mass approximation:

$$\omega_1 = \sqrt{\frac{k}{m_{\text{beam}} + 2.3m_{\text{tip}}}}, \tag{7.1}$$

where ω_1 is the fundamental frequency, k is the beam stiffness, m_{beam} is the mass of the beam, and m_{tip} is the mass of the tip mass at the free end. A more accurate model for

obtaining natural frequencies is based on the Euler–Bernoulli theory. The equation of motion for free out-of-plane vibration is (Karami & Inman, 2011)

$$YI\frac{\partial^4 w(x,t)}{\partial x^4} + \rho A\frac{\partial^2 w(x,t)}{\partial t^2} = 0, \tag{7.2}$$

where Y, I, ρ, and A are the Young's modulus, area moment of inertia, density, and surface area of the beam, respectively, and w represents the out-of-plane displacement of the beam as a function of distance along the beam length (x) and time (t). By using a separation of variables approach, we can express the beam displacement (w) and twist (β) as

$$\begin{aligned} w(x,t) &= W(x)\eta(t) \\ \beta(x,t) &= B(x)\eta(t), \end{aligned} \tag{7.3}$$

leading to spatial general solutions of the form

$$\begin{aligned} W(x) &= \sum_{i=1}^{4} a_i e^{\gamma_i x} \\ B(x) &= \sum_{i=5}^{6} a_i e^{\gamma_i x}, \end{aligned} \tag{7.4}$$

where

$$\gamma_i = \pm\left(\frac{\omega_n^2 \rho A}{YI}\right)^{\frac{1}{4}}, \tag{7.5}$$

and the values of $\boldsymbol{a_i}$ are numerical constants. The values of the numerical constants, natural frequencies ($\boldsymbol{\omega_n}$), and mode shapes, $W(x)$, can be obtained by applying the following boundary conditions,

$$\begin{aligned} &W(x=0) = 0 \\ &W'(x=0) = 0 \\ &B(x=0) = 0 \\ &M(x=l) = -YIW''(x=l) = 0 \\ &Q(x=l) = -YIW'''(x=l) = m_{\text{tip}}\omega_n W(x=l) \\ &T(x=l) = -GJB'(x=l) = 0, \end{aligned} \tag{7.6}$$

to Eqn (7.4) and solving computationally. In Eqn (7.6), W', M, Q, T, G, and J represent the beam slope, bending moment, transverse shear force, twist torque, shear modulus, and polar moment of inertia, respectively.

The piezoelectric harvester response to external excitation can be derived based on the Timoshenko beam theory (Timoshenko, 1921; Timoshenko & Young, 1968). The electrically coupled governing equation of motion for a simple bimorph piezoelectric harvester with tip mass in response to external sinusoidal excitation is given as (Erturk & Inman, 2009)

$$YI\frac{\partial^4 w_{\mathrm{rel}}(x,t)}{\partial x^4}+c_{\mathrm{s}}I\frac{\partial^5 w_{\mathrm{rel}}(x,t)}{\partial x^4\partial t}+c_{\mathrm{a}}\frac{\partial w_{\mathrm{rel}}(x,t)}{\partial t}+\rho A\frac{\partial^2 w_{\mathrm{rel}}(x,t)}{\partial t^2}+\vartheta V(t)\times\left(\frac{\mathrm{d}\delta(x)}{\mathrm{d}x}-\frac{\mathrm{d}\delta(x-L)}{\mathrm{d}x}\right)=-(\rho A+m_{\mathrm{tip}}\delta(x-L))\frac{\partial^2 w_{\mathrm{b}}(x,t)}{\partial t^2}, \tag{7.7}$$

from which the time-dependent voltage response for on- and off-resonance can be obtained. In Eqn (7.7), c_{s}, c_{a}, w_{rel}, w_{b}, δ,ϑ, and V denote the coefficient of strain rate damping, coefficient of viscous air damping, displacement of the beam relative to its base, displacement of the base, dirac delta function, coupling constant, and voltage, respectively. The coupling constant is dependent on the type of electrical connection (series or parallel) applied to the piezoelectric layers.

The steady state voltage response from a bimorph piezoelectric cantilever when excited transversely at a resonance, is therefore given as

$$V_{\mathrm{series}}=\frac{j2\omega R_{\mathrm{load}}\kappa_r F_r \mathrm{e}^{jwt}}{\left(2+jwR_{\mathrm{load}}C_p\right)\left(\omega_r^2-\omega^2+j2\zeta_r\omega_r\omega\right)+j2\omega R_{\mathrm{load}}\kappa_r\chi_r}, \tag{7.8}$$

where ω, ω_r, κ_r, F_r, ζ_r, χ_r, C_p, R_{load}, and j are the forcing frequency, resonance frequency, modal electrical circuit coupling term, amplitude of the modal forcing function, mechanical damping ratio, modal electromechanical coupling term, internal capacitance of the piezoelectric layer, load resistance, and unit imaginary number ($\sqrt{-1}$), respectively. The equations of motion and voltage response can be further simplified for unimorph harvesters and harvesters without tip mass (Erturk & Inman, 2008). Some piezoelectric materials (mostly polymers), such as polyvinylidene flouride (PVDF), have been found to be promising for the VEH in resonance-independent conditions, which involves the application of alternating or uniform forces (or stresses) directly to the harvester, as shown in Figure 7.3. In this mode, the harvester functions like a capacitor.

The electric energy available under AC stress excitation from a parallel plate capacitor is given as

$$U=\frac{1}{2}CV^2 \quad \text{or} \quad \text{energy per unit volume,} \quad u=\frac{1}{2}d\cdot g\cdot X^2, \tag{7.9}$$

where U is the energy, C is the capacitance, V is the voltage, and X is the applied stress. A piezoelectric material with high energy density is characterized by a high product of piezoelectric voltage constant (g) and piezoelectric strain constant (d), given as ($d\cdot g$), along with high magnitude of g coefficient. There are two extreme

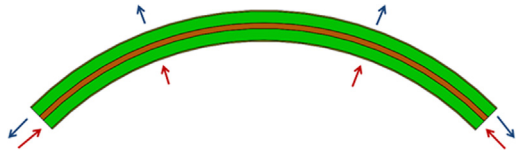

Figure 7.3 Forces applied to flexible piezoelectric bimorph harvester. Red arrow = compressive force, blue arrow = tensile force.

cases to the high energy density material, PVDF piezoelectric polymer ($d_{33} = 33$ pC/N, $\varepsilon_{33}/\varepsilon_o = 13$, $g_{33} = 286.7 \times 10^{-3}$ m^2/C) and relaxor piezoelectric single crystals, such as PZN − 7%PT ($d_{33} = 2500$ pC/N, $\varepsilon_{33}/\varepsilon_o = 6700$, $g_{33} = 42.1 \times 10^{-3}$ m^2/C). It can be seen from these data that piezoelectric polymer has the highest piezoelectric voltage constant g_{33} of 286.7×10^{-3} m^2/C and relaxor-based single crystals have the highest product ($d_{33} \cdot g_{33}$) of the order of $105{,}250 \times 10^{-15}$ m^2/N.

For most electromagnetic harvesters, the working principle involves vibration of a magnet (or magnet composite) through a coil. The modeling of such systems depends on the spring force(s) present. When a return spring is attached to the magnet, the response behavior of the system is mostly linear (just like piezoelectric cantilevers), and the vibration characteristics can be modeled using a simple lumped mass approach:

$$\omega_1 = \sqrt{\frac{k_{sp}}{m_{mag}}}, \tag{7.10}$$

where ω_1 is the fundamental frequency, k_{sp} is the spring stiffness, and m_{mag} is the mass of the beam. However, some electromagnetic systems incorporate abstract spring systems based on magnetic repulsion. For such systems, the dynamic and voltage responses typically exhibit nonlinear and broadband behavior (Saha et al., 2008). As shown in Figure 7.4, a novel design for electromagnetic harvesters was introduced by Apo and Priya (2014a,b) based upon a double repulsion configuration in the moving magnet composite. The magnet composite is suspended between two stationary magnets as it vibrates through two sections of coils.

Finite element analysis can be used to obtain the force field (F) and magnetic flux field (B) while a computational model can be used to simulate the dynamics and voltage response of the harvester. As shown in Figure 7.5, the electromagnetic harvester is modeled as a moving mass restricted by two nonlinear springs and two dampers. The model can be simplified to one mass, one nonlinear spring, and one damper since the two springs are based on magnetic repulsion forces, which are similar.

Thus, dynamics of the oscillating moving magnet composite can be mathematically modeled by using a nonlinear spring−mass−damper mechanical system with an external applied base excitation given as

$$m\ddot{z}(t) + c_m\dot{z}(t) + c_e(t)\dot{z}(t) + kz(t) + k_3 z(t)^3 = -m\ddot{y}(t) - mg, \tag{7.11}$$

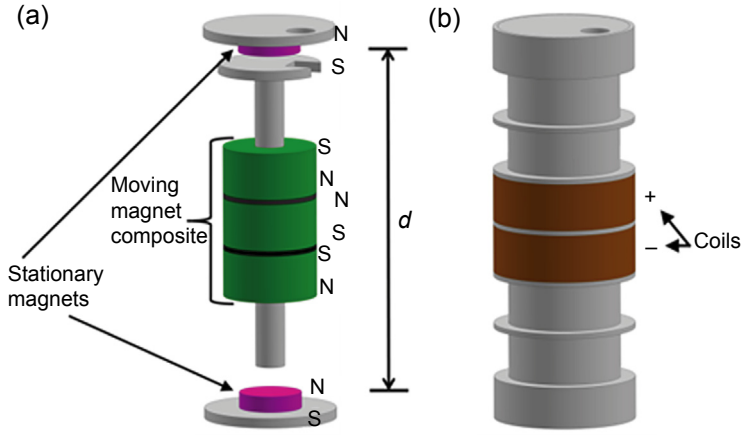

Figure 7.4 Electromagnetic harvester with magnetic repulsion spring: (a) magnet configuration with three magnet discs and two steel discs in the moving magnet composite and (b) harvester casing and coils.

where m is the moving magnet composite mass, c_m is the mechanical damping constant, $c_e(t)$ is the instantaneous electrical damping, k is the linear stiffness constant of the spring, k_3 is the nonlinear stiffness constant of the spring, $\ddot{z}(t)$ is the relative acceleration between the base of the structure $\ddot{y}(t)$ and the vibrating mass $\ddot{X}(t)$, g is the gravitational constant, and $\dot{z}$ and z are the velocity and displacement of the moving magnet composite, respectively. The acceleration of the vibrating mass $\ddot{X}(t)$ includes the moving magnet and the base of the structure, that is, $z(t) = x(t) - y(t)$. Thus, the value of z defines the vibration of the moving magnet only. Gravitational force is normally included in the analysis of vibrating nonlinear systems (unlike linear systems) to account for the nonlinear stiffness constant (Zavodney & Nayfeh, 1989). The nonlinear mathematical spring refers to the repulsion between the moving magnet

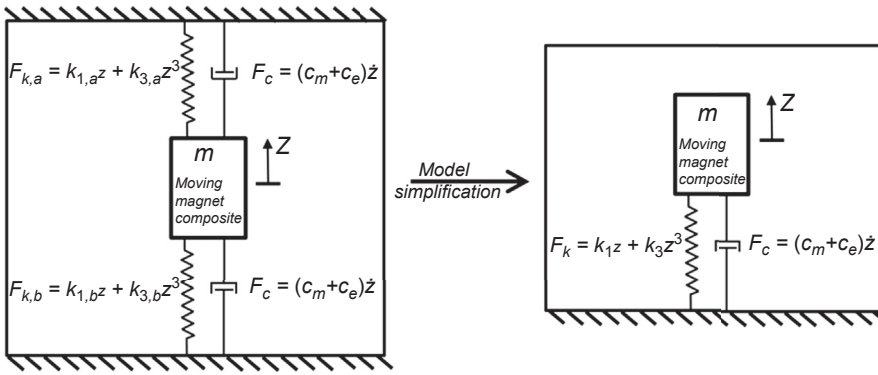

Figure 7.5 Schematic representation of the dynamic modeling for electromagnetic harvesters.

composite and the stationary magnets, and it is related to the instantaneous magnetic repulsion force (F) and the moving magnet displacement by

$$F(t) = kz(t) + k_3 z(t)^3. \tag{7.12}$$

In order to solve the dynamic system, the damping terms, c_m and c_e, can be obtained and added to the model. The mechanical damping constant is defined by

$$c_m = 2\zeta_m \sqrt{km}, \tag{7.13}$$

where ζ_m is mechanical damping ratio. The damping ratio can be empirically determined by measuring the amplitude of displacement decay after the moving magnet composite was initially displaced from its rest position. This approach assumes a linear decay and therefore allows the damping ratio to be obtained from

$$\ln\left|\frac{A_0}{A_n}\right| = \frac{2\pi n \zeta_m}{\sqrt{\left(1-\zeta_m^2\right)}}, \tag{7.14}$$

where A_0 is the first amplitude of motion and n is the decaying cycle. The electrical damping can be estimated from

$$c_e(t) = \frac{(B(t)\times l)^2}{R_e + R_l}, \tag{7.15}$$

where $B(t)$ is the instantaneous magnetic flux density, l is the length of coil, R_e is the total coil resistance, and R_l is the optimum coil resistance. The B-field values apply to the instantaneous B-field region cutting through the coil. The output response of the harvester can be predicted by discretizing the coil volume and applying looping forms of the equations below:

$$V = \frac{Bl\dot{z}}{R_L + R_e} R_L \quad V_{\text{rms}} = \sqrt{\frac{1}{n}\sum_{i=1}^{n} V_i^2}, \tag{7.16}$$

$$P = \left(\frac{Bl\dot{z}}{R_L + R_e}\right)^2 R_L \quad P_{\text{rms}} = \sqrt{\frac{1}{n}\sum_{i=1}^{n} P_i^2}, \tag{7.17}$$

where n is the number of discrete points applied.

7.1.3 The need for magnetoelectric energy harvesters

ME energy harvesting is a relatively new concept with a limited number of investigations on quantifying the variety of harvester architectures. The voltage can be induced

in a ME composite through external magnetic fields and vibrations. Various devices and structures around us generate stray magnetic fields as a result of the components inherent to their operation. In addition, a ME EH can be made to work as a vibration EH to create an additive voltage effect (Zhou, Apo, & Priya, 2013). In this chapter, we will systematically describe the development of ME composites and their application as ME EH. Self-biased ME composite that can generate voltage in the absence of DC bias will be discussed in detail. Principles behind the design to harvest energy from mechanical vibrations and magnetic fields individually or simultaneously will be illustrated. Other considerations, such as the arc-based concept that ensures low resonance frequency across different length scales while providing the wideband, will also be discussed.

7.2 Development of magnetoelectric energy harvester

ME effect is product property of ferromagnetic and piezoelectric materials that is expressed as polarization change in response to an externally applied magnetic field and vice versa (Fiebig, 2005; Spaldin & Fiebig, 2005). This ferroic coupling provides great opportunity toward developing new applications, such as sensors, tunable transformers, filters, memory devices, and EH (Nan, Bichurin, Dong, Viehland, & Srinivasan, 2008; Priya et al., 2009; Priya, Islam, Dong, & Viehland, 2007). Prior research on ME materials has mainly focused on improving the ME coefficient and sensitivity for their application in sensors. Between 2000 and 2010, research has started on energy recovery from unused power and developing self-powered sensors and electronics (Beeby et al., 2006; Paradiso & Starner, 2005; Priya et al., 2009). ME composites with various connectivity and structures have been developed in order to scavenge the ambient magnetic and mechanical energies (Dong, Zhai, Li, Viehland, & Priya, 2008; Lafont et al., 2012; Li, Wen, & Bian, 2007). These experimental investigations have been complemented by the theoretical modeling which has led to the understanding of the role of various materials and structure parameters. In this section, we will overview the working principle, development, and design concept of the ME EH. Detailed information on the ME EH will be provided in the following sections.

7.2.1 Working principle

For energy harvesting applications, by utilizing the product property of the ME composite, one is able to generate the electricity from a stray AC magnetic field present in the surroundings and additionally from converting the mechanical vibrations into electricity with higher efficiency. The scavenging mechanism can be described as follows: when the ME composite is placed in an AC magnetic field, the magnetostrictive layer responds by elongating or contracting, thereby straining the piezoelectric layer that results in output voltage across the electrical load through a direct piezoelectric effect. Due to the existence of the piezoelectric phase in the composite, mechanical

oscillation applied on to the composite can directly create electrical voltage. Thus, an ME EH can harness energy from both vibrations and the AC magnetic field at the same time. The combination is expected to enhance the power output and conversion efficiency.

7.2.2 Magnetoelectric energy harvesters

ME composites working as generators can produce high output voltages as the strain in the piezoelectric material can be maximized with the aid of magnetostrictive material. In the following section, we review the current status of an ME energy harvesting system as a function of source, as schematically depicted in Figure 7.6.

7.2.2.1 Stray magnetic field

Stray magnetic fields are widely present around power cables, vehicles, and industrial machines. For example, large electric motors commonly used in industrial manufacturing plants have presence of periodic stray magnetic field from the inductive windings. The oscillating magnetic field can induce an AC stress on the piezoelectric layer through magnetostriction and thereby create an electric charge through direct piezoelectric effect. The electric charge can be further processed and stored by the circuit. Recently, Li et al. developed an ME composite consisting of a magnetostrictive Terfenol-D plate, multiple piezoelectric plates, and a copper ultrasonic horn, which can produce a maximum power of 6.5 μW at an AC magnetic field of 1 Oe (Li et al., 2007). Alternatively, Gao et al. designed an unsymmetrical bilayered Metglas/Pb(Zr,Ti)O_3

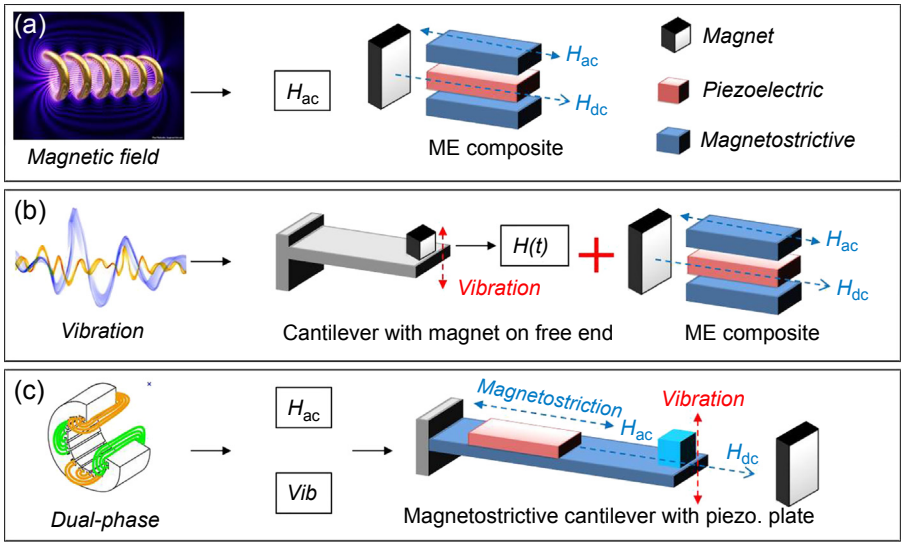

Figure 7.6 Schematic diagram depicting (a) magnetic field ME energy harvester; (b) vibration ME energy harvester; (c) dual-phase ME energy harvester.

laminate in push−pull configuration with tunable resonance frequency for a 60 Hz magnetic field EH and experimentally observed a power output of 16 μW/Oe with the power density of ≥200 μW/cm^3 (Gao et al., 2012). Dong et al. have demonstrated a ME cantilever based on the push−pull type Metglas/Pb(Zr,Ti)O_3 laminate and demonstrated a power output of 420 μW/Oe across a 50 kΩ load under an AC magnetic field of 1 Oe at ∼21 kHz (Dong et al., 2008).

7.2.2.2 Mechanical vibration

VEH devices widely employ the piezoelectric or electromagnetic transduction mechanisms (Anton & Sodano, 2007; Beeby et al., 2006; Priya, 2007). However, either the narrow bandwidth or the relatively low power density of these designs hinders their potential for the practical applications. If mechanical vibration or rotation is present, AC magnetic field can be created by oscillating or rotating a mechanical assembly that consists of magnets as schematic shown in Figure 7.6(b). Dai et al. have recently demonstrated a series of devices based on this approach, where the harvester uses magnets arranged on the free end of a cantilever beam with a single or multiple ME transducers placed in the air gap between the magnets (Bai et al., 2012; Dai, Wen, Li, Yang, & Li, 2011; Dai, Wen, Li, Yang, & Zhang, 2009; Li, Wen, Li, Yang, & Dai, 2011; Yang, Wen, Li, 2011; Yang, Wen, Li, Bai, 2011). The ME transducers move through a concentrated magnetic flux variation and were able to provide a maximum power of ∼7.13 mW (1.1 mW/cm^3) under acceleration of 2.5 g at 35 Hz (Dai et al., 2011). Moss et al. have reported a bi-axial oscillator using a permanent-magnet/ball bearing arrangement, which can produce a peak power of 121 μW from a vibration of 61 mg at 9.8 Hz (Moss, McLeod, Powlesland, & Galea, 2012). Ju et al. have designed a vibration EH using a freely movable spherical permanent magnet to create a time-varying magnetic field for ME conversion (Ju et al., 2013). All these approaches reported in literature take advantage of the fact that if vibration and magnetic fields are available, then a ME transducer can be used to harvest the energy simultaneously with higher power density. A vibration source can be used to create the AC magnetic field with the same frequency.

Alternative approaches have been proposed in literature to transform the mechanical rotation into magnetic field variation, thereby generating power through an ME transducer. When a permanent magnet rotates above ME composites, the induced magnetostriction depends on the angular position alternating between λ_{11} and λ_{12}; thus, the piezoelectric layer is stressed and generates electrical charges (Lafont et al., 2012). In their experiment, Li et al. attached a cantilever beam with a magnet at the free end on a rotating host, thereby creating a sinusoidal magnetic wave. The rotation induced magnetic field variation was able to generate a power of 157 μW across a 3.3 MΩ load at the rotation rate of 599 rpm (Li et al., 2011).

7.2.2.3 Dual-phase: stray magnetic field & mechanical vibration

To further enhance the efficiency and power output of the ME EH researchers have made an attempt toward generating power from mechanical vibration and alternating magnetic field simultaneously, termed as dual-phase mode. Since the ME effect in

composites is a product property of magnetostrictive and piezoelectric mechanism, the induced strain from different phases can be expected to be combined together. Based on this hypothesis, several ME EH have been developed (Dong et al., 2008; Kambale, Yoon, et al., 2013; Zhou et al., 2013). As schematically depicted in Figure 7.6, by utilizing the magnetostrictive layer as both magnetic field-strain conversion layer under magnetic field and flexible substrate under mechanical vibration, the composite structure can provide an additive effect. In dual mode operation, ME EH have demonstrated the potential to scavenge magnetic field energy and vibration energy with high conversion efficiency. Detailed discussion on the dual-phase ME EH is provided below.

7.2.3 Design concept

There are several fundamental challenges in realization of a high-performance ME EH. The performance of an ME EH is tightly related with the materials selection, structure, processing method, operating mode, size effect, and other dynamic parameters. Table 7.2 illustrates a list of factors to be considered in the design of ME EH and provides an overview of the features and challenges, as well as the suggested fabrication methods.

One of the biggest challenges for practical application of ME composites has been the magnitude of ME voltage coefficient $\alpha_{ME,}$ which represents the magnetic field output voltage conversion. The characteristic ME behavior can be explained by taking into account the constitutive piezoelectric and magnetostrictive behavior. Thus, the selection of appropriate piezoelectric and magnetostrictive materials is the primary

Table 7.2 List of factors to be considered in the design of magnetoelectric energy harvester

Design factors	Features	Challenges	Realization
Materials	Piezoelectric	α_{ME}	Appropriate combination
	Magnetostrictive		
Synthesis	Epoxy bonding	Low coupling	Cofiring
	Thin film deposition	Low power	Thick film printing
Characterizations	ME vs H_{DC}	H_{bias}	Self-biased ME
		Narrow bandwidth	Wideband
	ME vs f_{AC}	f_r	Low frequency
		Narrow bandwidth	Broadband
	ME vs Configuration	Volume ratio	Demagnetization
		Size effect	MEMS

step toward achieving a high-performance ME transducer. Next, the effect of synthesis techniques on the ME response should be considered.

In general, under a constant applied AC magnetic field (H_{ac}), the ME coupling coefficient (α_{ME}) shows a peak behavior in response to varying DC bias (ME vs H_{dc}) and AC magnetic field frequency (ME vs f_{ac}). The peak behavior clearly indicates the necessity for optimizing the magnitude of DC magnetic bias and AC frequency to obtain the maximum output voltage. However, from the practical point of view, the ME behavior also presents two challenges: (1) the requirement of DC magnetic bias dramatically increases the device size due to the use of solenoid or permanent magnet, and (2) the peak behavior limits the operating bandwidth in terms of magnetic DC bias and AC frequency.

In summary, comprehensive understanding of these factors provides guidance toward the design of a high-performance ME EH. In the following sections, we will discuss some of these factors, including ME composite, self-biased ME EH, multimode ME EH, low-frequency/wideband ME EH and micro-electro-mechanical system (MEMS) ME EH.

7.3 Magnetoelectric composite

ME composite can be realized through the interactions between the magnetostrictive and piezoelectric materials (Zhai, Xing, Dong, Li, & Viehland, 2008). The transfer of magnetic field induced strain (magnetostriction) from the magnetostrictive phase to the piezoelectric phase occurs through the elastic coupling. Prior research on ME materials has shown that composites exhibit much higher magnitude of ME coefficient than single-phase materials (Nan et al., 2008; Priya et al., 2007; Zhai et al., 2008). In addition, the design and synthesis of ME composites offers more flexibility, resulting in cost-effectiveness and freedom in meeting the shape and size constraints. Between 2000 and 2010, ME composites with a diverse set of materials, connectivity, and microstructure have been developed through a variety of processing techniques (Kambale, Jeong, & Ryu, 2012; Martins & Lanceros-Méndez, 2013; Nan et al., 2008; Srinivasan, 2010).

7.3.1 Classification

In general, ME composites can be categorized into different groups based upon the phase connectivity, materials selection, operation mode, and synthesis method, as listed in Table 7.3.

Based upon the applied input, the ME effect can be described as direct magnetoelectric (DME) effect and converse magnetoelectric (CME) effect. In DME effect, the coupling coefficient is the ratio of the applied H_{ac} and induced AC electric field (E_{ac}); DME coefficient $= \frac{\text{Magnetic}}{\text{Mechanical}} \times \frac{\text{Mechanical}}{\text{Electric}}$. In CME effect, the coupling coefficient is the ratio between the applied AC electric field and induced AC magnetic field; CME coefficient $= \frac{\text{Electric}}{\text{Mechanical}} \times \frac{\text{Mechanical}}{\text{Magnetic}}$.

Table 7.3 Classification of magnetoelectric composites

Characterization	Classes		
Applied input	DME	CME	
Connectivity	0−3	2−2	1−3
Operation mode	L−T/T−L	T−T	L−L
Material	All ceramics	Ceramic-metal	Polymer-metal
Synthesis	Bonding	Cofired	Thin/thick film

Considering the phase connectivity (Newnham, Skinner, & Cross, 1978), a two-phase ME composite system can be typically classified into three common groups (Nan et al., 2008): (1) 0−3 type particulate composite, where the first number denotes the magnetic phase (0 dimension particles) embedded in the matrix of the piezoelectric phase (3 dimension); (2) 2−2 type laminate, where the layer-by-layer architecture consists of alternate magnetic and piezoelectric phase; and (3) 1−3 type cylinder-matrix composite, where nano/microrods of magnetic phase are embedded in the piezoelectric matrix (Priya et al., 2007). The 2−2 type ME laminate structures preserve the physical characteristics of individual phases, minimize the interfacial damping, and exhibit negligible leakage, thereby resulting in higher ME coupling. A sandwich-type configuration with two distinct phases is a commonly utilized structure in this category (Zhai et al., 2008). The 1−3 composites have been mainly explored at the micro and nanoscale where they can be easily synthesized through the self-assembly process (Ramesh & Spaldin, 2007). The 2−2 type laminates have been widely investigated due to the ease of fabrication and design flexibility (Priya et al., 2007; Zhai et al., 2008). The most common configurations for 2−2 type laminates are magnetostrictive/piezoelectric (MP) bilayer structure and magnetostrictive/ piezoelectric/magnetostrictive (MPM) trilayer structure. Based on different combinations of poling and magnetization direction, we can identify four basic operation modes, including L−T/T−L, T−T, L−L, where the first letter represents magnetization orientation, the second letter denotes polarization direction, L stands for longitudinal, and T stands for transverse. All these modes can be easily realized by fabricating structures through epoxy bonding of layers with different magnetization/poling conditions. Both theoretical calculation and experiments have demonstrated that the magnitude of ME voltage coefficient for laminates follows the order (L−L) > (L−T/T−L) > (T−T) (Zhai et al., 2008). Generally, the ME voltage coefficient of L−L mode structure is nearly an order of magnitude higher than those of L−T type laminates (Dong, Zhai, Li, & Viehland, 2006). This is due to the efficient stress transfer ($d_{33} > 2d_{31}$ since Poisson's ratio is smaller than 0.5) when the piezoelectric layer is longitudinally poled. The low value of (T−T) mode is the result of the demagnetization effect of the magnetostrictive phase. It is also important to mention here that other more complex modes, such as composites in the form of bimorph, unimorph, ring, and cylindrical structure have also been developed and provide

more choices toward designing suitable harvester structure (Dong et al., 2005; Dong, Li, & Viehland, 2004; Zhai, Xing, Dong, Li, & Viehland, 2006).

7.3.2 Materials selection

A suitable selection of piezoelectric and magnetostrictive materials is an essential step toward realization of a high-performance ME composite.

7.3.2.1 Piezoelectric materials

Generally, piezoelectric materials exhibiting high magnitude of piezoelectric voltage constant ($g = d/\varepsilon$), low dielectric, and piezoelectric losses are desired. The choice of microstructure is diverse, including random ceramics, textured ceramics, single crystals, and polymers, as listed in Table 7.4. In this table, d_{33} is the longitudinal piezoelectric constant, d_{31} is the transverse piezoelectric constant, ε_r is the relative dielectric constant, k_{33} is the longitudinal electromechanical coupling coefficient, and T_c is the Curie temperature.

One of the first ME composites was developed by using $BaTiO_3$ (BTO) as the piezoelectric phase (Van Den Boomgaard, Van Run, & Suchtelen, 1976). To further enhance the ME coupling, Pb(Zr,Ti)O_3 (PZT) based compositions have replaced BTO as the piezoelectric phase due to its larger electromechanical coefficients. With the development of relaxor-based single crystals, such as $Pb(Zn_{1/3}Nb_{2/3})O_3$−$PbTiO_3$ (PZN-PT) and $Pb(Mg_{1/3}Nb_{2/3})O_3$−$PbTiO_3$ (PMN-PT), the performance of ME composites can be dramatically enhanced based on their ultra-high electromechanical properties ($d_{33} > 2000$ pC/N and $k_{33} > 92\%$) (Priya et al., 2007). However, the low Curie temperature and high cost hinders the application for ME composites. In addressing this challenge, the alternative strategy of texturing ceramics has been proposed. Yan et al. have demonstrated a template grain growth (TGG) technique

Table 7.4 List of typical piezoelectric materials (Maurya, Zhou, Yan, & Priya, 2013; Priya et al., 2007; Yan, Cho, et al., 2013; Zhai et al., 2008)

	Materials	d_{33} (pC/N)	d_{31} (pC/N)	ε_r (1 kHz)	k_{33}	T_c(°C)
Random ceramics	$BaTiO_3$	190	−78	1700	0.49	120
	PZT-5	400	−175	1750	0.72	360
Textured ceramics	NBT-BT	322			0.57	90
	PMN-PZT	1100		2310	0.84(k_p)	204
Single crystal	PMN-PZT	1530		4850	0.93	211
Polymer	PVDF		−28	6	0.2(k_t)	170

that yields microstructure with ⟨001⟩ preferred grain orientation, resulting in high d and g value comparable to that of single crystal (Yan, Cho, et al., 2013). By utilizing these textured ceramics as the piezoelectric layer in the ME composites, a 3.4 times improvement of α_{ME} was realized as compared to that of random ceramics (Yan, Cho, et al., 2013). Lead-free random and textured ceramics have also been considered for fabricating ME composites (Maurya et al., 2013). Other than these ceramic materials, polymeric piezoelectric compositions, such as PVDF, have been utilized for developing highly flexible ME devices (Fukada, 2000; Martins & Lanceros-Méndez, 2013).

7.3.2.2 Magnetostrictive materials

Magnetostrictive materials undergo a change in shape due to the variation of the magnetization state under external magnetic field. The magnetic domains in these materials can be reoriented along the direction of applied external magnetic field. During the process of magnetization, the material deformation can be quantified through a magnetostriction (λ) coefficient whose saturation value (λs) is used for the comparative material analysis. Table 7.5 provides a list of commonly used magnetostrictive materials for ME composites.

Among the magnetostrictive materials listed in Table 7.5, ferrites have larger electrical resistance in comparison to the metal/alloy magnetic materials but smaller magnetostriction. Ferrites are widely used in coprocessing with piezoelectric ceramics due to their stability under high temperature. Magnetic alloy Terfenol-D exhibits large magnetostriction (1400 ppm) with small permeability (≈ 10). Terfenol-D is suitable for high-performance ME laminate but requires large DC magnetic bias to reach the saturation magnetostriction. Metglas has extremely high relative permeability of $>10{,}000$ and high piezomagnetic coefficient (q) but requires low processing

Table 7.5 List of typical magnetostrictive materials (Priya et al., 2007; Zhai et al., 2008)

	Materials	λs(ppm)
Ceramic	Fe_3O_4	40
	$NiFe_2O_4$	−26
	$CoFe_2O_4$	−110
Metal	Fe	−9
	Co	−62
	Ni	−33
Alloy	Terfenol-D ($Tb_{1-x}Dy_xFe_2$)	1400
	Galfenol (Fe-Ga)	200
	Metglas ($Fe_{81}Si_{3.5}B_{13.5}C_2$)	40

temperatures. Metglas-based ME laminates require extremely small H_{bias} (Dong et al., 2006; Wang, Gray, Berry, Gao, et al., 2011).

7.3.2.3 Synthesis of ME composite

A variety of synthesis techniques have been used for fabricating ME composites, including epoxy bonding, cofiring, thick film printing, and thin film deposition.

Epoxy bonding

Epoxy bonding is widely used for synthesizing ME laminates due to the ease of fabrication and low cost (Zhai et al., 2008). Since this process does not require high temperature, most of the material combinations are suitable for the design of ME composites. Epoxy bonding reduces the misfit strain at the interface arising due to the thermal expansion mismatch between the different layers. It also eliminates the atomic interdiffusion and/or chemical reaction between the layers. Thus, this method offers greater design flexibility than that of conventional ceramic processing techniques. However, the epoxy layer with low mechanical strength will dampen the generated strain, induce noise floor, and therefore limit the ME response (Wang, Gray, Berry, Li, et al., 2012). Further, the manual fabrication process presents another challenge in implementation of industrial manufacturing (Li, Berry, et al., 2011; Wang, Gray, Berry, Gao, et al. 2012).

Cofiring

To optimize the ME interface coupling, direct bonding that completely excludes the epoxy in the composite is necessary. The cofiring technique not only enhances the elastic coupling between phases, but also dramatically decreases the cost due to its compatibility with an industrial production process that is commonly used for multilayer capacitors. Considering the sintering conditions of different materials and phases, cofiring techniques for piezoelectric and ferromagnetic ceramics has been developed (Priya et al., 2007; Srinivasan et al., 2001; Srinivasan, Rasmussen, Levin, & Hayes, 2002). However, cofiring is challenging due to the large difference in the shrinkage rates and thermal expansion mismatch among the different phases.

Thin film deposition

It has been widely accepted that strong interfacial bonding between two phases is required for a large ME response. However, either the low mechanical strength from the epoxy bonding or the possibility of interdiffusion during the high-temperature cofiring process may limit the bonding between the two phases. More importantly, these two methods result in another issue: the large sample size may limit its implementation for MEMS-scale functional ME devices. In addressing these issues, the thin film deposition method has been widely employed in the development of ME composites (Jahns et al., 2013; Martin et al., 2008; Prellier, Singh, & Murugavel, 2005; Ramesh & Spaldin, 2007). Nanostructure thin film composites, including 0−3 type particular films, 2−2 type layered heterostructures, and 1−3 type vertical heterostructures have been investigated using either physical

vapor deposition (PVD) methods (pulsed laser deposition, sputtering, molecular beam epitaxial) or chemical vapor deposition (CVD) methods (sol−gel spin coating, metal-organic CVD). By optimizing the deposition parameters and materials selection, ME composite thin films with coherent interfaces in various nanostructures have been developed by precise control of the lattice mismatch and thickness between the two phases (Martin et al., 2008; Vaz, Hoffman, Anh, & Ramesh, 2010).

Thick film printing

For energy harvesting systems, the weak magnitude of ME voltage output due to the size effect cannot be neglected, even though large ME coupling can be achieved in the thin film composites. For a film with 100 nm scale thickness, the real ME voltage detected from the films might be negligibly small at the magnitude of μV level (Kambale et al., 2012). Therefore, to enhance the voltage output of the ME films, thick films in micron scale are required. Ryu et al. demonstrated an efficient method for fabricating thick films using aerosol deposition (AD) (Kambale et al., 2012; Park et al., 2009). Piezoelectric and magnetostrictive nano-powders were sprayed on the substrate through high pressure gas flow at room temperature. A high print rate with the magnitude of several μm/min can therefore be obtained. Composite films with varying materials, thickness, and configuration can be printed on metal/ceramic substrates with high density and good interfacial bonding strength (Kambale, Patil, et al., 2013; Oh et al., 2012; Park et al., 2009).

7.3.3 Characterization

It can be seen from the above discussion that the possibilities are numerous (materials, connectivity, operation mode, synthesis method, and so on) for obtaining the ME composites. To better utilize these composites, investigation on their working behaviors would contribute an understanding of the effect of some variables associated with the performance. In the following section, we will discuss the characteristic behavior of conventional ME composites.

7.3.3.1 ME versus H_{dc}

In a ME composite, the measured DME coupling coefficient is the field conversion ratio between applied H_{ac} and induced E_{ac} under H_{dc}, $\alpha_{ME} = \delta E_{ac}/\delta H_{ac}$. In general, under a constant applied AC magnetic field, the ME coupling coefficient first increases with increasing H_{dc}, reaching a maximum at an optimized DC bias (H_{bias}), and then decreases with further increasing H_{dc}. This peak behavior in response to varying H_{dc} can be further explained by taking the interaction coupling relationship as given below (Cho & Priya, 2011):

$$\alpha_{ME} = \left|\frac{\partial T}{\partial S} \times \frac{\partial D}{\partial T} \times \frac{\partial E}{\partial D}\right| \times \frac{\partial S}{\partial H}, \tag{7.18}$$

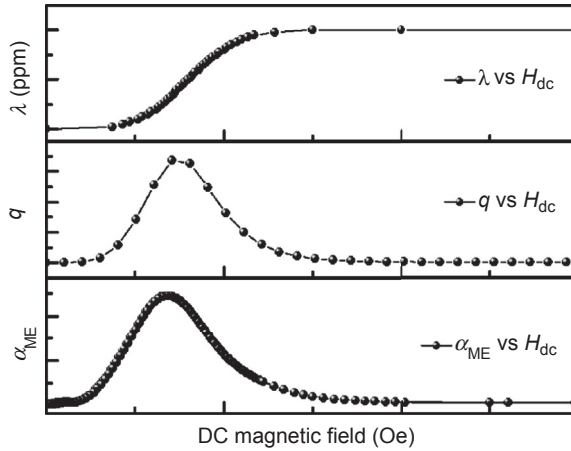

Figure 7.7 Typical magnetoelectric behaviors as a function of DC magnetic field.

where S is the mechanical strain, T is the mechanical stress, D is the electric displacement, E is the electric field, and H is the magnetic field. Since the first part of the above expressions is a nonmagnetic factor, one can re-write Eqn (7.18) as

$$\alpha_{\mathrm{ME}} \propto \frac{\partial S}{\partial H} = \frac{\mathrm{d}\lambda}{\mathrm{d}H} = q, \tag{7.19}$$

which indicates that the ME coefficient is directly related to the nature of the ferromagnetic phase (λ: magnetostriction, q: piezomagnetic coefficient) and the effectiveness of elastic coupling between the two phases. The dependence of α_{ME} on q indicates the requirement for additional H_{dc}. In summary, the typical behavior of the α_{ME}, λ, q, and their relationship as a function of H_{dc} are shown in Figure 7.7.

7.3.3.2 ME versus f_{ac}

Another important phenomenon of the ME composite is the ME coupling as a function of applied AC magnetic field (ME vs f_{ac}). When the AC magnetic field is applied at a frequency corresponding to electromechanical resonance (EMR) for the piezoelectric phase or ferromagnetic resonance (FMR) for the magnetic phase in the ME composite, the ME voltage coefficient shows a peak behavior with the magnitude increased by a factor of up to 100X (Srinivasan, 2010; Zhai et al., 2008). Bichurin et al. developed a theoretical analysis for bilayer NFO-PZT laminates that showed a 40 times increase in $a_{\mathrm{ME},33}$ at electromechanical resonance compared to that of off-resonance (Bichurin et al., 2003). Similar theoretical models have been developed for the ME effect at ferromagnetic and magnetoacoustic resonance in the composites (Bichurin, Petrov, Kiliba, & Srinivasan, 2002; Bichurin, Petrov, Ryabkov, Averkin, & Srinivasan, 2005). Cho et al. analyzed the direct and CME effect in laminate composites and found that DME is maximized at f_{a} while the CME is maximized at f_{r}, as shown in Figure 7.8 (Cho & Priya, 2011). This phenomenon can be further explained by using piezoelectric

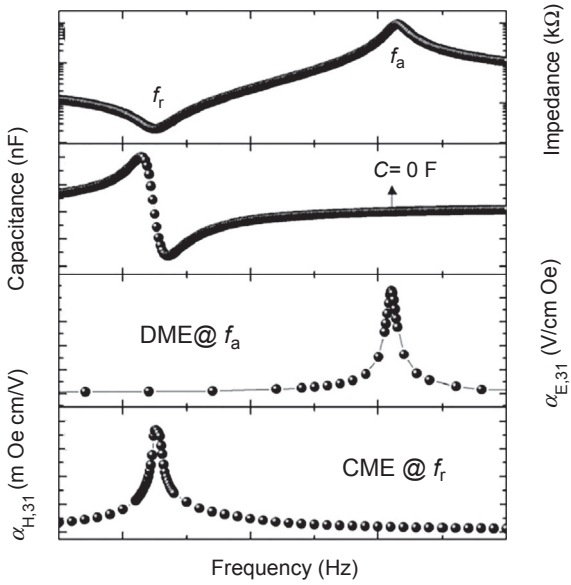

Figure 7.8 Impedance, capacitance, and ME behaviors as a function of AC frequency. Reproduced with permission from (Cho & Priya, 2011), Copyright 2011, AIP Publishing LLC.

constitutive equations and combining them with frequency-dependent capacitance of the piezoelectric layer.

Generally, for application of ME composites in EMR range, the fundamental resonance frequency can be tuned by the length of the laminates (l) where the first longitudinal resonance $f_L = 1/(2l\sqrt{\rho s_{11}})$ (ρ is the laminate density, s_{11} is the elastic compliance of the laminate) (Zhai et al., 2008). However, for practical use of the composites at low frequency, the corresponding composite dimension would be largely prohibitive. A recently developed analysis for bilayer ME composites operating at bending mode shows enhancement of the coupling at low frequency in unimorph configuration (Petrov, Srinivasan, Bichurin, & Galkina, 2009). Alternative approaches that utilize unique laminate configurations have been proposed to achieve low resonance frequency. Using these approaches, resonance enhancement of the ME coefficient has been achieved in the frequency range of 100 Hz, using cm-long laminates.

7.3.3.3 ME versus configuration

It is known that ME response as a function of DC magnetic field is tightly related with the nature of magnetostrictive materials. From the functional devices point of view, it is important to control the magnitude of ME voltage coefficient and its response. Thus, there are several investigations on shapes (disk, cylinder, plate, toroid, sphere, etc.) and dimensions (numbers of layers, layer thickness, length, and width) of the magnetostrictive material toward obtaining high ME voltage coefficient (Nan et al., 2008). It is widely accepted that an ME composite in a rectangular shape with a large length/width

aspect ratio, small thickness, and an optimized volume ratio will generate high ME voltage coefficient (Zhai et al., 2008). To better explain the ME versus configuration relationship, the size-induced demagnetization effect was taken into consideration. For ferromagnetic materials, the demagnetization field is directly proportional to the demagnetization factor (N_d), $H_d = MN_d$ (M is the magnetization), where N_d is dependent on the dimension and geometry. Thus, the internal effective magnetic field (H_{eff}) in the magnetic phase can be written as $H_{eff} = H_{bias} - H_d$, where H_{bias} is the induced external magnetic field. Therefore, in order to achieve the same magnitude of H_{eff}, one needs to apply larger H_{bias} when H_d is larger and vice versa (Zhou, Yang, Apo, Maurya, & Priya, 2012). Furthermore, this can also be corelated with the magnetic flux concentration (B_{eff}) in magnetic phase:

$$B_{eff} = \mu_0(H_{eff} + M) = \mu_0(H_{bias} + M) - \mu_0 M N_d, \tag{7.20}$$

where a smaller N_d will result in a stronger B_{eff}. It has been shown that high magnetic flux concentration in the magnetic phase has a positive effect on the ME response of ME laminates (Fang et al., 2009; Gao, Gray, Shen, Li, & Viehland, 2011). Thus, some researchers use the enlarged magnetic layer to enhance the effective magnetic flux density along the piezo/magnetic interface for obtaining a larger ME coefficient.

7.4 Self-biased magnetoelectric energy harvester

The dependence of a_{ME} on q indicates the requirement for additional DC magnetic bias. Depending on the optimum magnetic DC bias, ME composites can exhibit a maximum ME voltage coefficient. One needs to use a permanent magnet or electromagnet to provide external H_{bias}, which in turn results in problems of large device size and electromagnet interference. Thus, a novel design is desired if one needs to obtain an ME composite with large tunable α_{ME} in the absence of a DC magnetic field, which will pave the way for on-chip devices utilizing ME phenomenon, such as EH AC magnetic field sensors, and high frequency circuit components. Figure 7.9 illustrates the schematic of conventional ME composites and self-biased ME composites.

7.4.1 Development of self-biased ME composite

Results reported in literature have shown the ability to tune the magnitude of optimum DC bias ranging from 6.8 kOe to 5 Oe by optimizing the composition and shape of the magnetostrictive phase (Dong et al., 2006; Nan et al., 2008; Srinivasan, 2010). Furthermore, ME composite structures with large tunable a_{ME} in the absence of DC magnetic field, namely "self-biased ME composites," have been developed in various configurations using different working principles.

As early as 2002, Srinivasan et al. have shown hysteresis and remanence of a_{ME} as function of H_{bias} in cofired LSMO (lanthanum strontium manganite)-PZT laminates (Srinivasan et al., 2002). Since then, similar behavior has been found in other

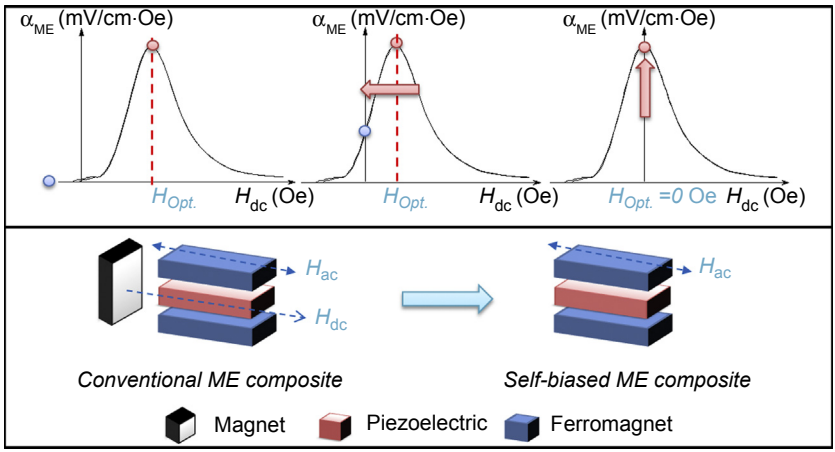

Figure 7.9 Schematic of conventional ME effect behavior and self-biased ME behavior.

laminates (Laletin et al., 2005). Recently, much effort has been focused on optimizing the materials, structures, and working mode to enhance the ME voltage coefficient and sensitivity (Nan et al., 2008; Zhai et al., 2008). In 2010, Mandal et al. demonstrated a compositionally graded ferrites/PZT laminate structure that generated non-zero ME voltage at zero DC magnetic bias (Mandal, Sreenivasulu, Petrov, & Srinivasan, 2010). This non-zero ME behavior was correlated with the presence of flexural deformation and grading induced out-of-plane internal magnetic field in the ferrite. Subsequently, Yang et al. presented a methodology that regular ME laminate composites can possess self-bias ME response by changing the vibration mode through electrical connections (Yang, Park, Cho, & Priya, 2010). Soon after that, Srinivasan et al. and his coworkers systematically investigated the hysteresis and remanence in ME effects in functionally graded magnetostrictive-piezoelectric layered composites (Laletin et al., 2012; Mandal, Sreenivasulu, Petrov, & Srinivasan, 2011; Sreenivasulu, Mandal, Bandekar, Petrov, & Srinivasan, 2011). Yang et al. first analytically studied the lead-free based self-biased laminates and proposed an electrically controlled core-free magnetic flux control device by using the self-biased CME effect (Yang et al., 2010; Yang, Ahn, et al., 2011; Yang, Cho, et al, 2011). Alternative approaches have been suggested for the case of thin films that rely on magnetic field dependence of resonance frequency and angular dependence of an exchange bias field (Lage et al., 2012; Onuta, Wang, Long, & Takeuchi, 2011). This phenomenon is promising for EH. The goal of studies on bulk structure has been mainly on understanding the nature of the self-biased effect in terms of grading of ferromagnetic composition and bending resonance. However, these structures present another level of practical difficulty for on-chip components as the synthesis process has to account for a heterogeneous graded structure or two-phase magnetic layers along with flexural deformation. Self-biased ME composites with a homogeneous magnetostrictive phase have also been developed. Yuan et al. first demonstrated a simple Ni/PZT bilayer laminate structure that

exhibits tunable self-bias phenomenon with single-phase magnetic material (Zhou et al., 2012). In this study, fundamental understanding of the role of domain structure and the demagnetization field of magnetic materials toward the self-biased effect was provided. The self-biased response was related to the nature of the magnetic phase and can be controlled by variation in the demagnetization state and the resultant differential magnetic flux distribution. Yan et al. have reported cofired self-biased composite NCZF/Ag/PMNPT/Ag/NCZF with a homogeneous magnetic phase (Yan, Zhou, et al., 2013). Cofired structure provides the opportunity of interfacial engineering to obtain the optimum strain transfer from two phases with a giant self-biased response >1 V/cm.Oe. The self-biased response in the cofired laminates is explained by the magnetostriction hysteresis of the magnetic phase and the built-in strain from the internal electrode during the cofiring process.

In summary, the working principle of the self-biased ME response can be categorized into three groups: (1) flexural deformation with graded ferromagnetic structure, (2) build-in stress arising from the inner electrode, and (3) nature of magnetization hysteresis in the magnetostrictive phase. The development of self-biased ME composites is schematically depicted in Figure 7.10. With the development of cofired techniques, self-biased ME response can be dramatically enhanced. Finally, with the discovery of tunable self-biased effect in homogeneous laminates, the self-biased behavior was successfully implemented into an energy harvesting device.

7.4.2 Working principle of Ni/PZT bilayer self-biased ME composite

Among all these different types of self-biased ME composites, the simple Ni/PZT bilayer laminate structure provides a promising design and potential toward the development of ME EH and MEMS scalable devices. Thus, we will discuss in detail the working principle of these Ni/PZT self-biased ME composites. To elucidate the reason for self-biased hysteretic behavior, a systematic study was conducted to compare Ni and Metglas under applied external magnetic field, as shown in Figure 7.11 (Zhou et al., 2012). The hysteretic behavior of magnetization for Ni can be immediately noticed in comparison with Metglas. This phenomenon could be attributed to the differences in the crystallinity and domain structure in both materials, as shown by magnetic force microscopy (MFM) images in the inset of Figure 7.11(a). Nanosized striped domains in Metglas can be easily aligned in the direction of applied H-field in comparison to that of macrosized domains in Ni. The absence of grain boundary in amorphous Metglas contributes toward the lower coercive field and high reversibility. However, nickel foil with long range ordering requires a higher field to achieve the random state, resulting in larger hysteresis in the magnetization curve. The magnetization behavior can be correlated with the magnetostriction through the relation given as (Ito, Aso, Makino, & Uedaira, 1980; Vlasko-Vlasov et al., 2000)

$$\varphi \sim \frac{3\lambda\sigma}{(K + 2\pi M^2)} \quad \text{or} \quad \lambda \propto M^2 \tag{7.21}$$

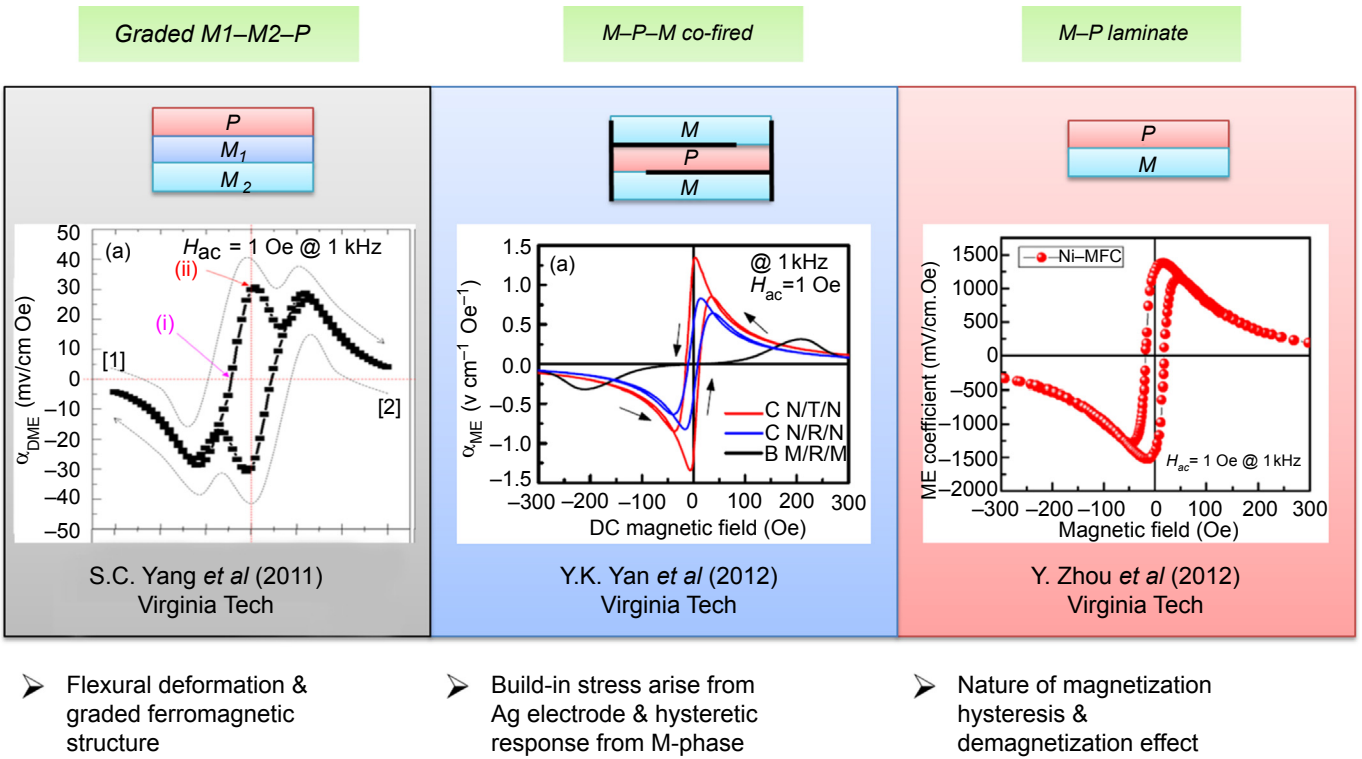

Figure 7.10 Development of self-biased magnetoelectric composite.
Reproduced with permission from Yan, Zhou, et al. (2013), Yang et al. (2011), Zhou et al. (2012), Copyright 2011, AIP Publishing LLC.

where φ is the angle of magnetic moments, and K and σ are the anisotropy constant and stress, respectively. Considering $\alpha_{ME} \propto q = d\lambda/dH$, the relationship $\alpha_{ME} \propto dM^2/dH$ can be used to predict the natural behavior of ME composites with respect to applied magnetic field. It was found that both of the M^2-H curve $(dM^2/dH)-H$ behaviors of Metglas and Ni match well with the experimental data of λ and q, as shown in Figure 7.11(b)–(d). Therefore, it is believed that the difference in the domain and microstructure of Metglas and Ni as observed by MFM and resultant different behavior of M^2-H and $(dM^2/dH)-H$ are the origin of the self-biased ME response. Thus, a ferromagnetic material like Ni, which has obvious hysteretic behavior of magnetostriction, and the non-zero piezomagnetic coefficient is essential for design of self-biased ME response.

From the point of view of functional ME devices, it is important to control the magnitude of self-biased ME voltage coefficient. As discussed earlier, ferromagnetic layer geometry plays an important role toward determining the demagnetization factor and the resultant effective internal magnetic field, leading to a shift of H_{bias} and tunability of the ME voltage coefficient. Thus, the self-biased response can be

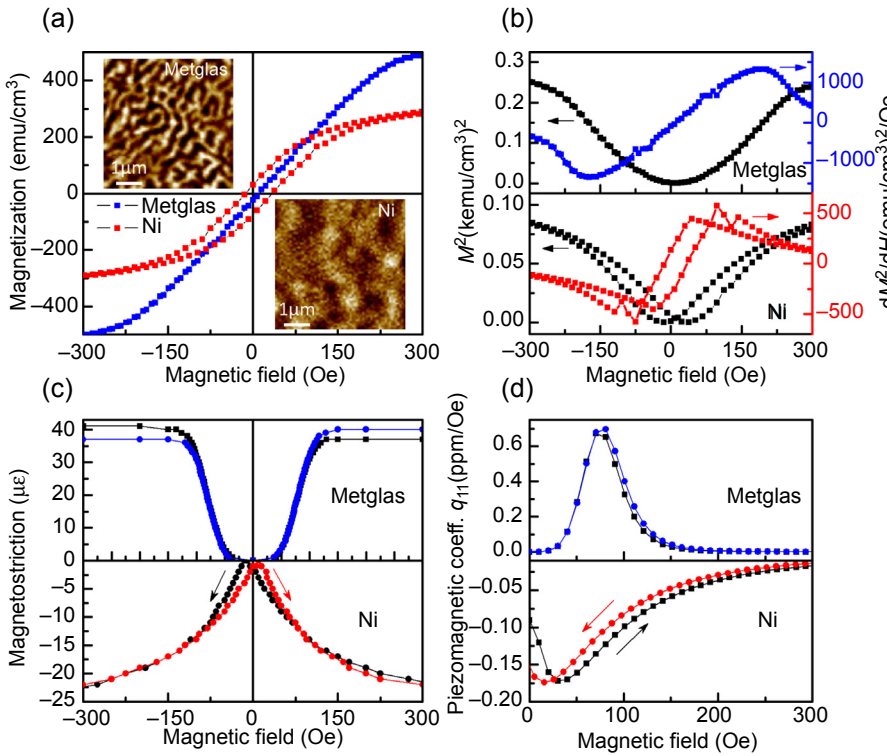

Figure 7.11 Magnetization, magnetostriction, and piezomagnetic coefficient of Metglas and Ni under applied DC magnetic field.
Reproduced with permission from Zhou et al. (2012), Copyright 2012, AIP Publishing LLC.

controlled by investigating the magnetostrictive phase geometry effect, as shown in Figure 7.12 (Zhou et al., 2012).

In all cases, a_{ME} shows a hysteretic loop with anticlockwise direction sweep. The values of increasing-field maximum (a_{H1}) and decreasing-field maximum (a_{H2}) with a thicker Ni layer were notably higher than that for thinner ones, while also requiring larger magnetic biases (increasing-field optimum, $H1$ and decreasing-field optimum, $H2$). The magnitude of self-biased point (a_{H0}) slightly decreases as thickness ratio increases, as shown in Figure 7.12(c). The maximum self-biased ME response was achieved at $t_{m/p} = 0.5$. With a fixed thickness ratio at $t_{m/p} = 0.5$, as shown in Figure 7.12(b), the magnitude of $a_{H0\sim H2}$ increased dramatically as lateral ratio ($L_{m/p}$) increased from 0.5 to 2. Notably, a giant self-bias coefficient (a_{H0}/a_{H2}) of 97% was achieved at $L_{m/p} = 2$, compared to 34.4% and 72.5% at $L_{m/p} = 0.5$ and 1, as shown in Figure 7.12(d). The hysteresis loop was tilted toward the y-axis as the optimum magnetic bias ($H1$ and $H2$) decreased. Based upon these results, one can obtain and tune the self-bias coefficient by selecting a suitable magnetic phase with proper geometry and dimension.

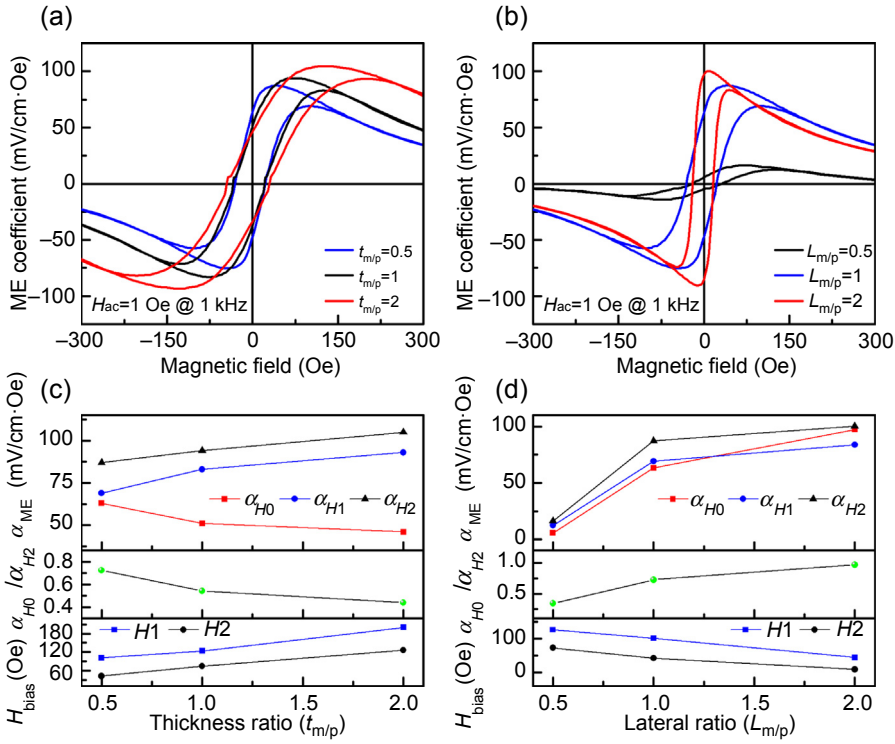

Figure 7.12 Magnetostrictive phase geometry effect on the tunablility of self-biased response for the Ni/PZT bilayer system.
Reproduced with permission from Zhou et al. (2012), Copyright 2012, AIP Publishing LLC.

7.4.3 Self-biased magnetoelectric energy harvester

Based on the understanding of Ni/PZT self-biased ME composite, Zhou et al. developed the ME EH that can scavenge stray AC magnetic field in the absence of DC magnetic field (Zhou et al., 2013). The device consists of a piezoelectric microfiber composite (MFC) bonded to a Ni plate in a cantilever configuration. Figure 7.13 illustrates the performance of the Ni−MFC self-biased EH.

As most of the ferromagnetic materials exhibit zero piezomagnetic coefficient near zero bias (Nan et al., 2008), the a_{ME} of a Metglas-MFC structure increases from zero to a peak value at the optimum bias and then decreases. In comparison, the a_{ME} of an Ni−MFC bilayer shows a hysteretic behavior during H_{dc} sweep (anticlockwise direction) with a large response of $\sim\pm1.25$ V/cm Oe at zero DC magnetic bias, $\sim$98% of the maximum ME value (1.38 V/cm Oe). This results from the hysteretic behavior of magnetostriction and non-zero piezomagnetic coefficient, as discussed in previous sections (Zhou et al., 2012).

Under zero-biased condition ($H_{dc} = 0$ Oe), resonance peaks with improved ME voltage output corresponding to bending modes were observed, as shown in Figure 7.13(b). It should be noted that even though there was no applied H_{dc}, self-biased ME response follows the same trend and exhibits enhanced magnitude

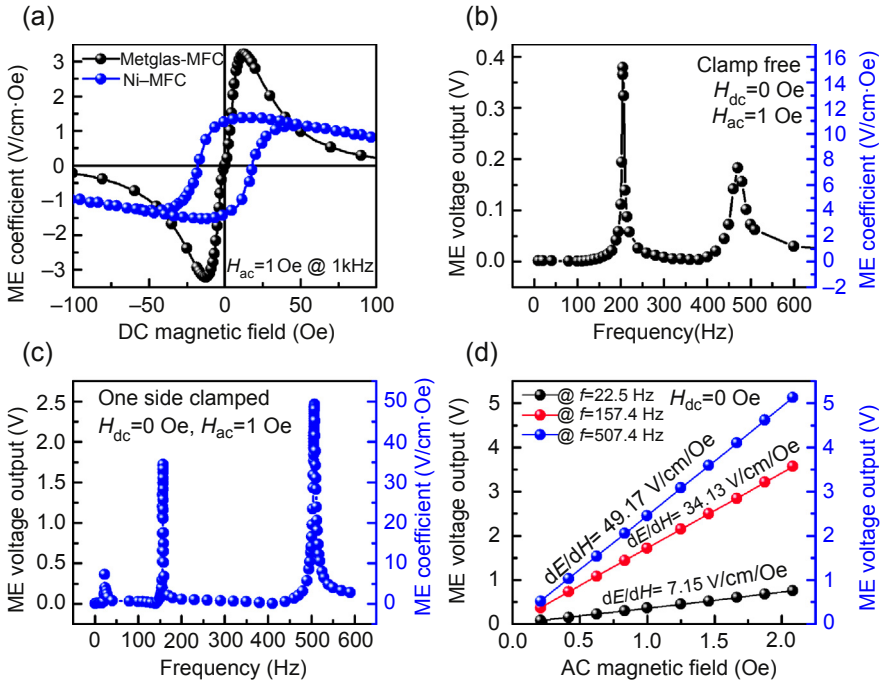

Figure 7.13 Performance of the Ni−MFC self-biased energy harvester.
Reproduced with permission from Zhou et al. (2013), Copyright 2013, AIP Publishing LLC.

of voltage coefficient at resonance frequency (Zhou et al., 2012). The ME laminate was further clamped at one end and attached a Ni tip mass at the free end for enhancing the bending vibration and reducing the resonance frequency, as shown in Figure 7.13(c). The ME voltage output increased with increasing frequency where the maximum ME coefficient with the magnitude of ~50 V/cm Oe was obtained at the resonance frequency of 507.4 Hz. Figure 7.13(d) shows that the ME voltage output linearly increased with increasing AC magnetic field at three longitudinal resonance frequencies. The a_{ME} calculated from the slope matches quite well with the measured value in Figure 7.13(c). Large ME voltage with the magnitude of >5 V was achieved at 507.4 Hz, $H_{ac} = 2$ Oe, which can be further increased with increasing H_{ac}. Alternatively, by changing the MFC into a single crystal fiber composite (SFC), Patil et al. was able to further enhance the ME coupling with ~82.9 V/cm Oe for the laminate with [011]-d_{32} SFC (Patil et al., 2014).

These results clearly demonstrate that, by using self-biased ME EH large ME voltage can be generated under zero-biased condition and can be further improved by increasing the AC magnetic field strength at resonance mode. It should be noted here that all the previous investigations on the ME harvesters have revealed that the requirement of DC magnetic field is indispensable to enhance the power output (Dai et al., 2009; Dong et al., 2008; Kambale & Yoon et al., 2013; Zhou et al., 2013). The simple structure of this self-biased ME EH provides great potential toward developing an MEMS-scalable high-performance energy harvesting system.

7.5 Multimode magnetoelectric energy harvester

7.5.1 Motivation for multimode energy harvester

Miniaturization and decrease in power consumption has given rise to the popularity of energy harvesting systems that can scavenge ambient energy to support power requirements in integrated circuits, sensors, and actuators (Paradiso & Starner, 2005). The majority of the work done in the energy harvesting system to date has focused on a single energy source, with most of the energy conversion coming from corresponding materials or structures (Anton & Sodano, 2007; Beeby et al., 2006; Priya, 2007). However, the target ambient energy is commonly in coexistence with other energy sources. For example, vibration fields generally can coexist with electromagnetic fields in industrial areas, solar energy can be commonly found together with wind in nature, and heat transfer is commonly associated with material property variation. Thus, an energy harvesting system that can simultaneously scavenge different forms of energy is desired, so that these unused energies can be more effectively and complementarily scavenged.

Recently, some researchers have made attempts at combining various mechanisms (solar, piezoelectric, magnetostrictive, electromagnetic, thermoelectric, and so on) to realize multimode EH with enhanced power density and harvesting efficiency. Yang

et al. proposed a flexible hybrid energy cell that is capable of simultaneously or individually harvesting thermal, mechanical, and solar energies to power electronic devices (Yang et al., 2013). In this design, a polarized PVDF nanogenerator was used for collecting thermal and mechanical energies and a ZnO-poly(3-hexylthiophene) (P3HT) heterojunction was designed for harvesting solar energy. The harvested energy can drive four red light-emitting diodes (LEDs) in parallel connection. Similarly, Gambier et al. developed a multilayer structure with flexible solar, piezoelectric ceramic, thin film battery, and metallic substructure layer in a cantilever configuration (Gambier, Anton, Kong, Erturk, & Inman, 2012). Using this device, they were able to charge 1 mA h of the thin film battery in 20 min using solar energy and in 8 h using vibration energy (0.5 *g* at 56.4 Hz). Other multimode EH have also been developed for scavenging sound and solar energies (Lee, Yang, Li, & Wang, 2010), thermal and solar energies (Guo et al., 2010), and biochemical and biomechanical energies (Pan, Li, Guo, Zhu, & Wang, 2011). These results provide a new trend toward developing multifunctional energy harvesting systems.

7.5.2 Development of multimode magnetoelectric energy harvester

The ME composites, combining piezoelectric and magnetostrictive phases, have been found useful in both magnetic and vibration harvesting applications, because of the coexistence of piezoelectric and ME effects. That is, the electric charges can be generated from mechanical vibration at the piezoelectric layer through a direct piezoelectric effect, and the magnetic field-induced magnetostriction can be converted into charges through a DME effect. The combination is expected to enhance the energy collection and conversion efficiency. Dong et al. demonstrated a multimodal system for harvesting magnetic and mechanical energy that consisted of a cantilever beam with tip mass and a ME laminate attached in the center of the beam. The device was shown to generate an open circuit voltage of $8V_{p-p}$ under vibration of 50 mg and AC magnetic field of 2 Oe (Dong et al., 2008). Further, by utilizing a PMN-PZT single crystal/Ni cantilever laminate, Kambale et al. were able to obtain a maximum a_{ME} and power output of 7.28 V/cm Oe and 1.31 mW at resonance mode under 0.7 g acceleration (Kambale & Yoon et al., 2013). However, in these combinations, solenoid and/or permanent magnet is required as the DC magnetic field source, which dramatically increases the size and therefore limits the power density.

In addressing these issues, Zhou et al. recently reported an ME energy harvesting system utilizing self-biased ME response, which can generate a giant output performance in the absence of DC magnetic field (Zhou et al., 2013). An additive effect was realized when the harvester operated under dual-phase mode. Large ME coefficient $\sim$50 V/cm Oe and power density $\sim$4.5 mW/cm^3 (1 g acceleration) were observed at the resonance frequency. These results on a dual-phase ME EH present significant advancement toward a high energy density harvesting system.

7.5.3 Dual-phase self-biased magnetoelectric energy harvester

The harvester was designed by combining self-biased ME laminate (Figure 7.14(a)) and piezoelectric unimorph (Figure 7.14(b)) structure in a cantilever configuration. The schematic design of the EH is illustrated in Figure 7.14(c). The prototype consisted of a magnetostrictive/piezoelectric (M/P) laminate structure fabricated by using an MFC and a layer of 0.25-mm-thick Ni beam. The composite was laminated by using epoxy resin. A series of Ni disks were added as tip mass at the free end of cantilever for dynamic force excitation at the mechanical resonance.

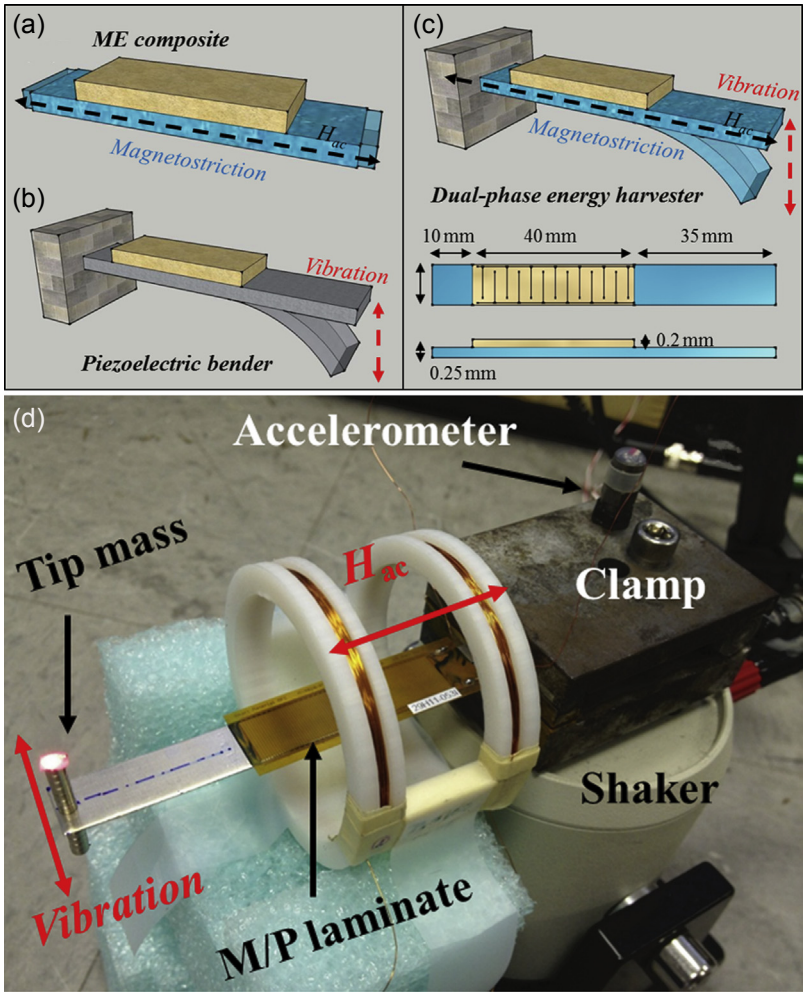

Figure 7.14 Schematic diagrams depicting the (a) ME composite, (b) piezoelectric bender, and (c) dual-phase self-biased ME energy harvester; (d) picture of the Ni−MFC dual-phase ME EH and its experimental setup for characterization.
Reproduced with permission from Zhou et al. (2013), Copyright 2013, AIP Publishing LLC.

The Ni beam plays several important roles in this configuration: (1) a magnetostrictive phase in the ME laminate, (2) a magnetic-field-active cantilever for the piezoelectric bender, and (3) a ferromagnetic phase with low field magnetic hysteresis and non-zero piezomagnetic coefficient that is essential for self-biased ME response (Zhou et al., 2012). When placed in an AC magnetic field, the magnetostrictive layer responds by elongating or contracting, thereby straining the piezoelectric layer that results in output voltage across electrical load. Under the external vibration, oscillation of the cantilever can directly create strain in the piezoelectric layer and therefore produce electrical voltage. In the absence of the applied DC magnetic field, large ME voltage can still be obtained via the self-biased ME effect. Thus, by incorporating a self-biased magnetostriction layer as a substrate for the piezoelectric layer, an ME harvester can be created for harnessing energy from both vibrations and AC magnetic field at the same time without the need for DC bias. The performance of the dual-phase harvester was demonstrated by exciting the bender with a stray magnetic field and mechanical vibration simultaneously, as shown in Figure 7.15. For comparison, open circuit voltage of the EH at the first three resonance frequencies was measured separately under: (1) stray magnetic field only ($H_{ac} = 1$ Oe), (2) mechanical vibration only ($a = 0.05$ g), and (3) dual-phase ($H_{ac} = 1$ Oe plus $a = 0.05$ g) mode.

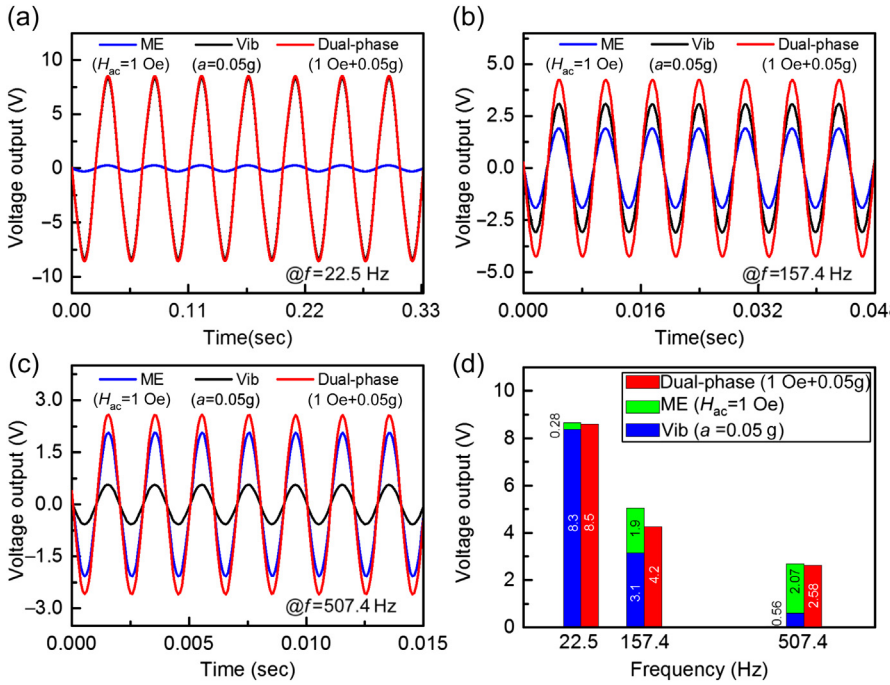

Figure 7.15 Performance of the dual-phase energy harvester working under mechanical vibration and magnetic field.
Reproduced with permission from Zhou et al. (2013), Copyright 2013, AIP Publishing LLC.

The output voltage under dual-phase mode was improved over a wide range of frequency, which implies that both power density and efficiency were enhanced through additive effect. To further quantify this combined response, the peak voltage at each single mode was added and compared with the dual-phase mode as a function of operating frequency, as shown in Figure 7.15(d). In this bar chart, it is obvious that the peak voltage under dual-phase mode is close to the summation of peak voltage under each single mode, implying an additive effect was found in the dual-phase EH. The increase in voltage output at the first three resonance frequencies under dual-phase mode was found to be 2.4%, 35.5%, and 360.7%.

In summary, large power density was achieved from the ME cantilever under mechanical excitation, which was further enhanced with the coexistence of AC magnetic field. The power output of the dual-phase, self-biased ME EH can be further improved by synchronizing the transversal (vibration) and longitudinal (magnetostriction) resonance frequency.

7.5.4 Theoretical modeling

As already mentioned above, the energy collection and conversion effectiveness are expected to be enhanced under magnetic and mechanical excitation. We consider a configuration designed by combining a bilayer of MFC and Ni and Ni unimorph, as shown in Figure 7.14. Theoretical modeling rests on the assumption that the sample undergoes the superposition of axial and bending strain (Bichurin & Petrov, 2014). These strains can be calculated by using the elastostatic/elastodynamic equations, and then they can be expressed in terms of stress components with the aid of elasticity law. To obtain the expression for the ME voltage coefficient, we substitute the found stress components into the open circuit condition.

The analysis described here is based on the equations for the strain, electric displacement, and magnetic induction of piezoelectric and magnetostrictive phases (Bichurin & Petrov, 2012):

$$\begin{aligned} {}^{p}S_i &= {}^{p}s_{ij}{}^{p}T_j + {}^{p}d_{ki}{}^{p}E_k; \\ {}^{p}D_k &= {}^{p}d_{ki}{}^{p}T_i + {}^{p}\varepsilon_{kn}{}^{p}E_n; \\ {}^{m}S_i &= {}^{m}s_{ij}{}^{m}T_j + {}^{m}q_{ki}{}^{m}H_k; \\ {}^{m}B_k &= {}^{m}q_{ki}{}^{m}T_i + {}^{m}\mu_{kn}{}^{m}H_n; \end{aligned} \tag{7.22}$$

where S_i and T_j are strain and stress tensor components, E_k and D_k are the vector components of electric field and electric displacement, H_k and B_k are the vector components of magnetic field and magnetic induction, s_{ij}, q_{ki}, and d_{ki} are compliance, piezomagnetic, and piezoelectric coefficients, ε_{kn} is the permittivity matrix, and μ_{kn} is the permeability matrix. The superscripts p and m correspond to piezoelectric and piezomagnetic layers, respectively. We assume the symmetry of piezoelectric to be ∞ m and the magnetic to be cubic. It should be noted that most ferromagnetic materials show the magnetostrictive effect; however, piezomagnetic effect in these materials is

not observed. Linearity in such composites is achieved by applying a bias magnetic field and AC magnetic field with amplitude, which is assumed to be small compared to bias field. Thus, the ME effect over a short range around this bias field can be approximated as a linear effect. Two types of magnetostriction have been known to date: Volume and Joule magnetostriction. In Volume magnetostriction, the magnetic field leads to an isotropic change of the shape in all dimensions. Joule magnetostriction leads to a change of shape in the direction of the magnetic field, while maintaining a constant volume. There is also a deformation associated with the Joule magnetostriction in the orthogonal direction to the field. This has the opposite sign and half the amplitude and is called transverse magnetostriction. We confine ourselves to consideration of Joule magnetostriction since, in general, volume magnetostriction is far smaller than Joule magnetostriction.

We consider a model for ME coupling at bending resonance in the sample (Bichurin, Petrov, & Petrov, 2012; Bichurin, Petrov, Petrov, & Priya, 2012). We assume the sample in the (x,y) plane with its thickness along the z-axis. The small-amplitude bending oscillations of the sample are governed by the following equations for the MFC−Ni bilayer and Ni unimorph:

$$\nabla^2\nabla^2 w + \frac{\rho\ t}{D}\frac{\partial^2 w}{\partial \tau^2} = 0, \tag{7.23}$$

$$\nabla^2\nabla^2 w_1 + \frac{{}^m\rho\ {}^m t}{{}^m D}\frac{\partial^2 w_1}{\partial \tau^2} = 0, \tag{7.24}$$

where $\nabla^2\nabla^2$ is biharmonic operator, w and w_1 are the deflections (displacements in z-direction) for MFC−Ni bilayer and Ni unimorph, t and ρ are thickness and average density of the bilayer, $t = {}^p t + {}^m t$, $\rho = ({}^p\rho\,{}^p t + {}^m\rho\,{}^m t)/t$, with ${}^p\rho$, ${}^m\rho$, ${}^p t$, and ${}^m t$ are densities and thicknesses of piezoelectric and magnetic layers, respectively, τ is the time, and D and ${}^m D$ is cylindrical stiffness for bilayer and Ni unimorph. The thickness of the sample is assumed to be small compared to other dimensions and its width small compared to its length. In that case, we can consider only one component of strain and stress. The MFC−Ni bilayer with length L is assumed to be joined at $x = L$ to an Ni plate with length L_1.

The cylindrical stiffness D of the bilayer can be calculated using the standard technique (Timoshenko & Young, 1968):

$$D = {}^p D + {}^m D + 3\left(\frac{(1-V)^2}{{}^m D} + \frac{V^2}{{}^p D}\right)^{-1}, \tag{7.25}$$

where V is the volume fraction of piezoelectric component. Cylindrical stiffness ${}^m D$ and ${}^p D$ of magnetostrictive and piezoelectric components are defined by well-known expressions: ${}^m D = 1/12\,{}^m Y {}^m t^3$, ${}^p D = 1/12\,{}^p Y {}^p t^3$ with ${}^m Y$ and ${}^p Y$ being the modules of elasticity of piezomagnetic and piezoelectric components at constant B and E, respectively.

The induced voltage is calculated at open circuit condition $\int_0^L {}^pD_3 \mathrm{d}x = 0$ with ${}^pD_3$ denoting the electric induction. Using Eqn (7.22), the ME voltage coefficient $\alpha_E = E_3/H_1$ can be found as

$$\alpha_E = -\int_A \frac{{}^pd_{31}{}^pT_1}{A\ H_1{}^p\varepsilon_{33}}\mathrm{d}S, \tag{7.26}$$

where A is the cross section of piezoelectric layer in (x,z) plane.

The expression for stress component ${}^pT_1$ in Eqn (7.26) was found from the law of elasticity (Eqn (7.22)) for the piezoelectric layer. The strains in Eqn (7.22) can be expressed in terms of deflection as ${}^pS_1 = -z\frac{\partial^2 w}{\partial x^2}$, where z is measured from the middle plane of the sample. The position of the middle plane is generally defined by equating the total force in x-direction to zero along the bilayer cross section. This force is determined by stresses in bilayer components.

In what follows, we restrict ourselves to the case of harmonic oscillations. Since solutions of Eqn (7.23) depend on sample's end conditions, we consider several types of end fixity conditions.

7.5.4.1 Sample free at both ends

For this case, the boundary conditions take on the form:

$$M_y = 0 \text{ and } V_y = 0 \text{ at } x = 0 \text{ and } x = L + L_1;$$

where M_y is the torque moment relative to y-axis produced by internal stresses per unit width, and V_y is the transverse force per unit width.

The torque moment of bilayer per unit width is calculated based on the expressions for internal stresses:

$$M_y = -\int_{z_0-{}^pt}^{z_0} {}^pY\left(-z\frac{\partial^2 w}{\partial x^2} - {}^pd_{31}{}^pE_3\right)z\mathrm{d}z - \int_{z_0}^{z_0+{}^mt} {}^mY\left(-z\frac{\partial^2 w}{\partial x^2} - {}^mg_{11}{}^mB_1\right)z\mathrm{d}z, \tag{7.27}$$

where piezomagnetic coefficient ${}^mg_{11}$ is defined as $\partial^m S_1/\partial^m B_1$.

For Ni unimorph, the torque moment of bilayer per unit width is determined in a similar way by setting the first term in Eqn (7.27) equal to zero.

The transverse force is defined by

$$V_y = \frac{\partial M_y}{\partial x}. \tag{7.28}$$

The final expression for ME voltage coefficient is not cited here because of space limitation, and we restrict ourselves to numerical calculations. Figure 7.16 shows the frequency dependence of ME voltage coefficient for a free-standing sample.

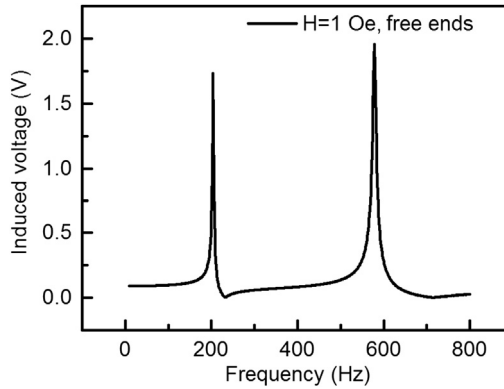

Figure 7.16 Frequency dependence of ME voltage coefficient for the sample free at both ends in applied magnetic field of 1 Oe.

7.5.4.2 MFC–Ni cantilever joined to Ni plate with tip mass

We use the boundary conditions for the bilayer rigidly clamped at one end (at $x = 0$) and joined to an Ni plate with length L_1 at $x = L$. Boundary conditions for the Ni plate take into account the end tip mass and can be written as

$$M_y = \partial w/\partial x\, I\omega^2/b \quad \text{and} \quad V_y = -m\, w\omega^2/b \ \text{ at } \ x = L + L_1,$$

where m and I are mass and moment of inertia of tip mass with respect to axis that is positioned in the middle plane along y-axis, correspondingly, and b is the sample width.

The frequency dependence of ME voltage coefficient for an MFC–Ni cantilever joined to Ni plate with end tip mass is shown in Figure 7.17.

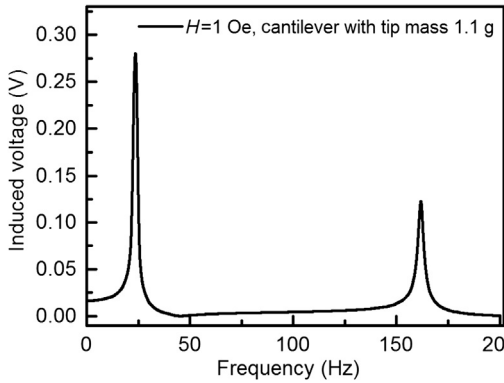

Figure 7.17 Frequency dependence of open circuit voltage in an applied magnetic field of 1 Oe.

7.5.4.3 *Dual-phase energy harvester under magnetic and mechanical excitation*

To enable the summation effect for both mechanical and magnetic energies, a configuration designed by combining a bilayer of MFC and Ni and Ni unimorph is considered (Figure 7.14). The stress and magnetic field energy could be converted into electric charges in the piezoelectric layer through a direct piezoelectric effect and ME effect, correspondingly. This combination should enhance energy collection.

In contrast to the case considered above, the boundary conditions for the bilayer should take into account the rigid clamping and acceleration $\boldsymbol{a}$ induced by a shaker along the z-axis at $x = 0$. So we have

$$\partial w/\partial x = 0 \quad \text{and} \quad \partial^2 w/\partial \tau^2 = a \ \text{ at } x = 0.$$

The frequency dependence of output voltage for this case is shown in Figure 7.18. The acceleration of the sample at clamped end is assumed frequency-independent.

The frequency dependence of output voltage under magnetic and acceleration of clamped end is shown in Figure 7.19.

Figure 7.19 shows that the output voltage from the vibration and AC magnetic field is much higher at first bending mode. For the case when the shaker provides peak displacement w_0 for any frequency, the boundary conditions for the bilayer take on the form:

$$w = w_0 \quad \text{and} \quad \partial w/\partial x = 0 \ \text{ at } x = 0.$$

The frequency dependence of output voltage for this case is shown in Figure 7.20. The displacement of the sample at clamped end is assumed frequency-independent.

The frequency dependence of output voltage under magnetic and displacement of clamped end is shown in Figure 7.21.

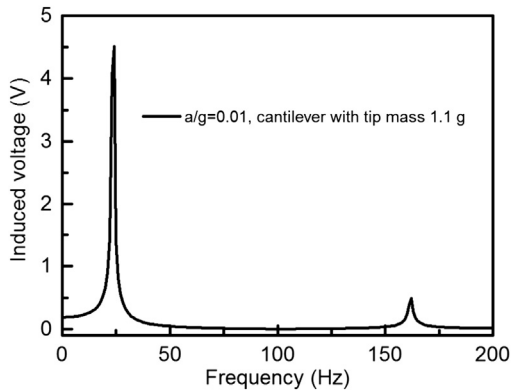

Figure 7.18 Frequency dependence of open circuit voltage induced by shaker acceleration of 0.01 g.

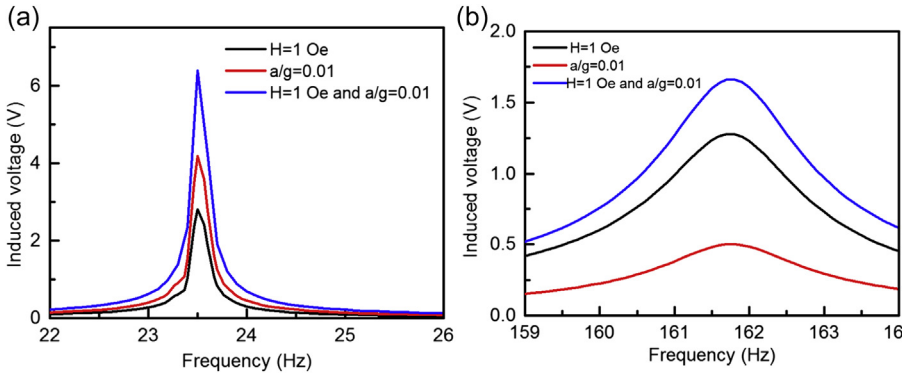

Figure 7.19 Frequency dependence of open circuit voltage induced by applied magnetic field and acceleration of shaker for the first (a) and second (b) resonance peaks.

One can see a qualitative agreement between the theoretical estimates and experimental data from Yuan et al. (Zhou et al., 2013) as discussed in previous sections. However, there are several reasons for some quantitative distinction between them: (1) incomplete clamping (clamping section should provide a zero slope angle, $\partial w/\partial x = 0$); (2) deviation of length and thickness of active zone and Ni plate; and (3) deviation of density and Young's modulus.

7.6 Low frequency and wideband magnetoelectric energy harvester

Most EH which rely on a piezoelectric layer for voltage generation (including ME EH) tend to produce significant power output only at the resonance frequency. Since most natural sources occur at low frequencies, the design of the EH must be suited to these

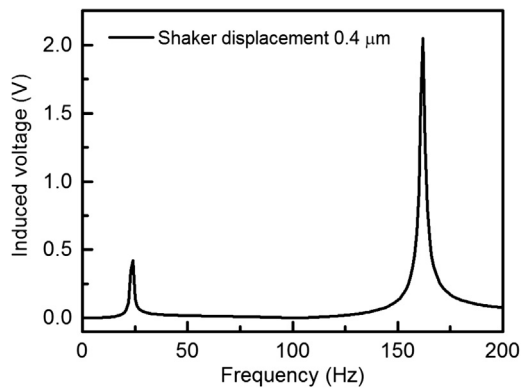

Figure 7.20 Frequency dependence of open circuit voltage induced by shaker displacement of 0.4 μm.

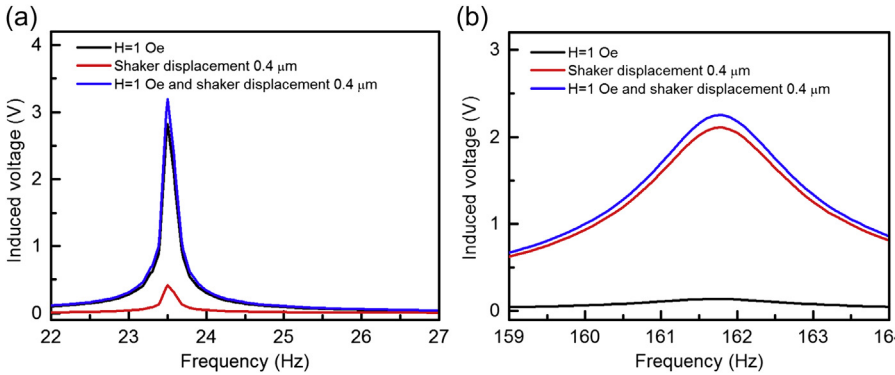

Figure 7.21 Frequency dependence of open circuit voltage induced by applied magnetic field and displacement of shaker for the first (a) and second (b) resonance peaks.

low frequencies to ensure the maximum power available is harvested. Furthermore, wideband energy harvesting has been pursued as a way to reduce the reliance on the exact resonance frequency of the EH, thus ensuring significant power is produced at a wide range of frequencies.

7.6.1 Low frequency structure—the ABC harvester

The arc-based cantilever (ABC) concept was introduced by Apo et al. (Apo, Sanghadasa, & Priya, 2013, 2014; Apo, Zhou, et al., 2014) to obtain low natural frequencies in MEMS EH and increase the surface area available for energy harvesting. An arc-based cantilever is a continuous cantilever that can be divided into circular arc segments, thereby making it a low frequency structure with dominant bending characteristics in the first (or fundamental) frequency mode. This unique design also ensures pure bending in the first mode when the cantilever is excited in the transverse direction. For dual mode energy harvesting, the circular arcs are strained transversely during vibrations, while the center disc is strained longitudinally in response to an applied magnetic field. As shown in Figure 7.22, a modified unimorph arc-based cantilever was designed for dual-phase ME energy harvesting, with PVDF and Metglas being the piezoelectric and magnetostrictive layers, respectively.

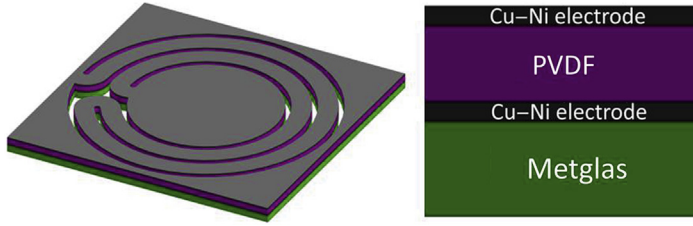

Figure 7.22 Design of the unimorph ABC magnetoelectric energy harvester.

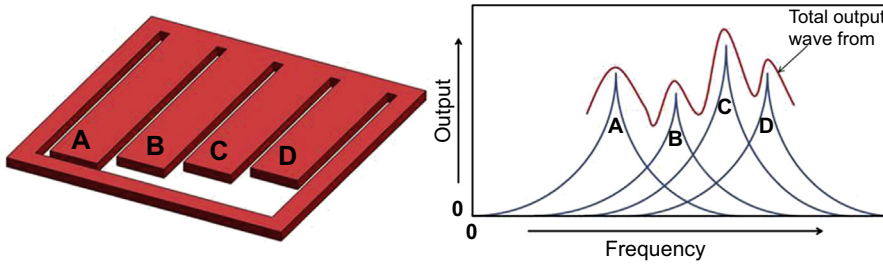

Figure 7.23 Design of the multiple cantilever harvester and typical output waveform from the cantilevers.

7.6.2 Wideband structure—the multiple cantilever harvester

The multiple cantilever design includes the simple straight cantilevers of different lengths that resonate at frequencies close to each other. Therefore, the entire device is quasi-broadband, as shown in Figure 7.23. The challenge with this design is reducing the losses associated with adding the individual voltages produced by the cantilevers. A series electrical combination will create significant losses, while separate connections of wires to the cantilever electrodes will be messy (Liu et al., 2008). The advantages of the multiple cantilever design include wideband energy harvesting and tunability of the output response.

Acknowledgments

The authors gratefully acknowledge the financial support from the Office of Basic Energy Science, Department of Energy (DOE) and Air Force Office of Scientific Research (AFOSR). The authors also thank the Office of Naval Research (ONR) for supporting the research (Y. Z.) through the Center for Energy Harvesting Materials and Systems (CEHMS).

References

Anton, S. R., & Sodano, H. A. (2007). A review of power harvesting using piezoelectric materials (2003−2006). *Smart Materials and Structures, 16*, R1−R21.

Apo, D. J., & Priya, S. (2014a). High power density levitation-induced vibration Energy harvester. *Energy Harvesting and Systems, 1*, 79.

Apo, D. J., & Priya, S. (2014b). Levitation-induced vibration energy harvesters. In *Proc. 12th international conference on motion and vibration control (MoViC 2014), Sapporo, Japan*.

Apo, D. J., Sanghadasa, M., & Priya, S. (2013). Low frequency arc-based MEMS structures for vibration energy harvesting. In *Proc. Nano/Micro engineered and molecular systems (NEMS), 2013 8th IEEE international conference on* (pp. 615−618).

Apo, D. J., Sanghadasa, M., & Priya, S. (2014). Vibration modeling of arc-based cantilevers for energy harvesting applications. *Energy Harvesting and Systems, 1*, 1−12.

Apo, D. J., Zhou, Y., Sanghadasa, M., & Priya, S. (2014). Vibration characteristics of low frequency arc-based microcantilevers. *Journal of Applied Physics*.

Bai, X., Wen, Y., Yang, J., Li, P., Qiu, J., & Zhu, Y. (2012). A magnetoelectric energy harvester with the magnetic coupling to enhance the output performance. *Journal of Applied Physics, 111*, 07A938−3.

Beeby, S. P., Torah, R. N., Tudor, M. J., Glynne-Jones, P., Donnell, T. O., et al. (2007). A micro electromagnetic generator for vibration energy harvesting. *Journal of Micromechanics and Microengineering, 17*, 1257.

Beeby, S. P., Tudor, M. J., & White, N. M. (2006). Energy harvesting vibration sources for microsystems applications. *Measurement Science and Technology, 17*, R175−R195.

Bichurin, M. I., Filippov, D. A., Petrov, V. M., Laletsin, V. M., Paddubnaya, N., & Srinivasan, G. (2003). Resonance magnetoelectric effects in layered magnetostrictive-piezoelectric composites. *Physical Review B, 68*.

Bichurin, M. I., & Petrov, V. M. (2012). Modeling of magnetoelectric interaction in magnetostrictive-piezoelectric composites. *Advances in Condensed Matter Physics*, 798310.

Bichurin, M. I., & Petrov, V. M. (2014). *Modeling of Magnetoelectric Effects in Composites. Springer Series in Materials Science* (Vol. 201).

Bichurin, M. I., Petrov, V. M., & Petrov, R. V. (2012). Direct and inverse magnetoelectric effect in layered composites in electromechanical resonance range: a review. *Journal of Magnetism and Magnetic Materials, 324*, 3548−3550.

Bichurin, M. I., Petrov, V. M., Petrov, R. V., & Priya, S. (2012). Electromechanical resonance in magnetoelectric composites: direct and inverse effect. *Solid State Phenomena, 189*, 129−143.

Bichurin, M., Petrov, V., Kiliba, Y., & Srinivasan, G. (2002). Magnetic and magnetoelectric susceptibilities of a ferroelectric/ferromagnetic composite at microwave frequencies. *Physical Review B, 66*.

Bichurin, M., Petrov, V., Ryabkov, O., Averkin, S., & Srinivasan, G. (2005). Theory of magnetoelectric effects at magnetoacoustic resonance in single-crystal ferromagnetic-ferroelectric heterostructures. *Physical Review B, 72*.

Byung-Chul, L., Md Ataur, R., Seung-Ho, H., & Gwiy-Sang, C. (2012). Low frequency driven electromagnetic energy harvester for self-powered system. *Smart Materials and Structures, 21*, 125024.

Cepnik, C., Radler, O., Rosenbaum, S., Ströhla, T., & Wallrabe, U. (2011). Effective optimization of electromagnetic energy harvesters through direct computation of the electromagnetic coupling. *Sensors and Actuators A: Physical, 167*, 416−421.

Ching, N. N. H., Wong, H. Y., Li, W. J., Leong, P. H. W., & Wen, Z. (2002). A laser-micromachined multi-modal resonating power transducer for wireless sensing systems. *Sensors and Actuators A: Physical, 97−98*, 685−690.

Cho, K.-H., & Priya, S. (2011). Direct and converse effect in magnetoelectric laminate composites. *Applied Physics Letters, 98*, 232904.

Dai, X., Wen, Y., Li, P., Yang, J., & Li, M. (2011). Energy harvesting from mechanical vibrations using multiple magnetostrictive/piezoelectric composite transducers. *Sensors and Actuators a-Physical, 166*, 94−101.

Dai, X., Wen, Y., Li, P., Yang, J., & Zhang, G. (2009). Modeling, characterization and fabrication of vibration energy harvester using Terfenol-D/PZT/Terfenol-D composite transducer. *Sensors and Actuators a-Physical, 156*, 350−358.

Dong, S., Bai, J. G., Zhai, J., Li, J.-F., Lu, G. Q., et al. (2005). Circumferential-mode, quasi-ring-type, magnetoelectric laminate composite—a highly sensitive electric current and/or vortex magnetic field sensor. *Applied Physics Letters, 86*, 182506.

Dong, S., Li, J. F., & Viehland, D. (2004). Voltage gain effect in a ring-type magnetoelectric laminate. *Applied Physics Letters, 84*, 4188.

Dong, S., Zhai, J., Li, J., & Viehland, D. (2006). Near-ideal magnetoelectricity in high-permeability magnetostrictive/piezofiber laminates with a (2-1) connectivity. *Applied Physics Letters, 89*, 252904.

Dong, S. X., Zhai, J. Y., Li, J. F., Viehland, D., & Priya, S. (2008). Multimodal system for harvesting magnetic and mechanical energy. *Applied Physics Letters, 93*.

Erturk, A., & Inman, D. J. (2008). A distributed parameter electromechanical model for cantilevered piezoelectric energy harvesters. *Journal of Vibration and Acoustics, 130*, 041002−041015.

Erturk, A., & Inman, D. J. (2009). An experimentally validated bimorph cantilever model for piezoelectric energy harvesting from base excitations. *Smart Materials and Structures, 18*, 025009.

Fang, Z., Lu, S. G., Li, F., Datta, S., Zhang, Q. M., & El Tahchi, M. (2009). Enhancing the magnetoelectric response of Metglas/polyvinylidene fluoride laminates by exploiting the flux concentration effect. *Appplied Physics Letters, 95*.

Fiebig, M. (2005). Revival of the magnetoelectric effect. *Journal of Physics D-Applied Physics, 38*, R123−R152.

Figueiredo, M., Santos-Tavares, R., Santin, E., Ferreira, J., Evans, G., & Goes, J. (2011). A two-stage fully differential inverter-based self-biased CMOS amplifier with high efficiency. *IEEE Transactions on Circuits and Systems-I, 58*, 1591−1603.

Figueras, R., Sabadell, J., Teres, L., & Serra-Graells, F. (2011). A 70-μm pitch 8-μW self-biased charge-integration active pixel for digital mammography. *IEEE Transactions on Biomedical Circuits and Systems, 5*, 481−489.

Fukada, E. (2000). History and recent progress in piezoelectric polymers. *IEEE Transactions on Ultrasonics, Ferroelectrics and Frequency Control, 47*, 1277−1290.

Gambier, P., Anton, S. R., Kong, N., Erturk, A., & Inman, D. J. (2012). Piezoelectric, solar and thermal energy harvesting for hybrid low-power generator systems with thin-film batteries. *Measurement Science and Technology, 23*, 015101.

Gao, J. Q., Gray, D., Shen, Y., Li, J. F., & Viehland, D. (2011). Enhanced dc magnetic field sensitivity by improved flux concentration in magnetoelectric laminates. *Applied Physics Letters, 99*.

Gao, J. Q., Hasanyan, D., Shen, Y., Wang, Y. J., Li, J. F., & Viehland, D. (2012). Giant resonant magnetoelectric effect in bi-layered Metglas/Pb(Zr,Ti)O-3 composites. *Journal of Applied Physics, 112*.

Glynne-Jones, P., Tudor, M. J., Beeby, S. P., & White, N. M. (2004). An electromagnetic, vibration-powered generator for intelligent sensor systems. *Sensors and Actuators A: Physical, 110*, 344−349.

Guo, X.-Z., Zhang, Y.-D., Qin, D., Luo, Y.-H., Li, D.-M., et al. (2010). Hybrid tandem solar cell for concurrently converting light and heat energy with utilization of full solar spectrum. *Journal of Power Sources, 195*, 7684−7690.

Hatipoglu, G., & Urey, H. (2009). FR4-based electromagnetic energy harvester for wireless tyre sensor nodes. *Procedia Chemistry, 1*, 1211−1214.

Ito, S., Aso, K., Makino, Y., & Uedaira, S. (1980). Magnetostriction and magnetization of iron-based amorphous-alloys. *Applied Physics Letters, 37*, 665−666.

Jahns, R., Piorra, A., Lage, E., Kirchhof, C., Meyners, D., et al. (2013). Giant magnetoelectric effect in thin-film composites. *Journal of the American Ceramic Society, 96*, 1673−1681.

Ju, S., Chae, S. H., Choi, Y., Lee, S., Lee, H. W., & Ji, C.-H. (2013). A low frequency vibration energy harvester using magnetoelectric laminate composite. *Smart Materials and Structures, 22*, 115037.

Kambale, R. C., Jeong, D. Y., & Ryu, J. (2012). Current status of magnetoelectric composite thin/thick films. *Advances in Condensed Matter Physics*, art. no. 824643.

Kambale, R. C., Patil, D., Ryu, J., Chai, Y. S., Kim, K. H., et al. (2013). Colossal magnetoelectric response of PZT thick films on Ni substrates with a conductive $LaNiO_3$ electrode. *Journal of Physics D: Applied Physics, 46*, 092002.

Kambale, R. C., Yoon, W.-H., Park, D.-S., Choi, J.-J., Ahn, C.-W., et al. (2013). Magnetoelectric properties and magnetomechanical energy harvesting from stray vibration and electromagnetic wave by $Pb(Mg_{1/3}Nb_{2/3})O_3$-$Pb(Zr,Ti)O_3$ single crystal/Ni cantilever. *Journal of Applied Physics, 113*, 204108.

Karami, M. A., & Inman, D. J. (2011). Analytical modeling and experimental verification of the vibrations of the zigzag microstructure for energy harvesting. *Journal of Vibration and Acoustics, 133*, 011002−011010.

Kim, H., Bedekar, V., Islam, R. A., Woo-ho, L., Leo, D., & Priya, S. (2008). Laser-machined piezoelectric cantilevers for mechanical energy harvesting. *IEEE Transactions on Ultrasonics, Ferroelectrics and Frequency Control, 55*, 1900−1905.

Lafont, T., Gimeno, L., Delamare, J., Lebedev, G. A., Zakharov, D. I., et al. (2012). Magnetostrictive-piezoelectric composite structures for energy harvesting. *Journal of Micromechanics and Microengineering, 22*.

Lage, E., Kirchhof, C., Hrkac, V., Kienle, L., Jahns, R., et al. (2012). Exchange biasing of magnetoelectric composites. *Nature Materials, 11*, 523−529.

Laletin, V. M., Paddubnaya, N., Srinivasan, G., De Vreugd, C. P., Bichurin, M. I., et al. (2005). Frequency and field dependence of magnetoelectric interactions in layered ferromagnetic transition metal-piezoelectric lead zirconate titanate. *Applied Physics Letters, 87*, 222507.

Laletin, U., Sreenivasulu, G., Petrov, V. M., Garg, T., Kulkarni, A. R., et al. (2012). Hysteresis and remanence in magnetoelectric effects in functionally graded magnetostrictive-piezoelectric layered composites. *Physical Review B, 85*.

Lee, M., Yang, R., Li, C., & Wang, Z. L. (2010). Nanowire−Quantum dot hybridized cell for harvesting sound and solar energies. *The Journal of Physical Chemistry Letters, 1*, 2929−2935.

Li, M. H., Berry, D., Das, J., Gray, D., Li, J. F., & Viehland, D. (2011). Enhanced sensitivity and reduced noise floor in magnetoelectric laminate sensors by an improved lamination process. *Journal of the American Ceramic Society, 94*, 3738−3741.

Li, P., Wen, Y. M., & Bian, L. X. (2007). Enhanced magnetoelectric effects in composite of piezoelectric ceramics, rare-earth iron alloys, and ultrasonic horn. *Applied Physics Letters, 90*.

Li, M., Wen, Y., Li, P., Yang, J., & Dai, X. (2011). A rotation energy harvester employing cantilever beam and magnetostrictive/piezoelectric laminate transducer. *Sensors and Actuators A-Physical, 166*, 102−110.

Liu, J.-Q., Fang, H.-B., Xu, Z.-Y., Mao, X.-H., Shen, X.-C., et al. (2008). A MEMS-based piezoelectric power generator array for vibration energy harvesting. *Microelectronics Journal, 39*, 802−806.

Mandal, S. K., Sreenivasulu, G., Petrov, V. M., & Srinivasan, G. (2010). Flexural deformation in a compositionally stepped ferrite and magnetoelectric effects in a composite with piezoelectrics. *Applied Physics Letters, 96*.

Mandal, S. K., Sreenivasulu, G., Petrov, V. M., & Srinivasan, G. (2011). Magnetization-graded multiferroic composite and magnetoelectric effects at zero bias. *Physical Review B, 84*.

Marin, A., Heitzmann, P., Twiefel, J., & Priya, S. (2012). *Improved pen harvester for powering a pulse rate sensor, 1, 8341*. San Diego, California, USA: SPIE, 83411D−10.

Marin, A., Turner, J., Ha, D. S., & Priya, S. (2013). Broadband electromagnetic vibration energy harvesting system for powering wireless sensor nodes. *Smart Materials and Structures, 22*, 075008.

Martin, L., Crane, S. P., Chu, Y. H., Holcomb, M. B., Gajek, M., et al. (2008). Multiferroics and magnetoelectrics: thin films and nanostructures. *Journal of Physics-Condensed Matter, 20*.

Martins, P., & Lanceros-Méndez, S. (2013). Polymer-based magnetoelectric materials. *Advanced Functional Materials, 23*, 3371−3385.

Maurya, D., Zhou, Y., Yan, Y., & Priya, S. (2013). Synthesis mechanism of grain-oriented lead-free piezoelectric $Na_{0.5}Bi_{0.5}TiO_3$−$BaTiO_3$ ceramics with giant piezoelectric response. *Journal of Materials Chemistry C, 1*, 2102.

Moss, S. D., McLeod, J. E., Powlesland, I. G., & Galea, S. C. (2012). A bi-axial magnetoelectric vibration energy harvester. *Sensors and Actuators A-Physical, 175*, 165−168.

Nan, C. W., Bichurin, M. I., Dong, S. X., Viehland, D., & Srinivasan, G. (2008). Multiferroic magnetoelectric composites: historical perspective, status, and future directions. *Journal of Applied Physics, 103*.

Newnham, R. E., Skinner, D. P., & Cross, L. E. (1978). Connectivity and piezoelectric-pyroelectric composites. *Materials Research Bulletin, 13*, 525−536.

Nibir, K., Dhar, P. S. W., & Dutta, Achyut K. (2011). Energy harvesting and storage: materials, devices, and applications II. In *Proceedings of SPIE, 8035*.

Oh, N.-K., Han, G., Yoon, W.-H., Choi, J.-J., Hahn, B.-D., et al. (2012). 2−2 structured magnetoelectric composites by aerosol deposition. *Journal of American Ceramic Society*.

Onuta, T.-D., Wang, Y., Long, C. J., & Takeuchi, I. (2011). Energy harvesting properties of all-thin-film multiferroic cantilevers. *Applied Physics Letters, 99*, 203506.

Pan, C. T., Hwang, Y. M., Hu, H. L., & Liu, H. C. (2006). Fabrication and analysis of a magnetic self-power microgenerator. *Journal of Magnetism and Magnetic Materials, 304*, e394−e396.

Pan, C., Li, Z., Guo, W., Zhu, J., & Wang, Z. L. (2011). Fiber-based hybrid nanogenerators for/as self-powered systems in biological liquid. *Angewandte Chemie, 50*, 11192−11196.

Paradiso, J. A., & Starner, T. (2005). Energy scavenging for mobile and wireless electronics. *IEEE Pervasive Computing, 4*, 18−27.

Park, C. S., Ryu, J., Choi, J. J., Park, D. S., Ahn, C. W., & Priya, S. (2009). Giant magnetoelectric coefficient in 3−2 nanocomposite thick films. *Japanese Journal of Applied Physics, 48*.

Patil, D. R., Zhou, Y., Kang, J. E., Sharpes, N., Jeong, D. Y., et al. (2014). Anisotropic self-biased dual-phase low frequency magneto-mechano-electric energy harvesters with giant power densities. *APL Materials, 2*.

Petrov, V. M., Srinivasan, G., Bichurin, M. I., & Galkina, T. A. (2009). Theory of magneto-electric effect for bending modes in magnetostrictive-piezoelectric bilayers. *Journal of Applied Physics, 105*, 063911.

Prellier, W., Singh, M. P., & Murugavel, P. (2005). The single-phase multiferroic oxides: from bulk to thin film. *Journal of Physics-Condensed Matter, 17*, R803−R832.

Priya, S. (2007). Advances in energy harvesting using low profile piezoelectric transducers. *Journal of Electroceramics, 19*, 167−184.

Priya, S., Islam, R., Dong, S., & Viehland, D. (2007). Recent advancements in magnetoelectric particulate and laminate composites. *Journal of Electroceramics, 19*, 149−166.

Priya, S., Ryu, J., Park, C. S., Oliver, J., Choi, J. J., & Park, D. S. (2009). Piezoelectric and magnetoelectric thick films for fabricating power sources in wireless sensor nodes. *Sensors, 9*, 6362−6384.

Ramesh, R., & Spaldin, N. A. (2007). Multiferroics: progress and prospects in thin films. *Nature Materials, 6*, 21−29.

Roundy, S., Wright, P. K., & Rabaey, J. (2003). A study of low level vibrations as a power source for wireless sensor nodes. *Computer Communications, 26*, 1131−1144.

Saha, C. R., O'Donnell, T., Wang, N., & McCloskey, P. (2008). Electromagnetic generator for harvesting energy from human motion. *Sensors and Actuators A: Physical, 147*, 248−253.

Shuo, C., & David, P. A. (2010). A study of a multi-pole magnetic generator for low-frequency vibrational energy harvesting. *Journal of Micromechanics and Microengineering, 20*, 025015.

Spaldin, N. A., & Fiebig, M. (2005). The renaissance of magnetoelectric multiferroics. *Science, 309*, 391−392.

Sreenivasulu, G., Mandal, S. K., Bandekar, S., Petrov, V. M., & Srinivasan, G. (2011). Low-frequency and resonance magnetoelectric effects in piezoelectric and functionally stepped ferromagnetic layered composites. *Physical Review B, 84*.

Srinivasan, G. (2010). Magnetoelectric composites. *Annual Review of Materials Research, 40*, 153−178.

Srinivasan, G., Rasmussen, E. T., Gallegos, J., Srinivasan, R., Bokhan, Y. I., & Laletin, V. M. (2001). Magnetoelectric bilayer and multilayer structures of magnetostrictive and piezoelectric oxides. *Physical Review B, 64*. art. no.-214408.

Srinivasan, G., Rasmussen, E. T., Levin, B. J., & Hayes, R. (2002). Magnetoelectric effects in bilayers and multilayers of magnetostrictive and piezoelectric perovskite oxides (vol B 65, art no 134402, 2002). *Physical Review B, 66*.

Timoshenko, S. (1921). On the correction factor for shear of the differential equation for transverse vibrations of prismatic bars. *Philosophical Magazine, 41*, 744−746.

Timoshenko, S., & Young, D. H. (1968). *Elements of strength of materials*. Princeton, NJ: Van Nostrand.

Van Den Boomgaard, J., Van Run, A. M. J. G., & Suchtelen, J. V. (1976). Magnetoelectricity in piezoelectric-magnetostrictive composites. *Ferroelectrics, 10*, 295−298.

Vaz, C. A. F., Hoffman, J., Anh, C. H., & Ramesh, R. (2010). Magnetoelectric coupling effects in multiferroic complex oxide composite structures. *Advanced materials, 22*, 2900−2918.

Vlasko-Vlasov, V. K., Lin, Y. K., Miller, D. J., Welp, U., Crabtree, G. W., & Nikitenko, V. I. (2000). Direct magneto-optical observation of a structural phase transition in thin films of manganites. *Physical Review Letters, 84*, 2239−2242.

von Büren, T., & Tröster, G. (2007). Design and optimization of a linear vibration-driven electromagnetic micro-power generator. *Sensors and Actuators A: Physical, 135*, 765−775.

Wang, Y., Gray, D., Berry, D., Gao, J., Li, M., et al. (2011). An extremely low equivalent magnetic noise magnetoelectric sensor. *Advanced materials, 23*, 4111−4114.

Wang, Y. J., Gray, D., Berry, D., Li, M. H., Gao, J. Q., et al. (2012). Influence of interfacial bonding condition on magnetoelectric properties in piezofiber/metglas heterostructures. *Journal of Alloys and Compounds, 513*, 242−244.

Wang, P., Liu, H., Dai, X., Yang, Z., Wang, Z., & Zhao, X. (2012). Design, simulation, fabrication and characterization of a micro electromagnetic vibration energy harvester with sandwiched structure and air channel. *Microelectronics Journal, 43*, 154−159.

Wang, J. W., Yang, A., Chen, Y. J., Chen, Z. H., Geiler, A., et al. (2011). Self biased Y-junction circulator at k-u band. *IEEE Microwave and Wireless Component Letters, 21*, 292−294.

Williams, C. B., Shearwood, C., Harradine, M. A., Mellor, P. H., Birch, T. S., & Yates, R. B. (2001). Development of an electromagnetic micro-generator. *Circuits, Devices and Systems, IEE Proceedings, 148*, 337−342.

Yan, Y., Cho, K.-H., Maurya, D., Kumar, A., Kalinin, S., et al. (2013). Giant energy density in [001]-textured $Pb(Mg_{1/3}Nb_{2/3})O_3$-$PbZrO_3$-$PbTiO_3$ piezoelectric ceramics. *Applied Physics Letters, 102*, 042903.

Yan, Y. K., Zhou, Y., & Priya, S. (2013). Giant self-biased magnetoelectric coupling in co-fired textured layered composites. *Applied Physics Letters, 102*.

Yang, S. C., Ahn, C. W., Cho, K. H., & Priya, S. (2011). Self-bias response of Lead-Free (1-x) [0.948 $K_{0.5}Na_{0.5}NbO_3$-0.052 $LiSbO_3$]-x$Ni_{(0.8)}Zn_{(0.2)}Fe_{(2)}O_{(4)}$-nickel magnetoelectric laminate composites. *Journal of the American Ceramic Society, 94*, 3889−3899.

Yang, S. C., Cho, K. H., Park, C. S., & Priya, S. (2011). Self-biased converse magnetoelectric effect. *Applied Physics Letters, 99*.

Yang, S. C., Park, C. S., Cho, K. H., & Priya, S. (2010). Self-biased magnetoelectric response in three-phase laminates. *Journal of Applied Physics, 108*.

Yang, J., Wen, Y., & Li, P. (2011). Magnetoelectric energy harvesting from vibrations of multiple frequencies. *Journal of Intelligent Material Systems and Structures, 22*, 1631−1639.

Yang, J., Wen, Y., Li, P., & Bai, X. (2011). A magnetoelectric-based broadband vibration energy harvester for powering wireless sensors. *Science China-Technological Sciences, 54*, 1419−1427.

Yang, Y., Zhang, H. L., Zhu, G., Lee, S., Lin, Z. H., & Wang, Z. L. (2013). Flexible hybrid Energy cell for simultaneously harvesting thermal, mechanical, and solar energies. *ACS Nano, 7*, 785−790.

Zavodney, L. D., & Nayfeh, A. H. (1989). The non-linear response of a slender beam carrying a lumped mass to a principal parametric excitation: theory and experiment. *International Journal of Non-Linear Mechanics, 24*, 105−125.

Zhai, J., Xing, Z., Dong, S., Li, J., & Viehland, D. (2006). Detection of pico-Tesla magnetic fields using magneto-electric sensors at room temperature. *Applied Physics Letters, 88*, 062510.

Zhai, J., Xing, Z., Dong, S., Li, J., & Viehland, D. (2008). Magnetoelectric laminate composites: an overview. *Journal of the American Ceramic Society, 91*, 351−358.

Zhou, Y., Apo, D. J., & Priya, S. (2013). Dual-phase self-biased magnetoelectric energy harvester. *Applied Physics Letters, 103*, 192909.

Zhou, Y., Yang, S. C., Apo, D. J., Maurya, D., & Priya, S. (2012). Tunable self-biased magnetoelectric response in homogenous laminates. *Applied Physics Letters, 101*.

Zorlu, Ö., & Külah, H. (2013). A MEMS-based energy harvester for generating energy from non-resonant environmental vibrations. *Sensors and Actuators A: Physical, 202*, 124−134.

This page intentionally left blank

Magnetoelectric current sensor

8

Y. Zhou, S. Priya
Virginia Tech, Blacksburg, VA, USA

8.1 Introduction

8.1.1 State-of-the-art current sensors

A current sensor is a system or device that can measure the magnitude of an electrical current in a cable/wire under either AC or DC conditions. Usually the current sensors encompass many aspects of physics and electronics. Based on their working mechanism, there are mainly four types of electrical current sensing techniques, including the Hall effect, induction transformer, resistive shunt, and Rogowski coil sensors, as shown in Figure 8.1.

1. Hall effect sensor (Figure 8.1(a)): It is a transducer that varies its output voltage in response to a magnetic field via the Hall effect, given as

$$V_{\mathrm{H}} = -\frac{IB}{nte} \tag{8.1}$$

where V_{H} is the Hall voltage, I is the current across the plate length, B is the magnetic field, t is the thickness of the plate, e is the elementary charge, and n is the charge carrier density of the carrier electrons. Generally, the Hall effect-based current sensor is mounted in a core at a right angle to the concentrated magnetic field along with a signal conditioning circuitry. When exposed to a magnetic field generated from a cable with current flow, the energized Hall sensor produces a potential difference that can be measured to identify the magnitude of the magnetic field or current. However, the use of iron cores dramatically enhances the electromagnetic interference, and the high sensitivity is obtained at the expense of high-quality signal conditioning electronics to monitor the inherently weak Hall voltage (Ramsden, 2006).
2. Inductive sensor (Figure 8.1(b)): It monitors the electrical energy changes between two or more circuits through electromagnetic induction, also named a current transformer. Generally, a current transformer consists of a wire-wound core and a signal conditioner. A varying current signal passing through the core magnifies the magnetic field; in return, the magnetic field induces a current in the winding. Thus, this type of current sensing possesses power supply-free measurement nature. However, it can only deal with an AC current with limited operating frequency range (40−60 Hz) due to the increased magnetic losses at elevated frequencies with a low detection sensitivity.
3. Resistive shunt (Figure 8.1(c)): It is a calibrated resistor placed in a current path that produces a voltage drop proportional to the current flow. Since its resistance is known, the measured voltage across the shunt can be scaled to reflect the current value. However, the shunt resistor will generate heat as current is passed through it. Therefore, this kind of sensing technique is

Composite Magnetoelectrics. http://dx.doi.org/10.1016/B978-1-78242-254-9.00008-1
Copyright © 2015 Elsevier Ltd. All rights reserved.

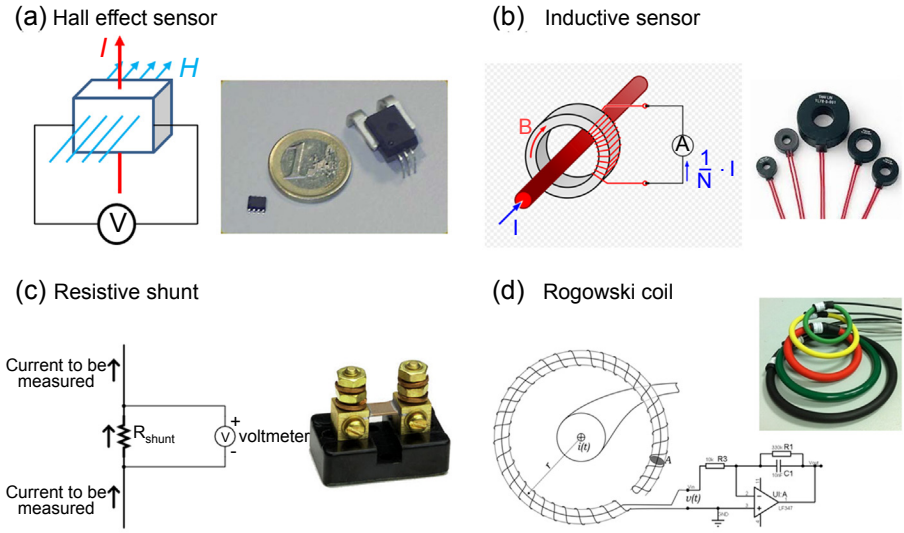

Figure 8.1 Schematic of the types of current sensors, including (a) Hall effect sensor, photograph of ±20 A and ±200 A current sensors; (b) Inductive sensor, photograph of wire lead current transformers/sensors; (c) Rogowski coil, examples of various Rogowski coils; (d) Resistive shunt, photograph of a DC ammeter shunt.
(a) © Allegro MicroSystems, LLC; (b) © Thai Lin; (c) © Yueqing Tengtai Electric Co., Ltd; (d) © Deltec Shunts, LLC.

generally used in applications where the emphasis is on accuracy and repeatability under low-current conditions. In addition, for practical application, although the shunt resistor is small in size and inexpensive, the need for cutting and reterminating the current carrier can be expensive to operate.

4. Rogowski coil (Figure 8.1(d)): It is a toroid of wire for measuring the AC current or high-speed current pulses. This type of coil has an air core with a helical coil of wire with the lead from one end returning through the center of the coil to the other end. The changes in magnetic field induce an electromotive force (EMF) within a wire loop, which is a voltage signal that is proportional to the changes in the magnitude field inside the loop: $\text{EMF} \propto \frac{dB(t)}{dt}$. Since $B(t) \propto i(t)$, the voltage output of the loop is therefore proportional to the time-differentiation of the current. The voltage produced by a Rogowski coil is

$$V = \frac{-AN\mu_0}{l}\frac{dI}{dt} \tag{8.2}$$

where $A = \pi a^2$ is the area of one of the small loops, N is the number of turns, $l = 2\pi a$ is the length of the winding, and dI/dt is the rate of change of the current. Since no iron core is needed, it is highly linear even when subjected to a large current. However, this type of coil can only be used with the support of an integrator circuit to obtain the current waveform, which needs external power support.

In summary, a comparison of these different current sensing technologies is listed in Table 8.1. The technology for sensing current has evolved, driven by the need for

Table 8.1 Comparison between different current sensing technologies

Sensing type	Hall sensor	Inductive sensor	Resistance shunt	Rogowski coil
Cost	High	Medium	Very low	Low
Linearity	Poor	Fair	Very good	Very good
High current capability	Good	Good	Very poor	Very good
Power consumption	Medium	Low	High	Low
Output variation with temperature	High	Low	Medium	Very low

improved sensitivity, smaller size, and compatibility with electronic systems. However, none of the above mentioned current sensors satisfy all the needs related to self-powered, miniature size, high performance, low detection limits, reliability, and cost-effectiveness. The development of a compact, low-noise, and low-cost passive current sensor is technologically important and much needed for variety of electronic systems.

8.1.2 Magnetoelectric sensors

Magnetoelectric (ME) composites can directly generate an electric signal in response to the external magnetic field, leading to a passive nature without the need of external power sources. In addition, by optimizing the composite materials and configurations, it can produce significantly large voltage and sensitivity over a wide range of frequency. Therefore, the development of ME composites and devices toward current/magnetic field sensing applications is technologically important. In this chapter, we will systematically describe the development of ME current sensors with respect to following aspects:

1. Sensing mechanisms, sensor designs, and challenges of typical ME-sensing elements.
2. Development of novel self-biased ME composites that can be used as ME passive current sensors in the absence of a DC magnetic field.
3. Development of ME transformers that can be used over a wide frequency range of magnetic signals based on their tunable features.
4. Classification of magnetic noises and corresponding noise-reduction methods.

8.2 Development of magnetoelectric current sensors

ME composites as magnetic field detection sensors have attracted lots of attention due to their simple implementation mechanism. Operation of conventional ME composites requires two input components: a magnetic DC bias and a magnetic AC field. Either of

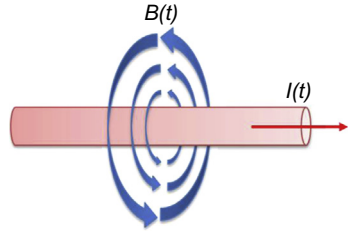

Figure 8.2 Schematic of current passes through a conductor induces a magnetic field.

these two components can be detected by providing one of the components, leading to a magnetic sensor for detecting AC or DC fields. Since the strength of the magnetic field depends on the current I in the wire, the electric current can be monitored by detecting the corresponding magnetic flux.

8.2.1 Sensing mechanism

For the case of a long, straight wire carrying a current I, the magnetic field generated is wrapped around the wire, as shown in Figure 8.2.

Depending upon the strength of the AC or DC current, the magnitude of the AC or DC magnetic field varies as a function of the distance from the wire, given as

$$H = \frac{I}{2\pi r} \tag{8.3}$$

where r is the radius of the vortex magnetic field. Accordingly, by using the ME composites, one can detect the change in magnetic field by monitoring the variation of the ME voltage and use that measurement to derive the status of the corresponding I. Therefore, the current sensing mechanism is similar to the magnetic field detection principle based on the ME coupling effect. The ME coupling can be explained as the following: on application of a magnetic field to the composite, a strain will be induced and transferred to the piezoelectric phase, and a proportional charge in the piezoelectric layer will be generated. The input magnetic field on the ME composite consists of an AC magnetic field along with a DC magnetic bias. One of these two variables can be detected by providing the other component. Thus, the ME composite can be utilized as an AC/DC magnetic field sensor (Dong, Zhai, Li, & Viehland, 2006a; Wang et al., 2011). By selecting the high-performance piezoelectric and magnetostrictive materials and combining them into a suitable structure, one can detect a small magnetic field as low as $\sim$1 pT at a frequency of only several Hz (Wang et al., 2011).

8.2.1.1 DC magnetic field-dependent response

For ME composites, the measured direct ME coupling coefficient is the field conversion ratio between applied H_{ac} and induced E_{ac} under applied H_{dc}, given as $\alpha_{ME} = \delta E_{ac}/\delta H_{ac}$. In general, under a constant applied AC magnetic field, the ME

coupling coefficient first increases with increasing H_{dc}, reaching a maximum at an optimized DC bias (H_{bias}), and then decreases with further increasing H_{dc}. This peak behavior in response to varying H_{dc} can be further explained by taking into account the relationship given below (Cho & Priya, 2011):

$$\alpha_{ME} = \left|\frac{\partial T}{\partial S} \times \frac{\partial D}{\partial T} \times \frac{\partial E}{\partial D}\right| \times \frac{\partial S}{\partial H} \tag{8.4}$$

where S is the mechanical strain, T is the mechanical stress, D is the electric displacement, E is the electric field, and H is the magnetic field. Since the first part of the above expression is a nonmagnetic factor, one can rewrite Eqn (8.4) as

$$\alpha_{ME} \propto \frac{\partial S}{\partial H} = \frac{d\lambda}{dH} = q \tag{8.5}$$

which indicates that the ME coefficient is directly related to the nature of the ferromagnetic phase (λ: magnetostriction, q: piezomagnetic coefficient) and the effectiveness of elastic coupling between the two phases. The dependence of α_{ME} on q indicates the requirement for additional H_{dc}. In summary, typical behavior of the α_{ME}, λ, q, and their relationship as a function of H_{dc} can be illustrated as shown in Figure 8.3.

From the above discussion, we can clearly notice that the ME coupling coefficient essentially tracks the strength of q, which is proportional to the rate of change in λ, and then vanishes when magnetostriction attains saturation. Depending on the magnitude of optimum magnetic DC bias, ME composites can exhibit maximum ME coefficient. The composition and geometry of the ferromagnetic phase can be tuned to tailor the magnitude of optimum DC bias ranging from 5 to 6.8 kOe (Dong, Zhai, Li, &

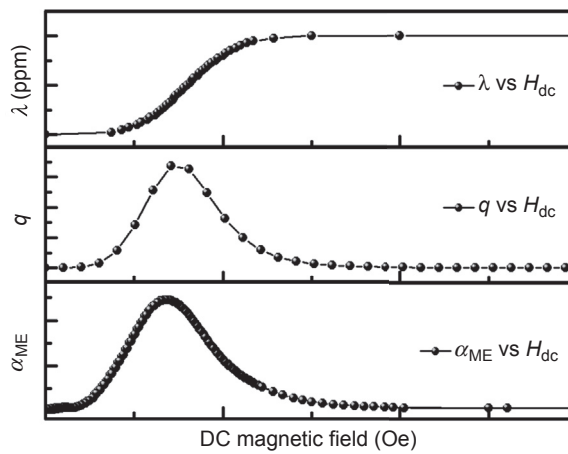

Figure 8.3 Typical magnetoelectric behaviors as a function of a DC magnetic field for a longitudinal magnetized and transversely poled ME composite.

Viehland, 2006b; Nan, Bichurin, Dong, Viehland, & Srinivasan, 2008; Srinivasan, 2010). Depending upon the materials utilized, ME composites will have different ME behavior due to the difference in coercive field, permeability, and magnetization. The volume fraction of the magnetostrictive phase affects the ME behavior and optimum H_{bias} and could also be used as a control parameter.

8.2.1.2 AC magnetic field-dependent response

Another important phenomenon of the ME composites is the change in ME coupling as a function of the applied AC magnetic field (ME vs f_{ac}). When the AC magnetic field is applied at a frequency corresponding to electromechanical resonance (EMR) for the piezoelectric phase or ferromagnetic resonance for the magnetic phase in the ME composite, the ME voltage coefficient shows a peak behavior with the magnitude increased by a factor of up to 100 (Srinivasan, 2010; Zhai, Xing, Dong, Li, & Viehland, 2008a). Bichurin et al. presented a theoretical analysis for the bilayer of NFO-PZT laminates and predicted a 40-times increase in $\alpha_{ME,33}$ at EMR compared to that of off-resonance conditions (Bichurin et al., 2003). Similar theoretical calculations have been developed for the ME effect at ferromagnetic and magnetoacoustic resonance (Bichurin, Petrov, Kiliba, & Srinivasan, 2002; Bichurin, Petrov, Ryabkov, Averkin, & Srinivasan, 2005). Cho et al. analyzed the direct and converse ME effect in laminate composites and showed that DME is maximized at f_a, while the CME is maximized at f_r, as shown in Figure 8.4 (Cho & Priya, 2011). This phenomenon

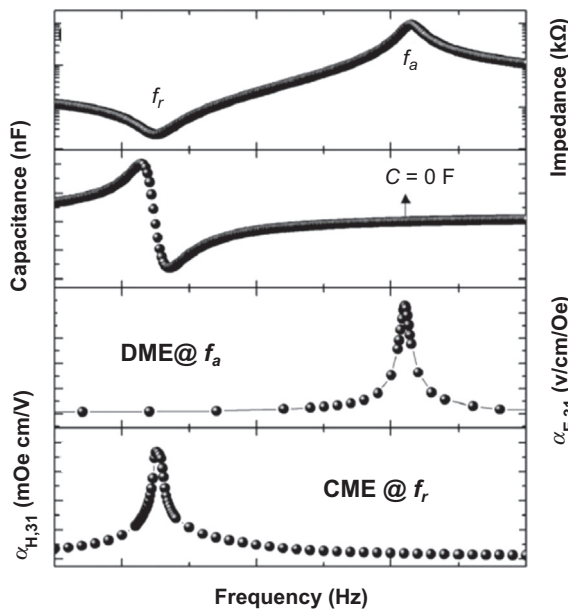

Figure 8.4 Impedance, capacitance, and ME voltage coefficient as a function of AC frequency. Reprinted with permission from Cho and Priya (2011), Copyright 2011, AIP Publishing LLC.

can be further explained by using piezoelectric constitutive equations and combining them with frequency-dependent capacitance of the piezoelectric layer. The fundamental resonance frequency can be tuned by the length of the laminates (l), where the first longitudinal resonance is expressed as $f_L = 1/(2l\sqrt{\rho s_{11}})$ (ρ is the laminate density and s_{11} is the elastic compliance of the laminate) (Zhai, Xing, Dong, Li, & Viehland, 2008b). However, for practical use of the composites at low frequency, the corresponding composite dimension would be prohibitively large. In order to overcome this problem, a unimorph configuration was proposed for bilayer ME composites working at the bending mode that showed enhancement in the coupling at low frequencies (Petrov, Srinivasan, Bichurin, & Galkina, 2009). Alternative approaches that utilize unique laminate configurations have been proposed to achieve low resonance frequency with a limited size of the components. Using these approaches, resonance enhancement of the ME coefficient has been achieved in the frequency range of 100 Hz, using cm-long laminates.

8.2.2 Theoretical model

A high field/current sensitivity can be obtained from an ME composite that exhibits high ME voltage coefficient and low signal-to-noise ratio. The sensitivity can be further increased by a factor of 10 or more at the mechanical resonance frequency. By optimizing materials combination and composites geometry, one is able to obtain detection sensitivity on the order of pT/Hz$^{1/2}$. The ME coefficients for the laminates can be determined by taking into account the constitutive piezoelectric and piezomagnetic behavior. A figure of merit for a conventional 2−2-type laminate ME composite can be derived as the following (Srinivasan et al., 2001):

$$\text{L}-\text{T mode}: \ \alpha_{E31} = \frac{\delta E_3}{\delta H_1} = \frac{-2d_{31}^{\text{p}} q_{11}^{\text{m}} v^{\text{m}}}{\left(s_{11}^{\text{m}} + s_{12}^{\text{m}}\right)\varepsilon_{33}^{T,P} v^{\text{p}} + \left(s_{11}^{\text{p}} + s_{12}^{\text{p}}\right)\varepsilon_{33}^{T,P} v^{\text{m}} - 2\left(d_{31}^{\text{p}}\right)^2 v_{\text{m}}} \tag{8.6}$$

$$\text{L}-\text{L mode}: \ \alpha_{E33} = \frac{\delta E_3}{\delta H_3} = \frac{-2d_{31}^{\text{p}} q_{13}^{\text{m}} v^{\text{m}}}{\left(s_{11}^{\text{m}} + s_{12}^{\text{m}}\right)\varepsilon_{33}^{T,P} v^{\text{p}} + \left(s_{11}^{\text{p}} + s_{12}^{\text{p}}\right)\varepsilon_{33}^{T,P} v^{\text{m}} - 2\left(d_{31}^{\text{p}}\right)^2 v_{\text{m}}} \tag{8.7}$$

where E_k and H_k are vector components of the electric and magnetic field, d_{31}^{p} is the piezoelectric coefficient, v^{m} and v^{p} are volumes of magnetostrictive and piezoelectric phases, s_{11}^{p}, s_{12}^{p} are elastic compliances for the piezoelectric phase, s_{11}^{m}, s_{12}^{m} are elastic compliances for the magnetostrictive phase, q_{11} is piezomagnetic coefficient of the magnetostrictive phase, and $\varepsilon_{33}^{T,P}$ is the permittivity of the piezoelectric phase.

The superscripts "m" and "p" represent the magnetostrictive and piezoelectric phase, respectively. This relationship clearly reflects the important role of material parameters of the piezoelectric phase ($g_{31,}$ S_{11}^{p}) and the magnetostrictive phase ($q_{11,}$ S_{11}^{m}) toward achieving a large ME response.

8.2.3 Design concepts and challenges

There are several fundamental challenges in the realization of high-performance ME current sensors. The performance of ME composites is tightly related with the materials selection, structure, processing method, operating mode, dimensionality, and other dynamic parameters. One of the biggest challenges in the implementation of ME composites has been the magnitude of ME voltage coefficient $\alpha_{ME,}$ which represents the magnetic field output voltage conversion. The characteristic ME behavior can be tuned by improving the constitutive piezoelectric and magnetostrictive behavior. Thus, the selection of appropriate piezoelectric and magnetostrictive materials is the primary step toward achieving a high-performance ME transducer. Next, the effect of synthesis techniques on the ME response should be considered. The epoxy bonding method provides an easy and simple fabrication process and provides more feasibility for the device configuration. However, the low mechanical strength of epoxy hampers the effective coupling between the magnetostrictive and piezoelectric phases. In addressing this issue, direct bonding between the consecutive phases through a low temperature cofiring technique can be used to enhance the effective coupling.

Magnetic noise in the environment (extrinsic noise: electromagnetic interference and thermal noise) and in the detection circuits (intrinsic noise: Johnson noise and $1/f$ noise) play an important role toward the detection capabilities of the ME laminated sensors (Wang et al., 2014). In addressing the extrinsic noise, appropriate rejection techniques can be used to reduce or eliminate the electromagnetic interference or thermal noise. By using a metallic shield placed between the ME component and external environment, it is possible to control the propagation of electromagnetic fields. A good thermal insulation helps in extending the sensor stability in a wide range of working temperatures. On the other hand, both the measurement circuit and sensor configuration need to be considered for sensor performance with regard to the inevitable intrinsic noise.

In the following sections, we will discuss the development of ME current sensors, covering conventional ME composite-based current sensors, self-biased ME composite-based current sensors, ME transformer-based current sensors, and noise-reduction methods.

8.3 Conventional ME composites-based current sensors

In considering the effective ME coupling, so far only bulk-sized ME laminate composites that exhibit a large ME effect above room temperature have the possibility to be implemented as current sensors for practical usage. There are three main promising

device configurations that can be used for current sensing, including rectangular shaped, ring-type shaped, and polymer-based flexible structures.

8.3.1 Rectangular-shaped sensor

It is well-known that the ME response as a function of a DC magnetic field is tightly related with the nature of magnetostrictive materials. From the functional device point of view, it is important to control the magnitude of the ME voltage coefficient and its response. Thus, there are several studies related to shapes (disk, cylinder, plate, toroid, sphere, etc.) and sizes (numbers of layers, layer thickness, length, and width) of the magnetostrictive material toward obtaining high ME voltage coefficient (Nan et al., 2008). It is widely accepted that ME composites with a rectangular shape, large length/width aspect ratio, and small thickness with optimized volume ratio will generate high ME voltage coefficient (Zhai et al., 2008a). To better explain the ME versus configuration relationship, the size-induced demagnetization effect has been taken into consideration. For ferromagnetic materials, the demagnetization field is directly proportional to the demagnetization factor (N_d), $H_d = MN_d$ (M is the magnetization), where N_d is dependent on the dimension and geometry. Thus, the internal effective magnetic field (H_{eff}) in the magnetic phase can be written as $H_{eff} = H_{bias} - H_d$, where H_{bias} is the induced external magnetic field. Therefore, in order to achieve the same magnitude of H_{eff}, one needs to apply larger H_{bias} when H_d is larger and vice versa (Zhou, Yang, Apo, Maurya, & Priya, 2012). Furthermore, this can also be corelated with the magnetic flux concentration (B_{eff}) in the magnetic phase:

$$B_{eff} = \mu_0(H_{eff} + M) = \mu_0(H_{bias} + M) - \mu_0 M N_d \tag{8.8}$$

where a smaller N_d will result in a stronger B_{eff}. It has been shown that high magnetic flux concentration in the magnetic phase has a positive effect on the ME response of ME laminates (Gao, Gray, Shen, Li, Viehland, 2011; Fang et al., 2009). Thus, some researchers use the enlarged magnetic layer to enhance the effective magnetic flux density along the piezo/magnetic interface for obtaining larger ME coefficient (Gao, Gray, et al., 2011).

Figure 8.5 illustrates a case study that describes the influence of Metglas length on the magnetic field concentration in ME laminate sensors (Gao, Gray, et al., 2011). As expected, it was found that the lengthening of the magnetostrictive layer increases the magnetic flux density along the center of the Metglas layer (Figure 8.5(a)) and therefore leads to an enhanced ME voltage coefficient (Figure 8.5(b)). As a result, the corresponding DC magnetic field detection sensitivity of Metglas/PZT laminates improved from 15 nT (Figure 8.5(c)) to 6 nT (Figure 8.5(d)) with respect to the Metglas length. Such high sensitivities can be further affected based on the magnitude and orientation of the local geomagnetic field.

For the implementation of the rectangular-shaped ME composites, Figure 8.6 shows a conceptual design of the ME current sensor. In this design, the rectangular-shaped ME laminate is mounted on the surface of an electrical cable. A pair of permanent magnets was placed at the two ends of the ME laminate to provide a DC bias H_{dc}.

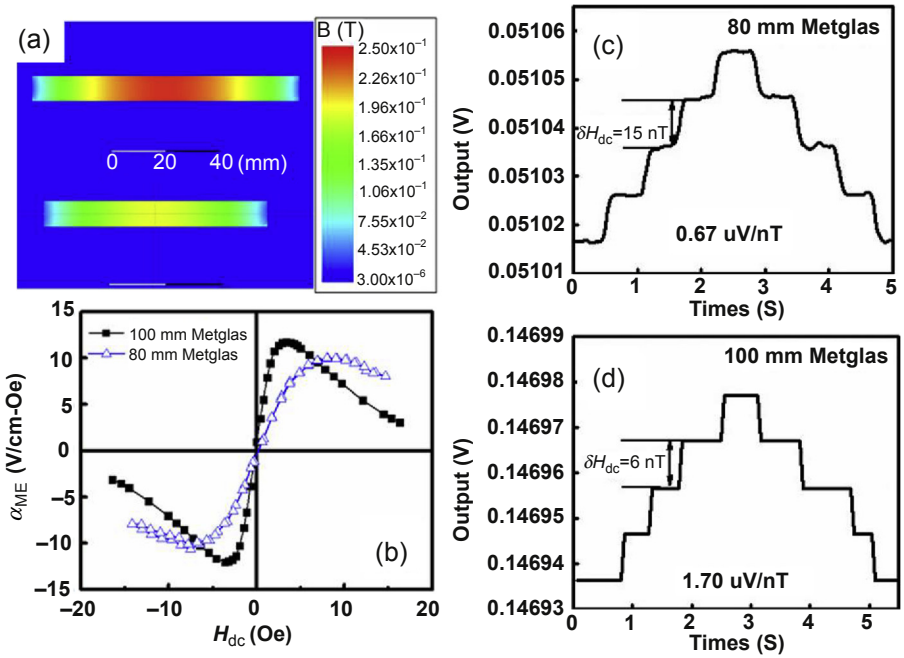

Figure 8.5 (a) In-plane magnetic field strength along the center-plane of Metglas foil in response to a low DC bias field, as simulated by Maxwell 3D; (b) the corresponding magnetoelectric voltage coefficient of Metglas/PZT laminate sensor with different Metglas length as a function of DC bias in response to $H_{ac} = 1$ Oe at 1kHz; (c) and (d) comparison of the DC field sensitivity for Metglas/PZT laminate sensor with different size Metglas under AC drive conditions at $f = 1$ kH and $H_{ac} = 0.1$ Oe.
Reprinted with permission from Gao, Gray, et al. (2011), Copyright 2011, AIP Publishing LLC.

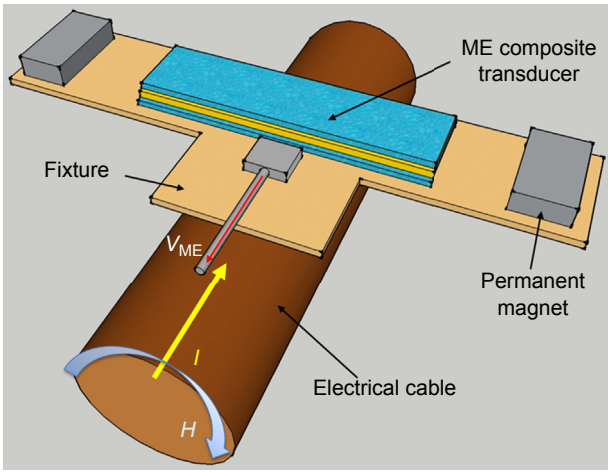

Figure 8.6 Conceptual design of a rectangular-shaped ME current sensor mounted on the surface of an electrical cable.

By optimizing the H_{dc} with the selected magnet, an enhanced ME voltage coefficient and the resultant high sensitivity was obtained. This design configuration provides a simple and flexible way for sensor installation and detection. However, the need of the permanent magnet hinders the way toward device miniaturization. More importantly, the sensor placement, with respect to the orientation of the cable, plays an important role toward maximum sensitivity and may produce another level of difficulty for sensor implementation.

8.3.2 Ring-type sensor

Previously, investigations on ME composites have focused on the simple construction of square or rectangular shapes based on the consideration of an effective demagnetization field and the leading magnetic flux density across the magnetostrictive phases. As-fabricated ME composites can be operated in either a transverse-transverse (T−T) mode, L−T mode, or L−L mode, which exhibit large ME effects for a specific direction of the applied magnetic field. Thus, the best sensitivity can only be achieved for the detection of an electric current (magnetic field) flowing in a certain direction. However, in most cases, it is important to utilize a stable and high-sensitivity sensor for detecting a current in electrical cables surrounded with AC vortex magnetic fields for a power integrated circuit (Bai, Lu, & Lin, 2003; Busatto, La Capruccia, Iannuzzo, Velardi, & Roncella, 2003). Accordingly, ring-type ME laminates were developed as ideal configurations for a vortex magnetic field or current detection. Dong et al. demonstrated a ring-type ME laminate consisting of two Terfenol-D rings magnetized in the circumferential direction and one PZT ring consisting of segments poled in the circumference direction, as shown in Figure 8.7(a) (Dong, Li, & Viehland, 2004a). In this design, the cable can be placed in the center of the ring-type sensor. An intensified strain will be generated and transferred to the piezoelectric layer when a vortex magnetic field is generated. Thus, by monitoring the induced ME voltage, one would be able to identify the electrical current. Figure 8.7(b) illustrates the induced ME voltage response to a square-wave current passing through the ring-type current sensor. In comparison with a toroidal-type reluctance coil with $N = 100$ turns, this ring-type sensor shows a near-flat ME response with higher voltage output as a function of frequency (Figure 8.7(c)), indicating its promise and advantage as a highly sensitive and stable current sensor. Furthermore, by selecting single-crystal materials with higher piezoelectric properties and optimizing the configuration of a ring-type structure, Dong et al. proposed a quasi-ring-type ME sensor, which is able to detect AC current as small as 10^{-7} A, and/or a vortex magnetic field as small as 6 pT, as shown in Figure 8.7(d) (Dong et al., 2005).

However, the requirement of a DC magnetic field source is still a concern. In addressing this challenge, Chung et al. proposed a modified ring-type ME current sensor, as shown in Figure 8.8(a) (Leung, Or, Zhang, & Ho, 2010). In this design, instead of using the whole Terfenol-D ring, an epoxy-bonded Terfenol short-fiber ring with an embedded NdFeB magnetic plate was used as the magnetostrictive phase. The permanent magnetic plates not only provide an

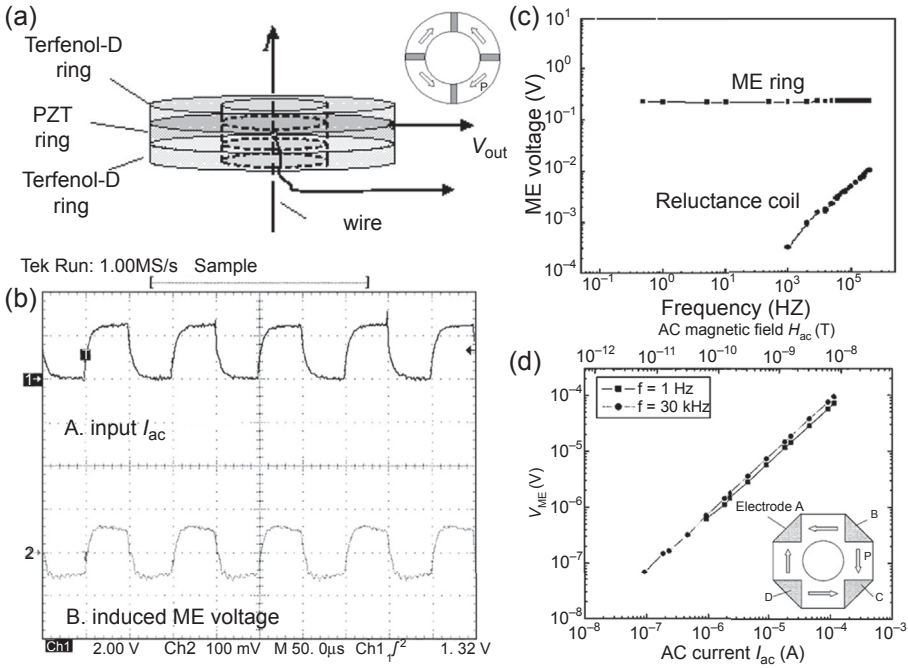

Figure 8.7 (a) Configuration of the ring-type Terfenol-D/PZT laminate composite, inset, illustrates the piezoelectric polarization direction in the circumferential direction; (b) induced ME response to switching currents; (c) ME response of a ring-type ME sensor and a reluctance coil as a function of driving frequency; (d) ME response as a function of AC magnetic field and current.
Reprinted with permission from Dong et al. (2005, 2004a), Copyright 2004, AIP Publishing LLC.

initial inner magnetic bias for a circumferential magnetization, but also eliminate the need of an external DC bias source for ME coupling optimization. Figure 8.8(b) plots the comparison of the electric current sensitivity (S) between the modified ring-type sensor and a reluctance coil with 100 turns. It can be seen that the sensitivity of the ring-type sensor possesses a stable response in a wide range of AC frequency. More details of the ring-type sensor current detection response can be found in Figure 8.8(c).

8.3.3 Polymer-based flexible sensor

Despite the large ME coefficient and high sensitivity achieved in bulk ceramic-based ME composites, there is concern with the brittleness of these materials. In particular, the piezoelectric material is usually rigid, fragile, and costly, leading to a high cost and difficulty in implementation. From a practical point of view, the need for some tolerance to external stresses is important. Accordingly, ME

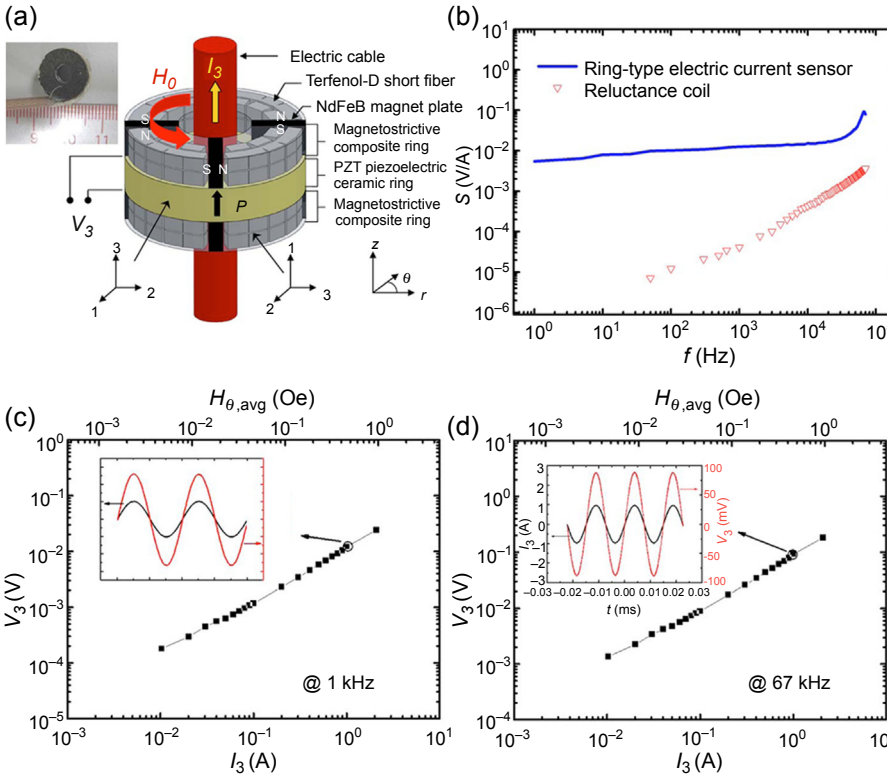

Figure 8.8 Design, ME response, and detection sensitivity of the modified ring-type ME current sensor.
Reprinted with permission from Leung et al. (2010), Copyright 2010, AIP Publishing LLC.

polymer-based composites with high flexibility and nonbrittle features were developed as promising alternatives for the ceramic-based sensors. Zhai et al. developed thin (<100 μm) and flexible Metglas/polyvinylldene-fluoride (PVDF) ME laminates in both unimorph and bimorph configurations (Figure 8.9) (Zhai, Dong, Xing, Li, & Viehland, 2006). Besides the flexible nature of this sensor, the composite was also able to provide a giant ME voltage coefficient of 7.2 V/cm.Oe at low frequency, and up to 310 V/cm.Oe under resonance frequency, leading to a high sensitivity (Zhai et al., 2006). Alternatively, Le et al. developed a flexible current sensor based on a bilayer structure consisting of the Cytop polymer and a magnetic tape filled with magnetically soft particles (Le et al., 2014). The Cytop polymer is an electret (or ferroelectret) material, which exhibits a high charge density and a large piezoelectric coefficient (25−700 pC/N). It was found that the laminate of a transversely charging electret, along with bias magnetic tape, could attain a large ME coefficient of 4.58 V/cm Oe at 1 kHz. In addition, two other types of polymer-based particulate nanocomposites and polymers as binder composites have been developed (Martins & Lanceros-Méndez, 2013).

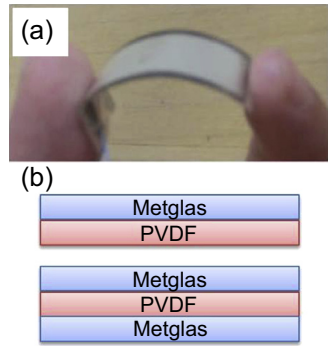

Figure 8.9 (a) Image and schematic of flexible Metglas/PVDF laminate composites; (b) DC sensitivity of a bimorph Metglas/PVDF sensor measured under $H_{ac} = 0.1$ Oe at $f = 50$ kHz. Adapted from Zhai et al. (2006), Copyright 2006, AIP Publishing LLC.

8.4 Self-biased ME composites-based current sensors

Although the above discussed current sensors based on conventional ME composites provide great potential for practical sensing application, most of them require an external DC magnetic bias field to obtain an optimum ME response and high current sensitivity. Considering the composition variation and geometry change, one can tune the optimum DC bias as low as several Oe. However, it is still a requirement to use a permanent magnet or electromagnet to provide DC magnetic bias, which, in turn, is a disadvantage for sensor implementation and miniaturization. Therefore, it is necessary to eliminate these limitations from DC bias. In particular, a novel design is desired if one needs to present a ME composite with large, tunable α_{ME} in the absence of a DC magnetic field. In this section, self-biased ME composites that can provide a giant ME coefficient at zero bias are introduced, and their application as current sensors have been demonstrated.

8.4.1 Self-biased ME composites

The self-biased ME effect is defined as ME composites that exhibit large nonzero α_{ME} in the absence of a DC magnetic field. Figure 8.10 illustrates the schematic of self-biased ME composites compared to that of conventional ME composites. Recently, self-biased ME composites have been developed in various configurations using different strategies.

The highlights in the development of self-biased ME composites can be summarized in Figure 8.11. Observation of self-biased ME effect was first reported by G. Srinivasan et al. in 2002, as they found hysteresis and remanence of α_{ME} as a function of H_{bias} in cofired LSMO-PZT laminates (Srinivasan, Rasmussen, Levin, & Hayes, 2002). Similar behavior was also found in other laminates (Laletin et al., 2005). However, this phenomenon did not attract much attention in the following decade, and most of the efforts have been focused on optimizing materials, structures,

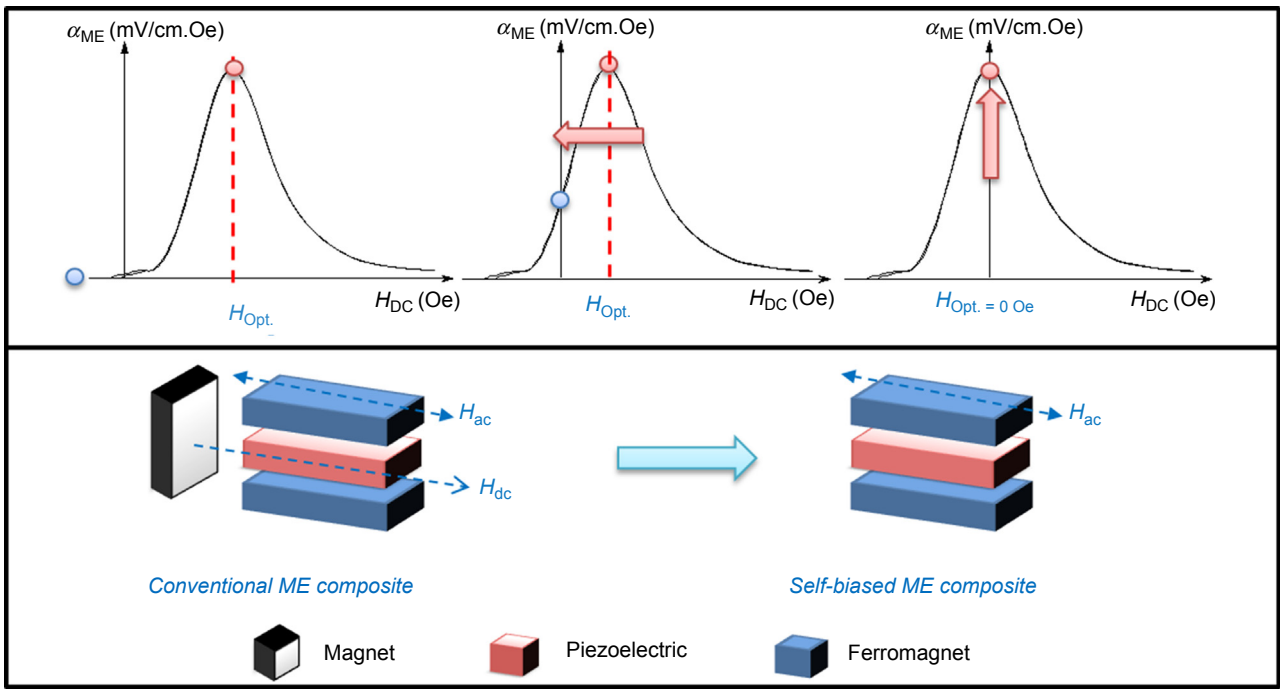

Figure 8.10 Schematic of conventional ME effect behavior and self-biased ME behavior.

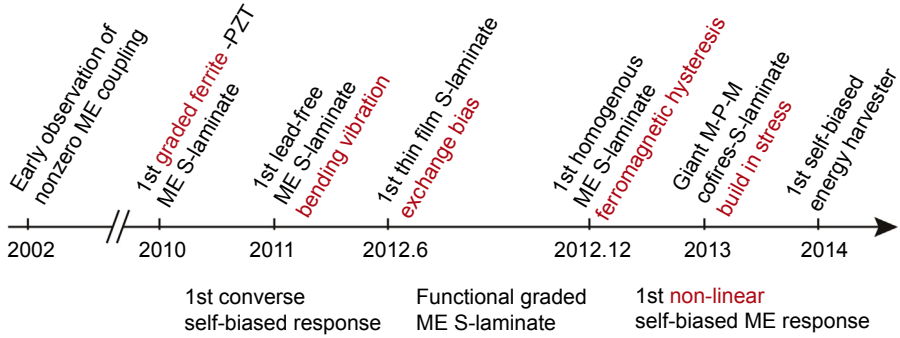

Figure 8.11 Milestones for the development of self-biased magnetoelectric composites.

and working modes to enhance the ME voltage coefficient and sensitivity (Nan et al., 2008; Zhai et al., 2008a).

In 2010, Mandal et al. demonstrated a compositionally graded ferrites/PZT laminate structure that produced nonzero ME voltage at zero DC magnetic bias (Mandal, Sreenivasulu, Petrov, & Srinivasan, 2010) They first correlated this nonzero ME behavior with the presence of flexural deformation and grading induced out-of-plane internal magnetic field in the ferrite. Subsequently, Yang et al. presented a methodology that regular ME laminate composites can possess a self-biased ME response by changing vibration mode through electrical connections, as shown in Figure 8.12(a) (Yang, Park, Cho, & Priya, 2010). Soon after that, Srinivasan et al. systematically investigated

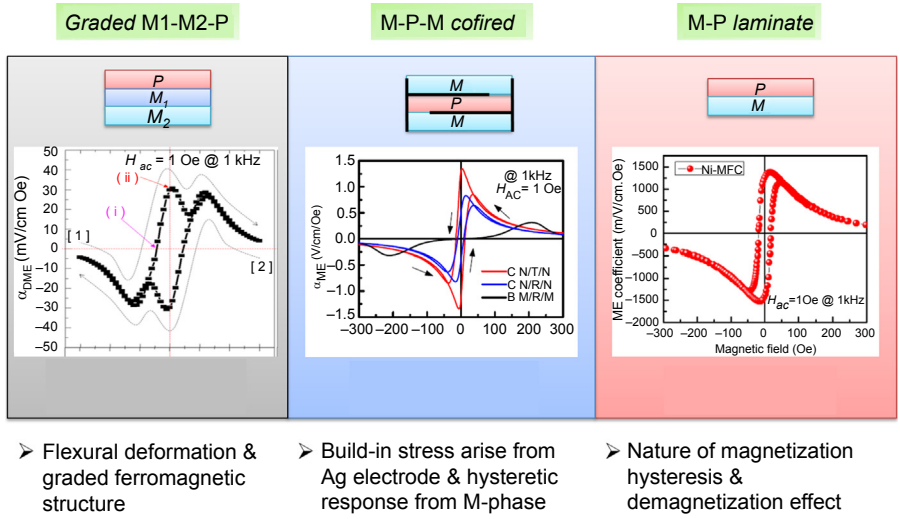

Figure 8.12 Development of self-biased magnetoelectric composite.
Reprinted with permission from Yang, Cho, et al. (2011); Yan et al. (2013); Zhou, Yang, et al. (2012), Copyright 2012, AIP Publishing LLC.

the hysteresis and remanence in ME effects in functionally graded magnetostrictive-piezoelectric layered composites; they further proposed a theoretical model for the self-biased graded composites (Laletin et al., 2012; Mandal, Sreenivasulu, Petrov, & Srinivasan, 2011; Sreenivasulu, Mandal, Bandekar, Petrov, & Srinivasan, 2011). Yang et al. first analytically studied the lead-free based self-biased laminates and proposed electrically controlled core-free magnetic flux control devices by using the self-biased converse ME effect (Yang, Ahn, Cho, & Priya, 2011; Yang, Cho, Park, & Priya, 2011; Yang et al., 2010). Alternative approaches have been suggested for the case of thin films that rely on the angular dependence of exchange bias field from a multicomponent magnetic system to provide a nonzero piezomagnetic coefficient at zero bias (Lage et al., 2012; Onuta, Wang, Long, & Takeuchi, 2011). The focus of these studies was mainly on understanding the nature of self-biased effect from multicomponent magnetic systems.

Subsequently, self-biased ME composites with a homogenous magnetostrictive phase have been developed. Yuan et al. first demonstrated a simple Ni/PZT bilayer laminate structure that exhibits tunable self-bias phenomenon with single-phase magnetic material (Figure 8.12(c)) (Zhou, Yang, et al., 2012). In this study, fundamental understanding of the role of domain structure and the demagnetization field of magnetic materials toward a self-biased effect was provided. The self-biased response was found to be related with the nature of the magnetic phase and hence could be controlled by variation in the demagnetization state and the resultant differential magnetic flux distribution. Meanwhile, Yan et al. successfully cofired a self-biased composite NCZF/Ag/PMNPT/Ag/NCZF with a homogeneous magnetic phase (Yan, Zhou, & Priya, 2013). Cofired structure provides the opportunity of interfacial engineering to obtain the optimum strain transfer from two phases with a giant self-biased response >1 V/cm/Oe, as shown in Figure 8.12(b). The self-bias response in the cofired laminates was explained by the low field magnetostriction hysteresis and the build-in stress from the internal electrode during the cofiring process. Further, by considering the nonlinear magnetic properties of the ferromagnetic phase, the self-biased phenomenon could also be observed in conventional ME composites that measured under the nonlinear region (Shen et al., 2013).

In summary, the working principle of the self-biased ME response can be categorized into three main groups: (1) flexural deformation with graded ferromagnetic structure; (2) build-in stress arising from an inner electrode; and (3) the nature of magnetization hysteresis in the magnetostrictive phase. The development of self-biased ME composites can be concluded, as shown in Figure 8.12. These discoveries of self-biased ME effect are technically important for applications of functional ME devices, especially for magnetic field/current sensors, core-free magnetic flux control devices, and electrically controlled magnetic memory devices (Jia, Or, Chan, Zhao, & Luo, 2006; Yang, Cho, et al., 2011; Wang et al., 2008). This phenomenon not only provides great potential toward devices miniaturization, but also reduced the electromagnetic interference that might be induced from the DC bias sources.

8.4.2 Application as current sensor

The early demonstration of using self-biased ME composites as an electric current sensor can be originated from the work done by Lu et al., as shown in Figure 8.13 (Lu et al., 2014). In this design, a PZT plate is bonded with graded ferromagnetic layers (Ni and FeCuNbSiB foils) in a cantilever configuration with one end clamped (Figure 8.13(a)). The self-biased effect is evoked due to the build-in magnetic bias formed in the graded ferromagnetic layers with different magnetic properties. A proof mass was added on the free end of the cantilever, which can be used to modify the natural resonance frequency of the ME cantilever to enhance the ME coefficient. By locating the current-carrying cable near the laminate sensor, the generated vortex magnetic field will be captured via the functional graded magnetic layers, thereby creating an ME voltage though the piezoelectric plate for current sensing in the absence of DC magnetic bias.

In order to detect the current of conventional power-line cables (50−60 Hz), the cantilever ME laminate was configured with adjusted geometry and tip mass (M_q). Moreover, the number of FeCuNbSiB layers (L) was optimized to achieve the largest self-biased ME coefficient. As a consequence, as shown in Figure 8.13(b), the self-biased ME voltage shows a peak behavior at 50 Hz in response to a power-line cable carried with an AC current of 50 Hz, indicating a good match of the optimized current sensor. Figure 8.13(c) plots the DC bias dependence of the ME voltage measured with

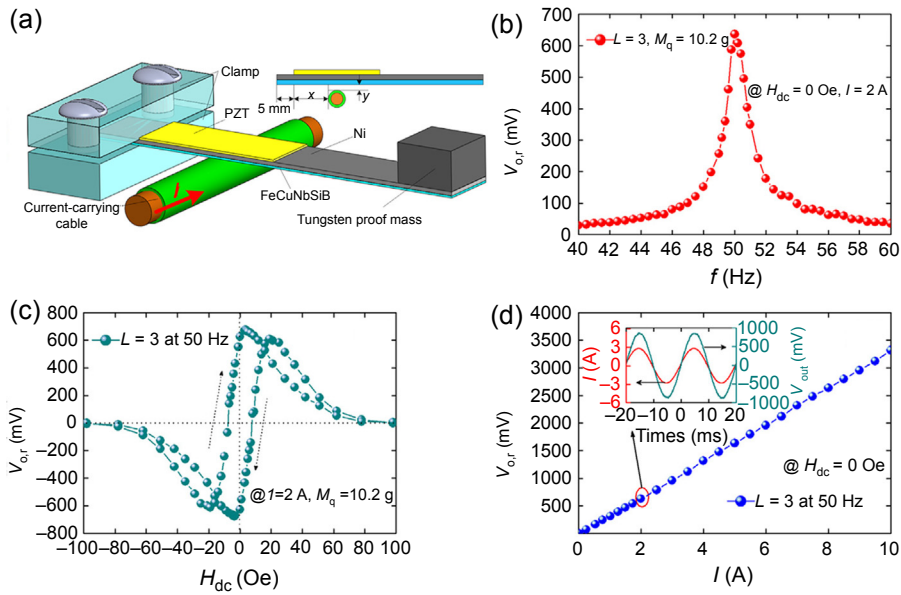

Figure 8.13 Demonstration of self-biased ME composites-based current sensor. (a) Schematic diagram of the cantilever-type ME current sensor design; (b) zero-biased ME voltage output as a function of frequency; (c) self-biased ME response as a function of DC bias; and (d) self-biased ME response as a function of detected current.
Reprinted with permission from Lu et al. (2014), Copyright 2014, Elsevier.

$I = 2$ A at 50 Hz. It can be clearly noticed that the maximum ME voltage output was obtained at zero-biased condition. Figure 8.13(d) illustrates the zero-biased ME voltage output under varied AC currents, and the inset shows the corresponding time-domain plot of I and V_{out} dependence. From these results, the self-biased ME sensor exhibits an excellent linearity and high sensitivity (330 mV/A) for monitoring the electric current in power-line cable.

Compared with the conventional ME current sensor, the presented self-biased-based sensor has high sensitive and DC-bias-free features. These features can be further expanded toward other types of self-biased ME composites. The development of self-biased-based ME composites is promising toward high sensitivity and miniaturized current sensor applications.

8.5 ME transformer-based current sensors

ME transformers as voltage gain devices have been investigated in literature, and it has been shown that a giant voltage gain can be obtained at the resonance frequency (Dong, Li, Viehland, Cheng, &Cross, 2004; Dong, Zhai, Priya, Li, & Viehland, 2009). With the application of a small DC magnetic bias, the ME transformer can provide a tunable voltage gain and/or a shift of resonance frequency, which is promising as a magnetic sensor. By configuring the characterization of ME composites and piezoelectric transformers, a variety of ME transformers have been developed (Dong et al., 2004b; Dong et al., 2009; Islam, Kim, Priya, & Stephanou, 2006a; Jia, Luo, Zhao, & Wang, 2008; Kim, Islam, & Priya, 2007; Leung, Or, Wang, & Ho, 2011). In the design proposed by Dong et al. (2004b, 2009) as shown in Figure 8.14(a), an input AC voltage was applied to the coil that generated an oscillating AC magnetic field (H_{ac}). The generated field interacted with the ME laminate and amplified the voltage output. In this design, the use of winding coil around the laminated ME composite poses challenges in its implementation. Alternatively, Zhang, Leung, Kuang, Or, and Ho (2013) demonstrated an ME transformer consisting of a ring-type Terfenol-D/PZT laminate composite directly connected with a Rosen-type PZT ceramic transformer, as shown in Figure 8.14(b) (Zhang et al., 2013). The ME transformer was characterized as a current sensor. The current sensitivity (S_I) in two concurrent operational modes was evaluated both theoretically and experimentally. A large enhancement in the resonance $S_I \sim 1000$ mV/A at 62 kHz (Figure 8.14(b)) was obtained as a result of the amplified vortex ME effect caused by the resonance voltage step-up effect in the piezoelectric transformer. However, the separate components of this ME transformer bring in another level of difficulty toward sensor implementation. Thus, even though these structures are intriguing, their implementation for realization of miniature transformer and magnetic sensors will be limited. In this chapter, we will discuss two different types of ME tunable transformers in addressing these challenges.

8.5.1 Epoxy-bonded ME transformer

Considering the high ME coupling of ME laminate and the easy fabricated unipoled piezoelectric transformer, epoxy-bonded ME transformers with different configurations

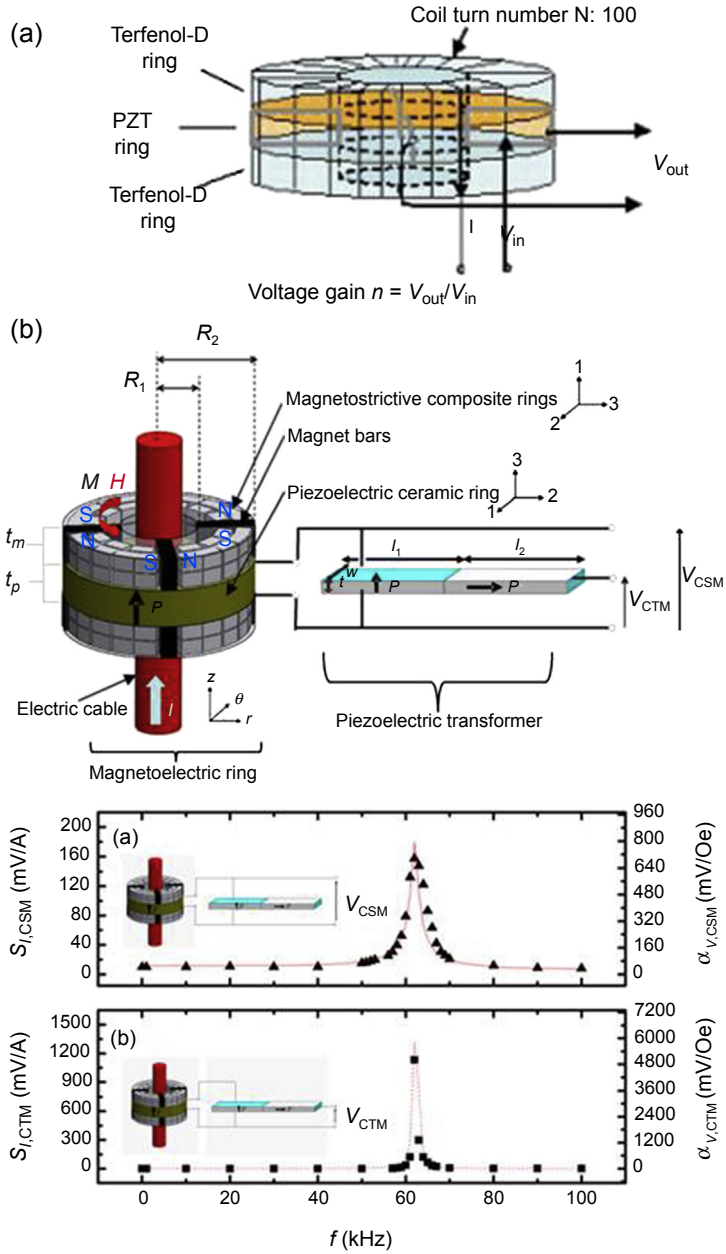

Figure 8.14 (a) Coil-winded-based ME transformer. (b) Ring-type ME composites connected with Rosen-type PZT ceramic transformer.
(a) Reprinted with permission from Dong et al. (2004b), Copyright 2004: AIP Publishing LLC;
(b) Reprinted with permission from Zhang et al. (2013), Copyright 2013: AIP Publishing LLC.

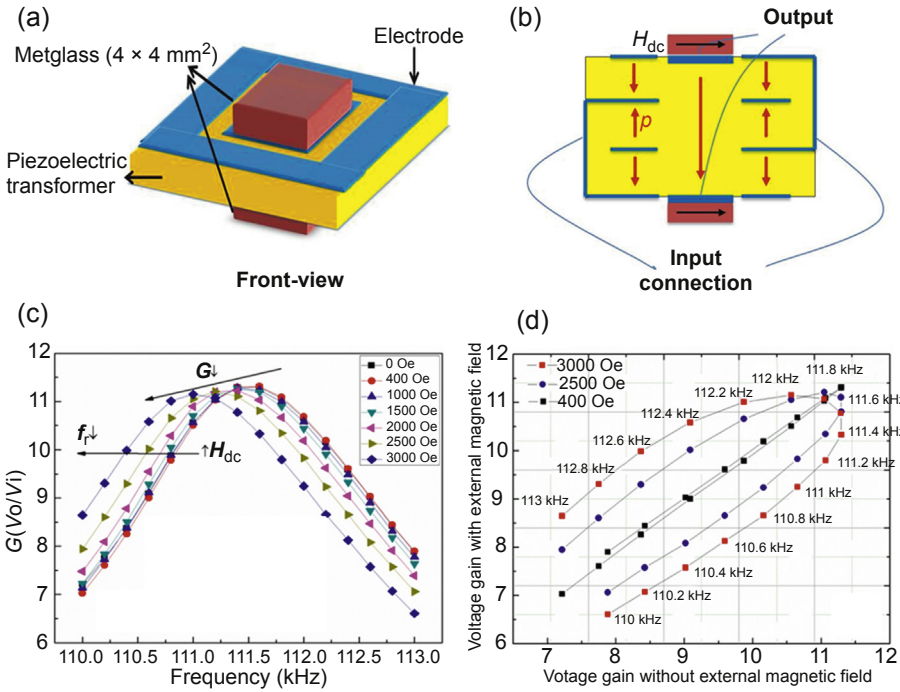

Figure 8.15 (a) and (b) Schematic diagram of the ME transformer, consisting of a multilayer piezoelectric ceramic transformer and two layers of Metglas. (c) and (d) ME transformer voltage gain variation as a function of frequency under varied DC magnetic bias.

were investigated (Jia et al., 2008; Leung et al., 2011; Zhou, Wang, et al., 2012). A 2−2-laminated ME transformer was designed and fabricated by directly bonding magnetostrictive layers onto the output port of a cofired multilayer piezoelectric transformer, as shown in Figure 8.15. The multilayered piezoelectric transformer was synthesized via a low temperature cofiring process (Park & Priya, 2011). Piezoelectric composition 0.2 $Pb(Zn_{1/3}Nb_{2/3})$-0.8 $Pb(Zr_{0.5}Ti_{0.5})O_3$ (PZNT) was chosen and synthesized by a conventional mixed oxide method due to its good piezoelectricity and low sintering temperature. Figure 8.15(a) illustrates the schematics of the ME transformer. In this design, the input and output electrodes are on the same side of the square plate and are isolated from each other by a fixed gap of 2 mm. The electrode pattern is a square/square structure with a floating connection among each layer. Metglas, with a dimension of 4 × 4 mm^2, are attached on both side of the output section. Figure 8.15(b) shows the electrical connection of the transformer in the step-up mode. In this case, on applying the electrical excitation to the external rectangle frame (input), the contour extensional vibration is generated and transferred to the center square (output) through the gap. At the output, the mechanical strain is converted to electrical voltage through a direct piezoelectric effect. The multilayer section is equivalent to connecting n units in parallel, where the input motional capacitance ($C_{a,\text{input}}$) is increased by n times. Simplistically, the gain of the transformer is given by: $\text{Gain} = \sqrt{\frac{C_{a,\text{input}}}{C_{a,\text{output}}}}$. Thus, the multilayered structure can

provide higher voltage gain. By locating the longitudinally poled transformer under a transverse DC magnetic field (H_{dc}), the peak value of the voltage gain was found to change with respect to different resonant frequency, as shown in Figure 8.15(c). Figure 8.15(d) plots the voltage gain with and without an external magnetic field, indicating the effectivity of voltage gain tunability under an induced magnetic field. There is a significant change in the magnitude of the voltage gain with an applied external magnetic field, which increases as the frequency approaches the resonance point. Furthermore, for the same magnitude of voltage gain, a large frequency shift can be noticed with the application of an external magnetic field. These results prove that both voltage gain and working resonance frequency are dependent on the external magnetic field.

The generation of voltage gain tunability and frequency shift under induced H_{dc} allows us to tailor the ME transformer with desired performance, offering the potential for the design of a magnetic-field-tunable sensor. The working mechanism can be simply explained as follows: when an external magnetic field is applied to the composite, the Metglas induces strain in terms of shape change on the center square section through magnetostriction. This strain is transferred to the output section of the transformer through elastic coupling. Next, a mechanical stress is generated in the center square, resulting in an electric polarization by direct piezoelectric effect. Meanwhile, the electric field-induced strain from the input piezoelectric phase is interfered with this magnetic field-induced strain from the magnetostrictive phase. The resulting differential strain is converted into voltage through the direct piezoelectric effect and will induce change in the magnitude of output voltage and working resonance frequency. In this case, external magnetic field affects the transformer performance through direct ME effect. Thus, it is expected that the magnitude of the voltage gain and working resonance frequency of the transformer will be tuned and shifted under an external magnetic field through the ME effect. In return, one can detect the ambient magnetic field/current by monitoring the performance of the ME transformer. This sensing mechanism can be further extended to other configurations by selecting high-performance magnetostrictive materials and piezoelectric transformers.

8.5.2 Cofired ME transformer

To achieve the best ME tunable performance, giant ME coupling and more efficient stress transfers are desired. However, the problems with epoxy-bonded laminate ME composites could not be neglected. (1) Device miniaturization is a concern since the processing requires manual operations like dicing, cutting, bonding, and wiring. (2) Low mechanical strength of the epoxy may deteriorate the ME coupling and sensitivity. The ideal solution to these problems is discovering an all-in-one ME composite, which possesses both giant ME coupling coefficient and transformer function.

In addressing these concerns, cofired ME transformers were developed. Islam et al. demonstrated a sintered ME transformer consisting of a particulate $Pb(Zr_{0.52}Ti_{0.48})O_3$-$Ni_{0.8}Zn_{0.2}Fe_2O_4$ (PZT-NZF) composite and utilizing the electrode pattern of a conventional unipoled transformer, as shown in Figure 8.16(a) (Islam, Kim, Priya, & Stephanou, 2006b). The unipoled ME transformer possesses a ring-dot type electrode pattern with an electrical connection in the step-up mode. On applying an electrical drive to the

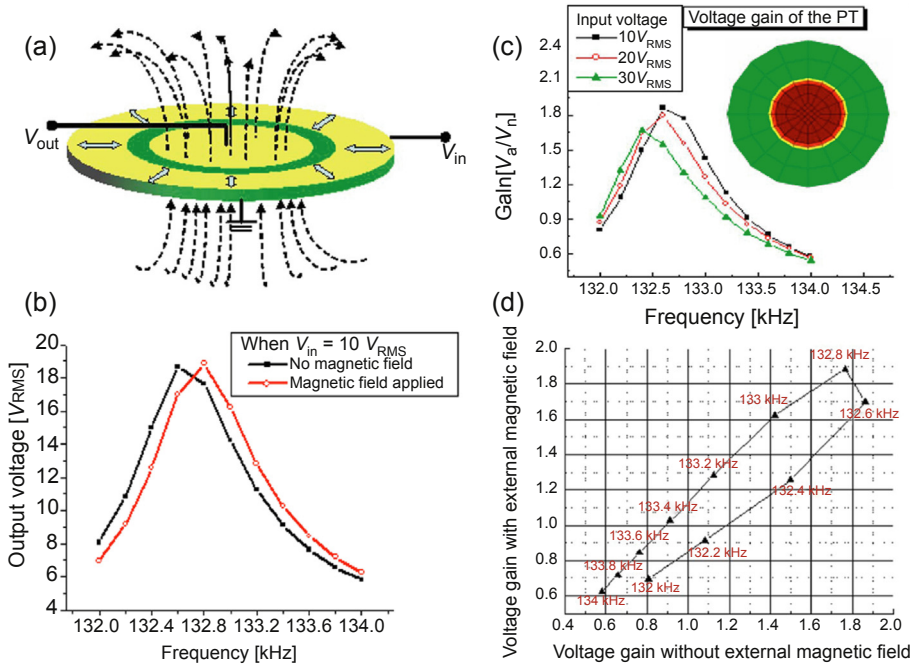

Figure 8.16 (a) Schematic diagram of the cofired particulate magnetoelectric transformer and its performance (b) with and without an applied DC magnetic field. (c) Voltage gain variation as a function of frequency under varied input voltage. (d) Change in voltage gain with and without the external magnetic field.
(a) and (b) Reprinted with permission from Islam et al. (2006b); Copyright: 2006 AIP Publishing LLC; (c) and (d) Reprinted with permission from Kim et al. (2007), Copyright: 2007 AIP Publishing LLC.

external ring (input), the radial extensional vibration is generated through converse piezoelectric effect and further transferred to the center dot (output). At the output, the mechanical strains are converted into electrical voltage through direct piezoelectric effect. Since NZF magnetostrictive particles were spread all over the transformer disk through the mixed oxide sintering route, the transformer performance is sensitive with respect to an external magnetic field. Figure 8.16(b) demonstrates a significant shift in the magnitude of resonance frequency with respect to the corresponding maximum voltage output under applied DC magnetic bias. In addition, the electric-field-induced strain will also interact with the magnetic particles, thereby generating magnetic flux through the ME transformer. This magnetic flux can interact with the external magnetic field, producing a flux gradient that can be detected through the tunable feature of the transformer. On the other hand, the change in voltage gain can be modulated by optimizing input voltage (Kim et al., 2007), as shown in Figure 8.16(c). The variation in voltage gain before and after applied magnetic bias was clearly demonstrated in Figure 8.16(d). These results indicate that the cofired ME transformer not only possesses a simple structure for fabrication and

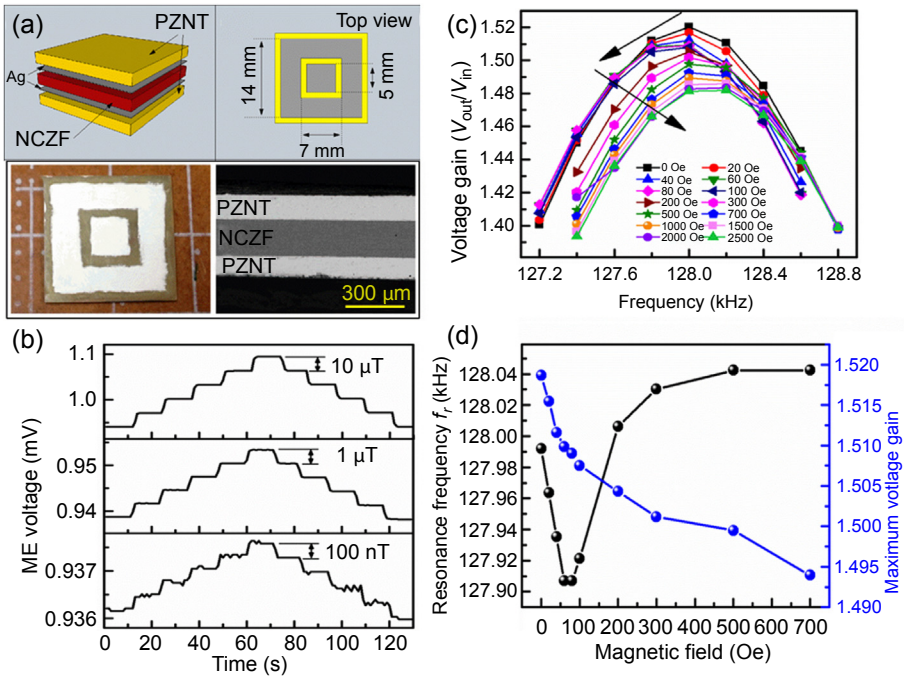

Figure 8.17 (a) Schematic and images of cofired laminate ME transformer; (b) DC sensitivity of the cofired ME laminate; (c) voltage gain variation as a function of frequency under varies DC magnetic bias; and (d) variation of resonance frequency and maximum voltage gain as a function of external DC magnetic field.
Reprinted with permission from Zhou et al. (2014), Copyright 2014, AIP Publishing LLC.

implementation, but also can be easily manipulated by changing the input driving voltage and ring-dot pattern. However, the small ME coupling of the particulate composites hinders its tunable feature under an applied DC magnetic field.

In order to further enhance the ME response, Yuan et al. designed and demonstrated a cofired ME transformer consisting of two unipoled piezoelectric transformers and a magnetostrictive layer in a laminate configuration (Zhou, Yan, & Priya, 2014). The ME transformer was designed by combining magnetostrictive material and a piezoelectric transformer in a piezoelectric/magnetostrictive/piezoelectric (PMP) laminate structure with an Ag inner electrode (Figure 8.17(a)). Composition corresponding to 0.2 $Pb(Zn_{1/3}Nb_{2/3})$−0.8 $Pb(Zr_{0.5}Ti_{0.5})O_3$ (PZNT) and $Ni_{0.6}Cu_{0.2}Zn_{0.2}Fe_2O_4$ (NCZF) were selected as piezoelectric and magnetostrictive materials, respectively. In this unipoled transformer design, the input electrode "square ring" and the center output electrode "square" are on the same side of the piezoelectric plate and are isolated from each other by a fixed gap of 1 mm (Laoratanakul, Carazo, Bouchilloux, & Uchino, 2002; Priya, Ural, Woo Kim, Uchino, & Ezaki, 2004). Two unipoled transformers were electrically connected in a series. Figure 8.17(b) illustrates the DC magnetic field sensitivity of the cofired transformer; magnetic field variation as small as $H_{dc} = 100$ nT

could be detected, indicating an enhanced ME coupling and sensitivity in the cofired 2−2-type laminate.

Figure 8.17(c) shows the measured voltage gain G as a function of frequency with H_{dc} varying from 0 to 2500 Oe. It is clearly noticed that the magnitude of maximum voltage gain decreased and the peak position (resonance frequency) shifted as a function of H_{dc}. The magnitude of maximum voltage gain and corresponding resonance frequency shift are summarized as a function of H_{dc} in Figure 8.17(d). It is obvious that the resonance frequency decreases first with increasing H_{dc}, showing a minimum magnitude of 127.9 kHz in the range of 60−80 Oe, and then increases with increasing H_{dc}. These results demonstrate that by optimizing the ME transformer configuration, large resonance frequency tunability $(f_{r.o} - f_{r.H})/H = 1.4$ Hz/Oe, where $f_{r.o}$ and $f_{r.H}$ are the resonance frequencies under zero and nonzero magnetic field condition was realized with a small DC magnetic field in the range of 60−80 Oe. The 2−2-type ME laminates presented a superior performance compared to the 0-3 type particulate composite. The performance of the structure presented in this study can be further improved by optimizing the input/output area ratio through multilayering, material composition, and electrical connectivity (Priya, 2006; Priya et al., 2004).

8.6 Magnetic noise and elimination

The detection capability of ME sensors not only depends on the ME voltage signals in response to an incident magnetic field, but is also affected by the noise that exists in the detection component, both internally and externally. In the case of ME sensors, the dominate noise sources can be classified as (1) extrinsic noises (vibration noise, thermal noise, and electromagnetic interference) and (2) intrinsic noises (Johnson noise and 1/*f* noise). Therefore, it is of great importance to identify the noise sources and eliminate their influence toward better detection sensitivity of the sensors.

8.6.1 Extrinsic noise

Extrinsic noise is referred to as any unexpected or unwanted disturbances that are originated from the environment. These disturbances can be mechanical vibration, magnetic field, temperature fluctuation, and so on. The main noise sources that can disturb the ME composites are thermal and vibration noises. In addressing these issues, Xing et al. systematically investigated the ability of various fundamental modes to eliminate environmental noise from thermal and vibration noise (Xing, Zhai, Li, & Viehland, 2009). The idea is based on designing the sensor signal and the noise signal in different fundamental modes. In a symmetrical structure, the neutral line sits in the center of the bending piezoelectric, where the vibration-induced charge can be canceled. In an unsymmetrical structure, both bending and longitudinal modes will be excited due to thermal expansion difference, where the thermal strain can be partially canceled. Figure 8.18 summarized various ME laminate configurations and their capability to reject thermal or vibration noises (Xing et al., 2009). Accordingly, SS-UN (symmetrical signal, unsymmetrical noise) modes have the ability to cancel

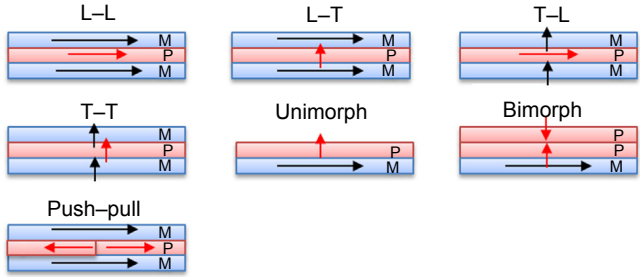

Model	Vibration cancellation	Thermal cancellation
Unimorph	No	No
Bimorph	Partially	Partially
L–T, T–T, L–L, T–L	Yes	No
Push–pull	Yes	No
SS–UN[a]	Yes	No
US–SN[b]	No	Yes

[a]SS–UN:symmetrical-signal, unsymmetrical noise
[b]US–SN:unsymmetrical-signal, symmetrical noise

Figure 8.18 ME laminate composite structures and their effect in noise cancellation. Adapted from Xing et al. (2009).

vibration noise, whereas US−SN (unsymmetrical signal, symmetrical noise) modes have the capability to reject thermal noise.

Thermal fluctuation noise affects the detection unit via the pyroelectric effect. This phenomenon can be originated from the nature of pyroelectric materials with lower crystal symmetry that can generate electricity in response to temperature changes. When considering the crystal structure, 10 of these 20 piezoelectric crystal classes are pyroelectric. In particular, the widely used PZT, 4 mm point group, has a pyroelectric effect. Thus, the ME composite sensors would be affected by the thermal noise in the piezoelectric (PZT-based) layer.

As discussed above, US−SN modes have the capability to reject thermal noise; one of the candidate configurations is ME laminate in a bimorph structure (Figure 8.18). Based on this concept, Zhai et al. demonstrate a design of Terfenol-D/PZT bimorph ME laminate that operates in a bending mode under an unsymmetrical magnetic bias (Zhai et al., 2008b), as shown in Figure 8.19(a). Unlike conventional bimorph, the magnetization directions are opposite in the two Terfenol-D layers by using two U-shaped magnetic biases. Thus, under an applied AC magnetic field, the bimorph laminate operates in bending modes with top and bottom PZT layers generating charges of opposite signs, where the differential output of the ME voltage will be doubled. However, when the temperature is changed, each layer will change shape in a longitudinal mode with induced thermal charges of the same sign, where the differential output of the thermal noise will be null. The comparative results in

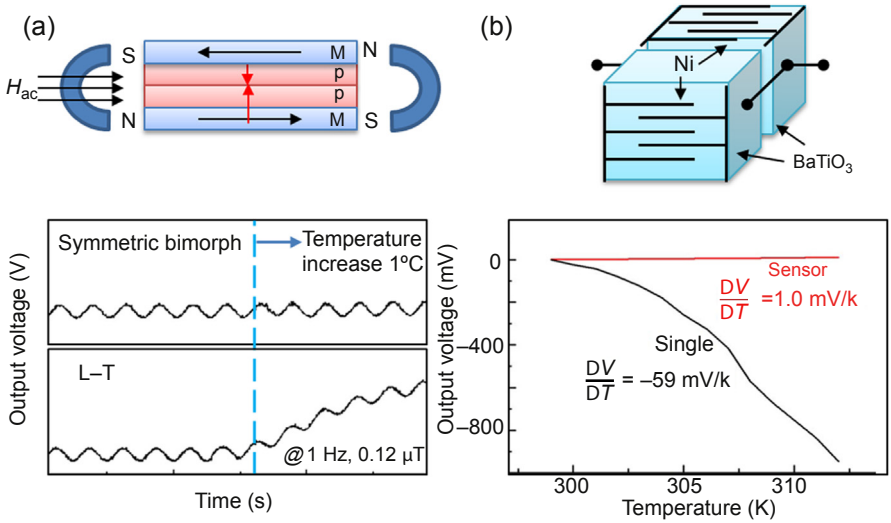

Figure 8.19 (a) Schematic illustration of symmetric ME bimorph design and its output signals under thermal fluctuations in time domain. (b) Schematic illustration of a temperature-compensated device based on two ME multilayer capacitors (MLCs) and its temperature dependence performance.
Adapted from Zhai et al. (2008b) and Israel et al. (2010).

Figure 8.19(a) clearly demonstrate the capability of thermal noise cancellation by using this bimorph structure. Alternatively, Israel et al. proposed a different thermal-noise-rejection ME sensor by connecting two ME multilayer $BaTiO_3$:Ni capacitors (Israel, Kar-Narayan, & Mathur, 2010), as shown in Figure 8.19(b). In this design, the two ME elements were electrically connected in parallel with oppositely oriented polarization and posses stable temperature dependence performance compared to that of a single ME element.

Vibration noise affects the ME sensor via the piezoelectric effect, which refers to spontaneous polarization coupled to pressure and/or stress changes. One can use a vibration isolation table to minimize the effect of vibration noise in a lab condition; however, this is not suitable for practical applications. According to Xing's investigation (Xing et al., 2008), it conceptually demonstrated that vibrational noise can be eliminated by using an ME laminate with a mechanically symmetrical structure. Gao et al. demonstrated a differential-mode Metglas/PZT ME laminate, where two layers of PZT with the same polarization were parallely connected to create a differential symmetric structure (Gao, Zhai, et al., 2011). Under an applied longitudinal magnetic field, the PZT layer contracts or expands longitudinally with identical signs of a generated charge, leading to a doubling of the signal. Conversely, an applied vibration noise will tend to cause an asymmetric bending deformation; the corresponding opposite signs of charges generated from top and bottom PZT layers will result in an attenuation of the output signal. Thus, the differential structure has the ability to reject external vibrational noise by separating the signal and noise with a different vibration mode.

8.6.2 Intrinsic noise

Intrinsic noise refers to disturbances that are originated from the detection unit and/or detection circuits inherently. In detection circuits, the main noise sources are (1) Johnson noise and (2) Flicker (1/*f*) noise.

Johnson noise is electronic noise generated by thermal agitation of electrons in resistors, which is random in nature. It can be represented as either a voltage noise source or a current noise source in series/parallel with a noiseless resistor, as shown in Figure 8.20. For a given bandwidth, the root mean square (RMS) voltage noise (V_n) and current noise (I_n) can be expressed as (Leach, 1994)

$$V_n = \sqrt{4k_B T \Delta f R} \tag{8.9}$$

$$I_n = \sqrt{4k_B T \Delta f / R} \tag{8.10}$$

where $k_B = 1.38 \times 10^{-23}$ J/K is Boltzmann's constant, T is absolute temperature in kelvins, Δf is the bandwidth in Hz over which the noise is measured, and R is resistance value in ohms. From these equations, we can see that both temperature and resistance play an important role toward the Johnson noise density at a fixed bandwidth.

Flicker noise (1/*f* noise), or contact noise, is present in all devices consisting of imperfect contact between two conductors. The various kinds of mechanisms for Flicker noise depends on the device type, where the random generation and recombination of electron−hole pairs in semiconductors are the most commonly found. It can be modeled by a noise current source in parallel with the device. For a given bandwidth Δf, the RMS flicker-noise current (I_f) can be expressed as (Leach, 1994)

$$I_f = \sqrt{K_f I^m \Delta f / f} \tag{8.11}$$

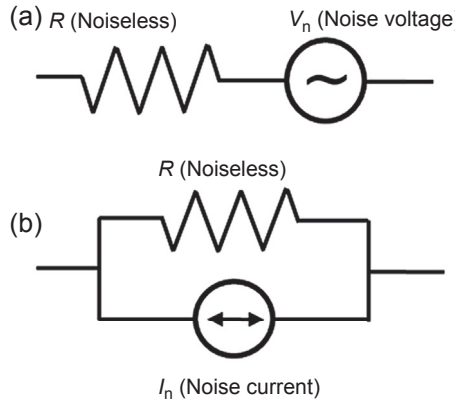

Figure 8.20 Equivalent circuit models of (a) noise voltage and (b) noise current.

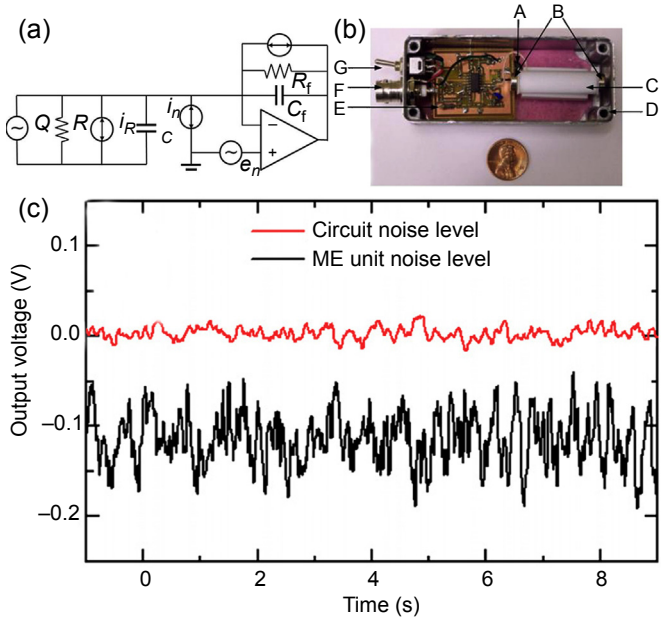

Figure 8.21 (a) Equivalent noise model for a magnetic sensor. (b) Photograph of a prototype ME detection system, consisting of an ME sensor and low-noise charge amplifier. (c) Output noise level of circuit and sensor unit.
Adapted from Wang et al. (2014) (a); Reprinted with permission from Xing et al. (2007), Copyright 2007, AIP Publishing LLC.

where K_f is the flicker-noise constant, I is the DC current, and m is the flicker-noise exponent. It can be noticed that the flicker noise is sensitive with respect to frequency, which is specifically high at a low frequency range.

Figure 8.21(a) shows an equivalent noise circuit model for an ME-based sensor (Wang et al., 2014; Xing, Li, & Viehland, 2007). In this noise model, five noise sources were considered as main contributions to the total noise density. The ME composite was modeled as a magnetic field-induced charge source in parallel with a capacitor C and resistor R. There are two noise sources for the ME detection unit: (1) the dielectric loss noise (N_{loss}) source and (2) the leakage resistance noise (N_R) source. The corresponding charge noise density is given as

$$N_{\text{loss}} = \sqrt{4k_{\text{B}}TC \tan \delta / 2\pi f} \tag{8.12}$$

$$N_R = \frac{1}{2\pi f}\sqrt{4k_{\text{B}}T/R} \tag{8.13}$$

where T is the temperature in kelvin, tan δ is the dielectric loss, R is the DC resistance of the ME sensor, and f is the frequency in Hz. For the detection circuit, there are three noise sources, including (1) current (N_i) and (2) voltage (N_v) noise from low-noise

amplifiers and (3) thermal noise (N_{R_f}) from feedback resistors. The noise charge density can be expressed as (Gao et al., 2012)

$$N_i = \frac{1}{2\pi f} i_n \tag{8.14}$$

$$N_v = \frac{e_n|1 + Z/Z_f|}{|H(s)|} \tag{8.15}$$

$$N_{R_f} = \frac{1}{2\pi f}\sqrt{4k_B T/R_f} \tag{8.16}$$

where i_n is the current noise density, e_n is the voltage noise density of the low-noise amplifier, and Z and Z_f represent the ME laminate and the feedback impedance. Thus, the total noise charge density (N^T) can be given as

$$N^T = \sqrt{N_{\text{loss}}^2 + N_R^2 + N_i^2 + N_v^2 + N_{R_f}^2} \tag{8.17}$$

Thus, one can use Eqns (8.12)−(8.17) to estimate and analyze the contributions from various noise sources.

Figure 8.21(b) illustrates a previous prototype ME detection system consisting of an ME composite (component C) and low-noise detection circuit (component E), as discussed above (Xing et al., 2008). In this prototype, the measured RMS value of the circuit is dramatically smaller than that of the ME detection unit (circuit + sensor), as shown in Figure 8.21(c). Accordingly, Wang et al. systematically reviewed the development of equivalent magnetic noise reduction for ME sensors (Wang et al., 2014). There are mainly three strategies toward noise reduction, including (1) reducing the detection circuit noise via a low-noise amplifier, (2) reducing the ME laminate noise via reducing dielectric loss and increasing resistance of piezoelectric materials, and (3) increasing the ME charge coefficient without introducing addition noise via interfacial bonding/poling condition/geometry design optimization.

Acknowledgments

The authors gratefully acknowledge the financial support from the Office of Basic Energy Science, the Department of Energy (DOE), and the Air Force Office of Scientific Research (AFOSR).

References

Bai, J. G., Lu, G. Q., & Lin, T. (2003). *Sensors and Actuators A-Physical, 109*(1−2), 9.

Bichurin, M. I., Filippov, D. A., Petrov, V. M., Laletsin, V. M., Paddubnaya, N., & Srinivasan, G. (2003). *Physical Review B, 68*(13).

Bichurin, M., Petrov, V., Kiliba, Y., & Srinivasan, G. (2002). *Physical Review B, 66*(13).
Bichurin, M., Petrov, V., Ryabkov, O., Averkin, S., & Srinivasan, G. (2005). *Physical Review B, 72*(6).
Busatto, G., La Capruccia, R., Iannuzzo, F., Velardi, F., & Roncella, R. (2003). *Microelectronics Reliability, 43*(4), 577.
Cho, K.-H., & Priya, S. (2011). *Applied Physics Letters, 98*(23), 232904.
Dong, S. X., Bai, J. G., Zhai, J. Y., Li, J. F., Lu, G. Q., Viehland, D., et al. (2005). *Applied Physics Letters, 86*(18).
Dong, S. X., Li, J. F., & Viehland, D. (2004a). *Journal of Applied Physics, 96*(6), 3382.
Dong, S. X., Li, J. F., & Viehland, D. (2004b). *Applied Physics Letters, 84*(21), 4188.
Dong, S. X., Li, J. F., Viehland, D., Cheng, J., & Cross, L. E. (2004). *Applied Physics Letters, 85*(16), 3534.
Dong, S. X., Zhai, J. Y., Li, J. F., & Viehland, D. (2006a). *Applied Physics Letters, 88*(8).
Dong, S. X., Zhai, J. Y., Li, J. F., & Viehland, D. (2006b). *Applied Physics Letters, 89*(25).
Dong, S. X., Zhai, J. Y., Priya, S., Li, J. F., & Viehland, D. (2009). *IEEE Transactions on Ultrasonics Ferroelectrics and Frequency Control, 56*(6), 1124.
Fang, Z., Lu, S. G., Li, F., Datta, S., Zhang, Q. M., & El Tahchi, M. (2009). *Applied Physics Letters, 95*(11).
Gao, J. Q., Gray, D., Shen, Y., Li, J. F., & Viehland, D. (2011). *Applied Physics Letters, 99*(15).
Gao, J. Q., Wang, Y. J., Li, M. H., Shen, Y., Li, J. F., & Viehland, D. (2012). *Materials Letters, 85*, 84.
Gao, J. Q., Zhai, J. Y., Shen, Y., Shen, L. G., Gray, D., Li, J. F., et al. (2011). *IEEE Transactions on Ultrasonics Ferroelectrics and Frequency Control, 58*(8), 1541.
Islam, R. A., Kim, H., Priya, S., & Stephanou, H. (2006a). *Applied Physics Letters, 89*(15).
Islam, R. A., Kim, H., Priya, S., & Stephanou, H. (2006b). *Applied Physics Letters, 89*(15), 152908.
Israel, C., Kar-Narayan, S., & Mathur, N. D. (2010). *IEEE Sensors Journal, 10*(5), 914.
Jia, Y. M., Luo, H. S., Zhao, X. Y., & Wang, F. F. (2008). *Advanced Materials, 20*(24), 4776.
Jia, Y. M., Or, S. W., Chan, H. L. W., Zhao, X. Y., & Luo, H. S. (2006). *Applied Physics Letters, 88*(24).
Kim, H., Islam, R. A., & Priya, S. (2007). *Applied Physics Letters, 90*(1).
Lage, E., Kirchhof, C., Hrkac, V., Kienle, L., Jahns, R., Knochel, R., et al. (2012). *Nature Materials, 11*(6), 523.
Laletin, V. M., Paddubnaya, N., Srinivasan, G., De Vreugd, C. P., Bichurin, M. I., Petrov, V. M., et al. (2005). *Applied Physics Letters, 87*(22), 222507.
Laletin, U., Sreenivasulu, G., Petrov, V. M., Garg, T., Kulkarni, A. R., Venkataramani, N., et al. (2012). *Physical Review B, 85*(10).
Laoratanakul, P., Carazo, A. V., Bouchilloux, P., & Uchino, K. (2002). *Japanese Journal of Applied Physics Part 1, 41*(3A), 1446.
Leach, W. M. (1994). *Proceedings of the IEEE, 82*(10), 1515.
Le, M. Q., Belhora, F., Cornogolub, A., Cottinet, P. J., Lebrun, L., & Hajjaji, A. (2014). *Journal of Applied Physics, 115*(19).
Leung, C. M., Or, S. W., Wang, F. F., & Ho, S. L. (2011). *Journal of Applied Physics, 109*(10).
Leung, C. M., Or, S. W., Zhang, S. Y., & Ho, S. L. (2010). *Journal of Applied Physics, 107*(9).
Lu, C. J., Li, P., Wen, Y. M., Yang, A. C., Yang, C., Wang, D. C., et al. (2014). *Journal of Alloys and Compounds, 589*, 498.
Mandal, S. K., Sreenivasulu, G., Petrov, V. M., & Srinivasan, G. (2010). *Applied Physics Letters, 96*(19).
Mandal, S. K., Sreenivasulu, G., Petrov, V. M., & Srinivasan, G. (2011). *Physical Review B, 84*(1).

Martins, P., & Lanceros-Méndez, S. (2013). *Advanced Functional Materials, 23*(27), 3371.
Nan, C. W., Bichurin, M. I., Dong, S. X., Viehland, D., & Srinivasan, G. (2008). *Journal of Applied Physics, 103*(3).
Onuta, T.-D., Wang, Y., Long, C. J., & Takeuchi, I. (2011). *Applied Physics Letters, 99*(20), 203506.
Park, C. S., & Priya, S. (2011). *Journal of the American Ceramic Society, 94*(4), 1087.
Petrov, V. M., Srinivasan, G., Bichurin, M. I., & Galkina, T. A. (2009). *Journal of Applied Physics, 105*(6), 063911.
Priya, S. (2006). *IEEE Transactions on Ultrasonics Ferroelectrics and Frequency Control, 53*(1), 23.
Priya, S., Ural, S., Woo Kim, H., Uchino, K., & Ezaki, T. (2004). *Japanese Journal of Applied Physics, 43*(6A), 3503.
Ramsden, E. (2006). *Hall-effect sensors: Theory and applications*. Burlington: Elsevier.
Shen, Y., Gao, J., Wang, Y., Finkel, P., Li, J., & Viehland, D. (2013). *Applied Physics Letters, 102*(17), 172904.
Sreenivasulu, G., Mandal, S. K., Bandekar, S., Petrov, V. M., & Srinivasan, G. (2011). *Physical Review B, 84*(14).
Srinivasan, G. (2010). *Annual Review of Materials Research, 40*, 153.
Srinivasan, G., Rasmussen, E. T., Gallegos, J., Srinivasan, R., Bokhan, Y. I., & Laletin, V. M. (2001). *Physical Review B, 64*(21).
Srinivasan, G., Rasmussen, E. T., Levin, B. J., & Hayes, R. (2002). *Physical Review B, 66*(2).
Wang, Y. J., Gao, J. Q., Li, M. H., Shen, Y., Hasanyan, D., Li, J. F., et al. (2014). *Philosophical Transactions. Series A, Mathematical, Physical, and Engineering Sciences, 372*(2009), 20120455.
Wang, Y. J., Gray, D., Berry, D., Gao, J. Q., Li, M. H., Li, J. F., et al. (2011). *Advanced Materials, 23*(35), 4111.
Wang, Y. J., Wang, F. F., Or, S. W., Chan, H. L. W., Zhao, X. Y., & Luo, H. S. (2008). *Applied Physics Letters, 93*(11).
Xing, Z. P., Li, J. F., & Viehland, D. (2007). *Applied Physics Letters, 91*(18).
Xing, Z. P., Zhai, J. Y., Dong, S. X., Li, J. F., Viehland, D., & Odendaal, W. G. (2008). *Measurement Science and Technology, 19*(1).
Xing, Z. P., Zhai, J. Y., Li, J. F., & Viehland, D. (2009). *Journal of Applied Physics, 106*(2).
Yang, S. C., Ahn, C. W., Cho, K. H., & Priya, S. (2011). *Journal of the American Ceramic Society, 94*(11), 3889.
Yang, S. C., Cho, K. H., Park, C. S., & Priya, S. (2011). *Applied Physics Letters, 99*(20).
Yang, S. C., Park, C. S., Cho, K. H., & Priya, S. (2010). *Journal of Applied Physics, 108*(9).
Yan, Y. K., Zhou, Y., & Priya, S. (2013). *Applied Physics Letters, 102*(5).
Zhai, J. Y., Dong, S. X., Xing, Z. P., Li, J. F., & Viehland, D. (2006). *Applied Physics Letters, 89*(8).
Zhai, J. Y., Xing, Z. P., Dong, S. X., Li, J. F., & Viehland, D. (2008a). *Journal of the American Ceramic Society, 91*(2), 351.
Zhai, J. Y., Xing, Z. P., Dong, S. X., Li, J. F., & Viehland, D. (2008b). *Applied Physics Letters, 93*(7).
Zhang, S. Y., Leung, C. M., Kuang, W., Or, S. W., & Ho, S. L. (2013). *Journal of Applied Physics, 113*(17).
Zhou, J. P., Wang, P., Yang, J., Liu, P., & Zhang, H. W. (2012). *Journal of Applied Physics, 111*(3).
Zhou, Y., Yang, S. C., Apo, D. J., Maurya, D., & Priya, S. (2012). *Applied Physics Letters, 101*(23).
Zhou, Y., Yan, Y., & Priya, S. (2014). *Applied Physics Letters, 104*(23).

Microwave and millimeter-wave multiferroic devices

9

G. Srinivasan
Oakland University, Rochester, MI, USA

9.1 Introduction

The nature of strain-mediated, high-frequency ME coupling and hybrid spin-electromagnetic modes in ferromagnetic−ferroelectric composites and their use for a new family of dual E- and H-tunable microwave and millimeter-wave signal processing devices are discussed in this chapter (Bichurin, Viehland, & Srinivasan, 2007; Lawes & Srinivasan, 2011; Srinivasan, 2010; Srinivasan & Fetisov, 2006; Sun & Srinivasan, 2012). The ferromagnetic phase in the composites for such high-frequency devices, in general, are low-loss ferrites, such as single-crystals or liquid phase epitaxy (LPE) grown films of yttrium iron garnet (YIG) and single-crystal nickel ferrite (NFO), lithium ferrite (LFO), Y-type hexagonal ferrites, and M-type hexagonal barium−aluminum and strontium−aluminum ferrites. Ferroelectric phases of interest are lead zirconate titanate (PZT), lead magnesium niobate-lead titanate (PMN-PT), and lead zinc niobate-lead titanate (PZN-PT) (Sun & Srinivasan, 2012).

A majority of devices discussed here are based on ferromagnetic resonance (FMR) in a layered ferrite−ferroelectric composite. FMR is a powerful tool for studies on the converse-ME (CME) effects in multiferroic composites. An electric field E applied to a ferrite−ferroelectric composite produces a mechanical deformation in the ferroelectric phase, which in turn is coupled to the ferrite, resulting in a shift in the resonance field. Information on the nature of CME coupling could therefore be obtained from data on the resonance field shift δH_E or frequency shift δf_E versus E. The first such study was on bulk samples of 90% YIG−10% PZT, and the ME coupling was quite weak because of low PZT concentration (Bichurin, Petrov, & Kiliba, 1997). But in samples with any higher PZT, FMR line broadening masked the electric-field effect on the resonance field. Such line broadening, however, could easily be eliminated in layered samples. Theoretical models for CME in ferrite−ferroelectric bilayers predict a strong interaction (Bichurin et al., 2001; Bichurin, Petrov, Kiliba, & Srinivasan, 2002). The effect also opens up the possibility of novel voltage-tunable ferrite signal processing devices (Sun & Srinivasan, 2012).

The CME effect discussed above takes place in ferrite−ferroelectric layered structures when the phases are *tightly bound*, that is, when the mechanical stress created in one is transferred to the second. There are, however, other ME phenomena that do not require bonding between the layers and take place simply due to the proximity of two materials having different dielectric and magnetic properties. An example of such a

Composite Magnetoelectrics. http://dx.doi.org/10.1016/B978-1-78242-254-9.00009-3
Copyright © 2015 Elsevier Ltd. All rights reserved.

phenomenon is the formation of hybrid spin-electromagnetic waves in the layered structures (Demidov, Kalinikos, & Edenhofer, 2002). Theoretical models for wave propagation in ferromagnetic−ferroelectric slabs predict intensive hybridization between the electromagnetic waves propagating in the ferroelectric film and the spin waves propagating in the ferromagnetic film. Also, the theory shows that the dispersion characteristics of the hybrid waves can be tuned with an electric field or a magnetic field (Ustinov et al., 2006).

The CME at FMR and the hybrid waves in multiferroic composites are of importance for dual E- and H-tunable microwave and millimeter-wave devices. Tunable microwave devices are widely used in radar, telecommunication, and RF devices. One class of such devices is based on ferrites (Adam, Daniel, Emtage, & Talisa, 1991; Adam, Davis, Dionne, Schloemann, & Stitzer, 2002). In particular, resonators fabricated from YIG films are attractive due to their planar geometry, small size (area on the order of several square millimeter), and high Q-factor (up to 4000). Their resonance frequency could be tuned over a wide frequency range (0.5−12 GHz) through changes in the magnetic permeability by varying the bias magnetic field created by an electromagnet (Adam et al., 2002). But such "magnetic" tuning is relatively slow and is associated with large power consumption. Another class of tunable microwave devices is based on ferroelectric materials (Cole, Nothwang, Hubbard, Ngo, & Ervin, 2003). The tuning of such devices is realized by applying an electric field that reduces the dielectric permittivity of the ferroelectric material. Advantages of this "electrical" tuning are fast resonant frequency adjustment and low power consumption because ferroelectric elements, essentially, draw zero static current. But ferroelectric devices in general have low Q and high insertion loss. The multiferroic composites provide a new promising technology for tunable microwave and millimeter-wave devices, which combines the advantages of ferrite and ferroelectric devices (Sun & Srinivasan, 2012). The devices are based on CME or the excitations of hybrid spin-electromagnetic waves in ferrite−ferroelectric layered structures. Such devices are dual tunable, with electrical tuning realized through the application of an electric field to the ferroelectric layer, while the magnetic tuning is realized through the application of a bias magnetic field.

This chapter is organized as follows. First, we discuss converse ME effects at FMR and the nature of hybrid waves in the composites. Composite materials for high-frequency devices, including tunable inductors, resonators, filters, phase shifters, and beam-forming antennas, are considered next. Finally, the details on multiferroic microwave and millimeter-wave devices and miniature antennas are provided.

9.2 Converse ME effects at ferromagnetic resonance

Ferrites are the materials of choice for microwave signal processing devices due to low losses, and the ferrite−piezoelectric composite is a promising candidate for high-frequency devices based on CME interactions. Theoretical models of the effects are provided in Bichurin et al. (2001) and Bichurin et al. (2002). In general, the composite

susceptibility under an applied magnetic field H and electric field E and the order of parameters are related by the following equations:

$$\begin{aligned} \boldsymbol{P} &= \chi^{\mathrm{E}}\mathbf{E} + \chi^{\mathrm{EM}}\mathbf{H}, \\ \boldsymbol{M} &= \chi^{\mathrm{ME}}\mathbf{E} + \chi^{\mathrm{M}}\mathbf{H}. \end{aligned} \tag{9.1}$$

Here $\boldsymbol{P}$ is the electric polarization, $\boldsymbol{M}$ is the magnetization, χ^{E} and χ^{M} are the electric and magnetic susceptibilities, and χ^{EM} and χ^{ME} are the ME susceptibilities. One has to consider two important interactions: (1) coupling between microwave magnetic field and DC electric field and (2) coupling between microwave magnetic and electric fields. The former is expressed in terms of electric-field effects on magnetic susceptibility, whereas the latter is described by magnetoelectric susceptibility. Here we are primarily concerned with the influence of the electric field that produces a piezoelectric strain in the composites that manifests as an induced magnetic anisotropy in the ferromagnetic phase, leading to a shift in the FMR profile.

A general theory, applicable to either bulk or layered composites subjected to DC and AC magnetic fields and a static electric field E, was considered in Bichurin et al. (2001) and Bichurin et al. (2002) and applied to layered lithium ferrite (LFO)−PZT, NFO−PZT, and YIG−PZT. The theoretical FMR profiles in terms of the real part of the magnetic susceptibility χ' versus H for E = 0 and 300 kV/cm are shown in Figure 9.1. The results are for a bilayer with H and E perpendicular to the sample plane and for a frequency of 9.3 GHz. The static field range is chosen to include FMR in the ferrite. For E = 0, one observes the expected resonance in the profiles. With the application of E = 300 kV/cm, a downshift in the resonance field occurs, since E essentially gives rise to an internal magnetic field. The condition for FMR, the resonance frequency ω_0 for H perpendicular to the plane of a ferrite−ferroelectric disk, is given by

$$\omega_0 = \gamma(\mathrm{H} + \mathrm{H_A} - 4\pi M). \tag{9.2}$$

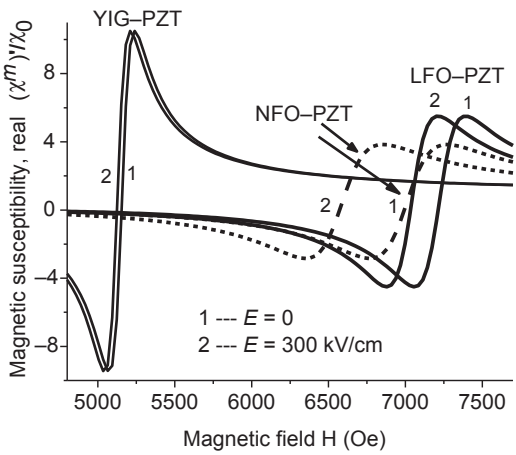

Figure 9.1 Susceptibility vs H profiles for bilayer ferrite−PZT at 9.3 GHz with (1) E = 0 and (2) E = 300 kV/cm. Fields E and H are perpendicular to the plane of disk-shaped samples of nickel ferrite (NFO)−PZT, lithium ferrite (LFO)−PZT, and yttrium iron garnet (YIG)−PZT (Bichurin et al., 2001).

where γ is the gyromagnetic ratio, H_A is the anisotropy field, and $4\pi M$ is the saturation induction. For an electric field E applied to a ferrite/piezoelectric bilayer, the piezoelectric deformation is equivalent to the effect of magnetostriction on FMR, leading to an internal magnetic field $\delta H_E = AE$, where A is the ME coupling constant. The ME effects at FMR can be taken into account by

$$\omega_0 = \gamma(H + H_A - 4\pi M + AE). \tag{9.3}$$

The E-induced shift δH_E in the resonance field is determined by the magnetostriction λ and piezoelectric coupling d. When E and H are directed along a symmetry axis, <100> for example, perpendicular to the plane (1, 2) of a bilayer, one obtains (Bichurin et al., 2001)

$$\delta H = \frac{3\lambda_{100} d_{31} E_3}{M_0[({}^p s_{11} + {}^p s_{12})(1 - v) + ({}^m s_{11} + {}^m s_{12})v]}, \tag{9.4}$$

where s is the compliance for magnetostrictive (m) and piezoelectric (p) phases and v is the volume (or thickness) fraction for the piezoelectric phase. The field shift δH_E in Figure 9.1 varies from a maximum of 330 Oe for NFO−PZT to a minimum of 22 Oe for YIG−PZT and is due to $\lambda \sim 2$ ppm for YIG versus -30 ppm for NFO (Bichurin et al., 2001).

The profiles in Figure 9.1 also reveal the possibility of voltage-controlled ferrite devices. In particular, one can envision E-tunable FMR-based devices such as ferrite resonators, filters, phase shifters, and attenuators. Such devices are discussed in Section 9.5.

9.3 Hybrid spin-electromagnetic waves in composites

Recently, a new promising technology for tunable microwave devices, which combines the advantages of ferrite and ferroelectric devices, has been developed (Sun & Srinivasan, 2012; Ustinov et al., 2006). The technique involves the excitations of hybrid spin-electromagnetic waves in ferrite−ferroelectric layered structures. Such excitations are dual E- and H-tunable, with electrical tuning realized through the application of an electric field to the ferroelectric layer, while the magnetic tuning is realized through the application of a bias magnetic field.

A theory of the hybrid waves in ferrite−ferroelectric bilayers based on a coupled-mode approach was developed in Ustinov et al. (2006). To find the resonance frequency of the hybrid modes in a rectangular bilayer, for example, one has to solve the Maxwell equations for the microwave electric and magnetic fields and the linearized Landau−Lifshits equation for the microwave component of the magnetization. For simplicity, one could ignore the exchange interactions in the ferrite, as well as any crystallographic magnetic anisotropy. The equations were solved together with the appropriate boundary conditions. The microwave magnetization can be expanded

in a series using the system of magnetostatic eigenmodes of a rectangular ferrite resonator. Similarly, the electromagnetic field of the ferroelectric resonator can also be developed in a series of eigen functions. A system of equations thus developed allows one to determine resonance frequencies of the composite resonator using only the information related to the uncoupled ferrite and ferroelectric subsystems, namely, their resonance frequencies and the distributions of microwave electromagnetic fields of the corresponding eigenmodes (Demidov et al., 2002; Ustinov et al., 2006).

In the general case, the system of equations for an infinite system describing coupling of *all* the ferromagnetic eigenmodes with *all* the ferroelectric eigenmodes could be solved only numerically. The frequency separation between the electromagnetic modes of the ferroelectric resonator is usually rather large (of the order of the frequency of the fundamental mode of the ferroelectric resonator) and, therefore, in most cases, one can ignore the possible excitation of the higher ferroelectric modes. In contrast, the frequency separation between the modes of the ferromagnetic resonator is much smaller, and a large number of these modes could be excited simultaneously. It should be noted that the simultaneous excitation of the several modes of a ferromagnetic resonator leads to a rather complicated shape and inhomogeneous broadening of the resonance curve of the hybrid ferrite−ferroelectric resonator, and, if possible, should be avoided (Ustinov et al., 2006).

While the reduction of the spurious influence of the higher ferromagnetic modes can be achieved by the use of small ferromagnetic resonators, having a larger frequency separation between the eigenmodes by using a highly symmetrical resonator geometry is also preferred. Namely, if the structures of the microwave electromagnetic fields of the ferromagnetic and ferroelectric eigenmodes are very similar, then each ferroelectric mode will be, for the most part, coupled to *only one* ferromagnetic mode. In particular, such a situation is approximately realized in the rectangular resonator geometry with equal in-plane sizes of the ferromagnetic and ferroelectric slabs. In this case, the coupling of the lowest ferroelectric mode to higher ferromagnetic modes is caused only by edge effects and the finite thickness of the ferromagnetic film, and, in most cases, can be neglected.

In the case when one (λ-th) ferroelectric mode of frequency Ω_λ interacts with only one (ν-th) ferromagnetic mode of frequency ω_ν, one obtains the following expression for the resonance frequencies of the hybrid ferrite−ferroelectric resonator (Ustinov et al., 2006):

$$\omega_{1,2}^2 = \frac{1}{2}\left(\omega_\nu^2 + \Omega_\lambda^2 + \xi\omega_M\omega_\nu \pm \sqrt{\left(\omega_\nu^2 + \Omega_\lambda^2 + \xi\omega_M\omega_\nu\right)^2 - 4\omega_\nu^2\Omega_\lambda^2}\right). \qquad (9.5)$$

Here ξ is a dimensionless coupling parameter for the ferroelectric and ferromagnetic eigenmodes and $\omega_M = \gamma\, 4\pi M$. For typical experimental conditions, ξ is on the order of 0.001−0.01. The above equation allows one to also determine the magnetic tuning $\partial\omega/\partial H$ and electric tuning $\partial\omega/\partial E$ of the resonance frequencies of the coupled hybrid resonator and to estimate the resonance line-width $\Delta\omega \approx |\partial\omega/\partial H_0|\Delta H + \varepsilon|\partial\omega/\partial\varepsilon|\tan\delta$, where ΔH is the line-width of the FMR in the ferrite layer and δ is the angle characterizing the dielectric losses in the ferroelectric layer.

The theory predicts superior tuning characteristics when one optimizes the resonator geometry, that is, *equal* in-plane dimensions of the ferrite and ferroelectric layers of this hybrid resonator. This geometry maximizes coupling between the ferromagnetic and dielectric resonant modes because the electromagnetic fields of the modes overlap efficiently. In addition, due to the strong dipolar pinning of magnetization at the lateral edges of a thin ferromagnetic layer (Cole et al., 2003) and the high dielectric permittivity of the ferroelectric medium, resonance modes of both the ferromagnetic and ferroelectric components have approximately the same spatial structure of electromagnetic fields. As a result, the main dielectric mode is coupled mostly to the main ferromagnetic mode, that is, the proposed geometry substantially reduces spurious influence of the higher-order resonance modes of the layered structure (Ustinov et al., 2006). Resonators and phase shifters based on hybrid waves are discussed later in this chapter.

9.4 Composites for high-frequency devices

Ferrites are the materials of choice for high-frequency devices due to low losses at microwave and millimeter-wave frequencies (Adam et al., 1991, 2002). Composites with spinel ferrites, YIG, and Y-, Z-, and M-type hexagonal ferrites are appropriate for use in E- and H-tunable devices over 1−110 GHz. The choice of ferrite for a specific frequency range is determined by (1) the desired anisotropy field for operation of the device without or with nominal bias magnetic field, (2) the magnetostriction λ that determines the strength of ME coupling, (3) saturation magnetization $4\pi M$, (4) FMR line-width ΔH, and (v) high-frequency dielectric and magnetic losses. The parameters of importance for the ferrites are listed in Table 9.1 (Hellwege & Springer, 1970). Thin films grown by liquid phase epitaxy and single-crystals of YIG have ΔH on the order of 0.5−1 Oe at frequencies up to 12 GHz and low magnetic and dielectric losses. For frequencies above X-band, however, the need of large external magnetic fields makes the use of YIG less attractive for ferromagnetic resonance-based devices. Two types of ferrites (1) nickel and lithium ferrites, $Ni\ Fe_2\ O_4$ and $Li_{0.5}\ Fe_{2.5}\ O_4$, are appropriate for devices up to 15 GHz; and (2) hexaferrites for 15−110 GHz devices. Spinel ferrites, including nickel ferrite and lithium ferrite, have $\Delta H \sim 5-50$ Oe. A large uniaxial or planar anisotropy field in the hexaferrites facilitates FMR over 15−110 GHz for moderate bias magnetic fields. The Y- and Z-type hexagonal ferrites with easy-plane anisotropy, $Ba_2Zn_2Fe_{12}O_{22}$ (Zn_2Y) and $Ba_3Co_2Fe_{24}O_{41}$ (Co_2Z), are preferred for use at 10−40 GHz. M-type hexaferrites, Me $Fe_{12-x}\ Al_x\ O_{19}$ (Me = Ba, Sr), have uniaxial anisotropy, and $BaFe_{12}O_{19}$ (BaM) or SrM are ideal for the frequency range 40−75 GHz. Aluminum-substituted hexaferrites, including (Ba, Al) M and (Sr, Al) M, have a uniaxial anisotropy field H_A on the order of 17−40 kOe and are ideal for 50−110 GHz devices (Hellwege & Springer, 1970).

Similarly, low-loss ferroelectrics with high piezoelectric coupling (PZT, PMN-PT, PZN-PT) and dielectrics that show rapid changes in ε with E are important for use as a ferroelectric/dielectric phase (Cross & Setter, 1993). The ferroelectric nature of PZT, $Pb(Zr_{1-x}Ti_x)O_3$, is critically dependent on the Zr/Ti ratio, with $PbZrO_3$ being an

Table 9.1 Key material parameters for ferromagnetic and ferroelectric phases for use in high-frequency multiferroic devices. The saturation magnetization $4\pi M$, FMR line-width ΔH, anisotropy field H_A, magnetostriction λ parallel to the applied magnetic field direction, and the piezoelectric coupling coefficient d are listed (Hellwege & Springer, 1970)

Ferromagnetic/ ferroelectric phase	$4\pi M$ (G)	ΔH (Oe)	H_A (kOe)	λ (ppm)	d (pm/V)
YIG	1750		0.05	−2	
Nickel ferrite				−30	
Lithium ferrite				−18	
Zn_2Y					
Ba−Al−M		6−50	17−37	−6 to −15	
Sr−Al−M		10−50	19−40	−6 to −10	
PZT					400−600
PMN-PT					1500−2500
PZN-PT					1600−3200

antiferroelectric and $PbTiO_3$ ferroelectric at room temperature. Much interest is focused on compositions close to the morphotropic phase boundary (MPB) for Ti ratio of ∼47% because of their large piezoelectric constants (Cross & Setter, 1993). PMN-PT, $(1-x)$ $Pb(Mg_{1/3}Nb_{2/3})O_3$−x $PbTiO_3$, is a relaxor ferroelectric with a diffused phase transition, frequency dependent dielectric maxima, nonlinear dielectric response for bias voltage and shows an MPB around 33%Ti. Single-crystal lead magnesium−lead titanates (0.68PMN−0.32PT) have desirable characteristics ($\varepsilon = 5000-7000$; $d_{33} = 2500-3200$ pC/N, $\tan\delta = 0.005$) (Cross & Setter, 1993). PZTs have high d_{33} (400−600 pC/N) for use in composites, but have high losses at microwave frequencies. Similarly, pure barium titanate (BTO) is lossy due to its domain structure. The losses can be reduced in a solid solution with strontium titanate (Cross & Setter, 1993). Bismuth strontium titanate (BST) compositions (0.5BTO−0.5STO) with a high dielectric constant and E-dependence are used in devices based on hybrid modes (Cross & Setter, 1993).

9.5 Multiferroic high-frequency devices

This section is devoted to discussions on multiferroic high-frequency devices. The devices could be classified into two broad categories, as in Table 9.2: E-tuning due

Table 9.2 Multiferroic high-frequency devices

Ferromagnetic/ ferroelectric composite	Frequency range	Devices	Reference
Strain-mediated E-tuning			
YIG/PZT/PMN-PT/ PZN-PT	1−12 GHz	Resonator	
Nickel ferrite/ PZT/ PMN-PT/PZN-PT	3−15 GHz	Filter	
Lithium ferrite/ PZT/ PMN-PT/PZN-PT	3−15 GHz	Phase shifter	
Zn2Y/ PZT/ PMN-PT/PZN-PT	12−24 GHz	Attenuator	
Ba−Al−M/ PZT/ PMN-PT/PZN-PT	47−110 GHz		
Sr−Al−M/ PZT/ PMN-PT/PZN-PT	47−110 GHz		
Hybrid waves			
YIG/PZT/PMN-PT	1−12 GHz	Delay lines	
YIG/BST	1−12 GHz	Resonator Phase shifter	
E-induced permeability			
FeB/PZT	1−4 GHz	Inductors	
High ε and μ-composites			
Ferrite/BST	10−100 MHz	antenna	

to mechanical strain and voltage tuning due to variation in dielectric constant or permeability. First, we discuss devices that utilize strain-mediated ME coupling. This includes resonators, band-pass and bandstop filters, phase shifters, and attenuators. Hybrid-wave resonators, phase shifters, and delay lines that utilize variation in ε with E for tuning are considered next. Multiferroic tunable inductors that take advantage of the variation in permeability with E are also discussed. Finally, we focus on antenna miniaturization with the use of high permeability−high permittivity multiferroic composites.

9.5.1 Strain-mediated E-tuning

Ferrite-ferroelectric resonators, filters, phase shifters, and attenuators that employ voltage tuning of FMR are considered (Fetisov & Srinivasan, 2006, 2008; Li et al., 2011;

Shastry, Srinivasan, Bichurin, Petrov, & Tatarenko, 2004; Tatarenko & Srinivasan, 2011; Tatarenko, Gheevarughese, & Srinivasan, 2006; Tatarenko, Murthy, & Srinivasan, 2012; Tatarenko, Srinivasan, & Bichurin, 2006; Tatarenko, Srinivasan, & Filippov, 2007; Tatarenko, Ustinov, Srinivasan, Petrov, & Bichurin, 2010; Yang et al., 2013; Yang, Obi, & Sun, 2012).

9.5.1.1 Resonators

Resonators are front-end elements in phased array radars and are also used in filters and phase shifters. One has to choose the appropriate ferrite for the specific frequency range. The fabrication and characterization of an electric-field-tunable 1−10 GHz YIG−PZT microwave planar resonator is discussed in Fetisov & Srinivasan (2006). Figure 9.2 shows the schematics of a YIG−PZT microstripline resonator that is based on voltage tuning of FMR by CME. An LPE YIG film of thickness of 15 μm and lateral dimensions of 1×2.2 mm^2 on 2-mm-thick gallium gadolinium garnet (GGG) substrate of (111) orientation was used. The film had an FMR linewidth of ∼0.6 Oe, measured at 5 GHz. A PZT plate with dimensions of $4 \times 4 \times 0.5$ mm^3 and with 5-μm-thick silver electrodes on both sides was bonded to the YIG film with a fast-dry epoxy. The bilayer was placed on a microstrip transducer and was subjected to a bias magnetic field H parallel or perpendicular to the bilayer plane. A (DC) electrical field E = 0−10 kV/cm was generated across PZT by applying a voltage.

Microwave measurements were carried out using a vector network analyzer. A cw input signal with $f = 2-10$ GHz and power $P_{in} = 0.1$ mW was applied to the microstrip transducer. Low input power was chosen to prevent heating of the sample due to power absorption at FMR. Profiles of reflected power $P_{ref}(f)$ versus f were recorded for a series of H and E. Figure 9.3 shows representative scattering parameter $S_{11}(f) = 10 \log[(P_{ref}(f)/P_{in}(f)]$ versus f for an out-of-plane H = 3.01 kOe. For E = 0, the spectra

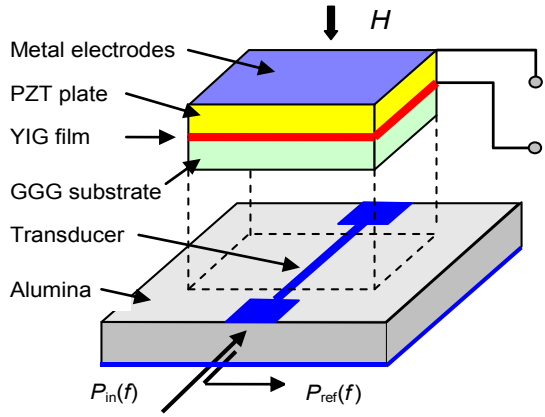

Figure 9.2 YIG−PZT resonator (Fetisov & Srinivasan, 2006).

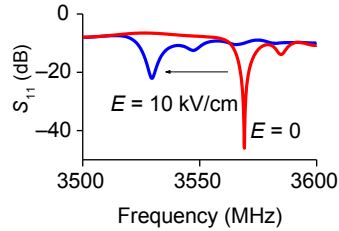

Figure 9.3 Electric-field-tunable YIG−PMN-PT resonator with perpendicular magnetization (H = 3010 Oe) (Fetisov & Srinivasan, 2006).

contained a well-defined FMR absorption peak at ∼3.57 GHz with a maximum insertion loss of −45 dB and a 3-dB line-width $\Delta f = 3.4$ MHz. The off-resonance loss could be partially due to ferroelectric losses in PZT. With the application of E = 10 kV/cm, the FMR peak shifted to a lower frequency by $\delta f_1 = 40$ MHz. When the polarity of E was reversed by reversing the voltage applied to PZT, the peak upshifted by $\delta f_1 = 38$ MHz. The CME coupling constant $A = \delta f$/E∼ 4 MHz cm/kV and the voltage tuning for E = ±10 kV/cm is around 2% of the central frequency.

The E-tuning discussed above could be nonlinear for large electric fields due to ferroelectric hysteresis, as discussed next. Figure 9.4 shows measured dependence

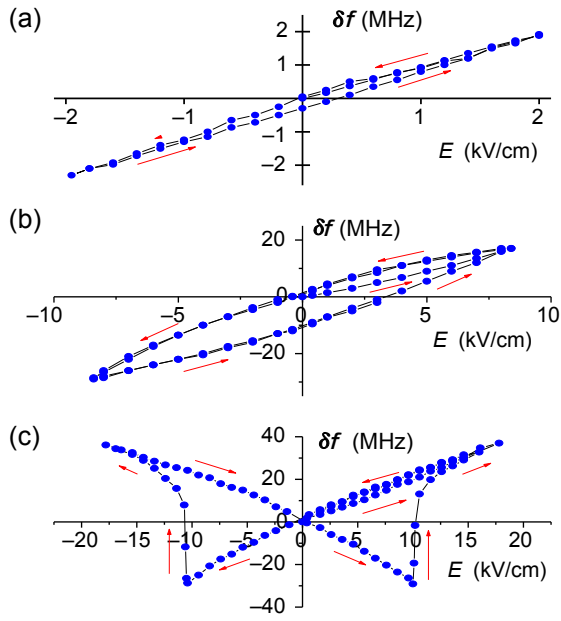

Figure 9.4 Shift in resonator frequency of a YIG−PZT resonator vs *E* for small, intermediate, and large electric-field values that indicate hysteresis and a flip in the frequency shift due to reversal of polarization (Fetisov & Srinivasan, 2008).

of the frequency shift δf as a function of E for small, intermediate, and large amplitudes (Fetisov & Srinivasan, 2008). For $|E| < 2$ kV/cm, it is shown in Figure 9.4(a) that δf first increases nearly linear with a slope $A = 1$ MHz/(kV/cm) as E increases from 0 to 2 kV/cm in the positive and negative directions.

Figure 9.4(b) shows similar δf versus E for intermediate values of E, for $|E| < 8$ kV/cm. One observes a nonlinear increase in δf as E increases from 0 to 8 kV/cm in the positive direction. After subsequent decrease of E to 0, δf decreases to zero as well, but along a different path. Then, as E reverses sign and increases in the negative direction, δf changes its sign and increases nonlinearly. As a result, after the variation in $E = -8$ kV/cm to 8 kV/cm, the tuning characteristics of hysteretic type is formed, and the loop is also shifted down on the vertical axis. For this nonlinear case, there is no single valued tuning coefficient A.

Figure 9.4(c) shows measured dependence of δf on E for large amplitudes of E, for $|E| < 18$ kV/cm. As E increases up to the maximum value in the positive direction and then decreases to zero, the shift δf similar to the intermediate case is measured. After reversal of E, δf changed its sign and at a threshold field $E_1 = -10$ kV/cm, δf switched abruptly from -30 MHz to $+10$ MHz. The time required for this transition at E_1 was $\sim 10-100$ s, and it decreased exponentially when E exceeded the threshold value. With further increase in the magnitude of E, δf increased and reached its maximum value of 40 MHz. Then, as E was decreased to zero and subsequently increased in the positive direction, δf was negative and increased with E until an abrupt switch from -30 MHz to $+10$ MHz occurred at $E_2 = +10$ kV/cm. As a result, a "butterfly-like" tuning characteristic, shown in Figure 9.4(c), was formed.

To understand the results in Figure 9.4, one has to consider the piezoelectric strain S versus E in PZT. The strain S in PZT to a linear approximation is given by $S = d_{13}E$, where $d_{13} \sim d_{33}/2$ is the in-plane piezoelectric coefficient of the PZT. The effective anisotropy field in YIG is proportional to the strain $H_a = 3(\lambda_{11}Y/M)S$, where λ_{11} is the magnetostriction, Y is Young's modulus, and M is the magnetization of YIG. Therefore, the theory (Bichurin et al., 2001, 2002) predicts a linear δf versus E since $\delta f = A \cdot \lambda_{11} d_{13} \cdot E$, where A is a coefficient that depends on material and bilayer parameters. An estimation based on the above formula and $E = 2$ kV/cm gives $\delta f = 1.3$ MHz, which is in good agreement with the data of Figure 9.4(a).

In order to account for the nonlinearity in the frequency shift in Figure 9.4, E dependence of the piezoelectric deformation of PZT was measured using a strain gage (Fetisov & Srinivasan, 2008). Figure 9.5 shows $S(E)$ vs E data for intermediate and high amplitudes of 9 kV/cm and 18 kV/cm, respectively. The arrows show direction of the field change. It is seen in Figure 9.5(a) that for intermediate amplitudes of E, the variation of S with E is linear only at the initial part of the curve, for $0 < E < 9$ kV/cm. After reversal of the field direction and cyclic variation in E, we observe hysteresis in $S(E)$ that resembles the dependence $\delta f(E)$ on E in Figure 9.4(b). Data on S for high amplitudes of E in Figure 9.5(b) is a "butterfly-like" type, symmetrical with respect to the vertical axis. An abrupt change in the sign and value of S is measured at the same threshold field $|E| = 10$ kV/cm, as for the frequency shift data in Figure 9.4(c). This transition corresponds to repolarization of an initially electrically poled PZT plate. It is obvious that deformation data in

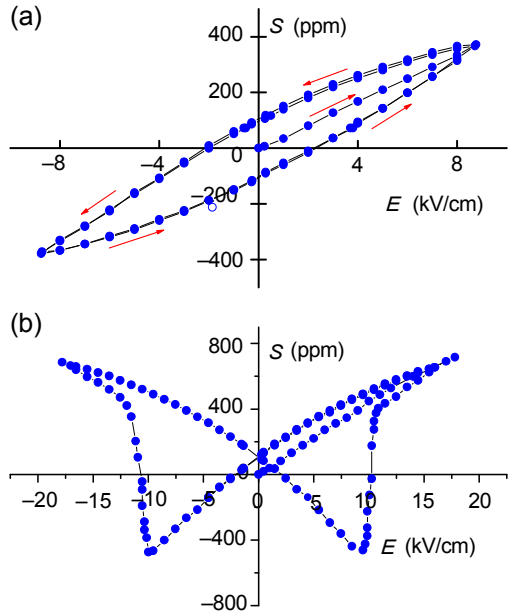

Figure 9.5 Piezoelectric strain *S* vs E for PZT (Fetisov & Srinivasan, 2008).

Figure 9.5(b) has an identical shape as the shift δf(E) in Figure 9.4(c). Thus, the E-tuning of the resonator could be linear or nonlinear, depending on the strength of E (Fetisov & Srinivasan, 2008).

Similar X-band resonator studies were reported for 1.5−2.0-μm-thick nickel ferrite ($NiFe_2O_4$) films grown heteroepitaxially on PZN-PT or PMN-PT substrates using direct liquid injection chemical vapor deposition (Li et al., 2011). A strong magnetoelectric coupling resulting in large shifts in the FMR profile was observed and is due to electrostatic field induced magnetic anisotropic field changes in these heterostructures. The data indicated an ME coefficient $A = \delta H/E \approx 20$ Oe cm/kV ($\sim$60 MHz cm/kV) at 9 and 11 GHz, which is an order of magnitude higher than for YIG−PZT. But the main drawback with the use of NFO is the large FMR line-width of around 300 Oe for the chemical-vopor-deposited (CVD) films, which is somewhat comparable to E-tuning with a field of 10 kV/cm (Li et al., 2011).

For resonators over the frequency range 12−110 GHz, hexagonal ferrites are used. Converse ME effects over 8−25 GHz were reported in bilayers of single-crystal Y-type hexagonal ferrite $Ba_2Zn_2Fe_{12}O_{22}$ (Zn_2Y) and polycrystalline PZT or single-crystal PMN-PT (Tatarenko et al., 2012). The bilayers were made by epoxy bonding or eutectic bonding the ferrite and piezoelectric. The strength of ME interactions *A* was measured from data, as in Figure 9.6, on electric field E tuning of FMR in the ferrite−ferroelectric in a stripline transducer. The resonator could be tuned by 120 MHz with E = 12 kV/cm, corresponding to ME coupling strength $A = 10$ MHz cm/kOe (Tatarenko et al., 2012).

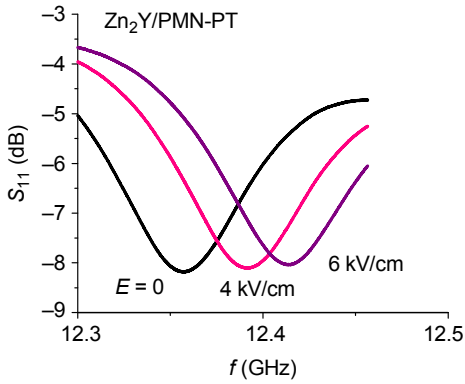

Figure 9.6 S_{11} vs f profiles for a series of E showing the shift in FMR in the ferrite−PMN-PT bilayer (Tatarenko et al., 2012).

Millimeter-wave resonators of barium or strontium hexaferrite and PZT were reported (Srinivasan, Zavislyak, & Tatarenko, 2006; Ustinov & Srinivasan, 2008). Since BaM has the desired high uniaxial anisotropy fields H_A, FMR and magnetic excitations could be observed at nominal external field H. For BaM with $H_A = 17$ kOe, FMR is expected in the frequency range 47−60 GHz for external fields $H_0 = 5-9$ kOe. Studies were performed on bilayers of single-crystal BaM prepared by floating-zone method and polycrystalline PZT. The measurement cell consisted of a coaxial-to-(WR-17) waveguide adapter. The bilayer was placed inside the waveguide section of the adapter. Studies were performed with E and H perpendicular to the bilayer plane and parallel to the magnetic easy axis of BaM. A vector network was used for data on scattering matrix element S_{11} versus f for a series of H_o and for $E = 0-10$ kV/cm. Figure 9.7 shows representative data on S_{11} versus f. One observes a series of absorption peaks for $H_o = 5980$ Oe and $E = 0$ that are identified as electromagnetic modes in BaM (Srinivasan et al., 2006). Due to the specific H orientation,

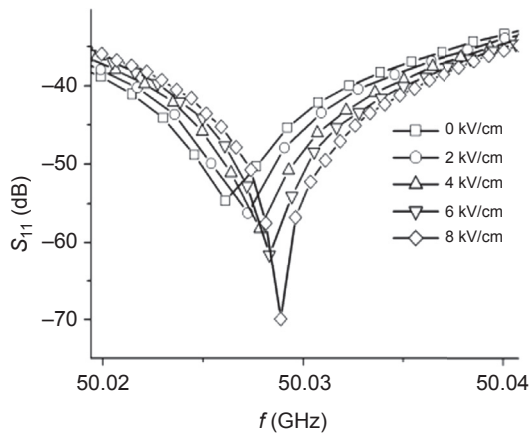

Figure 9.7 Electric-field effects on magnetic modes in barium hexaferrite PZT bilayer (Srinivasan et al., 2006).

that is, perpendicular to the sample plane, magnetostatic forward volume waves are hybridized with dielectric modes (Ustinov et al., 2006). The mode in Figure 9.7 shows a 3-dB line-width of 1 MHz that corresponds to a quality factor $Q = 5 \times 10^4$.

The electric-field effects on absorption profiles for the mode of interest are shown in Figure 9.7. One notices an upshift in the mode frequency with the application of E. Two significant changes are observed as E is increased from 0 to 8 kV/cm: a frequency shift of 4 MHz and an increase in absorption by 10−20 dB. The E-induced shift δf is much higher than the width of excitation. Data on the E-dependence of δf showed hysteresis and remanence, and the variation in δf with E tracks the dependence of the piezoelectric deformation on E in PZT. A maximum shift of 8 MHz is measured for $E = \pm 10$ kV/cm. Thus, the ME coupling constant $A = \delta f/E = 0.8$ MHz cm/kV must be compared with $A = 3-15$ MHz cm/kV for single-crystal YIG−PMN-PT and Zn_2Y−PMN-PT bilayers.

A frequency-agile hexaferrite−piezoelectric composite resonator for potential device applications at subterahertz frequencies was reported (Ustinov & Srinivasan, 2008). The bilayer was composed of aluminum substituted barium hexagonal ferrite ($BaAl_2Fe_{10}O_{19}$) and lead zirconate titanate (PZT). The bilayer showed FMR at 108 GHz and demonstrated a magnetoelectric interaction coefficient of about 1 MHz cm/kV (Ustinov & Srinivasan, 2008).

To summarize, strain-mediated E-tuning of ferrite resonators has been demonstrated in composites with PZT, PMN-PT, or PZN-PT. The resonators could be stripline planar structures for frequencies up to 40 GHz. For higher frequencies, one has to utilize waveguide structures.

9.5.1.2 Filters

An electric-field-tunable microwave band-pass filter based on FMR in a bilayer of YIG−PZT was designed and characterized. The device showed a 125-MHz tuning range for $E = 0-3$ kV/cm and an insertion loss of 5 dB at 6.5 GHz (Tatarenko, Gheevarughese et al., 2006). The single-cavity ME filter, shown in Figure 9.8, consisted of a 1-mm-thick dielectric ground plane (permittivity of 10), input and output microstrips of nonresonance lengths, and an ME element. The input−output decoupling is determined by the gap between the microstrips. Power is coupled from input to output under FMR in the ME element.

The ME element consisted of an epitaxial YIG film bonded to PZT. A 110-μm-thick YIG film grown by LPE on a (111) GGG substrate was used. The film had the dimensions of 5.5×1.5 mm^2, saturation induction $4\pi M$ of 1750 G, and FMR line-width of 1 Oe. A PZT plate with the dimensions $4 \times 1 \times 0.5$ mm^3 was initially poled by heating up to 150 °C and cooling back to room temperature in an electric field of 10 kV/cm perpendicular to the sample plane. The layered structure was made by bonding the YIG film surface to PZT with a 0.08-mm-thick layer of ethyl cyanoacrylate, a fast-dry epoxy. The sample was placed between the transducers, as in Figure 9.8, and was subjected to a field H parallel to the sample plane and perpendicular to the microstrips.

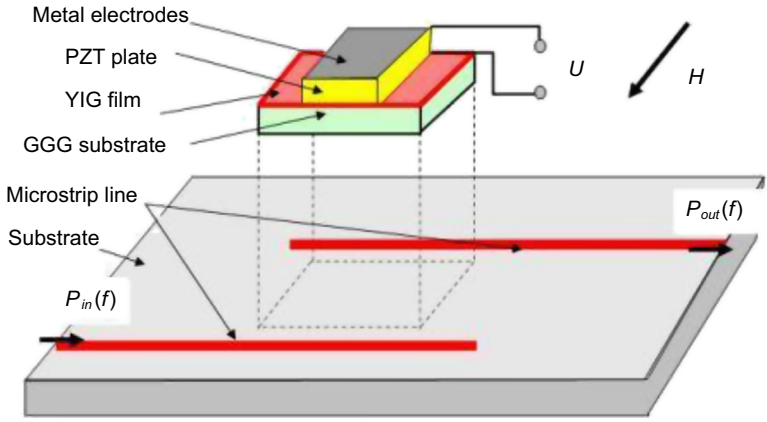

Figure 9.8 A magnetoelectric (ME) band-pass filter. The ME resonator consisted of a 110 μm-thick (111) YIG on GGG bonded to PZT (Tatarenko, Gheevarughese et al., 2006).

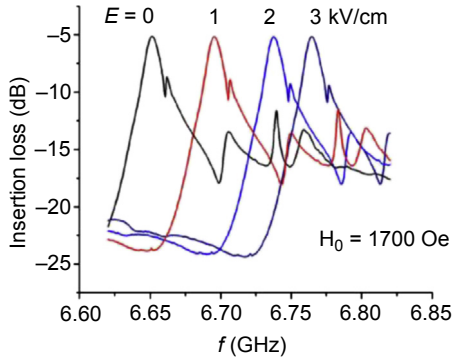

Figure 9.9 Loss vs f characteristics for a series of E for the YIG−PZT filter (Tatarenko, Gheevarughese et al., 2006).

The frequency f dependence of the insertion loss L, that is, the transmitted power through the ME element, was measured at 4−10 GHz as a function of H and E. Representative results on L versus f are shown in Figure 9.9. Consider first the profile for E = 0. The maximum input−output coupling is observed at $f_r = 6.77$ GHz that corresponds to FMR in YIG for an in-plane H = 1.7 kOe, $4\pi M = 1.75$ kG, and gyromagnetic ratio $\gamma = 2.8$ GHz/kOe. The loss increases sharply $f < f_r$ and the off-resonance isolation is 20−25 dB. For $f > f_r$, secondary maxima due to magnetostatic modes are seen in Figure 9.9. A significant modification of L versus f profile is observed in Figure 9.9 when $E = 1$ kV/cm is applied across PZT; f_r is upshifted by $\delta f = 28$ MHz. The shift arises due to strain at the YIG−PZT interface caused by the piezoelectric deformation in PZT. A further increase in E results in an increase

in the magnitude of the up shift, as shown in Figure 9.9. We observed a down shift in f_r when the direction of E was reversed by reversing the polarity of applied voltage. This is attributed to a switch from compressive to tensile strain in YIG. The filter can be tuned by 2% of the central frequency with a nominal electric field of 3 kV/cm (Tatarenko, Gheevarughese et al., 2006).

A majority of resonators and filters utilizing CME in ferrite−ferroelectric composites so far, however, were carried out for FMR in magnetically saturated ferrites. But similar studies under resonance in unsaturated ferrites is of interest for high-frequency device applications. Recent efforts in this regard include resonances in partially magnetized YIG and in YIG−ferroelectric composites for use as band-pass filters (Yang et al., 2012, 2013). Yang et al. studied H-tuning of FMR over 2.7−3.7 GHz and 5.9−6.4 GHz in YIG and showed that the resonance frequency f_r scales as $1/\sqrt{\mu_r}$, where μ_r is the real part of the permeability. They also demonstrated H-tunable filters based on the modes (Yang et al., 2012, 2013). Their work was extended to E-tuning of the FMR and 10% tuning of the pass-band through CME in YIG/PZN-PT (Yang et al., 2013). Such filters under low bias field resonances in ferrites are of particular interest for microwave device applications since providing a high bias magnetic field is usually the biggest challenge for ferrite devices. One also could obtain a large E-tuning under such conditions.

9.5.1.3 Phase shifters

Microwave phase shifters are important elements for use in oscillators and phased array antenna systems. Traditional ferrite phase shifters are based on the Faraday rotation for electromagnetic waves in axially magnetized ferrite rods in waveguides. The devices require an electromagnet or solenoidal magnetic field for phase tuning and involve large power dissipation (Adam et al., 2002). A desirable alternative is the latching ferrite phase shifter that operates at the remanent magnetization for the ferrite element and requires current pulses for switching the magnetization state (Adam et al., 1991). Phase shifts could also be realized through magnetostatic wave (MSW) propagation or FMR in planar ferrites in microstripline structures. The MSW wavelength and group velocity are 2−3 order in magnitude smaller than that for electromagnetic waves of the same frequency. This makes possible a phase shift of decades of π for propagation distances of several millimeters. In the case of phase shifters operating close to FMR, a rapid change in the permeability and phase shift can be achieved by tuning the bias magnetic field (Tatarenko, Srinivasan et al., 2006). But all of the above ferrite phase shifters, in general, require high electrical power for operation and cannot be miniature in size or compatible with the integrated circuit technology.

Ferroelectric phase shifters, on the other hand, can be tuned with an electric field (Cross and Setter, 1993). But such phase shifters are very lossy at frequencies above 1−5 GHz. With a ferrite−ferroelectric layered structure, it is possible to achieve both magnetic- and electric-field tunability of the phase shift. An electric-field-tunable YIG−PZT phase shifter based on FMR was designed and characterized. The electric field control of the phase shift $\delta\varphi$ arises through magnetoelectric interactions (Tatarenko, Srinivasan et al., 2006). The piezoelectric deformation in PZT in an

electric field E leads to a shift in the FMR frequency in YIG and a phase shift. For E = 5−8 kV/cm applied across PZT, $\delta\varphi = 90-180^{\circ}$ and an insertion loss of 1.5−4 dB was obtained. It was possible to realize linear or nonlinear $\delta\phi$ versus E characteristics with proper choice for bias magnetic field or frequency. The insertion loss is on the order of 1.5−4 dB, somewhat close to the desirable 0.5 dB for practical applications. Theoretical estimates of $\delta\phi$ versus E are in very good agreement with the data (Tatarenko, Srinivasan et al., 2006).

The design for the ME microwave phase shifter is shown in Figure 9.10. It consists of a 1-mm-wide microstrip on a 1-mm-thick aluminum oxide ground plane (relative permittivity of 10), a YIG−PZT resonator, and microstrip loops of length $\lambda/8$ and $3\lambda/8$ that produce a circularly polarized microwave magnetic field in the resonator. The ME resonator consisted of a 0.5-mm-thick, 5 × 5-mm plate of PZT and a 4 × 2.5 mm epitaxial (100) YIG film of thickness 124 μm on a 0.5-mm-thick gadolinium gallium garnet (GGG) substrate. Silver electrodes were deposited on PZT that was poled by heating up to 150 °C and cooling back to room temperature in an electric field of 20 kV/cm perpendicular to the sample plane. The YIG film with a saturation magnetization of 1750 Oe and an FMR line-width of 1 Oe was bonded to PZT with a 0.08-mm-thick layer of ethyl cyanoacrylate, a fast-dry epoxy.

The device characteristics were studied with a vector network analyzer. The operating frequency was chosen by applying appropriate bias magnetic field H parallel to the sample plane. An electromagnet was used for the magnetic field generation. For a given frequency f, FMR is expected in YIG for $H = H_r$. One has to choose $H > H_r$, to obtain low-insertion loss and a linear or nonlinear variation of the real part of the permeability μ' with H. An input cw signal $P_{in}(f)$ of frequency $f = 1-10$ GHz and power $P_{in} = -10$ dBm was applied to the input transducer. The frequency dependences of the insertion loss $L(f) = 10\log[P_{out}(f)/P_{in}(f)]$ and phase shift $\varphi(f)$ of the output signal were measured as a function of H and E. Representative data on the electric-field-tunable YIG−PZT phase shifters are shown in Figure 9.11. The bias field H = 2700 Oe corresponds to the region in which the variation of μ' versus H is nonlinear. For E = 0, one observes a smooth variation in ϕ versus f and an expected discontinuity at $f = 9.6$ GHz. Application of

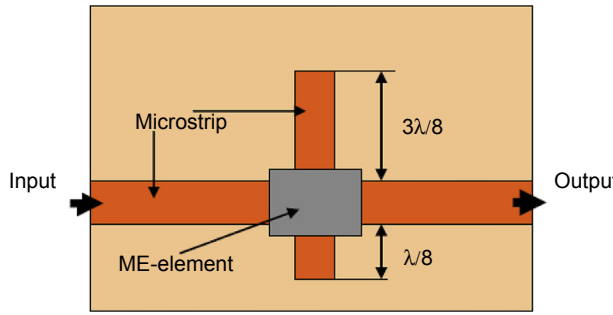

Figure 9.10 Diagram showing the schematics of a YIG/PZT phase shifter (Tatarenko, Srinivasan et al., 2006).

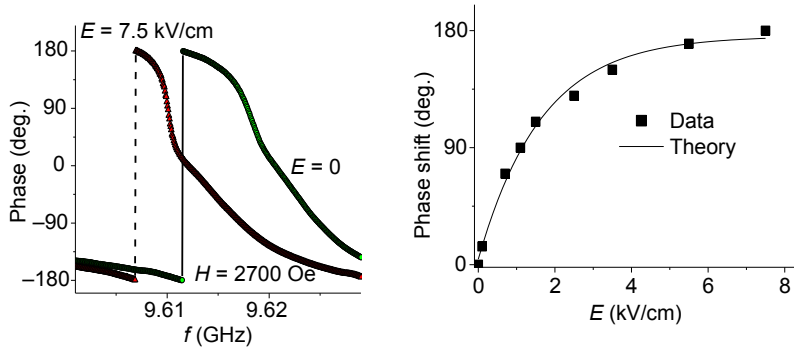

Figure 9.11 The phase angle ϕ vs frequency f at 9.6 GHz for E = 0 and 7.5 kV/cm and differential phase shift vs E at 9.615 GHz (Tatarenko, Srinivasan et al., 2006).

E = 7.5 kV/cm to PZT resulted in a downshift in frequency $\delta f = 6$ MHz and a corresponding differential phase shift of $\delta\phi = 180°$. By increasing the bias field to 2720 Oe, it was demonstrated that $\delta\phi$ showed a linear dependence on E (Tatarenko, Srinivasan et al., 2006).

Similar phase shifters with hexaferrite/ferroelectric elements in waveguides could be realized. Bilayers of Co_2Z (20−40 GHz), Zn_2Y (15−40 GHz) (Tatarenko & Srinivasan, 2011), or BaM (45−67 GHz) and PZT could be used. For a stripline Zn_2Y/PMN-PT phase shifter, data on differential phase shift versus E indicated a differential phase shift of 50 ° for E = 12 kV/cm, a linear variation in the phase shift with E, and an insertion loss of 4−8 dB. Device optimization will have to include studies on (1) ferroelectric leakage current, which will affect the electrical tuning, (2) ferroelectric fatigue, and (3) ferroelectric and loss parameters of PZT.

Other devices on strain mediated E-tuning include an attenuator. An electric-field-tunable YIG/PMN-PT attenuator operating at 7.2 GHz was reported (Tatarenko et al., 2007). The device is based on FMR in YIG. Electric-field (E) tuning of the attenuation was accomplished through magnetoelectric interactions in the bilayer. Theoretical estimates of attenuation versus E were in very good agreement with data.

9.5.2 Hybrid spin-electromagnetic wave devices

Here we discuss resonators, phase shifters, and delay lines of multiferroic composites, in which hybrid waves are excited and E-tuning is achieved by changes in the dielectric permittivity (Fetisov & Srinivasan, 2005a,b; Kim et al., 2000; Pettiford, Dasgupta, Lou, Yoon, & Sun, 2007; Semenov et al., 2006; Ustinov & Srinivasan, 2010; Ustinov, Srinivasan, & Kalinikos, 2007; Ustinov, Kalinikos, Tiberkevich, Slavin, & Srinivasan, 2008).

An electric-field-tunable, microwave resonator with a YIG−BST layered structure was investigated (Semenov et al., 2006). In this case, the ferrite and the ferroelectric were placed on top of each other since bonding for strain transfer is not a requirement in this tuning. The measured characteristics at 3.6 GHz, corresponding to the

proximity of magnetic and dielectric resonance modes, showed a broad-band electrical tunability. A tuning range of 1.5% of the central resonance frequency was obtained for nominal electric fields.

The device was constructed in two steps. First, a straight-edge YIG film resonator was fabricated and characterized. The resonator was made from a 7-μm-thick (111) YIG film on a 500-μm-thick GGG substrate. Its in-plane dimensions were chosen to be 0.5 mm by 1.5 mm in order to excite hybridized wave modes with the wave number that would allow efficient electrical tuning. The measured resonance spectrum of the YIG film resonator exhibited several well-defined peaks with all of them identified as eigenmodes of a rectangular magnetostatic wave (MSW) straight-edge resonator.

Second, a rectangular BST resonator was fabricated and characterized. Through an electrodynamical analysis of dispersion in relation to TE waves in a dielectric layer, the dimensions of the rectangular BST resonator were calculated for a frequency range of around 3650 MHz. Then, the amplitude−frequency characteristic of the fabricated BST resonator was measured, and the resonant modes were identified. For the specific design, which is described below, the main working ferroelectric mode was labeled as (032). This mode demonstrated a maximum quality factor.

A schematic diagram of the coupled resonator construction is given in Figure 9.12. To excite the ferrite−ferroelectric resonator, a microstrip transmission line patterned on 3-μm-thick copper film deposited on alumina substrate was used. The YIG film straight-edge resonator was placed on the microstrip line, which was directed along its longer edge. The resonator was magnetized in its plane with a bias magnetic field H parallel to the microstrip line main axis. The rectangular ferroelectric resonator with in-plane dimensions $3 \times 5\ \text{mm}^2$ was cut from the $0.5BaTiO_3{-}0.5SrTiO_3$ ceramic layer of thickness 500 μm, prepared from the carbonate and oxide precursors, and annealed at 1400 °C. Metal electrodes were deposited on the both sides of the ferroelectric resonator: the upper 3-μm-thick Cu by magnetron sputtering and the lower 50-nm-thick Cr by vacuum evaporation. The Cr thickness was smaller than the skin depth, so there was no attenuation of the microwave fields at the YIG film. The Cu and Cr electrodes were used to apply a voltage to tune the permittivity of BST.

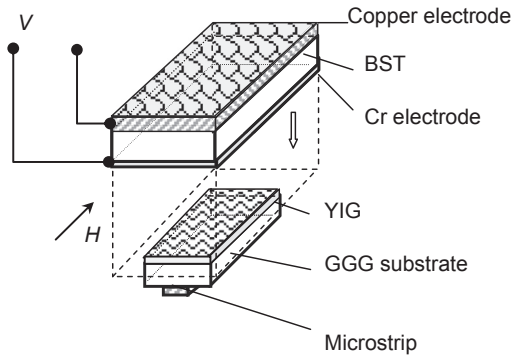

Figure 9.12 Schematics of a ferrite/ferroelectric resonator comprised of BST ceramic plate and YIG film (Semenov et al., 2006).

In the bilayer resonator, electromagnetic coupling among the MSW modes and the ferroelectric mode occurred, and the resonance branches repulsed each other and became hybridized in the region of the frequency degeneration of the MSW eigenmodes and the ferroelectric mode. The degree of the repulsion depended on the value of the bias magnetic field. Figure 9.13 presents the reflected power versus frequency profiles showing the resonance for voltages 0−900 V across BST. These profiles were recorded for the main, (011)-mode of the YIG film. One observes a tuning range of 54 MHz, corresponding to 1.5% of the central resonant frequency of the YIG/BST resonator.

Electrical tunability could be substantially improved and losses could be reduced by choosing the ferroelectric layer to have resonant properties (Semenov et al., 2006; Ustinov et al., 2006). To improve the tuning characteristics, resonators with *equal* in-plane dimensions of the ferrite and ferroelectric layers were proposed (Ustinov et al., 2006). This geometry maximizes coupling between the ferromagnetic and dielectric resonant modes because the electromagnetic fields of the modes overlap efficiently. A tuning range of 100 MHz for the resonator frequency was realized at 5 GHz through the variation of magnetic permeability and dielectric permittivity of the YIG−BST structure.

A microwave planar phase shifter based on a ferrite−ferroelectric bilayer as a waveguide for hybrid spin-electromagnetic waves was studied (Fetisov & Srinivasan, 2005a,b; Ustinov et al., 2007). The ferroelectric layer was a ceramic BST slab of the composition $Ba_{0.6}Sr_{0.4}TiO_3$ of dimensions $5 \times 10 \times 0.5$ mm. Chromium electrodes of thickness 50 nm were deposited on both surfaces of BST. The dependence of the permittivity versus applied voltage measured for BST showed a 20% variation for E = 20 kV/cm. A 5.7-μm-thick (111) YIG film on GGG was placed on BST in a microstripline phase shifter, as shown in Figure 9.14. Representative data on the return loss, insertion loss, and differential phase shift are shown in Figure 9.15. These data were obtained for H = 1413 Oe. As is clear from the figure, the return loss of −10 dB and the insertion loss of −15 dB were observed at 6.15 GHz. The differential phase shift $\Delta\varphi$ in Figure 9.15 was calculated from the measured phase-frequency characteristics for 0, 500, and 1000 V. The electric-field tunability data indicate a continuous variable $\Delta\varphi$ with increasing voltage. The values of $\Delta\varphi$ depended on the signal frequency. In other words, they were a function of the spin wave number. Note that

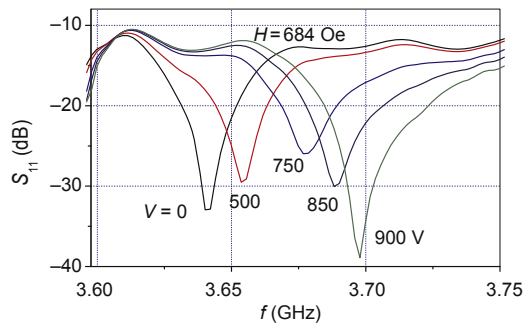

Figure 9.13 Electrical tuning characteristics of the YIG/BST composite resonator (Semenov et al., 2006).

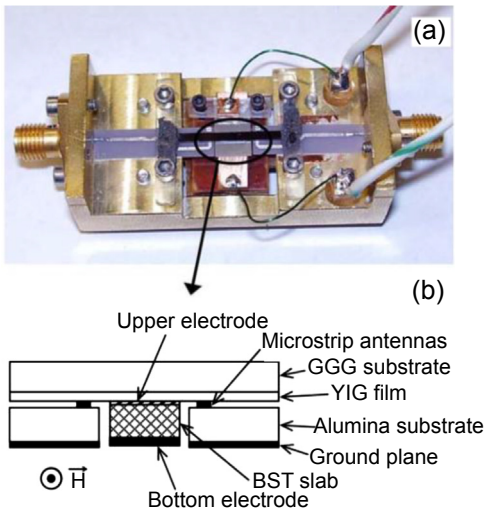

Figure 9.14 YIG/BST hybrid wave phase shifter (Ustinov et al., 2007).

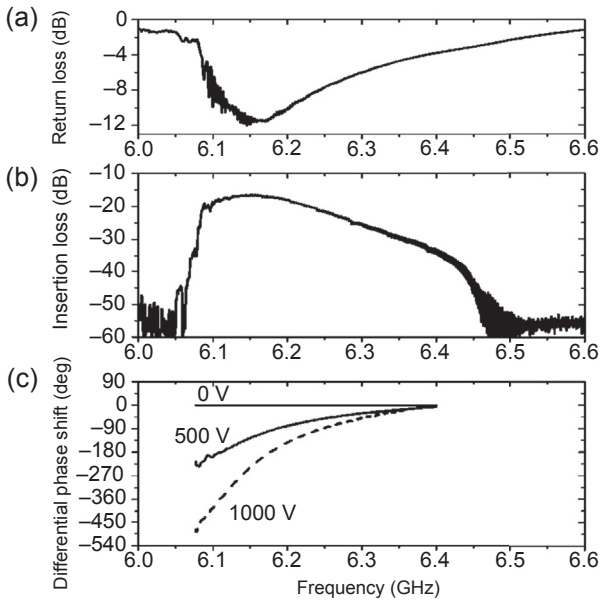

Figure 9.15 Frequency dependences of the return loss (a), insertion loss (b), and electrically induced differential phase shift.

the value of the differential phase shift more than 180° was obtained for the frequencies around 6.15 GHz. A substantial reduction in the insertion loss is required for practical use of the device.

Finally, the *electric-field* control of delay time was observed in a ferrite–ferroelectric microwave delay line. A microstrip delay line with a bilayer of (111) YIG film and (001)

PMN-PT was studied (Fetisov & Srinivasan, 2005a,b). A 10−25% variation in delay time was measured when the electric field applied to the PMN-PT layer was increased from 0 to 8 kV/cm. The tunability was attributed to variations in the permittivity for PMN-PT in an electric field and its effect on the dispersion characteristics of hybrid spin-electromagnetic waves that were excited in the bilayer.

9.5.3 Other multiferroic microwave device applications

Several other devices that utilize unique properties of multiferroic composites were reported in recent years (Petrov, Tatarenko, Srinivasan, & Mantese, 2008; Petrov et al., 2008; Petrov, Murthy, Sreenivasulu, & Srinivasan, 2013; Yang, Obi, & Sun, 2012; Yang, Xing, Daigle, Obi et al., 2010; Yang, Xing, Daigle, Liu et al., 2009). Notable among them include tunable inductors, ferrite−ferroelectric substrates for antenna miniaturization, and ferrite−ferroelectric phase shifters in slot antenna for beam forming.

9.6 Conclusion

Multiferroic composite materials having mechanically coupled magnetic/ferroelectric phases can lead to strong magnetoelectric coupling, which allows for electric-field control of magnetic properties (converse ME coupling), as well as magnetic field tuning of electrical polarization (direct ME coupling). Of particular interest is the converse ME coupling, which leads to voltage-tunable FMR or voltage-tunable permeability with minimum power consumption, thereby enabling voltage-tunable magnetic devices. Voltage control of magnetism in multiferroic composites has led to a variety of novel devices, including microwave resonators, band-pass and band-stop filters, and phase shifters.

Similarly, a microwave ME coupling of importance is there is excitation of hybridized spin-electromagnetic waves in multiferroic composites. Such excitations arise due to overlap of magnetic modes in the ferromagnet and dielectric resonance in the ferroelectric, and the two layers need not be bonded. Microwave devices, including resonators, phase shifters, and delay lines, have been demonstrated based on the hybrid modes.

There are several challenges, however, for these voltage-tunable RF multiferroic devices. Primary limitations for practical use include (1) a limited frequency tuning range of 1−10%, although the theory predicts a strong ME coupling, and (2) very high insertion loss for hybrid wave devices. Thus, the full potential of voltage-tunable RF multiferroic devices is yet to be realized.

References

Adam, J. D., Daniel, M. R., Emtage, P. R., & Talisa, S. H. (1991). In M. H. Francombe, & J. L. Vossen (Eds.), *Physics of thin films: Thin films for advanced electronic devices* (vol. 15, pp. 1−141). New York: Academic Press.

Adam, J. D., Davis, L. E., Dionne, G. F., Schloemann, E. F., & Stitzer, S. N. (2002). *IEEE Transactions on Microwave Theory and Techniques, 50*, 721.

Bichurin, M. I., Petrov, R. V., & Kiliba, Yu V. (1997). *Ferroelectrics, 204*, 311−319.
Bichurin, M. I., Kornev, I. A., Petrov, V. M., Tatarenko, A. S., Kiliba, Yu V., & Srinivasan, G. (2001). *Physical Review B, 64*, 094409.
Bichurin, M. I., Petrov, V. M., Kiliba, Yu V., & Srinivasan, G. (2002). *Physical Review B, 66*, 134404.
Bichurin, M. I., Viehland, D., & Srinivasan, G. (2007). *Journal of Electroceramics, 19*, 243.
Cole, M. W., Nothwang, W. D., Hubbard, C., Ngo, E., & Ervin, M. (2003). *Journal of Applied Physics, 93*, 9218.
Cross, L. E. (1993). Ferroelectric ceramics: tailoring properties for specific applications. In N. Setter (Ed.), *Ferroelectric ceramics*. Basel: Birkhäuser.
Demidov, V. E., Kalinikos, B. A., & Edenhofer, P. (2002). *Journal of Applied Physics, 91*, 10007−10016.
Fetisov, Y. K., & Srinivasan, G. (2005a). *Electronics Letters, 41*, 1066.
Fetisov, Y. K., & Srinivasan, G. (2005b). *Applied Physics Letters, 87*, 103502.
Fetisov, Y. K., & Srinivasan, G. (2006). *Applied Physics Letters, 88*, 143503.
Fetisov, Y. K., & Srinivasan, G. (2008). *Applied Physics Letters, 93*, 033508.
Hellwege, K.-H., & Springer, A. M. (Eds.). (1970), *Magnetic and other properties of oxides Vol. 4(b). Landolt-Bornstein; Numerical data and functional relationships in science and technology, Group III, crystal and solid state physics*. New York: Springer-Verlag.
Kim, W. J., Chang, W., Qadri, S. B., Wu, H. D., Pond, J. M., Kirchoefer, S. W., et al. (2000). *Applied Physics A, 71*, 7−10.
Lawes, G., & Srinivasan, G. (2011). *Journal of Physics D: Applied Physics, 44*, 243001.
Li, N., Liu, M., Zhou, Z., Sun, N. X., Murthy, D. V. B., Srinivasan, G., et al. (2011). *Applied Physics Letters, 99*, 192502.
Petrov, R. V., Murthy, D. V. B., Sreenivasulu, G., & Srinivasan, G. (2013). *Microwave and Optical Technology Letters, 55*, 533.
Petrov, R., Tatarenko, A. S., Pandey, S., Srinivasan, G., Mantese, J. V., & Azadegan, R. (2008). *Electronics Letters, 44*, 528.
Petrov, R., Tatarenko, A., Srinivasan, G., & Mantese, J. V. (2008). *Microwave and Optical Technology Letters, 50*, 3154.
Pettiford, C., Dasgupta, S., Lou, J., Yoon, S. D., & Sun, N. X. (2007). *IEEE Transactions on Magnetics, 43*, 3343.
Semenov, A. A., Karmanenko, S. F., Kalinikos, B. A., Srinivasan, G., Slavin, A. N., & Mantese, J. V. (2006). *Electronics Letters, 42*, 641.
Shastry, S., Srinivasan, G., Bichurin, M. I., Petrov, V. M., & Tatarenko, A. (2004). YIG-PMN-PT. *Physical Review B, 70*, 064416.
Srinivasan, G. (2010). *Annual Review of Materials Research, 40*, 153.
Srinivasan, G., & Fetisov, Y. K. (2006). *Ferroelectrics, 342*, 65.
Srinivasan, G., Zavislyak, I. V., & Tatarenko, A. S. (2006). *Applied Physics Letters, 89*, 152508.
Sun, N. X., & Srinivasan, G. (2012). *SPIN, 2*, 1240004.
Tatarenko, A. S., & Srinivasan, G. (2011). *Microwave and Optical Technology Letters, 53*, 261.
Tatarenko, A. S., Gheevarughese, V., & Srinivasan, G. (2006). *Electronics Letters, 42*, 540.
Tatarenko, A. S., Srinivasan, G., & Bichurin, M. I. (2006). *Applied Physics Letters, 88*, 183507.
Tatarenko, A. S., Murthy, D. V. B., & Srinivasan, G. (2012). *Microwave and Optical Technology Letters, 54*, 1215.
Tatarenko, A. S., Srinivasan, G., & Filippov, D. A. (2007). *Electronics Letters, 43*, 674.
Tatarenko, A. S., Ustinov, A. B., Srinivasan, G., Petrov, V. M., & Bichurin, M. I. (2010). *Journal of Applied Physics, 108*, 063923.
Ustinov, A. B., Kalinikos, B. A., Tiberkevich, V. S., Slavin, A. N., & Srinivasan, G. (2008). *Journal of Applied Physics, 103*, 063908.

Ustinov, A. B., & Srinivasan, G. (2008). *Applied Physics Letters, 93*, 142503.
Ustinov, A. B., & Srinivasan, G. (2010). *Technical Physics, 55*, 900.
Ustinov, A., Srinivasan, G., & Kalinikos, B. A. (2007). *Applied Physics Letters, 90*, 031913.
Ustinov, A. B., Tiberkevich, V. S., Srinivasan, G., Slavin, A. N., Semenov, A. A., kamanenko, S. F., et al. (2006). *Journal of Applied Physics, 100*, 093905.
Yang, X., Wu, J., Lou, J., Xing, X., Oate, D. E., Dionne, G. F., et al. (2012). *Electronics Letters, 48*, 1070.
Yang, G.-M., Obi, O., & Sun, N. X. (2012). *Microwave and Optical Technology Letters, 54*, 230.
Yang, X., Wu, J., Beguhn, S., Nan, T., Gao, Y., Zhou, Z., et al. (2013). *IEEE Microwave and Wireless Components Letters, 23*, 184.
Yang, G. M., Xing, X., Daigle, A., Liu, M., Obi, O., Stoute, S., et al. (2009). *IEEE Transactions on Antennas and Propagation, 57*, 2190.
Yang, G.-M., Xing, X., Daigle, A., Obi, O., Liu, M., Lou, J., et al. (2010). *IEEE Transactions on Antennas and Propagation, 58*, 648.

Magnetoelectric composites for miniature antennas

10

G. Yang[1], *N.X. Sun*[2]
[1]School of Information Science and Technology, Fudan University, Shanghai, China;
[2]Northeastern University, Boston, MA, USA

10.1 Introduction

This chapter, which is subdivided into five sections, details the various types of magnetoelectric composites and their effects on miniature antennas. The first section discusses the effect of a high permeability/permittivity ratio on antenna performance. In the second section, high permeability RF/microwave films are introduced. Bulk composite materials, including hexagonal Z-type ferrites, hexagonal M-type ferrites, mixed ferrites, and (Ba,Sr)TiO_3 (BST) material are presented in the third section. The fourth section deals with the layered system of sandwich ferrite films and woodpile bulk ferrite materials, while the last section investigates antenna design and characterization with novel magnetoelectric materials.

10.2 Effect of high permeability/permittivity ratio on antenna performance

The benefits of magneto-dielectrics (or magnetoelectric) are obvious. In general, antenna size can be minimized using a substrate with high relative permittivity (Balanis, 1989; Vittoria, 1993; Buell, 2005). However, antennas with high-permittivity substrates result in decreased bandwidth, as well as the excitation of the surface waves, thus leading to lower radiation efficiency. Another problem associated with antennas on high relative permittivity substrates is that it is difficult to achieve good impedance matching because the input impedance is quite sensitive to the feeding point location on the patch, especially for circular polarization. To analyze the effect of a high permeability/permittivity ratio on antenna performance, the effects of ferrite substrate on antenna resonant frequency, radiation patterns, polarization, radiation efficiency, and tunable radiation beams will be investigated in this section with the finite element-boundary integral (FE-BI) method, method of moments (MoM), cavity model, and experiments.

Composite Magnetoelectrics. http://dx.doi.org/10.1016/B978-1-78242-254-9.00010-X
Copyright © 2015 Elsevier Ltd. All rights reserved.

10.2.1 Effects of ferrite substrate on antenna resonant frequency and radiation patterns

To demonstrate the effects of ferrite substrate on antenna resonant frequency and radiation patterns, a geometry that consists of a patch situated in a cavity is considered. The substrate in the rectangular cavity is made of ferrite material.

As shown in Figure 10.1, the patch antenna is fed by a probe and the parameters for the anisotropic substrate are $4\pi M_s = 650$ G, $H_0 = 600$ Oe, and $\varepsilon_r = 10$. A hybrid FE-BI method is employed to calculate the input impedance and radiation patterns, which are shown in Figures 10.2 and 10.3, respectively. To calculate the unknown field in the context of finite element method, the following equation should be solved (Brown et al., 1999)

$$\delta F(\mathbf{E}) = 0 \tag{10.1}$$

where

$$F(\mathbf{E}) = \frac{1}{2}\int\int\int_V \left[\frac{1}{\mu_r}(\nabla \times \mathbf{E})\cdot(\nabla \times \mathbf{E}) - k_o^2 \varepsilon_r \mathbf{E}\mathbf{E}\right] dV + \int\int\int_V \left[jk_o J^{\text{int}}\cdot\mathbf{E} - \frac{1}{\mu_r}\mathbf{M}^{\text{int}}\cdot(\nabla \times \mathbf{E})\right] dV + jk_o Z_o \int\int_S (\mathbf{E}\times\mathbf{H})\cdot\hat{z}\, dS \tag{10.2}$$

where V denotes the cavity volume, S is the cavity aperture, ε_r and μ_r are the relative permittivity and permeability of the ferrite substrate, and J^{int} and M^{int} are internal electric and magnetic sources due to the antenna feeds and the last term in the BI term (Brown et al., 1999).

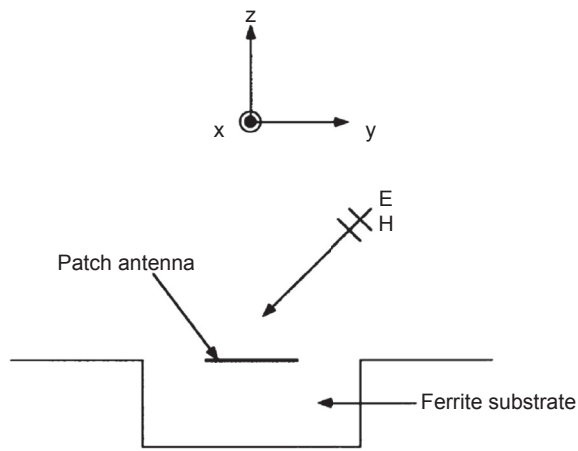

Figure 10.1 Geometry for a patch antenna on an anisotropic substrate (Brown, Volakis, Kempel, & Botros, 1999).

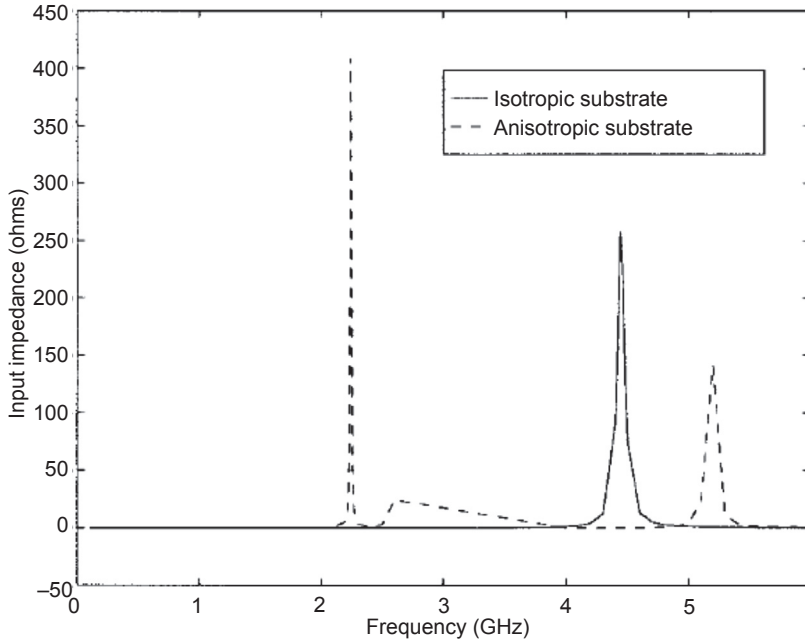

Figure 10.2 Real input impedance (Brown et al., 1999).

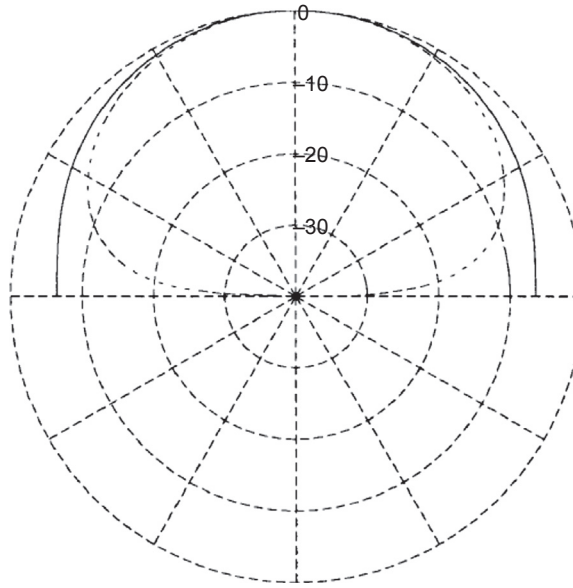

Figure 10.3 Radiation pattern in the *yz*-plane on an x-biased ferrite substrate (frequency = 2.2 GHz, — isotropic substrate, - - anisotropic substrate) (Brown et al., 1999).

The anisotropic substrate with biasing field shows a frequency shift in Figure 10.2, and the resonant frequency for the ferrite substrate is about 2.24 GHz, while it is 4.4 GHz for the isotropic substrate. That means the antenna dimension can be greatly minimized for a substrate with anisotropic material (rather than the isotropic counterpart). A null is observed along the horizontal direction for the anisotropic substrate, as shown in Figure 10.3.

10.2.2 Effects of ferrite substrate on antenna polarization and radiation efficiency

To verify the effects of ferrite substrate on antenna polarization and radiation efficiency, a basic geometry of a single rectangular microstrip patch antenna on a normally biased ferrite substrate is considered in Figure 10.4. In this study, the permeability tensor of the ferrite can be written as

$$[\mu] = \begin{bmatrix} \mu & j\kappa & 0 \\ -j\kappa & \mu & 0 \\ 0 & 0 & \mu_0 \end{bmatrix} \tag{10.3}$$

where $\mu = \mu_0\left(1 + \frac{\omega_0\omega_m}{\omega_0^2 - \omega^2}\right)$, $\kappa = \mu_0\frac{\omega\omega_m}{\omega_0^2 - \omega^2}$, $\omega_0 = \mu_0\gamma H_0$, $\omega_m = \mu_0\gamma M_s$

where H_0 is the internal bias field, M_s is the saturation magnetization, and the internal bias field is related to the externally applied field H_e with the equation $H_0 = H_e - M_s$. The ferrite substrate is supposed to be magnetically saturated in this case. The polarity of both M_s and H_0 will be changed by varying the polarity of the bias magnetic field, which will change the sign of κ, while μ will not be changed.

A full-wave MoM is used to calculate the resonant frequency with a different applied bias field. The cavity model results are plotted in the same figure for comparison. The circular polarization is derived with two orthogonal feeds that used to drive the square patch. The data in Figure 10.5 show that the left hand circular polarization

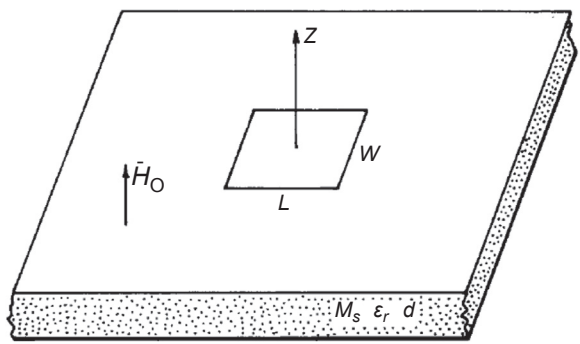

Figure 10.4 Geometry of a rectangular probe-fed microstrip patch antenna on a normally biased ferrite substrate (Pozar, 1992).

(LHCP) and right hand circular polarization (RHCP) modes have different resonant frequencies; this is because the RHCP and LHCP modes form the eigenmodes for this structure, and the propagation constants for these two modes are different (Pozar, 1992). From this figure, we also can see that the resonant frequency of each mode can be tuned by changing the bias field strength. In the range of bias field of 0−1200 Oe, the LHCP mode can be tuned by about 6%, and the RHCP mode can be tuned by about 12%. The sense of polarization can be reversed by simply reversing the polarity of the bias field, which means that a tuning range of 12% can be achieved for this design for either RHCP or LHCP operation. If the applied field strength is enlarged, a greater tuning range can be obtained (Pozar, 1992).

It is possible to achieve circular polarization by feeding a square patch at a midpoint of one edge, and RHCP or LHCP will be achieved by operating the antenna at the same operating point. For example, for a bias field of 800 Oe, LHCP can be obtained by operating the antenna at about 5.6 GHz; RHCP can be obtained by operating the antenna at about 7.1 GHz. In both cases, the antenna will be matched and will have a nominal gain of about 4.5 dB. The radiation patterns are not significantly affected by the normally biased ferrite substrate. Also, the RHCP and LHCP can be easily switched by reversing the polarity of the bias magnetic field.

The impedance bandwidths for both RHCP and LHCP are about 1%, which is a typical value for a substrate with this thickness and dielectric constant. The axial ratio versus normalized frequency for a patch with a single feed is shown in Figure 10.6. The 3 dB bandwidth for the RHCP is about 4%, while the LHCP has a bandwidth of about 13%. These bandwidths reverse as the bias polarity is reversed. Therefore, it is possible to obtain an axial ratio bandwidth of 13% for either RHCP or LHCP. As can be seen from this figure, the axial ratio bandwidth is much larger than the impedance

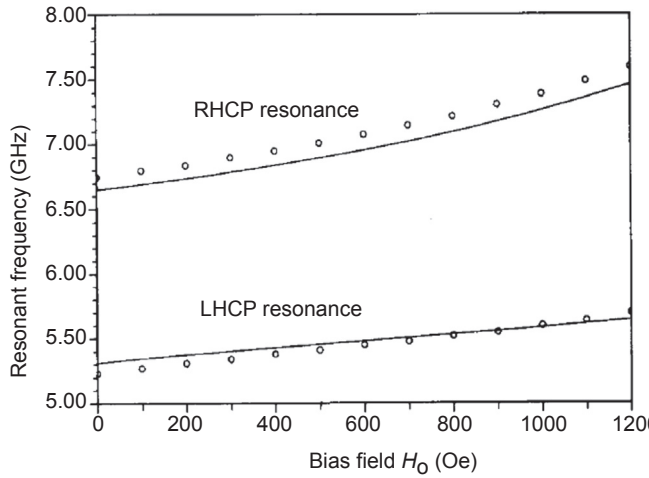

Figure 10.5 Resonant frequency for RHCP and LHCP modes for a square patch on a normally biased ferrite substrate versus bias field. $\varepsilon_r = 15$, $d = 1.27$ mm, $L = W = 6.1$ mm, $4\pi M_s = 650$ G. The solid lines are results from full-wave solutions; circles are cavity model results (Pozar, 1992).

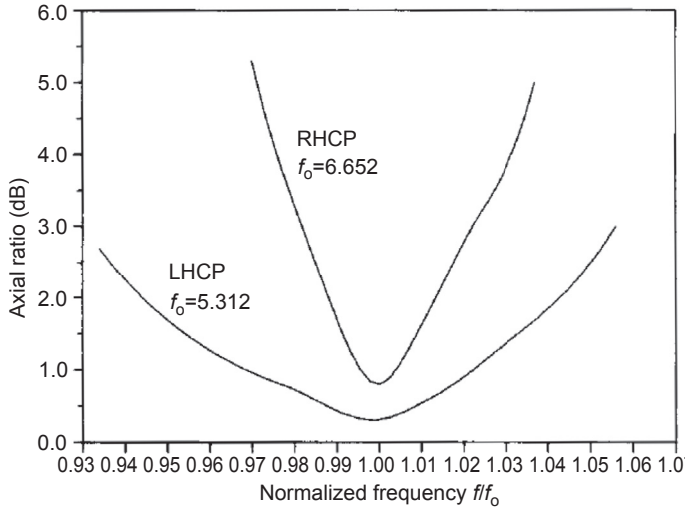

Figure 10.6 Axial ratio versus normalized frequency for RHCP and LHCP resonant modes (Pozar, 1992).

bandwidth, which means that the phenomenon of obtaining circular polarization in this manner is a fairly robust effect and not one that is limited to only a narrow bandwidth (Pozar, 1992). The gain of the antenna is about 4.5 dB for both RHCP and LHCP over the tuning range. These results are calculated with the MoM method with either a single feed point or two feeds, and the gain calculation includes losses due to surface waves, as well as dielectric and magnetic losses in the ferrite substrate.

The radiation efficiency of the circularly polarized antenna is shown in Figure 10.7. The main loss mechanism is due to the excited surface wave. The efficiency is plotted versus bias field, where the frequency of operation corresponds to the RHCP or LHCP resonances shown in Figure 10.4 (Pozar, 1992). Since the resonant frequency of the RHCP mode is greater than that for the LHCP mode, the substrate looks electrically thicker for the RHCP mode, resulting in a slightly lower efficiency (Pozar, 1992). Note that the efficiency of both cases is on the order of 70% and changes only slightly with bias field. This relatively low value of efficiency causes a drop in gain of about 1.5 dB because the dielectric constant of the substrate is fairly high (Pozar, 1992). The two solid dots at the left edge of Figure 10.7 are the efficiencies for an antenna with an ordinary dielectric substrate with the same permittivity and thickness, where $H_0 = 0$. It should be noted here that these values are quite close to the efficiencies for the ferrite case.

10.2.3 Effects of ferrite substrate on antenna tunable radiation beams

To evaluate the effects of ferrite substrate on tunable antenna radiation beams, a schematic layout of an array of ferrite patch antennas with 2×4 elements is shown in Figure 10.8(a). An antenna array is fabricated by using yttrium iron garnet substrate

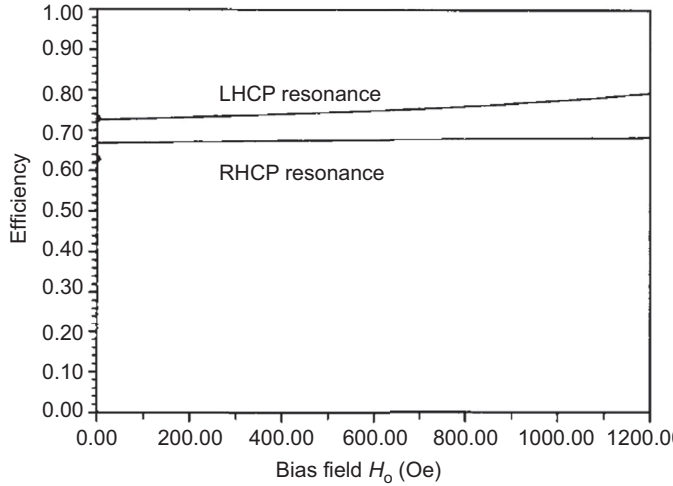

Figure 10.7 Efficiency versus bias field for the square microstrip antenna. Solid dots at the left edge of the plot are corresponding efficiencies for a dielectric substrate with the same permittivity and thickness (Pozar, 1992).

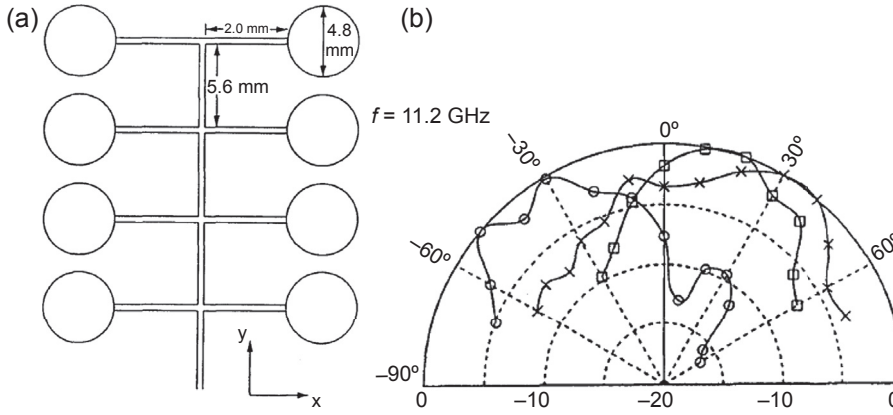

Figure 10.8 (a) Schematic drawing of the microstrip antenna array of circular geometry. (b) Radiation profile in the y-z plane. ×: without a magnetic field; □: with a magnetic field perpendicular to the feeder line; ○: with a magnetic field parallel to the feeder line (900 Oe) (How, Fang, Guan, & Vittoria, 1994).

with dimension $2'' \times 2'' \times 0.02''$ (G1010, Trans-Tech, MD). The diameter of the circular patches is 0.48 cm, and the dimensions of the feeder lines are shown in Figure 10.8(a). The antenna array is magnetically biased by using a horseshoe permanent magnet. The magnetic field is applied either along the x or the y axis. The radiation patterns of the designed antenna array are measured with an X-band waveguide horn antenna. Figure 10.8(b) shows the measured radiation intensity in the

y−z plane with in-plane polarization. The traces in Figure 10.8(b) are corresponding to different biasing field configurations. The maximum radiation intensity is at an angle $\theta = 47^\circ$ for the radiation without an applied biasing field ($\times$ dotted in the figure). The peak radiation is at an angle $\theta = 15^\circ$ when the antenna array is biased along the *x*-axis direction ($\square$ dotted in the figure) and at $\theta = -51^\circ$ when the biased magnetic field is along *y*-axis direction ($\circ$ dotted in the figure). Therefore, the radiation patterns of the ferrite patch antenna array depend on the biasing of the ferrite substrate. A tunable radiation beam can be obtained by varying the magnitude and direction of the applied biasing magnetic field (How et al., 1994).

10.3 High permeability RF/microwave thick film materials

Most recently, magnetic films have developed great interest in the device industry, as they can be used as an electromagnetic means in enhancing the performance of microwave devices, such as antennas, filters, phase shifters, and inductors (Abe & Tamaura, 1983, 1984; Abe, 2000; Kondo et al., 2008; Kondo, Yoshida, Ono, & Abe, 2007; Lou et al., 2007; Matsushita, Chong, Mizutani, & Abe, 2002; Obi, 2008; Pettiford et al., 2006; Sun & Wang, 2000; Sun, Wang, Silva, & Kos, 2002; Wang, Sun, Yamaguchi, & Yabukami, 2000; Zhang, Itoh, Abe, & Tamaura, 1993). Improving the fabrication process of these magnetic films, thereby increasing their practical applications, is highly desired. Typical thin films are deposited utilizing conventional methods like physical vapor deposition (for $(Fe_{60}Co_{40})_{85}B_{15}$ metal magnetic films), sol−gel process (SGP), molecular beam epitaxy (MBE), pulsed laser deposition (PLD), etc. The spin spray ferrite plating process, as an alternative deposition method, is currently being investigated. Unlike the other processes, the spin spray process uses low temperature and no vacuum for film production and thus can increase the range of substrates and practical applications of these thin films. Also, its cost of production is a lot less than that of the other conventional methods like PLD, MBE, etc.

Ferrite plating was invented in 1983 by Masanori Abe and Yutaka Tamaura (Abe & Tamaura, 1983). It is an electroless type of plating that involves the direct deposition of ferrite from an aqueous solution at low temperature, usually below 100 °C, onto a substrate. Since it is a low temperature process, metals (as well as nonheat resistant materials like organic materials and plastics) can be used as substrates (Abe, 2000; Abe & Tamaura, 1984; Obi, 2008).

The principle of ferrite plating involves the following:

1. Absorption of the Fe^{2+} and M^{n+} (Fe, Mn, Zn, Ni, Co, etc.) ions on the surface of the substrate brought about by the OH^- group on the substrate.
2. Oxidation of some of the Fe^{2+} to Fe^{3+} ions by an oxidizing agent (e.g., $NaNO_3$, O_2, etc.). The chemical equation for this reaction can be expressed as

$$Fe^{2+} \rightarrow Fe^{3+} + e^- \tag{10.4}$$

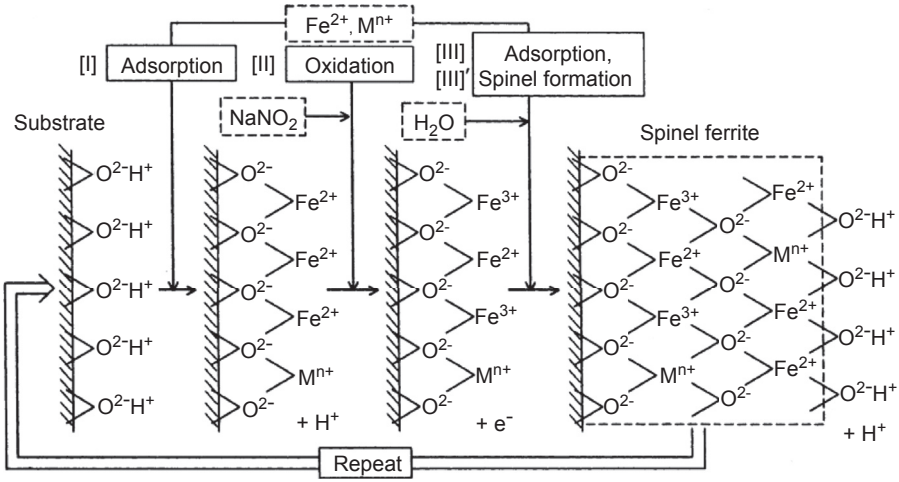

Figure 10.9 Principle of ferrite plating (Abe, 2000).

3. Reabsorption of the Fe^{2+} and M^{n+} ions on the surface of the substrate with the layered preabsorbed ions Fe^{2+} and M^{n+} and Fe^{3+} ion. This leads to the ferrite layer formation. This process is accompanied by the hydrolytic dissolution with the release of H^+ and can be expressed by the equation (Abe & Tamaura, 1984):

$$x\mathrm{Fe}^{2+} + y\mathrm{Fe}^{3+} + z\mathrm{M}^{n+} + 4\mathrm{H_2O} \rightarrow \left(\mathrm{Fe}^{2+}, \mathrm{Fe}^{3+}, \mathrm{M}^{n+}\right)_3\mathrm{O_4} + 8\mathrm{H}^{+} \tag{10.5}$$

$$x + y + z = 1 \tag{10.6}$$

$$2x + 3y + nz = 8 \tag{10.7}$$

This entire process is repeated and the ferrite thickness is increased since the OH^- group is still on the surface of the substrate (Abe, 2000; Abe & Tamaura, 1984). The schematic for the ferrite plating principle is shown in Figure 10.9.

There are different types of ferrite plating, which include the following:

1. Reactor Ferrite Plating
2. Ultrasound Enhanced Ferrite Plating
3. Inner/Outer Wall Ferrite Plating
4. Thin-Liquid Film (laser enhanced) Ferrite Plating
5. Spin Spray Ferrite Plating

10.3.1 Spin spray process

The spin spray process consists of two solutions: reaction/precursor and oxidizing solution, simultaneously sprayed on to a spinning substrate on a heating table in the presence of nitrogen gas (Abe, 2000; Matsushita et al., 2002; Obi, 2008).

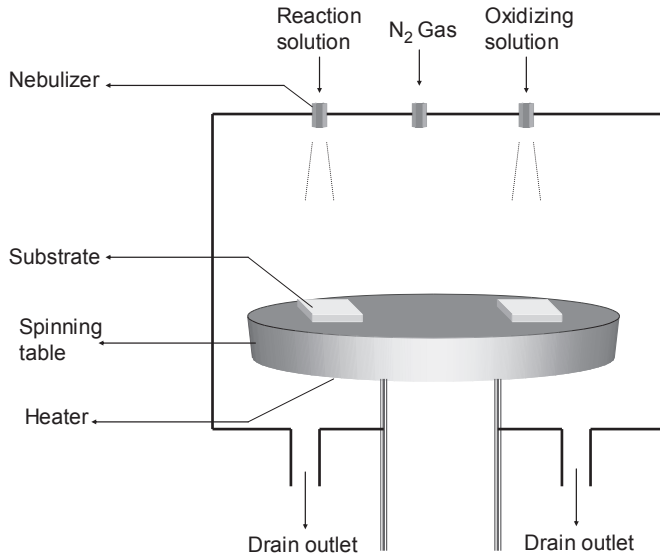

Figure 10.10 Schematics of spin spray setup (Obi, 2008).

The reaction solution is composed of $FeCl_2$ and MCl_2 (where M is a metal ion like Zn, Co, Mn, Ni, etc.) while the oxidizing solution is a mixture of a buffer (an acetate, e.g., CH_3COONa, CH_3COOK, CH_3COONH_4) and an oxidant ($NaNO_3$). Temperature range is between 70 and 90 °C, and speed of rotation of the plates is between 120 and 200 rpm for high-quality films. A schematic layout for the spin spray process is shown in Figure 10.10.

10.3.2 Magnetic thin films by spin spray process

Several spinel ferrites have been fabricated using spin spray process. Some of these materials and their properties include the following:

10.3.3 Nickel zinc (Ni−Zn) ferrite thin films

Polycrystalline Ni−Zn ferrite thin films with various compositions have been studied and fabricated over the years. These fabricated films have been found to have well-defined spinel structures. Coercivity as low as 15 Oe and ferromagnetic resonance (FMR) frequency as high as 1.2 GHz have been reported. Also, large saturation magnetization (M_s) greater than 400 emu/cc has been observed (Kondo et al., 2007; Zhang et al., 1993). Initial permeability and magnetic resonance in the GHz frequency spectra makes this film applicable for integrated circuits and microwave devices working in the GHz range.

10.3.4 Nickel zinc cobalt (Ni−Zn−Co) ferrite thin films

Magnetically isotropic Ni−Zn−Co ferrite thin films with low magnetic losses even at 900 MHz have been fabricated. These films are reported to have high real permeability (μ'), greater than that of bulk films, and low imaginary permeability (μ'') with loss tangent much lower than that for composite-type magnetic sheets. Ni−Zn−Co ferrite thin films can be used as a shielding material against electromagnetic interference for radio frequency identification (900 MHz or 2.45 GHz) (Obi, 2008).

10.3.5 Manganese zinc (Mn−Zn) ferrite thin films

The following properties for Mn−Zn ferrite thin films have been reported. These include the following:

1. High permeability in GHz range
2. Film resistivity, $\rho > 10^4$ Ω, which increased as the amount of Fe content decreased
3. High surface resistance $R > 108$ Ω/sq for film with an Fe content <2.6
4. Large M_s (380−460 emu/cc)
5. Low coercivity ($H_c = 11-29$ Oe)
6. Very large transmission loss per thickness (as a microstrip), about 10 times larger than that of the commercialized composite sheets
7. Sufficiently low reflection coefficient $S_{11} < -10$ dB
8. FMR frequency of about 300 MHz

Mn−Zn ferrite thin films can be used as noise suppressors for multilayered printed circuit boards (Matsushita et al., 2002).

10.3.6 XRD spectra and other material characteristics

Crystallographic structures of these magnetic thin films are obtained by X-ray Diffractometer (XRD) (Yang et al., 2010a). For most of the ferrite films, pure phases of the ferrites are clearly identified from the XRD spectrum, although no preferential crystallographic orientation is observed. The XRD spectrum of NiCo-ferrite films (NCFO) is shown in Figure 10.11. It is clear from the XRD data that the NiCo-ferrite film has a single phase spinel structure without preferential orientation.

The in-plane and out-of-plane magnetic hysteresis loops of the NiCo-ferrite films are measured with a vibrating sample magnetometer (VSM) with the external magnetic field applied in the film plane or out of the film plane, respectively (Yang et al., 2010a). The hysteresis loops indicate the dependence of magnetization M on the applied magnetic field H. As shown in Figure 10.12, the in-plane hysteresis loop shows an in-plane coercivity of 165 Oe, as well as the self-biased magnetization of the film under zero applied magnetic fields. There is a huge difference between the in-plane hysteresis and the out-of-plane hysteresis, indicating that the magnetization stays in the film plane under zero bias magnetic field. The NiCo-ferrite film showed an in-plane homogeneous magnetization with an in-plane relative permeability of about 10. The in-plane resistivity of the NiCo-ferrite film is measured to be 5.6×10^3 Ω cm.

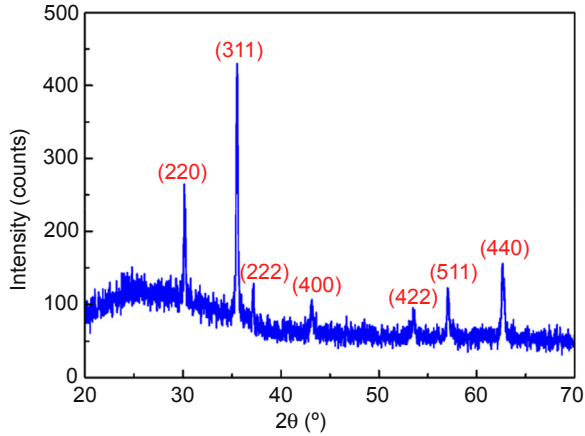

Figure 10.11 XRD spectrum for NCFO thin films (Yang et al., 2010a).

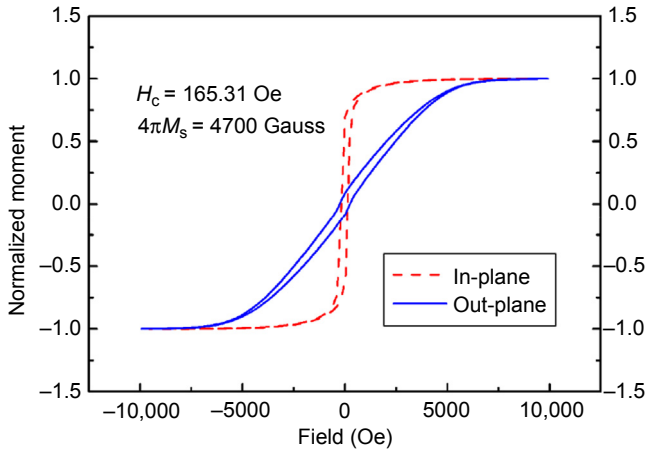

Figure 10.12 Hysteresis loop of NiCo-ferrite film (Yang et al., 2010a).

The physical properties have been examined by atomic force microscope (AFM) and scanning electron microscope (SEM). The resonance frequencies of the NiZn ferrites produced appear to be around 1 GHz. The resonance of the NiCo-ferrite film is much higher. The material parameters of NiCo-ferrite film can be seen in Figure 10.13(a) and (b).

10.4 Bulk composites

One of the most promising ceramics ferrite for offering low-loss operation in the microwave region is the hexagonal ferrites. The descriptors 'hexagonal' refer to the geometric crystal structure that the ceramic forms, and some of the most important

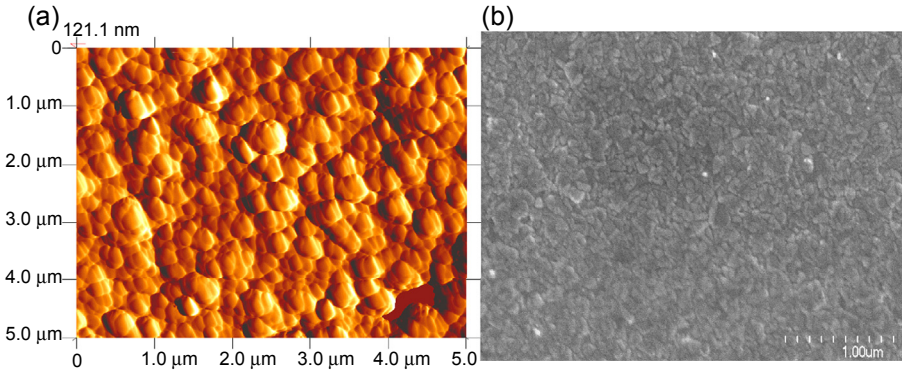

Figure 10.13 (a) AFM data for NiCo-ferrite film. (b) SEM data for NiCo-ferrite film (Zhang et al., 1993).

classes are 'Z-type' hexaferrites and 'M-type' hexaferrites. What's more, mixed ferrites and bismuth strontium titanate (BST) materials will be introduced as well.

10.4.1 Hexagonal Z-type ferrites

Hexagonal *Z*-type hexaferrite has the characteristics of high permeability and low loss property below 300 MHz (Bae et al., 2009). One of such hexaferrites is $Ba_3Co_2Fe_2O_{41}$ (Co_2Z), which is fabricated with starting materials such as $Ba(NO_3)_2$, $Co(NO_3)_2 \cdot 6H_2O$, $Fe(NO_3)_3 \cdot 9H_2O$ for SGP, and $BaCO_3$, CoO, and α-Fe_2O_3 used for conventional ceramic process (CCP) according to an Fe/Ba mole ratio of 7.2 and 8.0, respectively. A mixture of starting materials is shake milled for 10 h with hardened-steel balls in a jar, which had a balls-to-powder weight ratio of 10:1. The shake milled precursors are subjected to two-step calcinations (Bae et al., 2009). The first-step calcination is performed at 1000 °C for 4 h and followed by the second-step calcination at 1300 °C with ambient O_2 pressure to obtain a pure *Z*-type phase. In order to prepare a sintered ring for dynamic-magnetic property measurements, the second-step calcined Co_2Z powder is mixed with polyvinyl alcohol binder and pressed with a steel mold. Green bodies were then sintered in O_2 at 1300 °C for 2 h (Bae et al., 2009).

Frequency dispersion of polycrystalline ferrite permeability can be written by the following equations (Bae et al., 2009):

$$\mu' = 1 + \frac{\omega_d^2 \chi_{d0}\left(\omega_d^2 + \omega^2\right)}{\left(\omega_d^2 - \omega^2\right)^2 \omega^2 \beta^2} + \frac{\chi_{s0}\omega_s^2\left[\left(\omega_s^2 + \omega^2\right) + \omega^2\alpha^2\right]}{\left[\omega_s^2 - \omega^2\left(1+\alpha^2\right)\right]^2 + 4\omega^2\omega_s^2\alpha^2} \tag{10.8}$$

$$\mu'' = \frac{\chi_{d0}\omega\beta\omega_d^2}{\left(\omega_d^2 - \omega^2\right)^2 + \omega^2\beta^2} + \frac{\chi_{s0}\omega_s\omega\alpha\left[\omega_s^2 + \omega^2\left(1+\alpha^2\right)\right]}{\left[\omega_s^2 - \omega^2(1+\alpha)^2\right]^2 + 4\omega^2\omega_s^2\alpha^2} \tag{10.9}$$

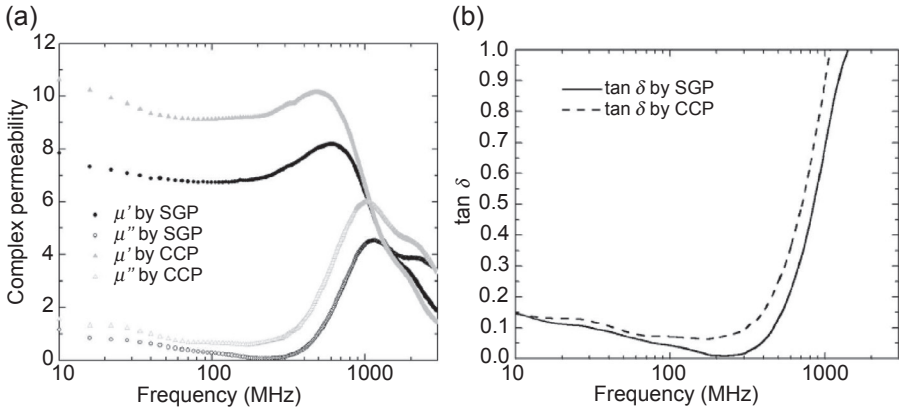

Figure 10.14 Frequency dependences of (a) complex permeability and (b) tan δ_μ of SGP and CCP Co_2Z rings (Bae et al., 2009).

The measured permeability data is given in Figure 10.14. The low loss tan δ of SGP Co_2Z at 200 MHz is attributed to a wider frequency gap between ω_d and ω_s than that of CCP Co_2Z. In addition, α and β of SGP Co_2Z are estimated around 0.88 and 2.0×10^8, respectively, while α and β are 0.91 and 8.5×10^8 for CCP Co_2Z. In order to minimize loss tan δ at 200 MHz, small (<10 μm) and uniform grain and $\mu_r < 7$ are desired. Furthermore, measured μ_r of Co_2Z at 200 MHz are 6.88 and 7.64 for SGP and CCP, respectively.

With regard to preparation of Co_2Z hexaferrite and Ni−Mn−Co (NMC) ferrite, the detailed processes have been reported by the authors (Kondo et al., 2008; Sun & Wang, 2000; Wang et al., 2000). The crystallized Co_2Z ferrite is water-quenched (WQ) to obtain the finer crystal grains and homogenous Z-phase. Magnetic properties of WQ Co_2Z hexaferrite are compared to those of air-cooled (AC) Co_2Z hexaferrite.

10.4.2 Hexagonal M-type ferrites

The most common type of M-type ferrite used for microwave devices is Co/Ti-substituted BaM. Soft $BaFe_{9.6}Co_{1.2}Ti_{1.2}O_{19}$ (Co/Ti-substituted BaM) powder is prepared by mixing and calcining $BaCO_3$, Fe_2O_3, CoO, and TiO_2 at 1100 °C for 5 h (Lee, Hong, Lee, Abo, & Park, 2012). The calcined powder is subject to shake-milling for 1.5 h or 8 h prior to sintering. The Co/Ti-substituted BaM green body (ring or rectangular shape) is heated to 1100 °C or 980 °C and rapidly quenched to 930 °C. The quenched sample is held at 930 °C for 8 h and then cooled to the room temperature. A VSM and impedance/material analyzer are used to characterize static- and dynamic-magnetic properties of Co/Ti-substituted BaM.

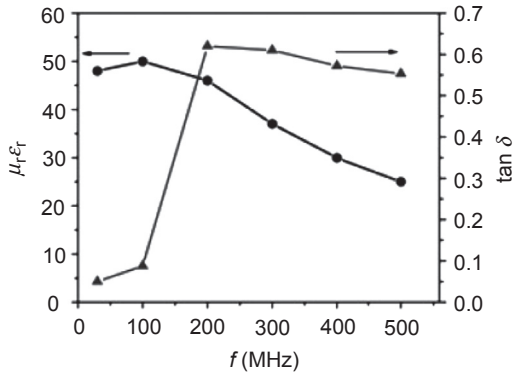

Figure 10.15 Variation with frequency of $\mu_r\varepsilon_r$ and loss tangent for 22 cm diameter and 1 cm thick disc of a composite of nickel zinc ferrite and barium strontium titanate (Petrov et al., 2008).

10.4.3 Mixed ferrite and BST materials

Substrates made of composites of nickel zinc ferrites (NZFO), $Ni_{1-x}Zn_xFe_2O_4$ ($x = 0-0.5$), and BST, $Bi_{1-x}Sr_xTiO_3$ ($x = 0.4-0.5$), are used for 20−100 MHz antennas (Petrov et al., 2008). Pure nickel zinc ferrites have $\mu_r = 10-50$ and loss factor $\tan\delta_\mu = 0.01-1$ at 100 MHz, depending on the Zn concentration, sample synthesis conditions, and microstructure (Sun et al., 2002). In the example below, NZFO with $x = 0.2$ is used as the magnetic phase in the ME composites. The dielectric phase is BST with $x = 0.5$, which has a high ε_r and low losses at 100 MHz (Petrov et al., 2008). Fine powders of NZFO and BST are prepared individually by ceramic processing techniques. They are mixed at a ratio of 98% ferrite and 2% BST, by weight, and sintered at 1250 °C to obtain a disc with a diameter of 10−22 cm and thickness of 0.1−1 cm. The addition of BST to NZFO resulted in a reduction both in μ_r and tan δ_μ. Analysis of magnetic and electric properties on a 10 cm diameter disc shows that the relative permeability and relative permittivity are both 16 and the loss tangent is about 0.005.

The miniaturization factor $n = \sqrt{\mu_r\varepsilon_r}$ and insertion loss and their frequency dependence are obtained on a 22 cm disc of the composite and are shown in Figure 10.15. The data are obtained using a series of half-wave radiators with lengths ranging from 1 to 22 cm, in steps of 1 cm. The half-wave radiators are mounted on the composite, and measurements of resonance frequency and transmission loss are performed to obtain $\mu_r\varepsilon_r$ and tan δ. With the increase in frequency, the miniaturization factor decreases while the loss tangent increases. This trend continues for the entire frequency range up to 500 MHz.

10.5 Layered thin film systems

To get a thick magneto-dielectric material substrate, the layered ferrite film composed of self-biased spinel NiCo-ferrite films is fabricated by a low-cost spin spray deposition process, which is a wet chemical synthesis process at a low temperature of 90 °C.

Figure 10.16 Schematic of Ferrite/Dielectric/Ferrite sandwich structure.

NiCo-ferrite films with the composition of $Ni_{0.23}Co_{0.13}Fe_{2.64}O_4$ are deposited onto both sides of the dielectric material substrate, and the thickness of ferrite film on each side ranges from 2 μm to 10 μm, which depends on the surface smooth conditions. Thus, one could get a Ferrite/Dielectric/Ferrite (F/D/F) sandwich structure, as shown in Figure 10.16.

10.5.1 Layered bulk ferrite systems

The geometry of an N-layer 3-D periodic magneto-dielectric woodpile structure is depicted in Figure 10.17. Each periodic layer is assumed to be made of both dielectric and magnetic materials with a fixed periodicity. The even numbered layers are similar to the odd numbered layers, except that they are rotated by 90°. In a twenty-layer magneto-dielectric woodpile structure, even layers are rotated 90° relative to the odd layers (Mosallaei & Sarabandi, 2004).

10.6 Antenna design and characteristics

10.6.1 Patch antenna with metal magnetic films

A conventional patch antenna operating at 2.13 GHz is designed on a square alumina substrate with a thickness of 2 mm (Sun et al., 2007). The copper patch size for the nonmagnetic antenna is $L = 22.2$ mm, $W = 30$ mm, and thickness of 3 μm. Two new magnetic antennas are designed and fabricated with the same alumina substrate and Cu patch dimensions as those of the nonmagnetic antenna, except that there is one 1-μm-thick metal magnetic film between the Cu patch and the alumina substrate. The shape of the magnetic layer is controlled to be the same as that of the Cu patch (excluding the feed line). Metal magnetic films used for magnetic patch antennas have an atomic composition of $(Fe_{60}Co_{40})_{85}B_{15}$ and are amorphous with a saturation

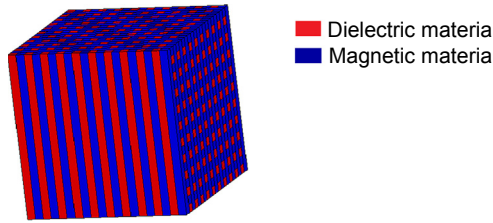

Figure 10.17 Magneto-dielectric woodpile.

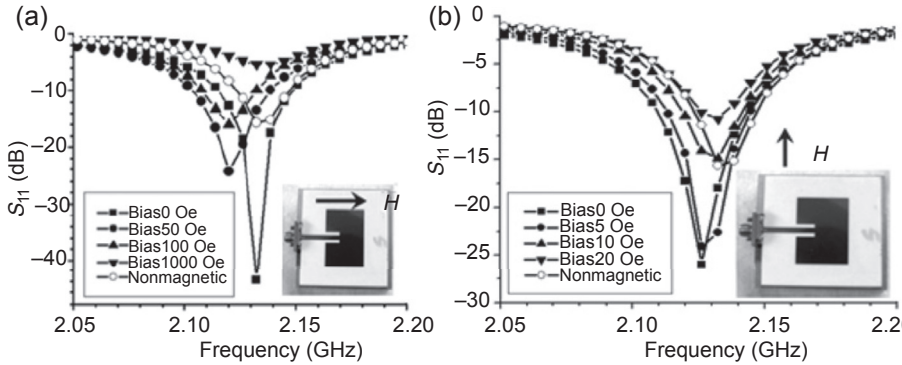

Figure 10.18 (a) Return loss of the magnetic patch antenna with different applied magnetic fields along feed line direction. (b) Return loss of the magnetic patch antenna with different applied magnetic fields perpendicular to feed line direction (Sun et al., 2007).

magnetization of 16 kG, a coercivity of <0.3 Oe, and a high resistivity of 100 μΩ cm. All FeCoB films are 1 μm thick, deposited by sputtering with an in situ magnetic field to preset the magnetization direction, thus achieving anisotropic in-plane permeability. Two magnetic antennas are made with magnetization of the FeCoB magnetic film preset to be either parallel or perpendicular to the feed line, as shown in Figure 10.18(a) and (b).

Return loss of the nonmagnetic antenna and the two magnetic antennas are measured and shown in Figure 10.18. The resonant frequency of the nonmagnetic antenna is 2.135 GHz and the −10 dB bandwidth is 24.3 MHz. The return losses of the two magnetic patch antennas are measured with the magnetic bias field parallel or perpendicular to the feed line. Figure 10.18(a) shows the return loss of the magnetic patch antenna (with magnetization preset to be parallel to the feed line) with the applied bias magnetic fields feed line, and Figure 10.18(b) shows the results of the magnetic patch antenna with bias magnetic fields feed line.

As can be seen from these two figures, the magnetic bias field has a strong effect on the magnetic antenna performance. The magnetic patch antenna without bias field shows a resonance frequency of 2.132 GHz and a −10 dB bandwidth of 37.3 MHz, which is 50% higher than that of the nonmagnetic antenna. With a bias magnetic field of 20−50 Oe along the feed line direction, the resonance frequency is shifted from 2.132 GHz down to 2.120 GHz, while the bandwidth of 37 MHz is maintained.

When the magnetic fields are applied perpendicular to the feed line, the magnetic antenna shows an upward shift of the resonance frequency, opposite to the case when magnetic field is applied parallel to the feed line. The shift is about 7 MHz at a low bias field of 10 Oe. Therefore, with a small applied field of <50 Oe, a total resonance frequency shift of 19 MHz can be achieved, which is about 50% of the −10 dB bandwidth of the magnetic antenna.

The far-field H-plane radiation pattern of the nonmagnetic antenna is shown in Figure 10.19. The magnetic antenna is tested and the directivity is enhanced from

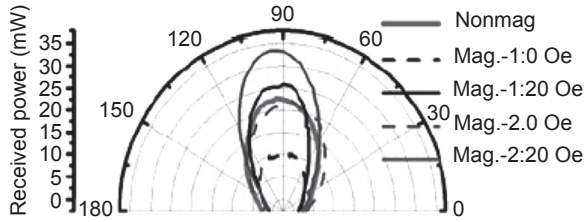

Figure 10.19 Comparison of H-plane received power for all three antennas (nonmagnetic, first magnetic antenna, second magnetic antenna) at different magnetic fields applied perpendicular to the feed line (Sun et al., 2007).

5.58 to 6.73 dB compared to that of the nonmagnetic antenna. The beam pattern of the first magnetic antenna shows strong bias field dependence. The H-plane beam pattern for another magnetic antenna, which has its magnetization preset to be perpendicular to the feed line, is shown in the same figure. Again, the directivity is enhanced at a bias field of 20 Oe, showing a 2.5 dB enhancement of the maximum radiated power. At a bias field of 20 Oe perpendicular to the feed line, the maximum radiated power of the first magnetic antenna is significantly enhanced compared to that at zero field, even slightly higher than that of the nonmagnetic antenna.

10.6.2 Patch antenna with self-biased ferrite films

The geometry of the designed rectangular patch antenna is shown in Figure 10.20 (Yang, 2010). The first study conducted with the use of NiCo-ferrite films is done to determine the correct placement of the film in regards to the antenna. To be more specific, four different antennas are designed and shown in Figure 10.21(a)–(d). The first antenna, named Antenna No.1, is a control antenna and has no ferrite films placed on it. The other antennas preceded as follows: Antenna No.2 has a ferrite

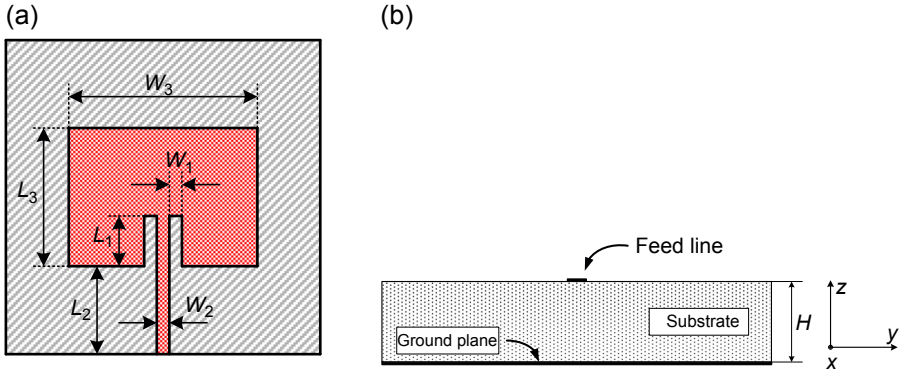

Figure 10.20 Geometry of the designed rectangular patch antenna. (a) Top view, $L_1 = 8.0$ mm, $L_2 = 14.3$ mm, $L_3 = 22.2$ mm, $W_1 = 2.0$ mm, $W_2 = 2.0$ mm, and $W_3 = 30.0$ mm. (b) Side view, $H = 2.0$ mm (Yang, 2010).

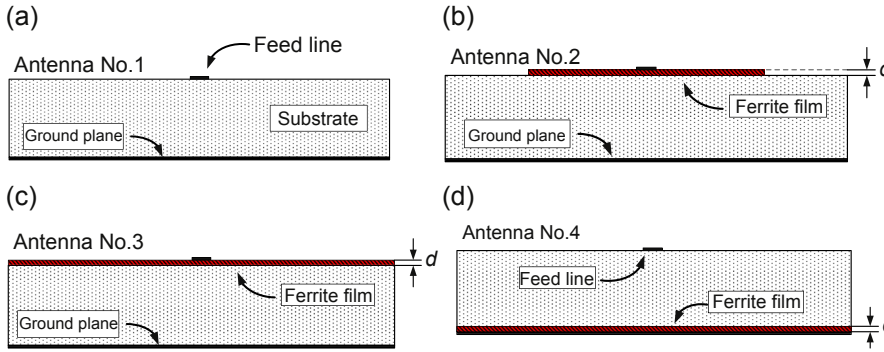

Figure 10.21 (a) Antenna without films (Antenna No.1). (b) Antenna with film under the patch (Antenna No.2). (c) Antenna with film on the whole dielectric surface (Antenna No.3). (d) Antenna with film above the ground plane (Antenna No.4). The film thickness $d = 2$ μm (Yang, 2010; Yang et al., 2008).

film placed underneath the radiating patch only, Antenna No.3 has a ferrite film placed over the entire area of the substrates top, and Antenna No.4 has the ferrite film placed between the ground and the substrate.

The ferrite film used in this study is a NiCo-ferrite with the following material parameters: thickness of 2 μm, relative permittivity of 13, relative permeability of 10, and a low loss tangent. Aside from differences in ferrite positioning, all antennas are fabricated to be identical.

The measurements are outlined in Figure 10.22. Antenna No.1 shows a resonant frequency of 2.147 GHz and a bandwidth of 18 MHz. Antenna No.2 shows a downward shift in the resonance peak down to 2.136 GHz. This indicates the miniaturization effect of the ferrite film in the antenna. This is also what is called the tunable range

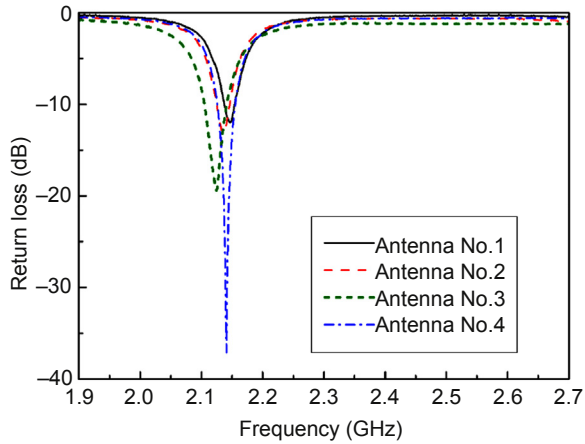

Figure 10.22 Measured return loss of the four antennas (Yang, 2010; Yang et al., 2008).

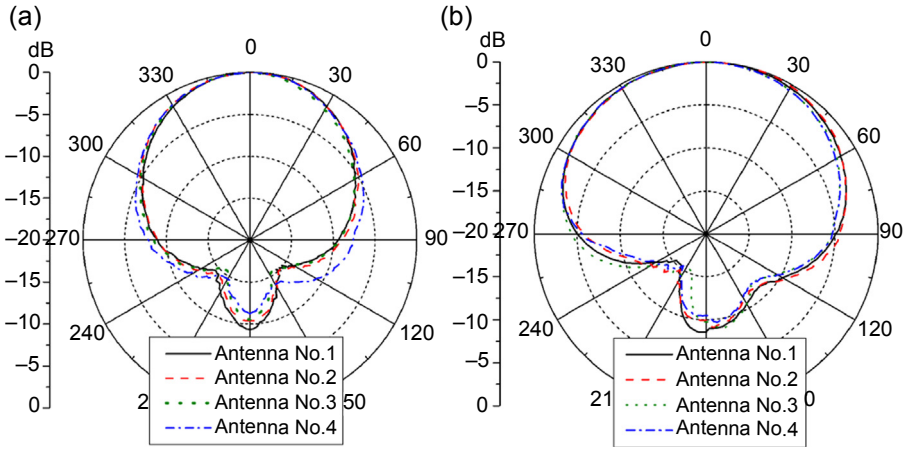

Figure 10.23 Measured normalized radiation pattern of the four antennas (No.1 to No.4). (a) H-plane. (b) E-plane (Yang, 2010).

offered by the film, and in this case is approximately 11 MHz. This value is more than 60% of the overall bandwidth of the nonmagnetic case. In addition to that enhancement, the second antenna also offered a larger bandwidth with about a 16% increase.

Antenna No.3 shows even better performance than that of Antenna No.2. The resonant frequency is shifted down further to 2.124 GHz, which is a shift of 23 MHz from the nonmagnetic antenna, or 127% of the bandwidth of the nonmagnetic antenna. This antenna also experienced a significant bandwidth enhancement. The −10 dB bandwidth is 37 MHz in this case, which is more than 200% of that of the nonmagnetic antenna. Finally, placing a ferrite film above the ground plane of the antenna led to significant enhancement of the impedance matching. As shown by the antennas, −38 dB return loss was indicated in Figure 10.22.

The normalized E- and H-plane radiation patterns of all these antennas are measured in the anechoic chamber. These measurements are given in Figure 10.23. As one can see from the figure, the radiation patterns are similar for each of the antenna, with the exception of the back lobes and high angle gain. The ferrite films seem to positively affect both of these parameters. In fact, antennas with ferrite films experienced a 1−2 dB reduction in the back lobes.

10.6.3 Planar microstrip antenna with magneto-dielectric loading

To investigate the loading effects of magneto-dielectric materials as an antenna's superstrate, five annular ring antennas with ferrite films are designed and fabricated as follows. Magnetic antennas with several layers of the NiCo-ferrite film loading on the top side are designed with the thickness of ferrite films varied with $T_{top} = 2$, 4, 6, 8, 10 μm, and shown in Figure 10.24 (Yang et al., 2010a). In order to compare the results with the nonmagnetic antenna, the measured reflection coefficient of five

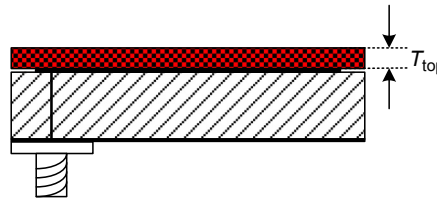

Figure 10.24 Annular ring antenna with ferrite films above the ring (Yang et al., 2010a).

magnetic antennas along with that of a nonmagnetic ring antenna are plotted and analyzed.

As shown in Figure 10.25(a), the central resonant frequency of the nonmagnetic antenna is about 1.72 GHz, and the −10 dB bandwidth is 5 MHz. When a ferrite film with thickness of 2 μm is added above the ring, the resonant frequency shifts down to 1.70 GHz. This indicates a frequency down shift of 20 MHz relative to the nonmagnetic antenna. When the thickness of the ferrite film is 4 μm, the resonance shifts down to 1.675 GHz, a frequency shift of 45 MHz, or is equivalent to five times the antenna bandwidth of nonmagnetic ring antenna. The resonant frequencies are 1.667, 1.664, and 1.649 GHz, when the thicknesses of the ferrite films are 6, 8, and 10 μm, respectively. The antenna gains are 0.57, 1.23, 1.4, 0.87, and 0.57 dB, respectively, for the antenna loaded with 2, 4, 6, 8, and 10 μm thick ferrite film. Clearly, ferrite film loading can lead to miniaturized antennas by downward shift of the resonant frequency. A summary of the variation of resonant frequency and antenna gain with ferrite film loading is shown in Figure 10.25(b).

The antenna gain and the radiation patterns of E-plane and H-plane are measured in the anechoic chamber and plotted in Figure 10.26(a) and (b), respectively. In order to compare the experimental results with the numerical results, the simulated E-plane and H-plane of the annular ring antenna are also given in the same figure. As shown in Figure 10.26(a), when the thickness of ferrite films is 4 μm or 6 μm, the upper-half pattern is almost the same, while the bottom-half pattern shrank. This can also be

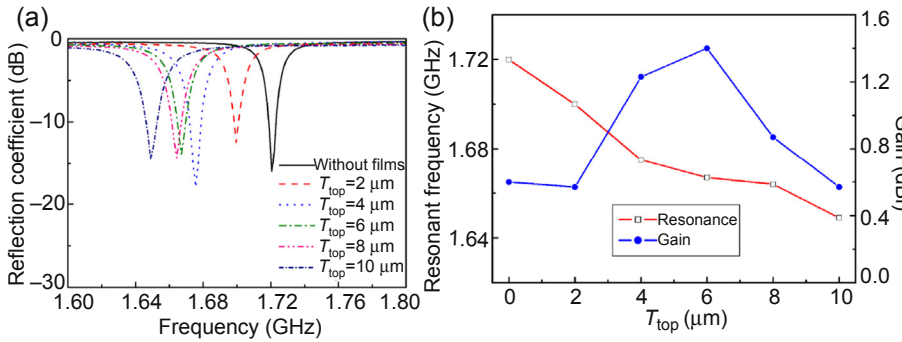

Figure 10.25 Measured reflection coefficient with $T_{top} = 2, 4, 6, 8, 10$ μm. (b) Measured resonant frequency and antenna gain with single-sided ferrite film loading (Yang et al., 2010a).

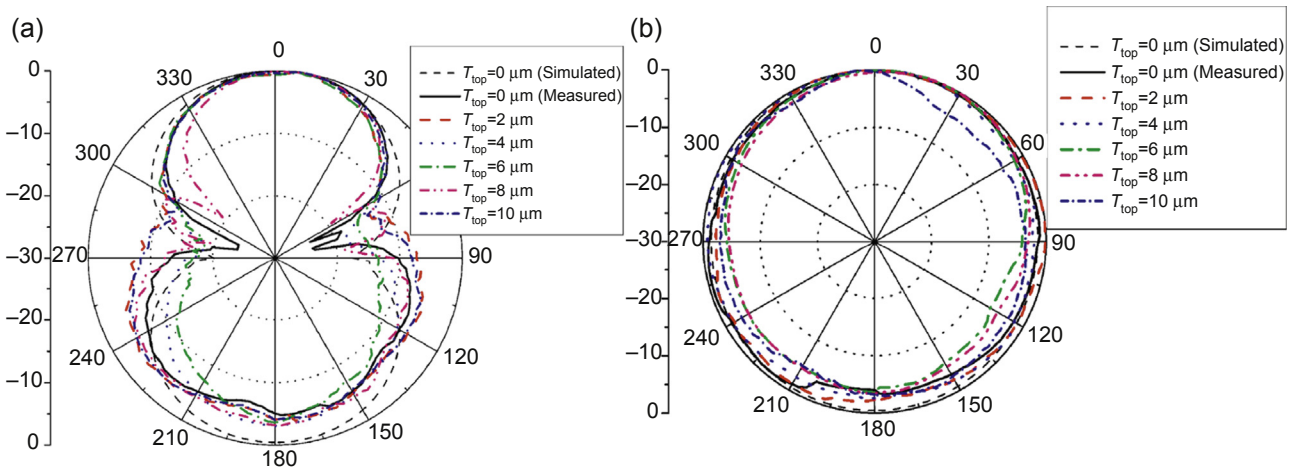

Figure 10.26 Normalized radiation pattern of (a) E-plane and (b) H-plane (Yang et al., 2010a).

observed in Figure 10.26(b). This shows that as an inductive loading acts as a superstrate, more energy will be radiated into forward free space. A maximum antenna gain of 1.4 dB is obtained when the thickness of ferrite films is 6 μm and coated above the ring. Similar enhanced gain is observed in patch antennas loaded with spin spray ferrite films (Yang et al., 2010b). All the measured gains are plotted in Figure 10.25(b). However, when the thickness is more than 6 μm, the antenna gain begins to decrease. From the radiation patterns of E-plane, we can see that more energy may be radiated between the elevation angles of 60°−120° and 240°−300°. The main reason for this may be that with an increase in the thickness of ferrite films, the surface wave may radiate more energy, which resulted in decreased antenna gain.

10.6.4 Antenna with hexagonal Z-type ferrite materials

In order to fabricate antennas, the CoZ and Ni−Mn−Co ferrite green blocks are prepared by pressing and sintering at 1100−1300 °C in an oxygen environment for 2 h (Bae et al., 2009). The fabricated antennas are shown in Figure 10.27. The first helical antenna is fabricated with an air cooling processed Co_2Z substrate (named AC antenna in this chapter). The second helical antenna is fabricated with WQ processed Co_2Z substrate (named WQ antenna in this chapter). The last helical antenna is fabricated with Ni−Mn−Co (NMC) ferrite substrate (named NMC antenna in this chapter).

Figure 10.28 shows the measured S-parameters for the AC antenna, WQ antenna, and NMC antenna. The resonant frequencies of the AC, WQ, and NMC antennas are measured to be 195, 201, and 209 MHz, respectively.

Radiation patterns of *yz*-planes are measured in terms of frequency, ranging from 174 to 228 MHz. The patterns of AC antenna, WQ antenna, and NMC antenna are shown in Figure 10.29, and all antennas show omnidirectional gain patterns in the *yz*-plane. The average gains increase up to about 195 MHz and then are followed

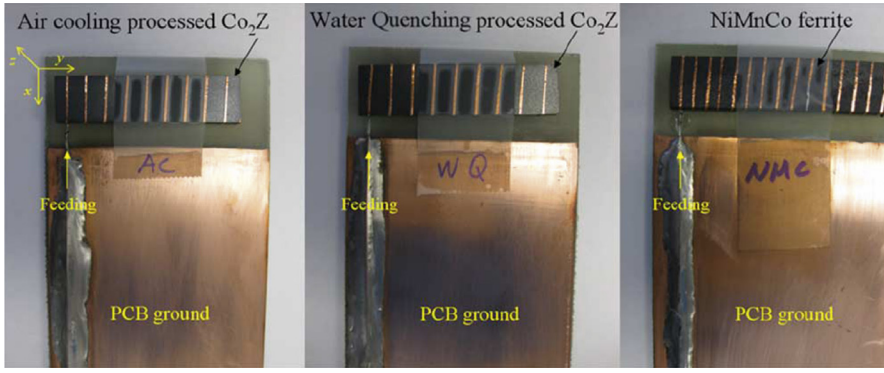

Figure 10.27 Fabricated AC, WQ CoZ, and Ni−Mn−Co ferrite T-DMB antennas (Bae et al., 2009).

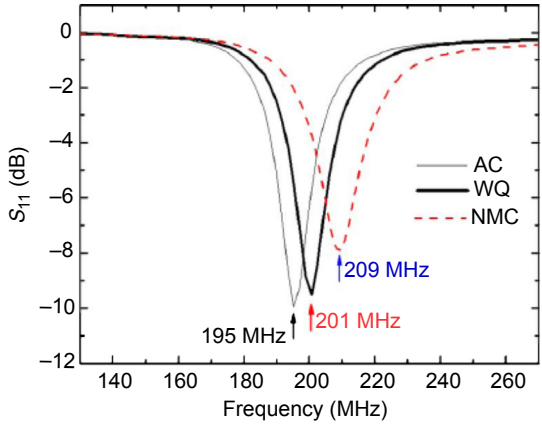

Figure 10.28 Frequency dependence of the S_{11}-parameter (Bae et al., 2009).

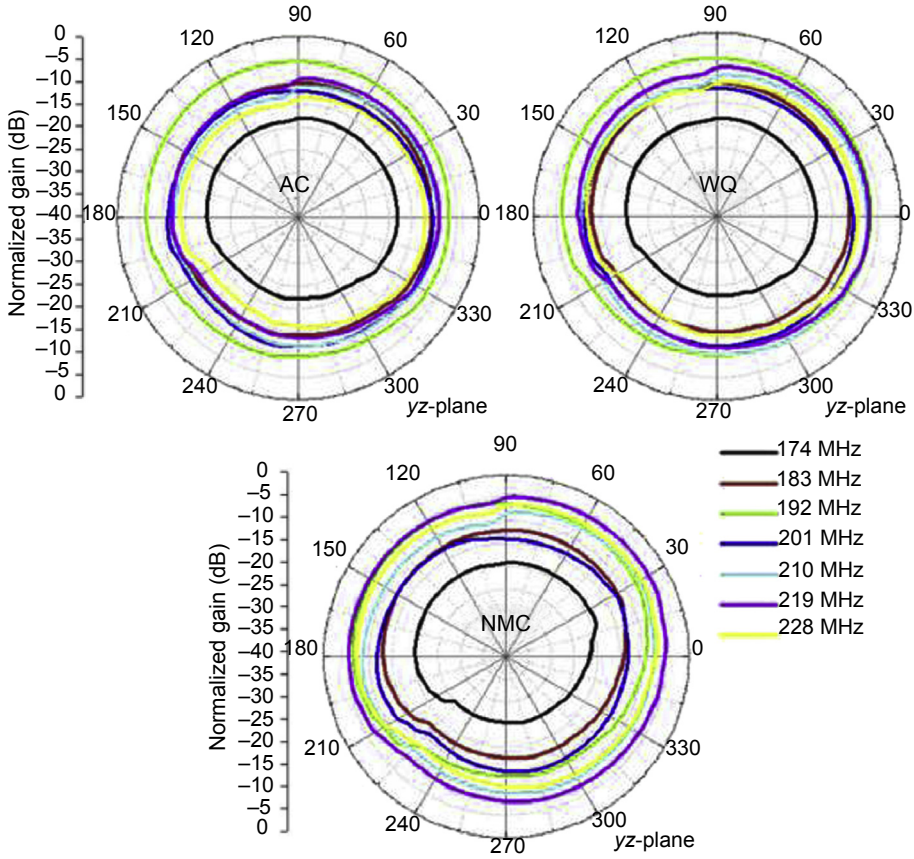

Figure 10.29 Radiation patterns at the *yz*-plane of the fabricated ferrite antennas (Bae et al., 2009).

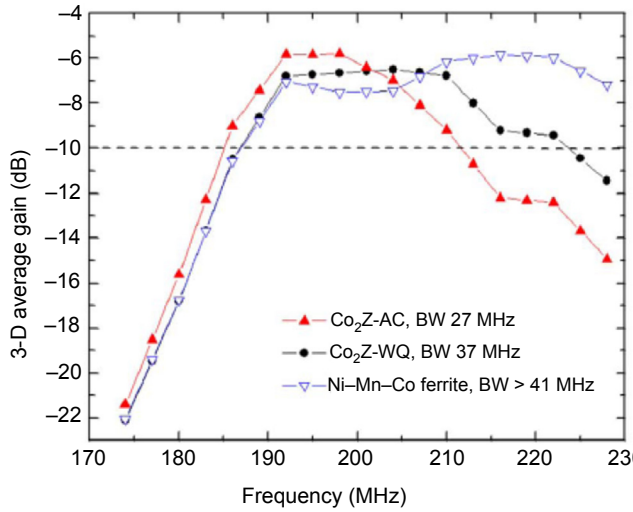

Figure 10.30 Frequency dependence of the 3-D average gain for the fabricated ferrite antennas (Bae et al., 2009).

by a gradual decrease for AC antenna and WQ antenna or sustaining for NMC, as depicted in Figure 10.30. The experimental bandwidth at 10 dB of AC, WQ, and NMC antennas are 27, 37, and 41 MHz, respectively, which are determined from the 3-D gain graphs in Figure 10.30.

10.6.5 M-type antenna

Helical antenna is fabricated on Co/Ti-substituted BaM substrate ($45 \times 11 \times 3.8$ mm^3 or $42 \times 11 \times 3.8$ mm^3) and then the antenna is mounted on an FR4 board (10×5 mm^2) with copper ground the size of 8×5 mm^2 (Bae et al., 2010). A 50-Ω coaxial cable is used to feed the antenna. The ferrite helical antenna performance is characterized with a network analyzer and the Wheeler cap. The wheeler cap is constructed by a copper (purity: 99.9%) cylinder with a radius of 24.5 cm and height of 0.5 mm and a copper circular ground with a radius of 50 cm.

The fabricated antenna is shown in Figure 10.31, and the measured return losses are shown in Figure 10.32. Antenna resonant frequency shifted from 231 to 201 MHz with the increasing permeability from 4.51 to 8.58. It should be noted that the number of coil turns remains the same (8.5 coil turns; 1 mm linewidth; 3 mm line spacing). In turn, the Co/Ti-substituted BaM antenna is miniaturized by 7% with the permeability of 8.58 with an equation of $\lambda_{\text{eff}} = \lambda_0/\sqrt{\mu_r \varepsilon_r}$. Therefore, the high relative permeability of BaM material needs less coil turns to meet the resonance frequency of 200 MHz. The low-loss Co/Ti-substituted BaM is an excellent soft magnetic material for miniature antenna applications in a very high frequency (VHF: 30−300 MHz) range.

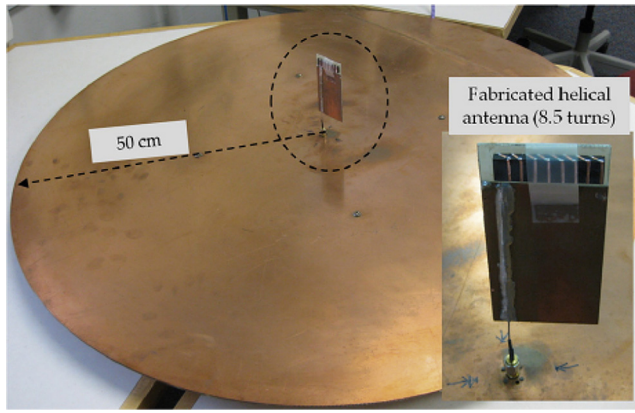

Figure 10.31 Fabricated ferrite helical antenna (8.5 turns) and Wheeler cap measurement for radiation efficiency (Bae et al., 2010).

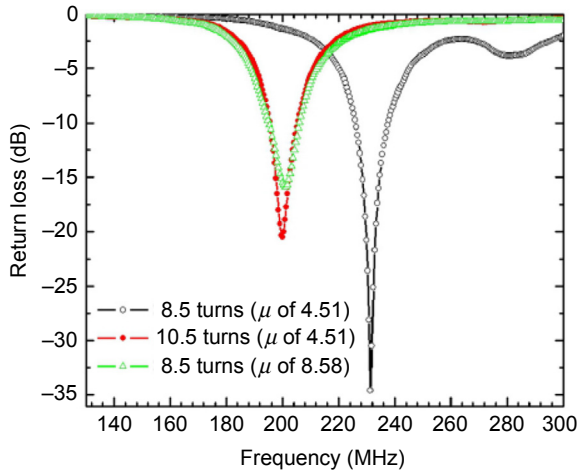

Figure 10.32 Measured return losses of ferrite helical antennas (Bae et al., 2010).

10.6.6 Mixed ferrites and BST materials antenna

Apart from the ferrite films and ferrite bulk materials mentioned above, a composite with large and equal relative permittivity and relative permeability is prepared for miniaturization and impedance match to free space (Petrov et al., 2008). This composite is made of nickel zinc ferrite and BST that is prepared by conventional ceramic processing. The geometry of the half-wavelength resonant microstrip antenna on the composite substrate is shown in Figure 10.33. The diameter of the composite disc is 22 cm and the thickness is 0.85 cm. The length of the microstrip is 22 cm and the width is 0.65 cm.

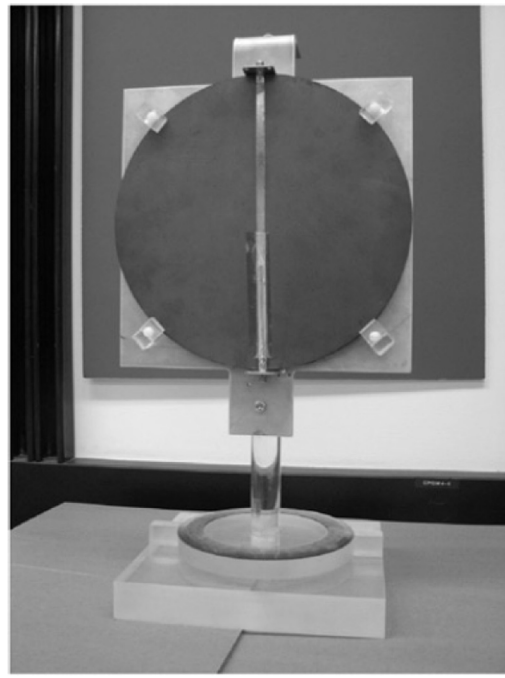

Figure 10.33 100 MHz miniature microstrip antenna on ferrite–ferroelectric composite substrate (Petrov et al., 2008).

The return loss and transmission loss are measured with a vector network analyzer. The predicted resonance frequency of 100 MHz and high insertion losses at the frequency of 150 MHz are in agreement with the data. The measured standing wave ratio (SWR) at resonance is close to 2.5 and indicates good impedance matching between the substrate and free space.

Return loss and radiation pattern are measured with the microstrip antenna as the receiver and shown in Figures 10.34 and 10.35, respectively. A transmitter made of traditional dipole antenna is used and the transmitter–receiver distance is 42 m. The radiation pattern and the signal level are close to expected data. The antenna has a signal amplitude of 0 dB at 0°. The back lobe of the radiation is sufficiently small and is measured to be −4.8 dB. The antenna has a high quality factor Q that represents the losses associated with the stripline and the substrate. A large Q leads to narrow bandwidth and low efficiency. However, Q can be reduced by increasing the thickness of the substrate.

10.6.7 Bulk composites

A patch antenna with the dimension of 10×8 cm^2 is printed on the four-layer magneto-dielectric materials with thicknesses of 2 cm and illustrated in Figure 10.36. The size of the ground plane is 20×20 cm^2. The return loss and radiation patterns are shown in Figure 10.37(a) and (b), respectively. The resonant frequency of the

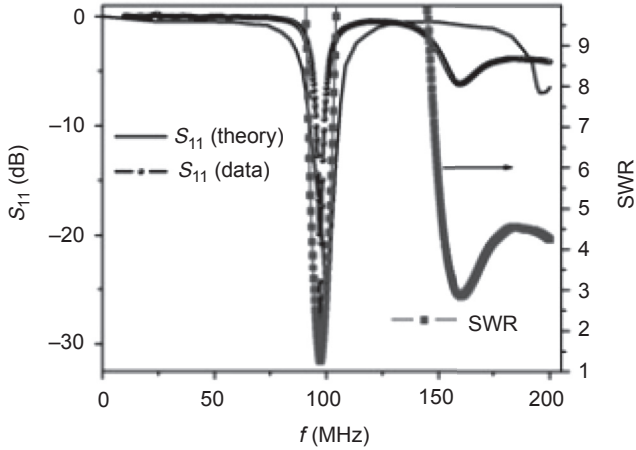

Figure 10.34 Measured and estimated return loss and measured SWR for miniature magnetoelectric microstrip antenna (Petrov et al., 2008).

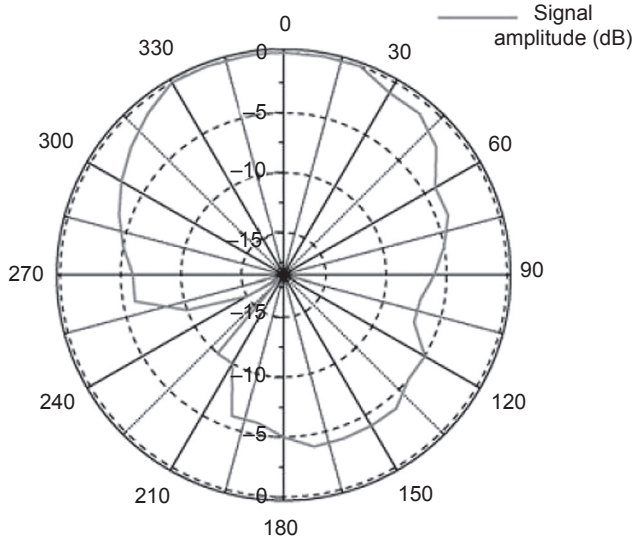

Figure 10.35 Radiation pattern for 100 MHz antenna (Petrov et al., 2008).

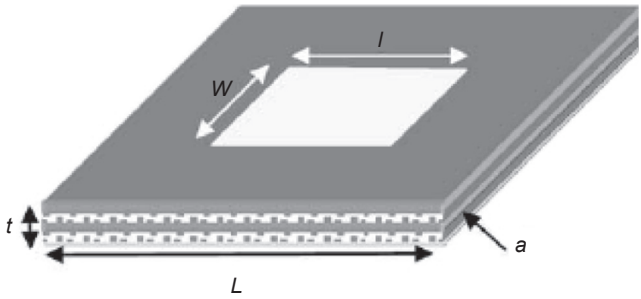

Figure 10.36 A patch antenna over the engineered magneto-dielectric meta-substrate (Mosallaei & Sarabandi, 2004).

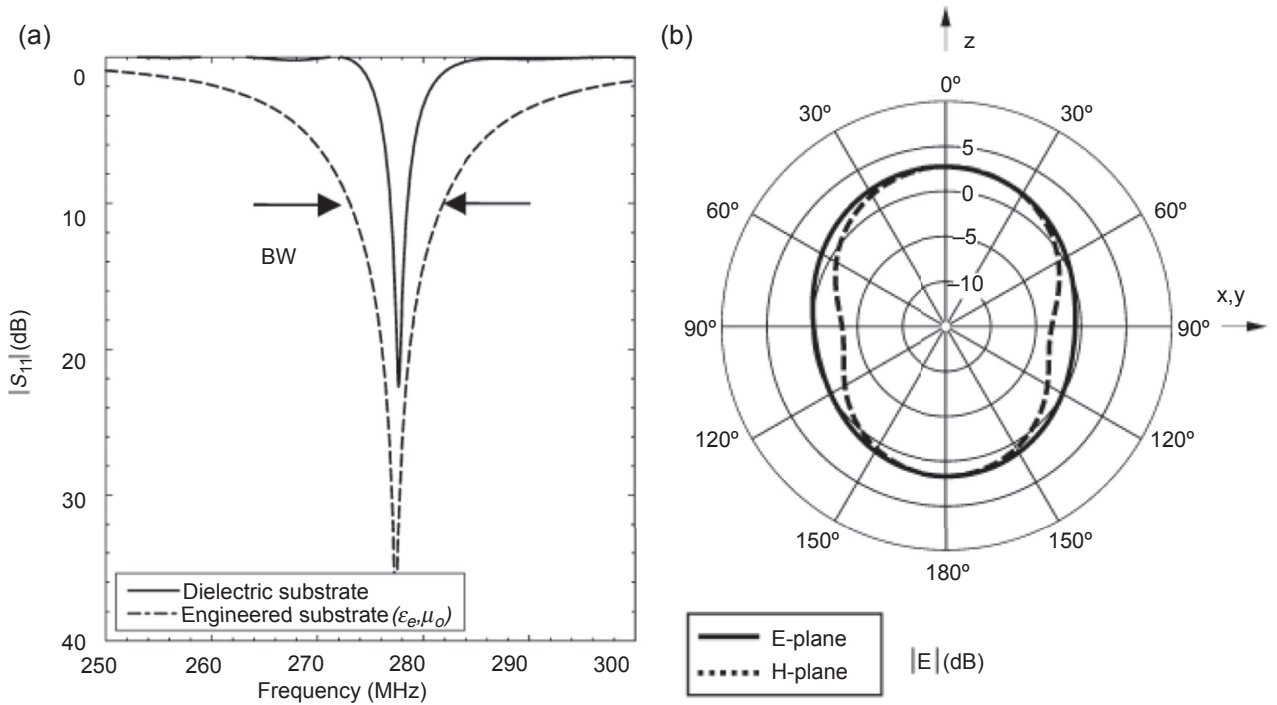

Figure 10.37 Patch antenna over the engineered magneto-dielectric meta-substrate: (a) return loss and (b) radiation patterns. The magneto-dielectric substrate enhances the antenna bandwidth significantly (about 600%) (Mosallaei & Sarabandi, 2004).

fabricated antenna is about 277 MHz, and it provides a wide bandwidth of about BW = 3.2%. The size of the antenna is around with a miniaturization factor of 5.4. The directivity of the antenna is $D_0 = 2.9$ dB, it has a front-to-back ratio of 1.3 dB with a ground plane size of $0.18\lambda_0 \times 0.18\lambda_0$, and the antenna efficiency is about $e_r = 67\%$. If a magneto-dielectric material with lower magnetic loss tangent of about 0.01 is used, the efficiency is increased to 82% while the bandwidth is decreased to BW = 2.8% (Mosallaei & Sarabandi, 2004).

It should be noted that to achieve the same miniaturization factor utilizing only a dielectric material ($\mu_r = 1$), the relative permittivity would be 23.7. This reduces the bandwidth to about BW = 0.5%, which is shown in Figure 10.37(a). The efficiency in this case for a dielectric loss tangent of 0.001 is about $e_r = 64\%$. Therefore, utilizing the magneto-dielectric meta-substrate, one can offer a miniaturized wideband planar antenna with high efficiency. The antenna bandwidth for the proposed magneto-dielectric substrate is about six times higher than that of the dielectric substrate.

References

Abe, M. (June 2000). Ferrite plating: a chemical method preparing oxide magnetic films at 24−100 °C, and its applications. *Electrochimica Acta, 45*(20), 3337−3343.

Abe, M., & Tamaura, Y. (August 1983). Ferrite-plating in aqueous solution: a new method for preparing magnetic thin film. *Japanese Journal of Applied Physics, 22*(8), L511−L513.

Abe, M., & Tamaura, Y. (March 1984). Ferrite plating in aqueous solution: new technique for preparing magnetic thin film. *Journal of Applied Physics, 55*(6), 2614−2616.

Bae, S., Hong, Y. K., Lee, J. J., Jalli, J., Abo, G. S., Lyle, A., et al. (2009). Low loss Z-type barium ferrite (Co_2Z) for terrestrial digital multimedia broadcasting antenna application. *Journal of Applied Physics, 105*, 07A515.

Bae, S., Hong, Y. K., Lee, J. J., Seong, W. M., Kum, J. S., Ahn, W. K., et al. (June 2010). Miniaturized broadband ferrite T-DMB antenna for mobile-phone applications. *IEEE Transactions on Magnetics, 46*, 2361−2364.

Balanis, C. A. (1989). *Advanced engineering electromagnetics*. Hoboken, NJ: John Wiley.

Brown, A. D., Volakis, J. L., Kempel, L. C., & Botros, Y. Y. (January 1999). Patch antennas on ferromagnetic substrate. *IEEE Transactions on Antennas and Propagation, 47*(1), 26−32.

Buell, K. (2005). *Development of engineered magnetic materials for antenna applications* (Ph.D. Dissertation). Ann Arbor, MI: The University of Michigan, Department of Electrical Engineering.

How, H., Fang, T. M., Guan, D. X., & Vittoria, C. (November 1994). Magnetic steerable ferrite patch antenna array. *IEEE Transactions on Magnetics, 30*(6), 4551−4553.

Kondo, K., Chiba, T., Ono, H., Yoshida, S., Shimada, Y., Matsushita, N., et al. (2008). Post-heat-treated spin-spray plated $Mn_xZn_yFe_{3-x-y}O_4$ films exhibiting high resistivity and noise suppressing properties. *Journal of Applied Physics, 103*, 07E502.

Kondo, K., Yoshida, S., Ono, H., & Abe, M. (2007). Spin sprayed Ni(-Zn)-coferrite films with natural resonance frequency exceeding 3 GHz. *Journal of Applied Physics, 101*, 09M502.

Lee, J. J., Hong, Y. K., Lee, W., Abo, G. S., & Park, J. H. (2012). Soft M-type hexaferrite for very high frequency miniature antenna applications. *Journal of Applied Physics, 111*, 07A520.

Lou, J., Insignares, R. E., Cai, Z., Ziemer, K. S., Liu, M., & Sun, N. X. (October 2007). Soft magnetism, magnetostriction and microwave properties of FeGaB thin films. *Applied Physics Letters, 91*, 18254.

Matsushita, N., Chong, C. P., Mizutani, T., & Abe, M. (October 2002). Ni-Zn ferrite films with high permeability at 1 GHz prepared at 90 °C. *Journal of Applied Physics, 91*, 7376−7378.

Mosallaei, H., & Sarabandi, K. (June 2004). Magneto-dielectric in electromagnetic: concept and applications. *IEEE Transactions on Antennas and Propagation, 52*(6), 1558−1567.

Obi, O. (2008). *Magnetic thin film characterization by spin spray process* (MS thesis). Boston, MA: The Northeastern University, Department of Electrical and Computer Engineering.

Petrov, R. V., Tatarenko, A. S., Pandey, S., Srinivasan, G., Mantese, J. V., & Azadegan, R. (April 2008). Miniature antenna based on magnetoelectric composites. *Electronics Letters, 44*(8), 506−507.

Pettiford, C. I., Zeltser, A., Yoon, S. D., Harris, V. G., Vittoria, C., & Sun, N. X. (April 2006). Magnetic and microwave properties of CoFe/PtMn/CoFe multilayer films. *Journal of Applied Physics, 99*, 08C901.

Pozar, D. M. (September 1992). Radiation and scattering characteristics of microstrip antennas on normally biased ferrite substrates. *IEEE Transactions on Antennas and Propagation, 40*(9), 1084−1092.

Sun, N. X., & Wang, S. X. (September 2000). Soft high saturation magnetization $(Fe_{0.7}Co_{0.3})_{1-x}N_x$ thin films for inductive write heads. *IEEE Transactions on Magnetics, 36*, 2506−2508.

Sun, N. X., Wang, J. W., Daigle, A., Pettiford, C., Mosallaei, H., & Vittoria, C. (April 2007). Electronically tunable magnetic patch antennas with metal magnetic films. *Electronics Letters, 43*, 434−435.

Sun, N. X., Wang, S. X., Silva, T. J., & Kos, A. B. (January 2002). Soft magnetism and high frequency behavior of Fe-Co-N thin films. *IEEE Transactions on Magnetics, 38*, 146−150.

Vittoria, C. (1993). *Microwave properties of magnetic films*. World Scientific Publishing Co.

Wang, S. X., Sun, N. X., Yamaguchi, M., & Yabukami, S. (September 2000). Sandwich films: properties of a new soft magnetic material. *Nature, 407*, 150−151.

Yang, G. M. (2010). *Tunable miniaturized RF devices on magneto-dielectric substrates with enhanced performance* (Ph.D. Dissertation). Boston, MA: The Northeastern University, Dept. of Electrical and Computer Engineering.

Yang, G. M., Xing, X., Daigle, A., Liu, M., Obi, O., Wang, J. W., et al. (November 2008). Electronically tunable miniaturized antennas on magnetoelectric substrates with enhanced performance. *IEEE Transactions on Magnetics, 44*(11), 3091−3094.

Yang, G. M., Xing, X., Daigle, A., Obi, O., Liu, M., Lou, J., et al. (March 2010). Planar annular ring antennas with multilayer self-biased NiCo-Ferrite films loading. *IEEE Transactions on Antennas and Propagation, 58*(3), 648−655.

Yang, G. M., Xing, X., Obi, O., Daigle, A., Liu, M., Stoute, S., et al. (September 2010). Loading effects of self-biased magnetic films on patch antennas with substrate/superstrate sandwich structure. *IET Microwaves Antennas and Propagation, 4*(9), 1172−1181.

Zhang, Q., Itoh, T., Abe, M., & Tamaura, Y. (May 1993). Preparation of NiZn ferrite films by spin-spray ferrite plating on oxygen=plasma-treated substrates. *Journal of Applied Physics, 73*, 6284−6286.

This page intentionally left blank

Magnetoelectric composites for medical application

11

M. Paluszek[1], *D. Avirovik*[1], *Y. Zhou*[1], *S. Kundu*[1], *A. Chopra*[1], *R. Montague*[2,3], *S. Priya*[1]

[1]Center for Energy Harvesting Materials and Systems (CEHMS), Virginia Tech, Blacksburg, VA, USA; [2]College of Science, Virginia Tech, Blacksburg, VA, USA; [3]Virginia Tech Carilion School of Medicine, Roanoke, VA, USA

As mentioned in the earlier chapters, the underlying principle behind the magnetoelectric (ME) laminate sensors is the magnetic-mechanical-electrical coupling. A voltage proportional to the applied magnetic field arises due to a giant elastic or mechanical coupling. When a magnetic field H is applied to the magnetostrictive layer, a mechanical strain is generated in that layer. Then, this strain is transferred to the piezoelectric layer, thus producing an electric field E via piezoelectricity. This phenomenon could be utilized in a variety of ways to address some of the challenges and needs in the medical applications. In this chapter, we describe promising nature of ME composites for the wireless endoscopy (Dragan, 2014) and brain imaging applications.

Endoscopy of the upper and lower gastrointestinal (GI) tract is considered to be a routine diagnostic and therapeutic outpatient procedure. Endoscopes are utilized for closer and noninvasive examination of the GI tract. They provide diagnosis and therapy of a wide variety of pathologies that originate in the epithelial tissue. Classical GI endoscopy involves the insertion of a flexible tube that contains the illumination component, lens/camera visual system, and an additional tube that enables the introduction of medical instruments or manipulators. Upper and lower GI endoscopies are considered to be powerful tools in the diagnosis of GI inflammatory disease (gastritis, esophagitis, Crohn's disease, inflammatory bowel disease) (Despot & Fraser, 2012), cancer (Schoen et al., 2012), and varicose venous structures (Wilkins, Khan, Nabh, & Schade, 2012). The same procedure can be utilized for minor therapeutic procedures, such as foreign body removal (Chen et al., 2012), sclerosis/banding of esophageal varices (Urso et al., 2006), esophageal stenting (Hirdes, Siersema, van Boeckel, & Vleggaar, 2012), and the removal of GI polyps (Pigò et al., 2013). Advances in fiber optics and imaging technology have greatly improved the visualization capabilities of conventional endoscopes. Nevertheless, the reach and maneuverability of tethered endoscopes is limited. Comprehensive endoscopy of the organs in the digestive system, such as the esophagus, stomach, and small and large intestines, is difficult. Only a decade ago, wireless capsule endoscopies (WCEs) were introduced, which leveraged the advances in telemetry, miniature optics, and microelectronics. WCE represents a paradigm shift in the visualization of the GI tract for clinical diagnosis. Currently WCEs are approved by the Food and Drug Administration (FDA) for the diagnosis of Crohn's disease, intestinal bleeding, and inflammatory bowel

Composite Magnetoelectrics. http://dx.doi.org/10.1016/B978-1-78242-254-9.00011-1
Copyright © 2015 Elsevier Ltd. All rights reserved.

syndrome. Patients are far more receptive to undergo a WCE procedure compared to conventional endoscopes since they are far less invasive. Nonetheless, WCE comes with a major disadvantage over conventional endoscopes because of their passive nature. They cannot be controlled or conduct biopsy. Images are acquired at random locations and orientations as the capsule moves along the GI tract. These images are wirelessly transmitted to a recorder worn by the patient around the waist or are saved onto a chip inside the WCE and then uploaded to a computer once removed from the GI tract. Coarse WCE position control is possible.

In order to be able to locate where the images of specific lesions are being taken, a high fidelity tracking of the WCE is required. So far, four methods of tracking have been explored: radio frequency (RF) triangulation, magnetic tracking, computer vision, and ultrasound. For both the RF triangulation and magnetic triangulation, an array of sensors outside the body are used to measure the signal originating from the capsule. Using magnetic theory-based models and a signal from a permanent magnet residing inside the capsule, an estimate of the location of the capsule can be found. An estimate instead of an exact location is obtained because the signals from the body go through different mediums; therefore, delays in acquiring the data occur. Due to signal noise, the experimental error can reach 37 mm using RF and 5 mm using magnetic tracking. A 95% accuracy is obtained using vector quantization, principle component analysis, and neural network (Toennies, Tortora, Simi, Valdastri, & Webster, 2010). Ultrasonic pulses emitted outside the body and echoed from the capsule can also provide a way of tracking the capsule. Another method can be tracking of radioactive material placed inside the capsule, whose emission is strong enough for radiation cameras, but weak enough to avoid adverse effect. As described later in this chapter, ME composites can be potentially tailored for meeting the requirements of the localization of WCE. To generate energy on demand, one can also envision incorporating a magnetic field energy harvesting component into the capsule that can be used to recharge the battery. Thus, if power in the system is less than the threshold, then one can just apply the AC magnetic field from outside the body (as simple as shaking a magnet by hand) and recharge the internal battery.

Another important development taking place is the improvement in the tools that can be used to understand the structure and function of the brain. Advances in magnetometers and signal processing have allowed imaging of the brain with significantly high resolution. The brain performs several bodily functions, such as maintaining body temperature, blood pressure, heart rate, and breathing, collection and processing of information around the person using various sensing organs (eyes, ears, nose, etc.), coordination of the physical motion during walking, talking, standing, or sitting, emotions, reasoning, and imagination. The brain is made of approximately 100 billion nerve cells called neurons, which gather and transmit electrochemical signals. Neurons within the brain may extend up to few millimeters and have different shapes depending on the function. For example, motor neurons that control muscle contractions have a cell body on one end, a long axon in the middle, and dendrites on the other end; sensory neurons have dendrites on both ends, connected by a long axon with a cell body in the middle. The structure of the neurons

controls the intraneuronal electric currents that generate the extracranial magnetic fields. Thus, detection of brain magnetic fields can allow us to investigate the neuronal activity in healthy and diseased brains. The key requirements for magnetic field sensors in this application are (1) sensitivity of $\sim$fT/$\sqrt{\text{Hz}}$ at low frequencies (10^{-3} Hz); (2) ambient temperature and wide bandwidth operation; and (3) small size, to promote portable imaging array systems. These requirements can be met by the advances being made in the synthesis and optimization of the ME composites as discussed in the following sections.

11.1 Detailed background on wireless capsule endoscopy

Misdiagnosis is a very common mistake that occurs in the medical field with an alarming 40% of the total cases, often resulting in consequences of severe magnitudes due to wrong or missed treatment. As a result, missed diagnostics have been responsible for $38.8 billion in spending between 1986 and 2010 (Grush, 2013), and this has been the cause for injuries for 80,000−160,000 patients yearly. Even though medical practitioners are trained to provide careful and systematic diagnoses, these are not 100% accurate. It is therefore necessary to understand that misdiagnosis occurs primarily due to the lack of information doctors acquire from their patients. Often the reason for this is that current technology does not provide conclusive analyses of the disease condition (diagnosis is never aimed at finding the cause of a disease; it usually identifies some symptom associated with one/many diseases). There might be many disease conditions associated with the symptoms exhibited by the patient, and therefore a correct diagnosis requires multiple tests. This could be both time-consuming and also a source for error. A potential solution to this problem is automation and continuous monitoring techniques that are able to utilize data analyses techniques to predict the right diseased state.

In addition to misdiagnosis, there are also medical errors that can result in deterioration of the sickness. According to the study conducted for Cable News Network (CNN) Health (Bonifield & Cohen, 2012), a quarter million causalities and several million injuries in United States occur due to the errors such as the ones listed in Figure 11.1. There have been recorded 1.7 million health care infectious diseases in US hospitals (Klevens et al., 2007), and around 100,000 deaths each year from such infections. These often occur due to the negligence of attending nurses and staff, costing the US health care system $1 billion annually (Wheeler, 2010).

Determining the disease of a patient can be achieved by identifying all the symptoms and then properly correlating them with the known disease conditions. One way to achieve this is through the development of equipment, sensors, and instruments that will be able to diagnose, treat, and communicate between each other in order to form a closed-loop system. This system will be able to acquire and analyze the collected data and correspondingly produce an appropriate response, such as alerting of medical staff, repeating diagnostics or conducting alternative ones, and/or executing treatment protocol. From a diagnostic point of view, some of the most

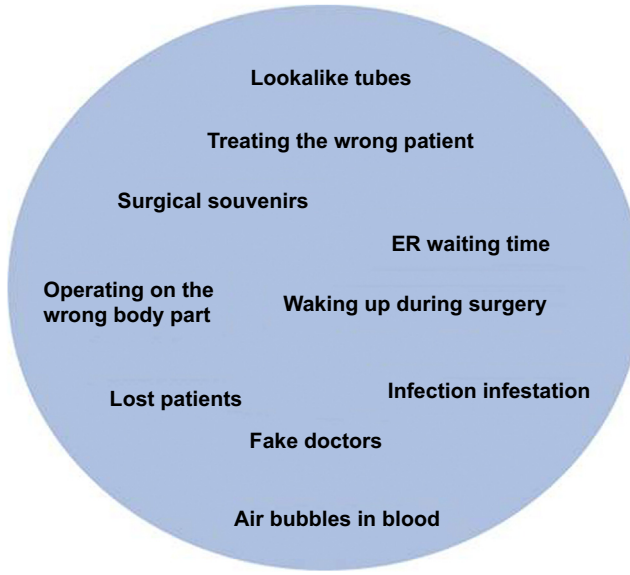

Figure 11.1 Most common medical errors.

commonly used technologies in hospitals are imaging instruments: magnetic resonance imaging (MRI), X-ray, photo acoustic imaging, thermography, ultrasound, endoscopes, etc. Endoscopy is widely utilized by medical doctors to examine the inside of the human body and provide diagnosis. Endoscopes (instruments used to perform endoscopy) are equipped with cameras and are mainly used for inspecting the GI tract of the human body but can also be used for inspecting the respiratory tract, the ear, the urinary tract, and the reproductive systems. Endoscopy of the upper and lower GI tract can be used as a routine diagnostic procedure or as a therapeutic outpatient procedure. It is a procedure for closer and noninvasive examination of the GI tract, conducted by insertion of endoscopes through the human esophagus or rectum. These medical instruments are defined by long, flexible tubes that contain an illumination component, a lens/camera visual system, and an additional tube that enables introduction of medical instruments or manipulators. For decades, these devices have assisted both simple and complex surgical procedures. Accordingly, they provide diagnosis and therapy of a wide variety of pathologies that originate in the epithelial tissue. Moreover, upper and lower GI endoscopies are considered to be powerful tools in the diagnosis of GI inflammatory disease (gastritis, esophagitis, Crohn's disease, inflammatory bowel disease) (Despot & Fraser, 2012), cancer (Schoen et al., 2012), and varicose venous structures (Wilkins et al., 2012). The same procedure can be utilized for minor therapeutic procedures, such as foreign body removal (Chen et al., 2012), sclerosis/banding of esophageal varices (Urso et al., 2006), esophageal stenting (Hirdes et al., 2012), and removal of GI polyps (Pigò et al., 2013). Advances in fiber optics and imaging technology have greatly improved the visualization capabilities of conventional endoscopes. However, because of their

tethered design, constraints in maneuverability, field of view, and dimensions occur, which limits the functions of current endoscopes. Comprehensive endoscopy of the organs in the digestive system, such as the esophagus, stomach, and small and large intestines is very difficult, if not impossible. Thus, there has been continued focus on miniaturizing current endoscopes and increasing their reach in three dimensions: through robotic assembly, wireless technology, and miniature optics. A new class of endoscopy, namely, WCE, is emerging.

It was in the earlier part of the last decade when the WCEs were introduced (Pillcam, Given Imaging Ltd.), which leveraged the advances in telemetry, miniature optics, and microelectronics. These achievements are responsible for a paradigm shift in visualization of the GI tract for clinical diagnosis. Currently, WCEs are approved by the FDA for the diagnosis of Crohn's disease, intestinal bleeding, and inflammatory bowel syndrome. Due to the size and less invasive functionality when compared to conventional endoscopes, patients are far more receptive to undergo a WCE procedure. Nonetheless, WCEs come with major disadvantages over conventional endoscopes because of their passive nature.

Currently available WCEs cannot be controlled or conduct a biopsy, and targeting specific areas of interest inside the GI tract is close to impossible. Consequently, the results of the WCE's operation as it moves along the GI tract are images acquired at random locations and orientations. These images are wirelessly transmitted to a recorder worn by the patient around the waist or are saved onto a chip inside the WCE and then uploaded to a computer once removed from the GI tract. Once acquired, these images aid in the development of a coarse medical diagnosis. In the past decade, considerable research has been conducted toward resolving some of the fundamental challenges associated with WCE. Designing a swallowable device that can replace conventional endoscopes is a challenging task and requires an interdisciplinary research approach with a focus on finding solutions for the following key functionalities presented in Figure 11.2 (Toennies et al., 2010). Below we describe in some detail the two components where an ME composite could find application.

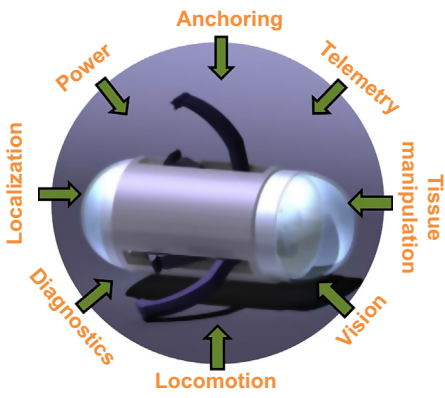

Figure 11.2 Key functionalities that complement the wireless capsule endoscopes.

11.1.1 ME composites for diagnostics and localization in WCE

Along with the vision system, additional sensors have the potential of being integrated into the device in order to acquire better information on the GI tract. Sensors, which will be able to provide information on the blood pressure, pH level, impedance, temperature, electrical conductivity, oxidation, etc., are viable. Hristoforou and Ktena explained the efficacy of ME materials for sensing applications (Hristoforou & Ktena, 2007). They have attributed that a large strain can be realized in magnetostrictive materials, and this is very useful when one wants to develop very sensitive stress sensors for precise determination of blood pressure, pH level, etc. A sandwich of piezoelectric and magnetostrictive layers or an ME composite that includes two phases can be developed to develop a system sensitive to surface stresses. Piezoelectric effect has been used to develop an arterial pressure wave sensor (Ghatak & Sur, 2005). Srinivasan has pointed out that ME composites are promising candidates for magnetic field and current sensors, energy harvesters, and miniature antennas for weak-signal detection (Srinivasan, 2010). More recently, Nan et al. developed a self-biased 215 MHz ME nanoelectromechanical systems (NEMS) resonator, which can be used to detect weak and DC magnetic fields (Nan, Hui, Rinaldi, & Sun, 2013). Marauska developed an ME microelectromechanical systems (MEMS)-based magnetic field sensor, which can detect biomagnetic signals for high spatial resolution and deep body region measurement (Marauska et al., 2013). The device offered ME coefficient of 2380 (V/m)/(A/m) with a corresponding sensitivity of 3800 V/T, which is effective for sensing a biomagnetic signal with low noise. MEMS manufacturing techniques provide the capability of developing such sensors on a small chip that can be integrated inside the capsule. It is also noteworthy to mention that optical biopsy has promising capabilities compared to the conventional biopsy of the colon that require $2-3\ mm^2$ tissue samples for diagnosis. It provides a more accurate, efficient, and low-cost approach to target biopsy of diseased tissue, thus reducing the number of required conventional biopsies and increasing the surveillance intervals (Wang & Van Dam, 2004; Toennies et al., 2010).

Current passive capsule endoscopes are equipped with cameras that image the GI tract and provide reliable diagnosis in a minimally invasive way. However, because clinicians have no control over the position and orientation of the capsules, there is a chance of missed diagnosis. Allowing the clinician to stop, move, and orient the capsule on demand would improve diagnostic capabilities by letting them take a closer look or backtrack to reexamine a region of interest. Furthermore, once reliable control is obtained to enhance the capabilities of the device, the capsule can be equipped with tools for performing tissue biopsy or for cleaning wound sites for drug deliveries. In some scenarios, it can be actively deformed in an axial direction using external magnetic actuation, which provides an extra degree of freedom that enables various advanced functions, such as axial position control, drug release, drug injection, or biopsy.

Inside the GI tract, the capsule travels from the esophagus through the stomach to the small and large intestines. As seen from the PillCam capabilities, images of the tract can be obtained via the integrated camera; however, the exact location of the capsule inside the body remains a mystery. In order to be able to locate where the images of specific lesions are taken, an accurate tracking of the robotic capsule is

required. This will improve the accuracy of the diagnosis, and it will be able to use this location as a reference for future treatments. So far, four methods of tracking the capsule have been explored: RF triangulation, magnetic tracking, computer vision, and ultrasound (Tortora, Toennies, Simi, Valdastri, & Webster, 2009). For the RF triangulation and magnetic triangulation, an array of sensors outside the body is used to measure the signal coming from the capsule. Using magnetic theory for the latter one and a permanent magnet inside the capsule, an estimate of the location of the capsule can be found. An estimate, instead of exact location, can be obtained because the signals from the body go through different mediums. Therefore, delays in acquiring the data occur. RF signals do not propagate efficiently through a water environment, and, due to the fact that the body is 65% water, RF is not the most accurate localization approach. Ultrasonic pulses emitted outside the body and echoed from the capsule can also present a way of tracking the capsule along with tracking of the radioactive material placed inside the capsule, which will emit signals that are strong enough to be detected using radiation cameras, but weak enough to avoid adverse effect to the patient's health (Tortora et al., 2009).

There are two practical methods that can be proposed for tracking the capsule inside the GI tract. One of these localization methods consists of two parts. A permanent magnet is placed inside the wireless capsule, which is located at *x, y, z* location inside the human GI tract with respect to a reference frame. Since the permanent magnet emits a magnetic field, it can be identified using a magnetic sensor, such as the 3-axis magnetic sensor that can approach nanotesla sensitivity. This array of magnetic sensors can be integrated on a vest, which the patient can wear while the endoscopic procedure is underway. An external power supply can be used to power the magnetic detection sensors and can be integrated with the vest. In the case of magnetic sensors, the power is only required for the conditioning electronics, as the sensors themselves are passive. Once the signal is detected, it is amplified, ran through a control circuit, and the data are acquired. Using a triangulation algorithm, an accurate positioning and orientation of the magnet, that is, the capsule, can be obtained. This approach has not yet been tested, but it is expected to provide an *estimated* visual representation of the movement of the capsule inside the digestive tract. Before the diagnosis begins, a scan of the human body can be obtained using any regular high-resolution technique, such as MRI. This will provide the information of the size and shape of the digestive tract specific to the patient's body. This image file will also provide three dimensional (3-D) representation of the GI tract. Combining the 3-D image with the data acquired from the magnetic sensor, a virtual graphical representation of the capsule moving through the patient's body can be created.

Multiferroic ME transducers are promising for providing the position feedback through their use in developing enhanced sensitivity magnetic field sensors. ME materials have coexistence of ferroelectric and ferromagnetic order, which makes them attractive for magnetic field sensors (Nan, Bichurin, Dong, Viehland, & Srinivasan, 2008; Spaldin & Fiebig, 2005). The magnetostrictive and piezoelectric phases can be combined in many ways, as shown in Figure 11.3, to develop miniature magnetic field sensing components. The ME coefficient can be tuned by controlling the phase connectivity (Priya & Inman, 2009). There has been significant progress in this area, and giant ME constants for both bulk and thick film structures have been

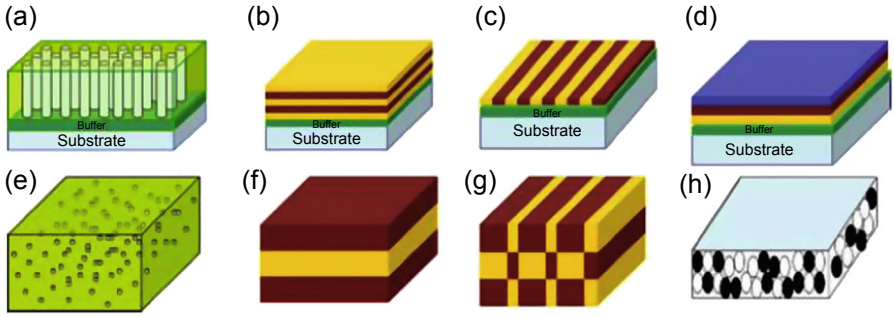

Figure 11.3 Schematic of the magnetoelectric composites, illustrating the multiple possibilities for two-phase connectivity: (a) self-assembled nanopillar structures, (b) layer-by-layer deposition, (c) deposition accompanied by masking and patterning, (d) three-phase depositions for gradient materials, (e) particles dispersed in a polymer matrix, (f) lamination, (g) checkerboard arrangement, and (h) sintered particulates.
Adopted from Priya and Inman (2009).

reported, which indicates the possibility of designing miniature sensors (Cho & Priya, 2011; Dussan, Kumar, Katiyar, Priya, & Scott, 2011; Park, Cho, Ali Arat, Evey, & Priya, 2010).

Recently, synthesis and characterization of ME 3-2 nanocomposite thick films using aerosol-deposition (AD) has been reported (Park et al., 2009). Piezoelectric and magnetostrictive materials were simultaneously deposited on a platinized silicon substrate using an AD method, and a 13 μm-thick nanocomposite film was realized with repeatable nozzle scanning. Upon annealing, the magnetostrictive phase was found to form a layered structure inside the piezoelectric matrix. This nanocomposite thick film was found to exhibit the ME coefficient of the order of 150 mV/cm/Oe, which is significantly higher in comparison to the other results reported in literature on ME thin/thick films. For WCE, the localization sensor structure could consist of two cantilever beams, one at each end of the capsule. Mechanical oscillations in the beam are introduced due to an applied external magnetic field. These oscillations will result in proportional voltage generation. The generated voltage will switch the transmitter built on the control circuit. The differential switching of the transmitter will provide the location of the two cantilever beams and thus the position of the cantilever. Stray magnetic fields that are generated by AC devices and propagate through earth, concrete, and most metals, including lead, can be a source of noise. However, the differential switching algorithm easily accommodates for the stray magnetic fields, as it requires that both the cantilevers activate the transmitter in a synchronized interval. Signal resolution at subhertz frequencies is often limited by low-frequency noise with a power spectrum that varies inversely with frequency, namely 1/f noise. Signal fluctuations are further accompanied by Johnson voltage noise $\sqrt{S_{v,J}} = \sqrt{(4k_B TR)}$, where k_B is the Boltzmann constant, R is the device resistance, and T is the temperature. Thus, the utilization of high frequency (close to resonance of the cantilever structure) for signal detection will be required to reduce the noise factor. The constant temperature of the body will reduce the baseline Johnson noise.

11.1.2 Power harvesting

Power is one of the limiting factors of the WCE. Current designs, such as the PillCam and the Olympus wireless capsules, use watch batteries with 3 V at 55 mA-h and can deliver 20 mW of power. Other researchers have used lithium metal oxide battery TLM-1030, which can provide enough power to supply energy to both DC brushless motors of 430 mW and the real-time vision system, which requires 180 mW. With this battery, the locomotion system of capsules can complete a 30 min colon transit (Dittrich, 2011). To reduce power consumption, the design of the WCE can be in such way that the actuators can be activated only at the area of interest. Besides having an on and off switch, alternative solutions, such as wireless power transmission and energy harvesting, can be established. Wireless power transmission can be created using inductive coupling (Carta & Puers, unpublished), where power can be derived from a magnetic field established by an external solenoid coil. The system employs a set of orthogonal ferrite coils embedded in the capsule and an external unit driven by a class E amplifier. A low-power energy harvesting system can harvest several milliwatts from an external low-frequency magnetic field. Mechanical vibrations (300 $\mu W/cm^3$) are an attractive power source at small scale (Roundy et al., 2005; Roundy, Wright, & Rabaey, 2003; Starner & Paradiso, 2004). Thus, if one can generate mechanical vibrations in the diaphragm-type structure built inside the capsule by applying a magnetic field from outside the body, then the power problem can be reduced. Stray magnetic fields that are generated by AC devices and propagate through earth, concrete, and most metals can also be a source of electrical energy. The actual AC magnetic field strengths encountered within a given commercial building typically range from under 0.2 mG in open areas to several hundred near electrical equipment. These fields could be harvested through the ME MEMS structure. The biggest advantage of these materials is that even if there are no mechanical vibration in the surroundings, one can create them by applying the AC magnetic field externally. Thus, power can be generated on demand as required for recharging the battery or supercapacitor.

Li et al. have studied rotation energy harvester composed of an ME transducer, a cantilever, and a magnetic circuit (Li, Wen, Li, Yang, & Dai, 2011). Their proposed structure is shown in Figure 11.4. The ME transducer consisted of one Lead-Zirconium-Titanate (PZT) layer sandwiched between the two Terfenol-D layers. The ME transducer is situated in the air gap of the magnetic circuit, and it induces the magnetic field when the magnetic circuit moves relative to the transducer. The magnetostrictive layer generates stress due to the variation of the magnetic field, which is transmitted to the piezoelectric layer and converted into electrical charge. The piezoelectric layer in this design was polarized in the thickness direction, and the magnetostrictive layers were magnetized along the longitudinal direction (Radousky & Liang, 2012).

The need for power harvesters within WCE is important to address the lifetime of the device (Onuta, Wang, Long, & Takeuchi, 2011). ME bulk laminates have been shown to effectively harvest the power at room temperature with high sensitivity (Dong, Zhai, Li, Viehland, & Priya, 2008; Finkel, Lofland, & Garrity, 2009;

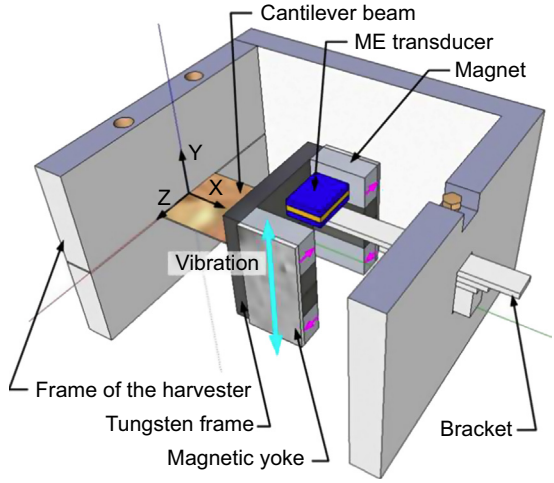

Figure 11.4 Schematic of ME transducer-based energy harvester. Reprinted with permission from Li et al. (2011), © 2011, Elsevier.

O'Handley, Huang, Bono, & Simon, 2008). However, these ME energy harvesters were at cm or mm-scale and thus not directly suitable for embedding into the wireless capsules. Recently, Onuta et al. demonstrated an MEMS-based ME energy harvester, where thin films of PZT and $Fe_{0.7}Ga_{0.3}$ were deposited on Si-micromachined cantilevers. Figure 11.5 shows the scanning electron microscope image of their structure. This device was shown to provide high ME coefficient (33.6 V/cm Oe) and Q-factor (~2000), and thus contributes toward high power density which can be obtained at resonance, which is quite favorable for energy harvesting purposes. Interestingly, this device can also operate at zero DC magnetic bias. Therefore, it can remove the necessity of extra DC bias, reducing the complexity in circuit design. However, to meet the power requirements of WCE within the constraints of size and shape, further work is required.

The existing body of work on low frequency mm-scale structure has not been able to simultaneously achieve high power density under the following environmental constraints: namely, low frequency (<50 Hz), broadband with low Q factor, less internal damping, and moderate operating amplitude (<0.1 g operation). Recently, 2-D complex MEMS structures have been proposed, as shown in Figure 11.6, to address some of the above-mentioned constraints. The main advantage lies in their inherently low natural resonance frequency. By examining the available low frequency geometries and investigating more the complicated configurations, one can tune the resonance frequency of the harvester to the magnetic field frequencies in the operation environment (~60 Hz). This frequency is much lower than the localization sensor working frequency, and so there will be negligible influence on its operation. In order to achieve a high magnitude of electromechanical coefficients, textured films are required. Synthesis of textured composite films can proceed

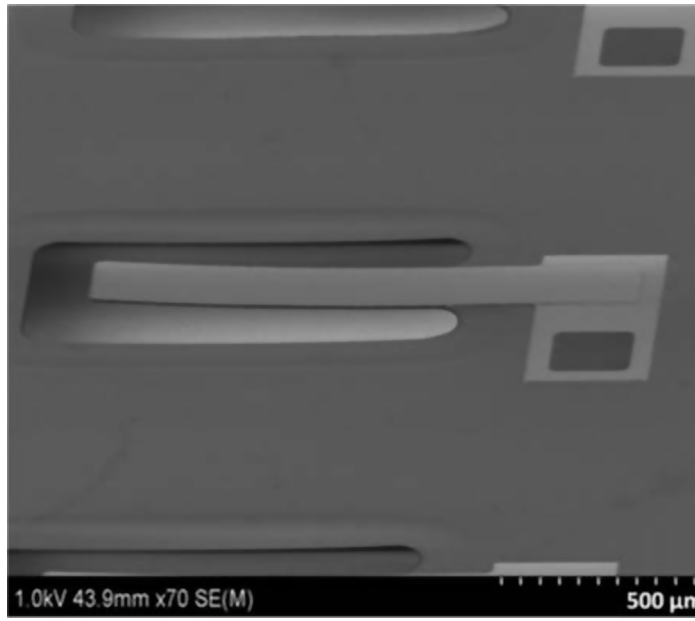

Figure 11.5 A scanning electron micrograph of ME MEMS-based energy harvester. The device is a 950-µm long and 200-µm wide released cantilever.
Reprinted with permission from Onuta et al. (2011), © 2011, AIP Publishing LLC.

in different forms: thick film heterostructures by seeded inkdeposition using micron size single crystals, layer-by-layer deposition of graded materials, and continuous film growth. These techniques need to be explored and compared against each other to identify the suitable path forward.

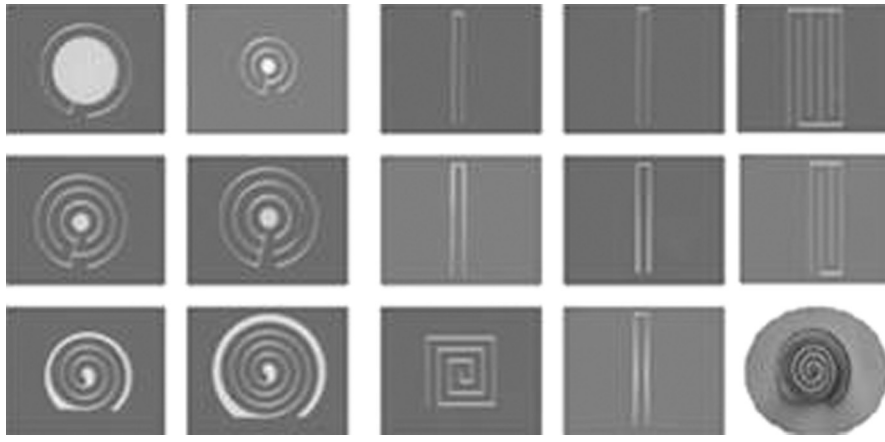

Figure 11.6 Example of low frequency energy harvesting structures fabricated on platinized silicon substrate.

11.2 Application of ME composites for noninvasive brain imaging

In the design of brain–machine interfaces, there is growing interest in developing methods that utilize the human biology to control the physical system as naturally as a human controls a limb. Such higher level of control has been pursued by obtaining signals directly from a user's muscles using electromyography (EMG). This method involves using a series of electrodes that observe electric membrane potentials created in a human's muscles during contraction, which in turn allows for direct observation of a subject's muscle contraction, typically for experiments involving biomechanics (Soderberg & Cook, 1984). EMG can come in two forms, surface and intramuscular. In surface EMG, leads are placed onto the surface of a subject's skin, just above the muscle being observed. This typically works better with larger muscles, as it is very susceptible to cross talk, which is where action potentials in other muscles interfere with the expected signal. Another option is intramuscular EMG, where small gold wires are surgically attached directly to the muscle fibers. This method, while slightly invasive, allows for excellent readings from muscles with limited cross talk. Using leads attached into an amputee's forearm or pectoral, an amputee can learn to control various upper limb positions using slight muscle activations and movements (Englehart & Hudgins, 2003). Recent research in neurology shows that the brain, which is the core part of the central nervous system, is one of the most complicated and powerful tools in the human body. It is contained in the cranial cavity of the skull and is responsible for both lower order as well as higher order functions of the human body. It is composed of multiple independent parts, each of which have a unique function (Scarabino & Salvolini, 2003). Different parts of the human brain are described below and are shown in Figure 11.7. A brief description for these parts is provided below for easy understanding of the readers.

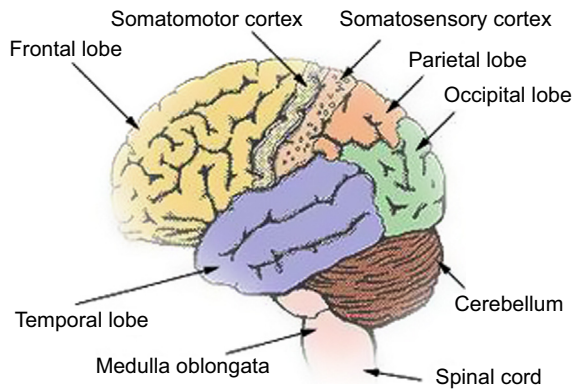

Figure 11.7 Locations of various brain functions. Of interest for BCI is the somatomotor cortex, also called the motor cortex, which controls the majority of muscle movement.
Image © 2013 National Cancer Institute.

Cerebrum: The cerebrum is the largest and most highly developed part of the brain. It is the uppermost, anterior part of the brain and consists of the left and right hemispheres. These two hemispheres are almost mirror images of each other and are connected through a deep bridge of nerve fibers known as the corpus callosum. Using nerve fibers, the corpus callosum works as a communication system between the two hemispheres and different organs of the body. The cerebrum (both right and left hemispheres) is divided into four sections: the frontal lobe, parietal lobe, temporal lobe, and the occipital lobe. These lobes have specific functions in the human body.

Frontal Lobe: The frontal lobe is one of the four lobes in the cerebrum hemisphere. It is the most anterior portion of the cerebrum and is superior to the eyes. This lobe consists of the somatomotor cortex, which is also known as the motor cortex. The motor cortex is the part that is responsible for the planning and implementation of the movements of different muscles. Additionally, this lobe also controls several elements, including creative thought, problem solving, intellect, judgment, behavior, attention, abstract thinking, physical reactions, smell, and personality.

Parietal Lobe: This lobe is located at the top of brain in the cerebrum hemisphere. This lobe consists of the somatosensory cortex, which functions similar to the motor cortex. It receives the information regarding the movement of various body parts through the spinal cord. Additionally, it also processes the sense of touch, including pressure, temperature, vibration, and texture. Visual functions, language, reading, and internal stimuli are also monitored in the parietal lobe.

Temporal Lobe: The temporal lobe is located at the inferior portion of the brain and is involved in controlling and processing visual and auditory memories. This lobe also contains a region called the hippocampus, which processes memory formation. It controls mood, thirst, hunger, and temperature. It also contains glands that control the hormonal processes throughout the body.

Occipital Lobe: The occipital lobe is located in the posterior portion of the brain and is involved in processing and controlling vision, recognizing, and identifying the visual world.

Cerebellum: The cerebellum is commonly known as the "little brain," and it is located at the inferior to the cerebrum and superior to the brainstem. The cerebellum controls essential body functions, such as balance, coordinating movements, and learning new motor tasks, allowing humans to move properly.

Brainstem: The brainstem is the part of the human brain that connects the rest of the brain with the spinal cord. It is composed of three parts: the midbrain, pons, and medulla, and controls basic life functions, such as heartbeat, blood pressure, swallowing, digestion, sleeping, walking, breathing, and sensory integration.

There have been attempts toward directly utilizing the user's brain to send, as well as receive, signals for a variety of electronic devices in a concept called Brain−Computer Interface (BCI). There are numerous purposes for BCI studies, such as neural prostheses for hearing (Gantz, Turner, Gfeller, & Lowder, 2005), seeing, and even for neuroprostheses (Velliste et al., 2008). Some BCIs have become a relatively common occurrence, such as in cochlear implants for certain hearing-impaired individuals.

To develop BCIs, first there must be a method to observe or quantify the brain signals in some capacity. This can be done both with invasive, as well as noninvasive

methods. Invasive methods involve cutting into the skull of a patient in order to implant a device, whether a net of electrodes or a small chip, to take readings directly from brain tissue. These methods, while notably difficult as well as potentially dangerous, offer some of the best data in terms of both spatial and temporal resolution. In comparison to the invasive techniques where one needs cuts and operations, noninvasive methods do not require any surgery.

11.2.1 Noninvasive BCI methods

As early as the nineteenth century, scientists have observed a correlation between the brain activity and electrical signals that are observable from the scalp of a subject. In 1924, Hans Berger took some of the first electrical signals from a human subject to observe brain activity (Haas, 2003). These early studies led to the establishment of electroencephalography (EEG). EEG is a noninvasive technique that uses small electrodes planted directly in the scalp of a subject; any fluctuations in the electrical activity of the brain are relayed through the surface of the subject's skin, as shown in Figure 11.8. In typical clinical applications, 21 electrodes, including ground and reference, are attached to a patient's scalp according to a standardized 10−20 system. Clinically, this system has applications for determining brain death, characterizing seizures, and monitoring brain activity for patients in comas, either induced or noninduced. Compared to other options for observing brain signals, EEG is relatively inexpensive, does not require a large amount of additional technology to maintain the

Figure 11.8 Subject with high-density EEG electrode array cap.
Image © Flinders University.

system, such as coolants or power, and has good temporal resolution. On the other hand, the data have a poor signal to noise ratio, as well as poor spatial resolution. In addition to these issues, EEG can only record surface brain signals, while deeper brain signals come with significant noise (Wolpaw et al., 2002).

The mechanics for observing brain signals based on electrical pulses created by brain activity can be measured by another method called magnetoencephalography (MEG). This method measures electrical signals produced within the brain, but unlike EEG, MEG observes brain activity by observing the changes in magnetic fields due to electric currents on the order of 10 fTesla. This method has both excellent temporal and spatial resolution for surface brain signals, allowing for revelation of high details of brain function (Cohen & Halgren, 2004). Because magnetic fields decay exponentially with distance, this method only works for brain activity close to the skull, as other signals cannot be observed. However, this method is very sensitive to external noise and must be performed in a controlled room with strong magnetic shielding, while the subject must remain absolutely immobile (Vrba & Robinson, 2001), as shown in Figure 11.9. Also, because the magnetic field produced by brain activity is so small,

Figure 11.9 A subject using an MEG interface. Note the large device size and cooling necessary to use this method.
Image © 2009 National Institute of Mental Health.

the Superconducting Quantum Interference Device (SQUID) sensors require significant cooling, needing a vacuum tube of liquid helium to obtain suitable cooling (Vrba & Robinson, 2001). Another important issue is that MEG sensing is subject to an inverse problem, which states that any given series of signals can have an infinite number of possible solutions for their source and magnitude within the brain. Even with a sizable array of sensors along a subject's brain, the sensors cannot fully determine the exact location and strength of each magnetic signal. For example, a single reading from a sensor could suggest a near source with a weak field or a further source with a strong field, which would be virtually indistinguishable between one another without a planned theoretical model (Uutela, Hamalainen, & Somersalo, 1999).

Another method to recording brain activity is using functional MRI. This method uses a high-power magnet on the order of 1 T to obtain detailed imagery of the brain itself by magnetizing a subject's brain tissue. A gradient field is applied to the tissue and subsequently removed. The magnetized tissue releases energy that can be observed and used to construct images. Different tissues are magnetized differently, which allows doctors to distinguish between different types of tissue and structures. This can be applied to arterial and venous blood flow due to the differences in the blood oxygenation levels. Arterial blood is oxygen-rich blood that is used to resupply oxygen in tissues, while venous blood is deoxygenated after having been used within tissues. This fundamental difference of oxygenated versus deoxygenated fluid allows functional magnetic resonance imaging (fMRI) to observe venous and arterial blood separately; de-oxygenated blood is more magnetic than oxygenated blood, allowing technicians to make distinctions between the two flows. As neurons are active, the tissue sees an influx of arterial blood, which is observable as a change of flow rate (Logothetis et al., 2001). The primary drawbacks of this method is that there is very low temporal resolution due to the physiology that is being observed, and it is phenomenally expensive, costing in the order of millions of dollars. Additionally, because this method uses powerful magnets, users should not have any metal objects, which includes metal implants such as pacemakers, catheters, or joint pins or replacements (Lebedev & Nicolelis, 2006).

ME sensors have the promise of performing all of the biomagnetic measurements analogous to that of MEG and fMRI. The advantages include operation at room temperature with no additional cooling, thereby greatly reducing the size of the device (Jahns et al., unpublished). The ME coefficient (α) of a material is defined as the ratio of the polarization change in response to the change of the field ($\alpha = \Delta P/\Delta H$). In a ME composite, α is a measure of performance of the multiferroic composite and is also defined as a figure of merit. Presently, these sensors have a ME coefficient in the range of 450 V/cm Oe at a resonance frequency of 678.5 Hz (Jahns et al., unpublished). Research is currently focused on achieving the same sensitivity at lower frequencies.

To assist the development of ME sensors for the medical imaging and other platforms, characterization techniques, such as ME scanning probe microscopes, are being designed. Hattrick-Simpers et al. have demonstrated working of such a microscope (Hattrick-Simpers, Dai, Wuttig, Takeuchi, & Quandt, 2007). This prototype design was developed to work at room temperature using a laminated ME sensor. The ME

sensor used in this microscope was a simple trilayer longitudinal-transverse mode sensor, which was fabricated using Metglas and polyvinylidene fluoride as the magnetostrictive layer and piezoelectric layer, respectively. The ME sensor used in the microscope demonstrated an AC field sensitivity of 467 μV/Oe in the measured frequency range of 0.2−8 kHz. The microscope displayed a successful functioning in imaging of a 2-mm diameter ring carrying an AC current as low as 10^{-5} A, and AC fields of magnitude of 3×10^{-10} T. This technique is still in the laboratory development stage and is limited to nonbiological tissues imaging.

Jahns et al. have explored the possibility of a thin films-based ME detector, which demonstrated a sensitivity value of 5.4 pT/√Hz at a resonance frequency of 330 Hz (Jahns, Greve, Woltermann, Quandt, & Knochel, 2011). This particular thin film ME sensor was designed for operation under longitudinal magnetization and transversal polarization (L-T) mode. The schematic of this sensor is shown in Figure 11.10. Since the sensor has a capacitor-like structure, the output voltage (V_{ME}) of such a sensor can be given as

$$V_{ME} = \alpha_{ME} \cdot \Delta H_{ac} \cdot T$$

where α_{ME}, H_{ac}, and T are ME coefficient, applied AC field, and thickness of the sensor. It consisted of a 20×3 mm^2 silicon cantilever, which was 625 μm thick. The Si cantilever used in the sensor was coated with a 0.3 μm thick molybdenum layer as a bottom electrode and a 1.8 μm thick piezoelectric aluminum nitride layer on the top. A 1.75 μm thick and 1.6×10^{-5} m^2 layer of FeCoBSi served as the magnetostrictive top electrode layer. In order to reduce the resonance frequency of the bending beam, a 7 mm broad trench was designed by standard etching techniques (Greve et al., 2010). However, biomagnetic measurements require a higher sensitivity over a wide frequency band of 0.1−100 Hz (Jahns, Greve, Woltermann, Quandt, & Knöchel, 2012). Work on transitioning the sensor into a practical design with sufficient sensitivity for biomagnetic measurements, such as magnetoencephalography and magnetocardiography at room temperature, is being conducted by various research laboratories around the world. In order to enhance the ME coupling and hence performance of these cantilever-type sensors, new materials and device designs are being explored.

With the development of new ME materials, new concepts are emerging to operate these sensors at room temperature with a limited requirement of additional circuitry and external field. In this regards, development of exchanged bias ME sensors is

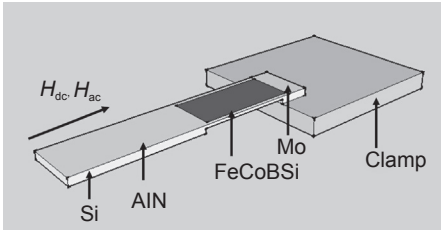

Figure 11.10 Structure of an L-T mode magnetoelectric sensor.
Adopted from Jahns et al. (2011).

evolving. Since in thin film ME composite sensors, both magnetic and piezoelectric parts are mutually mechanically coupled, tuning the high response one will always need external bias, which is a complication. This issue was addressed by using antiferromagnetic−ferromagnetic exchange coupling (Jahns et al., 2013; Lage et al., 2012; Lage, Woltering, Quandt, & Meyners, 2013). Internally biased sensors were fabricated to show an anisotropic sensitivity, which later was used to identify the orientation of AC magnetic fields. This approach was successfully implemented for the detection of a 2-D magnetic vector field. To fabricate the self-biased ME sensors, a magnetostrictive layer was fabricated on a piezoelectric cantilever, as shown in Figure 11.11. The magnetostrictive layer, consisting a multilayer stack of 5 nm Ta/3 nm Cu/8 nm $Mn_{70}Ir_{30}$/100 nm $Fe_{70.2}Co_{7.8}Si_{12}B_{10}$, was coated on a piezoelectric cantilever. The final stack was capped with Ta layer. The total thickness of the stack was 1 μm by repeating the stack 10 times. A unidirectional anisotropy was induced using a filed cooling procedure. A unidirectional anisotropy was induced using a field cooling procedure, which manifests to a unidirectional anisotropy with an angle of 45° with respect to the long cantilever axis, as shown in Figure 11.8(a) (Jahns et al., 2013). This anisotropy eliminates the need of external DC bias field. This is demonstrated in Figure 11.8(b), where ME voltage is plotted as a function of applied DC magnetic field. An AC excitation field of 10 μT with a frequency of 365 Hz, which matches to the mechanical resonance, was employed paralleled on a varying DC field (Jahns et al.,

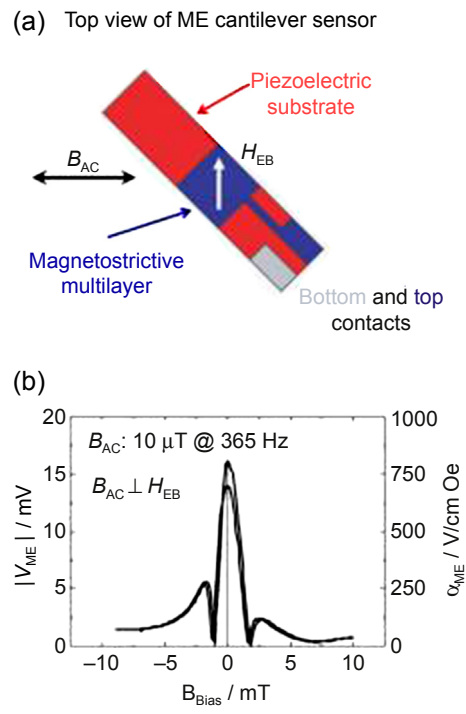

Figure 11.11 (a) Schematic of a self-biased ME sensor. (b) Corresponding ME voltage response of the self-biased sensor. Reprinted with permission from Jahns et al. (2013), © 2013, John Wiley and Sons.

2013). Due to the integrated magnetic self-bias, the maximum response was observed at zero field and corresponds to a ME coefficient of 800 V/cm·Oe. Still much work is required on improving the materials, reducing the impact of electrodes (Jahns et al., 2013), and canceling the noise.

11.2.2 Invasive methods

Another option to obtain brain signals is to implant electrodes directly into a patient's brain. This option, while notably dangerous due to necessitating brain surgery in order to implant the device into a patient's brain, offers unparalleled spatial resolution, as the device is placed close to the signal and has little noise. One of these methods is called electrocorticography (ECoG), which operates using the same concept as EEG, using a series of electrodes in an array attached just below the dura mater to read action potentials between various points of the brain without interference from the scalp and skull, as shown in Figure 11.12. To place this array, a craniotomy is necessary, where doctors remove a portion of the patient's skull to implant the electrode array to the surface of the cortex. This method is considered one of the prime options for evaluating severe epilepsy patients' conditions in preparation for surgery, due to the high signal to noise ratio, along with high temporal resolution (Kuruvilla & Flink, 2003). However, this method is only employed in human patients in preparation for surgery, due to the need to perform a craniotomy for the surgery. This method has been employed on rats (O'Keefe & Dostrovsky, 1971), as well as primates for BCI studies. In one prime example, monkeys with an ECoG interface were given control of a robotic hand to obtain some desired treats with a joystick. However, after some time, the monkeys

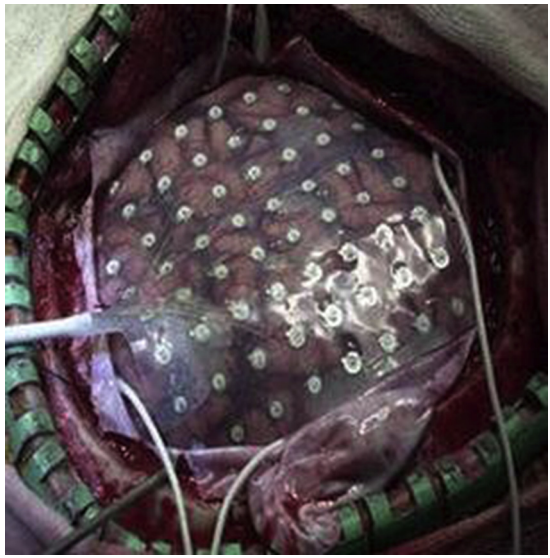

Figure 11.12 Electrocorticography array attached to a skull of a patient prior to surgery.
Image © 2011 Futurepredictions.com.

began to learn the act of wishing to control the hand was sufficient to obtain the treats, producing a full BCI (Velliste, Perel, Spalding, Whitford, & Schwartz, 2008).

A far more invasive method that offers unparalleled spatial and temporal resolution is implanting microelectrodes directly into the brain of a subject. Compared to ECoG, this method is significantly more invasive, as the process involves penetrating the subject's gray matter with small electrodes, which can observe electric signals directly at the source, allowing incredible spatial resolution, such as observing the activity of a single neuron (Quiroga et al., 2005). Depending on the desired task, the electrode array is placed into the appropriate portion of the brain, which in the case of neuroprosthesis would be the motor cortex. In some of the more recent research, it has been applied to patients with locked-in syndrome, where the patient has little or no motor function below the neck, making simple tasks such as drinking or eating all but impossible without assistance from a caretaker, despite the patient having full cognitive awareness. In several studies from Brown, using one of these electrodes implanted into the head of several human trials, subjects have been able to successfully control, with multiple degrees of freedom, robotic hands mounted to their wheelchairs to accomplish simple tasks (Hochber et al., 2006). However, because this method requires surgical procedures, it is considered as a last option. Numerous concerns exist, between complications during surgery, chip deterioration, or further complications due to a lack of human testing. Thus, this option is limited to all but patients with very severe disabilities, such as those with tetraplegia. Table 11.1 lists advantages and disadvantages of various BCI methods.

Table 11.1 Table of advantages and disadvantages of various BCI methods

Method	Created	Advantages	Disadvantages
EEG	1924	Good temporal resolution, inexpensive	Poor spatial resolution, only able to observe surface signals at noise threshold
MEG	1968	Good temporal and spatial resolution	Unable to read deep brain signals, inverse problem, subject must remain very still
fMRI	1990	Excellent spatial resolution, deep brain information	Low temporal resolution, large magnets needed, subject must remain very still
ECoG	1950	Good spatial resolution, good temporal resolution	Involves partially invasive surgery
Microelectrode array	1972	Excellent spatial and temporal resolution into deep brain signals	Requires intense brain surgery

11.2.3 Example demonstration of a brain-controlled robotic hand: a pathway toward brain-controlled machines

For control of a robotic hand, it is important to find a robust model of brain activity. To simplify the controls, in this example, the user will be using simple left and right hand activity in order to clearly draw a distinction between the two different states. Because the left and right hand are controlled by two different sides of the brain, this will allow for a very clear distinction between either the left or right brain activation, which, in turn, will allow for early phase control of the robotic hand. Preliminary experiments were performed at Virginia Tech—Carillion Research Institute in order to achieve the left and right brain activation along with left and right hand usage. To develop a mathematical model, the subject was given cues from within the fMRI to press some kind of controller with either their left or right hand, while the blood flow in the subject's brain was observed. To obtain the necessary data, a subject was placed within the fMRI with no metal. The person was laid on a table with a magnetic coil around their face to achieve higher resolution images of the brain, as shown in Figure 11.13. Due to the loud noises of the active scanner, the subject wore ear protection for the full duration of the test. The subject was also given two fiber optic button boxes, one for each hand, which can be used to transmit button press information without using metal wires. The room was then pressure sealed, while the controls operators worked in an adjoining room that was magnetically shielded. The fMRI operators could then speak to the subject in order to give directions through speakers in the room and also hear the subject through pressure microphones.

The subject then uses a mirror placed on the head apparatus to view a computer screen that is projected onto the back of the fMRI, allowing the subject to view visual cues for the experiment, as well as view the evoked potentials they are projecting to better track their progress. Once the user is fully situated, a 5 min long scan takes place to obtain a high-resolution image of the subject's brain (Figure 11.14), giving

Figure 11.13 A subject being prepared for fMRI readings. Pictures for this must be taken from a distance to prevent the magnetic field from destroying the camera.

Figure 11.14 High-resolution image of the subject's brain.

a resolution of about 1 mm^3 of the user's brain in a series of slices, which is used to overlay the lower resolution blood flow images. Once this is complete, the subject begins conditioning the brain to respond to set stimuli paired with specific motor function, as shown in Figure 11.15. In this case, the subject will be cued to press the buttons in either the left or right hand, which will allow for the Python program to build a model to correlate which portions of the brain are activating. Figure 11.16 shows a subject's brain, specifically blood flow during a gripping action of the right hand.

Once a suitable model has been built, the robotic hand can be controlled using evoked potentials. To build a robust model, the subject is still given the same cues and continues to press the same buttons. However, the buttons no longer have any link to the computer, and the end result for robotic hand control is the user's brain. The user receives the same cues as before, being told to press either the left or right

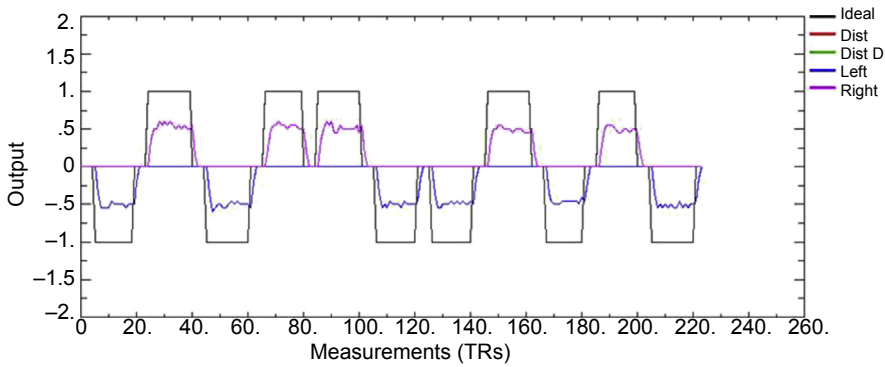

Figure 11.15 Plot showing the training phase of the experiment. The black lines indicate the ideal response, while the blue lines indicate left hand button presses and pink shows right hand button presses.

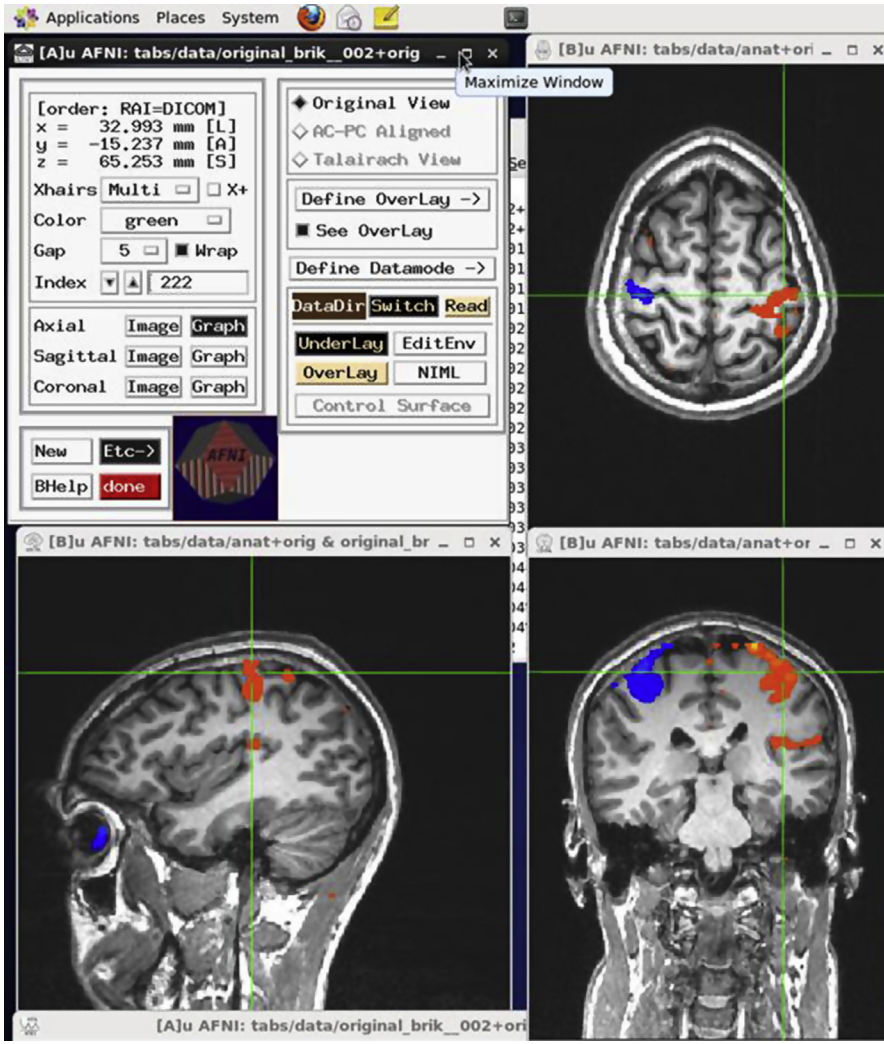

Figure 11.16 Image showing a subject's brain, specifically blood flow during a gripping action of the right hand.

buttons, though now a slider bar shows the results of the brain activity, sliding further to the left for highly negative values and to the right for highly positive values. This can be seen in Figure 11.17, which plots the expected values in red against the actual values in black. A camera feed of the robotic hand is also shown to the user, which allows the subject to confirm that the robotic hand is giving the appropriate response.

The results are as expected, showing consistent activation for the contralateral motor cortex for activity with each hand, allowing for successful control of the robotic hand using evoked potentials. However, the expected delay was also present, creating a 2 s delay between the changes of state for the robotic hand control following a change

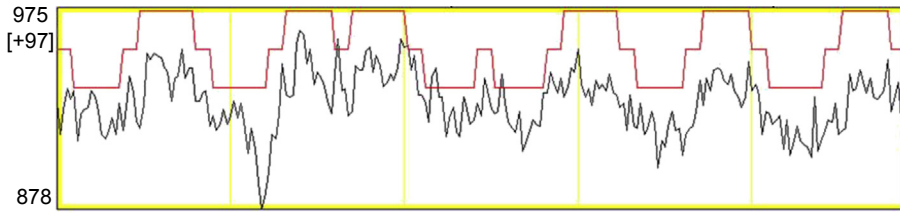

Figure 11.17 Ideal and actual brain response over time. Red shows the ideal response, while black shows the actual response.

of cues to the subject. Despite this, the created model was sufficient to control a robotic hand. While there is a general trend of the evoked potential following the ideal response, there was significant noise in the signal compared to an ideal response. This is indicative of the subject being a novice with BCIs, and would be expected to improve with additional training. This method was effective, but it is important to acknowledge that using fMRI as an industry standard of BCI work is not feasible. In particular, any BCI subject must remain very still during testing. Significant movement will cause data to become skewed, as the brain will shift relative to the expected model, causing blood flow in other sections of the brain to be incorrectly attributed to the trained model. Furthermore, it takes at least 2 s for a subject's blood flow to indicate a noticeable evoked potential, which would make a control system relying entirely around fMRI input very ineffective. Regardless of the improvements in fMRI technology, this time delay cannot be improved, as the limitation is caused by the physiology of the action. However, a major benefit to using the fMRI is to further the understanding of the human brain, particularly with respect to learning the use of an external machine−brain interface. While proving that an operator can control a robotic hand using only their brain from an fMRI is commendable and appealing to a wide audience, this example only serves as a motivation to develop ME sensors that could allow a portable helmet-type device to replace the fMRI and achieve a better brain-controlled system (Lee, Ryu, Jolesz, Cho, & Yoo, 2009).

One of the most intriguing applications of the above example is finding more complex control algorithms to apply in tandem with brain control (for example, using a semiautonomous control system that allows the robotic arm to perform various tasks at the user's directions). With this system, a subject could even use an abstract idea in their head, rather than a direct motor cortex interpretation, to perform a variety of tasks. What is particularly exciting about this concept is how this methodology would mimic a human controlling their limbs through the peripheral nervous system. While the main control center for a human is the brain, a large amount of the tasks that are performed are hardwired into the peripheral nervous system. Take, for example, flipping a coin in the air. A human wants to do this task, and takes some time to learn to consistently flip the coin. However, once the task is trained, the majority of the task is known subconsciously through the peripheral nervous system. Small details of the task, such as sensory feedback of the coin's position, suitable muscle torques to accomplish desired joint velocity, and hand position during the follow through to catch the coin are all trained and then delegated to the peripheral nervous system. By

emulating this concept, a human operator could plan a desired task, while the robot will be preprogrammed with a variety of tasks. While the human operator builds up the brain potential to select a desired task, the robot could perform autonomously or wait for additional feedback from the user. This concept could also provide interesting insights on human-machine learning. For example, a human learning to perform a task in tandem with a machine that is also learning how to perform the task could provide an interesting dynamic for cooperative human-machine learning, as well as understanding the process for a subject to become familiar with BCI work. This research could be used to provide better machine-learning algorithms, as well as for developing methods for teaching and maintaining BCI skills.

11.3 MEs for minimally invasive surgery

Minimally invasive surgical techniques are widely performed in procedures due to the advantages of tiny incisions, fast recovery time, and less discomfort when compared to conventional surgery. During a minimally invasive procedure, through the aid of several small incisions in the skin, either a miniature camera or surgical tools will be inserted and passed through the human body to perform the surgery, including monitoring, microcutting, or repairing. Smart materials could play an important role toward minimally invasive surgical tools development. The most commonly investigated and practical surgical tools are based on smart materials, such as ionic polymer actuators (Aw & McDaid, 2014; Bahramzadeh & Shahinpoor, 2012), shape memory alloys (SMA) (Fischer, Vogel, Gruhagen, Brhel, & Kaiser, 2001; Machado & Savi, 2003), and piezoelectric materials (Labanca, Azzola, Vinci, & Rodella, 2008). Ionic polymer-based actuators, which have properties similar to that of human tissue and muscle, demonstrate potential toward replacing traditional robotic actuators in medical robotics applications, such as a surgical hand (Aw & McDaid, 2014). SMA take advantage of its shape memory effect and are widely used as fixation devices for osteotomies and self-expanding stents for blood vessels (Fischer et al., 2001; Machado & Savi, 2003). Ultrasonic vibrations that are caused by the piezoelectric effect have been used to cut tissues and bones in oral, maxillofacial, cranial, and spinal procedures (Labanca et al., 2008). The working mechanism is simple: the applied electrical voltage across certain piezoelectric ceramic or crystals cause oscillations. By manipulating the ultrasonic frequency of the devices, it is possible to have selective microcut toward hard or soft tissues without harming the other. For example, at a frequency of 25−29 kHz, only mineralized tissue can be cut, while neurovascular tissue and other soft tissue is cut at frequencies higher than 50 kHz (Labanca et al., 2008). Due to the controllable and high precision feature of a piezoelectric ultrasonic generator, this technique is favorable for minimal invasive surgical tools due to the minimum risk of damage toward surrounding soft tissues and important structures, such as nerves, vessels, and mucosa (Labanca et al., 2008).

However, these existing technologies of minimally invasive surgical tools have some drawbacks, including the need of high voltage for actuation, lack of tactile feedback information, and bulky size. Specifically, the lack of feedback in

conventional piezoelectric surgical tools provides another level of safety concerns, such as internal bleeding resulting from nicking of tissues. Thus, surgical tools made from self-sensing smart materials would provide great advances toward increasing safety in the surgery process and make surgical treatment accessible. In addressing these issues, a ME composite-based new surgical tool was proposed, as shown in Figure 11.18 (Sundaresan, Atulasimha, & Clarke, 2013). The surgical tool consists of a ME composite cantilever fixed to a catheter, which can be inserted into the human body, acting as a scraping tool. The ME cantilever includes at least one piezoelectric layer and one magnetostrictive layer, where either the electric or magnetic polarization can be induced under an external magnetic/electric field through ME coupling. By taking advantage of this ME coupling effect, several functionalities can be realized: (1) the ME cantilever "up and down" motion can be produced and manipulated (frequency and displacement) under an applied external magnetic field, acting as a remote-controlled microblade; (2) the magnetic field-induced displacement of the ME cantilever will create a corresponding electric signal through the piezoelectric layer and in return act as a feedback signal in regard to the status (frequency, displacement, strain, and so on) of the ME surgical tip; (3) with use of an additional ME segment at the end of the cantilever, damping of undesired vibrations and subsequent stabilization of the ME surgical tip can be achieved. These features not only provide an alternative method of microcutting in minimally invasive surgery, but also dramatically enhance the surgery safety by collecting feedbacks from the self-sensing ME element itself.

Generally, a good ME coupling coefficient is achieved in layered laminates with a symmetrical configuration operating under longitudinally magnetized and transverse polarized (L-T) mode, as shown in Figure 11.19(a) (Atulasimha & Sundaresan, 2009). However, in considering the ablation motion of the ME cantilever tip, an ME composite with asymmetric configuration (Figure 11.19b) is preferred for the following reasons: (1) the bending vibration motion of the structure is more favorable in mimicking the cutting action and (2) the relatively low resonance frequency of the bending vibration mode is more favorable for practical usage. The dynamic behavior of an applied magnetic field, tip displacement, and current output has been systematically investigated for the development of an ME cantilever (Clarke & Sundaresan, unpublished-a, unpublished-b).

Figure 11.19c illustrates a conceptual schematic of a ME surgical tip proposed by Sundaresan et al. (Atulasimha & Sundaresan, 2009). The ME surgical tip is attached on the catheter and produces the required displacement (cutting force) through an external magnetic field. The corresponding electrical signal created by the strain in the piezoelectric layer acts as a feedback to determine the displacement of the cutting tip, therefore providing precise positioning control. The self-sensing feature of this ME surgical tip is ideal for the ablation of arterial plaque, as schematically shown in Figure 11.19d. By modulating the external magnetic field, the ME surgical tip can be precisely maneuvered and cause a scraping action. Furthermore, the feedback signal from the piezoelectric layer can be used to operate the ME tip in closed loop. The use of a second ME composite to the cantilever end will dynamically stabilize the ME surgical tip. In summary, ME composites are highly suitable for designing self-sensing actuators

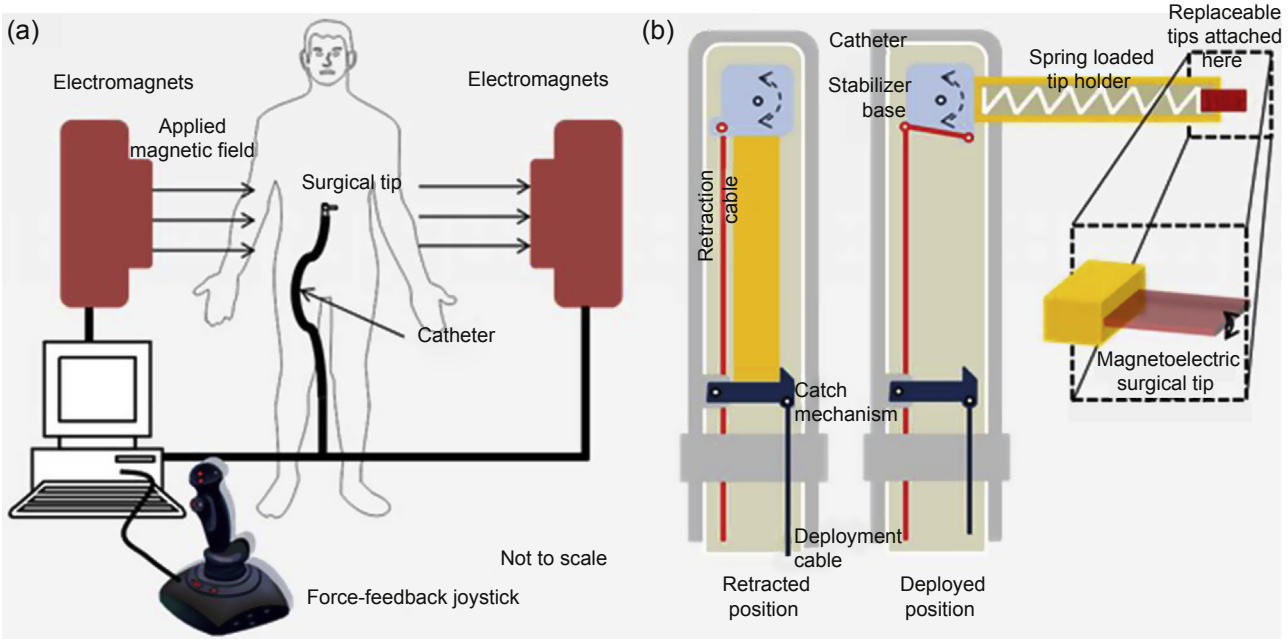

Figure 11.18 (a) Overview of the surgical system. (b) Surgical catheter with magnetoelectric cantilever cutting tip. Reprinted with permission from Sundaresan et al. (2013), © Vishnu Baba Sundaresan and Jatulasimha Atulasimha.

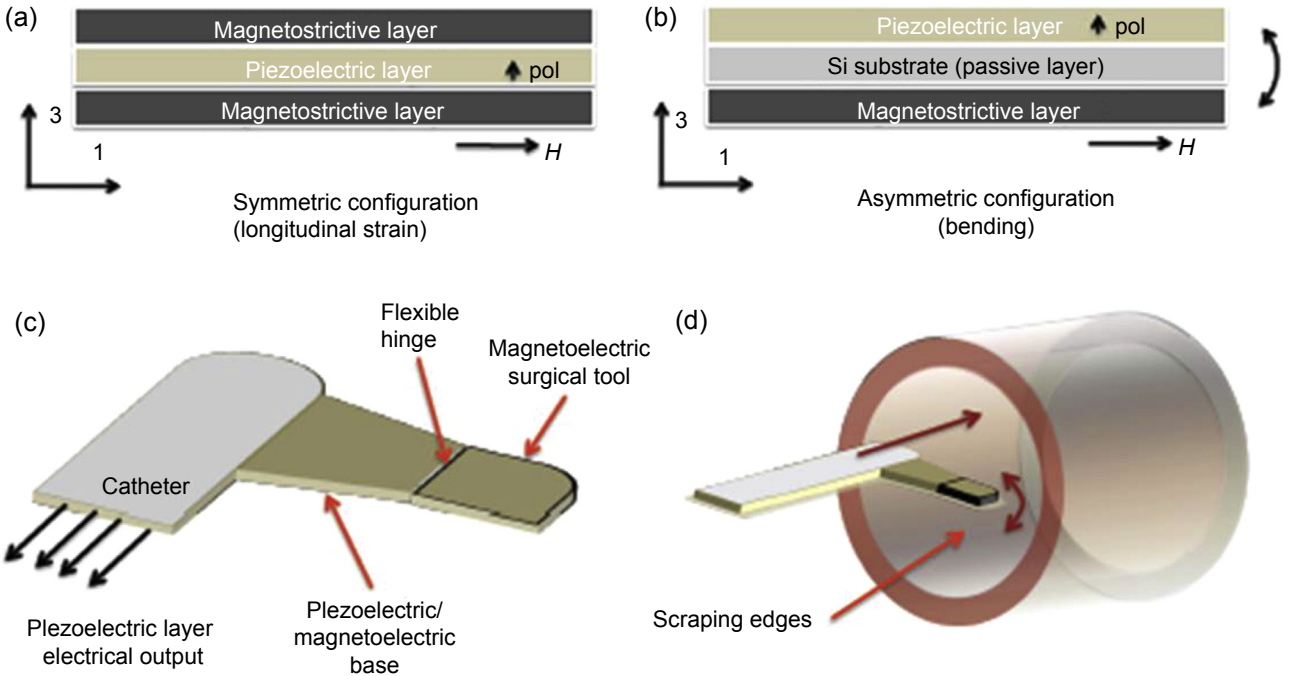

Figure 11.19 Schematic of the magnetoelectric (ME) composites in (a) symmetric and (b) asymmetric configuration; (c) schematic of the concept ME surgical tip; and (d) a concept for its application in an artery with plaque.
Adopted from Atulasimha and Sundaresan (2009), © 2009, ASME.

that can be used in a closed-loop system for precisely controlled surgical tools in minimally invasive surgery. Although it is only a conceptual design for the medical application, the current investigations of ME cantilever as a magnetic-field-induced actuator have been proven to have the potential for a small ablation tool (Clarke & Sundaresan, 2010, 2011).

Acknowledgments

The authors gratefully acknowledge the financial support from the Office of Basic Energy Science, Department of Energy (DOE), and Air Force Office of Scientific Research (AFOSR).

References

Atulasimha, J., & Sundaresan, V. B. (2009). ASME 2009 conference on smart materials, adaptive structures and intelligent systems. In *active materials, mechanics and behavior; modeling, simulation and control (SMASIS2009-1350)* (Vol. 1).

Aw, K. C., & McDaid, A. J. (2014). *Smart Materials and Structures, 23*(7), 074005.

Bahramzadeh, Y., & Shahinpoor, M. (2012). *Proc. SPIE 8340, Electroactive Polymer Acuators and Devices (EAPAD),* 834020.

Bonifield, J., & Cohen, E. (2012). CNN Health.

Carta, R., & Puers, R. Presented at the communications and vehicular technology in the Benelux (SCVT), 18th IEEE symposium on 2011, unpublished.

Chen, T., Wu, H. F., Shi, Q., Zhou, P. H., Chen, S. Y., Xu, M. D., et al. (2012). *Diseases of the Esophagus, 26*(8), 799.

Cho, K.-H., & Priya, S. (2011). *Applied Physics Letters, 98*(23).

Clarke, J., & Sundaresan, V. B. (2010), *Proc. SPIE 7644, Behavior and Mechanics of Multifunctional Materials and Composites,* 764413.

Clarke, J., & Sundaresan, V. B. (2011), *Proc. SPIE 7978, Behavior and Mechanics of Multifunctional Materials and Composites,* 79781A.

Cohen, D., & Halgren, E. (2004). *Encyclopedia of neuroscience*. Amsterdam: Elsevier.

Despot, E. J., & Fraser, C. (June 2012). *Best Practice & Research Clinical Gastroenterology, 26*(3), 279.

Dittrich T. (2011). http://mdtmag.com/Articles/2011/10/High-Powered-Medicine/

Dong, S., Zhai, J., Li, J. F., Viehland, D., & Priya, S. (2008). *Applied Physics Letters, 93*(10).

Dragan, A. (2014). *PhD thesis, "System Level Approach towards Intelligent Healthcare Enviroment"*. Virginia Tech.

Dussan, S., Kumar, A., Katiyar, R. S., Priya, S., & Scott, J. F. (2011). *Journal of Physics: Condensed Matter, 23*(20), 202203.

Englehart, K., & Hudgins, B. (2003). *IEEE Transactions on Biomedical Engineering, 50*(7), 848.

Finkel, P., Lofland, S. E., & Garrity, E. (2009). *Applied Physics Letters, 94*(7).

Fischer, H., Vogel, B., Gruhagen, A., Brhel, K. P., & Kaiser, M. (2001). *Materials Science Forum, 394*(3), 9.

Gantz, B., Turner, C., Gfeller, K., & Lowder, M. (2005). *Laryngoscope, 796*.

Ghatak, S.K., & Sur, S. (2005). arXiv:physics/0512071 [physics.med-ph].

Greve, H., Woltermann, E., Jahns, R., Marauska, S., Wagner, B., Knöchel, R., et al. (2010). *Applied Physics Letters, 97*(15).

Grush, L. (2013). Fox News.

Haas, L. (2003). *Journal of Neurology, Neurosurgery, and Psychiatry, 74*(1), 9.

Hattrick-Simpers, J. R., Dai, L., Wuttig, M., Takeuchi, I., & Quandt, E. (2007). *Review of Scientific Instruments, 78*(10).

Hirdes, M. M., Siersema, P. D., van Boeckel, P. G., & Vleggaar, F. P. (2012). *Endoscopy, 44*(7), 649.

Hochber, L., et al. (2006). *Nature, 442*, 164.

Hristoforou, E., & Ktena, A. (2007). *Journal of Magnetism and Magnetic Materials, 316*(2), 372.

Jahns, R., Greve, H., Woltermann, E., Quandt, E., & Knochel, R. H. (2011). *IEEE Transactions on Instrumentation and Measurement, 60*(8), 2995.

Jahns, R., Greve, H., Woltermann, E., Quandt, E., & Knöchel, R. (2012). *Sensors and Actuators A: Physical, 183*(0), 16.

Jahns, R., KnÃchel, R., Greve, H., Woltermann, E., Lage, E., & Quandt, E. Presented at the medical measurements and applications. Proceedings (MeMeA), IEEE International Workshop on 2011, unpublished.

Jahns, R., Piorra, A., Lage, E., Kirchhof, C., Meyners, D., Gugat, J. L., et al. (2013). *Journal of the American Ceramic Society, 96*(6), 1673.

Klevens, R. M., Edwards, J. R., Richards, C. L., Horan, T. C., Gaynes, R. P., Pollock, D. A., et al. (2007). *Public Health Reports, 122*(2), 160.

Kuruvilla, A., & Flink, R. (2003). *Seizure, 12*, 577.

Labanca, M., Azzola, F., Vinci, R., & Rodella, L. F. (2008). *British Journal of Oral and Maxillofacial Surgery, 46*(4), 265.

Lage, E., Kirchhof, C., Hrkac, V., Kienle, L., Jahns, R., Knöchel, R., et al. (2012). *Nature Materials, 11*(6), 523.

Lage, E., Woltering, F., Quandt, E., & Meyners, D. (2013). *Journal of Applied Physics, 113*(17).

Lebedev, M., & Nicolelis, M. (2006). *Trends in Neurosciences, 29*(9), 536.

Lee, J.-H., Ryu, J., Jolesz, F., Cho, Z.-H., & Yoo, S.-S. (2009). *Neuroscience Letters, 450*(1), 1.

Li, M., Wen, Y., Li, P., Yang, J., & Dai, X. (2011). *Sensors and Actuators A: Physical, 166*(1), 102.

Logothetis, N., et al. (2001). *Nature, 412*(6843), 150.

Machado, L. G., & Savi, M. A. (2003). *Brazilian Journal of Medical and Biological Research, 36*(6), 683.

Marauska, S., Jahns, R., Kirchhof, C., Claus, M., Quandt, E., Knöchel, R., et al. (2013). *Sensors and Actuators A: Physical, 189*(0), 321.

Nan, C. W., Bichurin, M. I., Dong, S. X., Viehland, D., & Srinivasan, G. (2008). *Journal of Applied Physics, 103*(3).

Nan, T., Hui, Yu, Rinaldi, M., & Sun, N. X. (2013). *Scientific Reports, 3*.

O'Handley, R. C., Huang, J. K., Bono, D. C., & Simon, J. (2008). *IEEE Sensors Journal, 8*(1), 57.

O'Keefe, J., & Dostrovsky, J. (1971). *Brain Research, 34*, 171.

Onuta, T.-D., Wang, Y., Long, C. J., & Takeuchi, I. (2011). *Applied Physics Letters, 99*(20).

Park, C.-S., Cho, K.-H., Arat, M. A., Evey, J., & Priya, S. (2010). *Journal of Applied Physics, 107*(9), 094109.

Park, C.-S., Ryu, J., Choi, J.-J., Park, D.-S., Ahn, C.-W., & Priya, Shashank (2009). *Japanese Journal of Applied Physics, 48*(8R), 080204.

Pigò, F., Bertani, H., Manno, M., Mirante, V., Caruso, A., Barbera, C., et al. (2013). *International Journal of Colorectal Disease, 28*(3), 399.

Priya, S., & Inman, D. J. (2009). *Energy harvesting technologies*. New York: Springer.
Quiroga, R. Q., et al. (2005). *Nature, 435*, 1102.
Radousky, H. B., & Liang, H. (2012). *Nanotechnology, 23*(50), 502001.
Roundy, S., Leland, E. S., Baker, J., Carleton, E., Reilly, E., Lai, E., et al. (2005). *IEEE Pervasive Computing, 4*(1), 28.
Roundy, S., Wright, P. K., & Rabaey, J. (2003). *Computer Communications, 26*(11), 1131.
Scarabino, T., & Salvolini, U. (2003). *Atlas of morphology and functional anatomy of the brain*. Napoli, Italy: Editoriale Idelson-Gonocchi.
Schoen, R. E., Pinsky, P. F., Weissfeld, J. L., Yokochi, L. A., Church, T., Laiyemo, A. O., et al. (2012). *The New England Journal of Medicine, 366*(25), 2345.
Soderberg, & Cook. (1984). *Physical Therapy, 64*, 1813.
Spaldin, N. A., & Fiebig, M. (2005). *Science, 309*(5733), 391.
Srinivasan, G. (2010). *Annual Review of Materials Research, 40*, 153.
Starner, T., & Paradiso, J. A. (2004). In C. Piguet (Ed.), *Low-power electronics design*. CRC Press.
Sundaresan, V. B., Atulasimha, J., & Clarke, J. (2013). Patent US 8,602,034 B2.
Toennies, J. L., Tortora, G., Simi, M., Valdastri, P., & Webster, R. J. (2010). *Proceedings of the Institution of Mechanical Engineers, Part C: Journal of Mechanical Engineering Science, 224*(7), 1397.
Tortora, G., Toennies, J. L., Simi, M., Valdastri, P., & Webster, R. J., III (2009). *Proceedings of the Institution of Mechanical Engineers, Part C: Journal of Mechanical Engineering Science, 224*.
Urso, G., Interlandi, D., Puglisi, M., Di Prima, P., Bertino, G., & La Rosa, G. (2006). *Minerva Gastroenterologica e Dietologica, 52*(3), 309.
Uutela, K., Hamalainen, M., & Somersalo, E. (1999). *NeuroImage, 10*(2), 173.
Velliste, M., et al. (2008). *Nature, 453*, 1098.
Velliste, M., Perel, S., Spalding, C., Whitford, A., & Schwartz, A. (2008). *Nature, 1098*.
Vrba, A., & Robinson, S. E. (2001). *Methods, 249*.
Wang, Thomas D., & Van Dam, Jacques (2004). *Clinical Gastroenterology and Hepatology, 2*(9), 744.
Wheeler, J. (2010). GE Healthcare.
Wilkins, T., Khan, N., Nabh, A., & Schade, R. R. (2012). *Am Fam Physician, 85*(5), 469.
Wolpaw, J., et al. (2002). *Clinical Neurophysiology, 113*, 767.

This page intentionally left blank

Progress toward magnetoelectric spintronics

12

T. Nan, N.X. Sun
Northeastern University, Boston, MA, USA

12.1 Introduction

Multiferroic materials and devices have attracted intensified recent interests due to the demonstrated strong magnetoelectric (ME) coupling with unique functionalities and superior performance characteristics (Fiebig, 2005; Ma, Hu, Li, & Nan, 2011; Nan, Bichurin, Dong, Viehland, & Srinivasan, 2008; Ramesh & Spaldin, 2007; Sun & Srinivasan, 2012; Vaz, 2012). Strong ME coupling has been demonstrated in a variety of multiferroic heterostructures, including bulk magnetic slab on ferro/piezoelectric, magnetic thin film on ferro/piezoelectric slab, thin film multiferroic heterostructures, etc (Dong, Cheng, Li, & Viehland, 2003; Liu et al., 2011; Liu, Lou, Li, & Sun, 2011; Ryu, Priya, Carazo, Uchino, & Kim, 2001; Thiele, Dörr, Bilani, Rödel, & Schultz, 2007; Wan et al., 2005; Zhou et al., 2007). The strong ME coupling offers great opportunities for achieving voltage control of spintronics devices with low energy consumption. In traditional magnetic materials-based magnetic random access memories (MRAM) devices, the binary information is stored as magnetization (Chappert, Fert, & Van Dau, 2007). The high coercivity of the hard ferromagnetic element requires a large magnetic field for switching the magnetic states, which consumes large amount of energy. In the modern MRAM information writing process, spin-torque technique is utilized by passing through a spin polarized current directly to the magnets to minimize the large energy for generating the magnetic field (Albert, Katine, Buhrman, & Ralph, 2000; Brataas, Kent, & Ohno, 2012). However, either method is able to decrease the energy consumption to a decent level (Tsymbal, 2011). With the presence of multiferroic or ME materials, spin is controlled by the electric field, which opens new opportunities for voltage control of spintronic devices with ultra-low energy consumption.

For artificial multiferroic or ME heterostructure, different coupling mechanisms are utilized for the demonstration of the voltage control of magnetism in spintronics: (1) strain-mediated ME coupling on the ferroelectric−ferromagnetic interface, where the magnetism is modified by the piezostrain induced by ferroelectric slab or thin film due to its piezoelectricity; (2) charge-mediated ME coupling on the ferroelectric−ferromagnetic or dielectric−ferromagnetic interface; and (3) exchange coupling between antiferromagnetic, ferroelectric, and ferromagnetic phases (Vaz, 2012).

Composite Magnetoelectrics. http://dx.doi.org/10.1016/B978-1-78242-254-9.00012-3
Copyright © 2015 Elsevier Ltd. All rights reserved.

12.2 Electric field control of magnetism in magnetoelectric composite mechanism

12.2.1 Strain-mediated magnetoelectric coupling

Strain-mediated ME coupling in layered ferromagnetic/ferroelectric heterostructures provides great opportunities in realizing novel multiferroic devices such as magnetoelectric random access memories (MERAMs) (Bibes, 2008; Hu, Li, Chen, & Nan, 2011; Hu, Nan, & Chen, 2011; Nan, Hui, Rinaldi, & Sun, 2013; Pertsev & Kohlstedt, 2009). Through the phase field simulations, Hu and coworkers demonstrated a new approach toward voltage-controlled MRAM through strain-mediated ME coupling in magnetic tunneling junction on a ferroelectric layered heterostructure (Hu, Li, et al., 2011). Strain-mediated ME coupling can lead to a 90° rotation of the in-plane magnetization of the free layer in the magnetic tunneling junctions. Simulation results show that these voltage-controlled MRAM devices have ultra-low writing energy (less than 0.16 fJ per bit), room temperature operation, high storage density, good thermal stability, and fast writing speed. Besides, voltage control of anisotropic magnetoresistance (AMR), giant magnetoresistance (GMR), exchange bias, and magnetic domain wall propagation were also realized experimentally by researchers.

12.2.1.2 Nonvolatile switching of magnetic anisotropy field

In a strain-mediated multiferroic system, the typical modification of the magnetism of the ferromagnetic phase as a function of bipolar electric field shows a "butterfly" like behavior (Hu, Nan, et al., 2011; Liu et al., 2009; Nan et al., 2012). That is due to the piezoelectricity of the ferroelectric phase, which has a "butterfly" like piezostrain as a function of the electric field resulting from ferroelectric domain wall switching. In this case, the magnetization state is volatile because of the disappearance of the piezostrain at zero electric field. However, the nonvolatile switching of magnetization would be more promising for information storage or MERAM devices with lower energy consumption, and the magnetic state can be further controlled by voltage impulse.

Nonvolatile switching of magnetism is experimentally demonstrated in ferromagnetic materials on different ferroelectric slabs, such as (001) and (011) oriented $[Pb(Mg_{1/3}Nb_{2/3})O_3]$-$[PbTiO_3]$ (PMN-PT) single crystal (011), oriented $Pb(Zn_{1/3}Nb_{2/3})O_3$-$PbTiO_3$ (PZN-PT) single crystal, and PZT ceramic slab.

Ferroelastic switching in PMN-PT (011) or PZT

Wu et al. have experimentally demonstrated a revisable and non-volatile magnetic anisotropy reorientation in a multiferroic Ni/(011)-oriented PMN-PT heterostructure (Wu et al., 2011a,b). In this system, they achieved a 300 Oe magnetic anisotropy field change. The change of the anisotropy field is stable without applying an electric field and is able to switch reversibly by an electric field below the electric coercive field.

Figure 12.1 shows the Kerr rotation hysteresis loop of Ni/PMN-PT in the application of a different electric field, which would lead to a different piezostrain state. Figure 12.1 inset shows the relative strain difference as a function of the

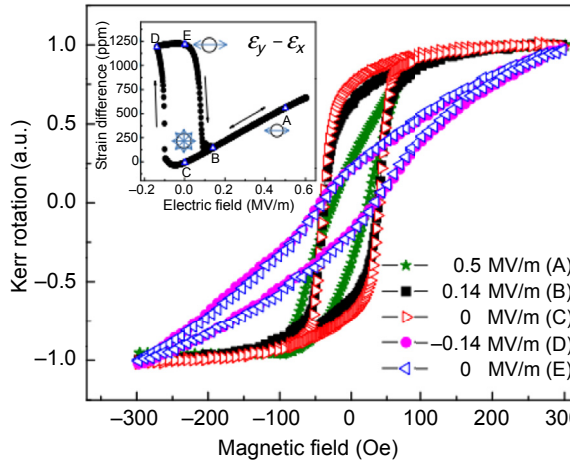

Figure 12.1 Normalized Kerr rotation hysteresis curves (M−H) along the *y* direction under different electric fields (letters are the representatives of the labeled strain states in the inset). The inset shows in-plane strain difference ($\varepsilon_y - \varepsilon_x$) as a function of electric field. The drawings indicate the magnetization state: (C) permanent easy plane, ((A) and (B)) temporary easy axis along x^-, and ((D) and (E)) permanent easy axis along x^- (Wu et al., 2011b).

electric field. By driving the electric field from A to C (A−B−C), due to the linear piezoelectric effect, the PMN-PT is in the linear ferroelectric regime. In that case, from the M−H hysteresis loop, the remnant magnetization increases linearly. However, in the linear regime, the magnetic anisotropy change is unstable and the magnetic state would change back to its initial state after removing the applied electric field. When decreasing the electric field from 0 to coercive field (D), the non-180° polarization reorientation takes place in PMN-PT and induces a sudden increase of strain. This would cause the large change of the magnetic anisotropy. When removing the electric field (E), the strain remains and the magnetization is retained. With further increase of the electric field from 0 to coercive field (B), another non-180° polarization reorientation occurs back to the initial poling direction. Thus, the remnant strain is released, and the magnetic state is switched back. However, the mechanism nonvolatile switching of the magnetism using non-180° polarization domain wall reorientation is unclear.

Most recently, Ming et al. used a unique ferroelastic switching pathway in (011) oriented PMN-PT ($0.71Pb(Mg_{1/3}Nb_{2/3})O_3$-$0.29PbTiO_3$) single crystal that allows up to 90% of polarization to rotate from an out-of-plane to a purely in-plane direction (71° and 109° switching), thereby producing two distinct, stable, and electrically reversible lattice strain states (Liu et al., 2013b). Domain distortion, polarization switching pathway, and lattice strain in response to in situ vertical voltage in PMN-PT (011) are clearly presented using reciprocal space mapping (RSM) and piezoforce microscopy (PFM) measurements.

As shown in Figure 12.2, the multilayer films with the structure of Au(5 nm)/$Fe_{60}Co_{20}B_{20}$(50 nm)/Ti(5 nm) were deposited on (011) oriented single crystalline

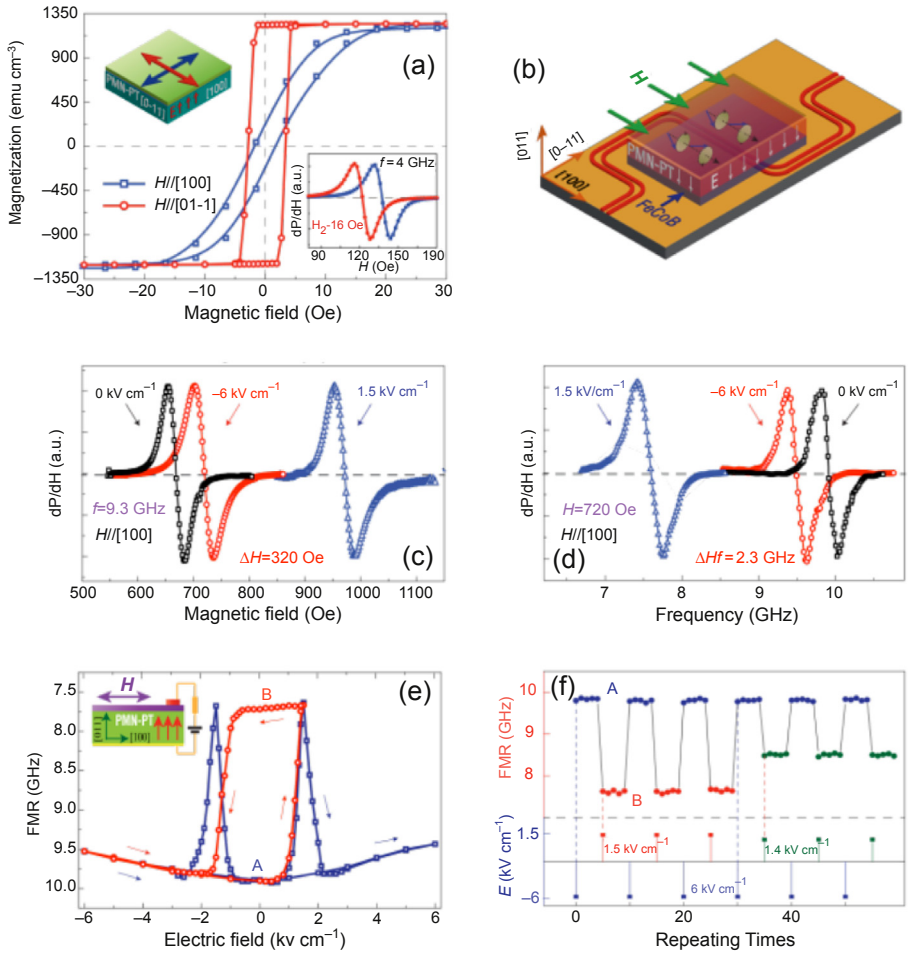

Figure 12.2 (a) In-plane magnetic hysteresis loops of FeCoB/PMN-PT (011). Insets are schematic (upper left) and ferromagnetic resonance (FMR) spectra (bottom right). (b) Schematic of FMR measurement for (c)−(f). The sample is laid face down on an S-shape coplanar waveguide. Magnetic fields are applied in the [100] direction and electric fields are applied along the [011] direction. (c) Electric field dependence of the FMR frequency in field sweeping mode. (d) Electric field dependence of the FMR field in frequency sweeping mode. (e) FMR frequency responses under unipolar (red) and bipolar (blue) sweeping of electric fields at room temperature. (f) Voltage-impulse-induced nonvolatile switching of FMR frequency (Liu et al., 2013b).

PMN-PT substrates, and the multiferroic heterostructure was characterized by electric field dependence of ferromagnetic resonance field using coplanar-waveguide FMR test unit. Figure 12.2(e) shows the resonance frequency in response to in situ electric fields applied normally to the sample. A "Butter-fly" curve (blue) is observed as cycling triangle electric fields. By applying a positive electric field on a negatively poled FeCoB/PMN-PT (011), a giant frequency jump takes place

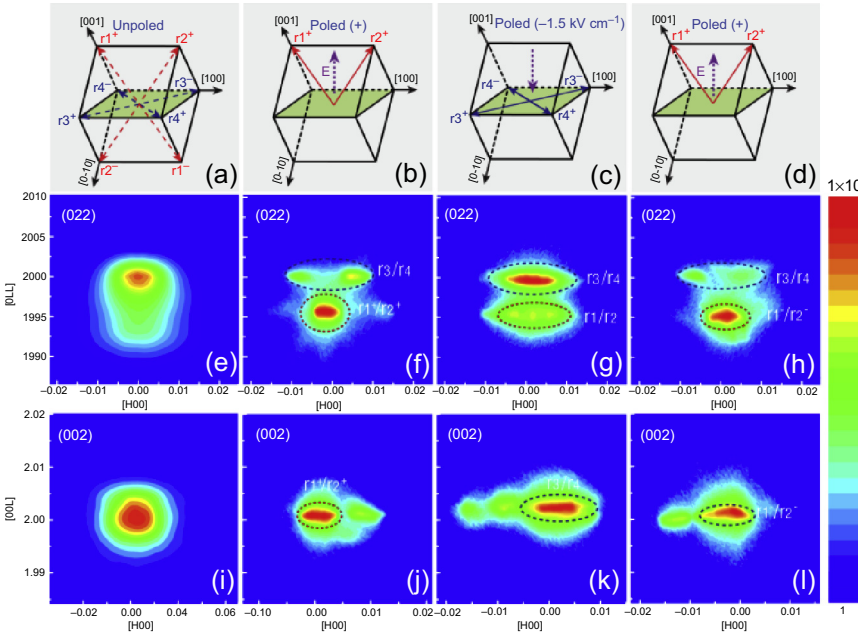

Figure 12.3 Schematics of domain structures and reciprocal space maps (RSMs) about (022) and (002) reflections of PMN-PT (011) under various applied electric fields and thus poling states. The first column (a, e, i) is for the unpoled state. The second column (b, f, j) is for the positive poling state with up to 90% of polarization pointing upward. The third column (c, g, k) is after applying a negative electric field of $-1.5\ \mathrm{kV\ cm^{-1}}$ and then switching it off. The fourth column (d, h, l) is achieved by applying a positive electric field of $5\ \mathrm{kV\ cm^{-1}}$ and then switching it off (Liu et al., 2013b).

near the coercive field of $1.5\ \mathrm{kV\ cm^{-1}}$. In this process, the polarization undergoes 71° and 109° ferroelastic switching from the out-of-plane to the in-plane direction associated with a lattice strain induced by the domain distortion. Therefore, the hysteresis loop of the FMR frequency as a function of the electric field is observed (Figure 12.2(e)). Similar to magnetic memory, two stable and reversible frequency remnant states A and B would facilitate the realization of nonvolatile frequency switching by reversing the applied electric field at the coercive field. The voltage impulse induced magnetization switching was also realized (shown in Figure 12.2(f)). As a PMN-PT (011) is subjected to an impulse of $-6\ \mathrm{kV\ cm^{-1}}$, the remnant strain in poling state A is retained and results in the maximum FMR frequency of 9.9 GHz. Upon applying an impulse field of $1.5\ \mathrm{kV\ cm^{-1}}$, the resonance frequency is reduced to 7.6 GHz, indicating that the strain state is switched to remnant state B.

High resolution X-ray diffraction (HRXRD) measurements were used to understand the polarization switching pathway and lattice strain in response to in situ electric fields. Figure 12.2 shows the electric field dependence of the reciprocal space maps (RSMs) in the vicinity of the (022) and (002) reflections of the bare PMN-PT (011) substrates. For the unpoled state of PMN-PT (011) (the first column in Figure 12.2),

a single broad spot is observed in both (022) and (002) reflections (Figure 12.2(e) and (i)). Analysis on RSM patterns suggests that two possible domain structures r3 and r4 are dominant in the unpoled state, and most of the polarization lies in the plane. As the sample is vertically poled with a strong positive voltage, the RSM in Figure 12.2(f) shows an additional high intensity (022) reflection spot with a lower Q_{022} value, corresponding to the r1/r2 domain structures. Meanwhile, the intensity of the spot corresponding to r3/r4 reduces dramatically. This indicates that 71° and 109° ferroelastic polarization switching from the in-plane direction to the out-of-plane direction takes place and results in a large out-of-plane lattice strain. After a small negative electric field of $-1.5\,\mathrm{kV\,cm^{-1}}$ is applied and removed, the domain distortion returns to r3/r4, and polarization is suppressed from the out-of-plane direction to the in-plane direction (Figure 12.2(g)). As a large positive electric field of $5\,\mathrm{kV\,cm^{-1}}$ is applied and then switched off, the domain structure is switched again and back to r1/r2 (Figure 12.2(h)). Therefore, a stable and reversible ferroelastic domain switching pathway is confirmed, which enables polarization rotation between the in-plane direction and the out-of-plane direction.

Ferroelastic switching induced nonvolatile magnetization reorientation has also been realized in PZT ceramic slab. Nan et al. demonstrated a voltage impulse induced reversible bistable magnetization switching at room temperature in a FeGaB/PZT heterostructure (Nan et al., 2012). The normalized magnetization as a function of E-field with the amplitude varied within -8 to $+8\,\mathrm{kV\,cm^{-1}}$ and -16 to $+16\,\mathrm{kV\,cm^{-1}}$ was shown in Figure 12.4, which showed a butterfly M−E curve when E-field amplitude was at $16\,\mathrm{kV\,cm^{-1}}$ and a loop-like M−E curve when the E-field amplitude was $8\,\mathrm{kV\,cm^{-1}}$. In the loop-like M−E curve, the magnetization ratio was varied from 71% to 56% with the change of E-field from -8 to $8\,\mathrm{kV\,cm^{-1}}$, leading to E-field induced bistable magnetization states that enabled reversible voltage impulse induced bistable magnetization switching, as shown in Figure 12.5.

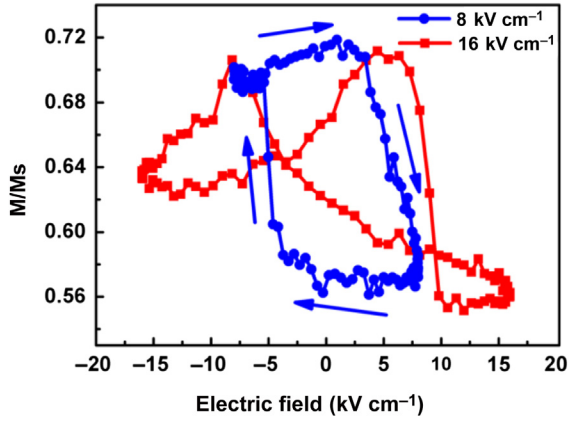

Figure 12.4 Magnetization ratio versus E-field with a magnetic bias field (i.e., 3 Oe) under application of E-field of 16 and $8\,\mathrm{kV\,cm^{-1}}$ (Nan et al., 2012).

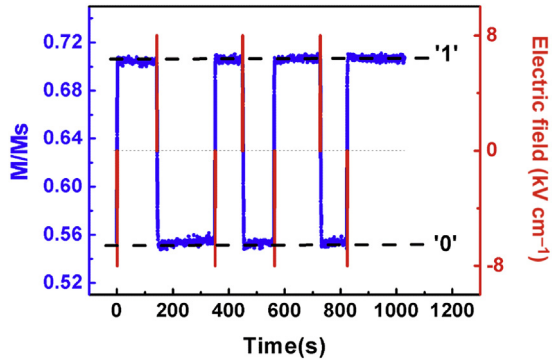

Figure 12.5 Magnetization ratio of FeGaB/PZT heterostructure switched by voltage impulse measured in length direction with a magnetic bias field (i.e., 3 Oe) in time-domain measurement (Nan et al., 2012).

(001) PMN-PT

In (001) oriented PMN-PT, different nonvolatile switching behavior was observed. Zhang et al. reported a large and nonvolatile bipolar-electric-field-controlled magnetization switching at room temperature in a CoFeB/(001) oriented PMN-PT multiferroic heterostructure, which exhibited an electric-field-controlled loop-like magnetization behavior (Zhang et al., 2012).

Figure 12.6(a)–(d) shows the XRD-RSM of the (113) peak under electric fields of $-8\,\mathrm{kV\,cm^{-1}}$, $-0\,\mathrm{V\,cm^{-1}}$, $+8\,\mathrm{kV\,cm^{-1}}$, and $+0\,\mathrm{kV\,cm^{-1}}$. The reflections are

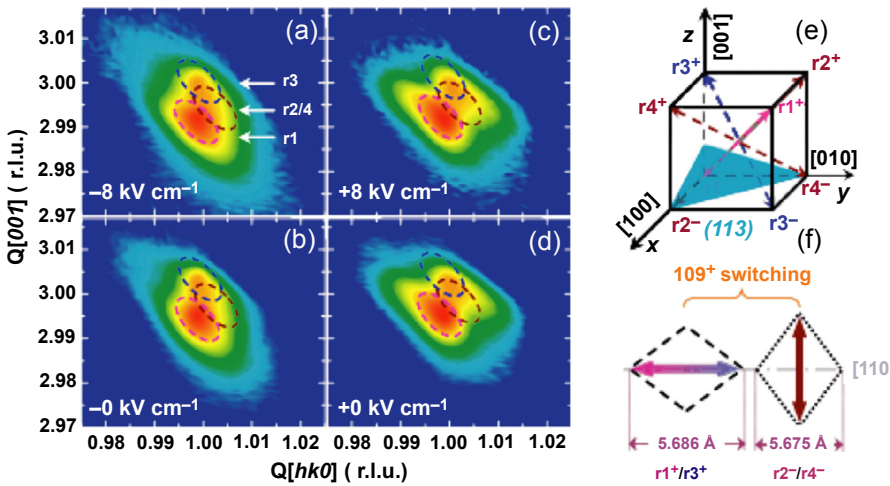

Figure 12.6 (a) to (d) show the electric-field tuned X-Ray diffraction reciprocal spacing mappings (XRD RSMs) around the (113) reflection. (e) Configuration of the (113) crystal face (translucent blue plane) and the rhombohedral distortions, as well as polarizations shown by the arrows, whose colors correspond to the colors of the ellipses in (a)–(d). (f) The 109° switching-induced changes of in-plane distortions along the [110] direction, as well as the corresponding lattice parameters and the in-plane projections of polarization vectors (broad arrows) (Zhang et al., 2012).

unchanged by removing the electric field, while the positive and negative poled cases displayed remarkable difference, which is the origin of the nonvolatile and reversible electrical control of magnetism. By analyzing the RSM data, the negatively and positively poled PMN-PT showed a change of the percentage of r2/r4 from 4% to 30%. Because the change between $r1^{+}/r3^{+}$ and $r2^{-}/r4^{-}$ corresponds to the 109° switching, percentage of the 109° switching is about 26% and the 71/180° switching have the percentage of 74%. This non-volatile control of magnetization in CoFeB/PMN-PT via electric field was believed to be related to the combined action of 109° switching have the percenching and the absence of magnetocrystalline anisotropy in the CoFeB film.

Phase change of PZN-PT

Besides ferroelastic switching, the phase transition of (011) oriented PZN-PT was also utilized for nonvolatile switching of magnetism. The rhombohedral-to-orthorhombic phase transition happened under sufficient poling conditions. The orthorhombic phase can also be reverted back when the electric field is removed. Liu et al. reported a bistable magnetization switching in a FeGaB/PZN-PT multiferroic heterostructure (Liu et al., 2013a).

Figure 12.7 shows loop-like FMR frequency under a bias magnetic field of 50 Oe and an FMR field at 12 GHz as a function of the electric field. At low electric field, the linear relation between the FMR field/FMR frequency and electric field indicates a linear piezoelectric effect in the rhombohedral phase of PZN-PT. By increasing the electric field to a critical threshold of 5.8 kV cm^{-1}, the phase transition of PZN-PT takes place from rhombohedral to orthorhombic with a large lattice change, which may lead to a giant ME coupling. This induced a dramatic and sudden change of the FMR field and FMR frequency. At high field, FMR field and frequency saturate with little strain variation. When the electric field decreased from 8 kV cm^{-1}, the orthorhombic phase and strain state were unchanged until the electric field was

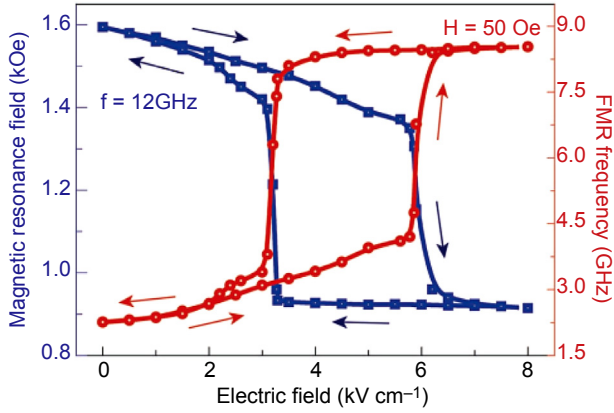

Figure 12.7 Hysteresis loops of E-field versus FMR frequency, measured under a bias magnetic field of 50 Oe and E-field versus FMR field with working frequency of 12 GHz.

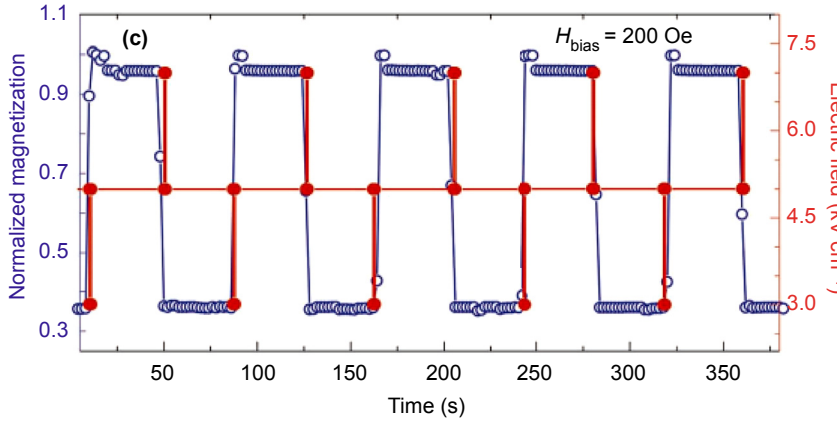

Figure 12.8 E-field-impulse-induced dynamic memory-type of magnetization switching.

lower than another critical field of 3 kV cm^{-1}. This also induced a large change of the magnetism.

Figure 12.8 shows the dynamic voltage-impulse-induced nonvolatile memory-type magnetization switching in FeGaB/PZN-PT heterostructure. In order to induce a phase transition in PZN-PT, an electric field bias of 5 kV cm^{-1} is maintained. When an electric field impulse of 3 kV cm^{-1} is applied, the magnetization of FeGaB increased and remains at a high magnetization ratio of 95%. The magnetization can be switched back to a low magnetization ratio of 35% by applying an electric field impulse of 7 kV cm^{-1}.

12.2.1.3 Voltage control of MERAM GMR exchange bias spin wave

Simulation on MERAM devices working principles

Strain-mediated magnetoelectric random access memory (MERAM) and magnetic tunnel junction on ferroelectric have been demonstrated theoretically (Hu, Li, Wang, & Nan, 2010; Pertsev & Kohlstedt, 2009). The piezoelectrically induced strain from the ferroelectric layer may lead to an in-plane 90° rotation of the magnetization in the free layer of the magnetic tunnel junction (MTJ). Thus an electric field is able to manipulate the resistance of the MTJ. As in the previous discussion, by sweeping the electric field below the ferroelectric coercive field of, for example, the (011) oriented PMN-PT, the ferroelectric layer provides a bistable and reversible strain state. This nonvolatile behavior could enable the electric field impulse induced magnetization switching in MTJ with ultra-low energy consumption. The nonvolatile switching of magnetization is the preference in amorphous rather than epitaxial magnetic thin film, which would provide good design flexibility.

Recently, Hu et al. proposed a high-density magnetoresistive random access memory operating at ultra-low voltage at room temperature by phase field simulation (Hu, Li, et al., 2011). (001) Ni film was chosen as the free layer, and a spin valve

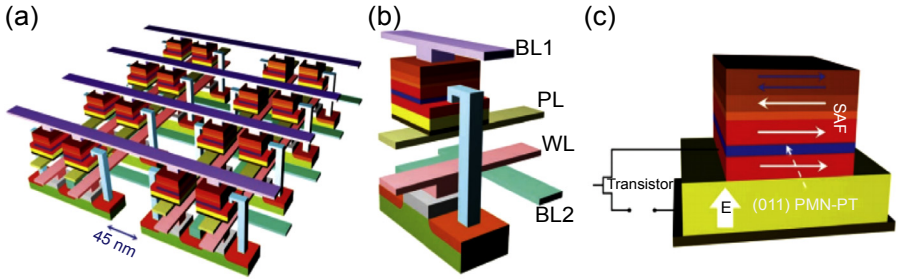

Figure 12.9 (a) Array design of the electric-field-controlled magnetoresistive random access memory (MRAM) device on complementary metal−oxide−semiconductor (CMOS) platforms. The space between neighboring cells is 45 nm, which is the typical channel length of its constituent MOS transistor. (b) Architecture of the 1-T (transistor)/1-magnetoresistive (MR) memory unit cell, where the writing voltage is applied between bitline (BL)2 and plateline (PL) controlled by wordline (WL) connecting to the gate of the transistor. (c) Schematic of the basic building block, where a spin valve or magnetic tunnel junction is integrated onto a PMN-PT layer, upon the application of a perpendicular voltage bias controlled by the transistor. (From top to bottom): antiferromagnetic pinning layer, a synthetic antiferromagnetic trilayer with a pinned layer and a reference layer separated by ultra-thin nonmagnetic spacer, tunneling barrier/nonmagnetic metallic layer, the magnetic-free layer, ferroelectric layer, and the bottom electrode. The arrows in the MR element denote the magnetization orientations (Hu, Li, et al., 2011).

consisting of an antiferromagnetic layer was shown in Figure 12.9. By the application of a perpendicular electric field to the bottom PMN-PT layer, and an in-plane anisotropic piezostrain was generated. Figure 12.2 shows the thickness-dependence magnetization switching in the Ni-free layer. A bistable magnetic state was shown at zero electric field, and the magnetization rotation is about 70°, shown by the vector diagram in Figure 12.10(b). The resistance change of the spin valve was shown in Figure 12.10(c) due to the magnetization rotation. The preferred lateral size of the spin valve and its thermal stability were also discussed. A lateral size between 64 and 160 nm showed a good thermal stability factor >40 with high information storage density. As a conclusion, the strain-mediated MERAM devices with low write time (<10 ns), low writing energy (0.16 fJ per bit), and high storage density would be promising for next-generation MRAM devices.

Devices demonstration

Some primary memory devices with strain-mediated ME coupling have been experimentally demonstrated. Li et al. have proposed an electrically write memory device in FeGa/BSPT multiferroic heterostructure with bistable magnetic states defined by different magnetic coercive field H_c (Li, Wang, Lin, & Nan, 2010; Yang et al., 2009).

Voltage control of GMR

Voltage control of AMR and GMR would be an important step toward electric field writing of magnetic bits for spintronics (Bibes, 2008; Garcia et al., 2010). Liu and coworkers have recently demonstrated an electric field modulation of

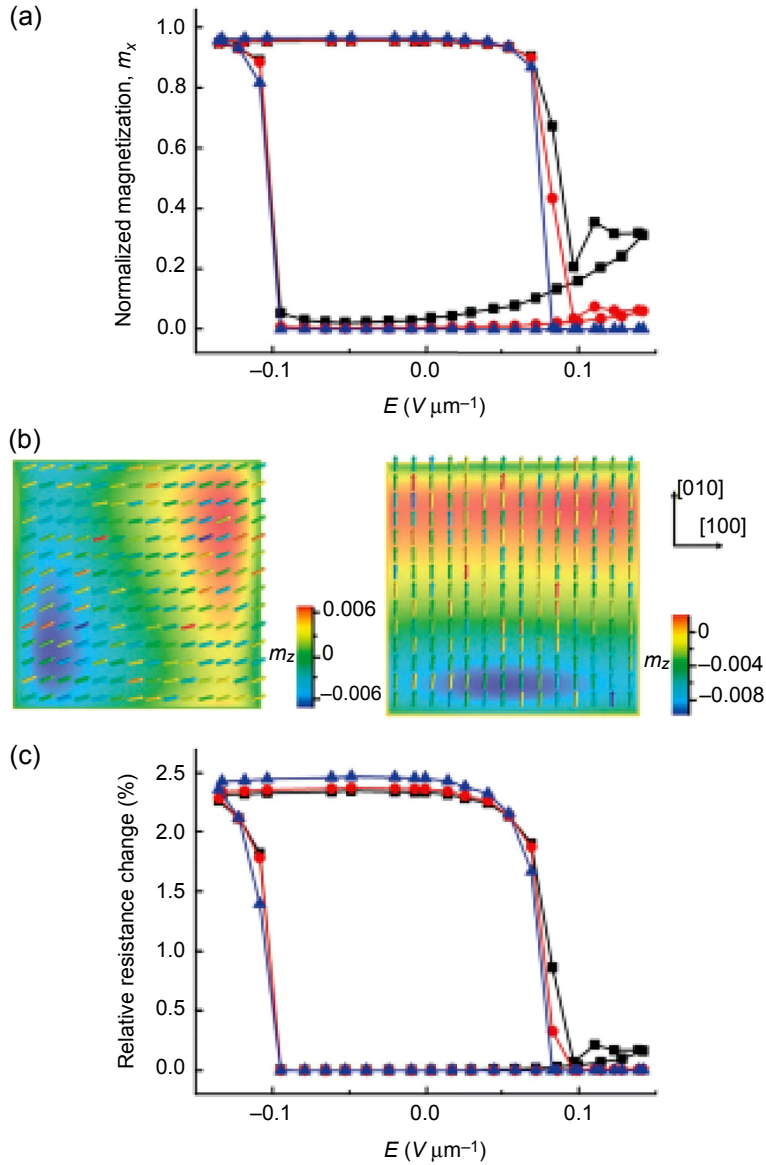

Figure 12.10 (a) Electric-field induced magnetization rotation in the Ni-free layers with thicknesses of 35 nm (squares), 15 nm (circles), and 5 nm (triangles), respectively. m_x indicates the normalized magnetization in the in-plane [100] direction. The lateral size (length and width) is set as 64 nm. (b) Vector diagrams of the bistable magnetization distributions at $E = 0$, that is, $m_x = 0.9538$ (left) and 0.0364 (right) in the $64 \times 64 \times 35$ nm three Ni-free layer. (Color bar) m_z indicates the normalized magnetization in the out-of-plane [001] direction. (c) Hysteric loops of relative device resistance change upon the perpendicular electric fields applied to the (011) PMN-PT layer, accompanied with the magnetization switching in the Ni-free layers with thicknesses of 35 nm (squares), 15 nm (circles), and 5 nm (triangles), respectively (Hu, Li, et al., 2011).

magnetoresistance with ultra-low power in multiferroic AMR and GMR structures of $Ni_{80}Co_{20}$/PZN-PT (lead zinc niobate-lead titanate) and FeMn/$Ni_{80}Fe_{20}$/Cu/Co/PZN-PT. The AMR of a $Ni_{80}Co_{20}$/PZN-PT multiferroic heterostructure was shown in Figure 12.11(a) under two external magnetic bias fields of 0 Oe (red) and 50 Oe (blue). The resistance of $Ni_{80}Co_{20}$ film was completely tuned by the electric field with an AMR ratio of 1.5% when the magnetic easy axis was parallel to $[0\ 1\ \bar{1}]$ and perpendicular to the measured current, indicating an E-field induced 90° magnetization rotation (Liu et al., 2011). Dynamic E-field modulation of AMR was shown in Figure 12.11(b) and (c), as the responses to the sine wave and square wave of applied electric fields. Figure 12.12 shows the typical E-field dependence of AMR curves while the external magnetic field is perpendicular to the magnetic easy axis and electric current direction along [100] of PN-PT. The magnetic field range of conventional AMR sensors can be significantly boosted from 20 Oe at $E = 0$ to >350 Oe at $E = 6\ \text{kV cm}^{-1}$. Clearly, multiband magnetic field sensors based on the E-field tunable AMR can be achieved based on the voltage control of the magnetoresistance in magnetic/piezoelectric multiferroic heterostructures (Figures 12.11 and 12.12).

Besides E-field modulation of AMR in multiferroic $Ni_{80}Co_{20}$/PZN-PT via a strain-induced 90° magnetization rotation, similar E-field dependence of GMR can also be observed in GMR multiferroic heterostructures (Liu et al., 2011). Spin-valve structure of Ta(10 nm)/FeMn(15 nm)/$Ni_{80}Fe_{20}$(8 nm)/Cu(2 nm)/Co(4 nm)/Ta(10 nm) was directly deposited onto PZN-PT substrate, where Co is the free layer and $Ni_{80}Fe_{20}$ is the pinned magnetic layer with near zero magnetostriction constant. E-field dependence of magnetic hysteresis loops for both configurations I and II are shown in Figure 12.13. As electric field was increased, opposite magnetization processes of the free layer (Co) were observed for the two configurations I and II due to strain-mediated ME coupling in the free layer, which was reflected in the opposite trend of the magnetic hysteresis loops for both configurations I and II. As a result,

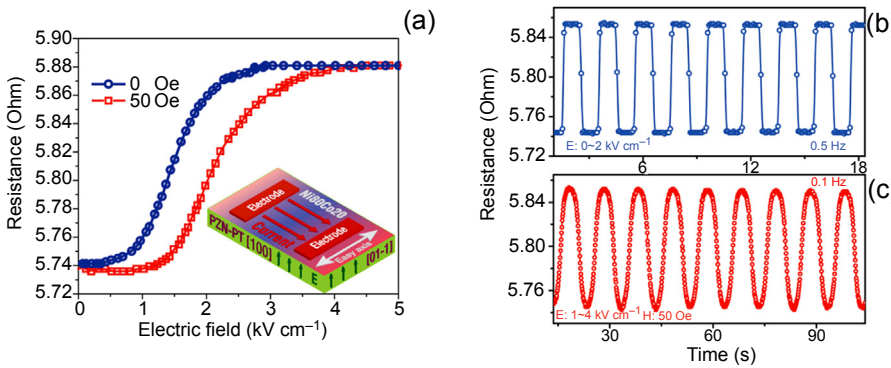

Figure 12.11 E-field manipulation of AMR in $Ni_{80}Co_{20}$/PZN-PT with magnetic bias fields of 0 Oe (red) and 50 Oe (blue), while magnetic easy axis is along $[0\ 1\ \bar{1}]$ direction and perpendicular to the measured current (a). E-field dynamically modulating AMR under various external magnetic bias field of 0 Oe (b) and 50 Oe (c) as a response to the sine wave and square wave of E-fields, respectively (Liu et al., 2011).

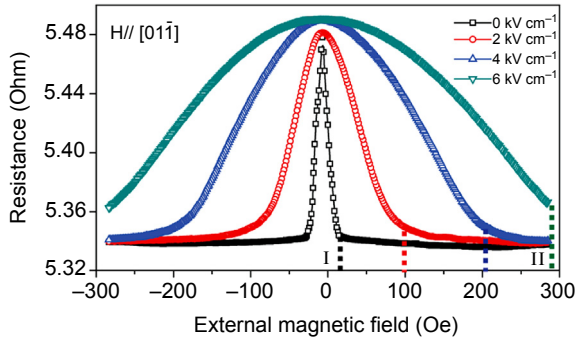

Figure 12.12 AMR curves under various E-fields while magnetic easy axis is parallel to the measured current and perpendicular to an applied external magnetic field (Liu et al., 2011).

E-field modulation of GMR in such a multiferroic spin-valve structure was demonstrated. Typical magnetoresistance hysteresis loops with a GMR ratio of 3% under various E-fields were obtained in the configuration I, as shown in Figure 12.14(a). E-field control of GMR ratio was shown in Figure 12.14(b) under two bias magnetic fields of 55 Oe (blue) and −55 Oe (red), respectively, corresponding to the dash arrow and solid arrow in Figure 12.14(a). In the configuration II, an opposite E-field dependence of magnetoresistance hysteresis loop was observed, as shown in Figure 12.14(c), due to the E-field-induced magnetic anisotropy field, which rotated magnetization direction by 90°. E-field dynamically modulating magnetoresistance was demonstrated as shown in Figure 12.14(d) under zero bias magnetic field, corresponding to the solid arrow in Figure 12.14(c). The demonstrated E-field control of magnetoresistance in AMR and GMR multiferroic heterostructures has a great implications for low-power electronics (Figures 12.13 and 12.14).

Voltage control of exchange bias

Voltage control of exchange bias has been achieved in BFO and Cr2O3 based multiferroic systems (Baek et al., 2010; Binek, Polisetty, He, & Berger, 2006; Borisov, Hochstrat, Chen, Kleemann, & Binek, 2005; Chen, Hochstrat, Borisov, & Kleemann, 2006; He et al., 2010; Martin et al., 2008; Ramesh & Ramesh, 2008). Most recently, Liu and coworkers demonstrated a new alternative approach in achieving E-field control of exchange bias in antiferromagnetic/ferromagnetic/ferroelectric (AFM/FM/FE) multiferroic heterostructures (Liu, Lou, et al., 2011). E-field induced near 180° magnetization switching at room temperature was achieved through E-field tuning of exchange bias.

Exchange-coupled multilayer films of Ta(5 nm)/FeMn(15 nm)/$Ni_{80}Fe_{20}$(2 nm)/FeGaB(14 nm)/Ta(20 nm) were deposited onto a (011) cut single-crystal ferroelectric PZN-PT substrate using magnetron sputtering to form the AFM/FM/FE multiferroic heterostructures (Liu, Lou, et al., 2011). [111] oriented FeMn film was deposited as the antiferromagnetic layer, which was facilitated by a 2 nm thick $Ni_{80}Fe_{20}$ between FeGaB and FeMn to induce a strong exchange coupling in the FeMn/$Ni_{80}Fe_{20}$/FeGaB multilayer. The FeGaB film was deposited under an in situ magnetic bias field, which

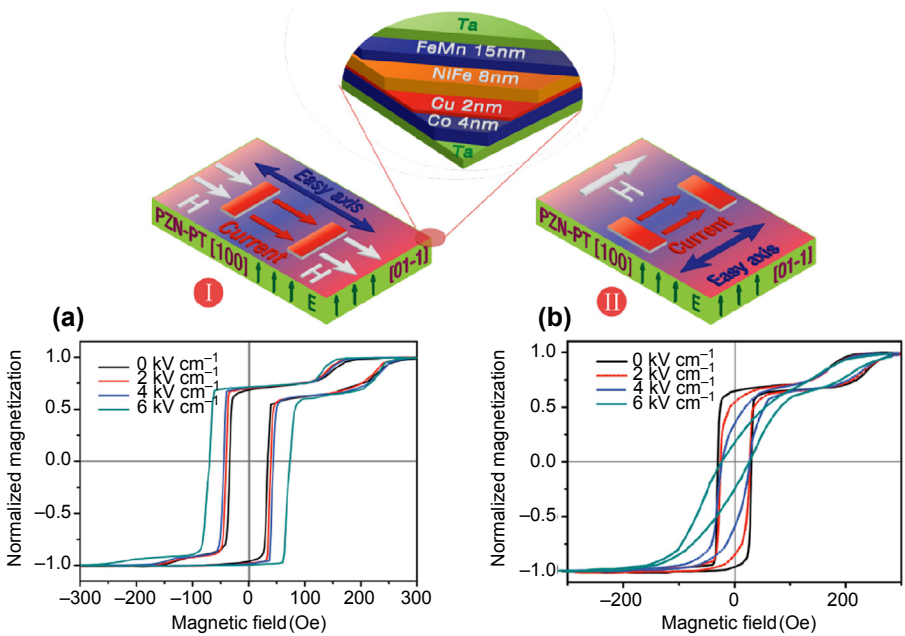

Figure 12.13 E-field control of magnetic hysteresis loops in multiferroic GMR structure of FeMn/$Ni_{80}Fe_{20}$/Cu/Co/PZN-PT for configuration I (a) and configuration II (b) (Liu et al., 2011).

led to an in-plane magnetic easy axis either alone [100] (configuration I) or [01−1] of PZN-PT (configuration II), as schematically shown in Figure 12.15.

Electric field control of magnetic hysteresis was also shown in Figure 12.15 for both configuration I and II at different θ angles, where θ is the angle between external magnetic field H and the magnetic easy axis of FeGaB. An exchange bias field of 48 Oe was observed for configuration I at $\theta = 0$ at zero E-field, which showed a slight reduction at an applied E-field. The magnetic hysteresis became more and more tilted due to an E-field induced effective magnetic field along the magnetic hard axis direction through strain-mediated ME coupling. As the external magnetic field was applied at $\theta = 55°$ from the magnetic easy axis, a much more pronounced E-field control of exchange bias was observed, exhibiting a downward shift of the exchange bias from 45 Oe to 3 Oe at an applied E-field of 6 kV cm^{-1}, as shown in Figure 12.15(b). In configuration II, an opposite trend of magnetic hysteresis loops and exchange bias shifts are observed at varying E-fields. An E-field induced magnetic field along the magnetic easy axis was achieved without noticeable variation of exchange bias fields for $\theta = 0°$, as shown in Figure 12.15(d). However, for $\theta = 45°$ and 60°, significant enhancement of exchange bias from 33 Oe to 50 Oe and from 22 Oe to 70 Oe with $\theta H_{ex}/H_{ex} = 218\%$ were achieved respectively as illustrated in Figure 12.15(e) and (f) (Figure 12.15).

Figure 12.16 summarizes the angular dependence of exchange bias H_{ex} under various E-fields for both configurations I and II. A strong θ angle dependence of the exchange bias on E-field was observed at intermediate θ angles between 0° and 90°. A maximum

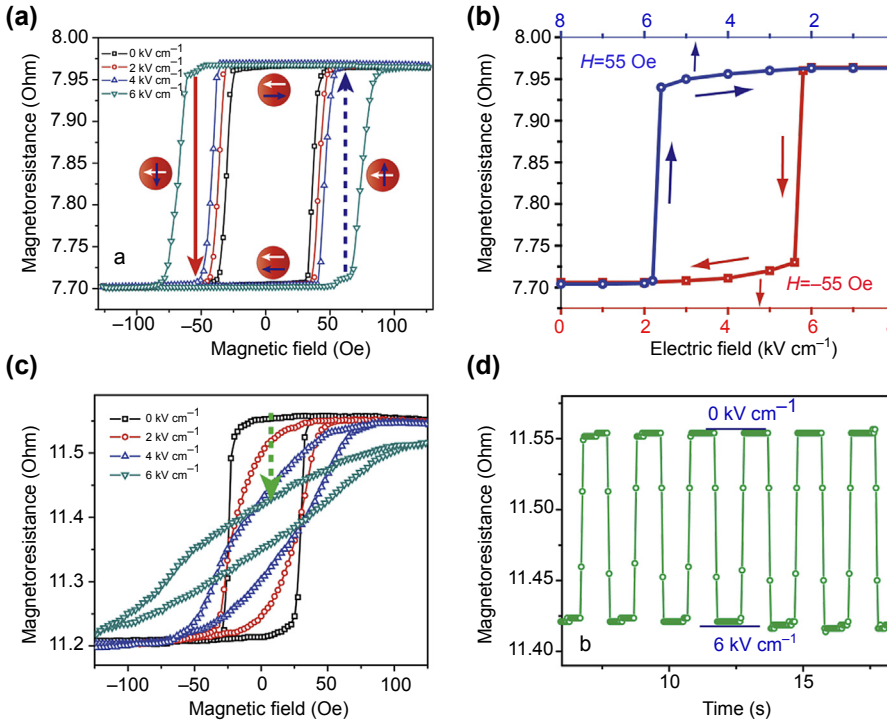

Figure 12.14 E-field dependence of GMR hysteresis loops in configuration I (a, b) and II (c) and E-field dynamically tuning of GMR at zero bias magnetic field (d) (Liu, Lou, et al., 2011).

E-field induced exchange field change of $-42°$ Oe was observed at $\theta = 55°$ for configuration I, as shown in Figure 12.16(a), while a significant enhancement of θH_{ex} up to 48 Oe was achieved in Figure 12.16(b) for configuration II. Repeatability of the exchange-bias field shift under various E-fields is shown in Figure 12.16(c), indicating a robust and repeatable E-field control exchange-bias.

The E-field dependence of exchange bias in AFM/FM/FE heterostructures provides great opportunities for realizing voltage controlled deterministic magnetization switching. Figure 12.17(a) shows the E-field manipulation of magnetization for configuration I at $\theta = 55°$ under an external magnetic bias field of 28 Oe. A near 180° deterministic magnetization switching can be realized by E-field, which is illustrated by the red arrow in the inset of Figure 12.17(a). Magnetization switching occurred when the applied E-field was changed from 6 kV cm^{-1} to 4 kV cm^{-1}. It is notable that such E-field induced deterministic magnetization switching is irreversible, that is, the magnetization can only be switched by near 180°, but cannot be switched back to the original orientation by changing the E-field from 4 kV cm^{-1} to 6 kV cm^{-1}.

This irreversibility of the E-field induced near 180° magnetization switching in AFM/FM/FE heterostructures could not meet the demand of reversible dynamic magnetization switching in ME memories. This issue can be resolved by employing

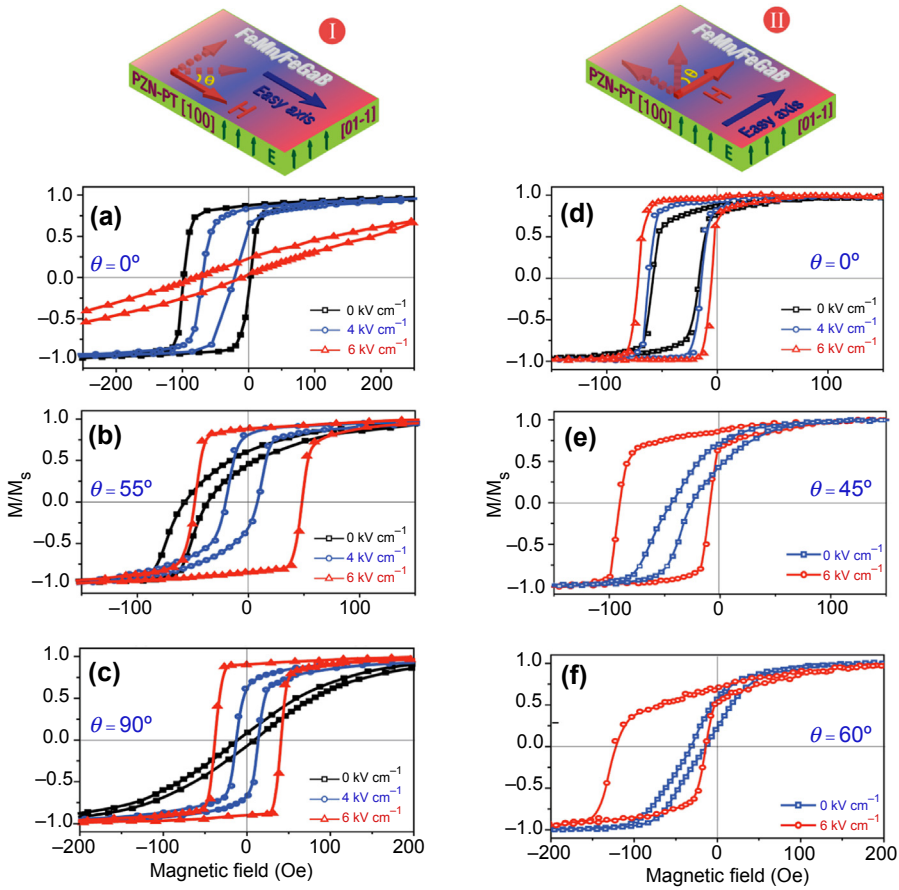

Figure 12.15 (a), (b), (c) E-field dependence of magnetic hysteresis loops in configuration I for $\theta = 0°$, 55°, and 90°. (d), (e), (f) E-field dependence of magnetic hysteresis loops in configuration II for $\theta = 0°$, 45°, and 60°.[18]

a magnetic impulse, which could switch the magnetization back and lead to a continuous magnetization switching. As shown in Figure 12.17(b), near 180° dynamic magnetization switching in FeGaB film can be observed as a response to a square wave of E-field combined with a magnetic impulse at an external constant bias magnetic field of 28 Oe, as illustrated by the red arrow in the inset of Figure 12.17(a). E-field assisted dynamic magnetization switching was also achieved without the aid of external bias magnetic field as presented in Figure 12.17(c), which corresponds to the green arrow in magnetic hysteresis loops. This E-field control exchange bias and realization of near 180° dynamic magnetization switching at room temperature in AFM/FM/FE multiferroic heterostructures constitute one important step toward voltage writing of magnetic bits (Figures 12.16 and 12.17).

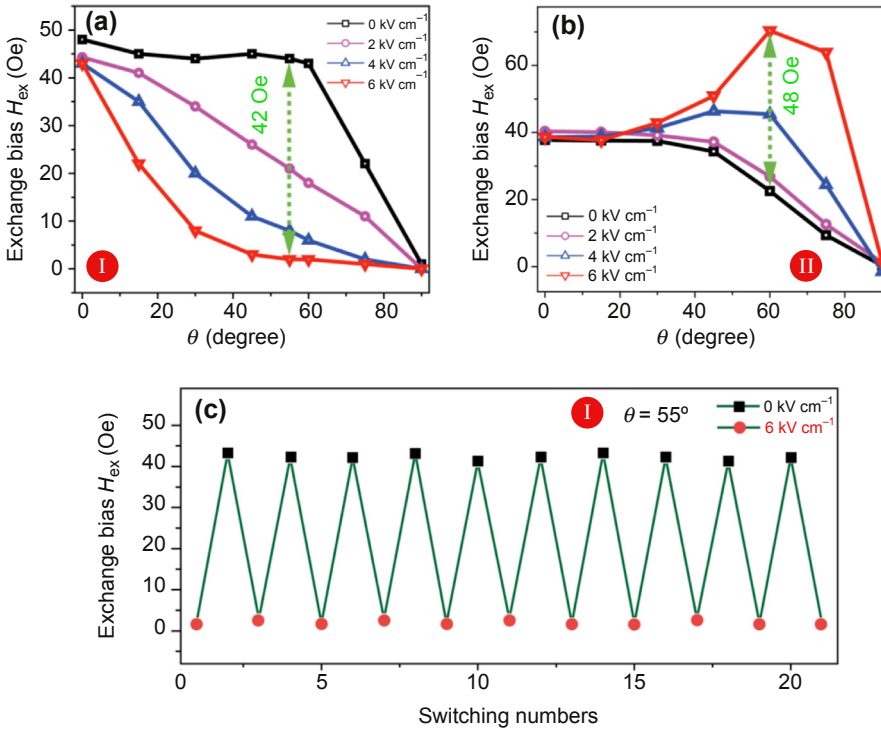

Figure 12.16 Angular dependence of exchange bias under various E-fields. (a) Correlation of exchange bias with E-field in configuration I. Arrow line indicates a remarkable E-field induced exchange bias downward shift up to 43 Oe at $\theta = 55°$. (b) Correlation of exchange bias with E-field in configuration II. Arrow line displays a significant E-field induced exchange bias upward shift up to 48 Oe or 218% at $\theta = 60°$. (c) Exchange-bias field versus switching number of E-fields between 6 kV cm^{-1} (red) and 0 kV cm^{-1} (black) (Liu, Lou, et al., 2011).

Voltage control of domain wall

Electric field control of magnetic nanostructure on ferroelectric layer using strain-mediated ME coupling has also been reported.

Todd et al. have demonstrated an in situ observation of reversible nanomagnetic switching induced by an electric field (Brintlinger et al., 2010). The author observed a real-time imaging of magnetic domain structure varied by applied electric field with Lorentz microscopy. The schematic and scanning electron microscope (SEM) image of the proposed device was shown in Figure 12.18. The ferromagnetic layer FeGa polycrystalline thin film was deposited on epitaxial $BaTiO_3$ ferroelectric thin film on a $SrTiO_3$ substrate. The $SrTiO_3$ substrate underneath the $BaTiO_3$ thin film was released for reaching high mechanical coupling. With an electric field of 7−11 MV m^{-1}, the domain wall motion happened in the devices, which is also repeatable and reversible within ±1 MV m^{-1}.

Voltage control of domain wall propagation has been widely reported (Bauer et al., 2014; Bauer, Przybylski, Kirschner, & Beach, 2012; Lahtinen, Franke, & van Dijken, 2012; Schellekens, van den Brink, Franken, Swagten, & Koopmans, 2012).

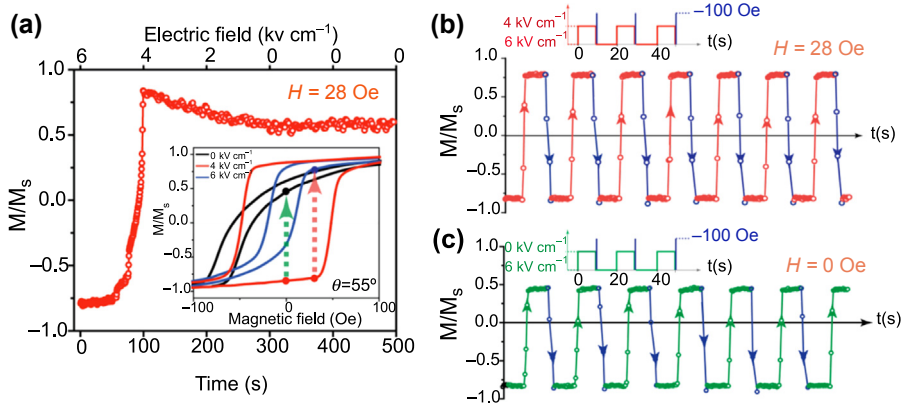

Figure 12.17 E-field deterministic switching of magnetization through E-field modulating exchange bias in AFM/FM/FE multiferroic heterostructures at configuration I at $\theta = 55°$. (a) Near 180° deterministic magnetization switching caused by reducing E-field in time domain with an external magnetic bias of 28 Oe. Inset is E-field dependence of magnetic hysteresis loops. The red and green arrow lines describe the magnetization switching directions as a response to the reduction of E-field with or without magnetic bias field. (b), (c) Near 180° dynamic magnetization switching as a response to a square wave of E-field combined with a magnetic pulse of −100 Oe.

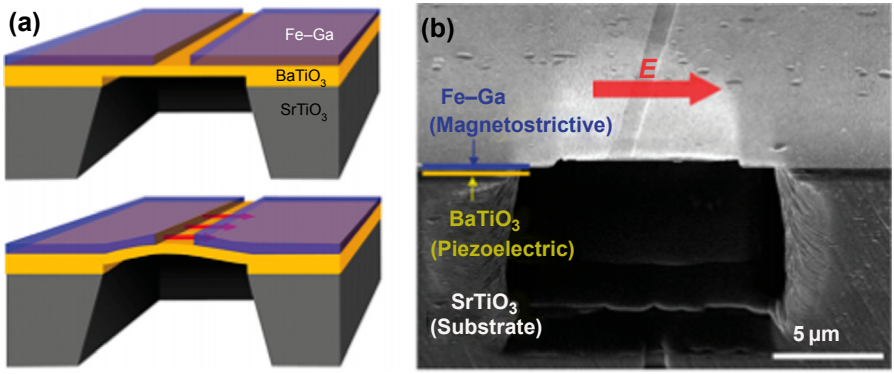

Figure 12.18 FeGa/$BaTiO_3$ thin film bilayer structure. (a) Schematic of device. Top image shows the sputter-deposited FeGa thin film with gap to form electrodes for application of electric field. $BaTiO_3$ is released from $SrTiO_3$ substrate in the region of interest beneath patterned FeGa. Bottom image shows schematic representation of electric field (red arrows) and resulting mechanical response in piezoelectric $BaTiO_3$. (b) Scanning electron micrograph of device. Patterned FeGa film is shown on top of $BaTiO_3$, with $SrTiO_3$ substrate removed via focused ion beam milling. Electric field direction is shown schematically with red arrow (Brintlinger et al., 2010).

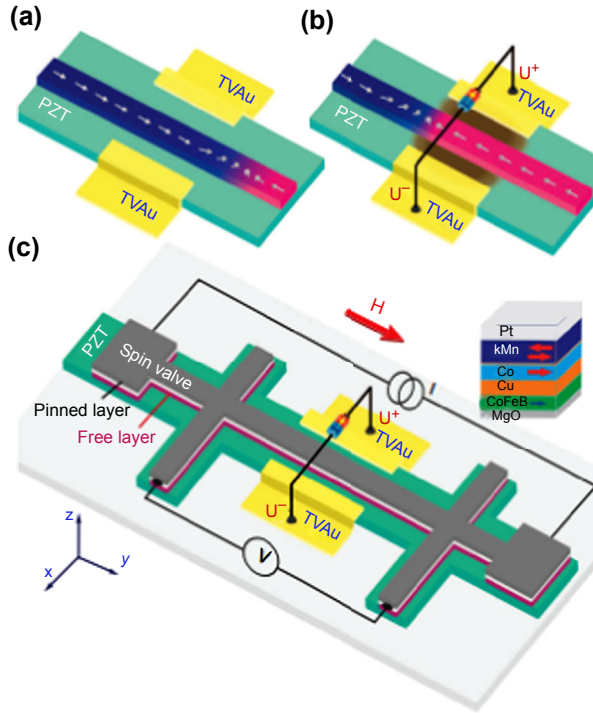

Figure 12.19 (a) In the absence of applied voltages on the piezoelectric layer, the domain wall (DW) propagates freely in the magnetic stripe. (b) DW propagation in the magnetic stripe can be controlled by voltages through the lateral ME coupling device. By applying a voltage onto the piezoelectric layer, a local stress is induced, followed by DW blockade. (c) Measurement configuration with hybrid PZT and spinvalve (SV) hall bar-shaped device; a single DW is injected from a large reservoir. The position of the DW is monitored by measuring the GMR between two electrodes. By applying a voltage on PZT, an induced stress results in a local modification of the domain wall dynamics. The SV multilayer structure is shown on the right (Lei et al., 2013).

Na et al. proposed low-power domain wall gates for magnetic logic devices based on the electric control of domain wall propagation in hybrid piezoelectric/ferromagnetic structures (Lei et al., 2013). Figure 12.19 shows the schematic of their proposed devices. A lateral spin valve was grown on top of a PZT thin film, which was then patterned into a Hall bar. With the application of a lateral electric field, a local strain can be induced. The results showed that because the coercive field is lower in the nonstrained PZT area, the domain nucleation occurs within this area (Figure 12.20).

Coexistence of strain and charge-mediated magnetoelectric coupling

Another way to achieve nonvolatile switching of magnetism is the coexistence of strain and charge-mediated ME coupling. With strain-mediated ME coupling, the nonvolatile behavior can only exist with 91° or 107° ferroelastic domain wall

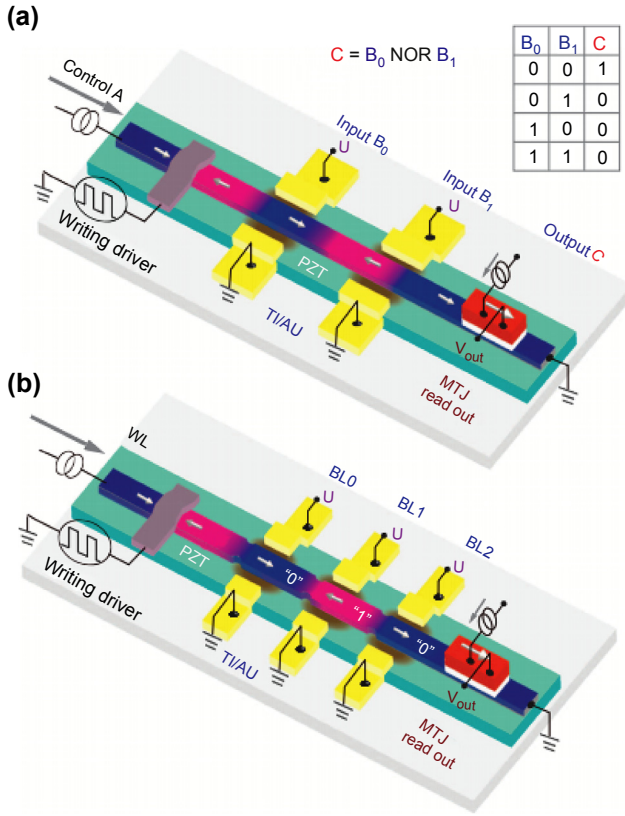

Figure 12.20 (a) Design of a multi-input NOR logic function by using voltage control of elementary domain wall (DW) gates. Control A is used for current-driven DW motion, and the writing line is used to generate a domain wall. Inputs B0 and B1 are piezoelectric-controlled DW gates, and output C serves as read out for the magnetization direction in the wire through the tunneling magnetoresistance effect. The device functions as follows. First, a domain wall is nucleated in the wire with the Oersted field generated by the current flowing through the write line, with the output "C" set to the low resistance state "0" (parallel magnetization state of the MTJ). If either or both of the gate voltages "B0" and "B1" are applied (that is, in the "1" state), then the induced anisotropy change at the gates concerned lead to a local pinning of the domain wall, which leaves the output "C" in the "0" state. However, if both gate voltages are off (inputs "B0" and "B1" set to "0"), then the generated domain wall can propagate free along the wire, driven by the spin-polarized currents controlled by "A", leading to magnetization reversal at the output "C" and thereby switching this state to "1". This scheme corresponds to a logical NOR operation and an NOR table is shown on top. (b) Design of a racetrack memory using voltage control of a DW gate. Proposed device scheme in which individual PZT electrodes supplement pinning sites defined by artificial notches. These electrodes act as bit lines (BL), as they allow individual domain walls to be pinned on demand by applied voltages, thereby allowing a content-addressable function to conventional racetrack memories. For example, in order to write the current state "1 0 1 0" to final state "1 0 0 0", the voltages on BL0 and BL2 are on and voltage on BL1 is off. By sending the domain wall-driven current (control A), the final state can be achieved (Lei et al., 2013).

switching (Liu et al., 2013b). In that case, a unique electric field sweeping pathway is needed. On the other hand, by decreasing the thickness of magnetic film below 1 nm, the magnetism of the ultra-thin magnetic films were observed to be modified by the spin-polarized charge at the interface between the magnetic and dielectric/ferroelectric films. Surface charge induced magnetic surface anisotropy change in $Fe/BaTiO_3$ heterostructure was estimated through density-functional calculations, and giant ME coupling behavior was experimentally demonstrated in Fe/MgO heterostructures (Duan et al., 2008a). Combined strain-mediated and charge-mediated ME coupling is expected in ultra-thin magnetic film/ferroelectric slabs, which has the potential for achieving even stronger ME coupling. For example, a multiferroic heterostructure with a magnetic semiconductor, 4 nm $La_{0.8}Sr_{0.2}MnO_3$, on PZT produced a hysteretic-like M−E curve at 100 K due to a charge-mediated ME coupling. A characteristic strain-mediated piezoelectric "butterfly" like M−E curve was observed in a heterostructure with 50 nm $La_{0.7}Sr_{0.3}MnO_3$ on PMN-PT (Vaz, Hoffman, Ahn, & Ramesh, 2010; Thiele et al., 2005). Shu et al. reported a thickness-dependent M−E behavior in Ni/BTO multiferroic heterostructures through the voltage-controlled magneto-optical Kerr signal, where the charge-mediated magnetic surface anisotropy increasingly dominates over the magnetoelastic anisotropy when decreasing the thickness of Ni thin film down to 5 nm (Li et al., 2011; Shu et al., 2012). However, it is theoretically difficult to detect the charge screening effect in such 5 nm magnetic thin film. The linear relation of the magnetism versus electric field on the BTO layer may also indicate an artificial magneto-optic effect.

Recently, Nan et al. reported the quantification of the coexistence of strain and surface charge-mediated ME coupling on ultra-thin $Ni_{0.79}Fe_{0.21}$/PMN-PT interface by using an $Ni_{0.79}Fe_{0.21}$/Cu/PMN-PT heterostructure with only strain-mediated ME coupling as a control (Nan et al., 2014). First, an ultra-thin ferromagnetic permalloy film of 1 nm was deposited on a (011) oriented PMN-PT ($0.71Pb(Mg_{1/3}Nb_{2/3})O_3$-$0.29PbTiO_3$) single-crystal substrate. Measurement of the voltage controlled ferromagnetic resonance of the ultra-thin NiFe/PMN-PT multiferroic heterostructures in an electron spin resonance (ESR) spectrometer demonstrated a strong combined strain and charge-mediated ME coupling. As a comparison, a 5 nm Cu film was inserted in between the NiFe and PMN-PT layers. The NiFe/Cu/PMN-PT heterostructure presented only strain-mediated ME coupling. By distinguishing the strain and surface charge ME effect strength, the hysteretic loop-like M−E curve was obtained, in which the voltage controlled switch of the magnetization corresponds to the switch of the ferroelectric polarization as shown in Figure 12.21.

12.3 Electric field control of a magnetic tunnel junction based on charge-mediated magnetoelectric coupling

A charge-mediated magnetoelectric effect was first reported by Weisheit et al. (2007), who stated that the magnetocrystalline anisotropy of an ultra-thin

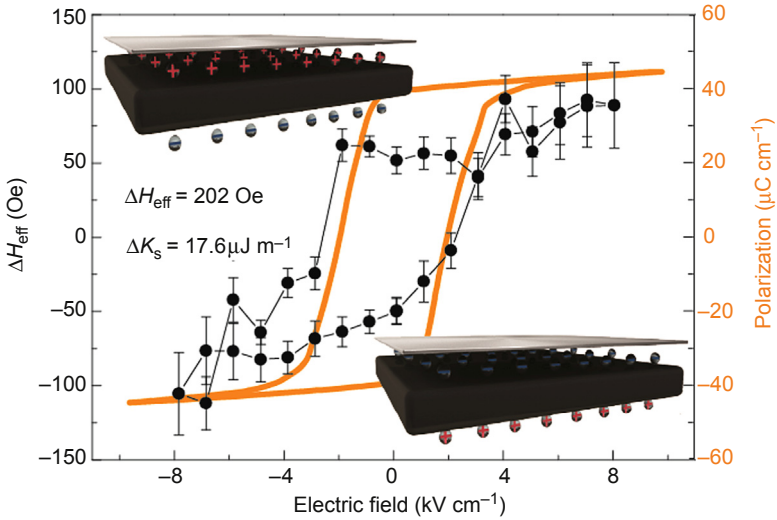

Figure 12.21 The change of the effective magnetic field upon the applied electric field, induced by pure screening charge effect in NiFe/PMN-PT (black) and P(E) loop of PMN-PT (orange). Insets show the schematics of the positive (up) and negative (down) screen charge on the NiFe interface (Nan et al., 2014).

iron−platinum and iron−palladium magnetic layer can be reversibly controlled by an electric field in an electrolyte. The screening charge provided by a liquid electrolyte modified the intrinsic magnetic properties (Chiba et al., 2011; Duan et al., 2008b; Endo, Kanai, Ikeda, Matsukura, & Ohno, 2010; Vaz, 2012; Wang, Li, Hageman, & Chien, 2012; Weisheit et al., 2007; Zhang, 1999; Zhu et al., 2012). This direct way of controlling magnetism through voltage offers an opportunity for an electric field-induced resistance change in magnetic tunnel junctions, the core portion of MRAM devices. Maruyama et al. (2009) also reported a change of magnetic anisotropy in a Fe(001)/MgO(001) junction. By applying an electric field to a dielectric MgO layer, the surface magnetic anisotropies in three-dimensional (3D) ferromagnetic metal/noble metal interfaces were changed by the electron filling of 3D orbitals. From this origin, they showed a 40% change in the magnetic anisotropy by a comparably small electric field, which could lead to various applications in low-power spintronic devices.

Previous research found that the charge-mediated ME coupling strength is highly dependent on magnetic film thickness. For instance, the ME coupling strength of an Fe/MgO heterostructure measured by a Kerr hysteresis looper was significantly dependent on Fe film thickness, where the maximum magnetic surface anisotropy change was obtained at spin reorientation Fe thickness. In a $Co_{20}Fe_{80}$/MgO heterostructure, the magnetic surface anisotropy decreased rapidly when $Co_{20}Fe_{80}$ film thicknesses were greater than 0.5 nm. Nevertheless, the mechanism causing the dependence of

charge-mediated ME coupling strength on magnetic film thickness is still not clear (Shiota et al., 2009). To optimize charge-mediated ME coupling tunability in real applications, Zhou et al. (2013) recently studied the voltage-dependent FMR in $Ni_{0.81}Fe_{0.19}$ (NiFe)/$SrTiO_3$ (STO) magnetic/dielectric thin film heterostructures to quantitatively determine the thickness dependence of charge-mediated magnetoelectric coupling. A voltage-induced FMR field change was carried out through a change in charge effect-induced magnetic surface anisotropy. A large voltage-induced FMR field shift of 65 Oe and a magnetic surface anisotropy change of 5.6 kJ/m^3 were obtained in NiFe/STO heterostructures. The voltage-induced magnetic surface anisotropy showed a strong dependence on the thickness of the magnetic thin films, which was discussed based on the thin-film growth model on the side with low thickness and on the charge screening effect on the side with large thickness. Thickness-dependent, surface charge−mediated ME coupling has been studied in bi-layered NiFe/STO thin-film heterostructures with thicknesses of the NiFe layer varying from 0.7 to 1.5 nm. A high ME coupling-induced FMR field shift of 65 Oe was obtained and measured using an ESR system, corresponding to a large voltage-tunable effective magnetic anisotropy of 5.6 kJ/m^3 and a surface anisotropy of 6.7 $\mu J/m^2$. This investigation established significant progress for the application of magnetic/dielectric heterostructures in novel interfacial charge−mediated magnetoelectric devices.

For the real application in magnetic tunnel junctions, Wang et al. (2012) demonstrated an electric-field−assisted switch in an MgO-based magnetic tunnel junction. For a traditional magnetic tunnel junction, a relatively thick ferromagnetic layer ($\geq$4 nm) is used with in-plane or perpendicular magnetic anisotropy. To enable a screening charge-induced magnetoelectric effect, an ultra-thin ferromagnetic layer with a good metal−oxide interface is needed in the magnetic tunnel junction (Wang et al., 2012). In that work the magnetic tunnel junction showed a TMR ratio of 118% with a core structure of CoFeB(1.3 nm)/MgO(1.4 nm)/CoFeB(1.6 nm). They demonstrated that the voltage-controlled MCA can be used to switch the magnetization of CoFeB from the perpendicular to the in-plane direction. The spin-torque effect was used to switch the magnetization back and forth. The electric field is actually used to reduce the coercive field of ferromagnets in an MTJ and thus the current that is used to switch the magnetization is two orders of magnitude smaller than the traditional one (Figure 12.22).

Shiota et al. (2012) also reported an induction of coherent magnetization switching in a few atomic layers of FeCo using voltage pulses. They realized coherent magnetization switching in an ultra-thin magnetic tunnel junction by a short voltage pulse of a specific duration. The FeCo layer was tilted from its initial in-plane magnetization to nearly perpendicular orientation by a biased magnetic field. The perpendicular anisotropy was enhanced by an electric field pulse and produced coherent rotation of the magnetization around the bias field. By applying the short electric field pulse for different amounts of time, the magnetization could be stopped at its initial state or the 90° with respect to this direction (Figure 12.23).

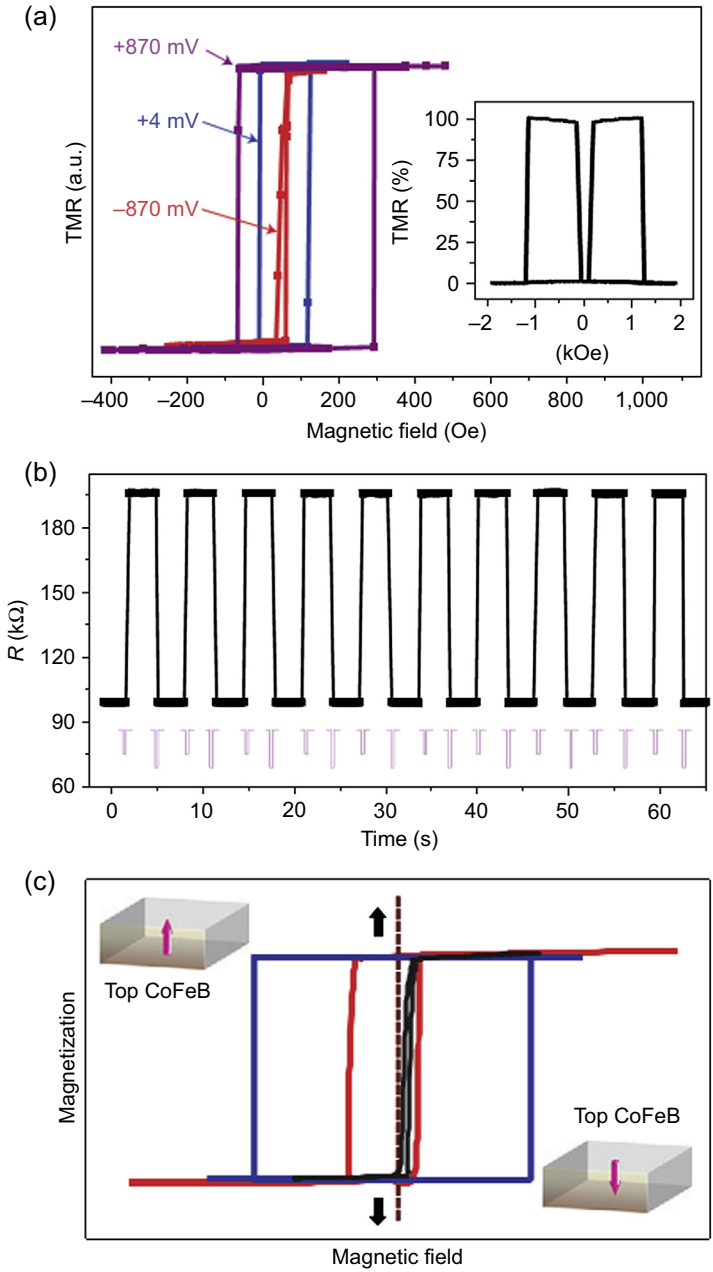

Figure 12.22 Electric field−induced unipolar switching. (a) Normalized minorloops of the TMR curve at different Vbias values. Inset: The full TMR curve at near-zero Vbias where both ferromagnetic layers are switched by a magnetic field. This MTJ has the structure of CoFeB (1.3 nm)/MgO (1.2 nm)/CoFeB (1.6 nm). (b) Unipolar switching of the MTJ by a series of negative pulses (schematically shown in purple at the bottom) with alternating amplitudes of −0.9 and −1.5 V. The corresponding electric fields are −0.75 and −1.25 V/nm, respectively. A constant biasing magnetic field of 55 Oe in favor of the antiparallel state at −0.9 V was applied. (c) Schematic diagram of the hysteresis loops of the top CoFeB layer showing the unipolar switching process: magnetization down−up switching at V = V1 (red) through STT with a greatly reduced energy barrier; magnetization up−down switching at V = V2 (black) by another negative electric field, where $|V2| > |V1|$. The loop for V = 0 is shown in blue. The vertical dotted line represents the position of the constant Hbias. The moment of the bottom CoFeB is fixed pointing down (Wang et al., 2012).

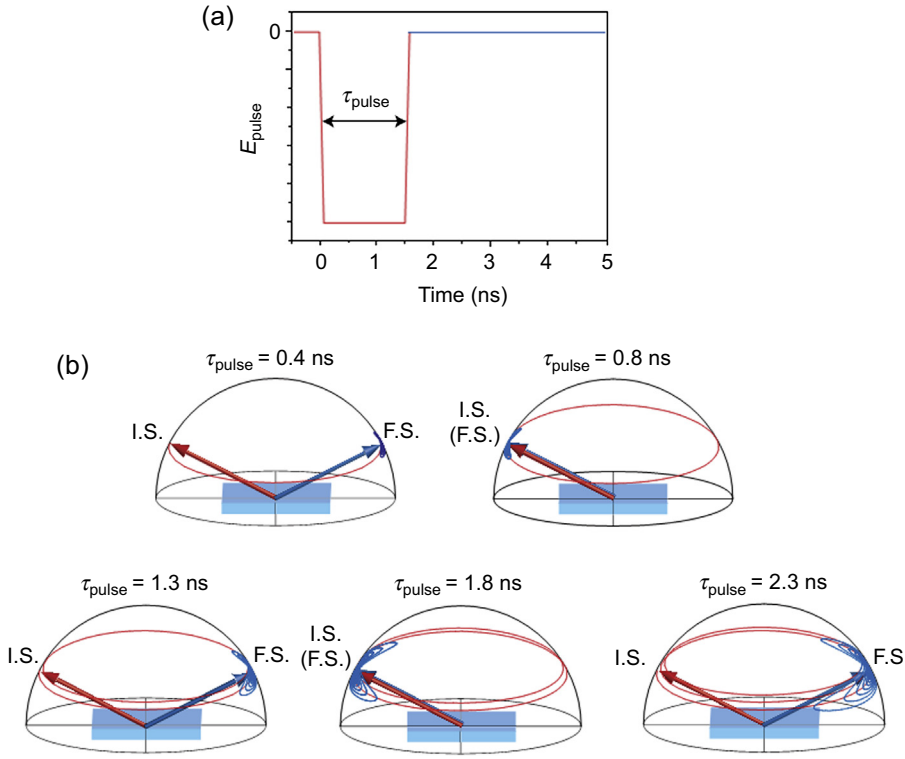

Figure 12.23 Macro-spin model simulation of coherent magnetization switching under various pulse duration conditions. (a) Shape of the applied voltage pulse used in the simulation. Pulse durations (pulse) are full widths at half-maximum with rise and fall times of 70 ps. (b) Examples of calculated trajectories induced by voltage pulse application. Initial state (I.S.) and final state (F.S.) represent the magnetization state before and after pulse voltage application (Shiota et al., 2012).

References

Albert, F. J., Katine, J. A., Buhrman, R. A., & Ralph, D. C. (2000). Spin-polarized current switching of a Co thin film nanomagnet. *Applied Physics Letters, 77*, 3809.

Baek, S. H., Jang, H. W., Folkman, C. M., Li, Y. L., Winchester, B., Zhang, J. X., et al. (2010). Ferroelastic switching for nanoscale non-volatile magnetoelectric devices. *Nature Materials, 9*, 309−314.

Bauer, U., Yao, L., Tan, A. J., Agrawal, P., Emori, S., Tuller, H. L., et al. (2014). Magneto-ionic control of interfacial magnetism. *Nature Materials, 14*, 174−181. http://dx.doi.org/10.1038/NMAT4134.

Bauer, U., Przybylski, M., Kirschner, J., & Beach, G. S. D. (2012). Magnetoelectric charge trap memory. *Nano Letters, 12*, 1437−1442.

Bibes, M. (2008). Towards a magnetoelectric memory out of the scalar sand box. *Nature, 7*, 425−426.

Binek, C., Polisetty, S., He, X., & Berger, A. (2006). Exchange bias training effect in coupled all ferromagnetic bilayer structures. *Physical Review Letters, 96*, 067201.

Borisov, P., Hochstrat, A., Chen, X., Kleemann, W., & Binek, C. (2005). Magnetoelectric switching of exchange bias. *Physical Review Letters, 94*, 1−4.

Brataas, A., Kent, A. D., & Ohno, H. (2012). Current-induced torques in magnetic materials. *Nature Materials, 11*, 372−381.

Brintlinger, T., Lim, S. H., Baloch, K. H., Alexander, P., Qi, Y., Barry, J., et al. (2010). In situ observation of reversible nanomagnetic switching induced by electric fields. *Nano Letters, 10*, 1219−1223.

Chappert, C., Fert, A., & Van Dau, F. N. (2007). The emergence of spin electronics in data storage. *Nature Materials, 6*, 813−823.

Chen, X., Hochstrat, A., Borisov, P., & Kleemann, W. (2006). Magnetoelectric exchange bias systems in spintronics. *Applied Physics Letters, 89*, 1−3.

Chiba, D., Fukami, S., Shimamura, K., Ishiwata, N., Kobayashi, K., & Ono, T. (2011). Electrical control of the ferromagnetic phase transition in cobalt at room temperature. *Nature Materials, 10*, 853−856.

Dong, S., Cheng, J., Li, J. F., & Viehland, D. (2003). Enhanced magnetoelectric effects in laminate composites of Terfenol-D/Pb(Zr,Ti)O_3 under resonant drive. *Applied Physics Letters, 83*, 4812−4814.

Duan, C.-G., Velev, J., Sabirianov, R., Zhu, Z., Chu, J., Jaswal, S., et al. (2008a). Surface magnetoelectric effect in ferromagnetic metal films. *Physical Review Letters, 101*, 137201.

Duan, C.-G., Velev, J. P., Sabirianov, R. F., Mei, W. N., Jaswal, S. S., & Tsymbal, E. Y. (2008b). Tailoring magnetic anisotropy at the ferromagnetic/ferroelectric interface. *Applied Physics Letters, 92*, 122905.

Endo, M., Kanai, S., Ikeda, S., Matsukura, F., & Ohno, H. (2010). Electric-field effects on thickness dependent magnetic anisotropy of sputtered MgO/$Co_{40}Fe_{40}B_{20}$/Ta structures. *Applied Physics Letters, 96*, 212503.

Fiebig, M. (2005). Revival of the magnetoelectric effect. *Journal of Physics D: Applied Physics, 38*, R123−R152.

Garcia, V., Bibes, M., Bocher, L., Valencia, S., Kronast, F., Crassous, A., et al. (2010). Ferroelectric control of spin polarization. *Science, 327*, 1106−1110.

He, X., Wang, Y., Wu, N., Caruso, A. N., Vescovo, E., Belashchenko, K. D., et al. (2010). Robust isothermal electric control of exchange bias at room temperature. *Nature Materials, 9*, 579−585.

Hu, J.-M., Li, Z., Chen, L.-Q., & Nan, C.-W. (2011). High-density magnetoresistive random access memory operating at ultralow voltage at room temperature. *Nature Communications, 2*, 553.

Hu, J. M., Li, Z., Wang, J., & Nan, C. W. (2010). Electric-field control of strain-mediated magnetoelectric random access memory. *Journal of Applied Physics, 107*, 1−10.

Hu, J.-M., Nan, C.-W., & Chen, L.-Q. (2011). Size-dependent electric voltage controlled magnetic anisotropy in multiferroic heterostructures: interface-charge and strain comediated magnetoelectric coupling. *Physical Review B, 83*, 134408.

Lahtinen, T. H. E., Franke, K. J. A., & van Dijken, S. (2012). Electric-field control of magnetic domain wall motion and local magnetization reversal. *Scientific Report, 2*, 1−6.

Lei, N., Devolder, T., Agnus, G., Aubert, P., Daniel, L., Kim, J.-V., et al. (2013). Strain-controlled magnetic domain wall propagation in hybrid piezoelectric/ferromagnetic structures. *Nature Communications, 4*, 1378.

Li, Z., Hu, J., Shu, L., Zhang, Y., Gao, Y., Shen, Y., et al. (2011). A simple method for direct observation of the converse magnetoelectric effect in magnetic/ferroelectric composite thin films. *Journal of Applied Physics, 110*, 096106.

Li, Z., Wang, J., Lin, Y., & Nan, C. W. (2010). A magnetoelectric memory cell with coercivity state as writing data bit. *Applied Physics Letters, 96*, 3−5.

Liu, M., Obi, O., Lou, J., Chen, Y., Cai, Z., Stoute, S., et al. (2009). Giant electric field tuning of magnetic properties in multiferroic ferrite/ferroelectric heterostructures. *Advanced Functional Materials, 19*, 1826−1831.

Liu, M., Li, S., Obi, O., Lou, J., Rand, S., & Sun, N. X. (2011). Electric field modulation of magnetoresistance in multiferroic heterostructures for ultralow power electronics. *Applied Physics Letters, 98*, 19−21.

Liu, M., Zhou, Z., Nan, T., Howe, B. M., Brown, G. J., & Sun, N. X. (2013a). Voltage tuning of ferromagnetic resonance with bistable magnetization switching in energy-efficient magnetoelectric composites. *Advanced Materials, 25*, 1435−1439.

Liu, M., Howe, B. M., Grazulis, L., Mahalingam, K., Nan, T., Sun, N. X., et al. (2013b). Voltage-impulse-induced non-volatile ferroelastic switching of ferromagnetic resonance for reconfigurable magnetoelectric microwave devices. *Advanced Materials, 25*, 4886−4892.

Liu, M., Lou, J., Li, S., & Sun, N. X. (2011). E-field control of exchange bias and deterministic magnetization switching in AFM/FM/FE multiferroic heterostructures. *Advanced Functional Materials, 21*, 2593−2598.

Ma, J., Hu, J., Li, Z., & Nan, C. W. (2011). Recent progress in multiferroic magnetoelectric composites: from bulk to thin films. *Advanced Materials, 23*, 1062−1087.

Martin, L. W., Chu, Y.-H., Holcomb, M. B., Huijben, M., Yu, P., Han, S.-J., et al. (2008). Nanoscale control of exchange bias with $BiFeO_3$ thin films. *Nano Letters, 8*, 2050−2055.

Maruyama, T., Shiota, Y., Nozaki, T., Ohta, K., Toda, N., Mizuguchi, M., et al. (2009). Large voltage-induced magnetic anisotropy change in a few atomic layers of iron. *Nature Nanotechnology, 4*, 158−161.

Nan, C. W., Bichurin, M. I., Dong, S., Viehland, D., & Srinivasan, G. (2008). Multiferroic magnetoelectric composites: historical perspective, status, and future directions. *Journal of Applied Physics, 103*, 1−35.

Nan, T., Zhou, Z., Liu, M., Yang, X., Gao, Y., Assaf, B. A., et al. (2014). Quantification of strain and charge co-mediated magnetoelectric coupling on ultra-thin permalloy/PMN-PT interface. *Scientific Reports, 4*, 3688.

Nan, T. X., Zhou, Z. Y., Lou, J., Liu, M., Yang, X., Gao, Y., et al. (2012). Voltage impulse induced bistable magnetization switching in multiferroic heterostructures. *Applied Physics Letters, 100*, 1−4.

Nan, T., Hui, Y., Rinaldi, M., & Sun, N. X. (2013). Self-biased 215 MHz magnetoelectric NEMS resonator for ultra-sensitive DC magnetic field detection. *Scientific Reports, 3*, 1985.

Pertsev, N. A., & Kohlstedt, H. (2009). Magnetic tunnel junction on a ferroelectric substrate. *Applied Physics Letters, 95*, 2009−2012.

Ramesh, R., & Ramesh, R. (2008). Electric-field control of local ferromagnetism using a magnetoelectric multiferroic. *Nature, 1*, 1−5.

Ramesh, R., & Spaldin, N. A. (2007). Multiferroics: progress and prospects in thin films. *Nature Materials, 6*, 21−29.

Ryu, J., Priya, S., Carazo, A. V., Uchino, K., & Kim, H.-E. (2001). Effect of the magnetostrictive layer on magnetoelectric properties in lead zirconate titanate/terfenol-D laminate composites. *Journal of American Ceramic Society, 84*, 2905−2908.

Schellekens, A. J., van den Brink, A., Franken, J. H., Swagten, H. J. M., & Koopmans, B. (2012). Electric-field control of domain wall motion in perpendicularly magnetized materials. *Nature Communications, 3*, 847.

Shiota, Y., Maruyama, T., Nozaki, T., Shinjo, T., Shiraishi, M., & Suzuki, Y. (2009). Voltage-assisted magnetization switching in ultrathin Fe80Co20 alloy layers. *Applied Physics Express, 2*, 1−3.

Shiota, Y., Nozaki, T., Bonell, F., Murakami, S., Shinjo, T., & Suzuki, Y. (2012). Induction of coherent magnetization switching in a few atomic layers of FeCo using voltage pulses. *Nature Materials, 11*, 39−43.

Shu, L., Li, Z., Ma, J., Gao, Y., Gu, L., Shen, Y., et al. (2012). Thickness-dependent voltage-modulated magnetism in multiferroic heterostructures. *Applied Physics Letters, 100*, 022405.

Sun, N. X., & Srinivasan, G. (2012). Voltage control of magnetism in multiferroic heterostructures and devices. *Spin, 2*, 121011044248002.

Thiele, C., Dörr, K., Bilani, O., Rödel, J., & Schultz, L. (2007). Influence of strain on the magnetization and magnetoelectric effect in $La_{0.7}A_{0.3}MnO_3$ PMN-PT(001) (A=Sr, Ca). *Physical Review B, 75*, 054408.

Thiele, C., Dörr, K., Bilani, O., Rödel, J., & Schultz, L. (2005). Voltage-controlled epitaxial strain in $La_{0.7}Sr_{0.3}MnO_3$ $Pb(Mg_{1/3}Nb_{2/3}O_3{-}PbTiO_3(001)$ films. *Applied Physics Letters, 87*, 262502.

Tsymbal, E. Y. (2011). Spintronics: electric toggling of magnets. *Nature Materials, 11*, 12−13.

Vaz, C. A. F. (2012). Electric field control of magnetism in multiferroic heterostructures. *Journal of Physics Condensed Matter, 24*, 333201.

Vaz, C. A. F., Hoffman, J., Ahn, C. H., & Ramesh, R. (2010). Magnetoelectric coupling effects in multiferroic complex oxide composite structures. *Advanced Materials, 22*, 2900−2918.

Wan, J. G., Wang, X. W., Wu, Y. J., Zeng, M., Wang, Y., Jiang, H., et al. (2005). Magnetoelectric $CoFe_2O_4{-}Pb(Zr,Ti)O_3$ composite thin films derived by a sol−gel process. *Applied Physics Letters, 86*, 122501.

Wang, W.-G., Li, M., Hageman, S., & Chien, C. L. (2012). Electric-field-assisted switching in magnetic tunnel junctions. *Nature Materials, 11*, 64−68.

Weisheit, M., Fähler, S., Marty, A., Souche, Y., Poinsignon, C., & Givord, D. (2007). Electric field-induced modification of magnetism in thin-film ferromagnets. *Science, 315*, 349−351.

Wu, T., Bur, A., Wong, K., Zhao, P., Lynch, C. S., Amiri, P. K., et al. (2011a). Electrical control of reversible and permanent magnetization reorientation for magnetoelectric memory devices. *Applied Physics Letters, 98*.

Wu, T., Bur, A., Zhao, P., Mohanchandra, K. P., Wong, K., Wang, K. L., et al. (2011b). Giant electric-field-induced reversible and permanent magnetization reorientation on magnetoelectric $Ni/(011)[Pb(Mg_{1/3}Nb_{2/3})O_3](1{-}x) - [PbTiO_3]_x$ heterostructure. *Applied Physics Letters, 98*, 1−4.

Yang, F., Zhou, Y. C., Tang, M. H., Liu, F., Ma, Y., Zheng, X. J., et al. (2009). Eight-logic memory cell based on multiferroic junctions. *Journal of Physics D: Applied Physics, 42*, 072004.

Zhang, S. (1999). Spin-dependent surface screening in ferromagnets and magnetic tunnel junctions. *Physical Review Letters, 83*, 640−643.

Zhang, S., Zhao, Y. G., Li, P. S., Yang, J. J., Rizwan, S., Zhang, J. X., et al. (2012). Electric-field control of nonvolatile magnetization in $Co_{40}Fe_{40}B_{20}/Pb(Mg_{1/3}Nb_{2/3})_{0.7}Ti_{0.3}O_3$ structure at room temperature. *Physics Review Letters, 108*, 1−5.

Zhou, J.-P., He, H.-C., Zhang, Y., Deng, C.-Y., Shi, Z., & Nan, C.-W. (2007). Electric and magnetic properties of $CoFe_2O_4/Pb(Zr_{0.52}Ti_{0.48})O_3$ bilayer thin films prepared by pulsed-laser deposition. *Applied Physics A, 89*, 553−558.

Zhou, Z., Nan, T. X., Gao, Y., Yang, X., Beguhn, S., Li, M., et al. (2013). Quantifying thickness-dependent charge mediated magnetoelectric coupling in magnetic/dielectric thin film heterostructures. *Applied Physics Letters, 103*.

Zhu, J., Katine, J. A., Rowlands, G. E., Chen, Y.-J., Duan, Z., Alzate, J. G., et al. (2012). Voltage-induced ferromagnetic resonance in magnetic tunnel junctions. *Physical Review Letters, 108*, 197203.

Index

Note: Page numbers followed by "f" and "t" indicate figures and tables respectively.

This page intentionally left blank